



저작자표시-변경금지 2.0 대한민국

이용자는 아래의 조건을 따르는 경우에 한하여 자유롭게

- 이 저작물을 복제, 배포, 전송, 전시, 공연 및 방송할 수 있습니다.
- 이 저작물을 영리 목적으로 이용할 수 있습니다.

다음과 같은 조건을 따라야 합니다:



저작자표시. 귀하는 원저작자를 표시하여야 합니다.



변경금지. 귀하는 이 저작물을 개작, 변형 또는 가공할 수 없습니다.

- 귀하는, 이 저작물의 재이용이나 배포의 경우, 이 저작물에 적용된 이용허락조건을 명확하게 나타내어야 합니다.
- 저작권자로부터 별도의 허가를 받으면 이러한 조건들은 적용되지 않습니다.

저작권법에 따른 이용자의 권리는 위의 내용에 의하여 영향을 받지 않습니다.

이것은 [이용허락규약\(Legal Code\)](#)을 이해하기 쉽게 요약한 것입니다.

[Disclaimer](#)

공학박사 학위논문

**Inelastic Lateral-torsional Buckling
of High-strength Steel I-shaped
Flexural Members**

고강도강 휨 부재의 비탄성 횡비틀림좌굴 거동

2015 년 2 월

서울대학교 대학원

건축학과

박 창 희

Inelastic Lateral-torsional Buckling of High-strength Steel I-shaped Flexural Members

지도 교수 이 철 호

이 논문을 공학박사 학위논문으로 제출함
2015 년 2 월

서울대학교 대학원
건축학과
박 창 희

박창희의 공학박사 학위논문을 인준함
2015 년 2 월

위 원 장 홍 성 결 (인)

부위원장 이 철 호 (인)

위 원 박 홍 근 (인)

위 원 이 은 택 (인)

위 원 김 진 호 (인)

Abstract

**Inelastic Lateral-torsional Buckling
of High-strength Steel I-shaped
Flexural Members**

Park, Changhee

Department of Architecture and Architectural Engineering

College of Engineering

Seoul National University

This research focuses on the inelastic behavior of structural I-shaped members fabricated from 800MPa high strength steel (HSA800). HSA800, a new generation of high performance steel, produced by thermo-mechanical controlling (TMC) process, has the advantages to acquire the high strength as well high toughness and relatively low carbon equivalent value (CEV). Due to these features, the high strength steel has attracted considerable attention in the construction industry for its use in new structural applications with the help of the appropriate design and fabrication methods. However, due to the lack of sufficient research on the effects of the different post-yield range characteristics of the high strength steel to the structural behavior, the current

code directly or indirectly restricts high strength steel by adopting limiting parameters such upper yield strength limit, upper yield-to-tensile (Y/T) strength ratio limit or a certain level of ductility capacity (rotation capacity). The primary target of this research is to experimentally and analytically quantify the effects of the post-yield range characteristics of mild and high strength steel on I-shaped flexural members. In addition, this study attempts to establish a methodology to provide adequate slenderness ratios to ensure inelastic lateral torsional buckling (LTB) strength and a certain level of rotation capacity, related to the existing AISC-LRFD specification and EC 3 code.

This work consists of four major sections: stress-strain curve idealizations, estimation of in-plane rotation capacities, and analytical and experimental studies of inelastic LTB behaviors.

In the stress-strain curve idealizations, tensile coupons of HSA800, SM570, and SM490 plates are tested and statistical regression curves were proposed to predict the Y/T strength ratio and tensile-to-yield (T/Y) strain ratio according to yield strength, which are pivotal values to idealize the initial portion of the stress-strain curve up to tensile strength. Four idealized material models (the traditional model (#1) and the Haaijer model (#2) for mild steel; the Ramberg-Osgood model (#3) for high strength steel; and the Piecewise linear model (#4) for both steel grades) with properly assumed parameter values are suggested and numerically verified with the tensile coupon data.

In the estimation of in-plane rotation capacities, a simplified method is proposed to calculate the in-plane rotation capacity at maximum moment of HSA800, SM570, and SM490 I-shaped members under uniform and moment gradient loading conditions by adopting the piecewise linear models. Under uniform moment loading condition, the in-plane rotation capacity is directly proportional to the T/Y strain ratio. On the other hand, at the moment gradient loading condition, three parameters including Y/T strength ratio, T/Y strain ratio, and yield plateau length together influence on the in-plane rotation capacity. Due to high Y/T strength ratio and low T/Y strain ratio of HSA800, the in-plane rotation capacity of HSA800 I-shaped member is inevitably low as compared to other grades (SM570 and SM490) of steel under moment gradient loading condition. Parametric studies were conducted to increase the rotation capacity level of the HSA800 I-shaped member under the moment gradient condition, demonstrating that lowering the Y/T strength ratio to 0.80 levels only does not ensure the satisfactory rotation capacity of the existing AISC-LRFD specification assumed; the increase of T/Y strain ratios is thus inevitably required.

In the analytical studies of inelastic LTB behaviors, the methods to quantify the inelastic section stiffness (effective flexural, warping, and torsional rigidities of I-shaped member fabricated from mild and high strength steel), including the presence of the residual stresses, are proposed by applying the tangent modulus theories. This inelastic section stiffness is crucial to develop

the LTB strength and rotation capacity curves of the I-shaped member under uniform and moment gradient loadings. After verifications of the derived strength and rotation capacity curves in current studies with the previous experimental data, parametric studies are conducted to evaluate the geometrical and material effects on the LTB capacity of I-shaped member. By comparing the results of the parametric models with the existing unbraced length limits specified in AISC-LRFD specifications, a methodology to design appropriate I-section geometry depending on the material selection of I-shaped member is proposed.

In the experimental studies, three types of welded I-shaped specimens (type A-[G:H-250x150x15x15]-[M:Ho-775], type B-[G:H-400x150x15x15]-[M:Ho-775], and type C-[G:H-400x150x15x15]-[M:Hy-349-822], where [G:] indicates the cross section geometry; [M:Ho] and [M:Hy] indicates the homogeneous and hybrid I-section respectively) were fabricated and tested under uniform moment to examine the geometrical and material effects of the I-section on LTB behaviors. All specimens failed by LTB, triggering a sinusoidal shape failure mode. The measured critical buckling strength and rotation capacity of both type A and type C specimens, where the effective section rigidities to plastic moment ratio are relatively high, satisfy the existing AISC-LRFD specification and EC 3 code. However, type B specimens, where a high height-to-width ratio is applied or the effective section rigidities to plastic moment ratio are relatively low, the current AISC-

LRFD unbraced length limit would not give conservative rotation capacity values. By comparing the experimental data with the analytically developed buckling curves, it is shown that the curves well predict experimental LTB strength and rotation capacity values.

Keywords : Carbon equivalent value ; Haaijer's stress-strain model; High strength steel; Inelastic section stiffness; In-plane rotation capacity; I-shaped member, LTB strength; Mild steel; Piecewise linear stress-strain model; Ramberg-Osgood stress-strain model; Rotation capacity; Slenderness ratio; Tensile-to-yield strain ratio; Traditional stress-strain model; TMC process; Unbraced length; Yield-to-tensile strength ratio; yield plateau length

Student Number : 2010-30165

Contents

Chapter 1. Introduction-----	1
1.1 Background -----	1
1.1.1 Production and mechanical properties of high strength steel -----	3
1.1.2 Specified limitation on high strength steels in building codes -----	12
1.2 Brief review of influence of post-yield range properties on member behavior -----	22
1.2.1 Post-yield range properties -----	23
1.2.2 In-plane behavior -----	23
1.2.3 Out-of-plane behavior -----	25
1.3 Limitation of recent studies and object of this study -----	27
1.3.1 Limitation of traditional stress-strain model to apply in high strength steel -----	27
1.3.2 Limitation of up-to-date theoretical and experimental researches ---	28
1.3.3 Objective of this study -----	30
1.4 Scope of work -----	31
1.4.1 Background -----	31
1.4.2 Development of analytical LTB model for I-shaped members -----	33
1.4.3 Development of LTB strength curve for homogeneous I-shaped member -----	33
1.4.4 Development of available rotation capacity curve for homogeneous I-shaped member -----	34
1.4.5 Development of LTB strength and rotation capacity curves for hybrid I-shaped member -----	35
1.5 Methodology -----	36
1.5.1 Experimental work -----	36
1.5.2 Theoretical work -----	36
1.6 Relevance of current studies -----	37
1.7 Summary -----	38

Chapter 2. Previous Researches -----	59
2.1 Introduction -----	59
2.1.1 Major buckling phenomenon and the significance of uncoupling approach -----	59
2.1.2 Rotation capacity under uniform moment and moment gradient ----	66
2.2 Experimental studies of inelastic LTB behavior -----	72
2.2.1 Rotation capacity of I-beam under uniform moment -----	72
2.2.2 Rotation capacity of I-beam under moment gradient -----	76
2.3 Analytical studies of inelastic LTB behavior -----	80
2.3.1 I-Beams under uniform moment -----	81
2.3.2 I-Beams under moment gradient -----	88
2.4. Summary -----	90
Chapter 3. Idealized Material Models and In-plane Rotation Capacity -----	121
3.1 Characteristics of stress-strain curves -----	121
3.1.1 Y/T strength ratio according to yield strength -----	122
3.1.2 T/Y strain ratio according to yield strength -----	123
3.2 Idealized material models -----	124
3.2.1 Traditional model -----	125
3.2.2 Haaijer model -----	128
3.2.3 Ramberg-Osgood model -----	129
3.2.4 Piecewise-linear model (Tri-linear, Bi-linear) -----	130
3.3 In-plane rotation capacity -----	133
3.3.1 Overview and assumption -----	133
3.3.2 In-plane rotation capacity at member maximum moment -----	136
3.4 Summary -----	146
Chapter 4. Analytical Studies of Inelastic LTB Behaviors -----	185

4.1 Derivation of inelastic section rigidities for analyzing inelastic buckling -	185
4.1.1 Tangent modulus theory and its application -----	186
4.1.2 Inelastic section rigidities in ideal I-section -----	191
4.1.3 Residual stress in I-section -----	201
4.1.4 Effects of residual stresses on inelastic section rigidities of I-beam -	208
4.1.5 Summary -----	221
4.2 LTB strength under uniform moment -----	224
4.2.1 Overview of LTB under uniform moment -----	225
4.2.2 Analytical parametric studies -----	230
4.2.3 Detailed approach to derive unbraced length limit for achieving plastic moment -----	236
4.2.4 Simplified approach to derive unbraced length limit for achieving plastic moment -----	238
4.2.5 Summary -----	242
4.3 Available rotation capacities (governed by LTB) under uniform moment-	246
4.3.1 Description of the behavior -----	246
4.3.2 Derivation of rotation capacity curve under uniform moment via inelastic section rigidities -----	248
4.3.3 Validation of the analytically developed rotation capacity curve with previous experiments -----	249
4.3.4 Analytical parameter studies -----	250
4.3.5 Detailed approach to derive unbraced length limit for target rotation capacity -----	254
4.3.6 Simplified approach to derive unbraced length limit for target rotation capacity -----	257
4.3.7 Summary -----	259
4.4 LTB strength under moment gradient -----	262
4.4.1 Overview of LTB under moment gradient -----	262
4.4.2 Simplified T-column approach to derive unbraced length limit for achieving plastic moment -----	273
4.4.3 Summary -----	276
4.5 Available rotation capacities under moment gradient -----	278
4.5.1 Description of the behavior -----	279

4.5.2 Derivation of rotation capacity curve under moment gradient via inelastic section rigidities -----	279
4.5.3 Simplified T-column approach to derive unbraced length limit for target rotation capacity -----	281
4.5.4 Summary -----	282
Chapter 5. Experimental Buckling Studies -----	353
5.1 Overview of the experimental study -----	353
5.1.1 Mechanical properties -----	356
5.1.2 Instrumentation plan for measurement -----	357
5.1.3 Data processing method -----	358
5.1.4 Description of test parameter -----	361
5.2 Experimental test results -----	365
5.2.1 Specimen Type A: [G:H-250x150x15x15]-[M:H0-775] -----	366
5.2.2 Specimen Type B: [G:H-400x150x15x15]-[M:H0-775] -----	369
5.2.3 Specimen Type C: [G:H-350x150x30x25]-[M:Hy-349-827] -----	372
5.3 Evaluation of the experimental results -----	374
5.3.1 Comparison with the code prediction -----	375
5.3.2 Comparison with the previous experiments -----	378
5.3.3 Comparison with the analytically developed buckling curves -----	384
5.4 Summary -----	389
Chapter 6. Conclusions -----	425
References -----	430

List of Tables

Table 1-1 Typical chemical composition of S690 and HSA800 according to the quality standards (EN, 2004 and KS, 2011)	54
Table 1-2 CVN value and maximum permissible element thickness (EN, 2004)	55
Table 1-3 Minimum preheat temperature according to steel grade and thickness (AIK, 2012)	56
Table 1-4 Classification of flexural ductility	57
Table 1-5 Flange, web slenderness limits and lateral slenderness limits in EC 3 and AISC LRFD	58
Table 2-1 Historical experimental uniform moment test data	113
Table 2-2 Historical experimental moment gradient test data	114
Table 3-1 Tensile coupon properties of HSA800 steel plates	171
Table 3-2 Tensile coupon properties of SM570 steel plates	172
Table 3-3 Tensile coupon properties of SM490 steel plates	173
Table 3-4 Relationship between yield stress and Y/T strength ratio	174
Table 3-5 Relationship between yield stress and T/Y strain ratio	175
Table 3-6 Geometric and material parameters for the in-plane behavior analysis	176
Table 3-7 In-plane rotation capacities (R_m) at maximum moment (M_m) under moment gradient ($m_R=0$) [Section: Type A]	177

Table 3-8 In-plane rotation capacities (R_m) at maximum moment (M_m) under moment gradient ($m_R=0$) [Section: Type B]	178
Table 3-9 Material parameters for analyzing the effects of T/Y strain ratios to the in-plane rotation capacity of HSA800 I-shaped member	179
Table 3-10 Effects of T/Y strain ratios to the in-plane rotation capacities (R_m) of HSA800 I-shaped member under moment gradient ($m_R=0$) [Section: Type A]	180
Table 3-11 Effects of T/Y strain ratios to the in-plane rotation capacities (R_m) of HSA800 I-shaped member under moment gradient ($m_R=0$) [Section: Type B]	181
Table 3-12 Material parameters for analyzing the effects of Y/T ratios to the in-plane behavior of HSA800 I-shaped member	182
Table 3-13 Effects of Y/T strength ratios to the in-plane rotation capacities (R) of HSA800 I-shaped member under moment gradient ($m_R=0$) [Section: Type A]	183
Table 3-14 Effects of T/Y strength ratios to the in-plane rotation capacities (R_m) of HSA800 I-shaped member under moment gradient ($m_R=0$) [Section: Type B]	184
Table 4-1 Residual stresses parameters for analyzing the effects on the effective rigidities	346
Table 4-2 Geometric and material parameters for LTB behavior analysis	347
Table 4-3 Unbraced length for achieving plastic moment under uniform moment by the detailed approach	348
Table 4-4 Unbraced length for achieving plastic moment under uniform moment by the simplified approach	349

Table 4-5 Unbraced length for achieving target rotation capacity $R_{cr}=2$ under uniform moment by the detailed approach	350
Table 4-6 Unbraced length for achieving target rotation capacity $R_{cr}=2$ under uniform moment by the simplified approach	356
Table 5-1 Tensile coupon properties of HSA800 steel plates	421
Table 5-2 Tensile coupon properties of SM490 steel plates	422
Table 5-3 Test matrix summary	423
Table 5-4 Test results	424

List of Figures

Fig. 1-1 Comparison of TMC process with Normalizing and Q&T processes (a) Normalizing (b) Q&T Process (c) TMC process	43
Fig. 1-2 Flow of TMCP and microstructure of steels	43
Fig. 1-3 Microstructure of TMC process steel compared with Normalizing (a) Normalizing (b) Q&T Process (c) TMC process	44
Fig. 1-4 Relationship between YS and CEV depending on steel making process	44
Fig. 1-5 Relationship between grain size and ductile-brittle transition temperature (DBTT) from Charpy impact energy testing results (a) Charpy testing (b) Charpy testing failure modes (c) Variation of DBTT according to steel making process (d) DBTT versus grain size	45
Fig. 1-6 Typical stress-strain curves of SM490, SM570 and HSA800	46
Fig. 1-7 Relationship between YP length and yield stress (Bannister, 1998a)	46
Fig. 1-8 Charpy-V notch impact energy versus DBTT depending on steel grades (Bannister, 1998a)	47
Fig. 1-9 Charpy-V notch impact energy value according plate thicknesses of HSA800 (RIST, 2011)	47
Fig. 1-10 Granville weldability diagram	48
Fig. 1-11 Relative frequency of use of high strength steel (Bannister et al, 2000)	48

Fig. 1-12 Definition of slenderness limits and rotation capacity (a) width-to-thickness ratios in EC 3 (b) width-to-thickness ratio in AISC (c) unbraced length (d) definition of rotation capacity	50
Fig. 1-13 Traditional stress-strain idealization curve	50
Fig. 1-14 Role of YP length (post-yield range properties) on in-plane rotation capacity under moment gradient loading condition (a) loading conditions (b) comparison of curvature diagram of mild and high strength steel at maximum moment	51
Fig. 1-15 Lateral torsional buckling with unbraced length (a) under uniform moment (b) moment under gradient	51
Fig. 1-16 Unbraced length limit versus critical buckling strength curves (a) AISC, (b) EC 3	52
Fig. 1-17 Unbraced length limit versus rotation capacity curve (a) Kemp (1985) (b) Adams, Lay and Galambos (1965) with analytically derived rotation capacity curve in this study	52
Fig. 1-18 Homogeneous high strength and mild steel I-section versus hybrid I-section	53
Fig. 2-1 Buckling shape of a simply-supported rectangular plate subjected to uniform compression	94
Fig. 2-2 Flange local buckling plate subjected to uniform compression with center line boundary conditions	94
Fig. 2-3 Value of compressive buckling stress coefficient for flat plates: (a) loaded edges simply-supported; and (b) loaded edges clamped [Stowell et al., 1951]	95

Fig. 2-4 I-shaped member under uniform moment loading	95
Fig. 2-5 Model of a simply-supported beam subjected to a uniform bending moment M_c [White, 1956] showing (a) elevation view, (b) part plan view with boundary conditions, and (c) typical cross-section with displacement degrees of freedom	96
Fig. 2-6 Typical beam behavior under uniform moment: (a) moment-rotation relationship and (b) moment-lateral displacement relationship	96
Fig. 2-7 Lateral buckling model of the cross-section by Lay and Galambos[1965] showing: (a) beam model; and (b) observed deformed shape	97
Fig. 2-8 Flange local buckling at the half of the compression flange after lateral torsional buckling triggered in current experimental study of HSA800 I-shaped member	97
Fig. 2-9 Experimental beam behavior under uniform moment from Lee and Galambos [1962]: (a) moment-midspan curvature relationship; (b) moment-lateral deflection relationship	98
Fig. 2-10 Typical beam behavior under moment gradient (a) Typical moment-end rotation curve (b) Experimental beam behavior under moment gradient from Lukey and Adams [1969] showing moment-end rotation relationship	98
Fig. 2-11 Compression flange model considering web restraint by Lay	99
Fig. 2-12 Peak and total rotations, experimental/theoretical values, from moment gradient tests performed by Lukey and Adams [1969]	99
Fig. 2-13 Experimental rotation capacity values under uniform moment performed by Lee and Galambos [1962]	100

Fig. 2-14 Experimental rotation capacity values under uniform moment performed by Adams, Lay and Galambos [1965]	100
Fig. 2-15 Experimental rotation capacity values under uniform moment performed by McDermott [1969]	101
Fig. 2-16 Experimental rotation capacity values under uniform moment performed by Holtz and Kulak [1973]	101
Fig. 2-17 Experimental rotation capacity values under moment gradient performed by Adams, Lay and Galambos [1965]	102
Fig. 2-18 Experimental rotation capacity values under moment gradient performed by (a) Lukey and Adams [1969] (b) Smith and Adams [1968]	103
Fig. 2-19 Experimental test data from Bansal [1971] showing relationships between rotation capacity, R and normalized lateral slenderness ratio according to end moment ratio, q (in U.S. Units)	104
Fig. 2-20 Local buckling conditions of the flange subjected to a moment gradient described by Lay[1965b]	104
Fig. 2-21 Experimental rotation capacity values under moment gradient performed by Roik and Kuhimann, [1987]	105
Fig. 2-22 Effects of torsional constraint to the rotation capacity to same flange slenderness specimens (No.4~No.6) described by Roik and Kuhimann, [1987]	105
Fig. 2-23 The methods to calculate (inelastic) effective rigidities by Galalbos [1963]	106
Fig. 2-24 Uniform moment buckling model by Lay and Galambos[1965]: (a) beam model; (b) lateral bracing; (c) cross-section deformations; (d) effective column model; and (e) lateral distortion showing axial and bending yield lines	107

Fig. 2-25 Rotation capacity of beams under uniform moment [Lay and Galambos, 1965]	108
Fig. 2-26 Lateral buckling model for a beam under moment gradient by Lay and Galambos [1967]	108
Fig. 3-1 Comparison of HSA800, SM570 and SM490 stress-strain relationships	149
Fig. 3-2 Y/T strength ratio as a function of yield stress	149
Fig. 3-3 T/Y strain ratio as a function of yield stress	150
Fig. 3-4 Traditional model No.1 for mild steel (a) stress-strain (b) modulus-strain	151
Fig. 3-5 Haaijer model No. 2 for mild steel (a) stress-Strain (b) modulus-Strain	152
Fig. 3-6 Ramberg-Osgood model No.3 for high strength steel (a) stress-strain (b) modulus-strain	153
Fig. 3-7 Determination of strain hardening parameter (n) for high strength steel by Ramberg-Osgood model	155
Fig. 3-8 Piecewise tri-linear model No.4 for high strength steel (a) stress-strain (b) modulus-strain	156
Fig. 3-9 Piecewise bi-linear model No.4 for high strength steel (a) stress-strain (b) modulus-strain	157
Fig. 3-10 Bending moment diagram and idealized curvature distribution along span with traditional model (Kemp, 1985)	158

Fig. 3-11 Idealized curves of HSA800, SM570 and SM490 (a) HSA800 by piecewise bi-linear model (b) SM570 by piecewise tri-linear model (c) SM490 by piecewise tri-linear model	160
Fig. 3-12 Inelastic curvature distributions according to moment level (a) moment-curvature relationship (b) curvature-moment relationship (c) HSA800 case (d) SM570 case (e) SM490 case	163
Fig. 3-13 Effects of stress-strain curve (piecewise bi-linear) on in-plane behavior under uniform moment (a) loading and beam geometry (b) deformed shape (c) moment capacity (d) curvature diagram of HSA800	164
Fig. 3-14 Effects of stress-strain curve (piecewise tri-linear) on in-plane behavior under uniform moment (a) loading and beam geometry (b) deformed shape (c) moment capacity (d) curvature diagram of SM570 and SM490	165
Fig. 3-15 Effects of stress-strain curve (piecewise bi-linear) on in-plane behavior under moment gradient (a) loading and beam geometry (b) deformed shape (c) moment capacity (d) curvature diagram of HSA800	166
Fig. 3-16 Effects of stress-strain curve (piecewise tri-linear) on in-plane behavior under moment gradient (a) loading and beam geometry (b) deformed shape (c) moment capacity (d) curvature diagram of SM570 and SM490	167
Fig. 3-17 Inelastic curvature distributions at maximum moment under moment gradient condition (a) HSA800 case (b) SM570 case (c) SM490 case	169
Fig. 3-18 Piecewise bi-linear model to consider the effects of T/Y strain ratios and Y/T strength ratios to inelastic rotation capacity of HSA800 (a) variation of tensile-to-yield strain ratios (b) variation of yield-to-tensile strength ratios	170
Fig. 4-1 Schematic overview of in-plane and out-of-plane behavior of I-shaped beam member (a) I-shaped member under uniform moment	284

loading (b) In-plane load- deflection behavior (c) load-deflection behavior degraded by LTB	
Fig. 4-2 Inelastic buckling theories (a) tangent modulus assumption (b) reduced modulus assumption	285
Fig. 4-3 Stress-strain relationships of typical mild steel (SM490)	285
Fig. 4-4 Traditional model No.1 for mild steel (a) stress-strain (b) modulus-strain	286
Fig. 4-5 Deformation of polycrystalline material: α brass strained 0.2% tension (Henkel and Pense, 2001)	287
Fig. 4-6 Analytical model for deriving tangent modulus by slip theory	287
Fig. 4-7 Haaijer model No. 2 for mild steel (a) stress-strain (b) modulus-strain	288
Fig. 4-8 Stress-strain relationships of typical high strength steel (HSA800)	289
Fig. 4-9 Ramberg-Osgood Model No.3 for high strength steel (a) stress-strain (b) modulus-strain	290
Fig. 4-10 Strain and stress distribution (a) residual strain (b) bending strain (c) total stress (Galambos , 1969)	291
Fig. 4-11 Beam cross-section (a) doubly symmetric section (b) monosymmetric section	292
Fig. 4-12 Variation of the neutral axis (N.A) and shear center (S.C) according to a curvature	292

Fig. 4-13 Dimension and coordinate of I-section	293
Fig. 4-14 Inelastic section characteristics of ideal I-beam fabricated from mild steel (SM490) (a) Strain distribution at plastic moment (b) Stress distribution at plastic moment (c) tangent modulus distribution at plastic moment	295
Fig. 4-15 Inelastic section characteristics of ideal I-beam fabricated from high strength steel (HSA800) (a) Strain distribution at plastic moment (b) Stress distribution at plastic moment (c) tangent modulus distribution at plastic moment	297
Fig. 4-16 Inelastic effective rigidities of ideal I-beam according to curvature (a) effective flexural stiffness (b) effective warping stiffness (c) effective torsional stiffness	299
Fig. 4-17 Inelastic effective rigidities of ideal I-beam according to moment (a) effective flexural stiffness (b) effective warping stiffness (c) effective torsional stiffness	301
Fig. 4-18 Fukumoto's measured residual stress patterns of rolled I beam (Fukumoto et al, 1980)	301
Fig. 4-19 Fukumoto's measured residual stress patterns of welded I beam (Fukumoto and Itoh, 1981)	302
Fig. 4-20 Residual stress pattern model No.1	302
Fig. 4-21 Residual stress pattern model No.2	303
Fig. 4-22 Residual stress pattern model No.3	303
Fig. 4-23 Meshed I-section for numerical calculation	304

Fig. 4-24 Stress and tangent modulus of HSA800 and SM490 according to strain used as subroutines in the numerical calculation program	306
Fig. 4-25 Variation of the inelastic rigidities of I-beam fabricated from mild steel (SM490) (a) N.A (b) S.C (c) Inelastic flexural rigidities with curvature (d) Inelastic warping rigidities with curvature (e) Inelastic torsional rigidities with curvature	309
Fig. 4-26 Variation of the inelastic rigidities of I-beam fabricated from high strength steel (HSA800) (a) N.A (b) S.C (c) Inelastic flexural rigidities with curvature (d) Inelastic warping rigidities with curvature (e) Inelastic torsional rigidities with curvature	311
Fig. 4-27 Variation of the inelastic rigidities of I-beam fabricated from mild steel (SM490) (a) N.A (b) S.C (c) Inelastic flexural rigidities with moment (d) Inelastic warping rigidities with moment (e) Inelastic torsional rigidities with moment	314
Fig. 4-28 Variation of the inelastic rigidities of I-beam fabricated from high strength steel (HSA800) (a) N.A (b) S.C (c) Inelastic flexural rigidities with moment (d) Inelastic warping rigidities with moment (e) Inelastic torsional rigidities with moment	316
Fig. 4-29 Schematic overview of LTB strength problem under uniform moment (a) Loading and beam geometry (b) Moment diagram (c) Deformed shape (in-plane and out-of-plane) (d) Curvature diagram (e) Effective rigidities diagram (f) Analytical model	317
Fig. 4-30 External moment decompositions (a) global coordinate and deformed shape (b) x-y plane (c) x-z plane (c) y-z plane	318
Fig. 4-31 Validation of the analytically developed critical buckling strength curve with previous experiments (a) Fukumoto, 1971 [G: H-250x100x6x8]-[M: Ho-336] (b) Fukumoto, 1971 [G: H-200x120x6x8]-[M: Ho-336] (c) Fukumoto, 1971 [G: H-300x100x6x8]-[M: Ho-336]	319
Fig. 4-32 Parametric models for analyzing the effects of geometrical and	320

material variations on inelastic LTB behavior (a) geometrical parameters (G1~G6) (b) material parameters (M1~M3)

Fig. 4-33 Effects of geometrical variation (flange, web and depth) on inelastic LTB strength curve (a) Material: $H_o-F_{yw}=F_{yf}=722\text{MPa}$ represented by AISC format (b) Material: $H_o-F_{yw}=F_{yf}=722\text{MPa}$ represented by EC 3 format (c) Material: $H_o-F_{yw}=F_{yf}=349\text{MPa}$ represented by AISC format (d) Material: $H_o-F_{yw}=F_{yf}=349\text{MPa}$ represented by EC 3 format 322

Fig. 4-34 Effects of material (high strength vs. mild) on inelastic LTB strength curve (a) Section: Type A [250x150 series] represented by AISC format (b) Section: Type A [250x150 series] represented by EC 3 format 323

Fig. 4-35 Effects of hybrid (homogeneous vs. hybrid) on inelastic LTB strength curve (a) Section: Type A [250x150 series] represented by AISC format (b) Section: Type A [250x150 series] represented by EC 3 format 324

Fig. 4-36 Effects of residual stresses (M1-C50-T100, M1-C100-T200) on inelastic LTB strength curve (a) Material: $H_o-F_{yw}=F_{yf}=722\text{MPa}$ represented by AISC format (b) Material: $H_o-F_{yw}=F_{yf}=722\text{MPa}$ represented by EC 3 format (c) Material: $H_o-F_{yw}=F_{yf}=349\text{MPa}$ represented by AISC format (d) Material: $H_o-F_{yw}=F_{yf}=349\text{MPa}$ represented by EC3 format 326

Fig. 4-37 Laterally unbraced length limit for achieving plastic moment under uniform moment by the detailed approaches (a) Material: $H_o-F_{yw}=F_{yf}=722\text{MPa}$ (b) Material: $H_o-F_{yw}=F_{yf}=349\text{MPa}$ (c) Material: $H_y-F_{yw}=349, F_{yf}=722\text{MPa}$ 327

Fig. 4-38 Laterally unbraced length limit for achieving plastic moment under uniform moment by the simplified approaches (a) Material: $H_o-F_{yw}=F_{yf}=722\text{MPa}$ (b) Material: $H_o-F_{yw}=F_{yf}=349\text{MPa}$ (c) Material: $H_y-F_{yw}=349, F_{yf}=722\text{MPa}$ 329

Fig. 4-39 Schematic overview of rotation capacity problem under uniform moment (a) LTB under uniform moment (b) maximum rotation capacity without LTB (c) Rotation capacity curves under LTB 330

Fig. 4-40 Validation of the analytically developed rotation capacity curve with previous experiments (a) Lee and Galambos (1962) (b) Prasad and Galambos (1963) (c) Adams, Lay and Galambos (1965)	332
Fig. 4-41 Effects of geometrical variation (flange, web and depth) rotation capacity curve (a) Material: Ho-Fyw=Fyf=722MPa represented by AISC format (b) Material: Ho-Fyw=Fyf=722MPa represented by EC 3 format (c) Material: Ho-Fyw=Fyf=349MPa represented by AISC format (d) Material: Ho-Fyw=Fyf=349MPa represented by EC 3 format	334
Fig. 4-42 Effects of material (high strength vs. mild) on rotation capacity curve (a) Section: Type A [250x150 series] represented by AISC format (b) Section: Type A [250x150 series] represented by EC 3 format	335
Fig. 4-43 Effects of hybrid (homogeneous vs. hybrid) on rotation capacity curve curve (a) Section: Type A [250x150 series] represented by AISC format (b) Section: Type A [250x150 series] represented by EC 3 format	336
Fig. 4-44 Laterally unbraced length limit for achieving target rotation capacity under uniform moment by the detailed approaches (a) Material: Ho-Fyw=Fyf=722MPa (b) Material: Ho-Fyw=Fyf=349MPa (c) Material: Hy-Fyw=349, Fyf=722MPa	337
Fig. 4-45 Laterally unbraced length limit for achieving target rotation capacity under uniform moment by the simplified approaches (a) Material: Ho-Fyw=Fyf=722MPa (b) Material: Ho-Fyw=Fyf=349MPa (c) Material: Hy-Fyw=349, Fyf=722MPa	339
Fig. 4-46 Schematic overview of LTB strength problem under moment gradient (a) Loading and beam geometry (b) Moment diagram (c) Deformed shape (in-plane and out-of-plane) (d) Curvature diagram (e) Effective rigidities diagram (f) Analytical model	340
Fig. 4-47 Inelastic effective rigidities of ideal I-beam according to moment level under moment gradient condition, $m_R=0$ (a) effective flexural stiffness (b) effective warping stiffness (c) effective torsional	342

stiffness

- Fig. 4-48** Schematic overview of the numerical procedure to calculate LTB strength under moment gradient condition for the detailed approach (a) modeling (b) lowest buckling mode 343
- Fig. 4-49** Laterally unbraced length limit for achieving plastic moment under moment gradient condition, $m_R=0$ by the detailed approaches (a) Material: Ho-Fyw=Fyf=722MPa (b) Material: Ho-Fyw=Fyf=349MPa 344
- Fig. 4-50** Schematic overview of the numerical procedure to calculate LTB strength under moment gradient condition for the simplified approach by Lay and Galambos (1967) 344
- Fig. 4-51** Schematic overview of rotation capacity problem under moment gradient (a) LTB under uniform moment (b) maximum rotation capacity without LTB (c) Rotation capacity curves under LTB 345
- Fig. 5-1** Schematic overview of experimental LTB testing under uniform moment (a) Initial geometry (b) Moment diagram (c) Deformed shape (d) In-plane curvature diagram (e) Lateral bending curvature after LTB triggered 394
- Fig. 5-2** Test set-up (a) Loading systems (b) Lateral bracing systems Lb=2800mm (c) Lateral bracing systems Lb=2400mm (d) Lateral bracing systems Lb=1,800mm (e) Lateral bracing systems Lb=1,400mm (f) Lateral bracing systems (A-A' section) (g) Overall view of test set-up (h) Side view of test set-up 398
- Fig. 5-3** Instrumentation plan for measuring In-plane and out-of-plan behavior 398
- Fig. 5-4** Instrumentation for measuring out-of-plane behavior (LTB bifurcation) (a) Cross-section rotation measurements (b) Lateral bending curvature measurements 399
- Fig. 5-5** Test specimens layout and fabrication details (a) Specimens [G: 400

H-250x150x15x15]-[M: Ho-775] (b) Specimens [G: H400x150x15x15]-
[M: Ho-775] (c) Specimens [G: 350x150x30x25]-[M: Hy-349-827]

Fig. 5-6 Global responses of the specimens [G: H-250x150x15x15]-[M: Ho-775] (a) Bending moment versus end rotation curves (b) Cross section rotation versus center vertical deflection curves (c) Failure modes 401

Fig. 5-7 Local responses of the specimens [G: H-250x150x15x15]-[M: Ho-775] (a) Strain response of the top flange (b) Strain responses of the web (c) Strain response of the bottom flange 402

Fig. 5-8 Global responses of the specimens [G: H-400x150x15x15]-[M: Ho-775] (a) Bending moment versus end rotation curves (b) Cross section rotation versus center vertical deflection curves (c) Failure modes 403

Fig. 5-9 Local responses of the specimens [G: H-400x150x15x15]-[M: Ho-775] (a) Strain response of the top flange (b) Strain responses of the web (c) Strain response of the bottom flange 404

Fig. 5-10 Global responses of the specimens [G: H-350x150x30x25]-[M: Hy-349-722] (a) Bending moment versus end rotation curves (b) Cross section rotation versus center vertical deflection curves (c) Failure modes 405

Fig. 5-11 Local responses of the specimens [G: H-350x150x30x25]-[M: Hy-349-722] (a) Strain response of the top flange (b) Strain responses of the web 406

Fig. 5-12 Critical buckling strength and rotation capacity of specimens [G: H-250x150x15x15]-[M: Ho-775] compared with current design codes (a) AISC, M_{cr} (b) AISC, R_n 407

Fig. 5-13 Critical buckling strength and rotation capacity of specimens [G: H-400x150x15x15]-[M: Ho-775] compared with current design codes (a) AISC, M_{cr} (b) AISC, R_n 408

Fig. 5-14 Critical buckling strength and rotation capacity of specimens [G: H-350x150x30x25]-[M: Hy-349-722] compared with current design 409

codes (a) AISC, M_{cr} (b) AISC, R_n

Fig. 5-15 Comparison critical buckling strength of specimens with previous experiments (a) Fukumoto, 1976 [M: Ho-336] series (b) Fukumoto, 1976 [M: Ho-769] (c) Fukumoto, 1976 [M: Hy-650-770] and [M:Hy-460-770] series 411

Fig. 5-16 Comparison rotation capacity of specimens with previous experiments (Lee and Galambos, 1962 [M:Ho-241] series; Prasad and Galambos, 1963 [M:Ho-296] series; Adams, Lay and Galambos, 1965 [M:Ho-375] series) 412

Fig. 5-17 Comparison rotation capacity of specimens with previous experiment (McDermott, 1969 [M:Ho-815] series) 412

Fig. 5-18 Validation of the analytically developed rotation capacities curves (a) Proposed curve by Kemp based on the Experimental Test Data (1986) (b) Proposed curve in current studies 413

Fig. 5-19 Critical buckling strength (M_{cr}) and rotation capacity (R_{cr} , R_m and R_n) measurement points in the $M-\Theta$ curve (a) R_{cr} , rotation capacities at bifurcation points (b) R_m , rotation capacities at maximum strength (c) R_n , rotation capacities at nominal strength 413

Fig. 5-20 Critical buckling strength and rotation capacity of specimens [G: H-250x150x15x15]-[M: Ho-775] compared with the analytically developed buckling curves (a) AISC, M_{cr} (b) AISC, R_{cr} (c) AISC, R_m 415

Fig. 5-21 Critical buckling strength and rotation capacity of specimens [G: H-400x150x15x15]-[M: Ho-775] compared with the analytically developed buckling curves (a) AISC, M_{cr} (b) AISC, R_{cr} (c) AISC, R_m 416

Fig. 5-22 Critical buckling strength and rotation capacity of specimens [G: H-350x150x30x25]-[M: Hy-349-722] compared with the analytically developed buckling curves (a) AISC, M_{cr} (b) AISC, R_{cr} (c) AISC, R_m 418

Fig. 5-23 Proposed rotation capacities curves (R_m) for HSA800 I-shaped 418

member

Fig. 5-24 Schematic post-buckling behaviors of mild and high strength I-shaped steel after LTB triggered (a) Moment-rotation relationship (b) comparison between tangent modulus versus reduced modulus approach 419 (c) application of reduced modulus concept to mild and high strength steel

List of Symbols

A, B, C, D, E, F are the unknown coefficients for shape function applied in F.E.M

$A = \frac{GJ}{EC_w}$, $B = \frac{1}{EI_y \cdot EC_w}$ is the coefficients for elastic LTB solution applied in Galerkin method

$A_{ij} = \frac{(GJ)_e}{(EC_w)_e}$, $B_{ij} = \frac{1}{(EI_y)_e \cdot (EC_w)_e}$ is the coefficients for inelastic LTB solution applied in Galerkin method

$A_{wy} = (h - 2t_f - h_{we})(t_w)$ is the area of the yielded web at the flange yield moment M_{yf} in hybrid I-section

[A] is the matrix containing the effective cross-section properties and destabilizing matrix

$\det|A| = 0$ is the determinant of the matrix A, resulting in a polynomial function with variable $M_{cr,1}, M_{cr,2}, \dots, M_{cr,n}$

B_1, B_2 is the inelastic reduction factor for weak and warping stiffness proposed in Galambos (1963)

C_{eq} is carbon equivalent value

$E_t(x, y, \phi)$ is tangent modulus at an element x,y in I-section according to a curvature ϕ

$E_R = \varepsilon_u / \varepsilon_y$ is elongation at tensile strength to yield strain ratio

$E_{t,R-O}$ is tangent modulus by Ramberg-Osgood model

$E_{t,R-O,HSS}(\varepsilon)$ is tangent modulus by Ramberg-Osgood model applied in high strength steel

$E_{t1}(\varepsilon) = E$ is elastic modulus at elastic region

$E_{t2,mild}(\varepsilon)$ is inelastic modulus at inelastic region according to strain ε in mild steel

$E_{t2,bi,HSS}(\varepsilon)$ is inelastic modulus at strain hardening region by bi-linear model applied in high strength steel

$E_{t2,tri,mild}(\varepsilon)$ is inelastic modulus at yield plateau region by tri-linear model applied in mild steel

$E_{t2,tri,HSS}(\varepsilon)$ is inelastic modulus at post-proportional region by tri-linear model applied in high strength steel

$E_{t2,Lay,mild}(\varepsilon)$ is inelastic modulus at yield plateau region applied in mild steel

$E_{t2,Galambos,mild}(\varepsilon)$ is inelastic modulus at yield plateau region applied in mild steel in 1963 Galambos's study

$E_{t2,Trahair,mild}(\varepsilon)$ is inelastic modulus at yield plateau region applied in mild steel in 1979 Trahair's study

$E_{t3,mild}(\varepsilon)$ is inelastic modulus at strain-hardening region according to strain ε in mild steel

$E_{t3,Haijer,mild}(\varepsilon)$ is inelastic modulus at strain hardening region in Haaijer model applied in mild steel

$E_{t3,tri,HSS}(\varepsilon)$ is inelastic modulus at strain hardening region by tri-linear model applied in high strength steel

$E_{t3,tri,mild}(\varepsilon)$ is inelastic modulus at inelastic region by tri-linear model applied in mild steel

$E_{st} = E / h$ is initial strain hardening modulus

$E_{st,R} = \varepsilon_{st} / \varepsilon_y$ is strain ratio onset of strain hardening point to the onset of yield

$E' = E / h$ is inelastic modulus at onset of strain hardening assumed in White (1956)

EC_w is elastic warping stiffness

$(EC_w)_e$ is effective warping stiffness

$(EC_w)_e(\phi)$ is effective warping rigidity according to a curvature ϕ

$(EC_w)_{e,mild}$ is effective warping stiffness of mild steel

$(EC_w)_{e,HSS}$ is effective warping stiffness of high strength steel

EI_y is elastic flexural stiffness

$(EI_y)_e$ is effective flexural stiffness

$(EI_y)_T$ is elastic flexural stiffness of T-column in elastic region

$(EI_y)_{e,mild}$ is effective flexural stiffness of mild steel

$(EI_y)_{e,HSS}$ is effective flexural stiffness of high strength steel

$(EI_y)_e(\phi)$ is the effective flexural rigidities at curvature ϕ

$(EI_y)_{e,T}(\phi)$ is effective flexural rigidities of T-column at the curvature ϕ

$(EI_y)_{e,gr}(z_1)$ is the effective flexural rigidities located at z_1 position under moment gradient condition

$(EI_y)_{e,T,gr}(z_1)$ is effective flexural rigidities of T-column located at z_1 position

$(EI_y)_{e,BF} = \int_{BF} E_t x^2 dA$ is flexural stiffness of bottom flange by tangent modulus concept

$(EI_y)_{e,TF} = \int_{TF} E_t x^2 dA$ is flexural stiffness of top flange by tangent modulus concept

$(EI_y)_{eq,T,gr}$ is equivalent effective stiffness value of T-column in inelastic portion length ($L_{ie} = \tau_i \cdot L_b$) under moment gradient condition

$(EI_y)_{eq,gr}$ is equivalent effective stiffness value in inelastic portion length ($L_{ie} = \tau_i \cdot L_b$) under moment gradient condition

$\int_{w,\#1} E_{t,R-O,HSS}(\varepsilon) \cdot x^2 dA$ is effective flexural rigidities at elastic web portion applied in high strength steel

$\int_{w,\#2} E_{t,R-O,HSS}(\varepsilon) \cdot x^2 dA$ is effective flexural rigidities at yield plateau web portion applied in high strength steel

$\int_{f,\#2} E_{t,R-O,HSS}(\varepsilon) \cdot x^2 dA$ is effective flexural rigidities at yield plateau flange portion applied in high strength steel

$\int_{w,\#1} E_{t,mild}(\varepsilon) \cdot x^2 dA$ is effective flexural rigidities at elastic web portion applied in mild steel

$\int_{f,\#2} E_{t,mild}(\varepsilon) \cdot x^2 dA$ is effective flexural rigidities at inelastic flange portion applied in mild steel

$\int_{w,\#2} E_{t,mild}(\varepsilon) \cdot x^2 dA$ is effective flexural rigidities at inelastic web portion applied in mild steel

$\int_{f,\#3} E_{t3,mild}(\varepsilon) \cdot x^2 dA$ is effective flexural rigidities at strain hardening flange portion applied in mild steel

F_{yf} is the flange yield strength

F_{yw} is the web yield strength

$[G]$ is the stability matrix representing the destabilizing effects of an initial set of applied loads

GJ is elastic torsional stiffness

$(GJ)_e$ is effective torsional stiffness

$[(GJ)_e - M_x(\beta_x)_t](\phi)$ is effective torsional rigidity according to a curvature ϕ

J is the number of terms required for convergence

$[K]$ is the stiffness matrix with elastic properties for eigenvalue analysis

$$K_{ij} = \int_i^j [H_i^{iv} H_j - A_{ij} H_i'' H_j] dz$$

K_s is web torsional stiffness proposed by Roik and Kuhmann (1987)

P is UTM force

P_{cm} is critical metal parameter

P_{cr} is critical buckling load proposed in Lay and Galambos (1965) T-column approach

R_m is the rotation capacity at maximum moment

$$S_{ij} = \int_i^j [B \cdot \{1 - (z/L) \cdot (1 - m_R)\}^2 H_i H_j] dz$$

L is test span length

L_a is a portion of T-column length in elastic property

L_{aj} is the adjacent span length which influences on the effective length in L_b

L_b is unbraced length for LTB testing

L_b is a portion of T-column length in inelastic property

$L_{b,ui}$ is required unbraced length for resisting uniform moment M_0

$L_{b,gr}$ is required unbraced length for resisting moment gradient M_0

$L_{d,gr}$ is required unbraced length in order to achieve target rotation capacity under moment gradient

$L_{d,T,gr}$ is required unbraced length for achieving target rotation capacity under moment gradient by T-column approach

$L_{d,ui}$ is unbraced length for achieving target rotation capacity

$L_{d,Ho,ui}$ is unbraced length for achieving target rotation capacity of homogeneous I beam

$L_{d,Hy,ui}$ is unbraced length for achieving target rotation capacity of hybrid I beam

L_{gr} is the span length under moment gradient to trigger uniform moment in L_{ui}

L_{nd} is unbraced length limit for a member to provide a highly ductile behavior in AISC

$L_{ie} = \tau_i L$ is the inelastic portion length

L_{md} is unbraced length limit for a member to provide a moderately ductile behavior in AISC

L_p is unbraced length limit for the full plastic moment in AISC

$L_{p,ui}$ is unbraced length for achieving plastic moment M_p under uniform moment

$L_{p,Ho,ui}$ is unbraced length for achieving plastic moment of homogeneous I beam

$L_{p,Hy,ui}$ is unbraced length for achieving plastic moment of hybrid I beam

L_{pd} is unbraced length limit for a plastic analysis, ensuring a minimum rotation capacity in AISC

$L_{pd,Lay}$ is unbraced length limit for ensuring adequate rotation capacity proposed by Lay

$L_{p,gr}$ is required unbraced length for achieving plastic moment under moment gradient

$L_{p,T,gr}$ is required unbraced length for achieving plastic moment under moment gradient by T-column approach

L_r is unbraced length limit for initiation of the inelastic lateral-torsion buckling in AISC

L_{ui} is the span length under uniform moment

L_{Δ} is the differential length between loading point and the end bracing point

M_0 is the external moment

M_b is the buckling resistance moment of a laterally unrestrained beam

$M_e = \frac{\pi}{k_y \cdot L_b} \sqrt{(EI_y)(GJ) + \frac{\pi^2 (EI_y)(EC_w)}{(k_z \cdot L_b)^2}}$ is the elastic LTB strength in the given unbraced length L_b

M_{cr} is the critical buckling strength at the given unbraced length L_b

$M_{cr,e}$ is the elastic lateral torsional buckling load at bifurcation point

M_m is the maximum moment calculated by strain compatibility method

$M_n(\phi)$ moment strength according to curvature (ϕ)

M_p is the plastic moment, Eq. (5-4a) is applicable to homogeneous I section, Eq. (5-4b) is applicable to hybrid I section

M_x is major x-axis loading

M_{yf} is the flange yield moments, Eq. (5-3a) is applicable to homogeneous I section, Eq. (5-3b) is applicable to hybrid I section

$M'_{x,ext}$ is the external moment applied on the x' -axis

$M'_{y,ext}$ is the external moment applied on the y' -axis

$M'_{z,ext}$ is the external moment applied on the z' -axis

$M'_{x,int}$ is the internal moment on the x' -axis

$M'_{y,int}$ is the internal moment on the y' -axis

$M'_{z,int}$ is the internal moment on the z' -axis

$R_{d,gr} = \frac{\theta_{cr,d,gr}}{\theta_p} - 1 \approx \frac{\int_0^L \phi_{cr,d,gr}(z) dz}{\int_0^L \phi_y(z) dz} - 1$ is target rotation capacity under moment gradient

$R_{d,ui} = \frac{\theta_{cr,d}}{\theta_p} - 1 \approx \frac{\phi_{cr,d}}{\phi_y} - 1$ is target rotation capacity under uniform moment

R_m is rotation capacity when the maximum moment of member is equal to M_m

$R_{m,ui}$ is the rotation capacity at maximum moment equal to M_m under uniform moment

$R_{m,gr}$ is the rotation capacity at maximum moment equal to M_m under moment gradient

$Y_R = F_y / F_u$ is yield to tensile strength ratio

$Z_x = Z_{xf} + Z_{xw}$ is plastic section modulus about x-x' axis

$Z_{xf} = (A_f / 2)(d - t_f)$ is the flange plastic section modulus

$Z_{xw} = (A_w / 2)[(1 / 2) \cdot (d - 2t_f)]$ is the web plastic section modulus

a_i are the undetermined coefficients

b_f is flange width

b_w is the transverse distance of two measurement instruments

b_{12} is the longitudinal distance of the two measurement instruments

c is the lateral flexural stiffness reduction factor at Lay and Galambos (1965) T-column approach

d is depth

$d_{wy} = 2 \cdot \left[\frac{2}{3}(h / 2 - t_f - h_{we} / 2) + h_{we} / 2 \right]$ is the distance between the centroid of the yielded web section at flange yield moment in hybrid I-section

f_z is longitudinal stress ($f_z = \frac{M_x \cdot y}{I}$)

$f_{0.2}$ is 0.2% offset yield stress at continuous yielding material

f_p is stress at the limit of proportionality at continuous yielding material

f_r is the residual stress at a point of I-section

f_{rf} is the residual stress distributed in flange

f_{rfc} is the maximum compressive residual stress in flange at the tip

f_{rw} is the residual stress distributed in web

f_{rwc} is the maximum compressive residual stress in web at center

$f_{rvt} = f_{rft} = \left[\frac{b_f t_f}{b_f t_f + (d - 2t_f)t_w} \right] f_{rfc}$ is the maximum tensile residual stress in

Lehigh residual stress model

$f_{rvt} = f_{rft} = \left[\frac{4(b_f - t_w)(t_f)}{dt_w} \right] f_{rfc}$ is the maximum tensile residual stress in

Dwight and White's residual stress model

f_u is tensile yield stress

$h = E / E_{st}$ is the ratio of elastic modulus to initial strain-hardening modulus

$h_{we} = \frac{F_{yw}}{F_{yf}} \cdot h$ is the elastic web height in hybrid I-section

i, j vary over the range $1 \leq (i, j) \leq J$ result in a square matrix

i, j are end joints in a sub-domain

k is effective (lateral bending) length factor adjusted by L_b and L_{aj}

$\frac{kL_b}{r_y}$ is effective lateral slenderness ratio

k_E is the constant for T/Y strain ratio, estimated $k_E = 3 \cdot 10^8$ in current study

k_Y is the constant for Y/T ratio, estimated $k_Y = 270$ in current study

$k_1 = \sqrt{\frac{P_0}{(EI_y)_T}}$ is constant representing elastic property in T-column approach

$k_2 = \sqrt{\frac{P_0}{(EI_y)_{eq,T}}}$ is constant representing inelastic property in T-column approach

$l = \frac{L_{ie}}{(L/2)}$ is the ratio of inelastic portion length(L_{ie}) to half-span length($L/2$)

m, K are the parameters for describing the shape of strain hardening in Haaijer model

$m_R = M_{e1} / M_{e2}$ is ratio of end moments where M_{e2} is the larger moment between two

n is hardening parameter in Ramberg-Osgood model

r is Pearson correlation coefficient

$s = \varepsilon_{st} / \varepsilon_y$ is the ratio of strain at the onset of strain-hardening (ε_{sh}) to yield strain (ε_y)

t_f is flange thickness

t_w is web thickness

u is the lateral bending deformation of top flange

$\{u\}$ is set of the out-of-plane displacement such rotation or lateral deflection, eigenvector

w is z-direction (out-of-plane) displacement in the analysis of the plate local buckling

x, y is coordinate of an element from geometrical center (=origin)

x_i, y_i are the values of the paired data

\bar{x}, \bar{y} are the means value of the paired data

y_n is coordinate of neutral axis

$y_n(\phi)$ is coordinate of neutral axis according to a curvature ϕ

y_{0r} is coordinate of shear center by tangent modulus concept

$y_{0r}(\phi)$ is coordinate of shear center by tangent modulus concept according to a curvature ϕ

z_i, z_j is the longitudinal location where lateral bending curvature is zero

z_1 is the coordinate for longitudinal direction

α, β, γ is stiffness reduction factor, the ratio of effective section stiffness to the elastic section stiffness, ranging from 0 to 1 ($0 \leq \alpha, \beta, \gamma \leq 1.0$)

$\alpha(\phi) = (EI_y)_e / (EI_y)$ is the ratio of effective flexural stiffness to the elastic section stiffness according to curvature ϕ

$\alpha_d = (EI_y)_e / (EI_y)$ is the flexural bending stiffness reduction factor at target rotation capacity

$\alpha_p = (EI_y)_e / (EI_y)$ is the flexural bending stiffness reduction factor at plastic moment M_p

$\beta(\phi) = (EC_w)_e / (EC_w)$ is the ratio of effective warping stiffness to the elastic section stiffness according to curvature ϕ

$\beta_d = (EC_w)_e / (EC_w)$ is the warping stiffness reduction factor at target rotation capacity

$\beta_p = (EC_w)_e / (EC_w)$ is the warping stiffness reduction factor at plastic moment M_p

$(\beta_x)_t(\phi)$ is mono-symmetry section constant by tangent modulus concept according to a curvature ϕ

$(\beta_x)_t$ is mono-symmetry section constant by tangent modulus concept in inelastic range, $(\beta_x)_t = 0$ is zero in ideal doubly symmetric beam since y_{0t} remain constant at its initial

γ is the rotation of the cross section

$\gamma(\phi) = ((GJ)_e - M(\beta_x)_e) / GJ$ is the ratio of effective torsional stiffness to the elastic section stiffness according to curvature ϕ

$\gamma_d = (GJ)_e / GJ$ is the torsional stiffness reduction factor at target rotation capacity

γ_{LT} is magnified cross section rotation by inelastic LTB behavior

γ_o is representing initial cross section rotation, first term of Fourier series

$\gamma_p = (GJ)_e / GJ$ is the torsional stiffness reduction factor at plastic moment M_p

Δ_L, Δ_R are measured vertical displacements for cross section rotation

Δ_1, Δ_2 is measured vertical displacement for end rotation

List of Symbols

ε is measured strain in tensile coupon test

$\varepsilon_L, \varepsilon_R$ are longitudinal strains for cross section rotation

$\varepsilon_{R,top} = \varepsilon_{top} / \varepsilon_y$ is the ratio of top flange strain to yield strain

$\varepsilon_b(x, y)$ is bending strain by flexural bending in I-section

ε_f is the elongation at fracture (EF)

$\varepsilon_{f0.2}$ is the strain corresponding to the $f_{0.2}$ at continuous yielding material

ε_p is proportional limit strain at continuous yielding material

$\varepsilon_r(x, y)$ is residual strain by residual stress in I-section

ε_{st} is the strain at the initiation of strain hardening at discontinuous yielding material

ε_u is the elongation at tensile strength (ET)

$\varepsilon_t(x, y)$ is total strain at a point of x, y in I-section

$\varepsilon_y = f_y / E$ is the strain at yield stress at discontinuous yielding material

$\varepsilon_{y,f0.2} = f_{0.2} / E$ is nominal yield strain at continuous yielding material

$\theta_{cr,d,ui}$ is the critical rotation when target rotation capacity achieved under uniform moment

$\theta_{cr,d,gr}$ is the critical rotation when target rotation capacity achieved under moment gradient

$\theta_{m,HSS}$ is the plastic end rotation when the maximum moment of member is equal to M_m in high strength steel

$\theta_{m,mild}$ is the plastic end rotation when the maximum moment of member is equal to M_m in mild steel

$\theta_{m1,HSS}, \theta_{m2,HSS}, \theta_{m3,HSS}, \theta_{m4,HSS}$ are the components of the plastic end rotation at maximum moment of member is equal to M_m in high strength steel

$\theta_{m1,mild}, \theta_{m2,mild}, \theta_{m3,mild}, \theta_{m4,mild}$ are the components of the plastic end rotation at maximum moment of member is equal to M_m in mild steel

λ is load factor, eigenvalue

λ_{1-2} is width-to-thickness ratio limit to provide adequate rotation capacity after reaching the full plastic moment in EC 3

λ_p is width-to-thickness ratio limit to provide adequate rotation capacity after reaching the full plastic moment in AISC

λ_{2-3} is width-to-thickness ratio limit to reach the full plastic moment but with little or no rotation capacity in the plastic range in EC 3

λ_{3-4} is width-to-thickness ratio limit that a section is able to reach yielding in the extreme fiber in EC 3

λ_r is width-to-thickness ratio limit that a section is able to reach yielding in the extreme fiber in AISC

$\bar{\lambda}_{LT}$ is non-dimensional slenderness for lateral torsional buckling curve in EC 3

$\bar{\lambda}_{LT,ui}$ is plateau length in lateral torsional buckling curve for resisting uniform moment M_0

$\bar{\lambda}_{LT,d,ui}$ is plateau length in lateral torsional buckling curve for satisfying target rotation capacity

$\bar{\lambda}_{LT,p,ui}$ is plateau length in lateral torsional buckling curve for achieving plastic moment

$\bar{\lambda}_{LT,0}$ is plateau length of the lateral torsional buckling curve for rolled section or equivalent welded section in EC 3

λ_{hd} is width-to-thickness ratio limit that a section is able to provide highly ductile behavior in AISC

λ_{md} is width-to-thickness ratio limit that a section is able to provide moderately ductile behavior in AISC

v is the in-plane displacement in the y-axis direction

σ_{cr} is critical buckling stress in the analysis of the plate local buckling

$\tau_i = \frac{[1 - (M_y / M_p)]}{1 - m_r}$ is inelastic portion factor at plastic moment achieved

Φ_{LT} is value to determine the reduction factor χ_{LT}

$\phi_{1-2} = M_p / EI$ is an elastic limit where the curvature is linearly increased

$\phi_{2-3,mild} = (\varepsilon_{st} / \varepsilon_y) \cdot \phi_y$ is a curvature limit where top flange strain reaches EST
($\varepsilon_{top} = \varepsilon_{st}$) in mild steel

$\phi_{2-3,HSS} = (\varepsilon_u / \varepsilon_y) \cdot \phi_y$ is a curvature limit where top flange strain reaches ET
($\varepsilon_{top} = \varepsilon_u$) in high strength steel

$\phi_{3-4,mild} = (\varepsilon_u / \varepsilon_y) \cdot \phi_y$ is a curvature limit where top flange strain reaches ET
($\varepsilon_{top} = \varepsilon_u$) in mild steel

ϕ_b is lateral bending curvature

$\phi_{cr,d,ui}$ is the critical curvature when target rotation capacity achieved under uniform moment

$\phi_{cr,d,gr}$ is the critical curvature when target rotation capacity achieved under moment gradient

$\phi_{cr,\alpha=0.05}$ is the critical curvature when effective flexural rigidities are under 5% of its elastic value

ϕ_i are independent continuous functions satisfying boundary conditions

$\phi_m(z)$ is longitudinal curvature distribution when the maximum moment of a member is equal to M_m

ϕ_n are independent continuous functions satisfying boundary conditions

List of Symbols

ϕ_p is curvature when the plastic moment achieved

ϕ_y is curvature when the yield moment achieved

$\phi_y(z)$ is longitudinal curvature distribution when the maximum moment of a member is equal to M_y

χ_{LT} is reduction factor for lateral-torsional buckling

ψ is reduction factor reflecting the magnitude of the yielding

Chapter 1 Introduction

1.1 Background

One of the principal objectives of many modern structures, nowadays, is optimizing the structural systems for satisfying various functional requirements (e.g. reducing self-weight of structures for the ease of mobility and installation) and improving their economic efficiency by applying new materials (Bannister and Trail, 1996). From the point of view, high strength steel (abbreviated as HSS) , yield stress (abbreviated as YS) of which is higher than 450MPa, as one of the new materials is gaining great attention since it enable a structure to reduce its weight and acquire economical advantage with the help of appropriate design and fabrication methods. In addition, some types of structures, regardless of the economical aspect, can only be realized through light weight design either due to the difficulty in installation and the necessity for mobility. Thus, the demand for HSS and the endeavor for practical application of it are expected to expand globally.

Despite the fact that many designers are now beginning to appreciate the advantages in using HSS, the full exploitation of the potential for such steels remains largely unrealized. This is predominantly due to code limitations, the upper yield strength (F_y) limit and yield to tensile stress ratio (abbreviated as

Y/T strength ratio) limit being particularly severe, restricting the advantages to be gained by using HSS (Bjorhovde, 2014). The principal driving forces leading to the introduction of those limits, in the codes, is the lack of clearly defined guidance about the influence of the different post-yield characteristics on the structural behavior and belief that such limits ensure the structural safety.

For example, traditionally, a Y/T ratio in the range of 0.6~0.85 has been only regarded as a strong limit to provide a safety margin and ductility against structural failure without sufficient research on the post-yield parameters such yield plateau length (abbreviated as YP length, $S=\epsilon_{st}/\epsilon_y$), elongation at tensile strength (abbreviated as ET, ϵ_u) and the strain hardening characteristic ($E_{st}(\epsilon)$) (Noordhoek et al, 1996). In other words, the lack of sufficient researches on the effect of those post-yield parameters on the structural behavior of members lead to subsequent reduced user confidence and curtails high strength steel application in many fields. A clear assessment of the role of post-yield region characteristic on the structural behavior is, therefore, required in order to revive the current interest of the construction industry in HSS. This dissertation work were planned to clarify the effect of post-yield parameters (characteristics) on inelastic behavior of a structural member. Further, based on the results of such studies, this work is performed to develop a HSS I-shaped member and its design methodology to satisfy the strength and ductility requirements the principal codes specified.

1.1.1 Production and mechanical properties of of high strength steel

This chapter briefly describes steel making process, chemical compositions, microstructure, and mechanical properties of HSS.

1.1.1.1 TMC process and chemical compositions

Improvements in production process and new developments in alloying compositions have led to a new generation of HSS produced by thermo mechanical controlled process (abbreviated as TMCP) or Q&T route. Such steels with tensile strengths up to 1000N/mm^2 have Y/T ratios in the range 0.8 to 0.95, offering not only an advantageous combination of high strength but also good toughness and low carbon equivalent value (abbreviated as CEV). Accordingly, considering the above properties, HSS often called as High Performance Steel (HPS).

(1) Steel making process and microstructure of TMCP steels

In the past, the role of hot rolling process was only to achieve the nominal dimensions like thickness, width and length. If the quality requirements were extremely high, an off-line heat treatment such as normalizing or quench and tempering (Q&T) was added to the process. However, as the quality requirements were increased, a new process for plate rolling had to be developed, TMCP. As shown in the [Fig. 1-1](#), TMCP are composed of TMR

(Thermo-mechanical rolling) and ACC (Accelerated Cooling) processes. With the TMCP process, the total control during reheating of slab, plate rolling and cooling after plate rolling is critical

Fig. 1-2 shows conceptual flow of TMCP and following microstructure of the steels. The concept of microstructure control of TMCP steel begins with the slab reheating stage. In this stage, prior-Austenite grain size is controlled carefully. The next stage is the hot rolling stage. By the controlled rolling in the Non-recrystallization region, fine and worked Austenite grains are formed. These fine Austenite grains are transformed into fine acicular ferrite or upper bainite in the following accelerated cooling stage after hot rolling.

Fig. 1-3 showed the microstructure of TMCP Steel compared with the conventional steels. The consequence of TMCP is to achieve a fine and uniform acicular ferrite microstructure instead of a ferrite/pearlite banded structure of conventional steels. According to this fine and uniform acicular ferrite, TMCP steels have superior mechanical properties as below. In detail, **Fig. 1-4** shows the relationship between yield strength and CEV. At the same CEV level, the strength of TMCP steel is higher than those of conventional steels. As shown in **Fig. 1-5**, toughness is improved with the decrease of grain size. Therefore it can generalize that TMCP steels have the lower CEV, the higher strength and the better toughness than conventional steels.

(2) Chemical composition

In general, depending on the mechanical properties required for a specific application, the amount and types of alloying element vary in chemical composition. Especially thermo-mechanically controlled high strength steel (TMCP/HSS) is not made to meet specific chemical composition but rather specific mechanical properties. Therefore the quantitative amount of chemical components of HSS is not easy to describe. However, some general information of HSS chemical composition is provided as below. It typically contain 0.05 to 0.12% range carbon (C), 1.5~2.5% manganese (Mn) and in various combinations of all small additions of nickel (Ni), niobium (Nb), titanium (Ti, usually max. 0.1%) and vanadium (V) (Bannister, 1998).

Table 1-1 showed the principal chemical compositions of principal HSS specified including HSA800 in a document somewhere (RIST, 2012). HSA800 is a type of HSS steels produced by TMCP, developed for building structure application, made in a steel-making company located in South Korea. It contain maximum 0.05% carbon (C), 2.45% manganese (Mn), 0.15% silicon (Si), 0.012% phosphorus (P), 0.003% sulfur (S) with other small amount alloying. As compared to A514 in the past, it has lower carbon content (C) and higher manganese (Mn) relatively. The Carbon Equivalent Value (CEV) and Critical Metal Parameter (PCM) of HSA800 is around to 0.55%, 0.22% respectively, calculated by Eq. 1-1, 1-2.

$$C_{eq} (\%) = C + Mn / 6 + Si / 24 + Ni / 40 + Cr / 5 + Mo / 4 + V / 16 \quad (1-1)$$

$$P_{cm} (\%) = C + Si / 30 + Mn / 20 + Cu / 20 + Ni / 60 + Cr / 20 + Mo / 15 + V / 14 + 5B \quad (1-2)$$

1.1.1.2 Mechanical properties and performances

A metallurgical point with respect to the TMC process is grain refining and formation of a fine bainitic microstructure. As a result, these micro-structural controls raise the yield strength and the toughness simultaneously. In this chapter, mechanical properties of HSS will be described as compared with the properties of conventional steels.

(1) Tensile properties

Fig. 1-6 gives representative curves of mild SM490, high strength SM570 and HSA800 steels. As shown in the figure, the stress-strain curves differ significantly between mild steels and high strength steels. Specifically, HSS does not have the yield plateau (the discontinuous yielding phenomenon) region which the mild steel generally has and it continuously yields. Subsequently, the yield strength of HSS is only defined by such 0.2 percent offset method.

The primary tensile properties of steels, the yield strength (YS), the tensile strength (TS), yield/tensile difference ratio (Y/T strength ratio), the length of the yield plateau are calculated based on the idealized stress-strain model (Fig.

1-13) and the value of the elongation at ultimate tensile strength (abbreviated ET, ϵ_u) and the elongation at rupture (abbreviated EF, ϵ_f) reported additionally.

The nominal YS and TS of SM570 are 450MPa and 570MPa; the YS and TS of HSA800 are 650MPa and 800MPa respectively. The HSS showed high Y/T ratio compared mild steel. The reason for the high Y/T ratio is that modern compositions and processing routes have less effect on the ultimate tensile strength than on impeding the movement of dislocations which in turn governs the yield stress. The values of Y/T ratios of SM490, SM570 and HSA800 as shown in Fig. 1-6 are 0.64, 0.79 and 0.81 respectively.

The YP length (S), exactly speaking, could not be clearly defined even in same grade of steel, since the YP length relatively become decreased, even in the conventional steel as the plate thickness larger. However, it is commonly believed and rationally adopted that the yield plateau length becomes gradually decreased as YS become increased since the maximum plate thickness of building structure are limited to certain value as shown in Fig. 1-7. The typical YP length of the conventional steel is in the range of 7 to 12. The YP length of HSS is zero due to continuous yielding phenomenon as mentioned earlier.

The parameters related with ductility are ET (ϵ_u) and EF (ϵ_f). Additionally, a material with yield plateau have additional ductility parameter, elongation at strain hardening (abbreviated as EST, ϵ_{st}). Generally increasing the carbon content produces a material with higher strength but lower ductility. In case of

the HSS by TMC process, it is possible to keep the carbon content at low levels satisfying the ductility provision of conventional steel grade specified in principal codes (AISC, EC 3). Typical ductility values of them are as follows. The ESH, ETS and EF values of SM490 are around 3%, 15% and 25%; the ETS and EF values of SM570 of are around 8% and 20%; the ETS, EF values of HSA800 are around 5% and 12% respectively.

(2) Toughness and Charpy V-notch toughness

Table 1-2 specifies maximum element thickness depending on the steel grade and minimum Charpy-V energy values in EC 3. Grades taken from this table and satisfying the condition given in the code for the lowest temperature, are assumed to have sufficient toughness and no further testing is needed against brittle fracture. Generally, shown in the table, as the strength becomes increased, the available maximum thickness becomes decreased. However, as shown in Fig. 1-8, even as yield strength becomes increased, the toughness of a material can be increased by the grain refinement and Mn solid solutioning.

As similar with S460ML, HSA800 with refined grain by TMC process and relatively high Mn composition have shown superior toughness than the conventional steel. Also, even at the 100mm thick plate, HSA shows satisfactory Charpy-V values at the testing temperatures (47J at -5°C) given in the KS D5994 standard (Fig. 1-9).

(3) Weldability (CEV, PCM)

In general, as the parent metal strength increased, greater precautions are needed to ensure that welding procedure is satisfactory. Carbon equivalent (CEV) is the most common measure for weldability, which is used to assess the combined effect of carbon and the other chemical elements on the cracking susceptibility of the material. Low values for CEV is important for good weldability. In other words, a very high carbon equivalent value indicated poor weldability and these steels are not suitable for structural applications, where welding is very important to assure structural safety, since steel with a higher CEV are more likely to transform into hard microstructures with less toughness, when cooled relatively rapidly after welding.

Various CEV formulas are available, but for structural steel are usually described by following equation proposed by the International Institute of Welding (IIW): Eq. 1-1. Steel grades with a $CEV < 0.4\%$ are often considered to have a good weldability and do not require special preparation nor post-treatment of the welds. Among the HSS, HSA800 have an improved weldability due to their relative low CEV and carbon content as compared to High-Strength Quenched and Tempered Alloy steels (e.g. A514). In spite of the CEV of HSA800 and A514 is around 0.50~65%, the carbon content of HSA800 (0.05%) is significantly lower than the value of A514 (0.15~0.20%) as shown in Table 1-1, resulting in beneficial effect in the weldability (e.g.

PCM). Finally HSA800 are suitable for SAW, GMAW and FCAW welding methods and they are generally required little or less preheat as compared to A514, shown in [Table 1-3 \(AIK, 2012\)](#).

As an alternative approach backing up the above statement, Granville weldability diagram, adopted from some countries, is shown in [Fig. 1-10](#) which separate steel into three zones rated by their ease of weldability-Zone I easily weldable, Zone II weldable with care, and Zone III difficult to weld. From this diagram can be seen that with increasing carbon equivalent the weldability decreases but it also emphasizes the extremely important effect of carbon content on weldability. Reducing the carbon content of steel is most effective way to improve its weldability ([Gogou, 2012](#)). As mentioned earlier, HSA800 show lower carbon content as compared to the carbon content of A514 and it is expected to show improved weldability.

(4) Hydrogen Induced Cracking (HIC)

In simple terms, ductility is the ability of a material to deform under stress rather than crack or fracture. When hydrogen atoms combine into steel molecules that exceeds the tensile strength and hardness thresholds, the steel are cracked under the stress increase. But if the tensile and hardness levels are below the critical threshold, the higher degree of ductility allows the steel to deform, absorbing and redistributing the stress increase, rather than cracking. The strength / susceptibility to hydrogen embrittlement relationship, in fact,

approach exponential levels. In other words, doubling the strength through heat treating, quadruples the steel's susceptibility to hydrogen embrittlement. However, steel with an ultimate tensile strength of less than 1,000MPa or hardness of less than Rockwell C35 are not generally considered susceptible to hydrogen environment. Therefore HSA800 the properties of which are below these tensile and hardness level are generally regarded to have an immune against HIC.

1.1.1.3 Relative frequency of use of high strength steel in building, bridges, offshores and mobile structures

Fig. 1-11 shows the relative frequency of use of high strength steels in buildings, bridges, offshore and mobile structures (Bannister and Trail, 1996). HSS is frequently used particularly where a reduction of weight is significantly important role on financial benefit (e.g. a fuel-efficient car) and efficient constructability (e.g. such a heavy weight structure construction) in mobile and offshore fields. In contrast to such areas, the building industry had been used relatively lower and mild steel. The reason was that the economical and constructional advantages by applying such high strength steel in building structure was relatively little or limited as compared to the application of it in other areas.

However, in recent years, to meet the increasing social demands for providing a special-purpose building structure to resist heavy live load such as

heavy mechanical facilities or crowded people and to span long-distance without intermediate columns, practical application of high strength steel into building areas draws a special attention (e.g. benefits from the replacing large and heavy cross section fabricated from the mild steel into smaller and lighter high strength members) and field applications of it become largely increased in world-wide.

1.1.2 Specified limitations on high strength steels in building codes

In spite of those attentions on the steels, currently HSS are not fully exploited in building structures, since the current AISC-LRFD and AASHTO-LRFD specifications limits specified maximum yield stress about 450MPa on the design via inelastic or plastic analysis method. Such inelastic analysis method is not mandatory requirements and most of structures nowadays efficiently designed by elastic design methods to determine the required force. However, even in the elastic design method, the inelastic properties of a material (for an example, partially or fully plastificated I section) are employed to achieve the strength exceeding yield moment limit M_y (i.e. plastic moment, M_p).

Moreover, a certain amount of member ductility measured by the inelastic rotation capacity required to accommodate modest force and stress redistribution depending on the type of building structure such as continuous

beam (e.g. moment redistribution from the points of support to the interior of the span in continuous beam) or indeterminate moment frames even in elastic design. As stated in AISC specification, the implied rotation capacity $R_n \geq 3$ (three times the elastic rotation at the plastic moment) is a quantified value for developing compactness section limit of the flexural members controlled by the buckling limit states. Please note that for a ductile material such as mild or high strength steel where the fracture strain of which are higher than 15% ($\epsilon_f \geq 15\%$), the inelastic rotation capacity of a member is governed by the buckling limit states, unless tension fracture limit states are attained. In this chapter, specified regulations with regard to material performance and stability limits in AISC and EC 3 specification are summarized.

1.1.2.1 General specification

(1) Materials requirement (Strength and ductility)

Principal codes specified a couple of requirements for a structural material. AISC specified minimum YS and TS and accompanying ductility requirement, EF. It is only ASTM A992 that has a limit for maximum Y/T ratio, 0.85 and a maximum CEV, 0.45 since there are a couple of noteworthy enhancements with A992 (Bjorhovde, 2014).

On the other hand, EC3 places a limit of 1.10 for tensile-to-yield ratio

(equal to Y/T ratio 0.91) for all steels. EC3 also specified that a steel must have the EF at least 15% ($\epsilon_f \geq 15\%$) and the ET at least 15 times the yield strain ($\epsilon_u \geq 15 \cdot \epsilon_y$). With the exception, for steel greater than S460 ($F_y=460\text{MPa}$) up to S700 ($F_y=700\text{MPa}$), the EF leniently defined at least 10% ($\epsilon_f \geq 10\%$). EC3 also gives detailed requirement for the through-thickness properties of steels, however in US it is not regarded as critical properties based on the [Dexter and Melendrez \(2000\)](#) research stated that through-thickness fracture are not a realistic limit state, even under the most demanding seismic condition.

(2) Member stability requirements

As has been noted earlier, the full cross-section capacity and assumed rotation capacity can be achieved only if certain geometrical slenderness limits are not exceeded. In other words, the flange and web must be compact and the member must be laterally braced at sufficiently close intervals. Section compactness criteria and lateral slenderness limits in AISC and EC 3 for achieving certain cross-section capacity and rotation capacity will be described below.

It should be noted that the definitions and limit values for geometrical slenderness are somewhat different between those specifications. For example, for the flange of an I-shaped member, EC 3 uses the distance from the flange

tips to the start of the filler that provides the transitions from the flange to the web. AISC simply uses one half of the flange with as shown in Fig. 1-12. With regard to the flange local buckling, Table 1-4~1-5 show the comparison of width-to-thickness ratios limits in AISC and EC 3 specification. Compact or Class 1 (λ_1) sections indicate that a section is able to provide adequate rotation capacity after reaching the full plastic moment. The maximum width-to-thickness ratios for compression parts of I-shaped member of EC3 and AISC are Eq. 1-3 and Eq. 1-4 respectively.

$$\lambda_{1-2} = 9.0 \sqrt{\frac{235}{F_y}} \quad (1-3)$$

where

λ_{1-2} is width-to-thickness ratio limit to provide adequate rotation capacity after reaching the full plastic moment in EC 3

F_y is yield strength

$$\lambda_p = 0.38 \sqrt{E / F_y} \quad (1-4)$$

where

λ_p is width-to-thickness ratio limit to provide adequate rotation capacity after reaching the full plastic moment in AISC

Class 2 (λ_2) section indicates that a section is able to reach the full plastic moment but with little or no rotation capacity in the plastic range. Different from EC 3 section classification, there is no appropriate corresponding

matching with the Class 2 in AISC specification. In US terminology, the class section could be defined as “semi-compact” (Bjorhovde, 2014). The maximum width-to-thickness ratio for compression parts of I-shaped member of EC 3 is Eq. 1-5.

$$\lambda_{2-3} = 10.0 \sqrt{\frac{235}{F_y}} \quad (1-5)$$

where

λ_{2-3} is width-to-thickness ratio limit to reach the full plastic moment but with little or no rotation capacity in the plastic range in EC 3

Noncompact or Class 3 (λ_3) sections indicate that a section is able to reach yielding in the extreme fiber (the yield moment). Local buckling limits the rotation capacity. The maximum width-to-thickness ratios for compression parts of I-shaped member of EC3 and AISC are Eq. 1-6 and Eq. 1-7 respectively.

$$\lambda_{3-4} = 14.0 \sqrt{\frac{235}{F_y}} \quad (1-6)$$

where

λ_{3-4} is width-to-thickness ratio limit that a section is able to reach yielding in the extreme fiber in EC 3

$$\lambda_r = 1.0 \sqrt{E / F_y} \quad (1-7)$$

where

λ_r is width-to-thickness ratio limit that a section is able to reach yielding in the extreme fiber in AISC

Slender or Class 4 (λ_4) sections indicate that the response of a section is entirely elastic, including elastic local buckling. It cannot achieve its yield moment and no inelastic rotation capacity.

With regard to lateral torsional buckling, [Table 1-4~1-5](#) show the unbraced length limits (L_b) in AISC and non-dimensional slenderness ($\bar{\lambda}_{LT}$) in EC 3 specification. Three equations are suggested in AISC as below. L_{pd} ([Eq. 1-8](#)) is unbraced length limit for a plastic analysis, ensuring a minimum rotation capacity ($R \geq 3$); L_p ([Eq. 1-9](#)) is unbraced length limit for the full plastic moment; L_r ([Eq. 1-10](#)) is unbraced length limit for the inelastic lateral-torsional buckling as shown in [Fig. 1-16](#).

$$L_{pd} = \left[0.12 - 0.076 \frac{M_{e1}}{M_{e2}} \right] \frac{E}{F_y} r_y \quad (1-8)$$

where

L_{pd} is unbraced length limit for a plastic analysis, ensuring a minimum rotation capacity in AISC

M_{e1} is smaller moment at end of unbraced length

M_{e2} is larger moment at end of unbraced length

r_y is radius of gyration about minor axis

$$L_p = 1.76 r_y \sqrt{E / F_y} \quad (1-9)$$

where

L_p is unbraced length limit for the full plastic moment in AISC

$$L_r = 1.95r_{ts} \frac{E}{0.7F_y} \sqrt{\frac{Jc}{S_x h_0} + \sqrt{\left(\frac{Jc}{S_x h_0}\right)^2 + 6.76\left(\frac{0.7r_y}{E}\right)^2}} \quad (1-10)$$

where

L_r is unbraced length for initiation of the inelastic lateral-torsional buckling in AISC

r_{ts} is effective radius of gyration

J is torsional constant

$c = 1$ for doubly symmetric I-shapes

$$c = \frac{h_0}{2} \sqrt{\frac{I_y}{C_w}} \quad \text{for channels}$$

h_0 is distance between the flange centroids

S_x is elastic section modulus taken about the x-axis

Different from AISC specifying unbraced length for preventing lateral torsional buckling, EC 3 adopted non-dimensional slenderness $\bar{\lambda}_{LT}$ (Eq. 1-11). For slenderness $\bar{\lambda}_{LT} \leq \bar{\lambda}_{LT,0} = 0.2$ lateral torsional buckling effect ignored and only cross section check applied. For rolled section (Eq. 1-12b), $\bar{\lambda}_{LT,0}$ is 0.4. For slenderness $\bar{\lambda}_{LT} \geq \bar{\lambda}_{LT,0}$, four lateral torsional buckling curves (Fig. 1-16-a, b, c and d) are proposed considering gross cross sectional properties (h/b) and correction factors ($\beta = 0.75$ for rolled section, $\beta = 1.0$ for welded section). The buckling resistance moment (M_b) of a laterally unrestrained beam is taken as Eq. 1-13. The reduction factor (χ_{LT} , Φ_{LT}) is taken as Eq. 1-14 and Eq. 1-15 respectively.

$$\bar{\lambda}_{LT} = \sqrt{\frac{W_y f_y}{M_e}} \quad (1-11)$$

where

$\bar{\lambda}_{LT}$ is non-dimensional slenderness for lateral torsional buckling in EC 3

W_y is the appropriate section modulus as follows:

- $W_y = W_{pl,y}$ for Class 1 or 2 cross-sections
- $W_y = W_{el,y}$ for Class 3 cross-sections
- $W_y = W_{eff,y}$ for Class 4 cross-sections

f_y is yield strength

$$M_e = \frac{\pi}{k_y \cdot L_b} \sqrt{(EI_y)(GJ) + \frac{\pi^2 (EI_y)(EC_w)}{(k_z \cdot L_b)^2}} \quad \text{is the elastic LTB strength in the}$$

given unbraced length L_b

$$\bar{\lambda}_{LT,0} = 0.2 \quad (1-12a)$$

$$\bar{\lambda}_{LT,0} = 0.4 \quad (\text{rolled section only}) \quad (1-12b)$$

where

$\bar{\lambda}_{LT,0}$ is plateau length of the lateral torsional buckling curves for rolled sections or welded sections in EC 3

$$M_b = \chi_{LT} W_y f_y \quad (1-13)$$

$$\chi_{LT} = \frac{1}{\Phi_{LT} + \sqrt{\Phi_{LT}^2 - \beta \bar{\lambda}_{LT}^2}} \quad (1-14)$$

$$\Phi_{LT} = 0.5[1 + \alpha_{LT}(\bar{\lambda}_{LT} - \bar{\lambda}_{LT,0}) + \beta \bar{\lambda}_{LT}^2] \quad (1-15)$$

where

M_b is the buckling resistance moment of a laterally unrestrained beam

χ_{LT} is reduction factor for lateral-torsional buckling

Φ_{LT} is value to determine the reduction factor χ_{LT}

α_{LT} is an imperfection factor (curve a=0.21, b=0.34, c=0.49, d=0.76)
 $\beta = 0.75$ is minimum value

1.1.2.2 Seismic provision

(1) Material requirement

The specified minimum yield stress of steel to be used for members in which inelastic behavior is expected shall not exceed 345MPa for such Moment-Frame Systems, Braced-Framed and Shear-Wall systems, except that Ordinary Moment Frame and Ordinary Concentrically Braced Frames limit shall not exceed 380MPa. Therefore HSS, the yield stress of which is higher than 450MPa, is not allowed to be used as lateral systems to resist seismic loading. However, these specified minimum yield stress limits are permitted to be exceeded when the suitability of material is determined by testing or other rational criteria.

(2) Member stability requirement

The inelastic rotation capacities for withstanding the seismic load with sustaining moderately and highly ductile member demand the more ductility than the values in general specification. Depending on the level of ductility demand, the section compactness criteria and lateral slenderness limit are more stringent.

The maximum width-to-thickness ratios as moderately ductile (λ_{md}) or highly ductile (λ_{hd}) member for compression parts of I-shaped member of AISC are Eq. 1-16 and Eq. 1-17 respectively. The bracing of moderately (IMF) or highly (SMF) ductile members in AISC Seismic Provision shall satisfy the following requirements. For moderately ductile member, a maximum spacing (L_{md}) is taken as Eq. 1-18; for the highly ductile members, a maximum spacing (L_{hd}) is taken as Eq. 1-19.

$$\lambda_{md} = 0.38\sqrt{E / F_y} \quad (1-16)$$

where

λ_{md} is width-to-thickness ratio limit that a section is able to provide moderately ductile behavior in AISC

$$\lambda_{hd} = 0.30\sqrt{E / F_y} \quad (1-17)$$

where

λ_{hd} is width-to-thickness ratio limit that a section is able to provide highly ductile behavior in AISC

$$L_{md} = 0.17r_y E / F_y \quad (1-18)$$

where

L_{md} is unbraced length limit for a member to provide a moderately ductile behavior in AISC

$$L_{hd} = 0.086r_y E / F_y \quad (1-19)$$

where

L_{hd} is unbraced length limit for a member to provide a highly ductile behavior in

AISC

1.2 Brief review of influence of post-yield range mechanical properties on member behavior

Current-code (AISC-LRFD, EC 3) section compactness criteria (λ_{1-2} , λ_{2-3} and λ_{3-4} in EC 3, λ_p and λ_r in AISC-Specification, λ_{md} and λ_{hd} in AISC-Seismic Provision), unbraced length limit (L_{pd} , L_p and L_r in AISC-Specification, L_{md} , L_{hd} in AISC-Seismic Provision) were developed on the theories assuming certain properties of the stress-strain curve: length of plastic plateau and strain-hardening modulus, as shown in Fig. 1-13 and backed-up by the extensive experiments which were used to simplify and modify the theoretical formulas (Galambos, 1997). However, as shown in Fig.1-6, the shapes of the stress-strain curves vary significantly depending on the grade of steel, the properties (e.g. YP length and strain-hardening rate and magnitude) of which are changed simultaneously. For example, SM490 grade steel typically have 7~12 YP length but HSA800 does not have yield plateau and strain hardening continuously occurred in post-yield ranges. In this chapter, principal post-yield range properties and its influences on the member behavior (in-plane and out-of-plane) will be briefly explained.

1.2.1 Post-yield range properties

Usually, the reported mechanical properties for plate material are only limited to YS, TS and EF. However, this information alone provides little indication to plastic deformation of the material and a careful analysis of the stress-strain curve in post-elastic range would give a better estimation. Principal post-elastic properties to influence the in-plane and the out-of-plane behaviors are summarized as below.

- 1) Yield/tensile difference, Y/T strength ratio
- 2) Length of yield plateau (if existed, S), YP length
- 3) Initial strain hardening modulus, E_{st}
- 4) Strain hardening rate ($E_{st}(\epsilon)$ or Ramberg-Osgood model, n)
- 5) Elongation at ultimate tensile strength (ϵ_u/ϵ_y), T/Y strain ratio
- 6) Elongation at fracture (ϵ_f), EF

1.2.2 In-plane behavior

In-plane behavior is a maximum load-deformation capacity which can be achieved in a member or frame fabricated from certain material without the out-of-plane behavior such as lateral torsional buckling and local buckling. In the in-plane behavior, the presence of yield plateau, YP length and the strain-hardening magnitude of a material play a significant role whether a member

can redistribute force and stress between a portion of other members and show ductile behavior.

With regard to the yield plateau, consider the simply-supported beam under a concentrated load as shown in Fig. 1-14. When moment reaches $M \approx M_p$, there is a strain or curvature jump in flange strain from yield strain (EYS) to the strain at strain hardening (EST) as shown in Fig. 1-13. This jump has a considerably effect on the ductility (deformation with sustaining its strength) in inelastic member behavior (Lay, 1964). Also, the yield plateau is desirable value in facilitating early relief of the stress constraint and the crack tip opening. That is, the yield plateau enables the gross section to participate on the yielding without the steel cracking (fracture) which often occurred by the high stress concentration at the limited region. This phenomenon is quite an important role on the ductile behavior of a connection and tension member in the post-yield ranges.

While not only the yield plateau but also the strain hardening magnitude ($F_u - F_y$) have an important role on the in-plane behavior. A well-known example backing up the statement was published by Hrennikoff (1965). A continuous beam experiment made from aluminum which had no strain-hardening portion in its stress-strain (stress-strain curve flattened out at the yield stress level without any increase until the material fractured) curve cannot achieve force redistribution and plastic mechanism as predicted by the authors' earlier paper. Backing up the statement, Lay (1964) also have on

similar conclusion on the importance of strain hardening to the in-plane behavior of members in a study of beams under moment gradient and shown that the plastic moment M_p and the strength above the plastic moment can only occurred if a material have the strain-hardening portion. He (1965) also pointed out that the collapse load of an indeterminate system, assumed in plastic design, is only attainable with the strain hardening properties by illustrating both fixed-ended beam and three span beam under the concentrated forces.

However, as has been noted earlier, HSS in general does not possess the yield plateau and the strain hardening characteristic is quite dissimilar to the conventional steel. Therefore the effect of absence of yield plateau and the unique strain hardening characteristic of HSS on the structural behavior needs to be analyzed.

1.2.3 Out-of-plane behavior

Out-of-plane behavior is primarily concerned with the local or global buckling. These two buckling phenomenon are important because their occurrence usually signifies the commencement of the strength unloading and degrade the rotation capacity of a member. Clearly, once such unloading begins, the member no longer fulfills the basic assumptions of the design.

The type of buckling can be classified into elastic and inelastic buckling.

As well known, the elastic buckling strength is not affected by the material strength increase since it does not accompany the variation of the elastic modulus (E). However, the inelastic buckling is closely related with the material strength increase since the post-yield properties of a material, especially strain hardening rate or modulus ($E_{st}(\epsilon)$), are significant relation with the inelastic buckling behavior. Backing up this statement, Lay (1964) pointed out that both inelastic lateral buckling and local buckling of steel members are functions of the strain hardening modulus of a material. He also stated that the lower this initial strain hardening modulus (E_{st}), the lower the resistance of the member to either lateral or local buckling in the post-elastic range.

Following the Lay's research, various researchers have stated that the strain hardening modulus of a material needs to be examined carefully to appropriately control the out-of-plane behavior of a member fabricated from a material. By adopting those research achievement, the current slenderness ratios (e.g. width-to-thickness ratio and unbraced length, Eq. 1-3~1-19) in AISC specification and EC 3 assumed the tri-linear stress-strain models (Fig. 1-6), which is able to reflect those post-yield range characteristics. The assumed the yield plateau length and the initial strain hardening modulus are about 7~11 and $E_{st}=E/45\sim E/33$ which reflecting the tensile coupon testing results of the steel where the yield strength are under 345MPa (Galambos 1997).

However, HSS is not applicable to the assumed stress-strain model and the values of the strain hardening modulus are difficult to define as a constant value. Therefore, it is questionable whether the current slenderness ratio could simply extend to the HSS member and the performances (the buckling strength and rotation capacity) of which are could be obtainable as the current code assumed.

1.3 Limitations of recent studies and object of this study

The literature reviews of recent studies will be extensively studied in chapter 2. Therefore, in this chapter, the limitations of recent studies to approach high strength are briefly summarized and the object of this study will be described.

1.3.1 Limitation of traditional stress-strain model to apply in high strength steel

Various stress-strain models were proposed to fit various stress-strain curves of the developed materials by many researchers (Galambos, 1997). However, the tri-linear stress-strain model (Fig. 1-13), which mentioned previously, composed of three linear curves is most typical and widely adopted in the development of the current codes. Fig. 1-13 show tri-linear

stress-strain model in detail. It composed of three lines, to depict the stress-strain curves of ordinary steel. The curve consists of an elastic part where stress and strain are proportional, a plastic plateau, and the initial part of the strain hardening range in which stiffness is defined by the strain-hardening modulus, $E_{st}=E/h=E/45\sim E/33$.

Unfortunately, the extension of the tri-linear model to represent HSS seems to be unacceptable. First of all, HSS does not have the plastic plateau. Also, the rate of strain hardening ($E_{st}(\epsilon)$) is not constant over the full range of plastic strain. It seems that the strain hardening rate and magnitude of HSS is initially large but diminished rapidly after undergoing a certain amount of the plastic strain. Therefore new type of stress-strain model appropriate for HSS must be proposed by considering the effect of these different stress-strain characteristics on the inelastic behavior.

1.3.2 Limitation of up-to-date theoretical and experimental researches

Many researchers have been attempted to propose slenderness ratio (e.g. section compactness or unbraced length) adequate for HSS. The methodology of the approaches could be classified into two categories. One is a mechanistic or an analytical approach (Lay, 1963, Kemp, 1985). The other is numerical approach (Earls, 1999, 200, 2001).

The mechanistic approach is to develop new theories by considering the

characteristics of material properties such as the phenomenon of yielding, strain-hardening and buckling phenomenon (plate buckling, lateral buckling and twisting) in concert. This approach has resulted in usable design rule and theoretical basis for current AISC and EC 3 specification, but its generality is limited by the material properties assumed in the model. For example, the formulas (Eq. 1-20) proposed by Lay theory are strongly dependent on the plastic plateau-length (S) and the strain-hardening ratio ($h=E/E_{st}$). As these parameters were used to describe the properties of the traditional steels but not of high strength steel as mentioned previously, the extrapolation of current mechanistic approaches to the HSS is not easily acceptable by many scholars (Galambos, 1997)

$$L_{pd,Lay} = \frac{\pi}{0.54} \cdot r_y \sqrt{\frac{E}{F_y}} \frac{1}{\sqrt{1 + F \left(\frac{hR}{s-1} \right)}} \quad (1-20)$$

where

$L_{pd,Lay}$ is unbraced length limit for ensuring adequate rotation capacity proposed by

Lay

$h = E / E_{st}$ is the ratio of elastic modulus to strain-hardening modulus

$s = \varepsilon_{st} / \varepsilon_y$ is the ratio of strain at the onset of strain-hardening (ε_{st}) to yield strain (ε_y)

$$F = \frac{\frac{1}{2} + \frac{1}{2\sqrt{h}} - \frac{1}{h}}{\frac{2}{\pi} + \frac{1}{2} \left(1 - \frac{2}{\pi} \right) \left(1 - \frac{1}{\sqrt{h}} \right)}$$

R is rotation capacity

The numerical approach is the methods using computing techniques. The approaches draw attentions since the late 1970 when the inelastic buckling has also been solved by numerical techniques such as the finite strip method and the finite element methods. Also, the complexity and limitation of mechanistic approaches which try to explain all-encompassing material properties and member behavior at once empower the numerical approaches as more fascinated and elaborated methods to the many researchers (Galambos, 1997). However, the numerical approach has not made tangible result for HSS up-to-date. It seems that the numerical approach is advantageous to simulate certain experimental results. It seems to possess high risk of numerical error and undertaking lengthy calculation and difficulty so as to derive generalized formulas.

1.3.3 Object of this study

As mentioned in previous chapter, the solution and direction of the researches of HSS in progress heavily relied on numerical approaches by using finite element method and the mechanistic approaches with carefully analyzing selected experiment are rare. Unfortunately it seems that the unique characteristics of numerical approaches has limitations (e.g. numerical instability and subjectivity for solving nonlinear problem as like inelastic

buckling) to provide tangible results to the section compactness criteria and laterally unbraced limit adequate for HSS members. Finally, it brings about the needs of the other approaches for solving the problems.

The motivation of this study came from the recognition of the limits of the current studies in domestic and overseas. With precisely prepared experiment and mechanistic approach by using analytical model seems to well describe the behavior of the steel members, including HSS members, by explaining the effect of the unique characteristics of each material such as the existence of the yield plateau and different strain hardening rate or magnitudes. In this work, the methodologies and objective of this study were established as below.

1) Establishment of a mechanistic approach to analyze the inelastic buckling behavior applicable to 400~800MPa TS steel member.

2) Establishment of a methodology propose inelastic buckling strength and available rotation capacity of 400~800MPa TS steel member.

1.4 Scope of work

1.4.1 Background

In AISC and EC 3 codes, a category of bucklings are classified into local buckling, flexural (Euler) buckling, lateral-torsional buckling and flexural-torsional buckling etc. Although, in actual structure, such phenomenon does not occur independently and taking place in complex manner with interacting

each other, traditionally AISC and EC 3 recommend and adopt dealing those buckling phenomenons independently neglecting the interaction of each other. Although some of recent studies relied on the numerical tools in commercial finite element software (Earls, 1999, 2000) has a significant emphasis on interaction between local flange and web-buckling and lateral-torsional buckling in HSS member, treating all buckling phenomenon at once is too complex to derive obtainable result and inadequate to provide efficient design methodologies for a structural designer.

Respecting the traditional approaches, the scope of this study has limited on the lateral torsional buckling (LTB) behavior of I-shaped steel beam member. The reasons for the selection of this research items are as follow. The I-shaped steel members (in Korea, H-section) are the most frequently used and have an several advantages in structural efficiency and an easiness of the connections as compared to the other sections. However, despite those advantages, the I-shaped member (as open-section) is likely to prone various buckling phenomenon. Therefore it is not too much say that the design of I-shaped member is governed by the prevention of the possible buckling. Also, LTB (Fig.1-15) is one of key buckling limit states, taking place when laterally unsupported member are under flexural behaviors, has a significant role to govern the member strength and available rotation capacity. In next 4.2~4.4 chapters, a detailed work scope of this study will be explained.

1.4.2 Development of analytical LTB model for I-shaped member

Buckling is a behavior that a structure undergoes a large deformation when the applied load is beyond the critical (at bifurcation point) load. The initiation and progress (post bifurcation point e.g. inelastic instability point) of the lateral torsional buckling are well described by an analytical model. Previous researchers (White or Lay) proposed “T-column” model for LTB behavior of I-shaped member and verify reasonable agreement between test and theory for conventional steel with yield plateau. However, as pointed out frequently, the model was developed to target steel material under 350MPa YS steel and the extension of the model to the HSS member seems to unacceptable. Therefore analytical LTB model applicable to 400~800MPa TS steel member are the other fundamental scope of this work.

1.4.3 Development of LTB strength curve for homogeneous I-shaped beam member

Fig. 1-16 shows the nominal flexural strength in AISC and EC 3 as a function of unbraced length. The laterally unbraced length limit (L_b) are significant role to set-up the flexural strength curve and provide available rotation capacities. It could be classified as follows.

-1) Laterally unbraced length limit ($L_b \leq L_{pd}$) able to provide adequate rotation capacity after reaching fully plastic moment (M_p)

-2) Laterally unbraced length limit ($L_b \leq L_p$) able to reach fully plastic moment (M_p) but with little or no rotation capacity

-3) Laterally unbraced length limit ($L_b \leq L_r$) able to reach yielding in the extreme fibers (the yield moment M_r)

As result, the fundamental and major target of this research is critically review those unbraced length limits and modify or develop adequate unbraced lengths (L_b) applicable to 400~800MPa TS steel member.

1.4.4 Development of available rotation capacity curve for I-shaped member

Fig. 1-17 shows the rotation capacity as a function of unbraced length. Rotation capacity is a major parameter to evaluate a ductility of a structural steel member (sometimes assessed by deformation capacity). Current code (AISC, EC 3) stipulates the slenderness limits for a steel material to achieve target or sufficient rotation capacity as discussed earlier. However, some analytical and experimental studies has frequently reported that the rotation capacity of HSS member is not satisfactory results under specified slenderness condition by the current specifications. The fact brings about strong demand to find influential factors on the rotation capacity of a member and establish formulas predicting the rotation capacity.

Historically much efforts has been attempted about the relationship of

slenderness parameters (unbraced length and flange and web width-thickness ratios) and material characteristics to rotation capacity, as shown in Fig. 1-17 (Kemp, 1985, 1996). However, no satisfactory analysis and formulas including HSS are provided presented yet (Yura, Galambos and Ravindra, 1978). If such a relationship did exist, it is useful for a designer to determine whether a material is applicable to a certain structural member under specific slenderness condition to provide a required level of rotation capacity in a building structure. Therefore, in this study, the influential factors and rotation capacity formulas applicable to 400~800MPa TS steel member will be critically analyzed.

1.4.5 Development of LTB strength and rotation capacity curves for hybrid I-shaped member

Studies have shown that hybrid beams (stronger steel in the flanges than in the web) are frequently more economical than the fabricated homogeneous beam (Fig. 1-18). Such beam are highly expected as adequate member to utilize 800MPa TS steel. However, the practical utilization of such beam have limited since the limited knowledge on such yielding and buckling behaviors. In this research, the inelastic behaviors (such as inelastic buckling strength and rotation capacity) of hybrid beam with 800MPa TS flanges are critically reviewed for practical application of such beams.

1.5 Methodology

1.5.1 Experimental work

The experimental portion of this research involves (1) tensile coupon tests; (2) full-scale flexural tests of I-shaped member subjected to a region of uniform moment, fabricated from 800MPa TS plate; (3) full scale flexural test of hybrid I-shaped member subjected to uniform moment, fabricated from 800MPa TS plate for the flange and 490MPa TS plate for the web; (4) Evaluation of the experimental results with current codes (5) Evaluation of the experimental results with the previous buckling experiments (6) Evaluation of the experimental results with the analytically developed curves in current studies

1.5.2 Theoretical work

The theoretical and analytical portion of this research involves (1) a metallurgical consideration and a numerical quantification to idealize the various stress-strain curves, applicable to 400~800MPa TS steel; (2) implementation of tangent modulus approach to analyze the inelastic buckling behavior of HSS; (3) development of the Modified Effective Section Method in order to evaluate an inelastic section rigidities such $(EI_y)_e$, $(EC_w)_e$, $(GJ)_e$ with additionally covering the effect of residuals stress f_r ; (4) mechanistic approach to predict critical buckling strength at the given slenderness and material condition (5) simplified approach to predict unbraced length limit for

plastic moment (6) mechanistic approach to predict available rotation capacity at the given slenderness and material conditions (7) simplified approach to predict unbraced length limit for achieving target rotation capacities.

1.6 Relevance of current study

New developments in material making technology such TMC (thermo-mechanical controlling) process enable the steel makers to product HSS with exhibiting significantly improved mechanical properties (e.g. low carbon equivalent, improved Charpy V-notch toughness and ductility), which was not obtainable in the past. High strength steel such HSA in Korea, HPS in US are one of this new class of materials. However, several restrictions on the maximum yield strength limit in principal codes and limited knowledge on the inelastic behavior of HSS have a major obstacle to practical application.

Historically, with the conformance of the inelastic behavior and the performances of a material (such inelastic buckling and rotation capacities), the restriction on the maximum yield strength limit in current building codes were alleviated or modified so as to reasonably adopt high strength (performance) steel in that times. Adoption of A572, which was regarded as high strength materials and forbidden in 1960~1970s, in AISC specification is the good example. The researches in that time, performed by many eminent researchers (Lay, Galambos and etc.), had a key role to enable the steel to be

adopted in AISC specification by expanding knowledge about the inelastic behavior of A572 material and providing adequate slenderness criteria for ensuring the structural performance of the I-shaped member.

As the case of the past researches, this thesis work try to provides experimental, analytical and numerical information on the inelastic behavior of HSS I-shaped member (especially HSA800 and other lower grades of steels most widely used in South Korea). From this knowledge base, a rational approach for a versatile structural design of HSS I-shaped member such as hybrid beam are enabled and the current existing barrier will be removed and modified so as to permit the full utilization of HSS in future steel construction projects.

1.7 Summary

1) HSA800, a new generation of high performance steel, produced by thermo-mechanical controlling (TMC) process, not only has the advantage to acquire the high strength but also provides good toughness and relatively low carbon equivalent value (CEV) with a fine and uniform acicular ferrite microstructure. The typical values of nominal yield strength (F_y), nominal tensile strength (F_u), Y/T strength ratio ($Y_R=F_y/F_u$), elongation at tensile strength (ϵ_u), and elongation at fracture (ϵ_f) are $F_y=650\text{MPa}$, $F_u=800\text{MPa}$, $Y_R=0.80\sim 0.90$, $\epsilon_u=5\sim 6\%$, and $\epsilon_f=12\sim 15\%$, respectively.

2) The high performance steel is attracting considerable attention in the

construction industry for its use in new structural applications with the help of the appropriate design and fabrication methods. However, due to a lack of sufficient research on the influence of the post-yield range characteristics of various steel grades on structural behavior, the current code directly or indirectly restricts high strength steel by adopting limiting parameters such as upper yield strength limit or upper yield-to-tensile (Y/T) strength limit or a certain level of ductility demand (=rotation capacity), which subsequently leads to reduced user confidence and curtails high strength steel field application. Therefore, a clear assessment of the role of post-yield range characteristics on structural behavior is required to renew confidence in the use of high strength steel in the construction industry.

3) In current codes (AISC and EC 3), both the material property requirement and member stability requirement directly or indirectly limit the application of high strength steel in building structures. With regard to the material property requirements, AISC specified minimum F_y , F_u , and minimum ϵ_f for individual grade of steel. On the other hand, EC 3 places limits such T/Y strength ratio (F_u/F_y), T/Y strain ratio ($E_R=\epsilon_u/\epsilon_y$), and minimum ϵ_f for all grades of steel.

With regard to the member stability requirements, compact section in AISC general specification or class 1 section in EC 3, which satisfy the width-to-thickness ratios limit in the codes, is required to provide adequate rotation

capacity level at nominal plastic moment, $R_n \geq 3.0$. Analogous to the section requirements, unbraced length limits in AISC general specification and lateral slenderness in EC 3 are also specified to provide the adequate rotation capacity and strength levels according to bracing spacing.

In addition, the level of the rotation capacities is further increased if the seismic provisions are applied, depending on the level of ductility demand in the inelastic range. Eventually, whether a member is designed according to the general specification or seismic provisions, a member must ensure a certain level of rotation capacity, at a minimum of $R_n \geq 3.0$.

4) By reviewing previous studies, it has been found that the in-plane and the out-of-plane behavior, which curtail the in-plane behavior, of a member in the inelastic range is greatly influenced by the post-yield mechanical properties such as the magnitude of strain hardening (F_u/F_y), length of yield plateau (S), and strain hardening modulus ($E_{st}(\epsilon)$). With regard to the in-plane behavior, the length of yield plateau is important for ensuring the sufficient rotation capacity of a mild steel member at moment gradient loading. Also, the existence of the strain hardening is significant for achieving plastic moment in a section.

With regard to the out-of-plane behavior, the initial strain hardening modulus is significant for estimating the resistance of a mild steel member against both lateral and local buckling, which curtails the member rotation

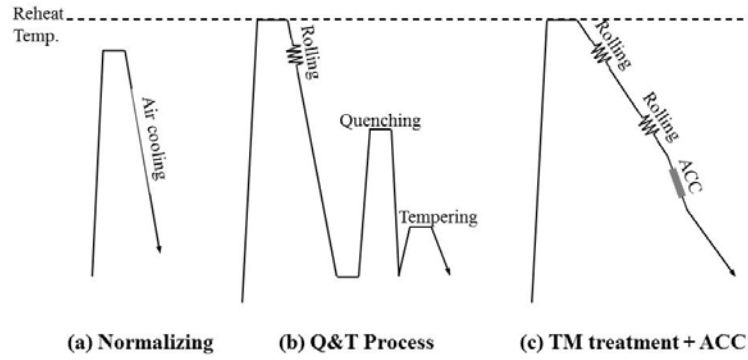
capacity significantly. By adopting those features, the current slenderness ratios (such as unbraced length limits and width-to-thickness ratios in AISC and EC 3) were established with a material model composed of three linear curves (tri-linear model: an elastic part where stress and strain are proportional, a plastic plateau part, and the initial part of the strain hardening).

However, high strength steel is not applicable to the assumed stress-strain model since the values of the strain hardening modulus are difficult to define as a constant value (E_{st}) over the full range of plastic strains. Therefore, it is questionable whether the current slenderness ratio could be simply extended to high strength steel members and whether its strength and rotation capacity could be obtained, as assumed in the current code.

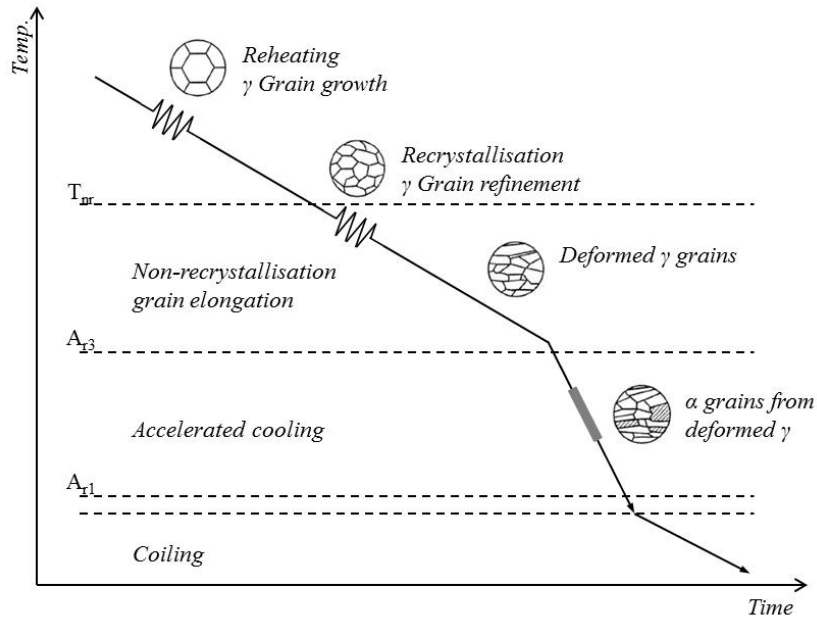
5) Until recently, numerous studies have been attempted to propose an adequate slenderness ratio for high strength steel I-shaped members using mechanistic and numerical approaches. However, these approaches have limitations in proposing useful design rules for HSS I-shaped members; especially, numerical approaches based on commercial finite element method (FEM) program tools do not give reliable results because of the numerical instabilities of the solver algorithm in the inelastic range. The motivation of this study is derived from the recognition of such limitations in recent studies, prevalent domestically and overseas. With precisely prepared experiments and a well prepared mechanistic approach, this study attempts to establish a methodology to provide adequate slenderness ratios to ensure a certain level

of the inelastic buckling strength and rotation capacity of I-members fabricated from all grades of steel materials.

6) The scope of this study was limited to the lateral-torsional buckling behavior of I-shaped members by respecting the tradition of treating each buckling phenomenon (=local, flexural, lateral-torsional, and flexural-torsional) independently (=or in decoupled manner) by neglecting their interaction with each other. Although some studies, which relied on numerical tools, emphasized the interaction between such local and lateral buckling for high strength I-shaped members, treating all buckling phenomena simultaneously is too complex to derive tangible results and is inadequate for providing design methodologies for a structural designer. Therefore, respecting the tradition and considering the practical purposes, the scope of this study is limited to the lateral-torsional buckling behavior of I-shaped members.



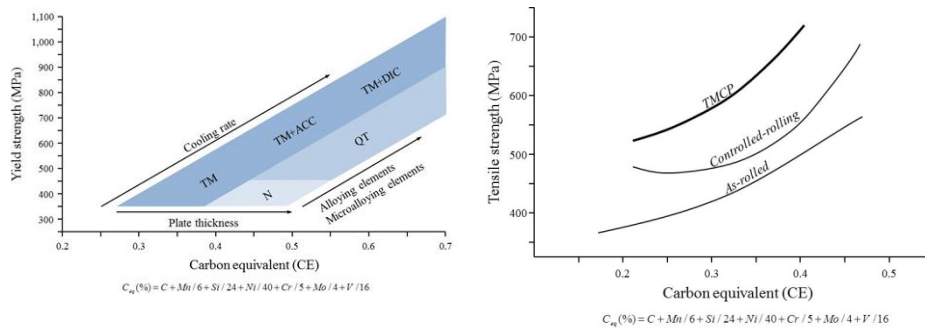
[1-1] Comparison of TMC process with Normalizing and Q&T processes (a) Normalizing (b) Q&T Process (c) TMC process



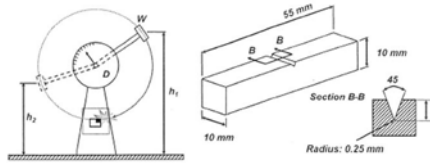
[1-2] Flow of TMCP and microstructure of steels



[1-3] Microstructure of TMC process steel compared with Normalizing (a) Normalizing (b) Q&T Process (c) TMC process

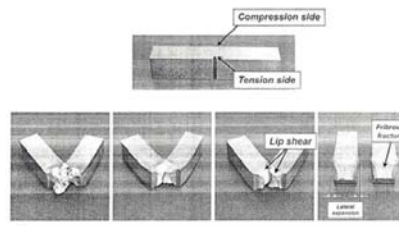


[1-4] Relationship between YS and CEV depending on steel making process



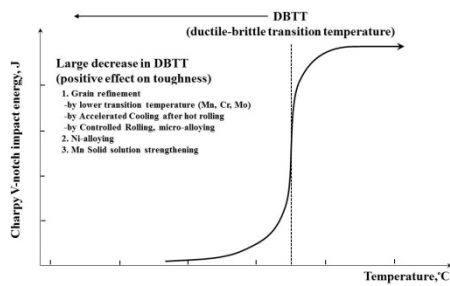
- Test conditions:**
1. Tri-axial stress state
 2. High strain rates
 3. Low temperatures

(a) Charpy V-notch impact energy testing

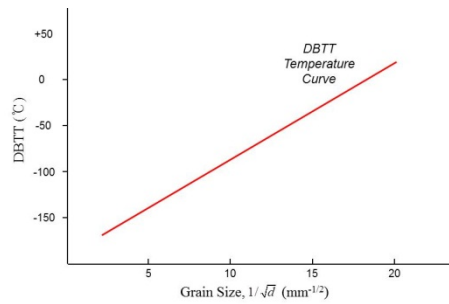


← **Increased toughness**

(b) failure modes with increased toughness

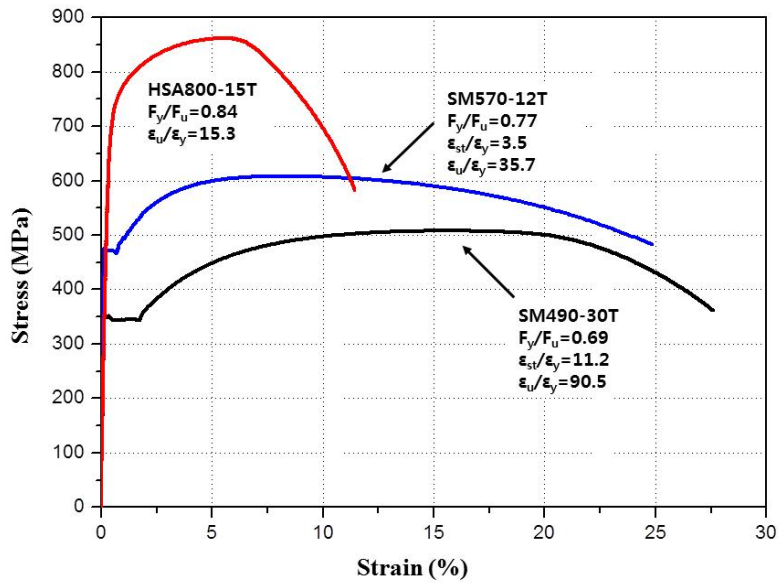


(c) Variation of DBTT according to steel making process

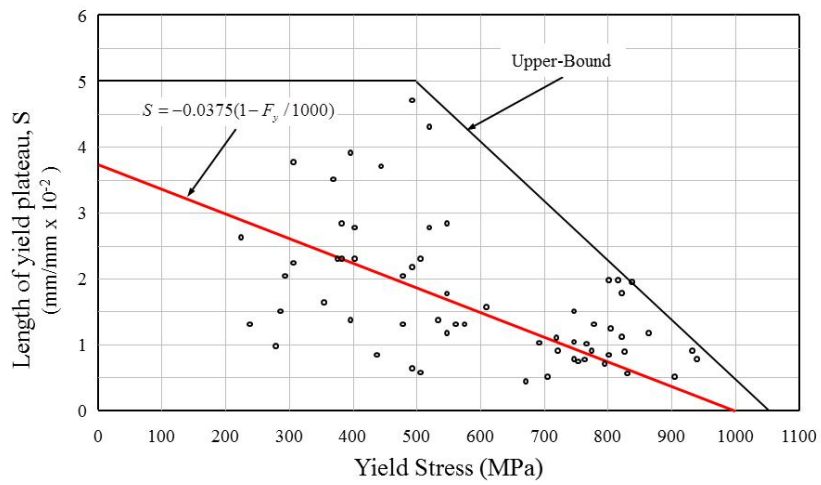


(d) DBTT versus Grain size

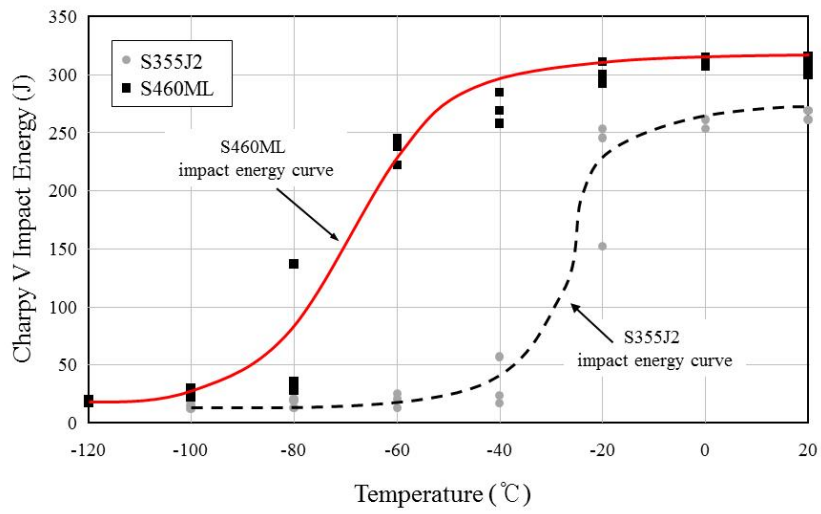
[1-5] Relationship between grain size and ductile-brittle transition temperature (DBTT) from Charpy impact energy testing results (a) Charpy testing (b) Charpy testing failure modes (c) Variation of DBTT according to steel making process (d) DBTT versus grain size



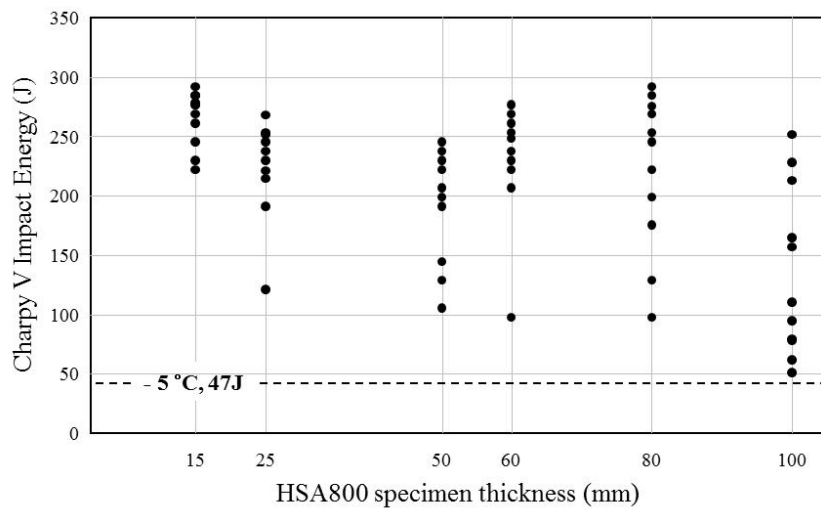
[1-6] Typical stress-strain curves of SM490, SM570 and HSA800



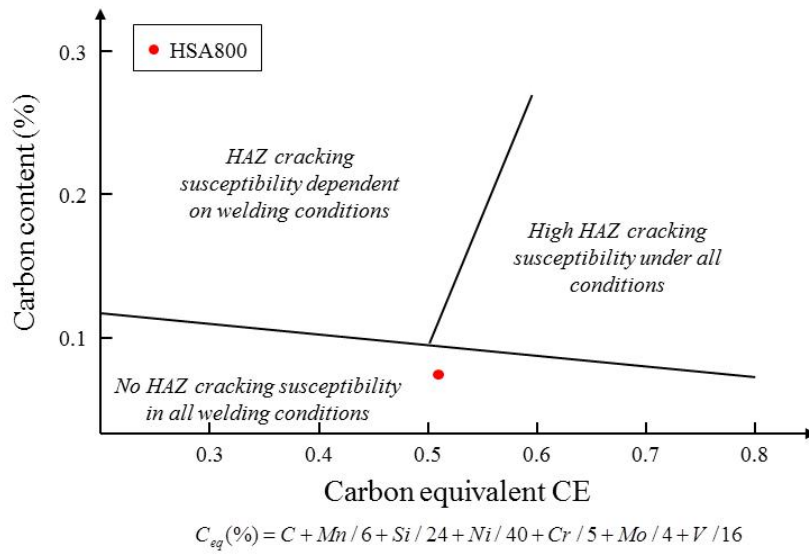
[1-7] Relationship between YP length and yield stress (Bannister, 1998a)



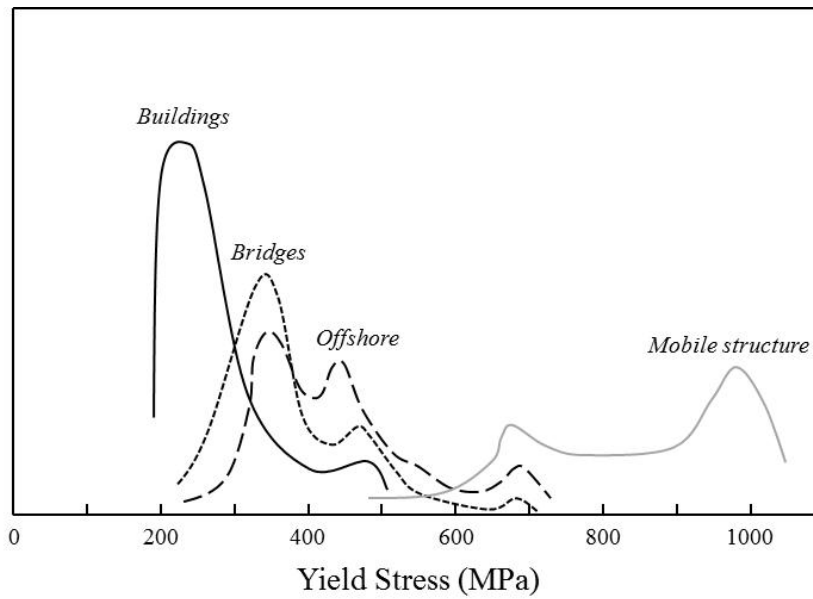
[1-8] Charpy-V notch impact energy versus DBTT depending on steel grades (Bannister, 1998a)



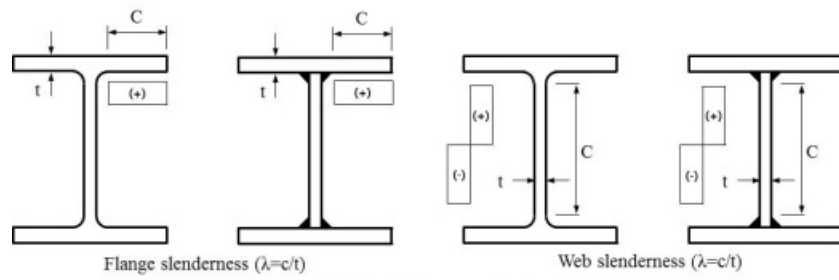
[1-9] Charpy-V notch impact energy value according plate thicknesses of HSA800 (RIST, 2011)



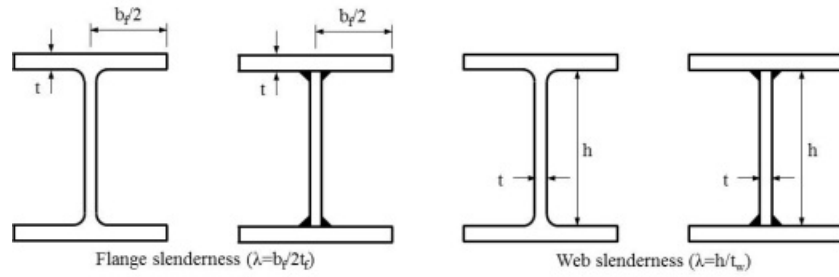
[1-10] Granville weldability diagram with CEV of HSA800



[1-11] Relative frequency of use of high strength steel (Bannister et al, 2000)

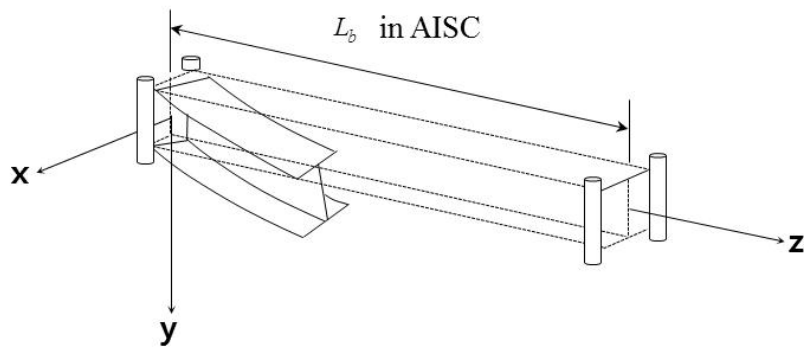


(a) width-to-thickness ratios in EC 3

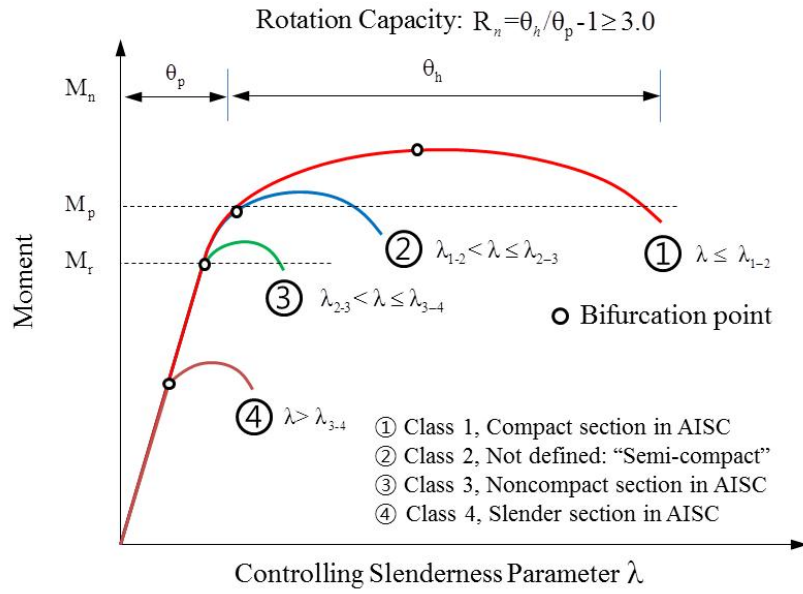


(b) width-to-thickness ratios in AISC

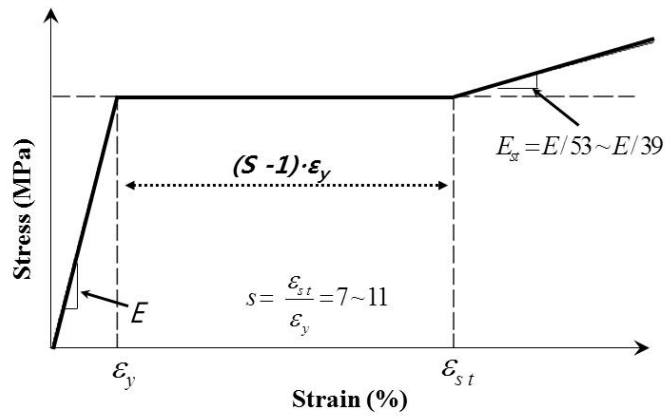
$$\bar{\lambda}_{LT} = \sqrt{M_p / M_e} \text{ in EC3}$$

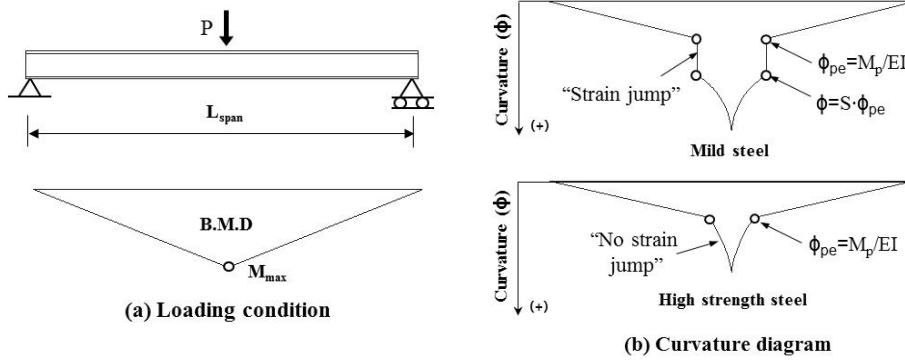


(c) Laterally unbraced length in AISC and EC3

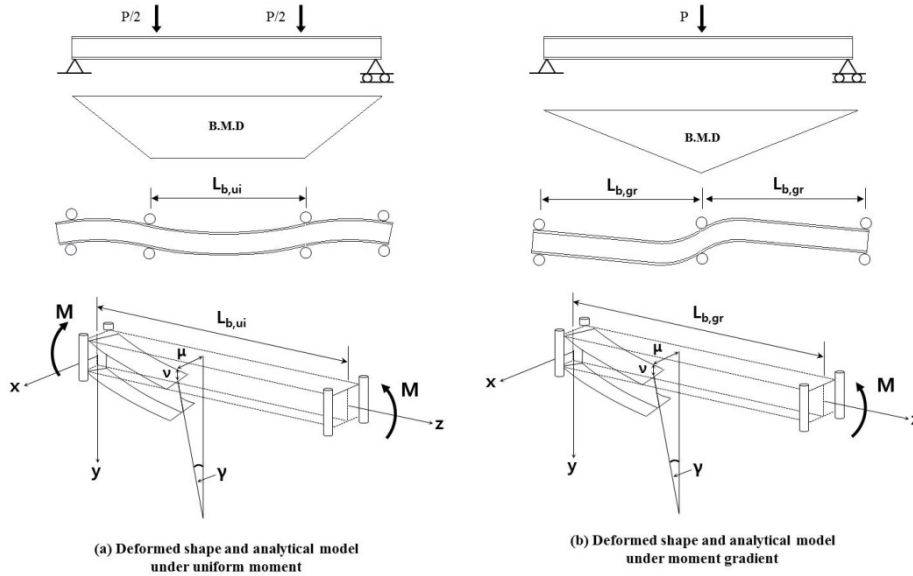


[1-12] Definition of slenderness limits and rotation capacity (a) width-to-thickness ratios in EC 3 (b) width-to-thickness ratio in AISC (c) unbraced length (d) definition of rotation capacity

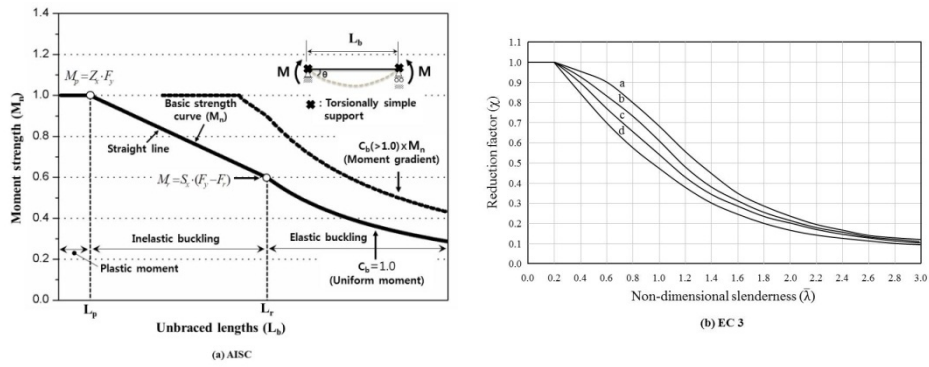




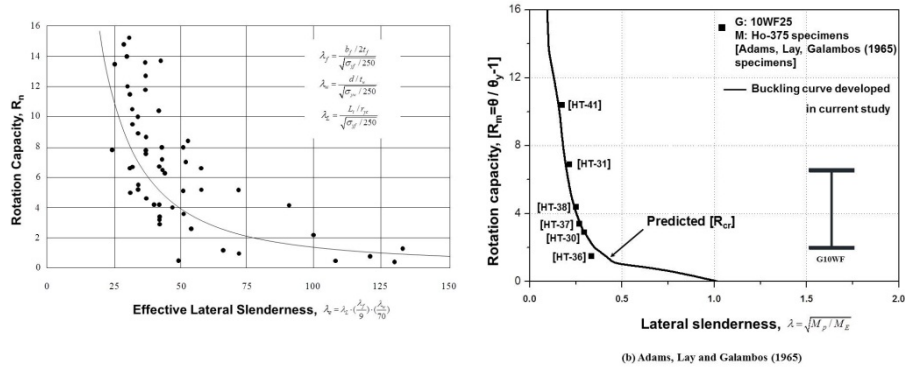
[1-14] Role of YP length (post-yield range properties) on in-plane rotation capacity under moment gradient loading condition (a) loading conditions (b) comparison of curvature diagram of mild and high strength steel at maximum moment



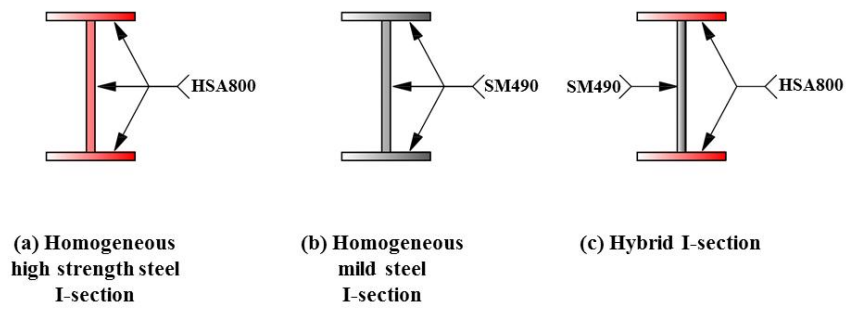
[1-15] Lateral torsional buckling with unbraced length (a) under uniform moment (b) moment under gradient



[1-16] Unbraced length limit versus critical buckling strength curves (a) AISC, (b) EC 3



[1-17] Unbraced length limit versus rotation capacity curve (a) Kemp (1985) (b) Adams, Lay and Galambos (1965) with analytically derived rotation capacity curve in this study



[1-18] Homogeneous high strength and mild steel I-section versus hybrid I-section

Chapter 1. Introduction

[1-1] Typical chemical composition of S690 and HSA800 according to the quality standards (EN, 2004 and KS, 2011)

	Grade	Thickness (mm)	C	Mn	P	S	Si	Cr	Ni	Mo	V	Cu	Ti	Nb	N	B	Zr	C _{eq}	P _{cm}
Quality Standard	S690Q ¹⁾	<150	.20 Max	1.70 Max	.20 Max	.010 Max	.80 Max	1.50 Max	2.0 Max	0.70 Max	.12 Max	.50 Max	.05 Max	.06 Max	.015 Max	.005 Max	.15 Max		
	HSA800 ²⁾	<100	.20 Max	3.00 Max	.015 Max	.006 Max	.55 Max											.60	.30
Typical	HSA800 ³⁾		.06	2.0	.012	.003	.15											.51 ⁴⁾	.21 ⁵⁾

1) EN 10025-6:2004 quality standard
2) KS D 5994 quality standard
3) Typical HSA800 chemical composition under 50mm thick plate
4), 5) Calculated by Equation 1-1, 1-2 respectively

[1-2] CVN value and maximum permissible element thickness (EN, 2004)

Steel Grade	Subgrade	Charpy Energy CVN		Reference temperature T_{Ed} [°C]																							
		T [°C]	J_{min}	$\sigma_{Ed}=0.75 f_y(t)$							$\sigma_{Ed}=0.50 f_y(t)$							$\sigma_{Ed}=0.25 f_y(t)$									
				10	0	-10	-20	-30	-40	-50	10	0	-10	-20	-30	-40	-50	10	0	-10	-20	-30	-40	-50			
S275	JR	20	27	55	45	35	30	25	20	15	80	70	55	50	40	35	30	125	110	95	80	70	60	55			
	J0	0	27	75	65	55	45	35	30	25	115	95	80	70	55	50	40	165	145	125	110	95	80	70			
	J2	-20	27	110	95	75	65	55	45	35	155	130	115	95	80	70	55	200	190	165	145	125	110	95			
	M,N	-20	40	135	110	95	75	65	55	45	180	155	130	115	95	80	70	200	200	190	165	145	125	110			
	ML,NL	-50	27	185	160	135	110	95	75	65	200	200	180	155	130	115	95	230	200	200	200	190	165	145			
S460	Q	-20	30	70	60	50	40	30	25	20	110	95	75	65	55	45	35	175	155	130	115	95	80	70			
	M,N	-20	40	90	70	60	50	40	30	25	130	110	95	75	65	55	45	200	175	155	130	115	95	80			
	QL	-40	30	105	90	70	60	50	40	30	155	130	110	95	75	65	55	200	200	175	155	130	115	95			
	ML,NL	-50	27	125	105	90	70	60	50	40	180	155	130	110	95	75	65	200	200	200	175	155	130	115			
	QL1	-60	30	150	125	105	90	70	60	50	200	180	155	130	110	95	75	215	200	200	200	175	155	130			
S690	Q	0	40	40	30	25	20	15	10	10	65	55	45	35	30	20	20	120	100	85	75	60	50	45			
	Q	-20	30	50	40	30	25	20	15	10	80	65	55	45	35	30	20	140	120	100	85	75	60	50			
	QL	-20	40	60	50	40	30	25	20	15	95	80	65	55	45	35	30	165	140	120	100	85	75	60			
	QL	-40	30	75	60	50	40	30	25	20	115	95	80	65	55	45	35	190	165	140	120	100	85	75			
	QL1	-40	40	90	75	60	50	40	30	25	135	115	95	80	65	55	45	200	190	165	140	120	100	85			
QL1	-60	30	110	90	75	60	50	40	30	160	135	115	95	80	65	55	200	200	190	165	140	120	100				

[1-3] Minimum preheat temperature according to steel grade and thickness (AIK, 2012)

Steel Grade	Welding method	Minimum preheat according to plate thickness [°C]			
		t≤25	25<t≤40	40<t≤50	50<t≤100
SM400	SMAW	No preheat ¹⁾	No preheat	50	50
	SAW, GMAW, FCAW	No preheat	No preheat	No preheat	No preheat
SM490	SMAW	No preheat	50	80	80
	SAW, GMAW, FCAW	No preheat	No preheat	50	50
SM570	SMAW	No preheat	80	80	100
	SAW, GMAW, FCAW	No preheat	50	50	80
HSA800	SMAW	80	100	100	100
	SAW, GMAW, FCAW	50	80	80	80

1) "No preheat" assume that the temperature of parent material is about 20°C.

[1-4] Classification of flexural ductility

Method of analyzing load effects	Method of calculating moment resistance	Eurocode 3	CSA 16.1	AISC LRFD (Specification)
Plastic analysis or elastic analysis with moment redistribution	Yielded stress blocks	Class 1	Class 1 Plastic	Compact ¹⁾
Elastic analysis with <u>limited redistribution</u>	Yielded stress blocks	Class 2	Class 2 Compact	
Elastic analysis with no redistribution	Elastic stress distribution limited to yield stress	Class 3	Class 3 Noncompact	Noncompact

1) AISC code compact sections are intended for plastic analysis or elastic analysis with moment redistribution providing a rotation capacity of at least three (Yura et al., 1978).

[1-5] Flange, web slenderness limits and lateral slenderness limits in EC 3 and AISC LRFD

Purpose of Classification	Analysis of load effects by	Plastic analysis	Elastic analysis	
	Calculation of moment resistance by	Yield stress blocks		Elastic yield stress
Classification by Eurocode 3		Class 1	Class 2	Class 3
Limiting slenderness of flange outstand (b/t)	Eurocode 3	$9.0\sqrt{235/F_y}$	$10.0\sqrt{235/F_y}$	$14.0\sqrt{235/F_y}$
	AISC	$0.38\sqrt{E/F_y}$	-	$1.0\sqrt{E/F_y}$
Limiting slenderness of web in flexural compression (h/t_w)	Eurocode 3	$72\sqrt{235/F_y}$	$83\sqrt{235/F_y}$	$124\sqrt{235/F_y}$
	AISC	$3.76\sqrt{E/F_y}$	-	$5.70\sqrt{E/F_y}$
Unbraced lateral slenderness ($\bar{\lambda}_{LT}$) or unbraced length (L_b)	Eurocode 3	$\bar{\lambda}_{LT,0} \leq 0.2$ $\bar{\lambda}_{LT,0} \leq 0.4$ (rolled section only)		Moment ($M_{b,Rd}$) is taken from the buckling curve ³⁾ [non-dimensional slenderness ($\bar{\lambda}$)-Reduction factor (χ)]
	AISC	$L_{pd} = [0.12 - 0.076 \frac{M_1}{M_2}] \frac{E}{F_y} r_y$	$L_p = 1.76 r_y \sqrt{E/F_y}$	$L_r = 1.95 r_{ts} \frac{E}{0.7 F_y} \sqrt{\frac{Jc}{S_x h_0} + \sqrt{(\frac{Jc}{S_x h_0})^2 + 6.76 (\frac{0.7 r_y}{E})^2}}$

1) See Figure 1-16

Chapter 2 Previous Researches

2.1 Introduction

As stated in chapter 1, current AISC specification and EC 3 specify the implied rotation capacity ($R_n=3.0$) for developing compactness section limits of the flexural members. Moreover, at seismic provisions, the required level of the rotation capacities ($R_n \geq 3.0$) are more increased for withstanding the strong and moderate seismic load, involving high ductility(=inelastic deformation capacity) demand for the flexural members. Therefore, previous researches have been extensively focused to find the adequate slenderness ratios to satisfy target inelastic deformation capacities by controlling the buckling phenomenon.

2.1.1 Major buckling phenomenon and the significance of uncoupling approach

In AISC and EC 3 codes, a category of bucklings for flexural member are classified into local buckling (FLB, WLB) and lateral-torsional buckling (LTB). Although, in actual structure, such phenomenon does not occur independently and taking place in complex manner with interacting each other (for example, under uniform moment, lateral-torsional buckling triggers first,

then flange local buckling are occurred later, whereas under moment gradient, provided that lateral bracing is adequately provided and yielded zone is sufficiently long to accommodate a full wavelength of the buckle, flange local buckling occurs first, then lateral-torsional buckling triggered), traditionally AISC and EC 3 recommend and adopt dealing those buckling phenomenons independently neglecting the interaction of each other.

Although some of recent studies relied on the numerical tools in commercial finite element software (Earls, 1999, 2000) has a significant emphasis on interaction between local flange and web-buckling and lateral-torsional buckling in HSS member, treating all buckling phenomenon at once is too complex to derive obtainable result and inadequate to provide efficient design methodologies for a structural designer. Respecting the traditional approaches, this study separately treat those buckling phenomena and manly focused on the lateral torsional buckling (LTB) behavior of I-shaped steel beam member.

2.1.1.1 Local buckling of I-shaped member

A I-shaped section can be regarded as assemblage of flat plates. In the analytical view, the flange local buckling could be idealized as the rectangular plate with center line boundary condition subjected to in-plane compression as shown in Fig. 2-1, 2-2. The loaded edge is simply supported and the longitudinal edge could be regarded as any boundary condition with rotational

stiffness. The governing differential equation for the isotropic plate as shown in Fig. 2-1 subjected to x-direction loading per unit length $N_x = \sigma_x \cdot t$ is described in Eq. 2-1.

$$\frac{\partial^4 w}{\partial x^4} + 2 \frac{\partial^4 w}{\partial x^2 \partial y^2} + \frac{\partial^4 w}{\partial y^4} = \frac{1}{D} N_x \frac{\partial^2 w}{\partial x^2} \quad (2-1)$$

where

w is z-direction (out-of-plane) displacement in plate local buckling

$D = \frac{Et^3}{12(1-\nu^2)}$ is the flexural rigidity of the plate

E is the modulus of elasticity

ν is Poisson's ratio (=0.3 for steel in the elastic range)

σ_x is the imposed stress

t is the plate thickness

Solving Eq. 2-1 gives the elastic critical buckling load as Eq. 2-2. The values of k are varied according to m and a/b as shown in Fig. 2-3 (Stowell et al., 1951). Since the aspect ratios of flange is very large as like long and narrow plate, the minimum value of k for given boundary condition should be applied. As an example, the flange of I-shaped beam could be regarded as a plate with one simply-supported (at the web) and one free edge, where the minimum value of k is 0.425. However, the web of I-shaped beam could be regarded as a plate being constrained between simply-supported and fully fixed, where the value of k can be taken as 4~7. This comparison between the k values of flange and web indicates that the flange is more vulnerable to local

buckling than web, requiring more stringent slenderness ratios.

$$\sigma_{cr} = k \frac{\pi^2 E}{12(1-\nu^2)(b/t)^2} \quad (2-2)$$

where

σ_{cr} is critical buckling stress in the plate local buckling

$k = \left(\frac{a}{mb} + \frac{mb}{a}\right)^2$ is the plate buckling coefficient, for simply supported boundary condition

m is the number of half-waves that occur in the loaded direction of the plate

a/b is the plate aspect ratio

Meanwhile, Eq.2-1 and Eq.2-2 are only applicable to elastic buckling of flat plates. For the inelastic buckling, which is applicable for stock plates, the governing equation are modified to include the altered stiffness properties of a material related with the plastic deformation prior to buckling. The altered stiffnesses are depended on the plasticity state and the modification is required. Depending on the applied plate buckling theory, the modification becomes quite different. Generally, there are two concepts to deal with the inelastic instability of plates; deformation theory and flow theory. Many researchers such Ilyushin (1947), Stowell (1948) and Shirvastava (1979) have shown that the deformation theory mainly have a good agreement with the experimental results. The differential equation for the inelastic buckling subjected to in-plane compression is written as Eq.2-3. The solution of Eq. 2-3 is obtainable depending on the numerical technique based on the energy

method such as Galerkin method. Detailed approach for the solution of Eq. 2-3 is omitted in this paper, since this paper mainly target on the lateral torsional buckling.

$$\frac{D_x}{\phi^2} \frac{\partial^4 W}{\partial \xi^4} + (2D_1 + 4D_{xy}) \frac{\partial^4 W}{\partial \xi^2 \partial \eta^2} + D_y \phi^2 \frac{\partial^4 W}{\partial \eta^4} + \left(\frac{12\sigma_x b^2}{t^2} \right) \frac{\partial^2 W}{\partial \xi^2} = 0 \quad (2-3)$$

where

$$W = w/t, \quad \phi = a/b, \quad \xi = x/a, \quad \eta = (y+b)/b$$

$$D_x = \frac{2E(\lambda + 3 + 3e)}{\lambda(5 - 4\nu + 3e) - (1 - 2\nu)^2}$$

$$D_1 = \frac{2E(\lambda - 1 + 2\nu)}{\lambda(5 - 4\nu + 3e) - (1 - 2\nu)^2}$$

$$D_{xy} = \frac{E}{2 + 2\nu + 3e}$$

$$D_y = \frac{4E\lambda}{\lambda(5 - 4\nu + 3e) - (1 - 2\nu)^2}$$

$$\lambda = E/E_t, \quad e = E/E_s - 1$$

E_s is secant modulus

E_t is tangent modulus

2.1.1.2 Lateral torsional buckling of I-shaped member

In addition to the local buckling, an I-shaped section member would fail suddenly by deflecting sideways and twisting at a certain critical value of the applied load, the phenomenon of which is terms as lateral-torsional buckling (Fig. 2-4). The phenomenon has much in common with the Euler buckling; a member that has been loaded in a stiff plane (major-axis bending of a beam) buckles in a weaker plane in combined with torsion and minor-axis flexure of

the beam.

The early studies of theoretical lateral instability were performed by Prandtl (1899) and Michell (1899). The authors limited the scope of the research to a narrow rectangular cross-section, simply supported at either end, loaded by uniform moment. Few years after, Timoshenko (1905) extended these solutions to I-sections, by including the effects of warping and torsional aspects of the problem. Then many authors have developed various topics such as the influence of the loading and lateral restraint conditions, monosymmetry (which further complicates torsional behavior) and inelastic material behavior have all been studied. The significant review of the subjects have been written by Lee (1960), Nethercot and Rockey (1971), Galambos (1977) and Trahair (1977).

The basic lateral torsional buckling problem is discussed following condition (Fig. 2-5). The beam, which is of doubly symmetrical cross section, is loaded by equal and opposite end moment M_x so as to cause bending about its major principal axis. At both ends it is supported in such a way that lateral deflection and twist are prevented but no resistance is offered to either lateral bending or warping (axial movement accompanying torsion which corresponds to the bending of the flanges in opposite sense about an axis through the web). Placing the beam in its slightly buckled state, allowing the lateral deformation (μ) and torsional deformation (γ) to occur and

decomposing M_x into its components about the deformed axis system (x' , y' , z') enables the distributing moments to be equated to the beams internal resistance as follows. (Timoshenko and Gere, 1961; Chen and Atsuta, 1977; Kirby and Nethercot, 1979)

$$(EI_y) \frac{d^2 u}{dz^2} = M \cdot \gamma \quad (2-4)$$

$$(GJ) \frac{d\gamma}{dz} - (EC_w) \frac{d^3 \gamma}{dz^3} = \frac{du}{dz} \quad (2-5)$$

where

EI_y is elastic flexural stiffness

EC_w is elastic warping stiffness

GJ is elastic torsional stiffness

Solving these two equations subject to the following boundary conditions (Eq. 2-6 and Eq. 2-7) gives the expression for the least value of M_x necessary to cause elastic instability $M_{cr,e}$ as Eq. 2-8.

$$u = \frac{d^2 u}{dz^2} = 0 \quad \text{at } z = 0, L \quad (2-6)$$

$$\gamma = \frac{d^2 \gamma}{dz^2} = 0 \quad \text{at } z = 0, L \quad (2-7)$$

where

u is the lateral bending deformation of top flanges

γ is the torsional deformation of a section

$$M_{cr,e} = \frac{\pi}{L_b} \sqrt{(EI_y)(GJ)} \sqrt{1 + \frac{\pi^2 (EC_w)_e}{(L_b)^2 (GJ)}} \quad (2-8)$$

where

L_b is the unbraced length

$M_{cr,e}$ is the elastic lateral torsional buckling load

For the inelastic LTB, new values of (EI_y) , (EC_w) , (GJ) must be re-calculated by either adopting the tangent modulus theory or reduced modulus theory. The method to calculate the tangent flexural stiffness $(EI_y)_t$ of I-section is proposed by Trahair and Kitipornchai (1972) and tangent torsional stiffness $(GJ)_t$, if each flange or web is idealized as bimetallic strip, is proposed by Booker and Kitipornchai (1971). Further, the altered position of shear center (y_{0t}) and following the tangent warping stiffness $(EC_w)_e$ in an inelastic beam is proposed by Trahair and Kitipornchai (1972). Detailed approach for the solution of inelastic LTB will be extensively discussed in chapter IV.

2.1.2 Rotation capacity under uniform moment and moment gradient

As mentioned previously, previous researches have been extensively focused on to find the adequate slenderness ratios (lateral slenderness ratio, flange and web width-to-thickness ratios) to satisfy target inelastic deformation capacities specified in the codes. Meanwhile, the inelastic behaviors of beams are significantly different according to loading conditions.

In other words, the inelastic behaviors (affecting to inelastic deformation capacity=rotation capacities) of a beam are quite different under uniform moment and under moment gradient, needs to investigate separately in detail.

2.1.2.1 Beams under uniform moment

Fig 2-6 shows the typical in-plane moment versus rotation relationship of a beam subjected to a uniform moment, fabricated from the mild steel, which have a considerable yield plateau length and strain hardening. The moment-end rotation curve could be categorized as four parts (Green, 2000).

- 1) The elastic range (OA segment) where the $M-\theta$ curve is linear
- 2) The partially yielding range (from out layer of top flange to inner side, AB segment) where the curves become nonlinear
- 3) The plateau range (BC segment) where most of beam section is fully yielded ($\varepsilon \geq \varepsilon_y$) and maintaining the moment strength
- 4) The unloading range (CD segment) where the beam becomes unstable because of magnified LTB or following FLB, no longer to resist additional moment

The behavior of a beam subjected to uniform moment involves both in-plane behavior and out-of-plane behavior (LTB). At the initial loading condition, a very slight lateral deflection is noticeable at the center of beam span. As the loading is increased, the compression flange begin to yield (=losing the elastic section stiffness), the lateral deflections become visually

pronounced and buckling bifurcated. As the end rotation becomes increased, the magnitude of the lateral deflection is more magnified, triggering additional 2nd-order moment at the center, degrading the beam capacity significantly.

It is not clearly defined when the beam degrades its strength. However, historically, it has been regarded that the beam is able to maintain the plastic moment until local buckling occurs (=strain hardening point) despite significant lateral deflection occurred (Green, 2000). (The point when the beam degrades its capacity under uniform moment is subject of discussion, will be treated in chapter IV.) As shown in Fig. 2-6b, during the all ranges of the loading process, the tension flange only slightly moves laterally (μ_t) in contrast to the compression flange (μ_c). Thus, the web becomes inevitably distorted because of the relative displacement between the compression and tension flange. This phenomenon seems to be a major motivation to propose T-column model (Fig. 2-7), with a hinge at the center of web, by Lay (1965). Also, the lateral movement (=bending) of the compression flange (μ_c) triggers the additional compressive strains to half of the beam flange as a result of compression flange bending about y-y axis. These movements eventually cause flange local buckling at the half of compression flanges as shown in Fig. 2-8.

Among the tests conducted by numerous researchers, Lee and Galambos (1962) experiment clearly showed that the rotation capacities are increased as

the length of the unbraced span are decreased (Fig. 2-9, Table 2-1). In detail, LB-11 specimen where $(L_b / r_y) \cdot \sqrt{\sigma_{yf} / E} = 1.18$ show higher rotation capacity ($R_m=12.8$) than that of LB-16 specimen with $R_m=5.0$ where $(L_b / r_y) \cdot \sqrt{\sigma_{yf} / E} = 1.69$. The major reason such phenomenon is come from that the closer bracing postpone or restrain the LTB buckling, which is the earliest symptom that leads to the member instability.

2.1.2.2 Beams under moment gradient

Beams under moment gradient show quite different behavior from the uniform moment case. Fig. 2-10 shows the typical in-plane moment versus rotation relationship of a beam subjected to a moment gradient, fabricated from mild steel, which have a considerable yield plateau length and strain hardening. The moment-end rotation curve could be categorized as four parts (Green, 2000).

- 1) The elastic range (OA segment) where the M- θ curve is linear
- 2) The partially yielding range (from out layer of top flange to inner side, AB segment) where the curves become nonlinear because of the cross-sections directly adjacent to the point of load are partially yielded
- 3) The strain-hardening range (BC segment) where the beam carries additional load as the maximum moment adjacent to the point of load carries additional load beyond the plastic moment, the spread of yielding are

continued along the longitudinal axis as the member is capable of resisting the additional moment. In contrast to the uniform moment condition, the plateau range could not be existed since the participation of yielding is not occurred simultaneously as like a member in uniform compression or tension.

-4) The unloading region (CD segment) where the beam becomes unstable because of FLB or following LTB, no longer able to resist additional moment.

The behavior of a beam subjected to moment gradient involves both in-plane behavior and out-of-plane behavior (FLB). At the initial loading condition the beam behaves elastically until yielding. Once the plastic moment M_p is exceeded, the end rotation increases measurably. The moment continues to increase beyond M_p and the spreading of yielding is sufficient to trigger local buckling (Lay (1965) indicate that the local buckling initiated when the compression flange has yielded over a length sufficient to accommodate a full wavelength of the buckled shape), local flange buckling is observed. However, the initiation of the local buckling does not directly cause any degradation in strength as shown Fig. 2-10a, performed by Lukey and Adams (1969), the moment continues to increase with increasing rotation until a lateral movement of the compression flange becomes pronounced as shown in Fig. 2-10b. The member strength starts to degrade as the corresponding lateral deflection increased rapidly.

It should be noted that, at moment gradient condition, yielding of a beam is confined to the region adjacent to the location of maximum moment, and it

cannot spread the yielding along the length of the beam unless the maximum moment is increased. Therefore, a material with no strain hardening, where plastic moment M_p could not be achieved, the inelastic rotation capacity also could not be obtainable since the member strength are under plastic moment. Also, as the level of the maximum moment become higher, the region of yielding along the length is more extensive, leading to large inelastic rotation capacity unless the local buckling are postponed.

It has been regarded that the beam is able to the plastic moment until lateral-torsional buckling is triggered. Thus, it is not local buckling but rather lateral-torsional buckling that cause a loss in capacity. After local buckling, the lateral stiffness of the compression flange is greatly reduced (only half of the section is effective) and lateral-torsional buckling is triggered. This phenomenon seems to be a major motivation to propose local buckling model (Fig. 2-11) by Lay. Depending on the magnitude of the constraint provided by web, the torsional stiffness (k) is determined.

Among the test conducted by numerous researchers, Lukey and Adams (1969) experiment clearly showed that the rotation capacities are increased as the flange width-to-thickness ratios are decreased (Fig. 2-12, Table 2-2). In detail, B-2 specimen where $(b/2t_f) \cdot \sqrt{\sigma_{yf}/E} = 0.30$ show higher rotation capacity ($R_m=10.4$) than that of B-1 specimen with $R_m=2.9$ where $(b/2t_f) \cdot \sqrt{\sigma_{yf}/E} = 0.42$. (It should be noted that the web width-to-thickness

ratios are also significant effect on the member rotation capacities, providing lateral resistance against the subsequent lateral-torsional buckling). The major reason such phenomenon is come from that the low flange width-to-thickness ratios postpone or restrain the FLB buckling, which is the earliest symptom that leads to the member instability.

2.2 Experimental studies of inelastic LTB behavior

Experimental test of steel members have been carried out since the later 1940's. The experiment could be grouped into uniform moment test and moment gradient test. Each type of test is related to one or more of the limit state such LTB, FLB and WLB to analyzed how it affect to a member capacity. A summary of all the experimental data is given in Table 2.1 and Table 2.2. The data have been normalized so that direct comparison of the works can be easily accomplished.

2.2.1 Rotation capacity of I-beam under uniform moment

2.2.1.1 Literature review: Lee and Galambos (1962) paper

A series of experiments (Specimens-LB 10, LB-S1, LB-S5 and LB-S6) were performed to study the behavior of the short, laterally braced wide flanges beams. The purpose of the experiment is to determine the maximum permissible spacing (=unbraced length limits) of the support beam subjected

to the uniform moment and to analyze the post-buckling strength. The experimental parameter was the unbraced length, positioned at $(L_b / r_y) \cdot \sqrt{\sigma_{yf} / E} = 1.18 \sim 1.69$ ranges. Controlled parameter such flange and web width-to-thickness ration is fixed to $(b / 2t_f) \cdot \sqrt{\sigma_{yf} / E} = 0.23$ and $(h / t_w) \cdot \sqrt{\sigma_{yw} / E} = 1.37$ level respectively. The yield strength of a material is $F_{yf} = 234MPa$.

From the experimental studies (Fig. 2-13 and Table 2-1), it was found that a beam (LB-10) with $(L_b / r_y) \cdot \sqrt{\sigma_{yf} / E} = 1.52$, failure is investigated by local buckling of the compression flange with rotation capacity, $R_m=7.0$ level. However, beam longer than above limit is failed by lateral buckling. All specimens have considerable post-buckling strength and sufficient rotation capacities.

2.2.1.2 Literature review: Adams, Lay and Galambos (1965) paper

A series of experiments (Specimens-HT29, HT30, HT31, HT36, HT37, HT41, HT38) were performed to study the behaviors of the wide flange beams fabricated from ASTM A441 ($F_{yf} = 409MPa$) steels. The purpose of the experiment is to determine the permissible spacing when the beams are subjected to the uniform moment. The experimental parameter was the unbraced length, positioned at $(L_b / r_y) \cdot \sqrt{\sigma_{yf} / E} = 1.12 \sim 2.01$ ranges.

Controlled parameter such flange and web width-to-thickness ratio is fixed to $(b/2t_f) \cdot \sqrt{\sigma_{yf}/E} = 0.30$ and $(h/t_w) \cdot \sqrt{\sigma_{yw}/E} = 1.74$ level respectively.

From the experimental studies (Fig. 2-14 and Table 2-1), it was found that a beam (HT-36) with $(L_b/r_y) \cdot \sqrt{\sigma_{yf}/E} = 2.01$ unloaded almost immediately on reaching the full plastic moment with the rotation capacity, $R=1.5$. Except HT-36, unloading of all specimens occurred only after severe local buckling of the compression flanges. It should be emphasized that local buckling did not coincide with unloading (Please note that it has been regarded that the local buckling followed by lateral torsional buckling is indicator of unloading) and the unloading is followed only after severe local bucklings. All specimens have sustained considerable inelastic capacities before unloading.

2.2.1.3 Literature review: McDermott (1969) paper

A series of experiments (Specimens-#1~#7) were performed to study the behaviors of the wide flange beam fabricated from ASTM A514 ($F_{yt}=793\sim 883\text{MPa}$) steel. The purpose of the experiment is to determine the permissible spacing and width-to-thickness ratios when the beams are subjected to the uniform moment. Except specimen 1 and 2, the main experimental parameter was the unbraced length, positioned at $(L_b/r_y) \cdot \sqrt{\sigma_{yf}/E} = 0.38 \sim 1.58$ ranges. The other parameters such flange and web width-to-thickness ratios are controlled to $(b/2t_f) \cdot \sqrt{\sigma_{yf}/E} = 0.20 \sim 0.38$

and $(h/t_w) \cdot \sqrt{\sigma_{yw}/E} = 1.22 \sim 2.15$ ranges respectively.

From the experimental studies (Fig. 2-15 and Table 2-1), the author indicate that the premature of inelastic buckling of A514 steel I-shaped member will not occur if the value of $(b/2t_f) \cdot \sqrt{\sigma_{yf}/E} = 0.31$ and if the value of $(L_b/r_y) \cdot \sqrt{\sigma_{yf}/E} = 1.31$ for uniform moment. It seems to be rather ambiguous how to derive those values in the paper. However, the experiments verified that, with appropriate width-to-thickness ratios and close bracing as shown in specimen 4 (the rotation capacity of which is $R_m=6.8$), such high strength steel could exhibit high level of rotation capacity.

2.2.1.4 Literature review: Holtz and Kulak (1973) paper

A series of experiments (WS-1, 2, 3, 4, 6, 7, 8, 9, 10 and 11) were performed to determine suitable limit for the web depth-to-thickness ratio where the beams are subjected to uniform moment. The major parameter is the web depth-to-thickness ratio, positioned at $(h/t_w) \cdot \sqrt{\sigma_{yw}/E} = 2.86 \sim 5.16$ ranges. The other parameters such flange and the unbraced length are controlled to $(b/2t_f) \cdot \sqrt{\sigma_{yf}/E} = 0.30 \sim 0.38$ and $(L/r_y) \cdot \sqrt{\sigma_{yf}/E} = 0.66 \sim 1.35$ ranges respectively.

From the experimental studies (Fig. 2-16 and Table 2-1), the authors proposed that a web slenderness limit be established for non-compact member

at $(h/t_w) \cdot \sqrt{\sigma_{yw}/E} = 1.52$. The authors felt this limit was conservative, but in light of the number of tests conducted, it was justified at this time.

2.2.2 Rotation capacity of I-beam under moment gradient

2.2.2.1 Literature review: Adams, Lay and Galambos (1965) paper

A series of experiments (HT-28, HT-43, HT-52) were performed to study the behaviors of the wide flange beam fabricated from A441 ($F_{yI}=405\text{MPa}$). The purpose of the experiment is to extended knowledge about the high strength I-shaped member at that time, subjected to moment gradient.

The major parameter was the unbraced length, positioned at $(L/r_y) \cdot \sqrt{\sigma_y/E} = 1.02 \sim 3.21$ ranges. The other parameter such flange and web slenderness are controlled to $(b/2t_f) \cdot \sqrt{\sigma_y/E} = 0.35$ and $(h/t_w) \cdot \sqrt{\sigma_w/E} = 1.55$ level respectively.

From the experimental studies (Fig. 2-17 and Table 2-1), the author conclude that the inelastic portion of the compression flange is relatively small, constrained to adjacent load point, when the beam subjected to moment gradient loading. Lateral deflection of the member is relatively very small until the local buckling occurs. After local buckling had commenced, the section is no longer maintain the symmetric condition, initiating lateral deflection and leading to a reduction in the ability of the beam to carry load.

2.2.2.2 Literature review: Lukey and Adams (1969); Smith and Adams (1968) paper

A series of experiments (A-S~A-W; B-S~B5; C1~C5; D1~D6; E1~E6) were performed to study the behaviors of the wide flange beam fabricated from a steel where the yield strength are 285~373MPa ranges. The purpose of the experiment is to determine where a relationship existed between the flange slenderness ratio and the rotation capacity of a simply-supported steel member. Also the studies tried to correlate the effects of changes in the slope of moment gradient, web width-to-thickness ratio and bracing spacing on the rotation capacities. At specimen type A, B and C, the unbraced length is controlled and flange and web slenderness become different. Whereas, at specimen type D and E, the unbraced length is variable and other parameter is controlled.

From the experimental studies (Fig. 2-18 and Table 2-1), the author concluded three facts as follows:

-1) The test result show that rotation capacity of members having the same effective slenderness was greatly influenced by the slope of the moment gradient. Specimen subjected to higher moment gradient could carry higher rotation capacity than those specimen subjected to low moment gradient. The major reason such phenomenon come from that uniform yielding region along the length trigger flange local buckling and following lateral deformation, which degrade the rotation capacities of the specimens. Similar tendency also

investigated at Bansal's 1971 experimental study (Fig. 2-19)

-2) The slope of moment gradient had a definite effect upon the wavelength of the local buckles. In specimens which were subjected to less severe moment gradient, the measured wavelength were approximately one-half of the yield length. In the case of high moment gradient, the buckling length were restricted to small extent of yielding along the compression flange. Similar investigated also reported by Lay (1965b) as shown in Fig. 2-20.

-3) Flange slenderness ratio had a definite effect on the measured member rotation capacity. The members with slender flange carry small rotation capacities than stockier flanges, although the flange buckling itself does not indicate the unloading of a member.

2.2.3.3 Literature review: Roik and Kuhmann (1987)

A series of experiments (Specimens-#1~#24) were performed to study the behaviors of the wide flange beam fabricated with the yield strength of steel ($F_{yf}=240\text{MPa}$). The purpose of the experiment is to find the effects of flange and web width-to-thickness ratios on the beam subjected to the moment gradients. Except specimen #3, the major parameters were the flange and web width-to-thickness ratios, positioned at $(b/2t_f) \cdot \sqrt{\sigma_y/E} = 0.30 \sim 0.40$ and $(h/t_w) \cdot \sqrt{\sigma_{yw}/E} = 1.57 \sim 2.60$. The unbraced lengths are controlled not so as to specimens failed by LTB by controlling $(L/r_y) \cdot \sqrt{\sigma_y/E} = 1.10 \sim 1.82$ ranges.

From the analytical and experimental studies (Fig. 2-21 and Table 2-2), the authors insist three major facts.

1) The torsional constraint provided by web play a significant role on rotation capacity. Even the specimens with same flange width-to-thickness ratios, the rotation capacity of each specimen are significantly different by comparing specimens #4~#6. As the specimens contained the more slender web, the less rotation capacities were exhibited. Although the flange was always the first to buckle, the web stiffness become very important since the buckled flange is restrained by the web bending resistance (Fig. 2-22). They propose new parameter, the web stiffness (K_s , Eq. 2-9), which represents the stiffness of a torsional spring formed by web, claiming that K_s is more significant characteristic, correlation with the experimental results, than the simple web slenderness such h/t_w .

$$K_s = \frac{G_t \cdot t_w^3}{3 \cdot (d - 2 \cdot t_f)} \quad (2-9)$$

where

K_s is web torsional stiffness proposed by Roik and Kuhmann (1987)

$$G_t = \frac{2 \cdot G}{1 + \frac{E/E_t}{4(1+\nu)}} \text{ is inelastic shear modulus}$$

E_t is the tangent modulus

ν is the Poisson's ratio

G is elastic shear modulus

2) The moment ratios (slope is high or low), also play a significant role on rotation capacity. The authors observed experimentally that the region where local buckling occurs limited to a length the width of the flange. Therefore, the more moment ratio is steep, the less the flange is participated on the inelastic ranges. Thus, member with a steep moment gradient buckle later and provide a greater amount of deformation capacity provided that the material could provide sufficient strain hardening.

3) Flange slenderness plays an important role on rotation capacity. The section containing the most slender flange delivers a rotation capacity only $R=1$, which in general is not sufficient to allow redistribution of bending moment in the structure. Meanwhile, the other section the rotation capacity lies above this value. However, it can be observed that for the same value of flange slenderness very different rotation capacities have been achieved. Therefore the flange slenderness is not the only criterion for the rotation capacity.

2.3 Analytical studies of inelastic LTB behavior

Elastic lateral-torsional buckling of wide-flange beams under uniform moment has been solved (Bleich, 1952; Timoshenko and Gere, 1961). In the elastic solution, following conditions are often assumed.

1) The elastic stiffnesses (such flexural, warping, torsional stiffness) does not

changed at the entire length

- 2) The shear center does not change in the original position
- 3) The cross-section remains plane before and after the buckling

However, except 3rd assumption, the assumptions are not valid in the inelastic ranges and the various modifications have been performed at the solution. In this chapter, key researches to provide solution of the inelastic lateral torsional buckling will be dealt with.

2.3.1 I-Beams under uniform moment

The first solution for lateral torsional buckling of wide-flange beams in the inelastic ranges (=especially strain hardening ranges) were proposed by **White (1956)**. Later, **Kusuda et al. (1960)** presented a simplified method from White's work and made a recommendation for plastic design. **Lee and Galambos (1962)** extended the White's work by considering the post-buckling, which reflects the unloading of the compression flange due to lateral-torsional buckling. **Galambos (1963)** contribute to present a solution for determining the inelastic lateral-torsional buckling strength. **Lay and Galambos (1965)** also extend the White's work, however, it seems to be first solution to present the rotation capacity of a beam according to lateral supporting under uniform moment.

2.3.1.1 Literature review: White (1956) paper

An analytical solution for the determination of the unbraced length was

presented to develop sufficient plastic rotation before lateral-torsional buckling occurs by assuming following conditions.

- 1) Lateral-torsional buckling occurs when the material has reached the onset of strain-hardening
- 2) No elastic unloading is considered (=tangent modulus theory is applied)
- 3) A material with initial strain hardening modulus ($E_{st} / E = 1/33$) was assumed
- 4) Simple end restraint (the ends of the beam cannot translate or twist but are free to rotate laterally and the end section are free to warp)

By modifying **Timoshenko and Gere (1961)** proposal (**Eq. 2-10**), the author presented following suggestions (**Eq. 2-11**). From the above assumption, the material constant E and G are replaced by their corresponding inelastic material properties, E_{st} and G_{st} respectively. Also, for relatively short beam (=closely braced beam), the equation can be further simplified since the contribution of St. Venant torsion term, GJ is relatively small (**Eq. 2-11a**). The limiting slenderness for this lower bound solution can be solved as **Eq. 2-11c**. If one use an average value of 1.2 for $A \cdot (d-t_f)/2Z_x$ for wide-flange sections and $h=33$ for A-F6 steel (**Eq. 2-11b**), the limiting L_b/r_y is about 18.

$$\frac{M_p}{EI_y} = \frac{\pi}{L_b} \sqrt{\frac{GJ}{EI_y} + \frac{\pi^2 C_w}{L_b^2 I_y}} = \frac{\pi}{L_b} \sqrt{\frac{GJ}{EI_y}} \approx 0 + \frac{\pi^2}{L_b^2} \left(\frac{d-t_f}{2}\right)^2 \quad (2-10)$$

where

M_p is the plastic moment

d is depth

t_f is flange thickness

$$\frac{Z_x \cdot \sigma_y}{E' I_y} = \left(\frac{\pi}{L_b}\right)^2 \left(\frac{d - t_f}{2}\right) \quad (2-11a)$$

$$E' I_y = \frac{1}{h} E I_y \quad (2-11b)$$

$$\frac{L_b}{r_y} = \pi \sqrt{\frac{E'}{\sigma_y}} \sqrt{\frac{A(d - t_f)}{2Z_x}} = \pi \sqrt{\frac{1}{h\varepsilon_y}} \sqrt{\frac{A(d - t_f)}{2Z_x}} \quad (2-11c)$$

where

Z_x is plastic section modulus about x-x' axis

$E' = E / h$ is inelastic modulus at onset of strain hardening assumed in white (1956)

$E' I_y$ is the effective flexural stiffness assumed in white (1956)

2.3.1.2 Literature review: Galambos (1963) paper

A method for the solution of the inelastic lateral buckling problem was presented to develop LTB strength curve in inelastic ranges by adopting the reduced lateral, warping and torsional stiffness due to yielding as shown in [Fig. 2-23](#). In the study, following conditions are assumed.

- 1) No external lateral forces are applied to the beam between supports.
- 2) The beam is initially straight and free of imperfection
- 3) The cross sectional and material properties are uniform along whole length of the beam
- 4) The beam is as-rolled steel wide-flange shapes. Fillets and variations of the

flange thickness are neglected in the derivations.

5) The cross section retains its original shape during buckling.

6) The vertical deflections are small.

7) The applied end bending moments are equal, causing single curvature deformation about the strong axis of the beam.

8) The ends of the may not translate or twist; however, they are free to rotate laterally and the end section are free to warp (=”simply supported end condition”)

9) The material properties are assumed to be uniform over the cross section.

The following values of these coefficients are used for computational purpose;

$$\sigma_y = 33\text{ksi} \approx 230\text{MPa}$$

$$E = 30,000\text{ksi} \approx 206,700\text{MPa}$$

$$E_w = 900\text{ksi} \approx 6,201\text{MPa}(= E / 33)$$

$$G = 11,500\text{ksi} \approx 79,235\text{MPa}$$

$$G_w = 2,400\text{ksi} \approx 16,536\text{MPa}(= G / 4.8)$$

The tangent modulus value at the plateau region is assumed, $E_t=0$.

10) The Lehigh’s residual stress pattern assumed. These stresses are assumed constant across the thickness of each thickness of each cross section element.

The stress σ_{rc} is the maximum compressive residual stress at the tips of flange, and σ_{rt} is the maximum tensile residual stress.

By adopting the effective cross section approach, the author presented

following suggestion to calculate inelastic stiffness of the yielded cross section (Eq. 2-12). Applying those inelastic stiffness into elastic buckling equation (Eq. 2-10), inelastic buckling strength curve is established for wide-flange I-shaped beams failed by lateral buckling. This solution could be widely adaptable for any cross sectional shape under any residual stress distributions provided that bending takes place in a plane of symmetry and that the residual stress are also symmetrical about the plane bending.

$$(EI_y)_e = (EI_y) \cdot B_1 = (EI_y) \cdot \left[\frac{1}{2} (1 + (1 - 2\alpha)^3 - 8 \cdot \psi^3) \right] \quad (2-12a)$$

$$(EC_w)_e = (EI_y) \cdot (d - t_f)^2 \cdot B_2 = (EI_y) \cdot (d - t_f)^2 \cdot \frac{(1 - 8\psi^3)(1 - 2\alpha)^3}{4B_1} \quad (2-12b)$$

$$(GJ)_e = GJ \quad (2-12c)$$

where

B_1, B_2 is the inelastic reduction factor for weak and warping stiffness proposed in Galambos (1963)

$(EI_y)_e$ is effective flexural stiffness in inelastic range

$(EC_w)_e$ is effective warping stiffness in inelastic range

$(GJ)_e$ is effective torsional stiffness in inelastic range

α, ψ is the reduction factor reflecting the magnitude of the yielding

Also, the extension of the work could be applied to the lateral buckling strength of beams subjected to unequal bending moment, where the distribution of yielding along the beam length is non-uniform. The solution would be obtainable by solving differential equations of LTB with methods such as finite difference method.

2.3.1.3 Literature review: Lay and Galambos (1965) paper

An analytical solution to predict the rotation capacity of a beam according to unsupported length is presented by adopting T-column model. In the study, following conditions are assumed.

- 1) A material having yield plateau and strain hardening were assumed
- 2) Slip theory is assumed to derive tangent modulus at the yield plateau region (Eq. 2-13c, the derivation of tangent modulus in yield plateau region extensively discussed in chapter IV)
- 3) The contribution of web to inelastic lateral stiffness neglected, yielding lower bound solution
- 4) The effects of lateral bending (the results of LTB) which trigger following local buckling could be considered by modifying the stiffness reduction factor c at Eq. 2-13c. Also, it assumed that local buckling occurs when the material has reached the onset of strain-hardening
- 5) The value of the effective length factor (k), provided when the continuous bracing applied, offered by adjacent span is taken 0.54 for elastic adjacent spans.

By adopting the T-column, the author presented following suggestion. The compressive part of a beam member under uniform moment could be idealized as a column under an axial force $P=A \cdot \sigma_y/2$, where A is the cross-section area of the beam. By assuming that the end of this column is simply

supported, the critical load of this T-column is derived as follows (Fig. 2-24).

$$P_{cr} = \frac{A\sigma_y}{2} = \frac{\pi^2 cEI}{L_b^2} \quad (2-13a)$$

$$\frac{k \cdot L_b}{r_y} = \pi \sqrt{c} \sqrt{\frac{E}{\sigma_y}} \quad (2-13b)$$

$$c = \frac{1}{1 + 0.7Rh\left(\frac{1}{s-1}\right)} \quad (2-13c)$$

$$L_{pd,Lay} = \frac{\pi}{0.54} \cdot r_y \sqrt{\frac{E}{F_y}} \frac{1}{\sqrt{1 + F\left(\frac{hR}{s-1}\right)}} \quad (2-13d)$$

where

P_{cr} is buckling load in T-column approach by Lay and Galambos (1965)

c is the flexural stiffness reduction factor in T-column approach by Lay and Galambos (1965)

$h = E / E_{st}$ is the ratio of elastic modulus to strain-hardening modulus

$s = \varepsilon_{st} / \varepsilon_y$ is the ratio of strain at the onset of strain-hardening (ε_{sh}) to yield strain (ε_y)

R is rotation capacity

$$F = \frac{\frac{1}{2} + \frac{1}{2\sqrt{h}} - \frac{1}{h}}{\frac{2}{\pi} + \frac{1}{2}\left(1 - \frac{2}{\pi}\right)\left(1 - \frac{1}{\sqrt{h}}\right)}$$

Applying $s=11.5$, $h=33$, $\sigma_y=35$ ksi for predicting Lee and Galambos (1962) experiment, $s=11.5$, $h=33$, $\sigma_y=43$ ksi for Prasad and Galambos (1963), $s=10.5$, $h=45$, $\sigma_y=54$ ksi for Adams, Lay, Galambos (1965), the proposed method very well predict the measured rotation capacities of previous experiments with lower bound solution (Fig. 2-25)

2.3.2 I-Beams under moment gradient

Contrary to the uniform moment loading, the moment in the gradient loading is a function of z . Consequently, the governing differential equation has a variable coefficient as Eq. 2-14. Therefore, a numerical procedure, such as finite difference, finite integral and finite element methods were required.

$$\frac{d^4 \gamma}{dz^4} - \frac{GJ}{EC_w} \frac{d^2 \gamma}{dz^2} - \frac{M_0^2}{EI_y \cdot EC_w} \cdot [1 - (z/L) \cdot (1 - m_R)]^2 \cdot \gamma = 0 \quad (2-14)$$

where

γ is the rotation of the cross section

$m_R = M_{e1} / M_{e2}$ is ratio of end moments where $M_{e2} = M_0$ is the larger moment between two

Furthermore, as the participation of yielding along the length become different for each load level from M_y to M_{max} , the inelastic sectional properties such $(EI_y)_e$, $(EC_w)_e$, and $(GJ)_e$ must be recalculated. In other words, the assumption (=the cross sectional and material properties are uniform along whole length of the beam) is not valid anymore. For the solution of such problems, many researchers have been attempted. Depending on the solution methods, the solution procedures were different. The procedure could be generalized as follows.

One-dimensional line element (having three dimensional degree of freedom) with the effective cross-section properties such $(EI_y)_e$, $(EC_w)_e$ and $(GJ)_e$ were used for inputting the geometrical and material information. Depending

on the load level whether it invokes yielding of a material, the complexity of the input procedure become significantly different. If the load does not trigger yielding of a material, the elastic properties could be used. However, if the load triggers yielding of a material, the inelastic properties depending on the load level should be inputted separately.

After setting up all the process, it lead to a set of linear equations as Eq. 2-15a. Computer methods of obtaining the matrix $[A]$ may be based on the differential equation which govern the bending and the out-of-plane line model of the beam, or on the balance between strain energy stored and work done during buckling. Then, the non-trivial solutions of these equation (Eq. 2-15b) are obtained by finding the buckling load levels and a corresponding series of buckled shapes obtained from the vector.

$$[A]\{u\} = 0 \quad (2-15a)$$

$$\det|A| = 0 \quad (2-15b)$$

where

$[A]$ is the matrix containing the effective cross-section properties and destabilizing matrix

$\{u\}$ is set of the out-of-plane displacement such rotation or lateral deflection, eigenvector

$\det|A| = 0$ is the determinant of the matrix A, resulting in a polynomial function

In detail, for elastic methods of buckling analysis, Eq. 2-15 can be developed as Eq. 2-16, which is a standard eigenvalue equation. However, in inelastic buckling problems, the stiffness and the stability matrices $[K]$ and $[G]$

must be recalculated for each load level because of the changes in the inelastic section properties. It seems that reasonable computation procedure is performed by iterating computing procedure through a series of load levels from first yield by reasonably small increments.

$$([K] - \lambda[G])\{u\} = 0 \quad (2-16)$$

where

$[K]$ is the stiffness matrix with elastic properties for eigenvalue analysis

$[G]$ is the stability matrix representing the destabilizing effects of an initial set of applied loads

$[\lambda]$ is load factor, eigenvalue

Lay and Galambos (1967) used the equivalent length concept to analyzed the lateral-torsional buckling of beams under moment gradient (Fig. 2-26). Nethercot (1972a,b, 1973a,b, 1974a,b, 1975a,b,c) applied the finite element method to the inelastic lateral buckling of steel beams. Kitipornchai and Trahiar (1975a,b, and c) applied the finite integral method to the inelastic lateral buckling of steel beams.

2.4 Summary

1) Previous studies have extensively (experimentally and analytically) focused on finding adequate each slenderness ratio such as lateral slenderness (L_b/r_y) or flange ($b/2t_f$) and web (h/t_w) width-to-thickness ratios independently by restraining early lateral and local buckling to ensure the target inelastic rotation capacity of a member.

2) Analytically, many researchers have proposed governing equations of inelastic lateral and local buckling and their solutions for providing the adequate slenderness ratios. However, the solutions of such equations mainly focus on mild steel, the material properties of which are well described with the tri-linear stress-strain model. No adequate inelastic solutions have been attempted for high strength steel, the post-yield range properties of which significantly differ from mild steel.

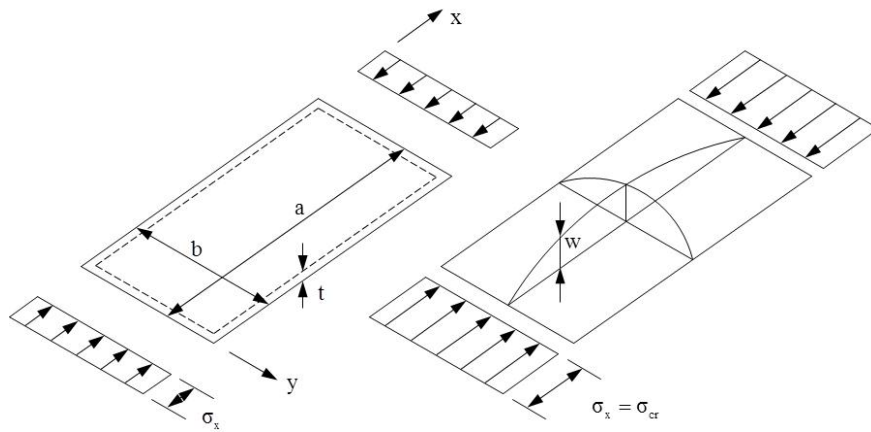
3) Experimentally, the inelastic behaviors of I-shaped member, affecting the strength and rotation capacity of a member, significantly differ between the uniform moment and moment gradient loadings conditions, and these behaviors have been separately investigated. The inelastic behaviors could be generalized as follows. Under the uniform moment loading case, at the initial loading condition, a very slight lateral deflection is noticeable at the center of the beam span. As the loading is increased beyond the yield moment, the compression flange begins to lose the elastic stiffness, due to flange yielding, and the lateral deflections become more visually pronounced. As the loading maintains the level (mild steel is under yield plateau region) and the end rotation is increased further, the magnitude of the lateral deflection is more magnified, triggering the bifurcation from the in-plane moment-rotation curve and inducing an additional 2nd-order moment at the beam center, which degrades the beam capacity significantly, which is known as inelastic lateral instability.

Meanwhile, in a moment gradient case, the beam behaves elastically until yielding. Once the maximum moment at the loading point exceeds the plastic moment, the end rotation starts to increase measurably. Contrary to the uniform moment case, the yielding only could spread from the loading point to the adjacent region when the maximum moment continues to increase above plastic moment level. The more the maximum moment continues to increase, the larger the portion of the beam participates the yielding from the loading point to the adjacent region. When the spreading of yielding is sufficient to trigger local buckling, Lay (1963) proposed that the local buckling initiated when the compression flange has yielded over a length sufficient to accommodate the full wavelength of the buckled shape, the flange local buckling starts to occur. However, the initiation of the local buckling does not directly cause any degradation, and the moment continues to increase with increasing rotation until the lateral movement of the compression flange and web distortion becomes pronounced. The member strength then starts to degrade significantly with the increase in lateral deflection.

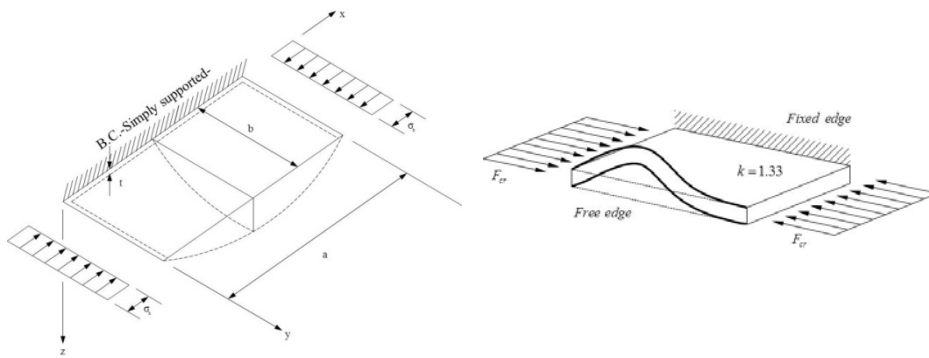
4) Regarding the key analytical studies under uniform moment, the researches by White (1956), Galambos (1963), and Lay and Galambos (1965) seems to be pivotal. The crucial analytical studies under moment gradient are the researches by Lay and Galambos (1967), Nethercot (1972-a,b, 1973-a,b, 1974-a,b, 1975-a,b,c), and Kitipornchai and Trahair (1975a,b,c). A summary

of each study is given in the main body of this paper.

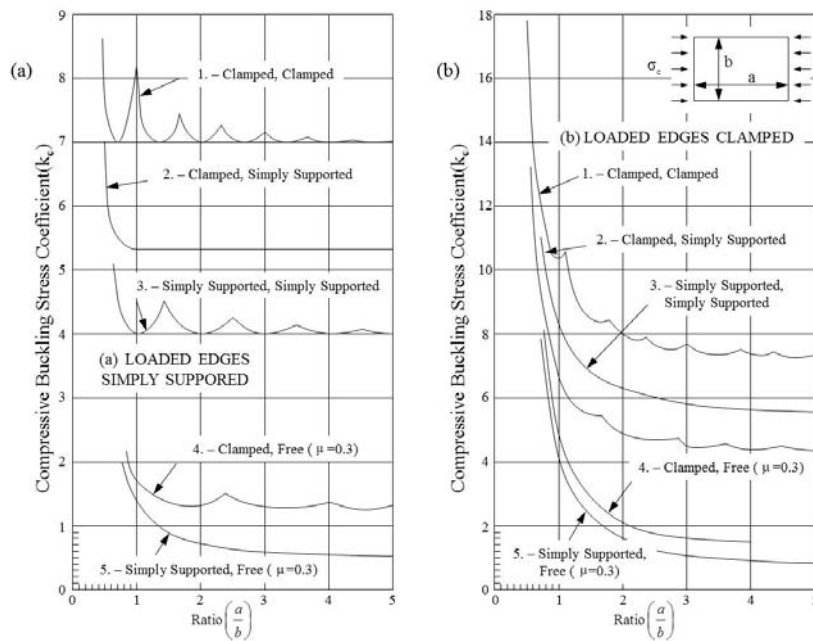
5) For the key experimental studies under uniform moment, the researches by Lee and Galambos (1962), Adams, Lay and Galambos (1965), McDermott (1969), and Holt & Kulak (1973) seem to be pivotal. The crucial experimental studies under moment gradient are the research by Adams, Lay and Galambos (1965), Lukey and Adams (1969), Smith and Adams (1968), and Roik and Kuhimann (1987). A summary of each study is given in the main body of this paper.



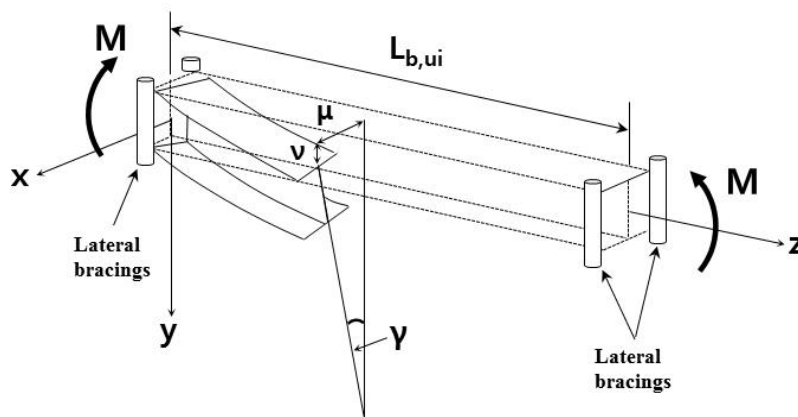
[2-1] Buckling shape of a simply-supported rectangular plate subjected to uniform compression



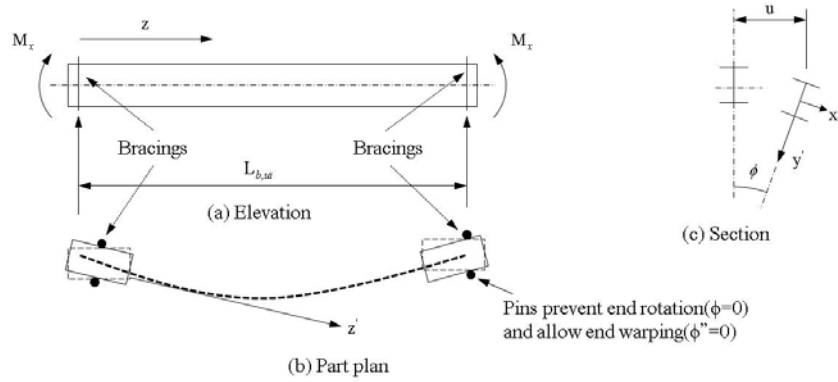
[2-2] Flange local buckling plate subjected to uniform compression with center line boundary conditions



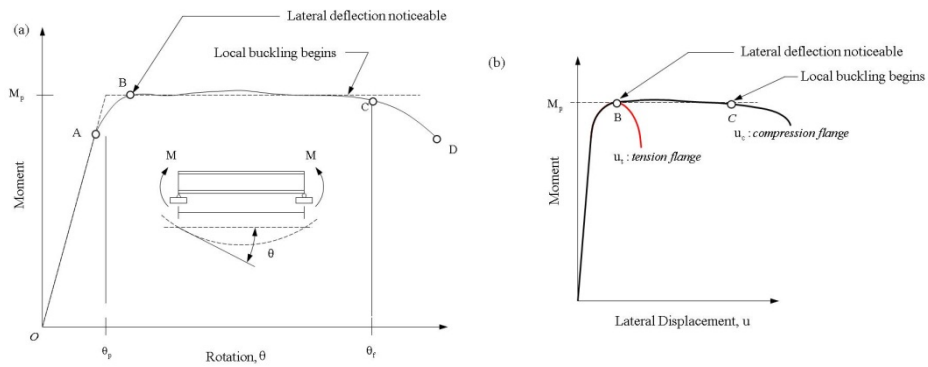
[2-3] Value of compressive buckling stress coefficient for flat plates: (a) loaded edges simply-supported; and (b) loaded edges clamped [Stowell et al., 1951]



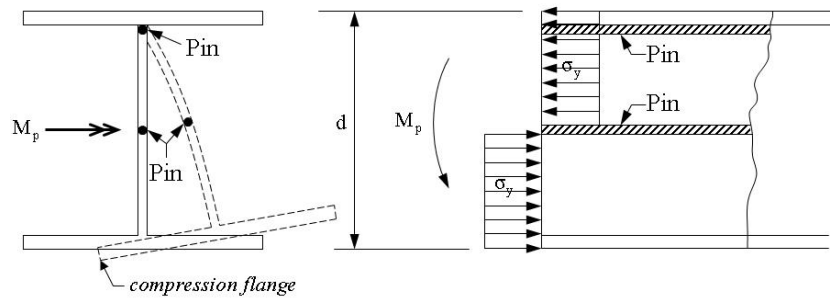
[2-4] Lateral torsional buckling of I-shaped member under uniform moment loading



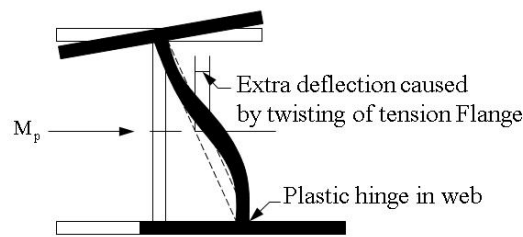
[2-5] Model of a simply-supported beam subjected to a uniform bending moment M_x [White, 1956] showing (a) elevation view, (b) part plan view with boundary conditions, and (c) typical cross-section with displacement degrees of freedom



[2-6] Typical beam behavior under uniform moment: (a) moment-rotation relationship and (b) moment-lateral displacement relationship

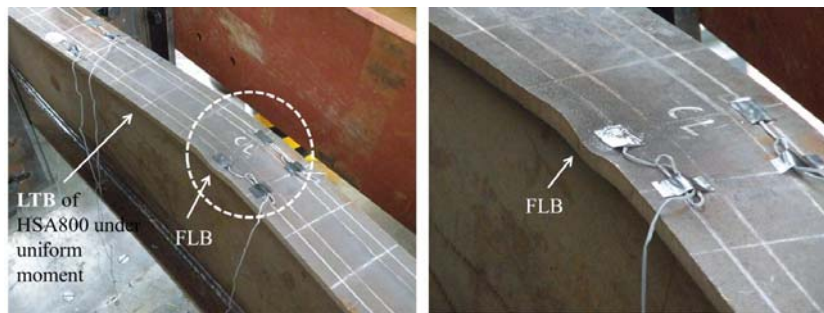


(a) Beam model

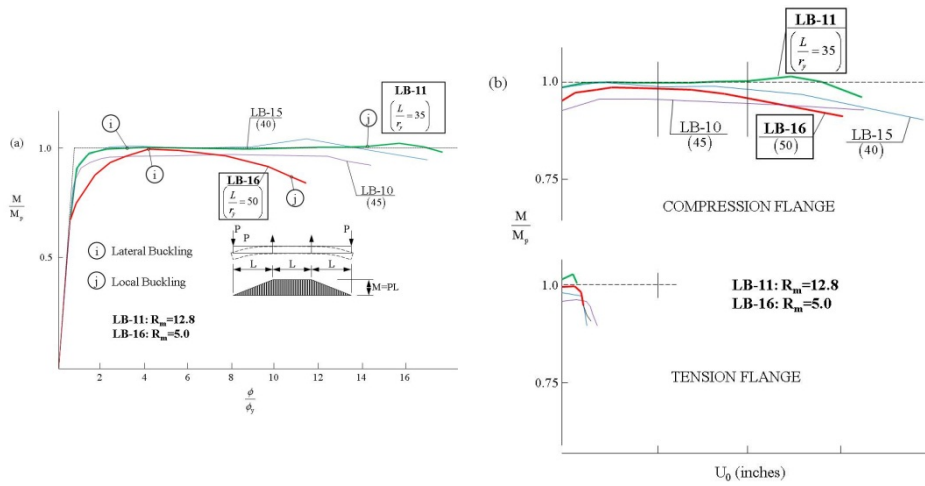


(b) Observed deformed shape

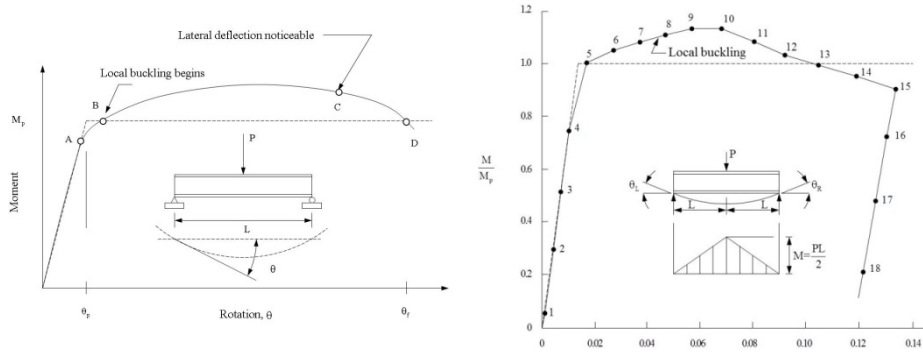
[2-7] Lateral buckling model of the cross-section under uniform moment by Lay and Galambos[1965] showing: (a) beam model; and (b) observed deformed shape



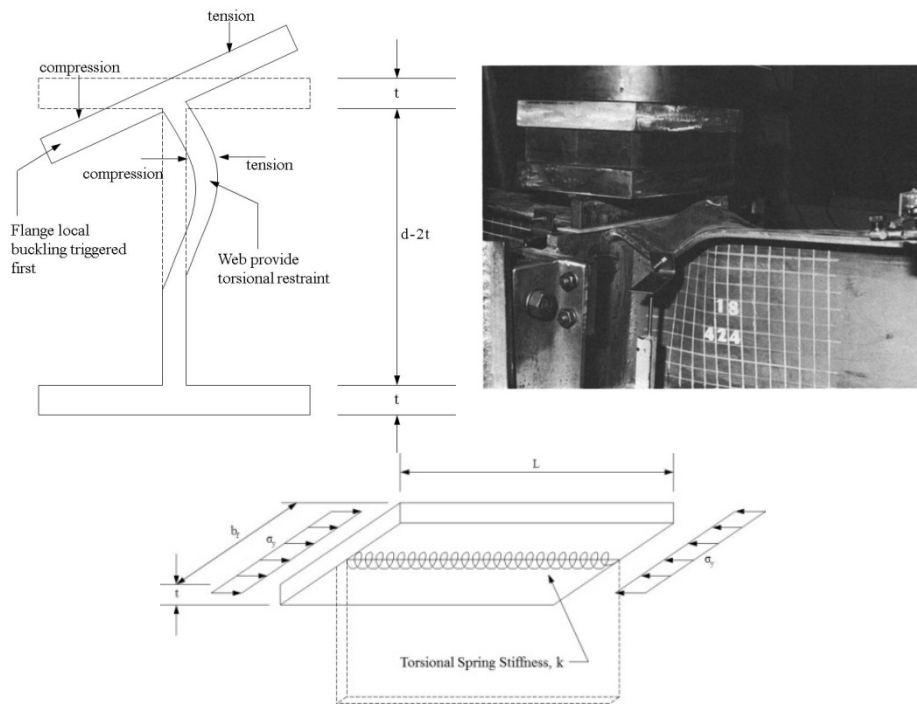
[2-8] Flange local buckling at the half of the compression flange after lateral torsional buckling triggered in current experimental study of HSA800 I-shaped member



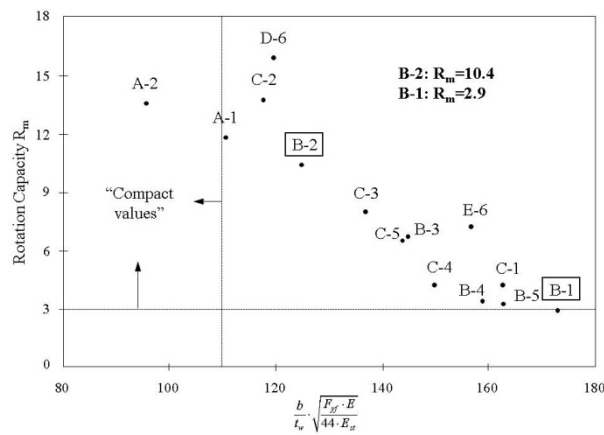
[2-9] Experimental beam behavior under uniform moment from Lee and Galambos [1962]: (a) moment-midspan curvature relationship; (b) moment-lateral deflection relationship



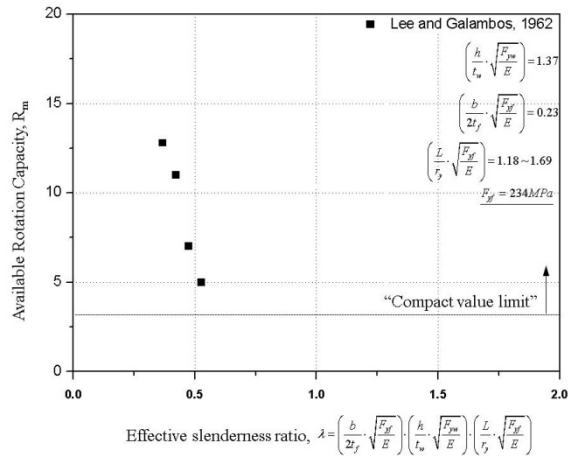
[2-10] Typical beam behavior under moment gradient (a) Typical moment-end rotation curve (b) Experimental beam behavior under moment gradient from Lukey and Adams [1969] showing moment-end rotation relationship



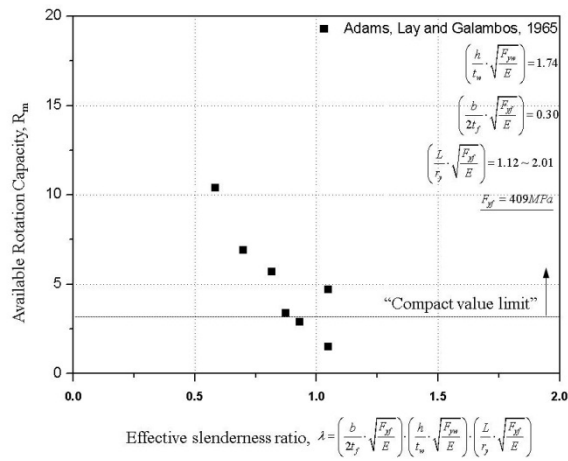
[2-11] Compression flange model considering web restraint by Lay



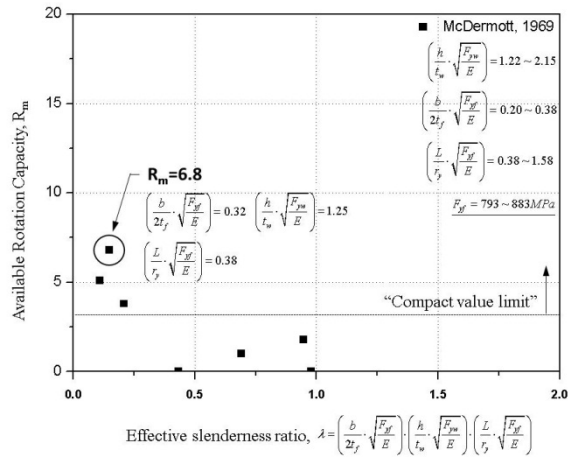
[2-12] Peak and total rotations, experimental/theoretical values, from moment gradient tests performed by Lukey and Adams [1969]



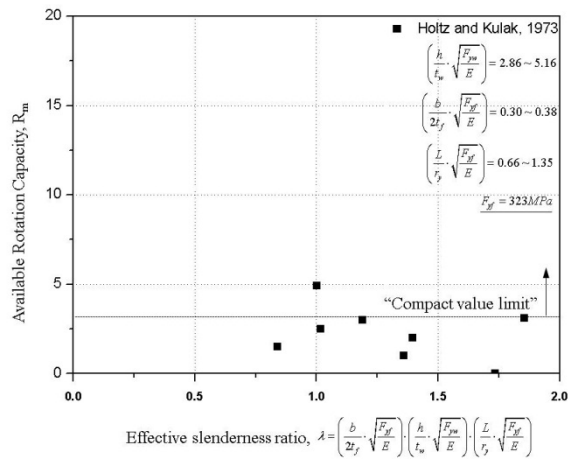
[2-13] Experimental rotation capacity values under uniform moment performed by Lee and Galambos [1962]



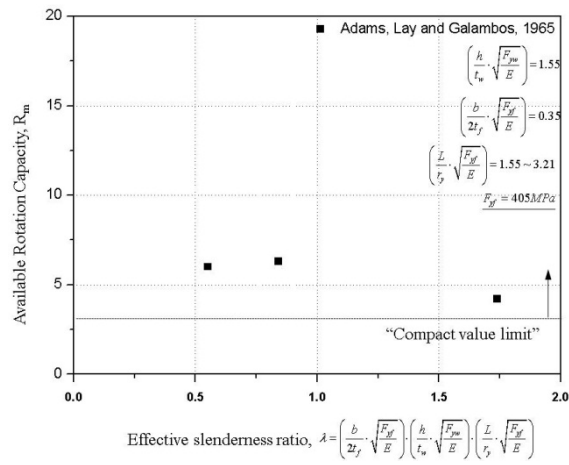
[2-14] Experimental rotation capacity values under uniform moment performed by Adams, Lay and Galambos [1965]



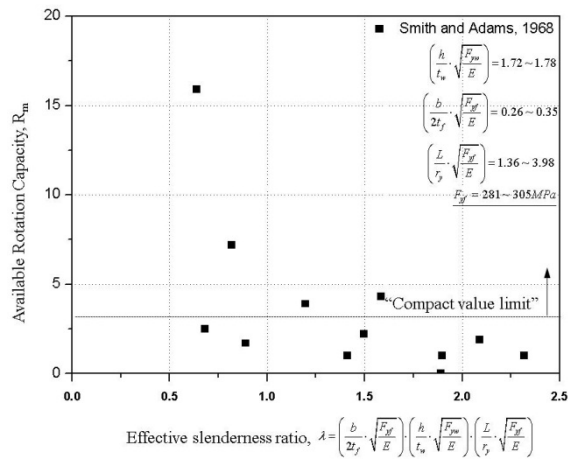
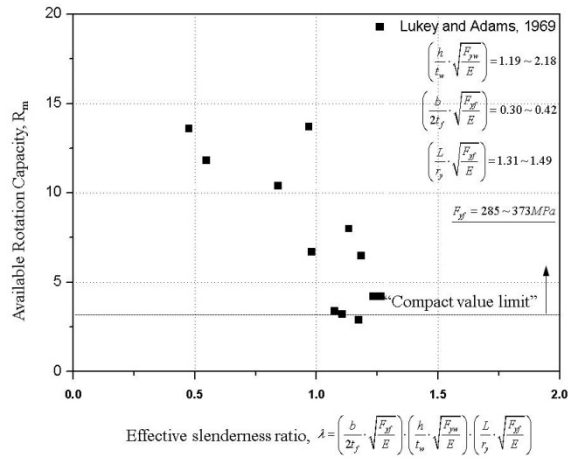
[2-15] Experimental rotation capacity values under uniform moment performed by McDermott [1969]



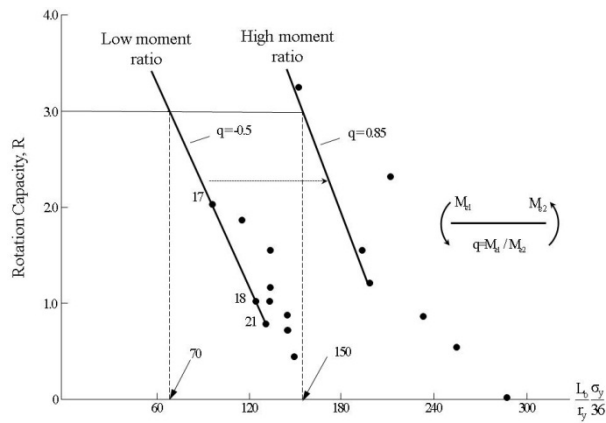
[2-16] Experimental rotation capacity values under uniform moment performed by Holtz and Kulak [1973]



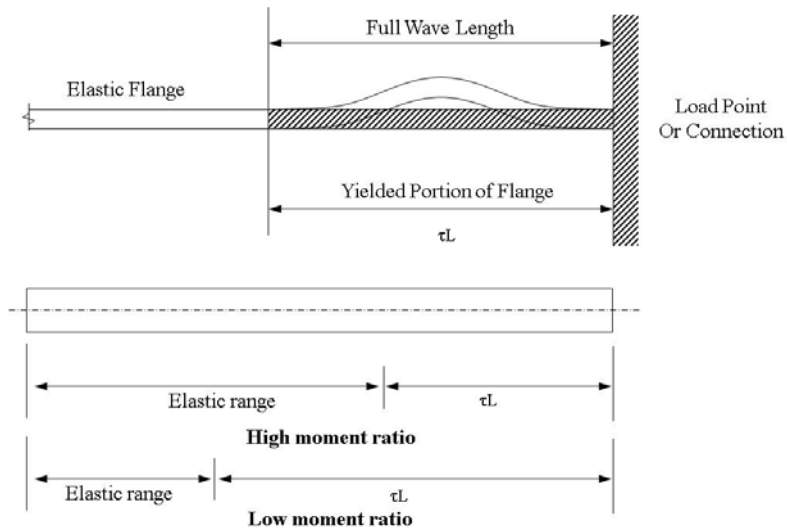
[2-17] Experimental rotation capacity values under moment gradient performed by Adams, Lay and Galambos [1965]



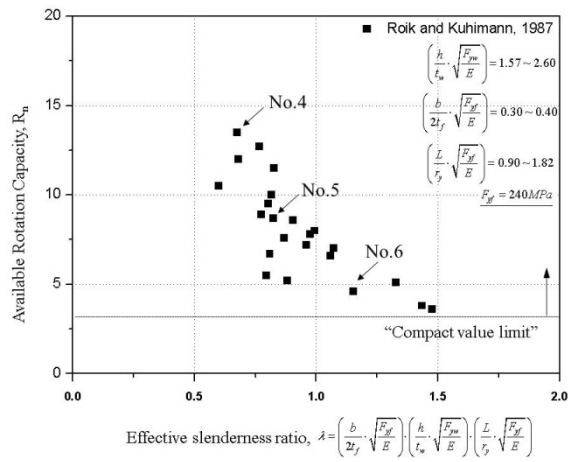
[2-18] Experimental rotation capacity values under moment gradient performed by (a) Lukey and Adams [1969] (b) Smith and Adams [1968]



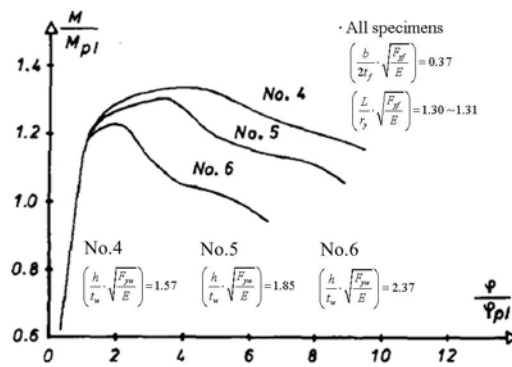
[2-19] Experimental test data from Bansal [1971] showing relationships between rotation capacity, R and normalized lateral slenderness ratio according to end moment ratio, q (in U.S. Units)



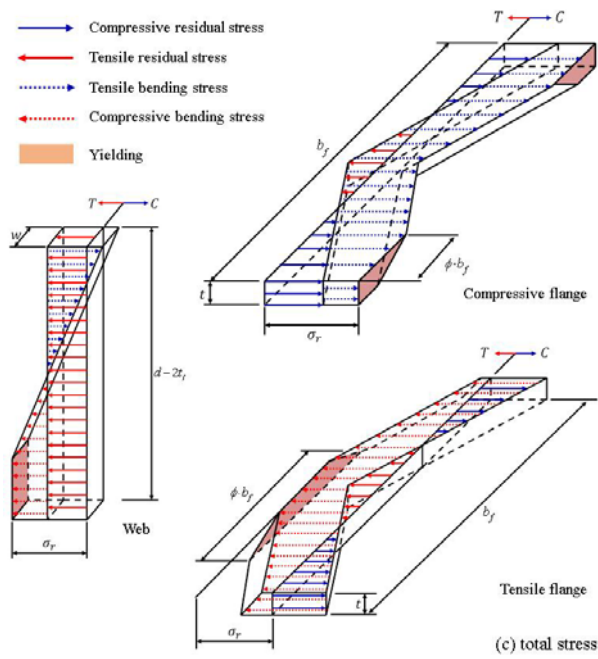
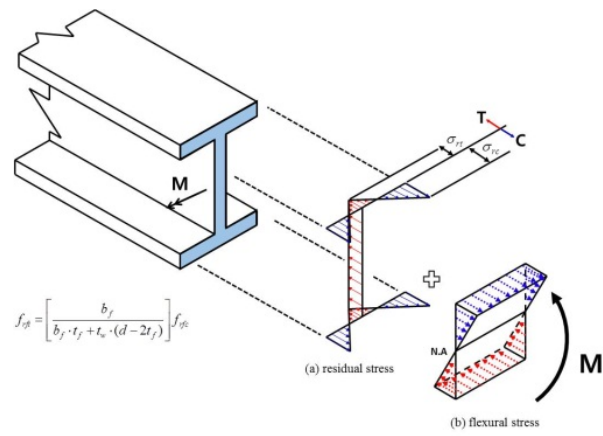
[2-20] Local buckling conditions of the flange subjected to a moment gradient described by Lay[1965b]



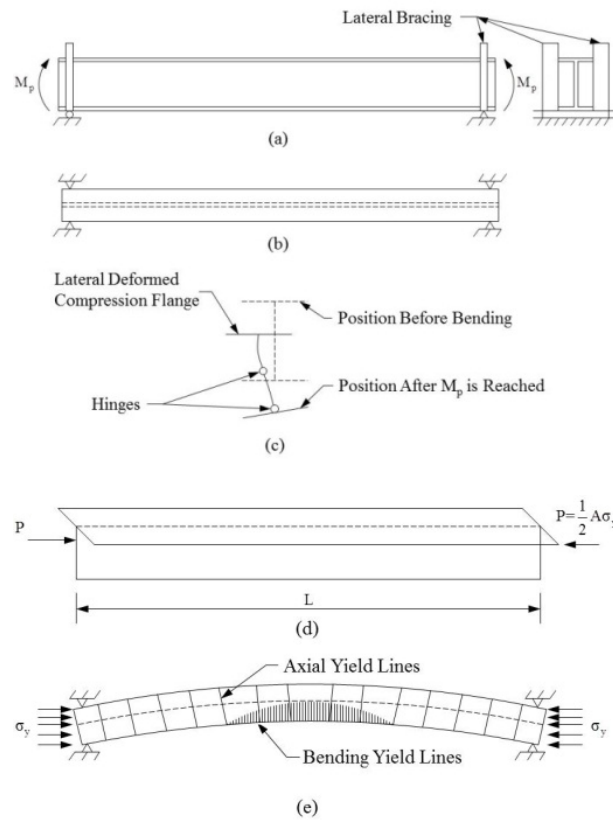
[2-21] Experimental rotation capacity values under moment gradient performed by Roik and Kuhmann, [1987]



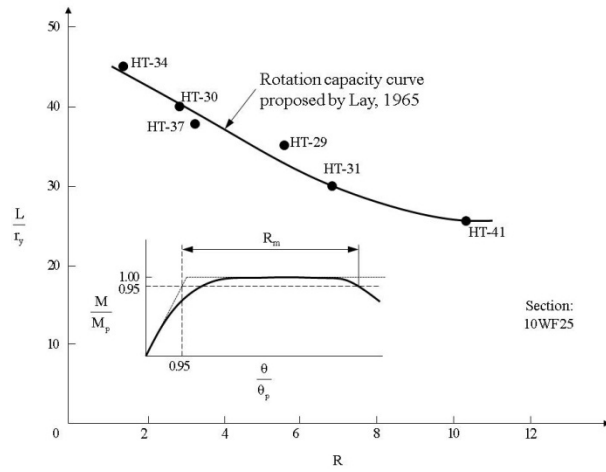
[2-22] Effects of torsional constraint to the rotation capacity to same flange slenderness specimens (No.4~No.6) described by Roik and Kuhmann [1987]



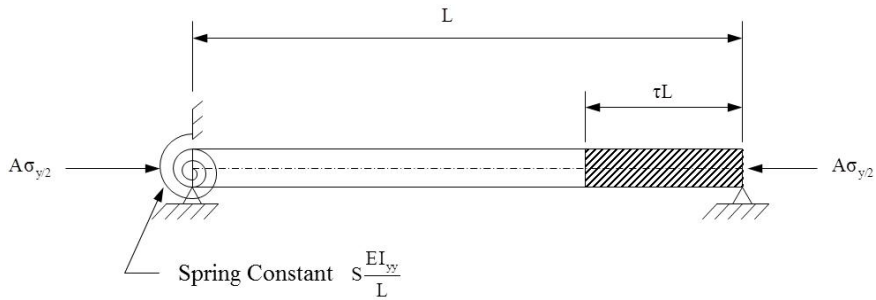
[2-23] The method to calculate (inelastic) effective rigidities by Galambos [1963]



[2-24] Uniform moment buckling model by Lay and Galambos[1965]: (a) beam model; (b) lateral bracing; (c) cross-section deformations; (d) effective column model; and (e) lateral distortion showing axial and bending yield lines



[2-25] Rotation capacity of beams under uniform moment [Lay and Galambos, 1965]



[2-26] Lateral buckling model for a beam under moment gradient by Lay and Galambos [1967]

[2-1] Historical experimental uniform moment test data

Lee and Galambos, 1962											
Test No.	σ_{yf} (MPa)	σ_{yw} (MPa)	$b/2t_f \cdot (\sigma_{yf}/E)^{0.5}$	$h_c/t_w \cdot (\sigma_{yw}/E)^{0.5}$	$L/r_y \cdot (\sigma_{yf}/E)^{0.5}$	R_m	M_p (kN-m)	M_u (kN-m)	θ_p (rad)	θ_u (rad)	θ_H (rad)
LB-10	234	267	0.23	1.37	1.52	7.0	116		0.0157		0.1100
LB-11	234	267	0.23	1.37	1.18	12.8	115		0.0120		0.1541
LB-15	234	267	0.23	1.37	1.35	11.0	116		0.0139		0.1526
LB-16	234	267	0.23	1.37	1.69	5.0	115		0.0173		0.0866
Notes:											
1) θ_p , θ_H calculated from given properties											
2) Nominal material yield strength is 228MPa											
3) R_m =Rotation capacity at maximum load											

Prasad and Galambos, 1963											
Test No.	σ_{yf} (MPa)	σ_{yw} (MPa)	$b/2t_f \cdot (\sigma_{yf}/E)^{0.5}$	$h_c/t_w \cdot (\sigma_{yw}/E)^{0.5}$	$L/r_y \cdot (\sigma_{yf}/E)^{0.5}$	R_m	M_p (kN-m)	M_u (kN-m)	θ_p (rad)	θ_u (rad)	θ_H (rad)
G9	296	296	0.28	1.58	1.52	2.6	76		0.0108		0.0280
G10	296	296	0.28	1.58	1.33	3.8	76		0.0094		0.0358
G11	296	296	0.28	1.58	1.71	1.5	76		0.0121		0.0182
G12	296	296	0.28	1.58	1.14	4.6	76		0.0081		0.0372
Notes:											
1) M_p , θ_p , θ_H calculated from given properties											
2) Nominal material yield strength is 248MPa											
3) R_m =Rotation capacity at maximum load											

Chapter 2. Previous researches

[2-1] Historical experimental uniform moment test data (continued)

Adams, Lay, Galambos, 1965											
Test No.	σ_{yt} (MPa)	σ_{yw} (MPa)	$b/2t_f \cdot (\sigma_{yt}/E)^{0.5}$	$h_c/t_w \cdot (\sigma_{yw}/E)^{0.5}$	$L/r_y \cdot (\sigma_{yt}/E)^{0.5}$	R_m	M_p (kN·m)	M_u (kN·m)	θ_p (rad)	θ_u (rad)	θ_H (rad)
HT-29	409	428	0.30	1.74	1.56	5.7	198		0.0208		0.1185
HT-30	409	428	0.30	1.74	1.79	2.9	198		0.0238		0.0689
HT-31	409	428	0.30	1.74	1.34	6.9	198		0.0178		0.1229
HT-36	409	428	0.30	1.74	2.01	1.5	198		0.0267		0.0401
HT-37	409	428	0.30	1.74	1.67	3.4	198		0.0223		0.0757
HT-41	409	428	0.30	1.74	1.12	10.4	198		0.0148		0.1544
HT-38	409	428	0.30	1.74	2.01	4.7	198		0.0267		0.1256

Notes:

- 1) For HT-38 only the center span was subjected to a moment that varied from a maximum at one interior support to $0.8M_{max}$ at the other; $L/r_y=35, 45, 45$
- 2) Rotation capacities were taken at $0.95M/M_p$ on the unloading branch of the M- θ curve
- 3) M_p, θ_p, θ_H calculated from given properties
- 4) Nominal material yield strength is 335MPa
- 5) R_m =Rotation capacity at maximum load

[2-1] Historical experimental uniform moment test data (continued)

McDermott, 1969											
Test No.	σ_{yf} (MPa)	σ_{yw} (MPa)	$b/2t_f \cdot (\sigma_{yf}/E)^{0.5}$	$h_c/t_w \cdot (\sigma_{yw}/E)^{0.5}$	$L/r_y \cdot (\sigma_{yf}/E)^{0.5}$	R_m	M_p (kN·m)	M_u (kN·m)	θ_p (rad)	θ_u (rad)	θ_H (rad)
1	862	862	0.80	1.63	0.75	0.0	402	313	0.0857		
2	883	883	0.53	1.40	0.59	0.0	488	474	0.0878		
3	793	793	0.38	1.22	0.45	3.8	441	445	0.0777		0.2978
4	814	814	0.32	1.25	0.38	6.8	391	399	0.0807		0.5512
5	821	821	0.25	1.24	0.34	5.1	327	334	0.0827		0.4203
6	827	800	0.20	2.15	1.58	1.0	347	354	0.0601		0.0626
7	821	800	0.30	2.07	1.51	1.8	490	490	0.0879		0.1547
Notes:											
1) Sections used for beam tests 1-5 were machined to the given dimensions											
2) Nominal material yield strength is 690MPa											
3) R_m =Rotation capacity at maximum load											

Chapter 2. Previous researches

[2-1] Historical experimental uniform moment test data (continued)

Holtz and Kulak, 1973											
Test No.	σ_{yf} (MPa)	σ_{yw} (MPa)	$b/2t_f \cdot (\sigma_{yf}/E)^{0.5}$	$h_c/t_w \cdot (\sigma_{yw}/E)^{0.5}$	$L/r_y \cdot (\sigma_{yf}/E)^{0.5}$	R_m	M_p (kN·m)	M_u (kN·m)	θ_p (rad)	θ_u (rad)	θ_H (rad)
WS-1	323	288	0.38	2.86	1.27	2.0	410	434	0.0334		
WS-2	323	288	0.38	3.58	1.35	3.1	549	555	0.0271		
WS-3	323	288	0.38	4.32	1.24	0.0	704	649	0.0286		
WS-4	323	288	0.38	5.16	1.11	0.0	866	771	0.0296		
WS-6	323	288	0.38	3.42	1.32	0.0	503	445	0.0287		
WS-7-P	323	288	0.32	3.06	1.22	3.0	382	382	0.0282		
WS-8-P	323	288	0.32	3.39	1.26	1.0	447	426	0.0254		
WS-9	323	288	0.38	2.80	0.95	2.5	394	442	0.0214		
WS-10	323	288	0.38	3.05	0.85	4.9	433	517	0.0199		
WS-11	323	288	0.38	3.33	0.66	1.5	489	540	0.0183		

Notes:

- 1) L' is the unbraced length of the uniform moment region
- 2) Nominal material yield strength is 303MPa
- 3) R_m =Rotation capacity at maximum load

[2-2] Historical experimental moment gradient test data

Sawyer, 1961											
Test No.	σ_{yf} (MPa)	σ_{yw} (MPa)	$b/2t_f(\sigma_{yf}/E)^{0.5}$	$h_c/t_w(\sigma_{yw}/E)^{0.5}$	$L/r_y(\sigma_{yf}/E)^{0.5}$	R_m	M_p (kN·m)	M_u (kN·m)	θ_p (rad)	θ_u (rad)	θ_H (rad)
4	283	317	0.25	1.25	0.69		92.6	127.1	0.0091	0.0952	
5	283	317	0.25	1.25	0.94	13.0	92.6	123.6	0.0124	0.0869	0.1608
6	283	317	0.25	1.24	1.30	10.	91.1	119.0	0.0169	0.0920	0.1691
7	286	390	0.26	0.83	0.63	27.0	47.5	69.8	0.0144	0.1921	0.3897
8	286	390	0.26	0.84	0.85	16.0	47.0	67.0	0.0193	0.1625	0.3096
9	286	390	0.26	0.84	1.19	14.0	47.5	66.4	0.0272	0.1985	0.3804
10	262	279	0.19	1.41	0.71	21.0	92.5	116.9	0.0050	0.0568	0.1052
11	262	279	0.19	1.42	0.96	19.0	91.5	122.9	0.0067	0.0682	0.1273
12	262	279	0.19	1.43	1.34	11.0	90.4	116.4	0.0092	0.0544	0.1017
13	268	326	0.26	1.61	0.68	12.0	201.4	248.2	0.0071	0.0447	0.0858
14	268	326	0.26	1.60	0.92	8.0	200.4	249.1	0.0096	0.0457	0.0769
15	268	326	0.26	1.64	1.28	9.0	201.0	253.8	0.0134	0.0695	0.1209
16	304	374	0.33	2.26	0.88	8.0	99.6	102.9	0.0058	0.0205	0.0468
17	304	374	0.34	2.30	1.19	1.0	99.0	97.3	0.0078	0.0141	0.0078
18	304	374	0.35	2.38	1.65	2.0	97.6	98.5	0.0107	0.0136	0.0214
19	284	308	0.35	0.99	0.63	8.0	146.5	171.7	0.0138	0.0673	0.1105
20	284	308	0.35	0.99	0.85	7.0	146.1	163.4	0.0187	0.0560	0.1306
21	284	308	0.35	1.00	1.19	7.0	147.0	154.3	0.0262	0.0902	0.1832

Notes:

- 1) Rotation Capacity information was estimated from the test data as given in ASCE-WRC (1971)
- 2) Nominal material yield strength is 228MPa
- 3) θ_p , θ_H calculated from given properties, R_m =Rotation capacity at maximum load

Chapter 2. Previous researches

[2-2] Historical experimental moment gradient test data (continued)

Adams, Lay, Galambos, 1965											
Test No.	σ_{yf} (MPa)	σ_{yw} (MPa)	$b/2t_f \cdot (\sigma_{yf}/E)^{0.5}$	$h_c/t_w \cdot (\sigma_{yw}/E)^{0.5}$	$L/r_y \cdot (\sigma_{yf}/E)^{0.5}$	R_m	M_p (kN·m)	M_u (kN·m)	θ_p (rad)	θ_u (rad)	θ_H (rad)
HT-28	405	459	0.35	1.55	1.55	6.3	71.8	82.0	0.0165	0.0740	0.1040
HT-43	405	459	0.35	1.55	1.02	6.0	66.5	75.1	0.0100	0.0390	0.0600
HT-52	405	459	0.35	1.55	3.21	4.2	100.2	114.0	0.0476	0.0860	0.2000
Notes:											
1) θ_H extrapolated for HT-52											
2) θ_H , M_p calculated from given properties											
3) Nominal material yield strength is 335 MPa, R_m =Rotation capacity at maximum load											

[2-2] Historical experimental moment gradient test data (continued)

Lukey and Adams, 1967											
Test No.	σ_{yf} (MPa)	σ_{yw} (MPa)	$b/2t_f \cdot (\sigma_{yf}/E)^{0.5}$	$h_c/t_w \cdot (\sigma_{yw}/E)^{0.5}$	$L/r_y \cdot (\sigma_{yf}/E)^{0.5}$	R_m	M_p (kN·m)	M_u (kN·m)	θ_p (rad)	θ_u (rad)	θ_H (rad)
Series A, B, and C Test Results- Total Rotations, Yielded Lengths and Peak Rotations											
A-1	285	309	0.35	1.19	1.31	11.8	179.1		0.0220	0.1134	0.2600
A-2	285	309	0.30	1.19	1.31	13.6	168.9		0.0200	0.1220	0.2720
B-1	373	396	0.42	1.89	1.49	2.9	47.8		0.0145	0.0282	0.0420
B-2	373	396	0.30	1.89	1.49	10.4	44.3		0.0115	0.04888	0.1200
B-3	373	396	0.35	1.89	1.49	6.7	48.9		0.0137	0.518	0.0920
B-4	373	396	0.38	1.89	1.49	3.4	52.3		0.0153	0.0302	0.0520
B-5	373	396	0.39	1.89	1.49	3.2	50.7		0.0150	0.0296	0.0480
C-1	373	352	0.41	2.18	1.41	4.2	72.8		0.0117	0.0236	0.0490
C-2	373	352	0.30	2.18	1.49	13.7	57.7		0.0082	0.0483	0.1120
C-3	373	352	0.35	2.18	1.49	8.0	62.9		0.0098	0.0296	0.0780
C-4	373	352	0.38	2.18	1.49	4.2	66.4		0.0107	0.0216	0.0450
C-5	373	352	0.36	2.18	1.49	6.5	65.8		0.0105	0.0316	0.0680
Notes:											
1) Lateral bracing at loadpoint and supports only						4) θ_p , M_p calculated from given properties					
2) $L=33r_y$ for C-1; $L=35r_y$ otherwise where L is the half span of the beam						5) Nominal material yield strength is 303 MPa					
3) R_m =Rotation capacity at maximum load											

Chapter 2. Previous researches

[2-2] Historical experimental moment gradient test data (continued)

Smith and Adams, 1968											
Test No.	σ_{yf} (MPa)	σ_{yw} (MPa)	$b/2t_f(\sigma_{yf}/E)^{0.5}$	$h_c/t_w(\sigma_{yw}/E)^{0.5}$	$L/r_y(\sigma_{yf}/E)^{0.5}$	R_m	M_p (kN·m)	M_u (kN·m)	θ_p (rad)	θ_u (rad)	θ_H (rad)
Series D and E Test Results- Total Rotations, Yielded Lengths and Peak Rotations											
D-1	286	370	0.26	1.77	2.60	3.9	33.5		0.0164	0.0318	0.0640
D-2	290	376	0.27	1.78	1.44	2.5	33.7		0.0244	0.0264	0.0610
D-3	301	373	0.27	1.78	3.98	0.0				0.0000	
D-4	281	382	0.25	1.77	3.15	1.0	32.6		0.0330	0.0156	0.0330
D-5	281	382	0.26	1.77	3.31	2.2	34.4		0.0214	0.0242	0.0470
D-6	305	380	0.27	1.73	1.36	15.9	34.8		0.0086	0.0624	0.1360
E-1	301	373	0.34	1.71	2.69	4.3	40.9		0.0228	0.0372	0.0980
E-2	286	370	0.34	1.76	1.48	1.7	37.8		0.0324	0.0300	0.0550
E-3	281	366	0.34	1.76	3.88	1.0	38.6		0.0330	0.0198	0.0330
E-4	281	366	0.34	1.76	3.17	1.0	38.4		0.0460	0.0190	0.0460
E-5	290	376	0.35	1.78	3.38	1.9	38.6		0.0284	0.0194	0.0540
E-6	305	380	0.35	1.72	1.35	7.2	40.8		0.0115	0.0360	0.083
Notes: 1) Lateral bracing at loadpoint and supports only Specimens D, E-1, 3, 5, 6; Lateral bracing at loadpoint, supports, and at L' away from midspan, Specimens D, E-2, 4											
2) Slenderness parameter based on L or L'											
3) θ_p , M_p calculated from given properties											
4) Nominal material yield strength is 303 MPa											
5) R_m =Rotation capacity at maximum load											

[2-2] Historical experimental moment gradient test data (continued)

McDermott, 1969											
Test No.	σ_{yf} (MPa)	σ_{yw} (MPa)	$b/2t_f \cdot (\sigma_{yf}/E)^{0.5}$	$h_c/t_w \cdot (\sigma_{yw}/E)^{0.5}$	$L/r_y \cdot (\sigma_{yf}/E)^{0.5}$	R_m	M_p (kN·m)	M_u (kN·m)	θ_p (rad)	θ_u (rad)	θ_H (rad)
Beam A	827	800	0.21	2.12	1.19	2.0	331.0	387.3	0.0354	0.1020	0.0716
Beam B	821	800	0.30	2.10	0.87	2.1	466.6	531.9	0.0519	0.1532	0.1074
Notes:											
1) Failures occurred abruptly at or near maximum load, therefore $\theta_H = \theta_{HM}$											
2) Nominal material yield strength is 690 MPa											
3) R_m = Rotation capacity at maximum load											

Chapter 2. Previous researches

[2-2] Historical experimental moment gradient test data (continued)

Kemp, 1986											
Test No.	σ_{yf} (MPa)	σ_{yw} (MPa)	$b/2t_f(\sigma_{yf}/E)^{0.5}$	$h_c/t_w(\sigma_{yw}/E)^{0.5}$	$L/r_y(\sigma_{yf}/E)^{0.5}$	R_m	M_p (kN·m)	M_u (kN·m)	θ_p (rad)	θ_u (rad)	θ_H (rad)
1C1	339	358	0.38	1.39	2.18	4.8	121.0	135.5	0.0302	0.0000	0.1454
2F4	285	329	0.25	1.27	1.98	6.0	120.5	139.2	0.0260		0.1570
3F12	332	387	0.30	2.05	3.46	1.7	117.7	116.1	0.0260		0.0445
4S5	340	358	0.36	1.36	1.09	6.2	127.0	147.3	0.0151		0.0935
5S7	294	300	0.33	1.25	1.02	8.5	107.2	132.2	0.0130		0.1102
6S6	288	329	0.24	1.29	1.03	9.9	119.7	153.3	0.0131		0.1294
7W3	374	403	0.37	2.76	2.58	2.6	250.1	265.3	0.0209		0.0537
8W9	313	300	0.31	0.64	1.83	8.6	70.0	86.4	0.0457		0.3903
9A2	340	358	0.33	1.51	2.19	4.5	128.5	142.6	0.0298		0.1330
10A13	307	387	0.29	2.13	3.42	0.0	109.1	109.1	0.0242		
11A1A	343	392	0.34	2.35	2.50	0.0	232.9	232.9	0.0369		
12A2A	317	351	0.30	2.07	4.15	1.8	101.0	105.2	0.0287		0.0517

Notes:

- 1) Letters denote predominant test factor: C=Control; F=Flange Slenderness; S=Lateral Slenderness; W=Web Slenderness; A=Coincident Axial Force Applied
- 2) Web slenderness h_c/t_w would be adjusted to account for axial force shifting N.A.
- 3) Rotation Capacity information was estimated from empirical equation developed based on effective lateral slenderness ration and yielded length
- 4) Nominal material yield strength is 248MPa
- 5) R_m =Rotation capacity at maximum load

[2-2] Historical experimental moment gradient test data (continued)

Roik and Kuhmann, 1987											
Test No.	σ_x (MPa)	σ_{yw} (MPa)	$b/2t_f(\sigma_{yf}/E)^{0.5}$	$h_c/t_w(\sigma_{yw}/E)^{0.5}$	$L/r_y(\sigma_{yf}/E)^{0.5}$	R_m	M_p (kN-m)	M_u (kN-m)	θ_p (rad)	θ_u (rad)	θ_H (rad)
1	236	217	0.30	1.85	1.80	8.0	97.1	118.5	0.0070	0.0303	0.0563
2	236	217	0.32	1.85	1.82	7.0	102.0	131.5	0.0076	0.0321	0.0535
3	449	217	0.44	1.67	2.53	10.0	197.2	209.1	0.0142	0.0242	0.0142
4	287	260	0.37	1.57	1.31	12.7	125.7	167.1	0.0068	0.0297	0.0859
5	287	252	0.37	1.85	1.31	8.6	118.7	154.3	0.0070	0.0245	0.0603
6	287	259	0.37	2.37	1.30	4.6	115.5	142.0	0.0072	0.0136	0.0330
7	287	252	0.37	2.01	0.90	13.5	130.5	171.0	0.0044	0.0301	0.0598
8	287	252	0.37	2.01	1.10	11.5	130.5	173.6	0.0054	0.0233	0.0623
9	287	252	0.37	2.00	1.31	7.8	130.0	176.7	0.0064	0.0193	0.0501
10	236	217	0.36	1.86	1.19	5.5	113.2	135.9	0.0057	0.0235	0.0315
11	236	217	0.39	1.67	1.20	8.9	121.3	155.3	0.0062	0.0241	0.0549
12	236	217	0.40	1.67	1.29	7.6	125.7	158.3	0.0064	0.0212	0.0489
13	333	709	0.28	2.66	1.79	5.1	175.6	210.7	0.0121	0.0326	0.615
14	333	709	0.30	2.65	1.79	3.8	180.1	217.9	0.0128	0.0333	0.0486
15	333	709	0.31	2.64	1.81	3.6	192.1	234.3	0.0138	0.0360	0.0498
16	333	709	0.32	1.69	1.12	10.5	107.8	135.9	0.0132	0.0607	0.1386
17	333	709	0.32	2.24	1.12	9.5	150.9	199.2	0.0100	0.0361	0.0952
18	333	709	0.32	2.97	1.10	6.6	220.1	281.8	0.0076	0.0227	0.0500
19	333	349	0.32	1.97	1.07	12.0	193.9	255.9	0.0059	0.0283	0.0708
20	333	349	0.32	1.97	1.29	8.7	194.7	260.9	0.0071	0.0318	0.0614
21	333	349	0.32	1.97	1.51	7.2	194.7	259.0	0.0082	0.0354	0.0593
22	333	349	0.34	1.97	1.21	10.0	204.4	267.7	0.0071	0.0226	0.0705
23	333	349	0.36	1.97	1.15	6.7	221.8	281.7	0.0073	0.0270	0.0488
24	333	349	0.38	1.97	1.19	5.2	227.0	286.0	0.0079	0.0267	0.0409

Chapter 2. Previous researches

[2-2] Historical experimental moment gradient test data (continued)

Boeraeve et al., 1992											
Test No.	σ_{yf} (MPa)	σ_{yw} (MPa)	$b/2t_f(\sigma_{yf}/E)^{0.5}$	$h_c/t_w(\sigma_{yw}/E)^{0.5}$	$L/r_y(\sigma_{yf}/E)^{0.5}$	R_m	M_p (kN·m)	M_u (kN·m)	θ_p (rad)	θ_u (rad)	θ_H (rad)
Steel D1	303	342	0.27	0.77	1.11	16.8	187.0		0.0262	0.1127	0.4402
Steel D2	375	421	0.29	0.78	1.24	12.1	236.0		0.0314		0.3799
Steel D3	445	462	0.31	0.83	1.34	10.0	287.0		0.0367		0.3670
Steel D4	261	291	0.25	0.65	1.04	24.3	166.0		0.0209		0.5079
Steel D5	409	426	0.30	0.83	1.30	9.2	266.0		0.0332		0.3054

Notes:

- 1) L is the half-span of the overall specimens
- 2) Nominal material yield strength are in MPa: D1(St37-2)=430; D2(St52-3)=510; D3(FeE460)=460; D4(FeE235)=235; D5(FeE420)=420
- 3) R_m =Rotation capacity at maximum load

Ito et al., 2005											
Test No.	σ_{yf} (MPa)	σ_{yw} (MPa)	$b/2t_f(\sigma_{yf}/E)^{0.5}$	$h_c/t_w(\sigma_{yw}/E)^{0.5}$	$L/r_y(\sigma_{yf}/E)^{0.5}$	R_m	M_p (kN·m)	M_u (kN·m)	θ_p (rad)	θ_u (rad)	θ_H (rad)
HY60	559.1	324.0	0.28	2.38	3.39	2.24	262.7		0.033		
HO60	559.1	599.3	0.28	2.46	2.29	1.52	292.7		0.025		
HY80	559.1	324.0	0.28	3.18	3.82	0.50	365.4		0.026		
HO80	592.8	613.0	0.28	3.22	2.92	0.47	412.5		0.024		
HY90	559.1	324.0	0.28	3.75	3.99	0.46	411.8		0.024		
HO90	559.1	599.3	0.28	3.69	2.78	0.32	488.3		0.019		

Notes:

- 1) R_m =Rotation capacity at maximum load

Chapter 3 Idealized Material Models and In-plane Rotation Capacities

As mentioned in Chapter I, current codes have been developed from the certain grades of the steel with the assumed material model. However, as the shapes of the stress-strain curve vary significantly according to the grades of steel, material models which are able to consider the unique properties of various grades of steel are essential. Unfortunately, the data of high strength steel is scant. Even for common grades, it is difficult to obtain the data such strain-hardening characteristics and yield stress, since these are not routinely measured in quality control test (Technical Memorandum 7 in Galambos, 1988). Carefully experimented tensile coupon data of the various steel grades (=including 800MPa tensile strength steel) performed by KS B 0802 testing procedure are presented in this chapter. The data presented in this study are the couponing specimens (KS B 0801) from SM490, SM570 and HSA800 plates developed in POSCO (A steel making company, headquarter of which are located in South Korea).

3.1 Characteristics of stress-strain curves

Fig. 3-1 and Table 3-1 ~ Table 3.3 showed the tensile coupon properties of HSA800, SM570 and SM490 steel plate respectively. The characteristics of the stress-strain curves are represented by the four parameters such as

magnitude of strain hardening (Y/T strength ratio, $Y_R = F_y/F_u$), length of yield plateau (Y/P length, $S = \epsilon_{st}/\epsilon_y$), elongation at ultimate tensile strength (T/Y strain ratio, $E_R = \epsilon_u/\epsilon_y$) and elongation at fracture (EF, ϵ_f). All parameter do not represent consistent trend according to steel grades. Even, at the same grade steel plate (for example 12mm thick and 25mm thick plates of SM570), the properties are significantly different depending on the plate thickness and others. However, two parameters (Y/T ratio and T/Y strain ratio) have been shown relatively significant correlation with the variation of the yield strength of steel plate, as presented below.

3.1.1 Y/T strength ratio according to yield strength

A Y/T strength ratios(Y_R), which are the most frequently and extensively appeared parameters in various material specification, product standard, design codes since it is convenient means to assess a material's ability. The Y/T ratios of 12mm, 25mm thick SM570 plates and 15mm, 25mm thick HSA800 plates are shown in [Table 3-4](#). The values of the Y/T ratio become higher, as the yield strength of steel plates are increased. By statistically analyzing the correlations between two variables calculated by [Eq. 3-1](#), Pearson correlation coefficient (r) is 0.964, implying relatively strong and positive correlation between two.

$$r = \frac{\sum_{i=1}^n ((x_i - \bar{x})(y_i - \bar{y}))}{\sqrt{\sum_{i=1}^n (x_i - \bar{x})^2 \sum_{i=1}^n (y_i - \bar{y})^2}} \quad (3-1)$$

where

x_i, y_i are the values of the paired data

\bar{x}, \bar{y} are the means value of the paired data

n is number of the paired data

r is Pearson correlation coefficient

In addition, by adopting the suggested fitting curve format from the previous research (Bannister, 1988), the Y/T strength ratio could be expressed as a function of yield stress as Eq. 3-2. The constant k_y is dependent on the applied steel making processes and alloying methods. Fig. 3-2 shows the validity of the curve. The curve well predicts the variation of Y/T strength ratio according to the yield stress with Pearson correlation coefficient (r) is 0.952.

$$Y_R = \frac{1}{[1 + 2 \cdot (\frac{K_Y}{f_y})^{2.5}]} \quad (3-2)$$

where

$Y_R = F_y / F_u$ is yield to tensile strength ratio

k_y is the constant for Y/T ratio, estimated $k_y = 270$ in current study

f_y is the yield stress

3.1.2 T/Y strain ratio according to yield strength

The T/Y strain ratios (E_R) of 12mm, 25mm thick SM570 plates and 15mm,

25mm thick HSA800 plates are shown in [Table 3-5](#). The values of the T/Y strain ratio become lower, as the yield strength of steel plates are increased. By statistically analyzing the correlations between two variables calculated by [Eq. 3-1](#), Pearson correlation coefficient (r) is -0.939, implying relatively strong and negative correlation between two.

$$E_R = \frac{K_E}{(f_y)^{2.55}} \quad (3-3)$$

where

$E_R = \varepsilon_u / \varepsilon_y$ is elongation at tensile strength to yield strain ratio

k_E is the constant for T/Y strain ratio, estimated $k_E = 3 \cdot 10^8$ in current study

By adopting the inversely proportional curve format, the T/Y strain ratio could be expressed as a function of yield stress as [Eq. 3-3](#). In [Eq. 3-3](#), the constant K_E is dependent on the applied steel making processes and alloying methods as the same as Y/T ratios. [Fig. 3-3](#) shows the validity of the curve. The curve well predicts the variation of T/Y ratio according to the yield stress with Pearson correlation coefficient (r) is 0.963.

3.2 Idealized material models

In order to analyze the effect of the different shape of the stress-strain curve on the global behaviors such in-plane and out-of-plane behavior, it is inevitable or useful to have a model to idealize the initial portions of the curve, at most up to tensile strength ([Galambos, 1997](#)). The idealization become

realized since both Y/T strength ratio and T/Y strain ratio (the major two parameters determining a shape of a stress-strain curve) are well predicted according to the yield strength (F_y) by the Eq. 3-2 and Eq. 3-3.

Five models are discussed in this study. First two models No.1, No.2 (Traditional model-Fig. 3-4, Haaijer model-Fig. 3-5) are discussed to idealize the shape of the stress-strain curve for a material with yield plateau such as mild steel. Second a model No.3 (Ramberg-Osgood model-Fig.3-6) are discussed to idealized the shape of the stress-strain curve for material without yield plateau such as recently developed high strength steel. Third two models No.4, No.5 (Tri-linear model-Fig.3-7, Bi-linear model-Fig.3-8) are discussed idealized the shape of the stress-strain curve for various materials.

3.2.1 Traditional model (No. 1)

Traditional model is the simplest one to idealize the shape of stress-strain curve with yield plateau. This model has been the most widely used in the past researches for the studies of structures in the inelastic ranges. Fig. 3-4a showed the stress-strain relationship of the traditional model. It consisted of three stress components as an elastic part (#1, Eq. 3-4a) where stress and strain are proportional, plateau part (#2, Eq. 3-4b) and the initial part of the strain hardening range (#3, Eq. 3-4c).

Fig. 3-4b showed the modulus-strain relation of the traditional model. Depending on the magnitude of strain at each elastic, plateau and hardening

region, three moduli are proposed. The elastic modulus $E_{t1,mild}=E$ is used for elastic region (Eq. 3-4d) and inelastic modulus $E_{t3,mild}=E/33\sim E/49$ is used for the strain-hardened regions (Eq. 3-4h). For the yield plateau region, two or three different values of the inelastic moduli ($E_{t2,Galambos,mild}$, $E_{t2,Lay,mild}$, and $E_{t2,Trahair,mild}$) have been applied. The major reasons for the difference come from whether a slip theory is admitted in the researches.

For example, in the Galambos' 1963 year paper, $E_{t2,Galambos,mild}$ (Eq. 3-4e) was applied for the yield plateau region. However, many experimental have indicated that the zero modulus values ($E_{t2,Galambos,mild}=0$) are extremely low and yield logical paradox such zero buckling load ($P_t=\pi^2 E_{t2,Galambos,mild} I/L^2=0$) in axially loaded column when the material of the column are strained corresponding to the plateau region ($\epsilon_u < \epsilon \leq S \cdot \epsilon_y = \epsilon_{st}$). In actual, no buckling phenomenon was observed when inelastic material is under the yield plateau region if a member properly designed.

White (1960) and Lay (1965) investigated and suggested that yielding may considered as a series of discontinuous slips (here and after 'slip theory'), and that all of the material in the yielded region is either elastic or strain hardened. This led to the first proposal that the tangent modulus for the yield plateau region should be properly suggested as considering the experimental discontinuous slip phenomenon (Fig. 4-4~Fig. 4-5). From the analytical studies of the slip behaviors, the inelastic modulus ($E_{t2,Lay,mild}$) adequate for the

yield plateau region as Eq. 3-4g were derived. Please see chapter IV for the details of the derivation.

Also, as simplified approach, Trahair(1979) proposed the inelastic modulus for the yielded region should be conservatively taken as equal to the strain hardening modulus ($E_{t2,Trahair,mild} = E/h$) as described in Eq. 3-4f.

$$f = E \cdot \varepsilon \quad [\text{when } 0 \leq \varepsilon \leq \varepsilon_y] \quad (3-4a)$$

$$f = f_y \quad [\text{when } \varepsilon_y < \varepsilon \leq s \cdot \varepsilon_y = \varepsilon_{st}] \quad (3-4b)$$

$$f - f_y = \frac{E}{h} \cdot (\varepsilon - \varepsilon_{st}) \quad [\text{when } \varepsilon_{st} < \varepsilon \leq \varepsilon_u] \quad (3-4c)$$

$$E_{t1}(\varepsilon) = E \quad [\text{when } 0 \leq \varepsilon \leq \varepsilon_y] \quad (3-4d)$$

$$E_{t2,Galambos,mild}(\varepsilon) = 0 \quad [\text{when } \varepsilon_y < \varepsilon \leq s \cdot \varepsilon_y = \varepsilon_{st}] \quad \text{in 1963} \quad (3-4e)$$

Galambos's study

$$E_{t2,Trahair,mild}(\varepsilon) = E / h \quad [\text{when } \varepsilon_y < \varepsilon \leq s \cdot \varepsilon_y = \varepsilon_{st}] \quad \text{in 1979} \quad (3-4f)$$

Trahair's study

$$E_{t2,Lay,mild}(\varepsilon) = \frac{1}{\left(\frac{1}{E_{st}} - \frac{1}{E}\right)\left(\frac{\varepsilon - \varepsilon_y}{\varepsilon_{st} - \varepsilon_y}\right) + \frac{1}{E}} \quad (3-4g)$$

[when $\varepsilon_y < \varepsilon \leq s \cdot \varepsilon_y = \varepsilon_{st}$] in 1965 Lay's study

$$E_{t3,mild}(\varepsilon) = E_{st} = E / h \quad [\text{when } \varepsilon_{st} < \varepsilon \leq \varepsilon_u] \quad (3-4h)$$

where

$E_{t1}(\varepsilon) = E$ is elastic modulus at elastic region

$E_{t2,Galambos,mild}(\varepsilon)$ is inelastic modulus at yield plateau region applied in mild steel in 1963 Galambos's study

$E_{t2,Trahair,mild}(\varepsilon)$ is inelastic modulus at yield plateau region applied in mild steel in 1979 Trahair's study

$E_{t2,Lay,mild}(\varepsilon)$ is inelastic modulus at yield plateau region applied in mild steel

$E_{t3,mild}(\varepsilon)$ is inelastic modulus at strain-hardening region according to strain ε in mild steel

f_y is yield stress

$h = E / E_{st}$ is the ratio of the elastic modulus to the initial strain-hardening modulus

3.2.2 Haaijer model (No.2)

Haaijer propose a model to improve and accurately represent the strain-hardened regions of the traditional. Fig. 3-5a showed the stress-strain relationship of Haaijer model. The shape of the stress-strain curve is the same as that of the previous model up to the initiation of strain-hardening (ε_{st}). Beyond that point it follows Eq.3-5c where the Ramberg-Osgood equation are somewhat modified to represent the strain-hardening behavior. The values of the constants m, K are dependent on strain hardening magnitude and rates of a material.

Fig. 3-5b showed the modulus-strain relation of Haaijer model. It consisted of three modulus components the elastic modulus ($E_{t1}=E$) for elastic region (#1, Eq. 3-5d), inelastic modulus ($E_{t2,Lay,mild}$) for yield plateau region (#2, Eq. 3-5e) and inelastic modulus ($E_{t3,Haaijer,mild}$) for strain hardened region (#3, Eq. 3-5d) by differentiating the Eq. 3-5c with regard to ε .

$$f = E \cdot \varepsilon \quad [\text{when } 0 \leq \varepsilon \leq \varepsilon_y] \quad (3-5a)$$

$$f = f_y \quad [\text{when } \varepsilon_y < \varepsilon \leq s \cdot \varepsilon_y = \varepsilon_{st}] \quad (3-5b)$$

$$\varepsilon - \varepsilon_{st} = \frac{f - f_y}{E/h} + K \left(\frac{f - f_y}{E/h} \right)^m \quad (3-5c)$$

$$[\text{when } \varepsilon_{st} < \varepsilon \leq \varepsilon_u \text{ or } f_y < f \leq f_u]$$

$$E_{t1}(\varepsilon) = E \quad [\text{when } 0 \leq \varepsilon \leq \varepsilon_y] \quad (3-5d)$$

$$E_{t2,Lay,mild}(\varepsilon) = \frac{1}{\left(\frac{1}{E_{st}} - \frac{1}{E}\right)\left(\frac{\varepsilon - \varepsilon_y}{\varepsilon_{st} - \varepsilon_y}\right) + \frac{1}{E}} \quad (3-5e)$$

[when $\varepsilon_y < \varepsilon \leq s \cdot \varepsilon_y = \varepsilon_{st}$] in 1965 Lay's study

$$E_{t3,Haijer,mild}(\varepsilon) = \frac{E/h}{\left[1 + K \cdot m \cdot \left(\frac{f - f_y}{E/h}\right)^{m-1}\right]} \quad (3-5f)$$

[when $\varepsilon_{st} < \varepsilon \leq \varepsilon_u$]

where

$E_{t3,Haijer,mild}(\varepsilon)$ is inelastic modulus at strain hardening region by Haaijer model
 m, K are the parameters for describing the shape of strain hardening in Haaijer model

3.2.3 Ramberg-Osgood model (No.3)

Ramberg-Osgood proposed a model which is adequate for fitting total range of non-linear stress-strain curve. The model has been widely used for idealizing stress-strain curves of aluminum alloys because its prediction is very closely fit the actual behavior. The model seems to be extensively applicable to the high strength steel since the shapes of stress-strain curve between two materials are very similar.

As many specification adopt 0.2% offset method for assessing yield stress of a non-linear material as shown in Fig. 3-6a, the Ramberg-Osgood equation could be modified as Eq. 3-6a with strain hardening parameter, n . When n become close to infinite values ($n = \infty$), it represent a material with no strain hardening. When n become close to zero values ($n=0$), it represent a linearly increased material with the slope of E. Usually, in the aluminum alloys, the

values of the strain hardening parameters are $n < 10-20$ for non-heat-treated alloy and $n < 20-40$ for heat treated alloy. By very close fitting the experimental tensile coupon data (Fig. 3-7), it seems that the adequate strain hardening parameter for HSA800 are in the range of $18 < n < 35$.

Fig. 3-6b showed the modulus-strain relation of the Ramberg-Osgood model. By differentiating the Eq. 3-6a with regard to ε , the modulus ($E_{t,R-O}$) in total range could be expressed by Eq. 3-6b.

$$\varepsilon = \frac{f}{E} + 0.002 \left(\frac{f}{f_{0.2}} \right)^n \quad (3-6a)$$

[when $0 \leq \varepsilon \leq \varepsilon_u$ or $0 \leq \varepsilon \leq f_u$]

$$E_{t,R-O} = \frac{E}{\left[1 + \frac{0.002nE}{f_{0.2}} \left(\frac{f}{f_{0.2}} \right)^{n-1} \right]} \quad (3-6b)$$

[when $0 \leq \varepsilon \leq \varepsilon_u$ or $0 \leq \varepsilon \leq f_u$]

where

$E_{t,R-O}$ is tangent modulus by Ramberg-Osgood model

$f_{0.2}$ is 0.2% offset yield stress at continuous yielding material

n is hardening parameter in Ramberg-Osgood model

3.2.4 Piecewise-linear (Tri-linear and bi-linear) models (No.4)

The simplified method for fitting the non-linear stress-strain curve is piecewise idealization. The number of lines composed of the piecewise linear model are determined by considering the nonlinearity of a material. Generally, three (tri-linear) or two lines (bi-linear) are selected.

Tri-linear piecewise linear model is composed of three lines to represent an

elastic-knee-strain-hardening portion as shown in Fig. 3-8a. The three referential points in this model are the proportional limit (ε_p), strain at the 0.2% offset ($\varepsilon_{f0.2}$) and strain at tensile strength (ε_u). By the points, it consisted of three stress components as proportional part (#1, Eq. 3-7a), knee part (#2, Eq. 3-7b) and strain hardening part (#3, Eq. 3-7c).

Fig. 3-8b showed the modulus-strain relation of the tri-linear piecewise linear model. It is characterized by three moduli $E_{t1}=E$, $E_{t2,tri,HSS}$ and $E_{t3,tri,HSS}$. A model similar to this, though on the safe side, has recently been used in the latest German aluminum specification (DIN 4113) by simply neglecting the strain hardening portions as zero ($E_{t3,tri,HSS}=0$)

$$f = E \cdot \varepsilon \quad [\text{when: } 0 \leq \varepsilon \leq \varepsilon_p] \quad (3-7a)$$

$$f - f_p = \frac{(f_{0.2} - f_p)}{(\varepsilon_{f0.2} - \varepsilon_p)} (\varepsilon - \varepsilon_p) \quad [\text{when: } \varepsilon_p \leq \varepsilon \leq \varepsilon_{f0.2}] \quad (3-7b)$$

$$f - f_{0.2} = \frac{(f_u - f_{0.2})}{(\varepsilon_u - \varepsilon_{f0.2})} (\varepsilon - \varepsilon_{f0.2}) \quad [\text{when: } \varepsilon_{f0.2} \leq \varepsilon \leq \varepsilon_u] \quad (3-7c)$$

$$E_{t1}(\varepsilon) = E \quad [\text{when: } 0 \leq \varepsilon \leq \varepsilon_p] \quad (3-7d)$$

$$E_{t2,tri,HSS}(\varepsilon) = \frac{(f_{0.2} - f_p)}{(\varepsilon_{f0.2} - \varepsilon_p)} \quad [\text{when: } \varepsilon_p \leq \varepsilon \leq \varepsilon_{f0.2}] \quad (3-7e)$$

$$E_{t3,tri,HSS}(\varepsilon) = \frac{(f_u - f_{0.2})}{(\varepsilon_u - \varepsilon_{f0.2})} \quad [\text{when: } \varepsilon_{f0.2} \leq \varepsilon \leq \varepsilon_u] \quad (3-7f)$$

where

f_p is stress at the limit of proportionality at continuous yielding material

$f_{0.2}$ is 0.2% offset yield stress at continuous yielding material

f_u is tensile yield stress

ε_p is proportionality limit strain at continuous yielding material

$\varepsilon_{f0.2}$ is strain corresponding to the $f_{0.2}$ at continuous yielding material

ε_u is ultimate strain

$E_{t1}(\varepsilon) = E$ is elastic modulus

$E_{t2,tri,HSS}(\varepsilon)$ is inelastic modulus at post-proportional region by tri-linear model applied in high strength steel

$E_{t3,tri,HSS}(\varepsilon)$ is inelastic modulus at strain hardening region by tri-linear model applied in high strength steel

Bi-linear piecewise linear model is composed of two lines to represent an elastic-strain-hardening portion as shown in Fig. 3-9a. The two referential points in this models are the yield strain (ε_y) and strain at tensile strength (ε_u). By the points, it consisted of two stress components as proportional part (#1, Eq. 3-8a) and strain hardening portions (#2, Eq. 3-8b). Fig. 3-9b showed the modulus-strain relation of the bi-linear piecewise linear model. It is characterized by two moduli $E_{t1}=E$ and $E_{t2,bi,HSS}$.

$$f = E \cdot \varepsilon \quad [\text{when: } 0 \leq \varepsilon \leq \varepsilon_{y,f0.2}] \quad (3-8a)$$

$$f - f_{0.2} = \frac{(f_u - f_{0.2})}{(\varepsilon_u - \varepsilon_y)} (\varepsilon - \varepsilon_y) \quad [\text{when: } \varepsilon_{y,f0.2} \leq \varepsilon \leq \varepsilon_u] \quad (3-8b)$$

$$E_{t1}(\varepsilon) = E \quad [\text{when: } 0 \leq \varepsilon \leq \varepsilon_{y,f0.2}] \quad (3-8c)$$

$$E_{t2,bi,HSS}(\varepsilon) = \frac{(f_u - f_{0.2})}{(\varepsilon_u - \varepsilon_y)} \quad [\text{when: } \varepsilon_{y,f0.2} \leq \varepsilon \leq \varepsilon_u] \quad (3-8d)$$

where

$\varepsilon_{y,f0.2} = f_{0.2} / E$ is nominal yield strain at continuous yielding material $E_{t1}(\varepsilon)$ is elastic modulus

$E_{t2,bi,HSS}(\varepsilon)$ is inelastic modulus at strain hardening region by bi-linear model in high strength steel

3.3 In-plane rotation capacities

In the previous chapter, material models appropriate for mild steel and high strength steel are determined. From this chapter, the inelastic behavior of I-beams will be introduced. The inelastic behaviors of I-beam fabricated from mild and high strength steel were analyzed by two procedures: in-plane behavior analysis and out-of-plane behavior analysis. By the analysis of the in-plane behavior, the maximum limiting load level and the maximum inelastic rotation capacity of a member could be assessed. By the analysis of the out-of-plane behavior (such LTB and LB, which significantly curtails the in-plane behavior capacity with causing large uncontrolled deflection), the adequate unbraced length and width-to-thickness ratios could be assessed. Since the analytical approach between the in-plane behaviors and out-of-plane behaviors are significantly different, each behavior will be dealt with separate chapter (Chapter 3: in plane behaviors, Chapter IV: out-of-plane behaviors).

3.3.1 Overview and assumption

In this chapter, the in-plane behavior of I-shaped beam subjected to flexure is dealt with. In the previous Galambos, Lay and Kemp researches, the (in-plane) rotation capacity under center concentrated loading (moment gradient) were derived as Eq. 3-9 via moment-curvature analysis. Fig. 3-10 shows the curvature distribution used for deriving the Eq. 3-9 at the researches. As

shown Fig. 3-10, the curvature distribution is dependent on the material model and loading type. It is also depended on the shape of cross-sections such as I-shape or rectangular shape. Therefore, for analyzing the influence of the different material models, loading conditions and cross section shapes, analytical parametric studies considering such effects are required.

$$R_{m,gr} = \frac{\theta_m}{\theta_p} = l \left(2s - 1 + \frac{h \cdot l}{1-l} \right) \quad (3-9)$$

where

$R_{m,gr}$ is the rotation capacity at maximum moment equal to M_m under moment gradient

θ_m is the plastic end rotation when the maximum moment of member is equal to M_m

$\theta_p = M_p / EI$ is the elastic end rotation at plastic moment achieved

$s = \varepsilon_{st} / \varepsilon_y$ is the ratio of strain at the onset of strain-hardening (ε_{sh}) to yield strain (ε_y)

$h = E / E_{st}$ is the ratio of elastic modulus to initial strain-hardening modulus

$l = \frac{L_{ie}}{L}$ is the ratio of inelastic portion length (L_{ie}) to half-span length (L)

For material models (Fig. 3-11), the piecewise linear models (which was model #4 and #5 in previous chapter) are selected. In detail, bi-linear model for fitting the stress-strain curve of HSA800 and tri-linear model for fitting the stress-strain curve of SM490 were applied. The referential points in the bi-linear model are two points (R.P₁₋₂, R.P₂₋₃): the nominal yield strain ($\varepsilon_{y,0.2} = f_{0.2}/E$) and the corresponding yield stress (f_y); the strain at tensile strength (ε_u) and the corresponding tensile strength (f_u) as shown in Fig. 3-11a.

The referential points in the tri-linear model (R.P₁₋₂, R.P₂₋₃, R.P₃₋₄) are three points: the yield strain ($\epsilon_y=f_y/E$) and the corresponding yield stress (f_y); the strain hardening point (ϵ_{st}) and the corresponding yield stress (f_y); the strain at tensile strength (ϵ_u) and the corresponding tensile strength (f_u) as shown in Fig. 3-11b. By adopting this model, the easier calculations are enabled for predicting the inelastic rotation capacity of two materials. Although some discrepancies between the real shape of stress strain curve and the idealization are presented, the discrepancies are negligible for the purpose of this analysis.

Fig. 3-12a and Fig. 3-12b show the moment-curvature distributions of each HSA800 and SM490 by adopting each model. The curvature of HSA800 can be analyzed in detail as shown in Fig. 3-12c. When the applied moments (M_0) are under the plastic moment ($M_0 < M_p$), the curvature ($\phi_1 \leq \phi_{1-2}$) is linearly increased according to the magnitude of moment ($\phi_1 = M_0/EI$). It should be noted that $\phi_{1-2} = M_p/EI$ is an elastic limit where curvature is linearly increased.

As the applied moments are higher than plastic moment ($M_0 \geq M_p$), the slopes of the curvature become changed and the curvature ($\phi_{1-2} \leq \phi_2 \leq \phi_{2-3, HSA800}$) is composed of two components (ϕ_2): the elastic curvature limit ($\phi_{1-2} = M_p/EI$) and the hardening region curvature by applied moment ($(M_0 - M_p)/(E_{t2, bi, HSS} \cdot I)$). It should be noted that $\phi_{2-3, HSS} = (\epsilon_u/\epsilon_y) \cdot \phi_y$ is a limit where top flange strain reaches ET ($\epsilon_{top} = \epsilon_u$) in high strength steel.

On the other hand, the curvature of SM570, SM490 can be analyzed in

detail as shown in Fig. 3-12d and Fig. 3-12e. When the applied moments are under the plastic moment ($M_0 < M_p$), the curvature ($\phi_1 \leq \phi_{1-2}$) is linearly increased according to the magnitude of moment ($\phi_1 = M_0/EI$).

As the applied moment is equal to the plastic moment ($M_0 = M_p$), the slope of curvature become almost zero and the curvatures (ϕ_2) are located between ϕ_{1-2} and $\phi_{2-3,mild} = (\epsilon_{st}/\epsilon_y) \cdot \phi_y$. This region often called as “curvature jump region”. The magnitude of jump is depends on the yield plateau length.

As the applied moments are higher than the plastic moment ($M_0 > M_p$), the slopes of the curvature become changed and the curvature ($\phi_{2-3} \leq \phi_3 \leq \phi_{3-4}$) is composed of three components (ϕ_3): the elastic curvature limit ($\phi_{1-2} = M_p/EI$), the jumped curvature ($(\phi_{2-3} - \phi_{1-2}) = (S-1) \cdot \phi_y$) and the hardening region curvature at applied moment ($(M_0 - M_p)/(E_{t3,tri,mild} \cdot I)$). It should be noted that $\phi_{3-4,mild} = (\epsilon_u/\epsilon_y) \cdot \phi_y$ is a limit where top flange strain reaches ET ($\epsilon_{top} = \epsilon_u$) in high strength steel.

3.3.2 In-plane rotation capacity at member maximum moment

The curvature distributions along the length are subjected to the loading condition: uniform moment and moment gradient. As the larger portions of the inelastic regions ($\tau \cdot L$) are participated along the length (L), the more rotation capacity are achieved as shown in Fig. 3-13~16. The length and magnitude of inelastic curvature are determined on loading condition and moment-curvature relationship of a material. In this chapter, the simplistic

method to calculate the maximum inelastic rotation capacity is summarized.

3.3.2.1 I-member under uniform moment loading

Fig. 3-13 and 14 shows the in-plane behavior under uniform moment. Fig. 3-13,14a shows the loading condition triggering uniform moment in the middle of I-beam. Fig. 3-13,14b showed the x-z plane (in-plane) deformed shape where the vertical degree of freedom is constraint at the ends. Fig. 3-13,14c shows the moment distribution when member strength (M) reached at maximum moment of a section (M_m) where m_R is the end moment ratio where $M_{e2}=M_m$ is the large moment. Fig. 3-13,14d showed the (in-plane) moment-curvature diagram at the loading condition. The curvature distributions in the elastic ($\phi_1 \leq \phi_{1-2}$) and inelastic ($\phi_2, \phi_3 \geq \phi_{1-2}$) range are shown depending on the stress-strain profiles of materials: HSA800 and SM490.

As described in Eq. 3-10a, when the end moment ratio ($m_R=M_{e1}/M_{e2}$) is higher than value of M_y/M_m , the applied loading could be regarded as uniform moment loading since the total member length participated in inelastic range (L_i) is the same as the length between loading point ($L_i=L$). The maximum inelastic rotation capacity under uniform moment could be calculated as Eq. 3-10b.

$$L_{ie} = \tau_i \cdot L = (1.0) \cdot L \quad [\text{when: } m_R \geq (M_p / M_m)] \quad (3-10a)$$

$$R_{m,ui} = \frac{\theta_m}{\theta_p} - 1 \approx \frac{\phi_m}{\phi_y} - 1 = \frac{\varepsilon_u}{\varepsilon_y} - 1 \quad (3-10b)$$

where

$L_{ie} = \tau_i L_b$ is the inelastic portion length

τ_i is the length of inelastic portion in total member length (L)

$m_R = M_{e1} / M_{e2}$ is ratio of end moment where M_{e2} is the larger moment

$M_p = Z_x \cdot F_y$ is the plastic moment

M_m is the maximum moment calculated by strain compatibility method

$R_{m,ui}$ is the rotation capacity at maximum moment equal to M_m under uniform moment

3.3.2.2 I-member under moment gradient loading

Fig. 3-15,16 shows the in-plane behavior under moment gradient. Fig. 3-15,16a shows the loading condition triggering moment gradient condition in the middle of I-beam (concentrated three point loading). Fig. 3-15,16b showed the x-z plane (in-plane) deformed shape where the vertical degree of freedom is constraint at the ends. Fig. 3-15,16c shows the moment distribution when member strength (M) reached at its maximum moment (M_m). Fig. 3-15,16d showed the moment-curvature diagram at the loading condition. The curvature distributions in the elastic ($\phi_1 \leq \phi_{1-2}$) and inelastic ($\phi_2, \phi_3 \geq \phi_{1-2}$) range are shown depending on the stress-strain profiles of a material: HSA800 and SM490.

As described in Eq. 3-11a, when the end moment ratio (m_R) is lower than value of M_p/M_m , the applied loading could be regarded as moment gradient loading since the member length participated in inelastic range (L_i) is constrained in ($\tau_i < 1.0$). The inelastic region participation ratio (τ_i) is determined as Eq. 3-11b. The maximum inelastic rotation capacity under

moment gradient could be calculated as Eq. 3-11c.

$$L_{ie} = \tau_i \cdot L \quad [\text{when: } m_R \leq (M_p / M_m)] \quad (3-11a)$$

$$\tau_i = \frac{(M_m - M_p)}{(1 - m_R)(M_m)} = \frac{[1 - (M_p / M_m)]}{(1 - m_R)} \approx \frac{(1 - Y_R)}{(1 - m_R)} \quad (3-11b)$$

$$R_{m,gr} = \frac{\theta_m}{\theta_p} - 1 \approx \frac{\int_0^L \phi_m(z) dz}{\int_0^L \phi_y(z) dz} - 1 \quad (3-11c)$$

where

$R_{m,gr}$ is the rotation capacity at maximum moment equal to M_m under uniform moment

$\phi_m(z)$ is longitudinal curvature distribution when the maximum moment of a member is equal to M_m

$\phi_y(z)$ is longitudinal curvature distribution when the maximum moment of a member is equal to M_y

The calculation procedure of Eq. 3-11 is as follow. The end rotation ($\theta_p \approx \theta_y$) when the maximum moment is equal to the plastic moment is calculated as Eq. 3-12.

$$\theta_p \approx \theta_y = \int_0^L \phi_y(z) dz = (1 + m_R) \cdot \left[\frac{L}{2} \right] \cdot \phi_y \quad (3-12)$$

where

$\theta_p = M_p / EI$ is the elastic end rotation at plastic moment achieved

The end rotation (θ_m) when the maximum moment is equal to (M_m) are calculated as Eq. 3-13 for HSA800 (Fig.3-17a) where yield plateau does not existed and Eq. 3-14 for SM570 (Fig.3-17b) and SM490 (Fig.3-17c) where yield plateau are existed.

$$\theta_{m,HSS} = \int_0^L \phi_m(z) dz = \theta_{m1,HSS} + \theta_{m2,HSS} + \theta_{m3,HSS} \quad (3-13a)$$

$$\theta_{m1,HSS} = \left[\frac{(1+m_R)}{2} \cdot (1-\tau_i) \right] \cdot \left[\frac{L}{2} \right] \phi_y \quad (3-13b)$$

$$\theta_{m2,HSS} = (\tau_i) \cdot \left[\frac{L}{2} \right] \phi_y \quad (3-13c)$$

$$\theta_{m3,HSS} = \left[\frac{(\varepsilon_u / \varepsilon_y - 1)}{2} \cdot \tau_i \right] \cdot \left[\frac{L}{2} \right] \phi_y \quad (3-13d)$$

where

$\theta_{m,HSS}$ is the plastic end rotation when the maximum moment of member is equal to M_m in high strength steel

$\theta_{m1,HSS}, \theta_{m2,HSS}, \theta_{m3,HSS}$ are the components of the plastic end rotation at maximum moment of member is equal to M_m in high strength steel

$$\theta_{m,mild} = \int_0^L \phi_m(z) dz = \theta_{m1,mild} + \theta_{m2,mild} + \theta_{m3,mild} + \theta_{m4,mild} \quad (3-14a)$$

$$\theta_{m1,mild} = \left[\frac{(1+m_R)}{2} \cdot (1-\tau_i) \right] \cdot \left[\frac{L}{2} \right] \phi_y \quad (3-14b)$$

$$\theta_{m2,mild} = (\tau_i) \cdot \left[\frac{L}{2} \right] \phi_y \quad (3-14c)$$

$$\theta_{m3,mild} = (s-1) \cdot (\tau_i) \cdot \left[\frac{L}{2} \right] \phi_y \quad (3-14d)$$

$$\theta_{m4,mild} = \left[\frac{(\varepsilon_u / \varepsilon_y - 1)}{2} \cdot \tau_i \right] \cdot \left[\frac{L}{2} \right] \phi_y \quad (3-14e)$$

where

$\theta_{m,mild}$ is the plastic end rotation when the maximum moment of member is equal to M_m in mild steel

$\theta_{m1,mild}, \theta_{m2,mild}, \theta_{m3,mild}, \theta_{m4,mild}$ are the components of the plastic end rotation at maximum moment of member is equal to M_m in mild steel

3.3.2.3 Simplified approach for estimating in-plane rotation capacity of SM490, SM570 and HSA800 I-members

Since the moment-curvature relationship is dependent on the shape of the cross-section, the shape of the stress-strain of a material and the type of loading, parametric study was performed for analyzing those effects on in-plane rotation capacity. Table 3.6 summarized the parameters being discussed in this study.

Geometrical parameter is designated as [G:] and the dimension of I-section designated as H-[depth x width x web thickness x flange thickness], the representation of which follows the Korea industrial standard. [G:A-S] ~ [G:A-F] show the selected section from 250(depth) x 150(width) series section. [G:A-S] is standard section assuming I-section fabricated from the same-thickness plate. The dimension of [G:A-S] is H-[250x150x14x14]. [G:A-W], the dimensions of which are H-[250x150x28x14], is web reinforced (thicker plate applied) I-section from [G:A-S]. [G:A-F], the dimensions of which are H-[250x150x14x28], is flange reinforced (thicker plate applied) I-section from [G:A-S]. By comparing the result of [G:A-S] ~ [G:A-F], the effect of thickness reinforcement on the in-plane behavior could be investigated.

From [G:B-S] to [G:B-F] showed the selected section from 400(depth) x 150(width) series section. In the 400x150 series section, no parameters were changed except the height of I-section from the 250x150 series section. By

comparing [G:B-S] with [G:A-S], [G:B-W] with [G:A-W], [G:B-F] with [G:A-F], the effect of the increased depth on the in-plane behavior could be investigated.

Material parameter is designated as [M:Ho- F_{yw} - F_{yf}]. The yield strength of flange and web are designated as F_{yf} and F_{yw} . When the yield strength of flange and web is identical the I-section are designated as [Ho] abbreviated from homogeneous. [M:Ho-722] indicate homogeneous I-section fabricated from HSA800 plate, the web and flange yield strengths are $F_{yf} = F_{yw} = 722\text{MPa}$. [M:Ho-471] indicate homogeneous I-section fabricated from SM570 plate, the web and flange yield strengths are $F_{yf} = F_{yw} = 471\text{MPa}$. [M:Ho-349] indicate homogeneous I-section, the web and flange yield strengths are $F_{yf} = F_{yw} = 349\text{MPa}$.

The values of inelastic rotation capacities show the larger value as the external loading is close to the uniform moment case as compared to the moment gradient case. The major reason such tendency come from that the length of inelastic portion ($\tau_i \cdot L$) become higher as loading is closer to uniform moment as compared to Fig. 3-13~16 respectively.

At the uniform moment loading condition, the inelastic rotation capacity ($R_{m,ui}$) is directly proportional to the T/Y strain (E_R) ratio. It could be expressed as follows: $R_{m,ui} = E_R - 1$. Other parameters such the Y/T ratio (Y_R) and the EST/EY ($E_{st,R}$) ratio are not influential to the inelastic rotation capacity under uniform moment loading since the total portion of the span

length ($\tau_i \cdot L = 1.0 \cdot L$) spatially participate the inelastic behavior at once. As E_R of SM490, SM570 and HSA800 is about 90.0, 35.0 and 15.0, the maximum inelastic rotation capacity ($R_{m,ui}$) of I-shaped member would be 89.0, 34.0 and 14.0 respectively, provided the in-plane behaviors are assumed only.

Please note that the in-plane rotation capacity is ideal value and, in reality, is not fully realized since the out-of-plane behavior such LTB and LB curtail the rotation capacity significantly, triggering severe buckling of compression flanges. This issue will be discussed in Chapter 4 in detail.

At the moment gradient loading condition, the inelastic rotation capacity ($R_{m,gr}$) is increased as the moment ratio ($m_R = M_{e1}/M_{e2}$) is close to the unit value ($m_R = 1.0$). The major reason such tendency comes from the wider inelastic participated length ($\tau_i \cdot L$) as the moment ratio become closer to the unit value. The most severe case (the least rotation capacity) is when the moment ratio is equal to zero ($m_R = 0$). Table 3-7 and Table 3-8 summarized the maximum inelastic rotation capacities at the moment gradient condition ($m_R = 0$), calculated by Eq. 3-10~3.14.

Three parameters such Y_R , E_R and $E_{st,R} = S$ are all together influential on the rotation capacity of such loading condition. As Y_R is become lower, the maximum moment (M_m) increased simultaneously, resulting in large inelastic participation length ($\tau_i \cdot L$) length. The maximum moment (M_m) of HSA800, SM570 and SM490 are 1.60~1.70, 1.45~1.60 and 1.35~1.50 respectively and the inelastic portion lengths ($\tau_i \cdot L$) are 0.26~0.32 L , 0.30~0.36 L and

0.38~0.42 L respectively.

The yield plateau length ($E_{st,R}=S$) contribute the inelastic rotation capacity as suggested in Eq. 3-14d. The inelastic rotation, contributed by yield plateau, of HSA800, SM570 and SM490 are 0, 0.79~0.91 and 3.86~4.21 respectively. Please note that the value is normalized by $(2/L) \cdot (1/\phi_{yf})$. It seems that without the enough yield plateau length such $S \geq 10.0$, the contribution to the in-plane rotation capacity is not significant.

The T/Y strain ratio (E_R) contribute the inelastic rotation capacity as Eq. 3-13d and Eq. 3-14e. The inelastic rotation, contributed by T/Y strain ratio, of HSA800, SM570 and SM490 are 1.90~2.30, 5.49~6.33 and 16.94~18.69 respectively. It is important that even without or little the existence of the yield plateau such SM570, the rotation capacity level ($R_{m,gr} \geq 3$) are assured if the enough value of T/Y strain ratio is presented in a material. The quantification of the T/Y strain ratio (E_R) to satisfy the sufficient rotation capacity will be dealt with in next chapter in detail.

3.3.2.4 Effects of Y/T strength and T/Y strain ratios to in-plane rotation capacities of HSA800 beam members

It should be noted that even the high Y/T strength condition, the high T/Y strain ratio could assure the sufficient inelastic rotation capacity. On the other hand even the low T/Y strain condition, the low Y/T strength ratio could assure the sufficient inelastic rotation capacity. Therefore the material

restriction in current standard codes with a restrictive parameter only such Y/T strength ratio (Y_R) is not appropriate approach to achieve target rotation capacity. Therefore, analytical studies have been performed to achieve sufficient rotation capacity of HSA800 I-shaped member by separately adjusting Y/T strength ratios and T/Y ratios as shown in Fig. 3-18 and Table 3-9, 3-12.

Table 3-10~3.11 summarized the effect of T/Y ratios to the inelastic rotation capacities of HSA800 I-shaped member at the moment gradient condition ($m_R=0$). The inelastic rotation capacities are proportionally increased as the T/Y strain ratios (E_R) are increased from 15.0 to 25.0. At the constant 0.84 Y/T strength ratio level ($Y_R=0.84$), to achieve target inelastic rotation capacities ($R_{m,gr} \geq 2$), the minimum value of T/Y strain ratio are about 20.0 ($E_R=20$).

Table 3-13~3.14 summarized the effect of Y/T strength ratios to the inelastic rotation capacities of HSA800 I-shaped member at the moment gradient condition ($m_R=0$). The inelastic rotation capacities are proportionally increased as the Y/T strength ratios are decreased from 0.90 to 0.80. At the controlled T/Y strain ratio level ($E_R=15.0$), the target inelastic rotation capacities ($R_{m,gr} \geq 2$) are only realized when the value of Y/T strength ratio is under 0.80 in a specific I-shaped section (such H-400x150x28x14). It seems that the variations of Y/T strength ratio from 0.90 to 0.80 are not considerably

increase rotation capacities as expected and the increase of the T/Y strain ratios from 15.0 to 25.0 are the more beneficial to considerably increase the inelastic rotation capacities.

3.4 Summary

1) From the tensile coupon testing results of HSA800, SM570, and SM490, the Y/T strength ratio and T/Y strain ratio were shown to have significant correlations with the variation of the yield strength. The Pearson correlation coefficients of the Y/T strength ratio and T/Y strain ratio with yield strength are about 0.95 and -0.94, respectively, implying strong positive and negative correlations between the two variables. Based on the tensile coupon test results, a statistical regression curve was proposed to predict the Y/T strength ratio and T/Y strain ratio according to the yield strength, which is a pivotal value used to idealize a stress-strain curve of mild and high strength steel.

2) Four idealized material models are discussed and numerically verified with the tensile coupon test data. The traditional model (#1) and Haaijer model (#2) were appropriate to idealize the shape of the stress-strain curve for a material such as mild steel. The Ramberg-Osgood model (#3) was adequate to idealize the shape of the stress-strain curve for a material without a yield plateau such as high strength steel. A piecewise linear model (#4) could easily idealize the shape of the stress-strain curves of various materials by increasing

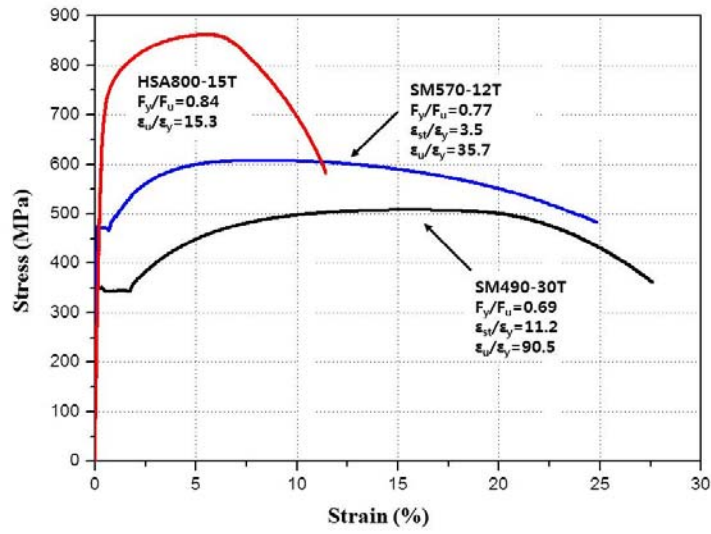
the number of polylines according to material nonlinearity. However, the value of the modulus from the piecewise linear model was not appropriate for utilizing in analytical studies for out-of-plane behavior since the different slopes between adjacent polygons give discontinuous modulus values along the strain distribution.

3) Among the in-plane behaviors of an I-shaped beam member, the maximum inelastic rotation capacities were analyzed. It should be noted that, because of the presence of the strain hardening in all grades of steel such as SM490, SM570, and HSA800, an I-shaped section fabricated from any grade of steels could achieve the plastic moment. Using the simplified method proposed in this study, by applying the piecewise linear model (#4) to integrate various curvature distributions along the longitudinal direction, the inelastic rotation capacities at member maximum moments (R_m) of HSA800, SM570, and SM490, the I-shaped member are predicted for uniform moment ($R_{m,ui}$) and moment gradient ($R_{m,gr}$) loading conditions.

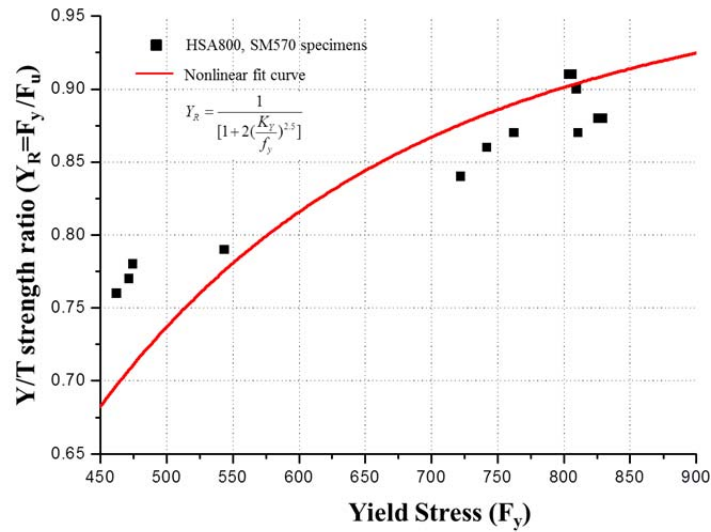
4) The effects of the Y/T strength ratio, T/Y strain ratio, and YP length on the inelastic rotation capacity of the I-shaped member were analyzed. At the uniform moment loading condition, the rotation capacity ($R_{m,ui}$) is directly proportional to the T/Y strain ratios. Other parameters such as Y/T strength ratio and YP length are not influential under the uniform loading condition. On the other hand, under the moment gradient loading condition, three parameters (Y/T strength ratio, T/Y strain ratio, and YP length) all together

influence the rotation capacity ($R_{m,gr}$) and their contributions are summarized.

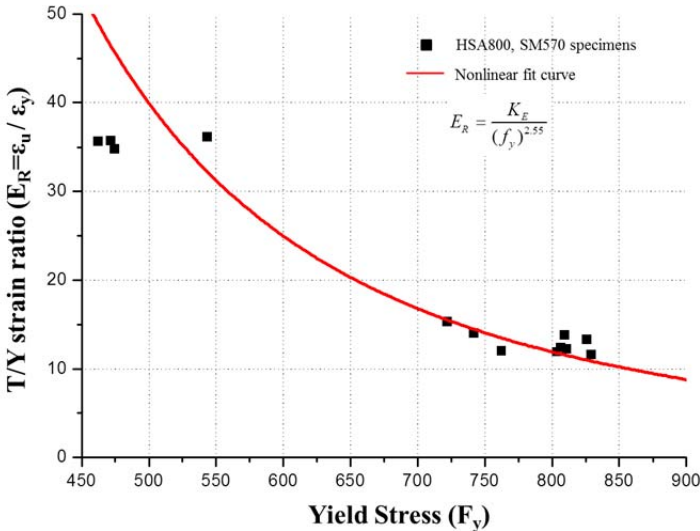
5) The analytical parametric studies were performed by independently adjusting the Y/T strength ratios ($Y_R=0.80\sim 0.90$) and T/Y strain ratios ($E_R=15.0\sim 25.0$) to achieve higher rotation capacity level (R_m) of the HSA800 I-shaped member under moment gradient loading condition. The inelastic rotation capacities proportionally increase as the T/Y strain ratios increase from 15.0 to 25.0. Similarly, the capacities improve as the Y/T strength ratios decrease from 0.90 to 0.80, by increasing the inelastic participation length. However, even at the Y/T strength ratio of level 0.80, the target rotation capacity level ($R_m=2.0$) is not easily realized. In other words, the strategy to only reduce the Y/T strength ratio does not ensure satisfactory rotation capacity for the HSA800 I-shaped member. To satisfy the target rotation capacity level, even at the high Y/T strength ratio of 0.90 level, the increase of the T/Y strain ratios in concert is significantly beneficial and inevitably required.



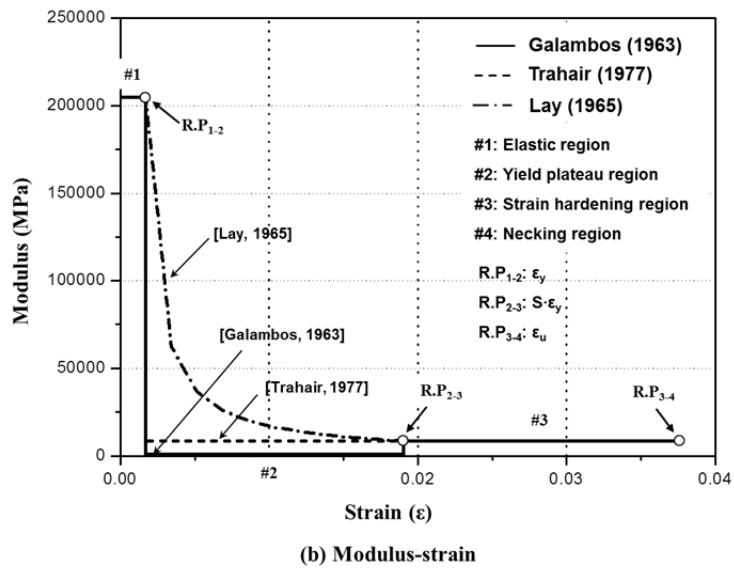
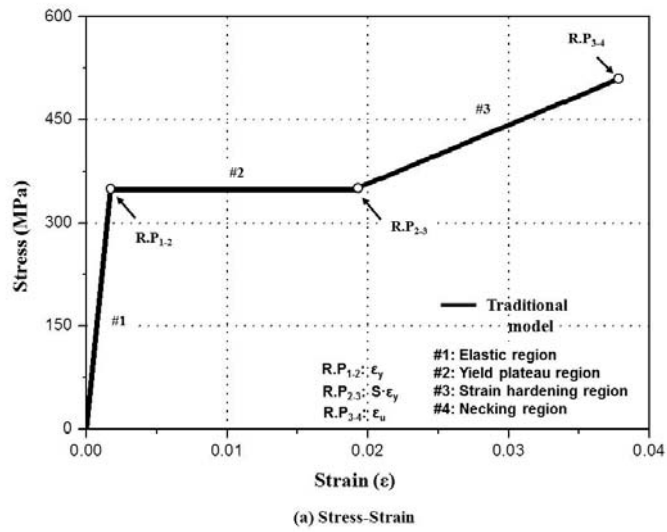
[3-1] Comparison of HSA800, SM570 and SM490 stress-strain relationships



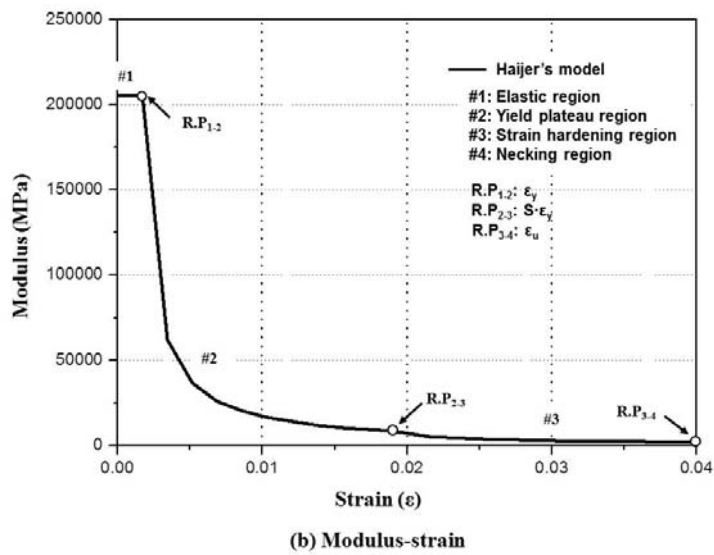
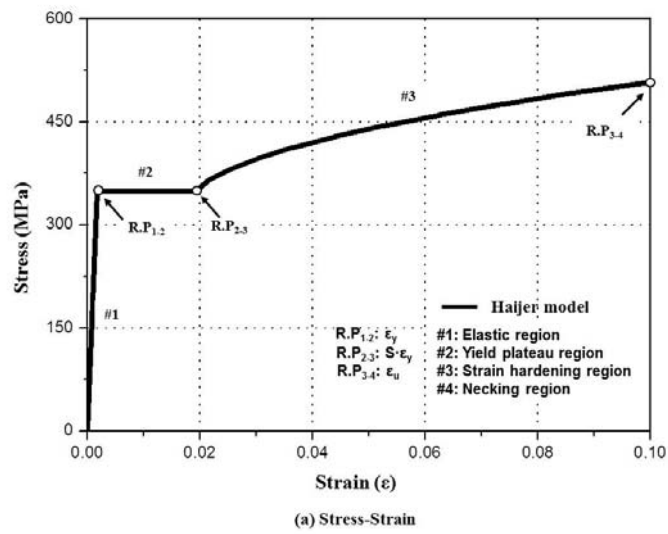
[3-2] Y/T strength ratio as a function of yield stress



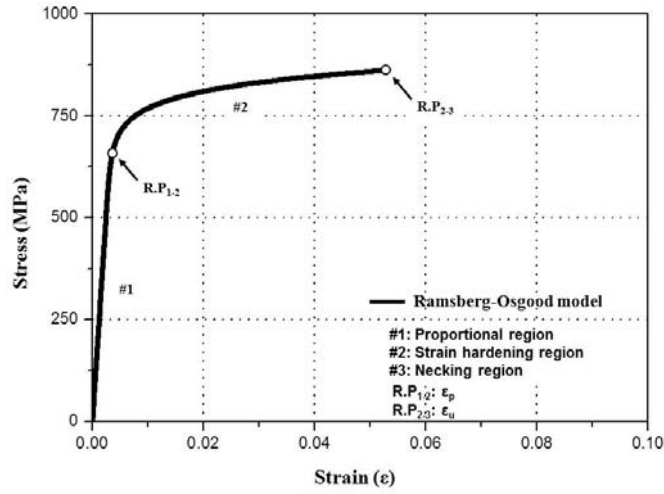
[3-3] T/Y strain ratio as a function of yield stress



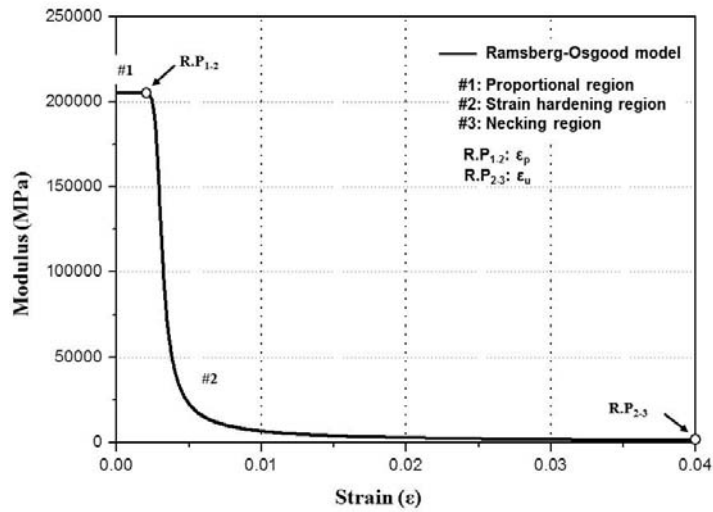
[3-4] Traditional model No.1 for mild steel (a) stress-strain (b) modulus-strain



[3-5] Haaijer model No. 2 for mild steel (a) stress-Strain (b) modulus-Strain

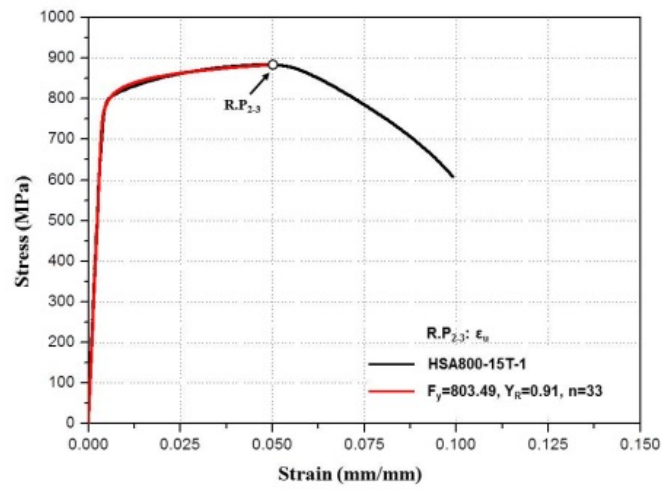


(a) Stress-Strain

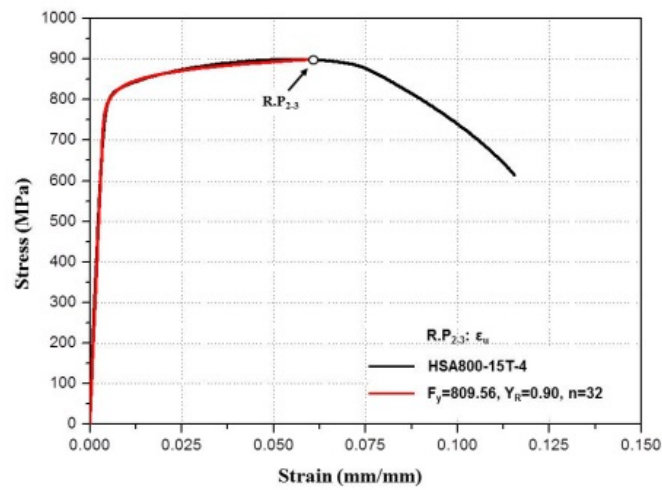


(b) Modulus-strain

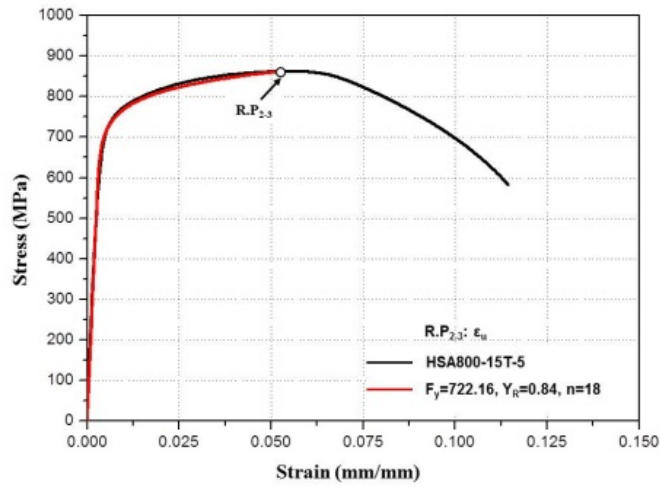
[3-6] Ramberg-Osgood model No.3 for high strength steel (a) stress-strain (b) modulus-strain



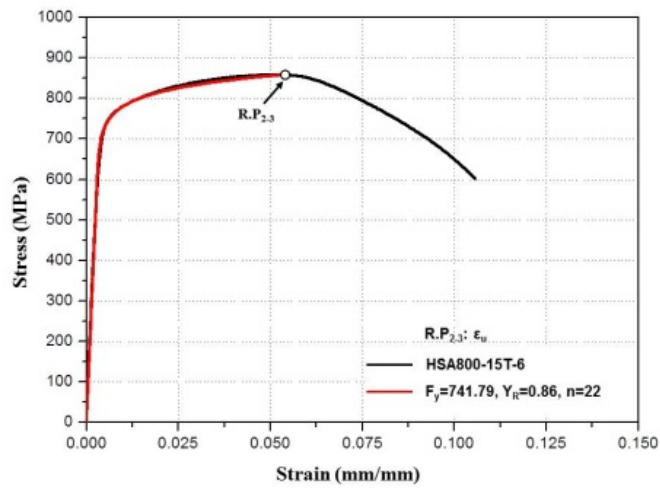
(a) HSA800-15T-1, Tab. 3-1



(b) HSA800-15T-4 in Table 3-1

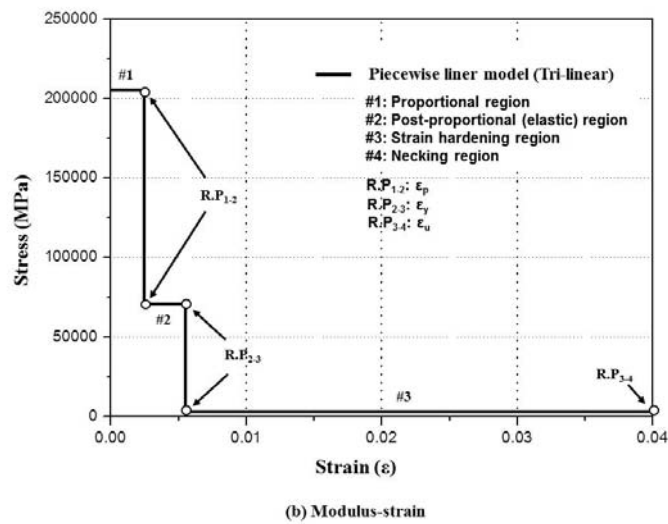
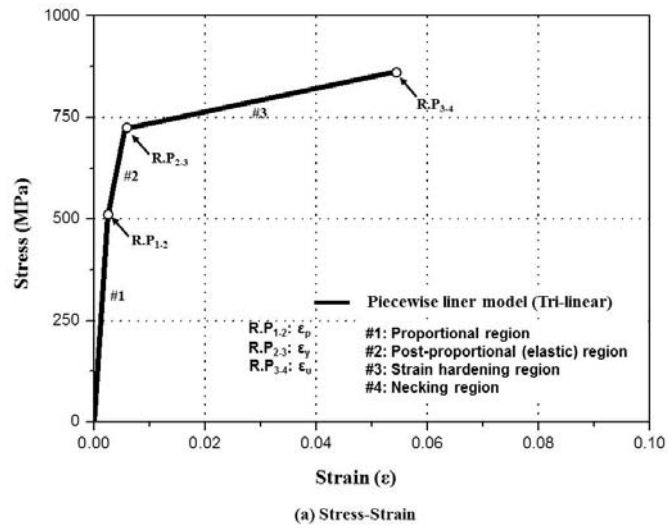


(c) HSA800-15T-5 in Table 3-1

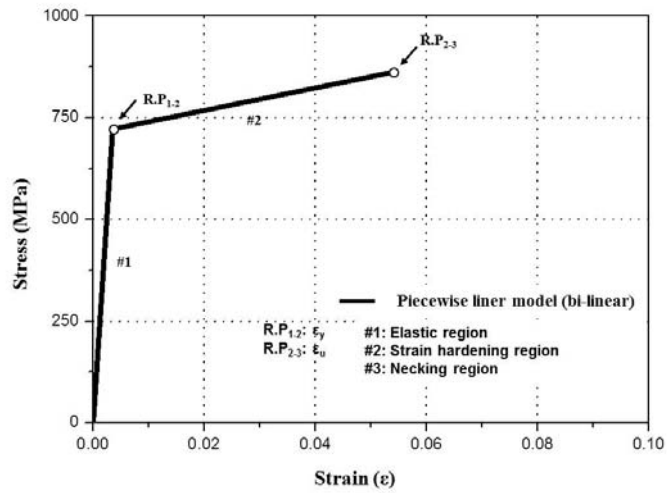


(d) HSA800-15T-6 in Table 3-1

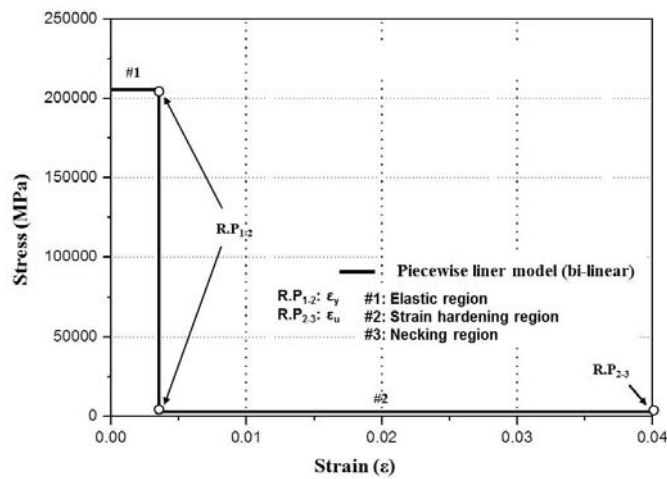
[3-7] Determination of strain hardening parameter (n) for high strength steel by Ramberg-Osgood model



[3-8] Piecewise tri-linear model No.4 for high strength steel (a) stress-strain (b) modulus-strain

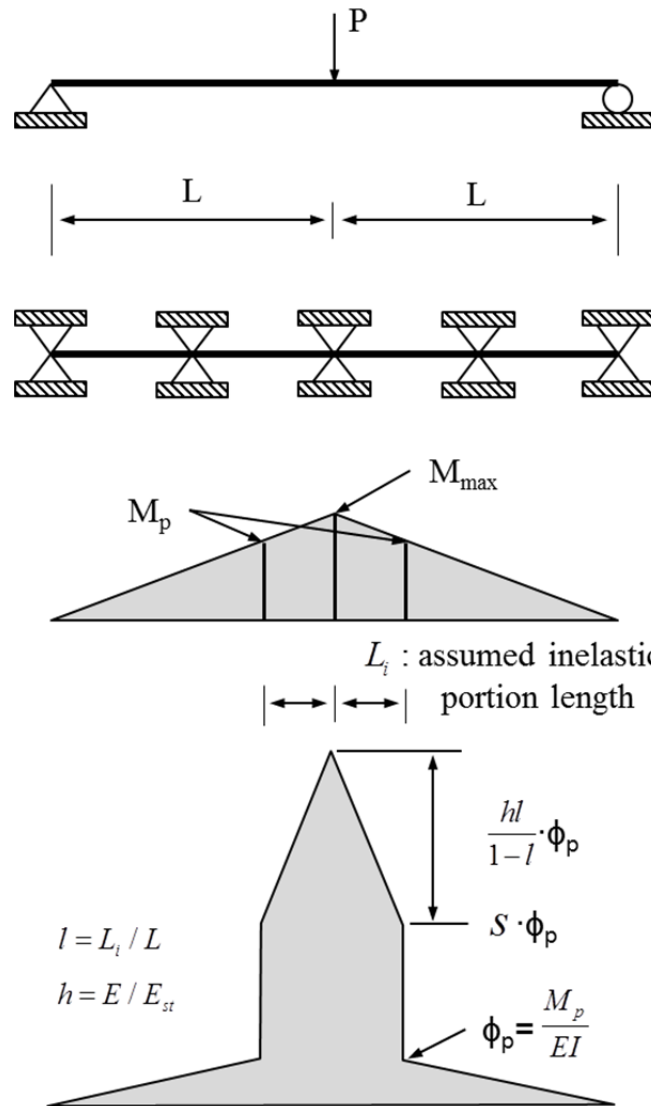


(a) Stress-Strain

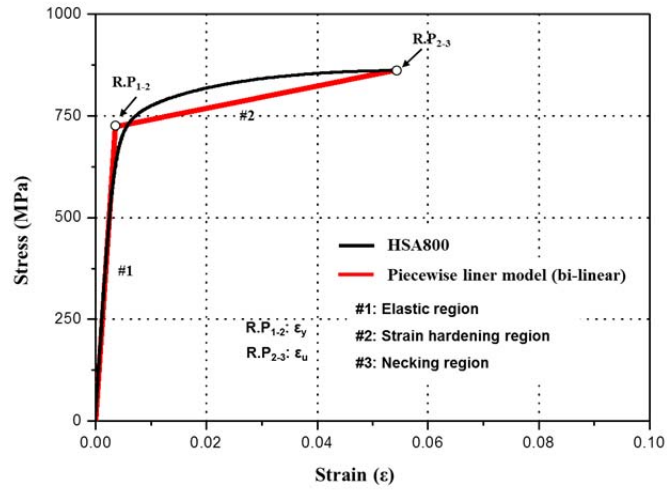


(b) Modulus-strain

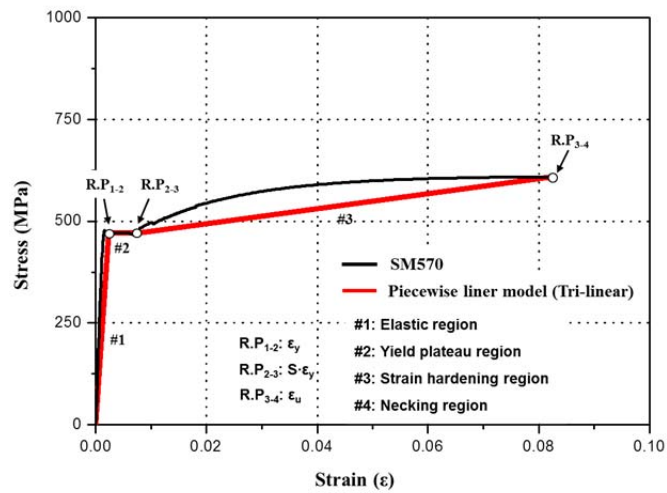
[3-9] Piecewise bi-linear model No.4 for high strength steel (a) stress-strain (b) modulus-strain



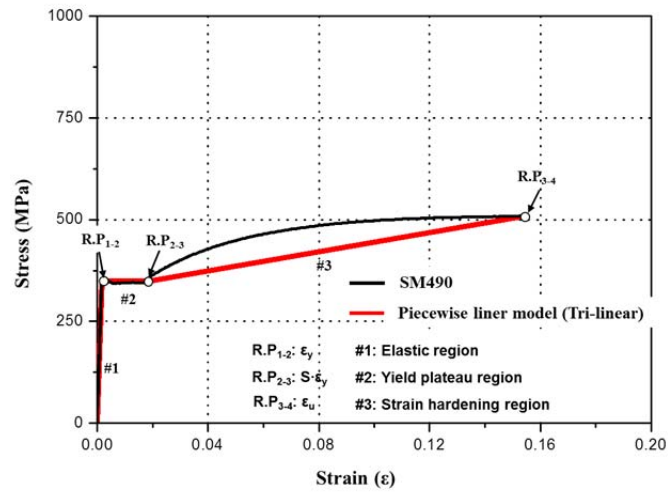
[3-10] Bending moment diagram and idealized curvature distribution along span with traditional model (Kemp, 1985)



(a) HSA800 by Piecewise bi-linear model

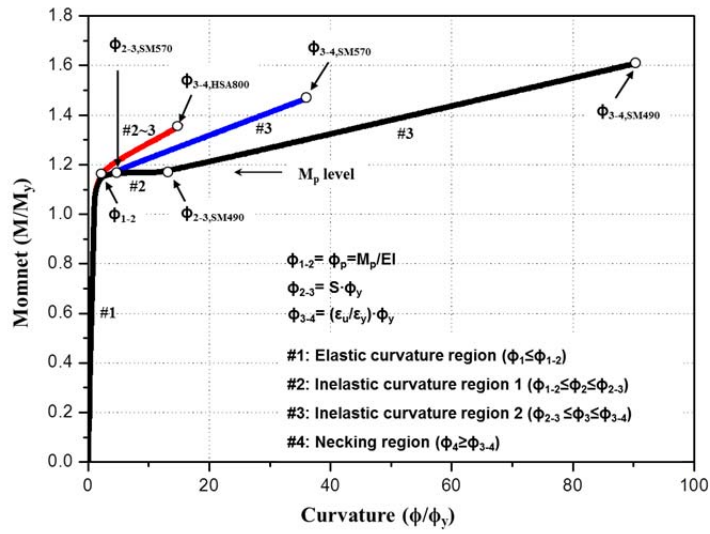


(b) SMS70 by Piecewise tri-linear model

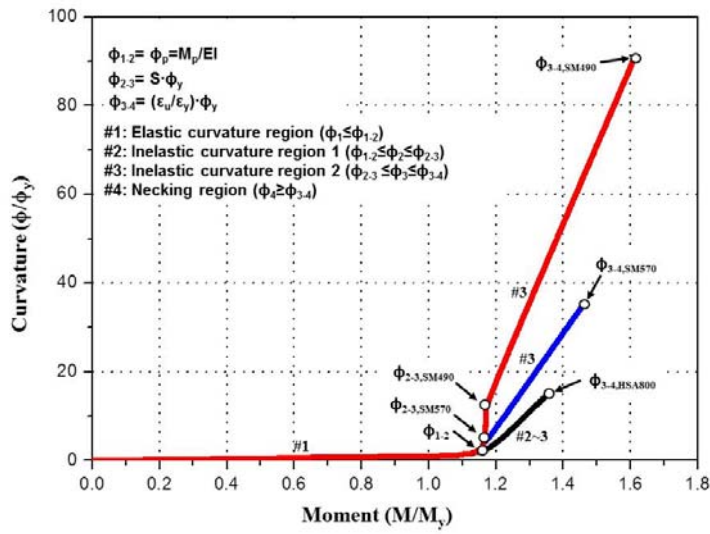


(c) SM490 by Piecewise bi-linear model

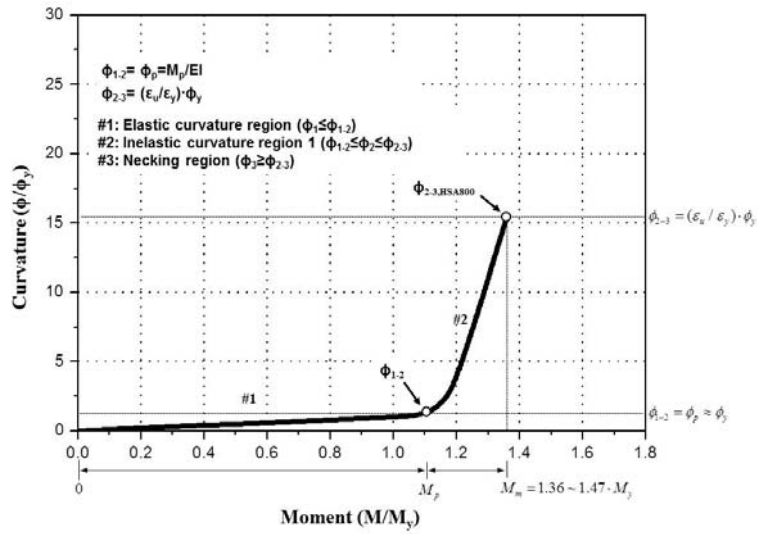
[3-11] Idealized curves of HSA800, SM570 and SM490 (a) HSA800 by piecewise bi-linear model (b) SM570 by piecewise tri-linear model (c) SM490 by piecewise tri-linear model



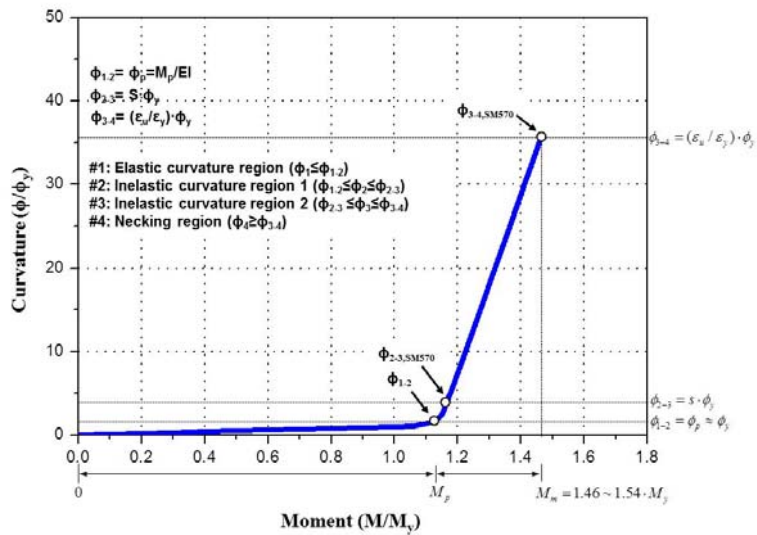
(a) Moment-curvature relationship



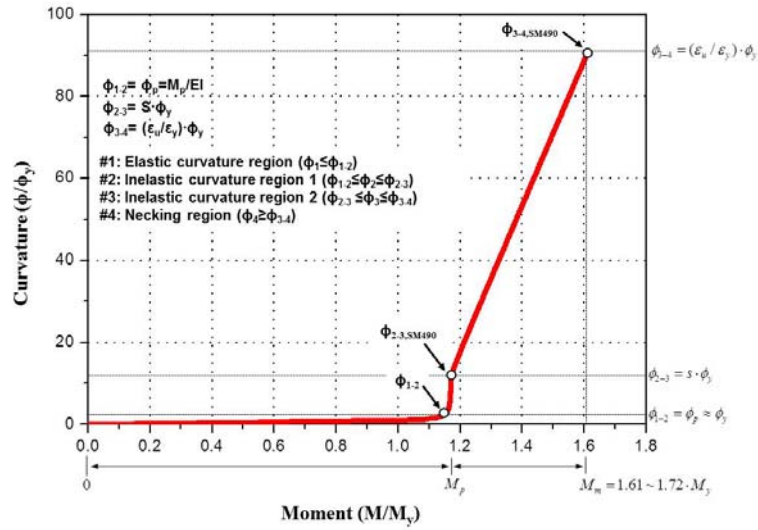
(b) Curvature-moment relationship



(c) Curvature-moment relationship of HSA800

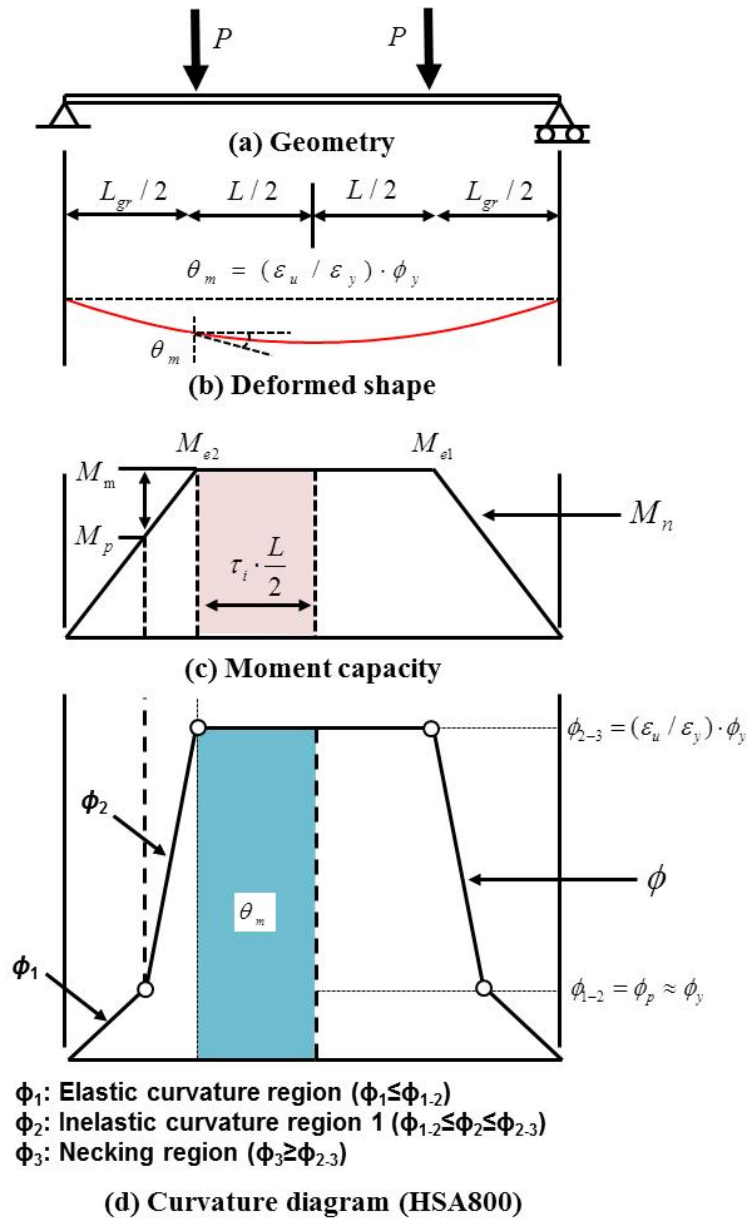


(d) Curvature-moment relationship of SM570

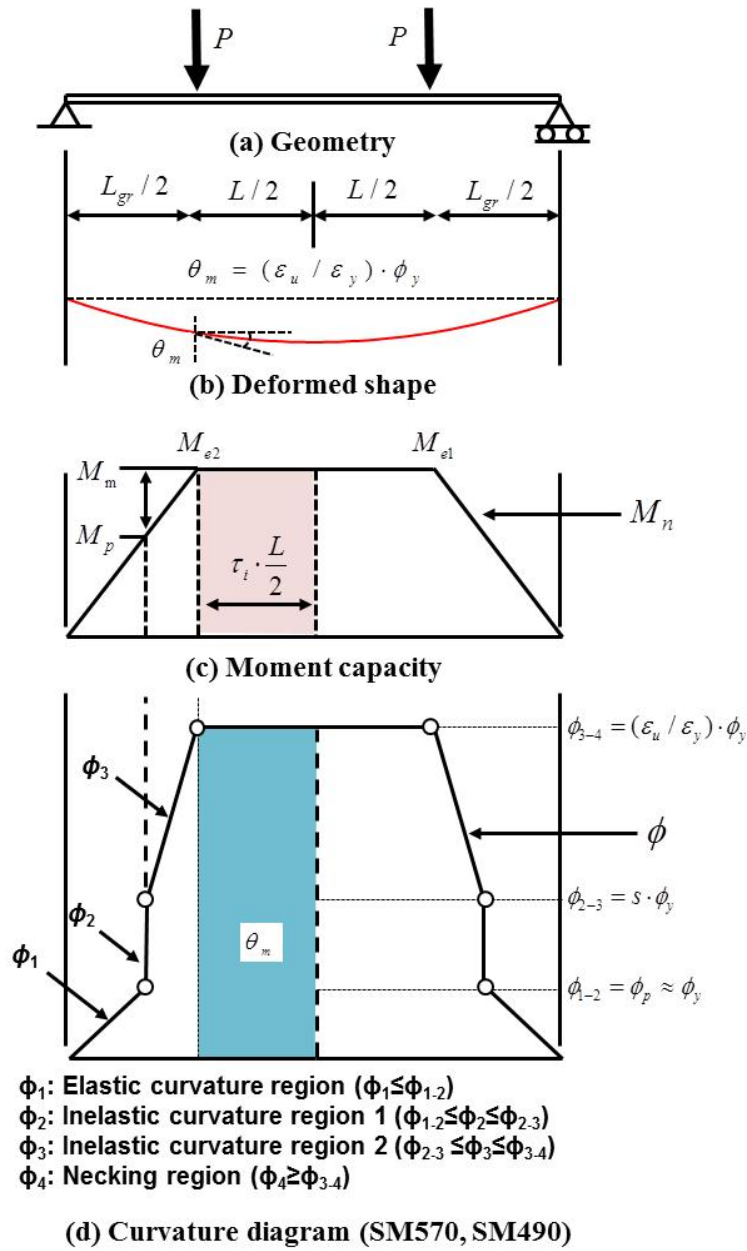


(e) Curvature-moment relationship of SM570

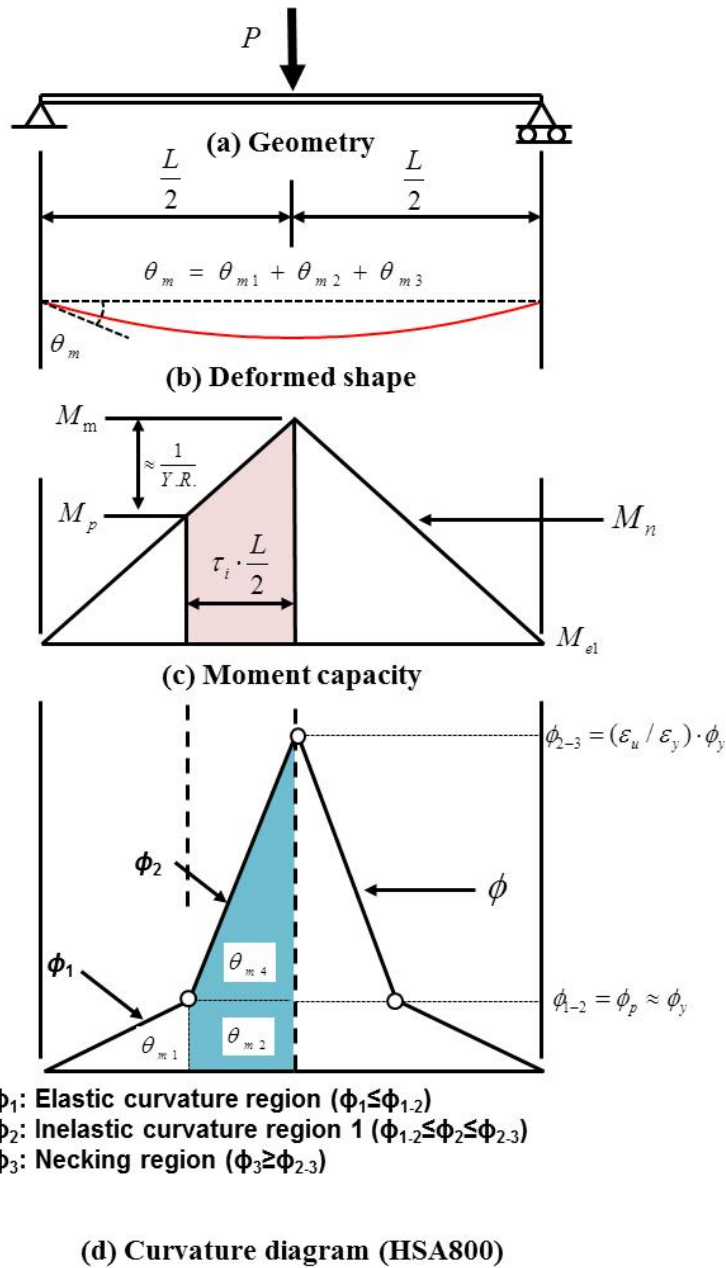
[3-12] Inelastic curvature distributions according to moment level (a) moment-curvature relationship (b) curvature-moment relationship (c) HSA800 case (d) SM570 case (e) SM490 case



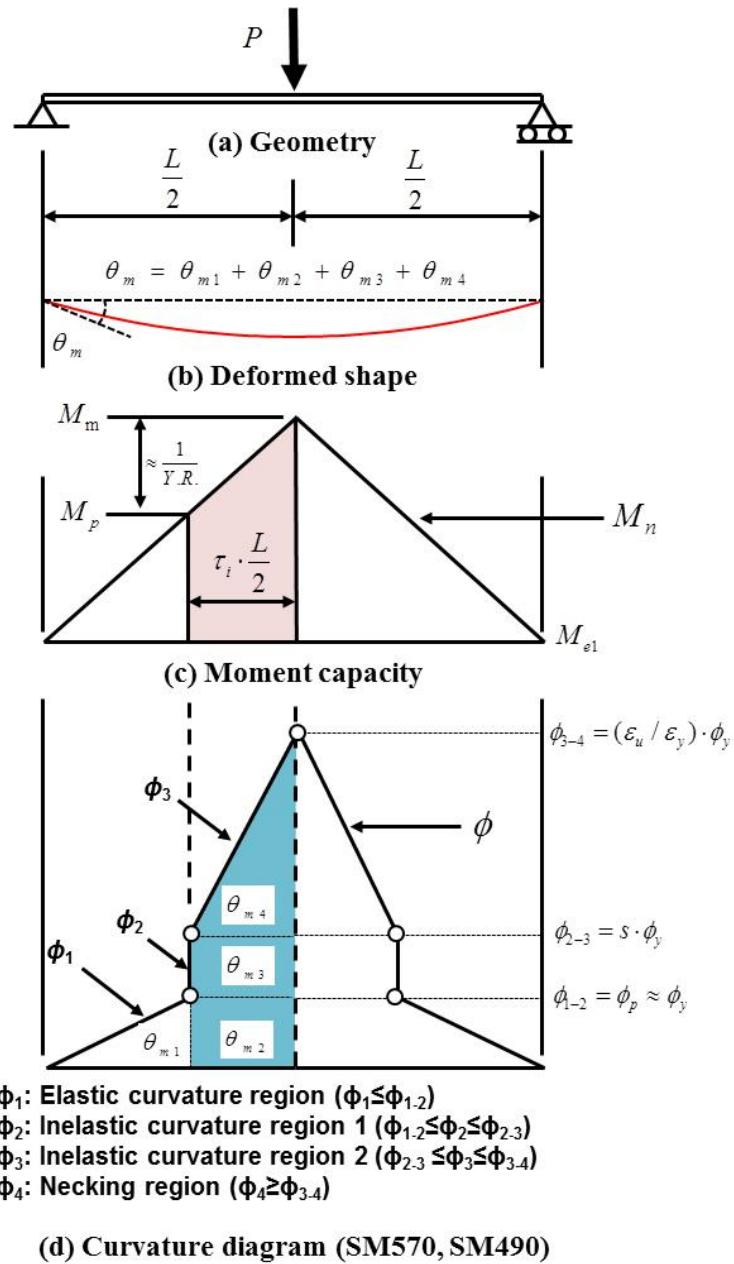
[3-13] Effects of stress-strain curve (piecewise bi-linear) on in-plane behavior under uniform moment (a) loading and beam geometry (b) deformed shape (c) moment capacity (d) curvature diagram of HSA800



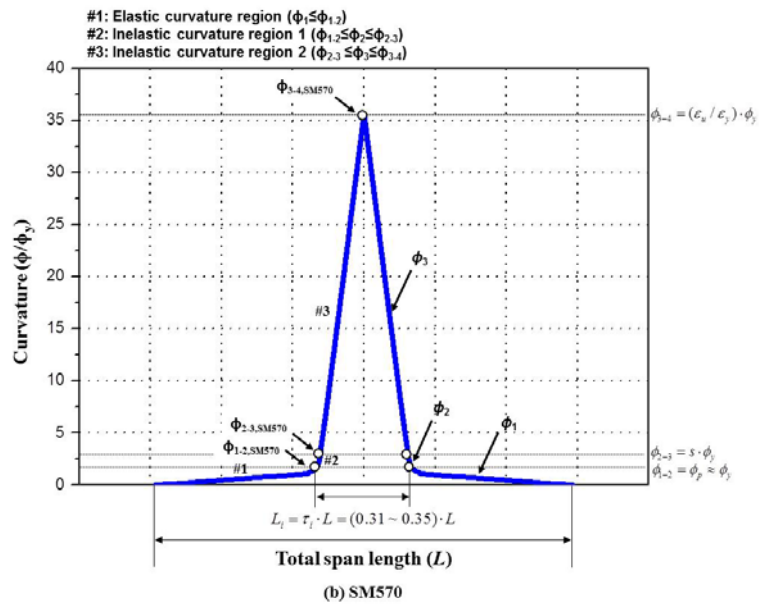
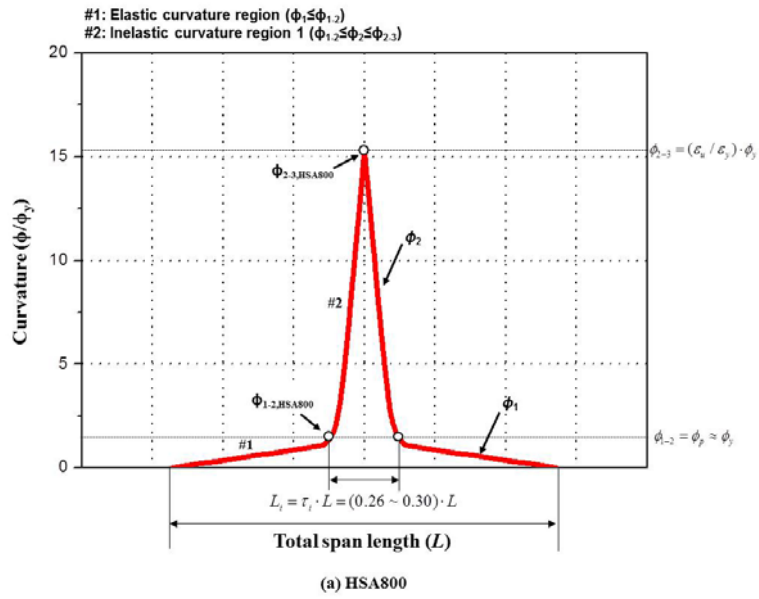
[3-14] Effects of stress-strain curve (piecewise tri-linear) on in-plane behavior under uniform moment (a) loading and beam geometry (b) deformed shape (c) moment capacity (d) curvature diagram of SM570 and SM490

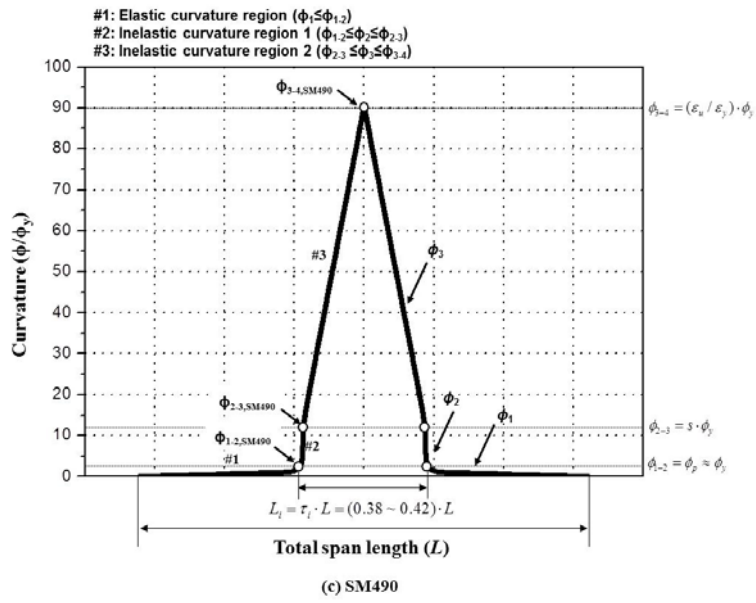


[3-15] Effects of stress-strain curve (piecewise bi-linear) on in-plane behavior under moment gradient (a) loading and beam geometry (b) deformed shape (c) moment capacity (d) curvature diagram of HSA800

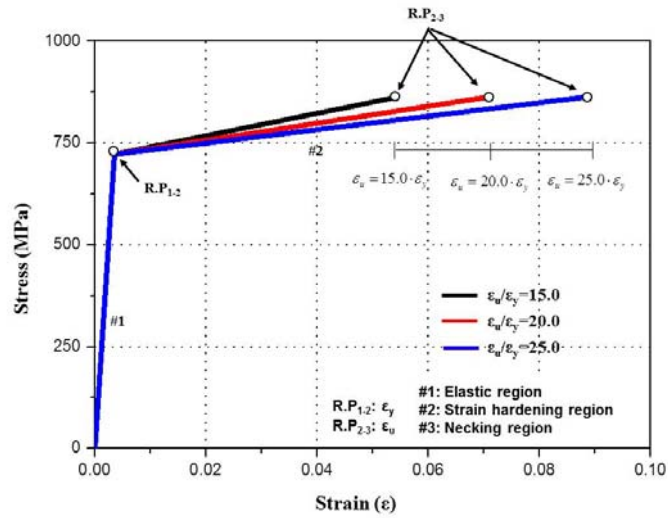


[3-16] Effects of stress-strain curve (piecewise tri-linear) on in-plane behavior under moment gradient (a) loading and beam geometry (b) deformed shape (c) moment capacity (d) curvature diagram of SM570 and SM490

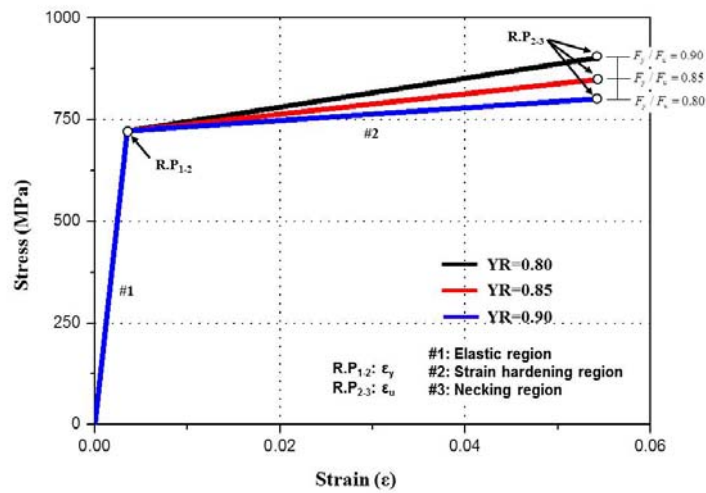




[3-17] Inelastic curvature distributions at maximum moment under moment gradient condition (a) HSA800 case (b) SM570 case (c) SM490 case



(a) T/Y strain ratios



(b) Variation of Y/T strength ratios

[3-18] Piecewise bi-linear model to consider the effects of T/Y strain ratios and Y/T strength ratios to inelastic rotation capacity of HSA800 (a) variation of tensile-to-yield strain ratios (b) variation of yield-to-tensile strength ratios

[3-1] Tensile coupon properties of HSA800 steel plates

Name of Specimen	E	F_y ¹⁾	F_u	$Y_R = F_y / F_u$	$E_{st,R} = \varepsilon_{st} / \varepsilon_y$ ²⁾	$E_R = \varepsilon_u / \varepsilon_y$	n ³⁾
	[MPa]	[MPa]	[MPa]				
HSA800-15T-1	205,000 ⁴⁾	803.49	888.53	0.91	1	11.9	33
HSA800-15T-2		806.33	883.24	0.91	1	12.4	35
HSA800-15T-3		762.43	875.76	0.87	1	12.0	22
HSA800-15T-4		809.56	898.54	0.90	1	13.8	32
HSA800-15T-5		722.16	861.87	0.84	1	15.3	18
HSA800-15T-6		741.79	858.10	0.86	1	14.0	22
HSA800-25T-1		826.09	940.26	0.88	1	13.3	25
HSA800-25T-2		810.94	927.97	0.87	1	12.2	23
HSA800-25T-3		829.38	943.00	0.88	1	11.6	24

1) 0.2% offset method applied
 2) $\varepsilon_y = F_y / E$
 3) Proposed hardening parameter according to Ramberg-Osgood model calculated by Eq. (3-6)
 4) Nominal value

Chapter 3. Idealized Material Models and In-plane Rotation Capacities

[3-2] Tensile coupon properties of SM570 steel plate

Name of Specimen	E	F_y ¹⁾	F_u	$Y_R = F_y / F_u$	$E_{st,R} = \varepsilon_{st} / \varepsilon_y$ ²⁾	$E_R = \varepsilon_u / \varepsilon_y$	n ³⁾	E / E_{st} ⁴⁾
	[MPa]	[MPa]	[MPa]					
SM570-25T-1 ¹⁾	205,000 ⁵⁾	543.56	688.16	0.79	1	36.10	16.5	
SM570-12T-1		471.56	608.53	0.77	3.46	35.71		20
SM570-12T-2		474.44	609.17	0.78	3.63	34.83		20
SM570-12T-3		462.20	610.61	0.76	3.06	35.57		20

1) 0.2% offset method applied
 2) $\varepsilon_y = F_y / E$
 3) Proposed hardening parameter according to Ramberg-Osgood model (Eq. (3-6))
 4) Stress-Strain relationship in strain-hardening range expressed by Haaijer model calculated by Eq. (3-5) with $m = 2$ and $K = 180$
 5) Nominal value

[3-3] Tensile coupon properties of SM490 steel plate

Name of Specimen	E	F_y ¹⁾	F_u	$Y_R = F_y / F_u$	$E_{st,R} = \varepsilon_{st} / \varepsilon_y$ ²⁾	$E_R = \varepsilon_u / \varepsilon_y$	E / E_{st} ³⁾
	[MPa]	[MPa]	[MPa]				
SM490-15T-1	205,000 ⁴⁾	426.26	548.74	0.78	14.7	74.4	30
SM490-15T-2		428.99	548.86	0.78	15.3	75.7	30
SM490-15T-3		427.20	548.60	0.78	14.8	73.2	30
SM490-30T-1		349.08	507.82	0.69	11.2	90.5	24
SM490-30T-2		328.67	518.13	0.63	9.7	90.3	20
SM490-30T-3		339.44	520.68	0.65	9.0	85.6	20

1) 0.2% offset method applied
 2) $\varepsilon_y = F_y / E$
 3) Stress-Strain relationship in strain-hardening range expressed by Haaijer model calculated by Eq. (3-5) with $m = 2$ and $K = 180$
 4) Nominal value

[3-4] Relationship between yield stress and Y/T strength ratio

Name of Specimen	F_y	$Y_R = F_y / F_u$	$r^{1)}$
	[non], (1)	[non], (2)	(1)-(2)
HSA800-15T-1	803.49	0.91	0.964
HSA800-15T-2	806.33	0.91	
HSA800-15T-3	762.43	0.87	
HSA800-15T-4	809.56	0.90	
HSA800-15T-5	722.16	0.84	
HSA800-15T-6	741.79	0.86	
HSA800-25T-1	826.09	0.88	
HSA800-25T-2	810.94	0.87	
HSA800-25T-3	829.38	0.88	
SM570-25T-1	543.56	0.79	
SM570-12T-1	471.56	0.77	
SM570-12T-2	474.44	0.78	
SM570-12T-3	462.20	0.76	

1) Pearson Corr. $r = \frac{\sum_{i=1}^n ((x_i - \bar{x})(y_i - \bar{y}))}{\sqrt{\sum_{i=1}^n (x_i - \bar{x})^2 \sum_{i=1}^n (y_i - \bar{y})^2}}$

[3-5] Relationship between yield stress and T/Y strain ratio

Name of Specimen	F_y	$E_R = \epsilon_u / \epsilon_y$	$r^{(1)}$
	[non], (1)	[non], (2)	(1)-(2)
HSA800-15T-1	803.49	11.9	-0.976
HSA800-15T-2	806.33	12.4	
HSA800-15T-3	762.43	12.0	
HSA800-15T-4	809.56	13.8	
HSA800-15T-5	722.16	15.3	
HSA800-15T-6	741.79	14.0	
HSA800-25T-1	826.09	13.3	
HSA800-25T-2	810.94	12.2	
HSA800-25T-3	829.38	11.6	
SM570-25T-1	543.56	36.1	
SM570-12T-1	471.56	35.7	
SM570-12T-2	474.44	34.8	
SM570-12T-3	462.20	35.6	

1) Pearson Corr. $r = \frac{\sum_{i=1}^n ((x_i - \bar{x})(y_i - \bar{y}))}{\sqrt{\sum_{i=1}^n (x_i - \bar{x})^2 \sum_{i=1}^n (y_i - \bar{y})^2}}$

[3-6] Geometric and material parameters for the in-plane behavior analysis

			Material parameters [MPa]			
			[M1: Ho ¹⁾ -F _{yw} =F _{yt} =722 (#5) ²⁾	[M2: Ho ¹⁾ -F _{yw} =F _{yt} =471 (#4) ³⁾	[M3: Ho ¹⁾ -F _{yw} =F _{yt} =349 (#4) ⁴⁾	
Geometrical parameters [mm]	[250x150 series] Type A	[G:A-S] H-250x150x14x14	A-P1: [G:A-S]-[M1:Ho-722]	A-P2: [G:A-S]-[M2:Ho-471]	A-P3: [G:A-S]-[M3:Ho-349]	
		[G:A-W] H-250x150x28x14	A-P4: [G:A-W]-[M1:Ho-722]	A-P5: [G:A-W]-[M2:Ho-471]	A-P6: [G:A-W]-[M3:Ho-349]	
		[G:A-F] H-250x150x14x28	A-P7: [G:A-F]-[M1:Ho-722]	A-P8: [G:A-F]-[M2:Ho-471]	A-P9: [G:A-F]-[M3:Ho-349]	
	[400x150 series] Type B	[G:B-S] H-400x150x14x14	B-P1: [G:B-S]-[M1:Ho-722]	B-P2: [G:B-S]-[M2:Ho-471]	B-P3: [G:B-S]-[M3:Ho-349]	
		[G:B-W] H-400x150x28x14	B-P4: [G:B-W]-[M1:Ho-722]	B-P5: [G:B-W]-[M2:Ho-471]	B-P6: [G:B-W]-[M3:Ho-349]	
		[G:B-F] H-400x150x14x28	B-P7: [G:B-F]-[M1:Ho-722]	B-P8: [G:B-F]-[M2:Ho-471]	B-P9: [G:B-F]-[M3:Ho-349]	
	1) Ho is abbreviation of homogenous I-section, the flange and web of which are the same grade steel are applied 2) Bi-linear model at the piecewise interpolation approach was applied ($F_y = 722MPa, Y_R = F_y / F_u = 0.84, E_R = \varepsilon_u / \varepsilon_y = 15.30$) 3) Tri-linear model at the piecewise interpolation approach was applied ($F_y = 471MPa, Y_R = F_y / F_u = 0.77, E_{st,R} = \varepsilon_{st} / \varepsilon_y = 3.46, E_R = \varepsilon_u / \varepsilon_y = 35.70$) 4) Tri-linear model at the piecewise interpolation approach was applied ($F_y = 349MPa, Y_R = F_y / F_u = 0.69, E_{st,R} = \varepsilon_{st} / \varepsilon_y = 11.2, E_R = \varepsilon_u / \varepsilon_y = 90.50$)					

[3-7] In-plane rotation capacities (R_m) at maximum moment (M_m) under moment gradient ($m_R=0$) [Section: Type A]

(1)	(2)	(3)	(4)	(5)	(6)	(7)	(8)	(9)	(10)	(11)	(12)	(13)	(14)
Analytical model	F_y	Y_R	s	E_R	$M_m / M_{yf}^{1)}$	τ_i	$\left(\frac{\theta_{yf}}{\phi_{yf}}\right) \cdot \left(\frac{2}{L}\right)$	$\left(\frac{\theta_{m1}}{\phi_{yf}}\right) \cdot \left(\frac{2}{L}\right)$	$\left(\frac{\theta_{m2}}{\phi_{yf}}\right) \cdot \left(\frac{2}{L}\right)$	$\left(\frac{\theta_{m3}}{\phi_{yf}}\right) \cdot \left(\frac{2}{L}\right)$	$\left(\frac{\theta_{m4}}{\phi_{yf}}\right) \cdot \left(\frac{2}{L}\right)$	$\left(\frac{\theta_m}{\phi_{yf}}\right) \cdot \left(\frac{2}{L}\right)$	$R_m = \frac{\theta_m}{\theta_y} - 1$
[Unit]	[MPa]	[non]	[non]	[non]	[non]	[non]	[non]	[non]	[non]	[non]	[non]	[non]	[non]
A-P1	722	0.84	0	15.3	1.36	0.26	1.00	0.37	0.26	0.00	1.90	2.53	1.53
A-P2	471	0.77	3.46	35.7	1.46	0.32	1.00	0.34	0.32	0.79	5.49	6.94	5.94
A-P3	349	0.69	11.2	90.5	1.61	0.38	1.00	0.31	0.38	3.86	16.94	21.49	20.49
A-P4	722	0.84	0	15.3	1.43	0.30	1.00	0.35	0.30	0.00	2.18	2.83	1.83
A-P5	471	0.77	3.46	35.7	1.54	0.35	1.00	0.32	0.35	0.88	6.08	7.63	6.63
A-P6	349	0.69	11.2	90.5	1.68	0.41	1.00	0.30	0.41	4.14	18.16	23.00	22.00
A-P7	722	0.84	0	15.3	1.37	0.27	1.00	0.37	0.27	0.00	1.94	2.57	1.57
A-P8	471	0.77	3.46	35.7	1.47	0.32	1.00	0.34	0.32	0.80	5.58	7.04	6.04
A-P9	349	0.69	11.2	90.5	1.62	0.38	1.00	0.31	0.38	3.90	17.11	21.70	20.70

1) Strain compatibility method was applied for the calculation of maximum moment, M_m
 2) θ_{m1} , θ_{m2} , θ_{m3} , θ_{m4} , is defined at Fig. 3-15, Fig. 3-16.

Chapter 3. Idealized Material Models and In-plane Rotation Capacities

[3-8] In-plane rotation capacities (R_m) at maximum moment (M_m) under moment gradient ($m_R=0$) [Section: Type B]

(1)	(2)	(3)	(4)	(5)	(6)	(7)	(8)	(9)	(10)	(11)	(12)	(13)	(14)
Analytical model	F_y	Y_R	s	E_R	$M_m / M_{yf}^{1)}$	τ_i	$\left(\frac{\theta_{mf}}{\phi_{yf}}\right) \cdot \left(\frac{2}{L}\right)$	$\left(\frac{\theta_{m1}}{\phi_{yf}}\right) \cdot \left(\frac{2}{L}\right)$	$\left(\frac{\theta_{m2}}{\phi_{yf}}\right) \cdot \left(\frac{2}{L}\right)$	$\left(\frac{\theta_{m3}}{\phi_{yf}}\right) \cdot \left(\frac{2}{L}\right)$	$\left(\frac{\theta_{m4}}{\phi_{yf}}\right) \cdot \left(\frac{2}{L}\right)$	$\left(\frac{\theta_m}{\phi_{yf}}\right) \cdot \left(\frac{2}{L}\right)$	$R_m = \frac{\theta_m}{\theta_y} - 1$
[Unit]	[MPa]	[non]	[non]	[non]	[non]	[non]	[non]	[non]	[non]	[non]	[non]	[non]	[non]
B-P1	722	0.84	0	15.3	1.38	0.28	1.00	0.36	0.28	0.00	1.99	2.63	1.63
B-P2	471	0.77	3.46	35.7	1.49	0.33	1.00	0.34	0.33	0.82	5.68	7.17	6.17
B-P3	349	0.69	11.2	90.5	1.63	0.39	1.00	0.31	0.39	3.95	17.33	21.98	20.98
B-P4	722	0.84	0	15.3	1.47	0.32	1.00	0.34	0.32	0.00	2.30	2.96	1.96
B-P5	471	0.77	3.46	35.7	1.57	0.36	1.00	0.32	0.36	0.91	6.33	7.93	6.93
B-P6	349	0.69	11.2	90.5	1.72	0.42	1.00	0.29	0.42	4.26	18.69	23.66	22.66
B-P7	722	0.84	0	15.3	1.35	0.26	1.00	0.37	0.26	0.00	1.88	2.51	1.51
B-P8	471	0.77	3.46	35.7	1.46	0.31	1.00	0.34	0.31	0.79	5.46	6.91	5.91
B-P9	349	0.69	11.2	90.5	1.61	0.38	1.00	0.31	0.38	3.85	16.88	21.41	20.41

1) Strain compatibility method was applied for the calculation of maximum moment, M_m
2) θ_{m1} , θ_{m2} , θ_{m3} , θ_{m4} , is defined at Fig. 3-15, Fig. 3-16.

[3-9] Material parameters for analyzing the effects of T/Y strain ratios to the in-plane rotation capacity of HSA800 I-shaped member

			Material parameter: [M1:Ho ¹]-F _{yw} =F _{yf} =722MPa ²]			
			$E_R: \varepsilon_u / \varepsilon_y = 15.0$	$E_R: \varepsilon_u / \varepsilon_y = 20.0$	$E_R: \varepsilon_u / \varepsilon_y = 25.0$	
Geometrical parameters [mm]	[250x150 series] Type A	[G:A-S] H-250x150x14x14	A-P1: [G:A-S]-[M:Ho-722]-[E _R -15.0]	A-P2: [G:A-S]-[M:Ho-722]-[E _R -20.0]	A-P3: [G:A-S]-[M:Ho-722]-[E _R -25.0]	
		[G:A-W] H-250x150x28x14	A-P4: [G:A-W]-[M:Ho-722]-[E _R -15.0]	A-P5: [G:A-W]-[M:Ho-722]-[E _R -20.0]	A-P6: [G:A-W]-[M:Ho-722, E _R -25.0]	
		[G:A-F] H-250x150x14x28	A-P7: [G:A-F]-[M:Ho-722]-[E _R -15.0]	A-P8: [G:A-F]-[M:Ho-722]-[E _R -20.0]	A-P9: [G:A-F]-[M:Ho-722, E _R -25.0]	
	[400x150 series] Type B	[G:B-S] H-400x150x14x14	B-P1: [G:B-S]-[M:Ho-722]-[E _R -15.0]	B-P2: [G:B-S]-[M:Ho-722]-[E _R -20.0]	B-P3: [G:B-S]-[M:Ho-722, E _R -25.0]	
		[G:B-W] H-400x150x28x14	B-P4: [G:B-W]-[M:Ho-722]-[E _R -15.0]	B-P5: [G:B-W]-[M:Ho-722]-[E _R -20.0]	B-P6: [G:B-W]-[M:Ho-722, E _R -25.0]	
		[G:B-F] H-400x150x14x28	B-P7: [G:B-F]-[M:Ho-722]-[E _R -15.0]	B-P8: [G:B-F]-[M:Ho-722]-[E _R -20.0]	B-P9: [G:B-F]-[M:Ho-722, E _R -25.0]	
	1) Ho is abbreviation of homogenous I-section, the flange and web of which are the same grade steel are applied					
	2) Bi-linear model at the piecewise interpolation approach was applied for the analysis ($F_y = 722MPa, Y_R = F_y / F_u = 0.84$)					

Chapter 3. Idealized Material Models and In-plane Rotation Capacities

[3-10] Effects of T/Y strain ratios to the in-plane rotation capacities (R_m) of HSA800 I-shaped member under moment gradient ($m_R=0$)
[Section: Type A]

(1)	(2)	(3)	(4)	(5)	(6)	(7)	(8)	(9)	(10)	(11)	(12)	(13)	(14)
Analytical model	F_y	Y_R	s	E_R	$M_m / M_{yf}^{1)}$	τ_i	$(\frac{\theta_{yf}}{\phi_{yf}}) \cdot (\frac{2}{L})$	$(\frac{\theta_{m1}}{\phi_{yf}}) \cdot (\frac{2}{L})$	$(\frac{\theta_{m2}}{\phi_{yf}}) \cdot (\frac{2}{L})$	$(\frac{\theta_{m3}}{\phi_{yf}}) \cdot (\frac{2}{L})$	$(\frac{\theta_{m4}}{\phi_{yf}}) \cdot (\frac{2}{L})$	$(\frac{\theta_m}{\phi_{yf}}) \cdot (\frac{2}{L})$	$R_m = \frac{\theta_m}{\theta_y} - 1$
[Unit]	[MPa]	[non]	[non]	[non]	[non]	[non]	[non]	[non]	[non]	[non]	[non]	[non]	[non]
A-P1	722	0.84	0	15.0	1.36	0.26	1.00	0.37	0.26	0.00	1.84	2.47	1.47
A-P2				20.0	1.36	0.26	1.00	0.37	0.26	0.00	2.51	3.14	2.14
A-P3				25.0	1.36	0.26	1.00	0.37	0.26	0.00	3.18	3.81	2.81
A-P4	722	0.84	0	15.0	1.43	0.30	1.00	0.35	0.30	0.00	2.12	2.77	1.77
A-P5				20.0	1.43	0.30	1.00	0.35	0.30	0.00	2.86	3.51	2.51
A-P6				25.0	1.43	0.30	1.00	0.35	0.30	0.00	3.61	4.26	3.26
A-P7	722	0.84	0	15.0	1.37	0.27	1.00	0.36	0.27	0.00	1.88	2.52	1.52
A-P8				20.0	1.37	0.27	1.00	0.36	0.27	0.00	2.57	3.20	2.20
A-P9				25.0	1.37	0.27	1.00	0.36	0.27	0.00	3.24	3.88	2.88

1) Strain compatibility method was applied for the calculation of maximum moment, M_m
2) θ_{m1} , θ_{m2} , θ_{m3} , θ_{m4} , is defined at Fig. 3-15, Fig. 3-16.

[3-11] Effects of T/Y strain ratios to the in-plane rotation capacities (R_m) of HSA800 I-shaped member under moment gradient ($m_R=0$)
 [Section: Type B]

(1)	(2)	(3)	(4)	(5)	(6)	(7)	(8)	(9)	(10)	(11)	(12)	(13)	(14)
Analytical model	F_y	Y_R	s	E_R	$M_m / M_{yf}^{1)}$	τ_i	$(\frac{\theta_{yf}}{\phi_{yf}}) \cdot (\frac{2}{L})$	$(\frac{\theta_{m1}}{\phi_{yf}}) \cdot (\frac{2}{L})$	$(\frac{\theta_{m2}}{\phi_{yf}}) \cdot (\frac{2}{L})$	$(\frac{\theta_{m3}}{\phi_{yf}}) \cdot (\frac{2}{L})$	$(\frac{\theta_{m4}}{\phi_{yf}}) \cdot (\frac{2}{L})$	$(\frac{\theta_m}{\phi_{yf}}) \cdot (\frac{2}{L})$	$R_m = \frac{\theta_m}{\theta_y} - 1$
[Unit]	[MPa]	[non]	[non]	[non]	[non]	[non]	[non]	[non]	[non]	[non]	[non]	[non]	[non]
B-P1	722	0.84	0	15.0	1.38	0.28	1.00	0.36	0.28	0.00	1.93	2.57	1.57
B-P2				20.0	1.38	0.28	1.00	0.36	0.28	0.00	2.62	3.25	2.25
B-P3				25.0	1.38	0.28	1.00	0.36	0.28	0.00	3.30	3.94	2.94
B-P4	722	0.84	0	15.0	1.47	0.32	1.00	0.34	0.32	0.00	2.30	2.90	1.90
B-P5				20.0	1.47	0.32	1.00	0.34	0.32	0.00	3.04	3.70	2.70
B-P6				25.0	1.47	0.32	1.00	0.34	0.32	0.00	3.84	4.50	3.50
B-P7	722	0.84	0	15.0	1.35	0.26	1.00	0.37	0.26	0.00	1.88	2.51	1.51
B-P8				20.0	1.35	0.26	1.00	0.37	0.26	0.00	2.46	3.09	2.09
B-P9				25.0	1.35	0.26	1.00	0.37	0.26	0.00	3.11	3.74	2.74

1) Strain compatibility method was applied for the calculation of maximum moment, M_m
 2) θ_{m1} , θ_{m2} , θ_{m3} , θ_{m4} , is defined at Fig. 3-15, Fig. 3-16.

[3-12] Material parameters for analyzing the effects of Y/T ratios to the in-plane behavior of HSA800 I-shaped member

			Material parameter: [M1:Ho ¹⁾ -F _{yw} =F _{yf} =722MPa ²⁾		
			$Y_R: F_y / F_u = 0.80$	$Y_R: F_y / F_u = 0.85$	$Y_R: F_y / F_u = 0.90$
Geometrical parameters [mm]	[250x150 series] Type A	[G:A-S] H-250x150x14x14	A-P1: [G:A-S]-[M:Ho-722]-[Y _R -0.80]	A-P2: [G:A-S]-[M:Ho-722]-[Y _R -0.85]	A-P3: [G:A-S]-[M:Ho-722]-[Y _R -0.90]
		[G:A-W] H-250x150x28x14	A-P4: [G:A-W]-[M:Ho-722]-[Y _R -0.80]	A-P5: [G:A-W]-[M:Ho-722]-[Y _R -0.85]	A-P6: [G:A-W]-[M:Ho-722]-[Y _R -0.90]
		[G:A-F] H-250x150x14x28	A-P7: [G:A-F]-[M:Ho-722]-[Y _R -0.80]	A-P8: [G:A-F]-[M:Ho-722]-[Y _R -0.85]	A-P9: [G:A-F]-[M:Ho-722]-[Y _R -0.90]
	[400x150 series] Type B	[G:B-S] H-400x150x14x14	B-P1: [G:B-S]-[M:Ho-722]-[Y _R -0.80]	B-P2: [G:B-S]-[M:Ho-722]-[Y _R -0.85]	B-P3: [G:B-S]-[M:Ho-722]-[Y _R -0.90]
		[G:B-W] H-400x150x28x14	B-P4: [G:B-W]-[M:Ho-722]-[Y _R -0.80]	B-P5: [G:B-W]-[M:Ho-722]-[Y _R -0.85]	B-P6: [G:B-W]-[M:Ho-722]-[Y _R -0.90]
		[G:B-F] H-400x150x14x28	B-P7: [G:B-F]-[M:Ho-722]-[Y _R -0.80]	B-P8: [G:B-F]-[M:Ho-722]-[Y _R -0.85]	B-P9: [G:B-F]-[M:Ho-722]-[Y _R -0.90]
1) Ho is abbreviation of homogenous I-section, the flange and web of which are the same grade steel are applied					
2) Bi-linear model at the piecewise interpolation approach was applied for the analysis ($F_y = 722MPa$, $E_R = \epsilon_u / \epsilon_y = 15.0$)					

[3-13] Effects of Y/T strength ratios to the in-plane rotation capacities (R_m) of HSA800 I-shaped member under moment gradient ($m_R=0$) [Section: Type A]

(1)	(2)	(3)	(4)	(5)	(6)	(7)	(8)	(9)	(10)	(11)	(12)	(13)	(14)
Analytical model	F_y	Y_R	$E_{st,R}$	E_R	$M_m / M_{yf}^{1)}$	τ_i	$\left(\frac{\theta_{yf}}{\phi_{yf}}\right) \cdot \left(\frac{2}{L}\right)$	$\left(\frac{\theta_{m1}}{\phi_{yf}}\right) \cdot \left(\frac{2}{L}\right)$	$\left(\frac{\theta_{m2}}{\phi_{yf}}\right) \cdot \left(\frac{2}{L}\right)$	$\left(\frac{\theta_{m3}}{\phi_{yf}}\right) \cdot \left(\frac{2}{L}\right)$	$\left(\frac{\theta_{m4}}{\phi_{yf}}\right) \cdot \left(\frac{2}{L}\right)$	$\left(\frac{\theta_m}{\phi_{yf}}\right) \cdot \left(\frac{2}{L}\right)$	$R_m = \frac{\theta_m}{\theta_y} - 1$
[Unit]	[MPa]	[non]	[non]	[non]	[non]	[non]	[non]	[non]	[non]	[non]	[non]	[non]	[non]
A-P1	722	0.80	0	15.0	1.42	0.29	1.00	0.35	0.29	0.00	2.06	2.70	1.70
A-P2		0.85			1.34	0.26	1.00	0.37	0.26	0.00	1.79	2.42	1.42
A-P3		0.90			1.28	0.22	1.00	0.39	0.22	0.00	1.53	2.14	1.14
A-P4	722	0.80	0	15.0	1.49	0.33	1.00	0.33	0.33	0.00	2.31	2.98	1.98
A-P5		0.85			1.42	0.30	1.00	0.35	0.30	0.00	2.07	2.72	1.72
A-P6		0.90			1.36	0.26	1.00	0.37	0.26	0.00	1.84	2.47	1.47
A-P7	722	0.80	0	15.0	1.43	0.30	1.00	0.35	0.30	0.00	2.09	2.74	1.74
A-P8		0.85			1.35	0.26	1.00	0.37	0.26	0.00	1.83	2.46	1.46
A-P9		0.90			1.29	0.22	1.00	0.39	0.22	0.00	1.57	2.19	1.19

1) Strain compatibility method was applied for the calculation of maximum moment, M_m
 2) θ_{m1} , θ_{m2} , θ_{m3} , θ_{m4} , is defined at Fig. 3-15, Fig. 3-16.

Chapter 3. Idealized Material Models and In-plane Rotation Capacities

[3-14] Effects of T/Y strength ratios to the in-plane rotation capacities (R_m) of HSA800 I-shaped member under moment gradient ($m_R=0$) [Section: Type B]

(1)	(2)	(3)	(4)	(5)	(6)	(7)	(8)	(9)	(10)	(11)	(12)	(13)	(14)
Analytical model	F_y	Y_R	$E_{st,R}$	E_R	M_m / M_{yf}^{-1}	τ_i	$\left(\frac{\theta_{yf}}{\phi_{yf}}\right) \cdot \left(\frac{2}{L}\right)$	$\left(\frac{\theta_{m1}}{\phi_{yf}}\right) \cdot \left(\frac{2}{L}\right)$	$\left(\frac{\theta_{m2}}{\phi_{yf}}\right) \cdot \left(\frac{2}{L}\right)$	$\left(\frac{\theta_{m3}}{\phi_{yf}}\right) \cdot \left(\frac{2}{L}\right)$	$\left(\frac{\theta_{m4}}{\phi_{yf}}\right) \cdot \left(\frac{2}{L}\right)$	$\left(\frac{\theta_m}{\phi_{yf}}\right) \cdot \left(\frac{2}{L}\right)$	$R_m = \frac{\theta_m}{\theta_y} - 1$
[Unit]	[MPa]	[non]	[non]	[non]	[non]	[non]	[non]	[non]	[non]	[non]	[non]	[non]	[non]
B-P1	722	0.80	0	15.0	1.44	0.31	1.00	0.35	0.31	0.00	2.14	2.79	1.79
B-P2		0.85			1.37	0.27	1.00	0.37	0.27	0.00	1.88	2.52	1.52
B-P3		0.90			1.30	0.23	1.00	0.38	0.23	0.00	1.63	2.25	1.25
B-P4	722	0.80	0	15.0	1.53	0.35	1.00	0.35	0.35	0.00	2.42	3.09	2.09
B-P5		0.85			1.46	0.31	1.00	0.34	0.31	0.00	2.20	2.85	1.85
B-P6		0.90			1.39	0.28	1.00	0.36	0.28	0.00	1.98	2.62	1.62
B-P7	722	0.80	0	15.0	1.41	0.29	1.00	0.35	0.29	0.00	2.04	2.69	1.69
B-P8		0.85			1.34	0.25	1.00	0.37	0.25	0.00	1.78	2.40	1.40
B-P9		0.90			1.28	0.22	1.00	0.39	0.22	0.00	1.51	2.12	1.12

1) Strain compatibility method was applied for the calculation of maximum moment, M_m
2) θ_{m1} , θ_{m2} , θ_{m3} , θ_{m4} , is defined at Fig. 3-15, Fig. 3-16.

Chapter 4 Analytical Studies of Inelastic LTB Behaviors

In previous chapter, the in-plane behavior of I-shaped member has been discussed. The performance of the inelastic behavior would not fully realized in actual since the out-of-plane behavior such lateral torsional buckling and local buckling curtails its performance according to slenderness ratios as described in Fig. 4-1. In this chapter, the out-of-plane behavior (=the inelastic lateral torsional buckling behavior) of I-shaped member will be discussed in detail.

4.1 Derivation of inelastic section rigidities for analyzing inelastic buckling

The resistance of elastic lateral torsional buckling (LTB) is depend on the minor axis flexural rigidity (EI_y), the warping rigidity (EC_w) and torsional rigidity (GJ). The rigidities can be simply calculated when a material remains in elastic range, as well described previous reference (Timoshenko, 1959). However, as the yielding commence and spread in the inner side of flanges and web of I-section according to the increased moment beyond the yield moment (M_y), the rigidities start to decrease steadily or somewhat radically reduced as the moment approach to the full plasticity. The decrease is

generated since some parts of the cross section have limited or no resistance according to the stress-strain or modulus-strain characteristics of a specific material and geometrical configuration. Therefore, the decreased rigidities $((EI_y)_e, (EC_w)_e, (GJ)_e)$ (abbreviated as effective rigidities) needs to carefully consider and quantified for solving the various inelastic LTB problems. The derivation procedure of effective rigidities is carefully described with adoption of the tangent modulus theory in below chapter.

4.1.1 Tangent modulus theory and its application

Tangent modulus is the most prevalent, principal design codes adopted, theory to analyzed and predict the inelastic buckling phenomenon. Although the theory sometimes partially inaccurate for inelastic material unloaded elastically as shown in Fig. 4-2, carefully performed experiments have shown that it leads more accurate and the closer and the safer (lower bound buckling load) solution than reduced modulus theory. Therefore, in this research, the tangent modulus theory was consistently applied for the analytical study and the points of bifurcation (the inelastic buckling begins) were measured carefully in the experimental study.

4.1.1.1 Tangent modulus for mild steel in yield plateau region

The derivation of tangent modulus for mild steel which have a yield plateau $(E_{t2,mild}(\epsilon))$ is described below. Fig. 4-3 shows the stress-strain curve of typical

SM490 with $Y_R=0.69$, $S=9.0$ and $E_{st}=E/24$. Fig. 4-4 shows the idealized material model applied in the Galambos' 1963 year, Lay's 1965 year and Trahair's 1977 paper. At the Galambos' 1963 year paper, the tangent modulus E for elastic region, $E_{t2, Galambos, mild}(\epsilon)=0$ for yield plateau region and $E_{t3}=E/33 \sim E/49$ for the strain-hardened regions was applied. For yield plateau region, however, many experimental have indicated that the zero modulus values ($E_{t2}=0$) are extremely low and yield logical paradox such zero buckling load ($P_t=(\pi^2 \cdot E_{t2} \cdot I)/L^2=0$) in axially loaded column under yield plateau region. In actual, no buckling phenomenon was observed when inelastic material is under the yield plateau region if a member properly designed.

From the experimental observations, White (1960) and Lay (1965) investigated and suggested that yielding may considered as a series of discontinuous slips (here and after 'slip theory'), and that all of the material in the yielded region is either elastic or strain hardened. This led to the first proposal that the tangent moduli for the yield plateau region should be properly suggested as considering the experimental phenomenon. In analogous to White and Lay's experimental investigation, a recent publication associated with a material science (Fig. 4-5) clearly shows the slip behavior via the micrograph of a single crystal of α brass strained 0.2% in tension. The dark show the undisturbed elastic surface and the light lines indicate the planes of slip (Daniel & Alan, 2001). As the same point of view with the

White and Lay's slip theory, Fig 4-5 well represents the slip behaviors in inelastic range. From those experimental backgrounds, an analytical model (Fig. 4-6) and tangent modulus formulas ($E_{t2,Lay,mild}(\varepsilon)$, Eq. 4-1) by adopting Lay's 1965 year consideration for the yield plateau region were selected in this study.

$$E_{t2,Lay,mild}(\varepsilon) = \frac{1}{\left(\frac{1}{E_{st}} - \frac{1}{E}\right)\left(\frac{\varepsilon - \varepsilon_y}{\varepsilon_{st} - \varepsilon_y}\right) + \frac{1}{E}} \quad (4-1)$$

where

$E_{t2,Lay,mild}(\varepsilon)$ is inelastic modulus at yield plateau region in this research applied in mild steel

ε is measured strain in tensile coupon test ()

$\varepsilon_y = f_y / E$ is the strain at yield stress in mild steel

4.1.1.2 Tangent modulus for mild steel in strain-hardening region

For the tangent modulus for strain hardened region (here and after, 'strain-hardening modulus'), Galambos and other researchers (Galambos, 1963; Trahair, 1993; Suzuki, 1970) prevalently adopted or idealize the initial part modulus as strain hardening modulus ($E_{t3}(\varepsilon)=E_{st}$). However, the strain-hardening modulus, in actual, also decreases steadily according to the magnitude of strain in analogous to the yield plateau region. The reason for the idealization in the past researches was to adopt the simplest stress-strain curve model (Fig. 4-4).

Different from the previous consideration, Haaijer (1959) proposed the improved idealization method for the strain hardened region as Eq. 4-2 and

Fig. 4-7. The shape of the stress-strain curve is the same as that of the traditional model up to the start of strain-hardening. Beyond that point it follows formula introduced by Haaijer. By this model, the idealization of strain hardening region for mild steel is well described as verified in **Fig. 4-7a**. In this study, as a consequence, Haaijer S-S model (**Eq. 4-2a**) and its derivative (**Eq. 4-2b**) was adopted for deriving strain hardening modulus ($E_{t3,Haaijer,mild}(\varepsilon)$) of mild steel as shown in **Fig. 4-7**.

$$\varepsilon - \varepsilon_{st} = \frac{f - f_y}{E/h} + K \left(\frac{f - f_y}{E/h} \right)^m \quad (4-2a)$$

[when $\varepsilon_{st} < \varepsilon \leq \varepsilon_u$ or $f_y < f \leq f_u$]

$$E_{t3,Haaijer,mild}(\varepsilon) = \frac{E/h}{\left[1 + K \cdot m \cdot \left(\frac{f - f_y}{E/h} \right)^{m-1} \right]} \quad (4-2b)$$

[when $\varepsilon_{st} < \varepsilon \leq \varepsilon_u$]

where

$E_{t3,Haaijer,mild}(\varepsilon)$ is inelastic modulus at strain hardening region in this research applied in mild steel

m, K are the parameters for describing the shape of strain hardening in Haaijer model

4.1.1.3 Tangent modulus for high strength steel

The application of the tangent modulus for high strength steel which does not have yield plateau is described below. **Fig. 4-8** shows the stress-strain curve of typical HSA800 with $Y_R=0.85$ and $E_R=\varepsilon_u/\varepsilon_y=15.0$. Up to now, no idealized stress-strain curve model for high strength steel have been suggested and established yet and are required to propose adequate for high strength

steel.

Contrary to the mild steel, the properties of which are easily distinguishable as the three portions of the regions (elastic, yield plateau, strain hardened), high strength steel are not able to separate each portions separately. As a result continuous form of idealization (Fig. 4-9) for non-linear stress-strain curve seems to be more appropriate in analogous to Haaijer approach to idealized strain hardening region. Actually, the continuous form of stress-strain curve idealization has been attempted in the idealizations of Aluminum alloy performed by Mazzolani (Mazzolani, 1997) via modifying Ramberg-Osgood model.

Eq. 4-3 showed proposed stress-strain model for high strength steel in this study. At the Eq. 4-3, the strain-hardening exponent (n) is the key parameter to represent non-linear stress-strain curve. As n approach to infinite value (∞), the stress-strain curve becomes close to the bi-linear (elasto-plastic) profile. While n approach to 1 the stress-strain curve becomes close to linearly increased profile. Mazzolani(1997) classify the values of strain-hardening exponent (n) according to class of aluminum alloys. The n -values of the non-heat-treated alloys are close 10-20 while the n -values of the heat-treated alloys are close to 20-40. As shown in Fig. 4-9, the strain hardening exponents for HSA800 are close to 18-25 and the values seem to closely predict the actual behavior of HSA 800 specimens as verified in chapter III. Finally,

derivative of Eq. 4-3a was adopted for tangent modulus ($E_{t,R-O}(\varepsilon)$) of high strength steel, in this study, as expressed by Eq. 4-3b.

$$\varepsilon = \frac{f}{E} + 0.002 \left(\frac{f}{f_{0.2}} \right)^n \quad (4-3a)$$

[when $0 \leq \varepsilon \leq \varepsilon_u$ or $0 \leq \varepsilon \leq f_u$]

$$E_{t,R-O,HSS}(\varepsilon) = \frac{E}{\left[1 + \frac{0.002nE}{f_{0.2}} \left(\frac{f}{f_{0.2}} \right)^{n-1} \right]} \quad (4-3b)$$

[when $0 \leq \varepsilon \leq \varepsilon_u$ or $0 \leq \varepsilon \leq f_u$]

where

$E_{t,R-O,HSS}(\varepsilon)$ is modulus by Ramberg-Osgood model adopted in this research applied in high strength steel

$f_{0.2}$ is 0.2% offset yield stress

n is hardening parameter in Ramberg-Osgood model

4.1.2 Inelastic section rigidities (stiffnesses) in ideal I section

As mentioned previously, the resistance against inelastic LTB depends on the effective flexural rigidities $(EI_y)_e$, effective warping rigidities $(EC_w)_e$ and effective torsional rigidities $(GJ)_e$. The calculation of effective rigidities is not easy task (inevitably numerical calculation are required when the effect of residual stresses are considered) since following reasons.

a) As shown in Fig. 4-7b and Fig. 4-9b, the value of the tangent modulus varies according to each strain level such elastic, inelastic and strain hardening region. Therefore, sophisticated formulas are required for acquiring the tangent modulus in inelastic ranges. Furthermore, if the residual stresses are considered, the initial residual strain disturbed bending strain of the loaded

I-section, resulting in complex strain distribution as shown in Fig. 4-10.

b) Also, as shown in Fig. 4-11, even geometrically doubly symmetrical I-section, the initial residual stress changes the I-section into mono-symmetrical I-section in inelastic range since the top and bottom flanges have different stiffness properties. As a result, location of neutral axis (y_n) varied depending on each strain level for satisfying axial equilibrium $\int_A f(x, y) dA = 0$ as shown in Fig. 4-12. Also, location of shear center (y_{0t}) varied depending on the relative flexural stiffness of top and bottom flanges as described in Eq.4-4.

$$y_{0t} = \left[\frac{(EI_y)_{e,BF}}{(EI_y)_{e,TF} + (EI_y)_{e,BF}} - \frac{1}{2} \right] (d - t_f). \quad (4-4)$$

where

y_{0t} is coordinate of shear center by tangent modulus concept

$(EI_y)_{e,BF} = \int_{BF} E_t x^2 dA$ is flexural stiffness of bottom flange by tangent modulus concept

$(EI_y)_{e,TF} = \int_{TF} E_t x^2 dA$ is flexural stiffness of top flange by tangent modulus concept

d is depth

t_f is flange thickness

c) Since the three varied parameters (E_t , y_n , y_{0t}) with the initial residual stresses, the effective warping rigidities $(EC_w)_e$ and effective torsional rigidities $(GJ)_e - M \cdot \beta_x$ need to be iteratively calculated including the variation of neutral axis and shear center as described in Eq.4-5 and Eq.4-6.

$$(EC_w)_t = (E_t I_y)_t \cdot \frac{(d - t_f)^2}{4} \cdot \left[1 - \frac{4 \cdot y_{0t}^2}{(d - t_f)^2} \right] \quad (4-5)$$

where

$(EC_w)_t$ is warping stiffness of I-section by tangent modulus concept $(E_t I_y)_t$ is

flexural stiffness of I-section by tangent modulus concept

y_{0t} is coordinate of shear center by tangent modulus concept calculated by Eq. 4-4

$$M_x (\beta_x)_t = \int_A f_z (x^2 + (y - y_{0t})^2) dA \quad (4-6)$$

where

f_z is longitudinal stress $(f_z = \frac{M_x \cdot y}{I})$

x, y is coordinate of an element from geometrical axis

M_x is x-axis moment

$(\beta_x)_t$ is mono-symmetry section constant by tangent modulus concept in inelastic range

By taking account of the above three considerations, the effective rigidities expressed by explicit formulas are only enabled in ideal I-beam which neglects the effect of residual stress. In next chapter, the formulation of effective flexural rigidities $(EI_y)_e$, effective warping rigidities $(EC_w)_e$ and effective torsional rigidities $(GJ)_e$ of ideal I section at inelastic range loading will be introduced.

4.1.2.1 Formulation of effective flexural stiffness $(EI_y)_e$ in ideal I-section

For clarification, H-250x150x14x14 section were selected and illustrated in plotting paper. The origin of I-section is located in geometrical center of I-section as shown in Fig. 4-13.

(1) Mild steel (SM490)

Fig. 4-14a shows the bending strain distribution of mild steel to achieve plastic moment (M_p). For the plastic moment, the required longitudinal strain for the top and bottom flange is larger the yield plateau length ($\epsilon_{top} \geq s \cdot \epsilon_y$). As shown in Fig. 4-14b, the location of neutral axis and shear center remains in the origin. Fig. 4-14c shows the stress distribution at the plastic moment. As shown in the profile of the web stress distribution, the stress component can be divided into three components ((a) elastic region ($f \leq f_y$), (b) yield plateau region ($f = f_y$) and (c) strain-hardened region ($f > f_y$)). Fig. 4-14d shows the tangent modulus distribution at plastic moment. The tangent modulus for calculating the effective flexural rigidities are composed of four components ((a) elastic web region ($w, \#1$), (b) yield plateau web region ($w, \#2$), (c) yield plateau flange region ($f, \#2$) and (d) strain hardened flange region ($f, \#3$)). From the four tangent modulus components, the effective flexural rigidities ($(EI_y)_{e, mild} = \int_A E_t(\epsilon) \cdot x^2 dA$) of ideal mild steel I-beam could be calculated as

Eq.4-7.

$$\begin{aligned} (EI_y)_{e, mild} &= \int_A E_t(\epsilon) \cdot x^2 dA \\ &= \int_{w, \#1} E_{t1, mild}(\epsilon) \cdot x^2 dA + \int_{w, \#2} E_{t2, mild}(\epsilon) \cdot x^2 dA \end{aligned} \quad (4-7)$$

$$\begin{aligned} &+ \int_{f, \#2} E_{t2, mild}(\epsilon) \cdot x^2 dA + \int_{f, \#3} E_{t3, mild}(\epsilon) \cdot x^2 dA \\ \int_{w, \#1} E_{t1, mild}(\epsilon) \cdot x^2 dA &= (E) \cdot \left(\frac{1}{12} \cdot (d / \epsilon_{R, top}) \cdot t_w^3 \right) \end{aligned} \quad (4-7a)$$

$$\begin{aligned}
 & \int_{w,\#2} E_{t2,mild}(\varepsilon) \cdot x^2 dA \\
 &= 2 \cdot \left[\int_{((d/2)/\varepsilon_{R,top})}^{(d/2-t_f)} \frac{1}{\left(\frac{1}{E_{st}} - \frac{1}{E}\right) \cdot \left(\frac{2(\varepsilon_{R,top}/d) \cdot y - 1}{(s-1)}\right) + \frac{1}{E}} dy \right] \cdot \left[\int_{-t_w/2}^{t_w/2} x^2 dx \right] \quad (4-7b)
 \end{aligned}$$

$$\begin{aligned}
 & \int_{f,\#2} E_{t2,mild}(\varepsilon) \cdot x^2 dA \\
 &= 2 \cdot \left[\int_{(d/2-t_f)}^{(d/2)(s/\varepsilon_{R,top})} \frac{1}{\left(\frac{1}{E_{st}} - \frac{1}{E}\right) \cdot \left(\frac{2(\varepsilon_{R,top}/d) \cdot y - 1}{(s-1)}\right) + \frac{1}{E}} dy \right] \cdot \left[\int_{-b_f/2}^{b_f/2} x^2 dx \right] \quad (4-7c)
 \end{aligned}$$

$$\int_{f,\#3} E_{t3,mild}(\varepsilon) \cdot x^2 dA = (E_{st}) \cdot \left[\frac{1}{12} \cdot [d \cdot (1 - (s/\varepsilon_{R,top}))] \cdot b_f^3 \right] \quad (4-7d)$$

where

$\int_{w,\#1} E_{t1,mild}(\varepsilon) \cdot x^2 dA$ is effective flexural rigidities at elastic web portion applied in mild steel

$\int_{w,\#2} E_{t2,mild}(\varepsilon) \cdot x^2 dA$ is effective flexural rigidities at inelastic web portion applied in mild steel

$\int_{f,\#2} E_{t2,mild}(\varepsilon) \cdot x^2 dA$ is effective flexural rigidities at inelastic flange portion applied in mild steel

$\int_{f,\#3} E_{t3,mild}(\varepsilon) \cdot x^2 dA$ is effective flexural rigidities at hardening flange portion applied in mild steel

$\varepsilon_{R,top} = \varepsilon / \varepsilon_y$ is the ratio of top flange strain to yield strain

t_w is web thickness

Figure 4-16 show the effective flexural rigidities of H-250x150x14x14/SM490 according to curvature variation, calculated by Eq. 4-7. The flexural rigidities (represented by $\alpha(\phi) = (EI_y)_e / (EI_y)$) remain elastic ($\alpha(\phi) = 1.0$) until the yielding commences (#1, $\phi/\phi_y \leq 1.0$). Then, $\alpha(\phi)$ start

to decrease from 1.0 to 0.05 as the yielding spread from the outer flanges into the inner flange and web according to the inelastic curvatures (#2, $1.0 \leq \phi/\phi_y \leq 10.0$). $\alpha(\phi)$ decrease continuously below 0.05, where inelastic buckling easily is prone, as the curvature reaches the ranges (#3, $\phi/\phi_y \geq 10.0$). Therefore, the critical curvature when the inelastic section stiffness is under 5% of its initial value is $10.0\phi_y$. Please note that the properties of SM490 plate were $Y_R=0.69$, $S=9.0$ and $E_{st}=E/24$.

(2) High strength steel (HSA800)

Fig. 4-15a shows the bending strain distribution of high strength steel to achieve plastic moment (M_p). For achieving the plastic moment, high strength steel require less longitudinal strain for the top and bottom flange than conventional steel about 2.0 times yield strain ($\varepsilon_f=2.0\cdot\varepsilon_y$). This phenomenon results from early and continuous strain hardening properties of high strength steel. **Fig. 4-15b** shows the location of neutral axis and shear center which remains in the origin as the same with the mild steel case. **Fig. 4-15c** shows the stress distribution at the plastic moment. As shown in the profile of the web stress distribution, the stress components are not easy to discrete into individual components. By the slope of the stress distribution, however, it can be divided into two component ((a) below proportional limit ($f \leq f_p$), (b) beyond proportional limit ($f > f_p$)). **Fig. 4-15d** shows the tangent modulus

distribution at plastic moment. The tangent modulus for calculating the effective flexural rigidities are composed of three components ((a) elastic web region ($w, \#1$), (b) strain hardened web region ($w, \#2$), (c) strain hardened flange region ($f, \#2$). From the four tangent modulus components, the effective flexural rigidities ($(EI_y)_{\epsilon, HSS} = \int_A E_t(\epsilon) \cdot x^2 dA$) of ideal high strength I-beam could be calculated as Eq.4-8.

$$(EI_y)_{\epsilon, HSS} = \int_A E_{t,R-O,HSS} \cdot x^2 dA$$

$$= \int_{w,\#1} E_{t,R-O,HSS}(\epsilon) \cdot x^2 dA + \int_{w,\#2} E_{t,R-O,HSS}(\epsilon) \cdot x^2 dA \quad (4-8)$$

$$+ \int_{f,\#2} E_{t,R-O,HSS}(\epsilon) \cdot x^2 dA$$

$$\int_{w,\#1} E_{t,R-O,HSS} \cdot x^2 dA = (E) \cdot \left(\frac{1}{12} \cdot (d / \epsilon_{R,top}) \cdot t_w^3\right) \quad (4-8a)$$

$$\int_{w,\#2} E_{t,R-O,HSS}(\epsilon) \cdot x^2 dA$$

$$= \frac{E}{\left[1 + \frac{0.002nE}{f_{0.2}} \left(\frac{f_{w,av}}{f_{0.2}}\right)^{n-1}\right]} \cdot \left[\frac{1}{12} \cdot (d - 2t_f - d / \epsilon_{R,top}) \cdot t_w^3\right] \quad (4-8b)$$

$$\int_{f,\#2} E_{t,R-O,HSS}(\epsilon) \cdot x^2 dA$$

$$= \frac{E}{\left[1 + \frac{0.002nE}{f_{0.2}} \left(\frac{f_{f,av}}{f_{0.2}}\right)^{n-1}\right]} \cdot \left[\left(\frac{1}{12} \cdot (2t_f) \cdot b_f^3\right)\right] \quad (4-8c)$$

where

$\int_{w,\#1} E_{t,R-O,HSS}(\epsilon) \cdot x^2 dA$ is effective flexural rigidities at elastic web portion at

continuous yielding material

$\int_{w,\#2} E_{t,R-O,HSS}(\epsilon) \cdot x^2 dA$ is effective flexural rigidities at inelastic web portion at

continuous yielding material

$\int_{f, \#2} E_{t,R-O,HSS}(\varepsilon) \cdot x^2 dA$ is effective flexural rigidities at inelastic flange portion at continuous yielding material
 $f_{w,av}$ is weighted average stress at the strain hardened web
 $f_{f,av}$ is weighted average stress at the strain hardened flange

Figure 4-16a shows the effective flexural rigidities of H-250x150x14x14/HSA800 according to curvature variation, calculated by Eq. 4-8. The flexural rigidities (represented by $\alpha(\phi) = (EI_y)_e / (EI_y)$) remain elastic ($\alpha(\phi) = 1.0$) until the vicinity of proportional limit (#1, $\phi / \phi_y \leq 0.75$). Then, $\alpha(\phi)$ starts to decrease rapidly from 1.0 to 0.05 as the yielding spread from the outer flanges into the inner flange and web of I-section according to the inelastic curvature region (#2, $0.75 \leq \phi / \phi_y \leq 2.5$). $\alpha(\phi)$ decrease continuously below 0.05, where inelastic buckling easily is prone, as the curvatures reaches the ranges (#3, $\phi / \phi_y > 2.5$). Therefore, the critical curvature when the inelastic section stiffness is under 5% of its initial value is $2.5 \cdot \phi_y$. Please note that the properties of HSA800 are $Y_R = 0.85$ and $E_R = \varepsilon_u / \varepsilon_y = 15.0$.

4.1.2.2 Formulation of effective warping stiffness $(EC_w)_e$ in ideal I-section

(1) Mild steel (SM490)

Effective warping rigidities fabricated by mild steel are formulated based on the inelastic flanges as described by Eq. 4-9 and Fig. 4-14d. Fig. 4-16b shows the effective warping rigidities (represented by $\beta(\phi) = (EC_w)_e / (EC_w)$) of H-250x150x14x14 section fabricated by SM490 material, calculated by Eq.

4-9. As compared to effective flexural stiffness in Fig. 4-16a, $(EC_w)_{e,SM490}$ showed similar tendency as $(EI_y)_{e,SM490}$. It seems that the reason for the similar tendency between two rigidities is resulted from that the contribution of flange is significant to the inelastic flexural rigidities of I-section.

$$(EC_w)_{e, mild} = \frac{1}{4}(d - t_f)^2 \cdot \left[\int_{f, \#2} E_{t2, mild}(\varepsilon) \cdot x^2 dA + \int_{f, \#3} E_{t3, mild}(\varepsilon) \cdot x^2 dA \right] \quad (4-9)$$

(2) High strength steel (HSA800)

Effective warping rigidities fabricated by high strength steel are formulated based on the inelastic flanges as described by Eq.4-10 and Fig. 4-15d. Fig. 4-16b shows the effective warping rigidities of H-250x150x14x14/HSA800 according to curvature variation, calculated by Eq. 4-10. The warping rigidities ($\beta(\phi) = (EC_w)_{e, HSS} / (EC_w)_{e, mild}$) remain elastic ($\beta(\phi) = 1.0$) until the vicinity of proportional limit (#1, $\phi/\phi_y \leq 0.75$). Then, $\beta(\phi)$ start to decrease rapidly from 1.0 to 0.05 as the yielding spread from the outer flanges into the inner flange and web of I-section according to the inelastic curvature region (#2, $0.75 \leq \phi/\phi_y \leq 3.0$). $\beta(\phi)$ decrease continuously below 0.05, where inelastic buckling easily is prone, as the curvatures reaches the ranges ((#3, $\phi/\phi_y > 3.0$)).

$$(EC_w)_{e, HSS} = \frac{1}{4}(d - t_f)^2 \cdot \left[\int_{f, \#2} E_{t, R-O, HSS} \cdot x^2 dA \right] \quad (4-10)$$

4.1.2.3 Formulation of effective torsional stiffness $(GJ)_e$ in ideal I-section

For the torsional rigidities $(GJ)_e$, Neal (1950) have shown that at the start of lateral buckling St. Venant's torsional rigidities is not dependent on the amount of yielding and the elastic torsional rigidities can be used for substitution in lateral buckling equation. Effective torsional rigidities fabricated both mild and high strength steels are formulated as described by Eq.4-11. Therefore the torsional rigidities remain elastic ($\gamma(\Phi)=1.0$) regardless of curvature variation as shown in Fig. 4-16c.

$$(GJ)_e - M_x(\beta_x)_t = G \cdot \left[\frac{1}{3}(d - 2t_f) \cdot t_w^3 + \frac{2}{3}b \cdot t_f^3 \right] = GJ \quad (4-11)$$

Where

$(\beta_x)_t = 0$ is zero in ideal beam since y_{0t} remain constant at its initial origin position even in inelastic range.

4.1.2.4 The effect of the post-yield properties to the effective rigidities

By the tangent modulus applicable both mild and high strength steel, the explicit formula (Eq. 4-7 and Eq. 4-8) for the inelastic section stiffness (flexural, warping and torsion) of ideal I-section are proposed. Except the effective torsional stiffness, it could be concluded as follow. For mild steel, as the initial strain-hardening modulus (E_{st}) is higher, the inelastic section rigidities ($(EI_y)_{e,mild}$, $(EC_w)_{e,mild}$) become higher. Meanwhile, for high strength steel, as the strain hardening parameter (n) is lower the inelastic section rigidities ($(EI_y)_{e,HSS}$, $(EC_w)_{e,HSS}$) become higher.

4.1.3 Residual stress in I-section

So far, the effective rigidities $((EI_y)_e, (EC_w)_e, (GJ)_e)$ of ideal I-beam have been dealt with. In this chapter, residual stress, which is well known as a factor significantly influential on the inelastic buckling strength of I-section member, will be discussed.

4.1.3.1 Complexity of developing residual stress model

Historically, many theoretical and experimental studies on residual stresses indicate that the residual stresses presented in rolled section are significantly different to those in welded section (Fukumoto, 1977; Nethercot, 1974; Yoshida, 1975). Also, residual stress distribution measured in experiment may differ significantly from the theoretical idealized pattern (Fukumoto et al., 1980; Fukumoto and Itoh, 1981). Considering the distribution pattern and the magnitude of residual stress, residual stress models adequate for the rolled and welded I-section are discussed.

4.1.3.2 Residual stresses in hot-rolled I-section

In a hot rolled beam, longitudinal residual stresses are induced during cooling after rolling, and as a result of any mechanical straightening process (Lay and Ward, 1969). Flange tips and web center are the location where the more highly exposed regions of the cross section during cooling. These early cooling regions shrink, inducing matching tensile stress in the high

temperature late-cooling regions at the flange-web junctions and for the axial equilibrium compressive residual stress induced in the late-cooling regions as shown in Fig. 4-18.

(1) Experimental study

Among the numerous experimental studies on residual stresses, Fukumoto (1980) reported sincerely prepared and performed experimental studies by the sectioning methods. Fig. 4-18 shows the measured residual stress pattern and magnitude in H-200x100x5.5x8 section from the reference. The residual stress pattern in the flanges ($f_{rf}(x)$) approximately showed linear or parabolic pattern and the residual stress pattern in the web ($f_{rw}(y)$) showed parabolic pattern. The magnitude of f_{rfc} , f_{rft} and f_{rwc} are 20.69MPa, 174.90MPa and 177.2MPa respectively where f_{rfc} is the maximum compressive residual stress in the flange tip; f_{rft} is the maximum tensile residual stress in web-to-flange junction; f_{rwc} is the maximum compressive residual stress in web. However, the magnitudes and distributions of residual stress vary considerably with the cross-section geometry and with the cooling and straightening process.

(2) Theoretical study

While the experimental flange and web residual stress pattern reported in Fukumoto (1980) are approximately parabolic, Lee et al. (1967) suggested that quadratic distribution of the form as shown in Eq. 4-13 so that satisfying axial and torsional equilibrium Eq. 4-12 .

$$\int_A f_r dA = 0 \quad (4-12a)$$

$$\int_A f_r (x^2 + y^2) dA = 0 \quad (4-12b)$$

where

f_r is the residual stress at a point of I-section

x, y is coordinate of an element from geometrical axis

$$f_{rf}(x) = a_1 + a_2 x^2 + a_3 x^4 \quad (4-13a)$$

$$f_{rw}(y) = a_4 + a_5 y^2 + a_6 y^4 \quad (4-13b)$$

where

f_{rf} is the residual stress distributed in flange

f_{rw} is the residual stress distributed in web

f_{rfc} is the maximum compressive residual stress in flange at the tip ($x = b_f / 2$, $y = d / 2 - t_f / 2$)

f_{rft} is the maximum tensile residual stress at web-to-flange junction ($x = 0$, $y = d / 2 - t_f / 2$)

f_{rwc} is the maximum compressive residual stress in web at center ($x = 0$, $y = 0$)

Eq. 4-12a ensures the resultant of the residual stresses have a zero axial force. Eq. 4-12b ensures the residual stresses have a zero axial torque effect when the member is twisted elastically. If this condition is not satisfied, the effective torsional rigidity of the cross-section should be changed to

$$(GJ - \int_A f_r (x^2 + y^2) dA).$$

Different from the Lee's suggestion, Galambos (1963) assumed linear distribution (here and after, "Lehigh's residual stress pattern") of the form as

shown in Eq. 4-14. Contrary to the quadratic distribution, this linear distribution only ensures the axial equilibrium (Eq. 4-12a) and torsional equilibrium (Eq. 4-12b) is not satisfied, inevitably resulting in torsional rigidities as follows ($GJ - \int_A f_r (x^2 + y^2) dA$).

$$f_{rf} = a_1 + a_2 x = f_{rft} + \frac{(f_{rfc} - f_{rft})}{b_f / 2} \cdot x \quad (4-14a)$$

$$f_{rw} = a_3 + a_4 x = f_{rwt} - \frac{f_{rwt}}{t_w / 2} \cdot x \quad (4-14b)$$

where

f_{rf} is the residual stress distributed in flange

f_{rw} is the residual stress distributed in web

$$f_{rwt} = f_{rft} = \left[\frac{b_f t_f}{b_f t_f + (d - 2t_f)t_w} \right] f_{rfc} \text{ is the maximum tensile residual stress in}$$

Lehigh residual stress model

4.1.3.3 Residual stresses in welded I-section

Residual stresses induced in welded beam are as a result of flame-cutting and welding the flanges and webs, causing uneven heating and cooling in I-section. The process is similar to that of hot-rolled I-section, with large tensile residual stress induced in the flange-web joints and equilibrated compression in the flange and webs as shown in Fig. 4-19.

(1) Experimental study

Among the numerous experimental studies on residual stresses, Fukumoto (1981) reported sincerely prepared and performed experimental studies by the

sectioning methods. Fig. 4-19 shows the measured residual stress pattern and magnitude in H-200x100x6x8 section from the reference. The residual stress pattern in the flanges ($f_{rf}(x)$) approximately showed approximately parabolic or quadratic pattern and the residual stress pattern in the web ($f_{rw}(y)$) showed linear in vicinity of web-to-flange junction and stepped function in the center. The magnitude of f_{rfc} , f_{rft} and f_{rwc} are about 40.8MPa, 340MPa (equal to the yield stress of the plates) and 175.0MPa respectively where f_{rfc} is the maximum compressive residual stress in the flange tip; f_{rft} is the maximum tensile residual stress in web-to-flange junction; f_{rwc} is the maximum compressive residual stress in web. As compared to the rolled I-section experiment performed by the author, the mean values of f_{rfc} in welded I-section about two times larger than that of rolled I-section. However, the magnitudes and distributions of residual stress vary considerably with the cross-section geometry and with the cooling and heating process.

(2) Theoretical study

Dwight and White (1977) have suggested that the maximum tensile stress can be assumed to be equal to the parent metal yield stress, and that the compressive stresses can be estimated from Eq. 4-15. However, the residual distribution and magnitude seems to only ensures the axial equilibrium (Eq. 4-12a) and torsional equilibrium (Eq. 4-12b) is not satisfied, inevitably resulting

in torsional rigidities reduction as follows ($GJ - \int_A f_r(x^2 + y^2)dA$).

$$f_{rf} = f_{rfc} \quad [\text{when: } x > |t_w / 2|] \quad (4-15a)$$

$$f_{rf} = a_1 + a_2 x = f_{rwt} - \frac{f_{rwt}}{t_w / 2} \cdot x \quad [\text{when: } x \leq |t_w / 2|] \quad (4-15b)$$

where

f_{rf} is the residual stress distributed in flange

f_{rwt} is the residual stress distributed in web

$f_{rwt} = f_{rft} = \left[\frac{4(b_f - t_w)(t_f)}{dt_w} \right] f_{rfc}$ is the maximum tensile residual stress in Dwight

and White s' residual stress model

4.1.3.4 Selected residual stress models in this study

Up to now, various residual stress distribution profile and magnitude are introduced via experimental and theoretical studies. Although the magnitude and distribution of residual stress vary considerably with the cross-section types and with the cooling and heating process, two facts are identified as follows:

a) Two equilibrium conditions are required for deriving ideal residual stress distributions. In other words, axial force equilibrium (Eq. 4-12a) and torsional force equilibrium (Eq. 4-12b) needs to be satisfied not to reduce effective rigidities in elastic stages. If this condition is not satisfied, the effective torsional rigidity of the cross-section inevitably reduced.

b) From the experimental studies (Fukumoto, 1980; 1981) in welded and rolled I-sections, residual stress in welded I-section show larger compressive

and tensile value (about two times) than that of rolled I-section.

Three models are proposed considering above the identified facts. Model 1 is idealized residual stress pattern applicable both welded and rolled I-section. Model 2 is Lehigh's residual stress pattern applicable only to rolled section. Model 3 is Modified Lehigh's residual stress pattern applicable to welded section only.

(1) Ideal residual stress pattern (Model #1 applicable for both rolled and welded)

Fig. 4-20 shows the residual stress distribution of Model 1. Both axial and torsional equilibrium are satisfied in the Model 1. Eq. 4-16 indicate how to determine the residual pattern coefficients ($a_1 \sim a_6$) as f_{rfc} , $f_{rft} = f_{rwt}$ are given. For rolled section, the magnitudes of f_{rfc} , $f_{rft} = f_{rwt}$ are assumed as 50.0MPa and 100.0MPa respectively. For welded section, the magnitudes of f_{rfc} , $f_{rft} = f_{rwt}$ are assumed as 100.0MPa and 200.0MPa respectively.

$$\begin{bmatrix} 1.0 & 0 & 0 & 0 & 0 & 0 \\ 1.0 & (b/2)^2 & (b/2)^4 & 0 & 0 & 0 \\ A(3,1) & A(3,2) & A(3,3) & A(3,4) & A(3,5) & A(3,6) \\ 0 & 0 & 0 & 1.0 & 0 & 0 \\ 0 & 0 & 0 & 1.0 & (h/2)^2 & (h/2)^4 \\ A(6,1) & A(6,2) & A(6,3) & A(6,4) & A(6,5) & A(6,6) \end{bmatrix} \begin{bmatrix} a_1 \\ a_2 \\ a_3 \\ a_4 \\ a_5 \\ a_6 \end{bmatrix} = \begin{bmatrix} f_{rfb} \\ f_{rfc} \\ 0 \\ f_{rft} \\ f_{rft} \\ 0 \end{bmatrix} \quad (4-16)$$

where

$$A(3,1) = 2 \cdot \int_{h/2}^{d/2} \int_{-b/2}^{b/2} dx \cdot dy, \quad A(3,2) = 2 \cdot \int_{h/2}^{d/2} \int_{-b/2}^{b/2} (x^2) dx \cdot dy,$$

$$A(3,3) = 2 \cdot \int_{h/2}^{d/2} \int_{-b/2}^{b/2} (x^4) dx \cdot dy, \quad A(3,4) = \int_{-h/2}^{h/2} \int_{-t_w/2}^{t_w/2} dx \cdot dy,$$

$$A(3,5) = \int_{-h/2}^{h/2} \int_{-t_w/2}^{t_w/2} (y^2) dx \cdot dy, \quad A(3,6) = \int_{-h/2}^{h/2} \int_{-t_w/2}^{t_w/2} (y^4) dx \cdot dy$$

$$A(6,1) = 2 \cdot \int_{h/2}^{d/2} \int_{-b/2}^{b/2} (x^2 + y^2) dx \cdot dy,$$

$$A(6,2) = 2 \cdot \int_{h/2}^{d/2} \int_{-b/2}^{b/2} (x^2) \cdot (x^2 + y^2) dx \cdot dy$$

$$A(6,3) = 2 \cdot \int_{h/2}^{d/2} \int_{-b/2}^{b/2} (x^4) \cdot (x^2 + y^2) dx \cdot dy,$$

$$A(6,4) = \int_{-h/2}^{h/2} \int_{-t_w/2}^{t_w/2} (x^2 + y^2) dx \cdot dy$$

$$A(6,5) = \int_{-h/2}^{h/2} \int_{-t_w/2}^{t_w/2} (y^2) \cdot (x^2 + y^2) dx \cdot dy$$

$$A(6,6) = \int_{-h/2}^{h/2} \int_{-t_w/2}^{t_w/2} (y^2) \cdot (x^2 + y^2) dx \cdot dy$$

(2) Lehigh's residual stress pattern (Model #2 applicable for rolled section)

Fig. 4-21 shows the residual stress distribution of Model 2. Axial equilibrium is only satisfied in the Model 2. The magnitudes of f_{rfc} is assumed as 100.0MPa and $f_{rft} = f_{rwt}$ are determined from the axial equilibrium.

(3) Modified Lehigh's residual stress pattern (Model #3 applicable for welded section)

Fig. 4-22 shows the residual stress distribution of Model 3. Axial equilibrium is only satisfied in the Model 3. Eq. 4-15 indicates how to determine the residual pattern for Model 2. The magnitudes of f_{rfc} is assumed as 100.0MPa and $f_{rft} = f_{rwt}$ are determined from the axial equilibrium.

4.1.4 Effects of residual stresses on inelastic section rigidities of I-beam

Up to now, residual stress model type (M1, M2 and M3) assumed in this study were discussed. In this chapter, the calculations of the inelastic effective

rigidities including the residual stresses are described. As mentioned previously, since the residual stress effect inherent in I-section become more complex as compared to that of the ideal I section, the explicit formulation is not capable and numerical calculation procedure are inevitable.

Four major factors need to be considered for the numerical calculation as follows:

- a) Location of neutral axis ($y_n(\phi)$) and shear center ($y_{0t}(\phi)$) according to curvature variation (ϕ);
- b) Residual stress distribution ($f_r(x,y)$) and its effect on elastic torsional rigidities [$GJ - \int_A f_r (x^2 + y^2) dA$];
- c) Distribution of tangent modulus and longitudinal stress according to total strain distribution ($E_t[\varepsilon(x,y)], f[\varepsilon(x,y)]$);
- d) Effective flexural rigidities ($EI_y)_e$, warping rigidities ($EC_w)_e$, torsional rigidities ($GJ)_e$ in the mono-symmetrical I-section

4.1.4.1 Numerical calculation procedures

The outline of the numerical calculation procedure to account above four major factors, developed and executed in this study, are described as follow:

Step-(1): Geometrically setting-up I-section

Fig. 4-23 showed I-section (H-250x150x14x14), which selected for

visualizing the numerical procedures. The section are composed of distributed elements (size: 1mm x 1mm) in two dimensional coordinate (x, y).

Step-(2): Input the residual strain ($\epsilon_r(x,y)=f_r/E$) from Model 1, 2 and 3

Fig. 4-20~4-22 and Table 4-1 showed the residual strain of Model 1, Model 2 and Model 3 respectively. From Model type 1, where the quadratic residual stress distributions are applied, two residual stress parameters (R1: C50-T100 and R2: C100-T200) are considered. The tensile residual stresses of the flange-to-web junction of R1 and R2 are $f_{rft}=f_{rwt}=100\text{MPa}$ and $f_{rft}=f_{rwt}=200\text{MPa}$ respectively. The compressive residual stresses of the flange tip of R1 and R2 are $f_{rfe}=50\text{MPa}$ and $f_{rfe}=100\text{MPa}$ respectively.

From Model type 2, where the linear and constant residual stress distribution are applied in the flange and web respectively, a residual stress parameter (R3: C100) are considered. The flange tips of the compressive stress are $f_{rfe}=100\text{MPa}$ and the residual stress magnitude of the flange-to-web junction is determined by axial equilibrium.

From Model type 3, where constant residual stress distribution are applied in the flange and web except the flange-to-web junction, a residual stress parameter (R4: C100) are considered. The flange tips of the compressive stress are $f_{rfe}=100\text{MPa}$ and the residual stress magnitude of the flange-to-web junction is determined by axial equilibrium.

Step-(3): Determine neutral axis position ($y_n(\phi)$) for satisfying axial equilibrium

Contrary to the ideal I-section, the neutral axis of which remains constant irrespective to curvature increase, the neutral axis of I-section varies its position according to the increase of the curvature since the residual stress in Step-(2). Eq. 4-17 describes the numerical algorithm to locate the neutral axis according to curvature (ϕ).

$$\int_A f(y_n(\phi)) dA = 0 \quad (4-17)$$

where

f is longitudinal stress ($f_z = \frac{M_x \cdot y}{I}$)

$y_n(\phi)$ is coordinate of neutral axis according to a curvature ϕ

Step-(4): Determine total strain [$\varepsilon_t(x,y)$] in the I-section

From the value of the initial strain ($\varepsilon_r(x,y)$) in Step-(2) and the bending strain ($\varepsilon_b(x,y)$) in Step-(3), total strains ($\varepsilon_t(x,y)$) in each element are determined as Eq. 4-18.

$$\varepsilon_t(x, y) = \varepsilon_b(x, y) + \varepsilon_r(x, y) = (y - y_n) \cdot \phi + f_r(x, y) / E \quad (4-18)$$

where

$\varepsilon_t(x, y)$ is total strain at a point of x,y in I-section

$\varepsilon_r(x, y)$ is residual strain by residual stress

$\varepsilon_b(x, y)$ is bending strain by flexural bending

Step-(5): Determine longitudinal stress ($f[\varepsilon_t(x,y)]$) and tangent modulus ($E_t[\varepsilon(x,y)]$) in the I-section

Fig. 4-24a and Fig. 4-24b show the stress-strain profile of SM490 and HSA800 used as subroutine in this program which described in Chapter III in

detail. When total strain of a certain element is given in Step-(4), the stress-strain profile of HSA800 and SM490 returns stress ($f[\varepsilon_t(x,y)]$).

Fig. 4-24c and Fig. 4-24d show the tangent modulus-strain profile of HSA800 and SM490 used as subroutine in this program which described previously in detail. When total strain of a certain element is given in Step-(4), the stress-strain profile of HSA800 and SM490 returns stress ($E_t[\varepsilon_t(x,y)]$).

Step-(6): Determine shear center position ($y_{0t}(\phi)$) and calculate torsional stiffness from mono-symmetric section $M_x(\beta_x)_{0t}$

The location of shear center is determined relative stiffness between top and bottom flanges. Eq. 4-19 described how to the position of the shear center are determined according to the curvature.

$$y_{0t}(\phi) = \left[\frac{(EI_y)_{e,BF}}{(EI_y)_{e,TF} + (EI_y)_{e,BF}} - \frac{1}{2} \right] (d - t_f) \quad (4-19)$$

where

$y_{0t}(\phi)$ is coordinate of shear center by tangent modulus concept according to a curvature ϕ

Eq. 4-20 described how the torsional stiffness from mono-symmetric section ($M_x(\beta_x)_{0t}$) are determined according to the curvature.

$$M_x \cdot (\beta_x)_t(\phi) = \int_A f(x^2 + (y - y_{0t})^2) dA \quad (4-20)$$

where

$(\beta_x)_t(\phi)$ is mono-symmetry section constant by tangent modulus concept according to a curvature ϕ

Step-(7): Calculate in-plane moment strength $[M_n(\phi)]$ and effective

rigidities $[(EI_y)_e, (EC_w)_e$ and $(GJ)_e - M_x(\beta_x)_{0t}]$

Up to Step-(6), all of properties required for calculation of the moment strength and effective rigidities of I-section are prepared. Eq. 4-21 described how the in-plane moment strength is calculated.

$$M_n(\phi) = \int_A f \cdot y \, dA \quad (4-21)$$

where

$M_n(\phi)$ moment strength according to curvature ϕ

Eq. 4-22 shows how the effective flexural rigidity is calculated according to the curvature.

$$(EI_y)_e(\phi) = \int_A E_t(x, y, \phi) \cdot x^2 \, dA \quad (4-22)$$

where

$(EI_y)_e(\phi)$ is the effective flexural rigidities at curvature ϕ

$E_t(x, y, \phi)$ is tangent modulus at an element x,y in I-section according to a curvature ϕ

Eq. 4-23 shows how the effective warping rigidity is calculated according to the curvature.

$$(EC_w)_e(\phi) = \int_{Flange} E_t(x, y) \cdot x^2 \, dA \cdot \frac{(d - t_f)^2}{4} \cdot \left[1 - \frac{4 \cdot y_{0t}^2}{(d - t_f)^2} \right] \quad (4-23)$$

where

$(EC_w)_e(\phi)$ is effective warping rigidity according to a curvature ϕ

Eq. 4-24 shows how the effective torsional rigidity is calculated according to the curvature.

$$[(GJ)_e - M_x(\beta_x)_t](\phi) = GJ - \int_A f(x^2 + (y - y_{0t})^2) dA \quad (4-24)$$

where

$[(GJ)_e - M_x(\beta_x)_t](\phi)$ is effective torsional rigidity according to a curvature ϕ

As shown in **Table 4-1**, by the numerical calculation procedure in this chapter, the effective rigidities are able to be represented and calculated according to curvature (ϕ) or moment strength (M). The effective rigidities representation in terms of curvature (ϕ) is closely related for deriving available rotation capacities (R_m) discussed in Chapter 4.2. The effective rigidities representation in terms of moment strength (M) is required for deriving LTB strength (M_{cr}) discussed in Chapter 4.3.

4.1.4.2 Effective rigidities according to curvature

In this chapter, the value of effective rigidities in terms of curvature (ϕ/ϕ_y) are described.

(1) Mild steel (SM490)

Fig. 4-25a and Fig. 4-25b show location of neutral axis (y_n) and shear center (y_{0t}) of H-250x150x14x14/SM490 according to the curvature variation. The neutral axis ($y_n(\phi)$) and shear center ($y_{0t}(\phi)$) remains its position until the curvature reaches yield curvature ($\phi/\phi_y \leq 1.0$). The position of neutral axis and shear center varied according to the residual stress (R1, R2, R3 and R4) from $\phi/\phi_y \geq 0.75$ to $\phi/\phi_y \leq 7.0$. After the curvature increased, the position of neutral

axis recovered its position at $\phi/\phi_y \geq 7.0$ since the inelastic properties of the upper-side and lower-side become similar. At this stage, the effect of the residual stress becomes insignificant and the inelastic properties between “ideal I-section” and “real I-section” become identical.

Fig. 4-25c shows the effective flexural rigidities $((EI_y)_e)$ of H-250x150x14x14/SM490 according to curvature variation. As compared to ideal I-section, the curvature regions affected by the residual stress pattern and magnitude (R1~R4) ranges from $\phi/\phi_y \geq 0.75$ to $\phi/\phi_y \leq 7.0$.

Fig. 4-25d shows the effective warping rigidities $((EC_w)_e)$ of H-250x150x14x14/SM490 according to curvature variation. As compared to Ideal I-section, the curvature regions affected by the residual stress pattern and magnitude (R1~R4) ranges from $\phi/\phi_y \geq 0.75$ to $\phi/\phi_y \leq 7.0$.

Fig. 4-25e shows the torsional rigidities $((GJ)_e - M_x(\beta_x)_{0t})$ of H-250x150x14x14/SM490 according to curvature variation. For the torsional rigidity component $(GJ)_e$, the elastic torsional rigidities (GJ) are still applicable in inelastic range by reflecting Neal’s consideration (Neal, 1960). Contrary to $(GJ)_e$, however, the torsional rigidity component $(M_x(\beta_x)_{0t})$ decreased from initial zero values to several times of the torsional rigidity component $(GJ)_e$. In detail, the $M_x(\beta_x)_{0t}$ value significantly decreased as the shear center move far away from the origin and recovering its zero value as the shear center relocate its initial position.

As compared to Ideal I-section, the curvature regions affected by the magnitude of residual stresses R1-C50-T100 and R1-C100-T200 are limited to the ranges from $\phi/\phi_y \geq 0.9$ to $\phi/\phi_y \leq 5.0$ and from $\phi/\phi_y \geq 0.75$ to $\phi/\phi_y \leq 7.0$ respectively. With same residual stresses pattern, the more residual stresses are increased, the larger the effective rigidities are decreased in the range. In case of R3-C100 and R4-C100, since no torsional equilibrium satisfied in initial stages, the torsional rigidities $((GJ)_e - M_x(\beta_x)_{0t})$ are rather different even in the elastic region. Among the two models, R4-C100 (constant residual stress pattern in flanges) yield lower torsional rigidity values than that of R3-C100 in the inelastic regions.

(2) High strength steel (HSA800)

Fig. 4-26a and Fig. 4-26b show location of neutral axis (y_n) and shear center (y_{0t}) of H-250x150x14x14/HSA800 according to the curvature variation. The neutral axis remains its position until the curvature reaches proportional limit ($\phi/\phi_y \leq 0.5$). The position of neutral axis and shear center varied according to the residual stress (R1, R2, R3 and R4) from $\phi/\phi_y \geq 0.5$ to $\phi/\phi_y \leq 3.0$. After the curvature increased, the position of neutral axis recovered its position at $\phi/\phi_y \geq 3.0$ since the inelastic properties of the upper-side and lower-side become similar. At this stage, the effect of the residual stress becomes insignificant and the inelastic properties between “ideal I-

section” and “real I-section” become identical.

Fig. 4-26c shows the effective flexural rigidities $((EI_y)_e)$ of H-250x150x14x14/HSA800 according to curvature variation. As compared to ideal I-section, the curvature regions affected by the residual stress pattern and magnitude (R1~R4) ranges from $\phi/\phi_y \geq 0.5$ to $\phi/\phi_y \leq 2.5$.

Fig. 4-26d shows the effective warping rigidities $((EC_w)_e)$ of H-250x150x14x14/HSA800 according to curvature variation. As compared to Ideal I-section, the curvature regions affected by the residual stress pattern and magnitude (R1~R4) ranges from $\phi/\phi_y \geq 0.5$ to $\phi/\phi_y \leq 2.5$.

Fig. 4-26e shows the torsional rigidities $((GJ)_e - M_x(\beta_x)_{0t})$ of H-250x150x14x14/HSA800 according to curvature variation. For the torsional rigidity component $(GJ)_e$, the elastic torsional rigidities (GJ) are still applicable in inelastic range by reflecting Neal’s consideration (Neal, 1960). Contrary to $(GJ)_e$, however, the torsional rigidity component $(M_x(\beta_x)_{0t})$ decreased from initial zero values to several times of the torsional rigidity component $(GJ)_e$. As compared to Ideal I-section, the curvature regions affected by the magnitude of residual stresses R1-C50-T100 and R2-C100-T200 are limited to the ranges from $\phi/\phi_y \geq 0.75$ to $\phi/\phi_y \leq 3.5$ and from $\phi/\phi_y \geq 0.50$ to $\phi/\phi_y \leq 5.0$ respectively. With same residual stresses pattern, the more residual stresses are increased, the larger the effective rigidities are decreased in the range.

In case of R3-C100 and R4-C100, since no torsional equilibrium satisfied in initial stages, the torsional rigidities $((GJ)_e - M_x(\beta_x)_{0t})$ are rather different even in the elastic region. Among the two models, R4-C100 (constant residual stress pattern in flanges) yield lower torsional rigidity values than that of R3-C100 in the inelastic regions.

4.1.4.3 Effective rigidities according to moment strength

In this chapter, the value of effective rigidities in terms of moment strength (M_n) are described.

(1) Mild steel (SM490)

Fig. 4-27a and Fig. 4-27b show location of neutral axis (y_n) and shear center (y_{0t}) of H-250x150x14x14/SM490 according to the moment variation. The neutral axis remains its position until the yield moment limit $(M_r = S_x \cdot (F_y - f_{rc}))$. The position of neutral axis and shear center varied according to the residual stress (R1, R2, R3 and R4) from $M/M_p \geq 0.45$ to $M/M_p \leq 1.0$. After plastic moment achieved, the position of neutral axis recovered its position since the inelastic properties of the upper-side and lower-side become similar. At this stage, the effect of the residual stress becomes insignificant and the inelastic properties between “ideal I-section” and “real I-section” become identical.

Fig. 4-27c shows the effective flexural rigidities $((EI_y)_e)$ of H-250x150x14x14/SM490 according to strength variation. As compared to Ideal

I-section, the moment regions affected by the residual stress pattern and magnitude R1 and R2 ranges from $M/M_p \geq 0.65$ to $M/M_p \leq 1.0$ and $M/M_p \geq 0.45$ to $M/M_p \leq 1.0$ respectively.

Fig. 4-27d shows the effective warping rigidities $((EC_w)_e)$ of H-250x150x14x14/SM490 according to strength variation. As compared to Ideal I-section, the moment regions affected by the residual stress pattern and magnitude (R1~R4) ranges from $M/M_p \geq 0.45$ to $M/M_p \leq 1.0$. No significant differences are investigated between effective flexural rigidities and effective warping rigidities in H-250x150x14x14/SM490.

Fig. 4-27e shows the torsional rigidities $((GJ)_e - M_x(\beta_x)_{0t})$ of H-250x150x15x15/SM490 according to strength variation. As compared to Ideal I-section, the moment strength regions affected by the magnitude of residual stresses R1-C50-T100 and R2-C100-T200 are limited to the ranges from $M/M_p \geq 0.65$ to $M/M_p \leq 1.0$ and from $M/M_p \geq 0.45$ to $M/M_p \leq 1.0$ respectively.

With same residual stresses pattern, the more residual stresses are increased, the larger the effective rigidities are decreased in the range. In case of R3-C100 and R4-C100, since no torsional equilibrium satisfied in initial stages, the torsional rigidities $((GJ)_e - M_x(\beta_x)_{0t})$ are rather different even in the elastic region. Among the two models, R4-C100 (constant residual stress pattern in flanges) yield lower torsional rigidity values than that of R3-C100 in the inelastic regions.

(2) High strength steel (HSA800)

Fig. 4-28a and Fig. 4-28b show location of neutral axis (y_n) and shear center (y_{0t}) of H-250x150x14x14/HSA800 according to the moment variation. As compared to the variation of neutral axis and shear center in the SM490 I-section, it shows similar tendency except the moment values are different depending on the material properties

Fig. 4-28c shows the effective flexural rigidities ($(EI_y)_e$) of H-250x150x14x14/HSA800 according to strength variation. As compared to Ideal I-section, the moment regions affected by the residual stress pattern and magnitude (M1~M4) ranges from $M/M_p \geq 0.40$ to $M/M_p \leq 1.0$.

Fig. 4-28d shows the effective warping rigidities ($(EC_w)_e$) of H-250x150x14x14/HSA800 according to strength variation. As compared to Ideal I-section, the moment regions affected by the residual stress pattern and magnitude (M1~M4) ranges from $M/M_p \geq 0.40$ to $M/M_p \leq 1.0$.

Fig. 4-28e shows the torsional rigidities ($(GJ)_e - M_x(\beta_x)_{0t}$) of H-250x150x14x14/HSA800 according to strength variation. As compared to Ideal I-section, the moment strength regions affected by the magnitude of residual stresses R1-C100-T200 and R2-C200-T400 are limited to the ranges from $M/M_p \geq 0.50$ to $M/M_p \leq 1.1$ and from $M/M_p \geq 0.40$ to $M/M_p \leq 1.1$ respectively. With same residual stresses pattern, the more residual stresses

are increased, the larger the effective rigidities are decreased in the range.

In case of R3-C100 and R4-C100, since no torsional equilibrium satisfied in initial stages, the torsional rigidities $((GJ)_e - M_x(\beta_x)_{0t})$ are rather different even in the elastic region. Among the two models, R4-C100 (constant residual stress pattern in flanges) yield lower torsional rigidity values than that of R3-C100 in the inelastic regions.

4.1.5. Summary

1) A universal method to apply tangent modulus theories for both mild and high strength steel is proposed. In addition, a method to quantify the inelastic section stiffnesses such effective flexural $((EI_y)_e)$, warping $((EC_w)_e)$, and torsional $((GJ)_e)$ rigidities of the I-section by using the tangent modulus is also proposed in this study. Using these methods, quantifying the inelastic section stiffness (which is crucial to analyze the inelastic LTB behavior under uniform moment or moment gradient loading) could be calculated for all types of I-shaped members, depending upon whether they are homogeneous or hybrid.

2) To quantify the tangent modulus value for mild steel such as SM490, a separate approach is applied to quantify the tangent modulus in the yield plateau region and strain hardening region as follows. First, at the yield plateau region, the tangent modulus was derived from the analytical slip theory model, which clearly describes the plastic deformation behavior of

metal. Second, at the strain-hardening region, by adopting Haaijer's stress-strain model for idealizing the strain hardening region, the derivative of the stress-strain curve was adopted for the tangent modulus. Meanwhile, to quantify the tangent modulus value for high strength steel such as HSA800, the Ramberg-Osgood stress-strain model is adopted for idealizing the entire non-linear stress-strain curve, and the values are proposed in a continuous form.

3) The explicit formulas for quantifying the inelastic section stiffnesses (flexure, warping and torsion) of an I-shaped member fabricated from various grades of steel are derived, which plays a significant role in LTB studies. Based on formula such as inelastic flexural stiffness for mild steel and for high strength steel), the following factors could be derived. For mild steel, as the initial strain-hardening modulus (E_{st}) increase, the inelastic section stiffness such $(EI_y)_{e,mild}$ increases. Meanwhile, for high strength steel, as the strain hardening parameter (n) decreases, the inelastic section stiffness such $(EI_y)_{e,HSS}$ increases.

4) By applying the formula to the HSA800 and SM490 I-sections (H-250x150x14x14), the variations of the inelastic section stiffnesses according to the values of curvatures and moment levels are compared. Except for the torsional rigidities, where the elastic torsional rigidity is constantly extended to the inelastic range, both the effective flexural (α) and warping (β)

rigidities decrease as the yielding commences from the outer side of the flanges to the inner side. The critical curvatures occur when the effective rigidities of two values decrease to less than 5% of the initial elastic rigidities ($\alpha_{2-3}=0.05$ and $\beta_{2-3}=0.05$) are $2.5 \cdot \phi_y$ and $10.0 \cdot \phi_y$ times the yield curvature of HSA800 and SM490 respectively. This implies that HSA800 would have little or weak resistance against sustaining rotation capacity and would buckle as the curvature reaches beyond three times the yield curvature unless very close lateral bracings or other geometrically high LTB resistance section are provided.

5) Considering the results of the residual stress experiments performed by Fukumoto (1977, 1980 and 1981), three residual stress models were studied. For model #1, which is applicable to both the welded and rolled I-section, adopting the quadratic residual stress pattern to satisfy the axial and torsional equilibrium simultaneously seems to be appropriate for a residual stress model of I-section. For models #2 and #3, which is applicable to rolled and welded I-section respectively, adopting the linear or constant residual stress patterns, satisfying the axial equilibrium only, but not satisfying the torsional equilibrium, seem to be inappropriate for a residual stress model of I-section since this generates the improper torsional stiffness values during the analysis.

6) In contrast to the ideal I-section case where the explicit formulas of the inelastic section stiffness are available, for the I-section with the residual

stress, the explicit formulas cannot be derived, and a numerical approach is required since the neutral axis (y_n) and shear center (y_{0t}) vary according to the curvature. Therefore, a numerical calculation method is developed to iteratively calculate the neutral axis and shear center, and following the inelastic section stiffness, reflecting the varied position of the neutral axis and shear center at each post-yield curvature. Applying the numerical method for HSA800 and SM490 I-sections, the variations of the inelastic section stiffness are compared. Depending on the residual stress magnitude and patterns, the inelastic section stiffnesses are altered and reduced from those of the ideal I-section. However, as the curvature increase above a certain level, the effect of residual stress becomes negligible and the inelastic section rigidities become almost identical to those of the ideal I-section.

4.2 LTB strength under uniform moment

In the previous chapter, the derivations of inelastic section rigidities (stiffness) in I-section with or without residual stresses were studied. From now, the LTB strength under uniform moment is deal with. As well known, among the various LTB formulas, the derivation of the inelastic LTB strength under uniform moment cannot be overemphasized and significantly meaningful to a structural designer and researchers since a large portion of practical I-beam and I- beam-columns have been designed by the inelastic

LTB strength curve under uniform moment.

4.2.1 Overview of LTB under uniform moment

4.2.1.1 Description of the behavior

Fig. 4-29 shows the overall information as inelastic LTB occurred under uniform moment. Fig. 4-29a shows the loading condition triggering uniform moment in the middle of I-beam. The position of the lateral constraint located same position with loading point. The laterally unbraced length is indicated by L_b . Fig. 4-29b shows the moment distribution when the maximum moment reached at the load level higher than the yield moment (M_y). Fig. 4-29c showed the x-z plane (in-plane) deformed shape where the vertical degree of freedom is constraint at the ends. Fig. 4-29c showed the y-z plane (out-of-plane) deformed shape where the lateral degree of freedoms is constraint at the bracing points and ends. It showed that the out-of-plane deformed shape showed sinusoidal profile with zero values at the constraints. Fig. 4-29d showed the (in-plane) moment-curvature diagram at the loading condition. The curvature distributions in the elastic ($\phi \leq \phi_y$) and inelastic ($\phi \geq \phi_y$) range are shown depending on the stress-strain profiles of a material. Fig. 4-29e showed the flexural rigidities at the loading condition. The distribution of rigidities in the elastic ($\alpha, \beta = 1.0$) and inelastic ($\alpha, \beta < 1.0$) range are shown depending on the stress-strain profiles of a material. Fig. 4-29f showed the

idealized analytical model with two equal end moments in the braced length region ($L_{b,ui}$). The lateral torsional buckling behavior is usually represented by the cross-sectional rotation ($\gamma(z)$) along the member length.

4.2.1.2 Derivation of LTB strength curve under uniform moment via inelastic section rigidities

Fig. 4-30 and Eq. 4-26 showed how to decompose the external force (M_0) into each axis components. x, y, z indicate the coordinate at the un-deformed configuration and x', y', z' indicate the coordinate at the deformed configuration. The applied moment (M_0) are decomposed into M_x', M_y' and M_z' via vector analysis.

$$\begin{aligned} M_{x,ext}' &= M_x \cdot \cos(\gamma) \approx M_x = M_0 \\ M_{y,ext}' &= -M_x \cdot \sin(\gamma) \approx -\gamma M_x = -\gamma M_0 \\ M_{z,ext}' &= d\mu / dz \cdot M_x = d\mu / dz \cdot M_0 \end{aligned} \quad (4-26)$$

where

- M_0 is the external moment
- $M_{x,ext}'$ is the external moment applied on the x' -axis
- $M_{y,ext}'$ is the external moment applied on the y' -axis
- $M_{z,ext}'$ is the external moment applied on the z' -axis
- u is the out-of-plane displacement in the x -axis direction
- γ is the rotation of the cross section

Eq. 4-27 showed the internal force in each axis components. The LTB resistances are represented by EI_y, EC_w and $GJ-M_x \cdot \beta_x$ in elastic ranges and $(EI_y)_e, (EC_w)_e$ and $GJ-M_x \cdot (\beta_x)_t$ in inelastic ranges.

$$\begin{aligned}
 M'_{x,int} &= -(EI_x)_e \frac{d^2 v}{dz^2} \\
 M'_{y,int} &= (EI_y)_e \frac{d^2 u}{dz^2} \\
 M'_{z,int} &= ((GJ)_e - M_x(\beta_x)_t) \frac{d\gamma}{dz} - EC_w \frac{d^3 \gamma}{dz^3}
 \end{aligned} \tag{4-27}$$

where

v is the in-plane displacement in the y-axis direction

$M'_{x,int}$ is the internal moment on the x' -axis

$M'_{y,int}$ is the internal moment on the y' -axis

$M'_{z,int}$ is the internal moment on the z' -axis

$(EI_y)_e$ is the effective weak axis bending stiffness

$(EC_w)_e$ is the effective warping stiffness

$(GJ)_e - M_x(\beta_x)_t$ is the effective torsional stiffness

Eq. 4-28 showed the governing equation of LTB. The major variable (shape function) is the rotation of the cross section ($\gamma(z)$), the value of which varies along the z axis. The exact solution or shape function of Eq. 4-28 is derived as Eq. 4-29.

$$\frac{d^4 \gamma}{dz^4} - \frac{(GJ - M_x(\beta_x)_t)}{EC_w} \frac{d^2 \gamma}{dz^2} - \gamma \frac{M_0^2}{EI_y \cdot EC_w} = 0 \tag{4-28}$$

Eq. 4-29a shows formulation of $\gamma(z)$ with unknowns (A, B, C and D). The assumed boundary condition (Torsionally simple support) of LTB is represented as Eq. 4-29b. The lowest eigenvalue satisfying the B.C is expressed in Eq. 4-29c.

$$\gamma(z) = A \cdot e^{m_1 \cdot z} + B \cdot e^{-m_1 \cdot z} + C \cdot \cos(m_2 \cdot z) + D \cdot \sin(m_2 \cdot z) \tag{4-29a}$$

$$\gamma(0) = 0, \gamma(L_b) = 0, \gamma'(0) = 0, \gamma'(L_b) = 0 \quad (4-29b)$$

$$\sin(m_2 L_b) \cdot \sinh(m_1 L_b) \cdot (m_1^2 + m_2^2) = 0 \quad (4-29c)$$

$$m_2 = \pi / L_b$$

where

$$m_1 = \sqrt{a + \sqrt{(a^2 + b)}}, m_2 = \sqrt{-a + \sqrt{(a^2 + b)}}$$

$$a = \frac{GJ}{2EC_w}, b = \frac{M_0^2}{EI_y \cdot EC_w}$$

The inelastic lateral torsional buckling strength (M_{cr}) according to given unbraced length (L_b) and effective rigidities ($(EI_y)_e$, $(EC_w)_e$, $(GJ)_e - M_x \cdot (\beta_x)_t$) is derived as **Eq. 4-30**.

$$M_{cr} = \frac{\pi}{k_y L_b} \sqrt{(EI_y)_e ((GJ)_e - M_x (\beta_x)_t) + \frac{\pi^2 (EI_y)_e (EC_w)_e}{(k_z L_b)^2}} \quad (4-30)$$

where

M_{cr} is the critical buckling strength at the given unbraced length L_b

$$(EI_y)_e = \alpha \cdot (EI_y)$$

$$(EC_w)_e = \beta \cdot (EC_w)$$

$$(GJ)_e - M_x (\beta_x)_t = \gamma \cdot (GJ)$$

α, β, γ is stiffness reduction factor, the ratio of effective section stiffness to the elastic section stiffness, ranging from 0 to 1 ($\alpha, \beta, \gamma \leq 1.0$)

$\alpha(\phi) = (EI_y)_e / (EI_y)$ is the ratio of effective flexural stiffness to the elastic section stiffness according to curvature ϕ

$\beta(\phi) = (EC_w)_e / (EC_w)$ is the ratio of effective warping stiffness to the elastic section stiffness according to curvature ϕ

$\gamma(\phi) = ((GJ)_e - M_x (\beta_x)_t) / GJ$ is the ratio of effective torsional stiffness to the elastic section stiffness according to curvature ϕ

By modifying the **Eq. 4-30** into explicit form in terms of L_b , the required

unbraced length ($L_{b,ui}$) for resisting uniform moment (M_0) can be expressed as

Eq. 4-31.

$$L_{b,ui} = \frac{1}{k} \sqrt{\frac{X_1 + \sqrt{(X_1)^2 + 4(M_0^2)(X_2)}}{2M_0^2}} \quad (4-31)$$

where

$L_{b,ui}$ is required unbraced length for resisting uniform moment M_0

$$X_1 = \pi^2 (EI_y)_e ((GJ)_e - M_x (\beta_x)_t)$$

$$X_2 = \pi^4 (EI_y)_e (EC_w)_e$$

$k = k_y = k_z$ is assumed effective length substituting the torsional and the flexural effective lengths in Eq. 4-30

Different from AISC specifying unbraced length ($L_{b,ui}$) for preventing LTB, EC 3 adopted normalized lateral slenderness $\bar{\lambda}_{LT} = \sqrt{M_p / M_e}$. By applying

Eq. 4-31 into $\bar{\lambda}_{LT,ui}$, required lateral slenderness for resisting uniform moment M_0 can be expressed as Eq. 4-32.

$$\bar{\lambda}_{LT,ui} = \sqrt{\frac{M_p}{M_e}} = \sqrt{\frac{M_p}{\frac{\pi}{k_y \cdot L_{b,ui}} \sqrt{(EI_y)(GJ) + \frac{\pi^2 (EI_y)(EC_w)}{(k_z \cdot L_{b,ui})^2}}}} \quad (4-32)$$

where

$\bar{\lambda}_{LT,ui}$ is plateau length in lateral torsional buckling curve for resisting uniform moment M_0

$M_e = \frac{\pi}{k_y \cdot L_{b,ui}} \sqrt{(EI_y)(GJ) + \frac{\pi^2 (EI_y)(EC_w)}{(k_z \cdot L_{b,ui})^2}}$ is the elastic LTB strength in the given unbraced length $L_{b,ui}$

4.2.1.3 Validation of the analytically developed critical buckling strength curve with previous experiments

To validate the analytically developed critical buckling strength curve in this study, Fukumoto's 1971 experiments were selected. By adopting Haaijer model, the material properties of the mild steel and following effective stiffness were inputted in Eq.4-32 for buckling strength curves.

Fig. 4-31a, Fig. 4-31b and Fig. 4-31c showed the critical buckling strengths of the specimens [G:H-250x100x6x8]-[M:Ho-336], [G:H-200x120x6x8]-[M:Ho-336] and [G:H-300x100x6x8]-[M:Ho-336] calculated by Eq. 4-32 with experimentally measured buckling(=at bifurcation point) strength. As shown in Fig.4-31, the analytically developed curves well predict the buckling strength and seems to be acceptable to utilize in the parametric studies in next chapter.

4.2.2 Analytical parametric studies

It has been reported that many parameters influence the stability of steel structures (Birnstiel and Iffland, 1980; McGuire, 1992; White and Chen, 1993; ASCE Task Committee on Effective Length, 1997; Ziemian, 2010). Among the many parameters (effecting on LTB), geometrical parameters (the effects of the height-to-width ratio, the effects of the compact/thick web or flanges), material parameters (the effects of the mild or high strength steel, the effects of the hybrid I-section) and the magnitude of residual stresses were selected

for the analytical studies since the inelastic effective rigidities $[(EI_y)_e, (EC_w)_e, (GJ)_e - M_x \cdot (\beta_x)_t]$, and were expected to be significantly affected from the parameters.

Fig. 4-32 and Table 4.2 summarized the parameters being discussed in this study. Geometrical parameter is designated as [G:#] and the dimension of I-section designated as H-[depth x width x web thickness x flange thickness], the representation of which follows the Korea industrial standard. [G:A-S]~[G:A-F] show the selected section from 250(depth) x 150(width) series section. [G:A-S] is standard section assuming I-section fabricated from the same-thickness plate. The dimension of [G:A-S] is H-[250x150x14x14]. [G:A-W], the dimensions of which are H-[250x150x28x14], is web reinforced (thicker plate applied) I-section from [G:A-S]. [G:A-F], the dimensions of which are H-[250x150x14x28], is flange reinforced (thicker plate applied) I-section from [G:A-S]. By comparing the result of [G:A-S]~[G:A-F], the effect of thickness reinforcement on the LTB could be investigated.

From [G:B-S] to [G:B-F] showed the selected section from 400(depth) x 150(width) series section. In the 400x150 series section, no parameters were changed except the height of I-section from the 250x150 series section. By comparing [G:B-S] with [G:A-S], [G:B-W] with [G:A-W], [G:B-F] with [G:A-F], the effect of the increased depth on the LTB behavior could be investigated.

Material parameter is designated as [M:Ho or Hy- F_{yw} - F_{yf}]. The yield strength of flange and web are designated as F_{yf} and F_{yw} . When the yield strength of flange and web is identical the I-section are designated as [Ho] abbreviated from homogeneous. Otherwise, the yield strength of flange and web is different the I-section are designated as [Hy] abbreviated from hybrid I. [M:Ho-722] indicate homogeneous I-section, the web and flange yield strengths are $F_{yf} = F_{yw} = 722\text{MPa}$. [M:Ho-349] indicate homogeneous I-section, the web and flange yield strengths are $F_{yf} = F_{yw} = 349\text{MPa}$. [M:Hy-349-722] indicate hybrid I-section, the web and flange yield strength are $F_{yw} = 349\text{MPa}$ and $F_{yf} = 722\text{MPa}$. By comparing [M:Ho-349] with [M:Ho-722], the effect of the high strength or mild strength steel on the LTB behavior could be investigated. By comparing [M:Hy-349-722] with [M:Ho-722], the effect of the hybrid on the LTB behavior could be investigated.

The residual stress parameter is designated as [R: C#-T#]. Since the residual stress pattern adopt the ideal quadratic stress pattern model, the values of f_{fc} and f_{ft} are entered in the designation. [C50-T100] indicate the compressive flange tip stress is 50MPa and the tensile web stress is 100MPa. [C100-T200] indicate the compressive flange tip stress is 100MPa and the tensile web stress is 200MPa.

4.2.2.1 Effect of the geometrical variation

(1) Variation of flange and web thickness

Fig. 4-33a, Fig. 4-33b showed the effect of flange and web thickness reinforcement on LTB in [M:Ho-722] I-section, calculated by Eq. 4-31 and Eq. 4-32. At the same normalized moment strength such as $M/M_p=1.0$, the unbraced length (L_b/r_y) of [G:A-W] and [G:A-F] indicate longer unbraced length, implying better buckling strength than that of [G:A-S]. The reason for the better buckling strength of [G:A-W] and [G:A-F] result from that the ratio of effective rigidities to plastic moment strength ($(EI_y)_e/M_p$, $(EC_w)_e/M_p$, and $(GJ)_e/M_p$) are higher than other [G:A-S] I-section. It is interesting that, although the required buckling strength (=plastic moment, $M_0=M_p=Z_x \cdot F_y$ is increased from [G:A-S]→[G:A-F]), [G:A-S] require shorter unbraced length than that of [G:A-F] since the effective rigidities ($(EI_y)_e$ and $(EC_w)_e$) of [G:A-S] is considerably lower than that of [G:A-F]. It clearly show that the unbraced length is not determined by the effective rigidities of I-section only but depended on the relative ratio of the effective rigidities to plastic moment(=required strength) ($(EI_y)_e/M_p$, $(EC_w)_e/M_p$, and $(GJ)_e/M_p$)

Fig. 4-33c and Fig. 4-33d showed the effect of flange and web thickness reinforcement on LTB in [M:Ho-349] I-section respectively, calculated by Eq. 4-31 and Eq.4-32. Regardless of the material properties changes, [G:A-W] and [G:A-F] showed better buckling strength than that of [G:A-S].

(2) Variation of depth

Fig. 4-33a and Fig 4-32b showed the effect of increased depth on LTB in

[M:Ho-722] and [M:Ho-349] I-section respectively, calculated by Eq. 4-31 and Eq. 4-32. It showed that at the same normalized moment strength such as $M/M_p=1.0$, the unbraced length (L_b/r_y) of [G:B-S, B-W and B-F] require shorter unbraced length than that of [G:A-S, A-W and A-F], implying that the increase of the depth without proportionally increasing the effective rigidities result in detrimental effect on the buckling strength.

4.2.2.2 Effect of the material properties

(1) Mild steel versus High strength steel

Fig. 4-34a and Fig.4-33b showed the effect of material properties on LTB in [G:A-S~A-F] section respectively, calculated by Eq. 4-31 and Eq.4-32. At the same normalized moment strength such as $M/M_p=1.0$, the unbraced length (L_b/r_y) of [M:Ho-722] require shorter unbraced length than that of [M:Ho-349].

This graph directly indicate that why the current code specify the unbraced length limit inversely proportional ($L_b \propto 1/\sqrt{F_y}$) to square root of yield strength. It also implies that the high strength steel needs to be examined in detail as it would adequate and properly controlled by the formulas provided in current specification in AISC and EC 3 codes. The issues will be dealt with in chapter 4.2.3.

It should be also noted that, as described in Eq. 4-7, for mild steel, as the initial strain-hardening modulus (E_{st}) is higher, the buckling strength will

become higher. For high strength steel, as described in Eq. 4-8, as the strain hardening parameter (n) is lower, the buckling strength will become higher. Therefore, the unbraced length limits of mild and high strength I-members could be varied depending on the post-yield properties such $E_{st}(\varepsilon)$ for mild steel and n (=strain hardening parameter) for high strength steel.

(2) High strength I section versus hybrid I section

Fig. 4-35a and Fig.4-34b showed the effect of hybrid I-section on LTB in [G:A-S~A-F] section respectively, calculated by Eq. 4-31 and Eq. 4-32. At the same normalized moment strength such as $M/M_p=1.0$, the unbraced length (L_b/r_y) of [M:Hy-349-722] require relaxed (=longer) unbraced length than that of [M:Ho-722], implying that the lower strength hybrid web result in positive effect on the buckling strength since it reduce the external force ($M_0=M_p=Z_{xf} \cdot F_{yf}+Z_{xw} \cdot F_{yw}$) with negligibly decreased the effective rigidities. It could be concluded that by taking advantage of the hybrid I-section, the required unbraced length for preventing lateral instability become considerably relaxed.

4.2.2.3 Effect of the residual stress

Fig. 4-36a and Fig.4-35b showed the effect of residual stress on LTB in [M:Ho-722], [M:Ho-349] and [M:Hy-349-722] I-section respectively, calculated by Eq. 4-31 and Eq.4-32. At inelastic moment ranges, the unbraced

length (L_b/r_y) of [R2:C100-T200] require more stringent unbraced length than that of [R1:C50-T100] and [Ideal], since the larger magnitude of the residual stress alter or reduced the inelastic section stiffness significantly as discuss in previous chapter. However, the residual stress effect and its duration become neglected at the level of $M/M_p=1.0$. Therefore, the effect of residual stress could be neglected with regard to unbraced length for achieving plastic moment ($L_{b,ui}$) or for acquiring adequate rotation capacities ($L_{d,ui}$).

4.2.3 Detailed approach to derive unbraced length limit for achieving plastic moment

In this chapter, an approach for deriving unbraced length for achieving plastic moment ($L_{p,ui}$) will be discussed. The unbraced length for plastic moment has significant meaning in LRFD code. Since the plastic moment (calculated the full plastic stress distribution) is designated as maximum moment of I-section, the unbraced length limit for achieving the maximum moment is remarkable in the code. Furthermore, the unbraced length limit is reference value to determine inelastic buckling strength ($M_y \leq M_{cr} \leq M_p$) of I-section as in inelastic range as described in AISC spec.

The unbraced length for plastic moment could be simply derived by modifying Eq. 4-31 as below. At the equation, the required buckling strength (M_0) become changed as the plastic moment, $M_p = Z_{xf} \cdot F_{yf} + Z_{xw} \cdot F_{yw}$. The values of the effective rigidities need to be estimated when the I-section reaches at

the plastic moment. By adopting the reduction factors, α_p , β_p , γ_p where $\alpha_p = (EI_y)_e / (EI_y)$ is the flexural bending stiffness reduction factor at plastic moment, $\beta_p = (EC_w)_e / (EC_w)$ is the warping stiffness reduction factor at plastic moment, $\gamma_p = ((GJ)_e - M_x \cdot (\beta_x)_t) / (GJ)$ is the torsional stiffness reduction factor at plastic moment, the effective rigidities at the plastic moment are easily calculated as shown in Fig. 4-17.

$$L_{b,ui} = \frac{1}{k} \sqrt{\frac{X_1 + \sqrt{(X_1)^2 + 4(M_0^2)(X_2)}}{2M_0^2}} \quad (4-31) \text{ again}$$

$$L_{p,ui} = \frac{1}{k} \sqrt{\frac{X_1 + \sqrt{(X_1)^2 + 4(M_p^2)(X_2)}}{2M_p^2}} \quad (4-31) \text{ modified}$$

$$X_1 = \pi^2 \cdot \alpha_p \cdot (EI_y) \cdot \gamma_p \cdot (GJ) \quad X_2 = \pi^4 \cdot \alpha_p \cdot (EI_y) \cdot \beta_p \cdot (EC_w)$$

$$\alpha_p = (EI_y)_e / (EI_y), \quad \beta_p = (EC_w)_e / (EC_w),$$

$$\gamma_p = ((GJ)_e - M \beta_x) / GJ$$

where

$L_{p,ui}$ is required unbraced length for achieving plastic moment M_p

$\alpha_p = (EI_y)_e / (EI_y)$ is the flexural stiffness reduction factor at plastic moment

$\beta_p = (EC_w)_e / (EC_w)$ is the warping stiffness reduction factor at plastic moment

$\gamma_p = ((GJ)_e - M \beta_x) / GJ$ is the torsional stiffness reduction factor at plastic moment

$k = k_y = k_z = 0.54$ is assumed effective length provided by adjacent span

Table 4-3 showed unbraced length limits ($L_{p,ui}/r_y$) and normalized slenderness limits ($\bar{\lambda}_{LT,ui}$) for achieving plastic moment calculated by the detailed approaches (Eq. 4-31). Fig. 4-37 shows the comparison between the analytically derived unbraced length limits and the unbraced length limit in

current AISC criteria $L_p / r_y = 1.76 \cdot \sqrt{E / F_y}$.

As indicated in the previous analytical parameter studies, the specimens with low height to width ratio [Type: A], relatively compact web [G: A-W, B-W] or compact flange [G: A-F, B-F] I-section and hybrid I-section [M: Hy-349-722] show higher buckling strengths, satisfying the unbraced length limit predicted in current AISC criteria. Comparing compact web I-sections [G: A-W, B-W] with compact flange I-sections [G: A-F, B-F], even the effective rigidities of compact flanges [G: A-F, B-F] I-section become higher than that of compact web [G: A-W, B-W] I-section, since the plastic moment(=required strength) are considerably increased simultaneously, the shorter unbraced lengths are required for compact flanges I-section cases in general.

The specimens, which could not satisfy the current criteria, are [G:B-S, H-400x150x14x14]-[M: Ho-722] and [G:B-S, H-400x150x14x14]-[M: Ho-349]. As indicated in previous analytical studies, the specimens with high height to width ratio [Type: B], relatively slender I-section [G: B-S] are vulnerable to LTB and the closer spacing than the current AISC limit is required.

4.2.4 Simplified approach to derive unbraced length limit for achieving plastic moment

In this chapter, simplified approach to derive the unbraced length for plastic moment will be introduced.

4.2.4.1 Overview and assumption

White (1960) suggested that a maximum support spacing(=unbraced length length limit) for a beam under uniform moment with simple end restraint(=torsionally simple condition) and describing that any closer spacing would not provide positive effect. His approach was later adopted and modified by **Lay's T-column approach**, become referential and simplistic format for providing unbraced length achieving for plastic moment in AISC spec. Therefore, his assumption will be briefly discussed and the suggested approach adopted in this study will be introduced in next chapter.

4.2.4.2 Derivation of unbraced length limit for plastic moment

The crucial assumption in **White's** derivation was neglecting the term $(EI_y)_e \cdot (GJ)_e$ as zero values since the contribution of $(EI_y)_e \cdot (GJ)_e$ in relatively short beam are negligible as compared to the term $\pi^2 \cdot (EI_y)_e \cdot (EC_w)_e / (L_b)^2$.

By adopting the assumption, the inelastic LTB strength formula could be simplified as **Eq. 4-33**. The beneficial effect of this simplification is the flexural rigidities reduction factor at plastic moment ($\alpha_p = (EI_y)_e / (EI_y)$) is only required for deriving the inelastic LTB strength at plastic moment.

$$\begin{aligned}
 M_{cr} &= \frac{\pi}{k_y L_b} \sqrt{(EI_y)_e (GJ)_e \approx 0 + \frac{\pi^2 (EI_y)_e (EC_w)_e}{(k_z L_b)^2}} \\
 &= \frac{\pi^2}{(k \cdot L_b)^2} \cdot (EI_y)_e \cdot \left(\frac{1}{2}(d - t_f)\right) \approx \alpha_p \cdot M_e
 \end{aligned} \tag{4-33}$$

where

$\alpha_p = (EI_y)_e / (EI_y)_p$ is the flexural bending stiffness reduction factor at plastic moment M_p

Meanwhile, the required buckling strengths ($M_0=M_p$) are determined from the plastic moment of the I-section as described in Eq. 4-34. As two types of I-section are proposed in this study, the plastic moment of the homogenous I-section is calculated as Eq. 4-34a and the plastic moment of the hybrid I-section is calculated as Eq. 4-34b.

$$M_{p,Ho} = Z_x F_{yf} \tag{4-34a}$$

$$M_{p,Hy} = Z_{xf} F_{yf} + Z_{xw} F_{yw} \tag{4-34b}$$

where

$M_{p,Ho}$ is plastic moment of homogeneous I beam

$M_{p,Hy}$ is plastic moment of hybrid I beam

$Z_x = Z_{xf} + Z_{xw}$ is plastic section modulus about x-x' axis

$Z_{xf} = (A_f / 2)(d - t_f)$ is the flange plastic section modulus

$Z_{xw} = (A_w / 2)((1 / 2) \cdot (d - 2t_f))$ is the web plastic section modulus

A_f is the flange area

A_w is the web area

F_{yf} is the flange yield strength

F_{yw} is the web yield strength

By setting equal the inelastic buckling strength (M_{cr}) to plastic moment

(M_p), the unbraced length for the homogeneous ($L_{p,Ho,ui}$) and hybrid ($L_{p,Hy,ui}$) I-section could be derived as Eq. 4-35a and Eq. 4-35b respectively.

$$\begin{aligned} L_{p,Ho,ui} &= \frac{\pi}{k} \cdot \sqrt{\frac{(EI_y)_e}{EI_y}} \cdot \sqrt{\frac{(A/2) \cdot (d-t_f)}{Z_x F_{yf}}} \cdot r_y \cdot \sqrt{E} \\ &= \frac{\pi}{k} \cdot \sqrt{\alpha_p} \cdot \sqrt{\frac{(A/2) \cdot (d-t_f)}{Z_x}} \cdot r_y \cdot \sqrt{\frac{E}{F_{yf}}} \end{aligned} \quad (4-35a)$$

$$\begin{aligned} L_{p,Hy,ui} &= \frac{\pi}{k} \cdot \sqrt{\frac{(EI_y)_e}{EI_y}} \cdot \sqrt{\frac{(A/2) \cdot (d-t_f)}{Z_{xf} F_{yf} + Z_{xw} F_{yw}}} \cdot r_y \cdot \sqrt{E} \\ &= \frac{\pi}{k} \cdot \sqrt{\alpha_p} \cdot \sqrt{\frac{(A/2) \cdot (d-t_f)}{Z_{xf} + Z_{xw} \cdot (F_{yw} / F_{yf})}} \cdot r_y \cdot \sqrt{\frac{E}{F_{yf}}} \end{aligned} \quad (4-35b)$$

where

$L_{p,Ho,ui}$ is unbraced length for achieving plastic moment of homogeneous I beam

$L_{p,Hy,ui}$ is unbraced length for achieving plastic moment of hybrid I beam

$$r_y = \sqrt{\frac{I_y}{A}}$$

$k=0.54$ assuming when continuous lateral bracings provided, $k=1.0$ without continuous bracings

For normalized lateral slenderness $\bar{\lambda}_{LT,0} = \sqrt{M_p / M_e}$ adequate for EC 3,

it can be expressed as Eq. 4-36.

$$\bar{\lambda}_{LT,p,ui} = \sqrt{\frac{M_p}{M_e}} = \sqrt{\alpha_p} \quad (4-36)$$

where

$\bar{\lambda}_{LT,p,ui}$ is plateau length in lateral torsional buckling curve for achieving plastic moment

$\alpha_p = (EI_y)_e / (EI_y)$ is the flexural bending stiffness reduction factor at plastic

moment M_p

Table 4-3 showed unbraced length limits ($L_{p,ui}/r_y$) and normalized slenderness limits (λ_p) for achieving plastic moment in calculated by the simplified approaches (Eq. 4-35 and Eq. 4-36). Fig. 4-38 graphically showed $L_{p,ui}/r_y$ values with the baseline (here and after ‘code limit’) predicted by the AISC Specification.

As indicated in the previous analytical parameter studies, the specimens with low height to width ratio [Type: A], relatively compact web [G: A-W, B-W] I-section and hybrid I-section [M: Hy-349-722] show higher buckling strengths, satisfying the unbraced length limit predicted in current AISC criteria. Compared with the detailed approach, by neglecting the torsional rigidities in this simplistic approaches, the buckling strength of relatively compact flange [G: A-F, B-F] I-section are underestimated.

As shown in Fig. 4-38, this approach underestimates the effective rigidities considerably and requires relatively closer bracing limits than the current AISC unbraced length limit for most models [M: Ho-349] and [M: Ho-722] except hybrid I-section model [M: Hy-349-722].

4.2.5 Summary

1) Based on the effective rigidities derived in this study, an analytical procedure to derive a buckling strength curve under uniform moment according to the unbraced length was proposed. Using the procedure, the

buckling strength curves of high strength and mild strength, and the hybrid I-section member are established. By comparing the buckling strength curve with that of Fukumoto's (1971) research, the curve well predicts the experimental buckling strength. By this verification, the analytical procedure is adopted for use in further parametric model studies required for suggesting appropriate design methodologies for controlling LTB of an I-shaped member fabricated from all grades of steels.

2) Parametric studies (six parameters, (a) ~ (f)) are performed to analyze the effects of geometrical and material variations on the LTB strength. Three geometrical parameter models are selected as follows: (a) the variation of height-to-width ratios [Type A: low height-to-width ratio model ($d=250\text{mm}$, $b=150\text{mm}$), Type B: high height-to-width ratio model ($d=400\text{mm}$, $b=150\text{mm}$)]; (b) the application of a relatively thicker web [G: A-W, B-W ($t_w=28\text{mm}$, $t_f=14\text{mm}$)] on the standard I-shaped section fabricated from plates of the same thickness [G: A-S, B-S ($t_w=t_f=14\text{mm}$)]; (c) the application of relatively thicker flange [G: A-F, B-F ($t_f=28\text{mm}$, $t_w=14\text{mm}$)] on the standard I-shaped section fabricated from plates of the same thickness [G: A-S, B-S ($t_w=t_f=14\text{mm}$)];

Three material parameters are selected as follows: (d) the application of homogeneous mild steel [M: Ho-349 ($F_{yw}=F_{yf}=349\text{MPa}$)]; (e) the application of homogeneous high strength steel [M: Ho-722 ($F_{yw}=F_{yf}=722\text{MPa}$)]; and (f) the application of hybrid I-section [M: Hy-349-722 ($F_{yw}=349\text{MPa}$,

$F_{yf}=722\text{MPa}]$.

3) From the analytical results, it could be concluded that the unbraced lengths limited at post-yield ranges are determined by the relative ratios of the effective flexural $((EI_y)_e/M_p)$, warping $((EC_w)_e/M_p)$, and torsional rigidities $((GJ)_e/M_p)$ to required buckling strength such plastic moment, M_p .

With regard to the geometrical aspect, the model with low height-to-width ratio [G: Type A ($d=250\text{mm}$, $b=150\text{mm}$)] shows higher inelastic buckling strength than the model with high height-to-width ratio [G: Type B ($d=400\text{mm}$, $b=150\text{mm}$)] since the required buckling strength ($M_p=Z_x \cdot F_y$) is increased at high height-to-width ratio without proportionally increasing the effective rigidities. Also, relatively thick web [G: A-W, B-W ($t_w=28\text{mm}$, $t_f=14\text{mm}$)] or thick flange [G: A-F, B-F ($t_f=28\text{mm}$, $t_w=14\text{mm}$)] models show higher inelastic buckling strength than the models with an I-section fabricated from plates of the same thickness [G: A-S, B-S ($t_w=t_f=14\text{mm}$)] since the application of thick plates increases the effective rigidities, especially flexural and torsional rigidities, without increasing the required buckling strength as the same proportion.

With regard to the material aspect, the mild steel I-section models [M: Ho-349 ($F_{yw}=F_{yf}=349\text{MPa}$)] show higher buckling strength than the high strength I-section models [M: Ho-722 ($F_{yw}=F_{yf}=722\text{MPa}$)] since the required buckling ($M_p=Z_x \cdot F_y$) is increased when high strength steel is applied without proportionally increasing the effective rigidities. The hybrid I-section [M: Hy-

349-722 ($F_{yw}=F_{yf}=349\text{MPa}$)] shows higher buckling strength than that of the high strength I-section [M: Ho-722] since it decreases the required buckling strength ($M_p = Z_{xf} \cdot F_{yf} + Z_{xw} \cdot F_{yw}$) considerably by applying a mild steel web while merely decreasing the effective section rigidities. Meanwhile, the effect of the residual stress is constrained in inelastic ranges only and the LTB strength at the vicinity of the plastic moment is not influenced by the presence of the residual stress.

4) The explicit formula to derive unbraced length limit ($L_{p,ui}$) for achieving plastic moment under uniform moment is proposed. By comparing the unbraced length limit ($L_{p,ui}$) with the current AISC limit ($L_p / r_y = 1.76 \cdot \sqrt{E / F_y}$), it is confirmed that most of the models satisfy the current AISC limit. However, the models, [G: B-S ($t_w=t_f=14\text{mm}$)]-[M: Ho-722] and [G: B-S ($t_w=t_f=14\text{mm}$)]-[M: Ho-349] with high height-to-width ratio [Type B ($d=400\text{mm}$, $b=150\text{mm}$)] without applying the thick flange or web plates, regardless of high strength steel or mild steel, are vulnerable to LTB, and a closer bracing spacing than the current AISC unbraced length limit is required. As mentioned previously, the effective rigidities to plastic moment (=required buckling strength) ratios of the models ($((EI_y)_e/M_p, (GJ)_e/M_p)$) are quite low, indicating that the models are inevitably vulnerable to LTB.

However, the model, hybrid I-section with high height-to-width ratio, [G: B-S ($t_w=t_f=14\text{mm}$)]-[M:Hy-349-722 ($F_{yw}=349\text{MPa}$, $F_{yf}=722\text{MPa}$)], satisfies

the current AISC unbraced length limit since it decreases the required buckling strength considerably with merely decreasing the effective section stiffness.

4.3 Available rotation capacity (governed by LTB) under uniform moment

As mentioned in chapter I, rotation capacity is a major parameter to evaluate a ductility of a structural steel member (sometimes assessed by deformation capacity). Current code (AISC, EC 3) stipulates the slenderness limits for a steel material to achieve sufficient (=in seismic design) or target rotation capacity. Some experimental studies have frequently reported that the rotation capacity of HSS member is not satisfactory results under specified slenderness condition suggested by the specifications. The fact brings about strong demand to find influential factors on the rotation capacity of a member and provide unbraced length formulas for restraining the initiation of inelastic LTB, which significantly curtails the rotation capacity of a member, to ensure target rotation capacity such as $R_n=3, 5$ or 7 for practical application of HSS.

4.3.1 Description of the behavior

Fig. 4-39 shows the overall information how the inelastic LTB behavior degrades the rotation capacity of a member. Fig. 4-39a shows the loading condition triggering uniform moment in the middle of I-beam. The position of

the lateral constraint located as the same position with the loading point. That is, the laterally unbraced length is designated as $L_{d,ui}$. Fig. 4-39b shows a moment-rotation curve considering the in-plane behavior only. However, the behavior is not fully realized since the out-of-plane behavior such LTB curtail the rotation capacity significantly as shown in Fig. 4-39c.

The behavior could be explained as below. As the effective rigidities are sufficient to resist the out-of-plane behavior such as elastic stages, the moment-rotation curve follows the in-plane behavior curve. However, as the effective rigidities are decreased according to the increase of the inelastic rotation (=curvature) and reached at the critical points ($M(\phi)-M_{cr}(L_b)$), the member bifurcate or the initial cross section is significantly magnified (assuming the member has initial imperfection) as described in Eq. 4-37.

$$\gamma = \frac{\gamma_0}{1 - \frac{M(\phi)}{M_{cr}(L_b)}} \quad (4-37)$$

where

γ_0 is the first term of Fourier series representing initial deformed shape

γ is the total rotation of the cross section

$M(\phi)$ is the moment according to curvature ϕ

$M_{cr}(L_b)$ is the critical buckling strength at the given unbraced length L_b , See Eq. 4-31

Since the deformed shape (γ) induce the additional instabilizing moment ($M_x \cdot \gamma_{LT}$) into $y'-y'$ axis (so called second-order effect, Eq. 4-38), the member finally reached the inelastic instability point where the member start

to degrade its strength.

$$M'_{y,ext} = M_x(\gamma) = M_x(\gamma_0 + \gamma_{LT}) \quad (4-38)$$

where

γ_{LT} is the magnified rotation of the cross section by inelastic LTB behavior

4.3.2 Derivation of rotation capacity curve under uniform moment via inelastic section rigidities

As the case of LTB strength under uniform moment, the required unbraced length ($L_{d,ui}$) for resisting target rotation capacity ($R_{d,ui}$) can be calculated as Eq. 4-39. As described in Eq. 4-39, under uniform moment case, the critical curvature ($\phi_{cr,d,ui}$) could be calculated as the target rotation capacity are determined. Please refer to chapter 3.2.1 for the background of the calculation. The effective rigidities ($(EI_y)_e$, $(EC_w)_e$, $(GJ)_e$) at the critical curvatures are easily calculated by Eq. 4-7 for mild steel and Eq.4-8 for high strength steel. By the derived values, the required unbraced length ($L_{d,ui}$) to resist target rotation capacity can be expressed as Eq. 4-39.

$$L_{d,ui} = \frac{1}{k} \sqrt{\frac{X_1 + \sqrt{(X_1)^2 + 4(M(\phi_{cr,d,ui}))^2(X_2)}}{2(M(\phi_{cr,d,ui}))^2}} \quad (4-39)$$

$$\phi_{cr,d,ui} = (R_{d,ui} + 1) \cdot \phi_y$$

$$X_1 = \pi^2 (EI_y)_e (GJ)_e = \pi^2 \cdot \alpha(\phi) \cdot (EI_y) \cdot \gamma(\phi) \cdot (GJ)$$

$$X_2 = \pi^4 (EI_y)_e (EC_w)_e = \pi^4 \cdot \alpha(\phi) \cdot (EI_y) \cdot \beta(\phi) \cdot (EC_w)$$

where

$L_{d,ui}$ is unbraced length for achieving target rotation capacity $R_{d,ui}$

$\phi_{cr,d,ui}$ is the curvature for satisfying target rotation capacity under uniform moment

$R_{d,ui} = \frac{\theta_{cr,d}}{\theta_p} - 1 \approx \frac{\phi_{cr,d}}{\phi_y} - 1$ is target rotation capacity under uniform moment

$\alpha(\phi) = (EI_y)_e / (EI_y)$ is the ratio of effective flexural stiffness to the elastic section stiffness according to curvature ϕ

$\beta(\phi) = (EC_w)_e / (EC_w)$ is the ratio of effective warping stiffness to the elastic section stiffness according to curvature ϕ

$\gamma(\phi) = ((GJ)_e - M\beta_x)_e / GJ$ is the ratio of effective torsional stiffness to the elastic section stiffness according to curvature ϕ

By modifying Eq. 4-39 into $\bar{\lambda}_{LT,d,ui} = \sqrt{M_p / M_e}$, required lateral slenderness for resisting target rotation capacity can be expressed as Eq. 4-40.

$$\bar{\lambda}_{LT,d,ui} = \sqrt{\frac{M_p}{M_e}} = \sqrt{\frac{M_p}{\frac{\pi}{k_y \cdot L_{d,ui}} \sqrt{(EI_y)(GJ) + \frac{\pi^2 (EI_y)(EC_w)}{(k_z \cdot L_{d,ui})^2}}}} \quad (4-40)$$

where

$\bar{\lambda}_{LT,d,ui}$ is plateau length in lateral torsional buckling curve for satisfying target rotation capacity $M_e = \frac{\pi}{k_y \cdot L_{b,ui}} \sqrt{(EI_y)(GJ) + \frac{\pi^2 (EI_y)(EC_w)}{(k_z \cdot L_{b,ui})^2}}$ is the elastic LTB strength in the given unbraced length $L_{b,ui}$

4.3.3 Validation of the analytically developed rotation capacity curve with previous experiments

To validate the analytically developed rotation capacity curve in this study, Lee and Galambos (1962), Prasad and Galambos (1963) and Adams, Lay and Galmbos (1965) experiments were selected.

At Lee and Galambos (1962) experiment, $s=11.5$, $h=33$, $\sigma_y=35$ ksi mild

steel were applied. At Prasad and Galambos (1963) experiment, $s=11.5$, $h=33$, $\sigma_y=43$ ksi mild steel were applied. At Adams, Lay, Galambos (1965) experiment, $s=10.5$, $h=45$, $\sigma_y=54$ ksi mild steel were applied. By adopting Haaijer model, the material properties and following effective stiffness were inputted in Eq.4-39 for deriving the rotation capacity curves.

Fig. 4-40a, Fig. 4-40b and Fig. 4-40c showed the rotation capacities of the specimens [G:10WF25]-[M:Ho-241], [G:10B-S5]-[M:Ho-296] and [G:10WF25]-[M:Ho-375] calculated by Eq. 4-40 with experimentally measured rotation capacities (R_m) at maximum moment. As shown in Fig.4-39, the analytically developed curves well predict the rotation capacity and seems to be acceptable to utilize in the parametric studies in next chapter.

4.3.4 Analytical parameter studies

As mentioned previously, many parameters influence the stability of steel structures. In analogy to previous chapter, the geometrical parameters (the effects of the height-to-width ratio, the effects of the compact/slender web or flanges) and the material parameters (the effects of mild or high strength steel, the effects of hybrid I-section) were selected for the analytical studies as shown in Fig.4-31d, Fig. 4-31e and Table 4-1.

4.3.4.1 Effect of geometrical variation

(1) Variation of flange and web thickness

Fig. 4-41a and Fig.4-40b showed the effect of flange and web thickness reinforcement on LTB in [M:Ho-722] I-section, calculated by Eq. 4-39 and Eq. 4-40. At the same rotation such as $R_m=2.0$, the unbraced length (L_b/r_y) of [G:A-W] indicate longer unbraced length, implying better buckling strength than that of [G:A-S] and [G:A-F].

The reason for the better rotation capacity [G:A-W] could be explained as below. As shown in Fig. 4-14 and Fig. 4-15, at the inelastic stages such as $R_m=2.0$, the effective rigidities contributed by the flanges become significantly lowered since the tangent modulus of the flanges ($E_{t,flange}$) are considerably reduced below one thirtieth or one fortieth of the elastic modulus ($E_{t,flange}=(1/40\sim 1/40)\cdot E$). Meanwhile the effective rigidities contributed by web could be relatively increased as since a portion of the web remains in elastic ranges and the tangent modulus of the rest portion are not decreased as that of the flanges. Therefore the geometrical compact/thick flange section [G:A-F] solely are not appropriate to ensure high rotation capacities and inevitably require compact web to ensure the performance.

Because of those phenomenon, the ratios of effective rigidities to plastic moment strength ($(EI_y)_e/M_p$, $(EC_w)_e/M_p$) of the geometrical compact web section [G:A-W] are higher than other [G:A-S] and [G:A-F] I-section. It should be noted that, although effective rigidities ($(EI_y)_e$, $(EC_w)_e$ and $(GJ)_e$) of [G:A-F] is higher than that of [G:A-W], the increased external force (such plastic moment, $M_0=M_p=Z_x\cdot F_y$ increase from [G:A-W] to [G:A-F]) requires

shorter unbraced length. As investigated previously, the unbraced length is not depended on the effective rigidities of I-section only but depended on the relative ratio of the effective rigidities to plastic moment(=required strength).

Fig. 4-41c and Fig 4-40d showed the effect of flange and web thickness reinforcement on LTB in [M:Ho-349] I-section respectively, calculated by Eq. 4-39 and Eq. 4-40. Regardless of the material properties change, [G:A-W] showed better buckling strength than that of [G:A-S] and [G:A-F].

(2) Variation of depth

Fig. 4-41 showed the effect of increased depth on LTB in [M:Ho-722] and [M:Ho-349] I-section respectively, calculated by Eq. 4-39 and Eq. 4-40. It showed that at the same rotation such as $R_m=2.0$, the unbraced length (L_b/r_y) of [G:B-S, B-W and B-F] require shorter unbraced length than that of [G:A-S, A-W and A-F], implying that the increase of the depth without increasing effective rigidities result in negative effect on the rotation capacities.

4.3.4.2 Effect of material properties

(1) Mild steel versus high strength steel

Fig. 4-42 showed the effect of material properties on LTB in [G:A-S~A-F] section respectively, calculated by Eq. 4-39 and Eq. 4-40. At the same rotation such as $R_m=2.0$, the unbraced length (L_b/r_y) of [M:Ho-722] require shorter unbraced length than that of [M:Ho-349].

Two major factors (effective section rigidities ($(EI_y)_e$ and $(EC_w)_e$) and

higher plastic moment (M_p) of [M:Ho-722] I-member result in the limited and less rotation capacity compared to [M:Ho-349] I-member. Firstly, as mentioned previously, a critical curvature (**here and after, critical curvature, $\phi_{cr,\alpha=0.05}$, $\phi_{cr,\beta=0.05}$**) when the effective flexural rigidities are under 5% of its initial elastic section rigidities would significantly meaningful to estimate the rotation capacity of a material since the out-of-plane buckling deformation is significantly increased and the rotation capacity is curtailed at this point.

Fig. 4-16a and Fig.4-16b compared the flexural rigidities and warping rigidities of [M:Ho-349] and [M:Ho-722] according to the curvatures. For the [M:Ho-349] of section, the critical curvature are $10.0 \cdot \phi_y$. However, the [M:Ho-722] I-section, the critical curvature are $2.5 \cdot \phi_y$. This clearly demonstrated that the I-section of [M:Ho-722] is more vulnerable to LTB than that of [M:Ho-349] in terms of ensuring the rotation capacity.

Secondly, the increase of the plastic moment itself ($M_{p,Ho,722}/M_{p,Ho,349}=722/349$) require more stringent unbraced length for [M:Ho-722] I-section. As verified in **Eq. 4-39**, regardless of the variation of the effective rigidities, the increased required buckling strength (=plastic moment) stipulate closer unbraced length.

In summary, in this chapter clearly show that why the high strength steel are more vulnerable and expected to more stringent unbraced length required as compared to the mild steel. It also implies that the high strength steel needs

to be examined in detail as it would adequate and properly controlled by the formulas provided in current specification to ensure the rotation capacity in current specification in AISC and EC 3 codes specified. This will be discussed later.

(2) High strength I section versus hybrid I section

Fig. 4-43 showed the effect of hybrid I-section on LTB in [G:A-S~A-F] section respectively, calculated by Eq. 4-39 and Eq. 4-40. At the same rotation such as $R_m=2.0$, the unbraced length (L_b/r_y) of [M:Hy-349-722] require relaxed (=longer) unbraced length than that of [M:Ho-722], implying that the lower strength hybrid web result in positive effect on the buckling strength since it reduce the external force ($Z_{xw} \cdot F_{yw, HSA800} \rightarrow Z_{xw} \cdot F_{yw, SM490}$) without or marginally decreased the effective rigidities [$((EI_y)_e$ and $(EC_w)_e$]. It could be concluded that by taking advantage of the hybrid I-section, the required unbraced length for preventing lateral instability become relaxed.

4.3.5 Detailed approach to derive unbraced length limit for target rotation capacity

In this chapter, an approach for deriving unbraced length for achieving target rotation capacity (L_d) will be discussed. As mentioned previously, current code has been stipulated the unbraced length limit for a member to ensure certain level of target rotation capacity. Therefore, the derivation method to achieve target rotation capacity is significantly meaningful.

The unbraced length for achieving target rotation capacity could be simply derived by modifying Eq. 4-39 as below. At the equation, the required buckling strength (M_0) changed into a moment ($M(\phi_{cr,d,ui})$) when a curvature satisfying target rotation capacity. The values of the effective rigidities need to be estimated when the I-section reaches at the critical curvature.

By adopting the reduction factor ($\alpha_d, \beta_d, \gamma_d$), where $\alpha_d=(EI_y)_e/(EI_y)$ is the flexural bending stiffness reduction factor, $\beta_d=(EC_w)_e/(EC_w)$ is the warping stiffness reduction factor, $\gamma_d=((GJ)_e-M\beta_x)/(GJ)$ is the torsional stiffness reduction factor at target rotation capacity, the effective rigidities at target rotation capacity are easily calculated as shown in Fig. 4-16.

$$L_{b,ui} = \frac{1}{k} \sqrt{\frac{X_1 + \sqrt{(X_1)^2 + 4(M(\phi_{cr}))^2(X_2)}}{2(M(\phi_{cr}))^2}} \quad (4-31) \text{ again}$$

$$L_{d,ui} = \frac{1}{k} \sqrt{\frac{X_1 + \sqrt{(X_1)^2 + 4(M(\phi_{cr,d,ui}))^2(X_2)}}{2(M(\phi_{cr,d,ui}))^2}}$$

$$\begin{aligned} \phi_{cr,d,ui} &= (R_{d,ui} + 1) \cdot \phi_y \\ X_1 &= \pi^2 \cdot \alpha_d \cdot (EI_y) \cdot \gamma_d \cdot (GJ), X_2 = \pi^4 \cdot \alpha_d \cdot (EI_y) \cdot \beta_d \cdot (EC_w) \end{aligned} \quad (4-31) \text{ modified}$$

$$\alpha_d = (EI_y)_e / (EI_y)$$

$$\beta_d = (EC_w)_e / (EC_w)$$

$$\gamma_d = ((GJ)_e - M\beta_x) / GJ$$

where

$L_{d,ui}$ is required unbraced length for achieving target rotation capacity

$\phi_{cr,d,ui}$ is the curvature for satisfying target rotation capacity under uniform moment

$$R_{d,ui} = \frac{\theta_{cr}}{\theta_p} - 1 \approx \frac{\phi_{cr}}{\phi_y} - 1 \text{ is target rotation capacity under uniform moment}$$

$\alpha_d = (EI_y)_e / (EI_y)$ is the weak axis bending stiffness reduction factor at target rotation capacity

$\beta_d = (EC_w)_e / (EC_w)$ is the warping stiffness reduction factor at target rotation capacity

$\gamma_d = ((GJ)_e - M\beta_x) / GJ$ is the torsional stiffness reduction factor at target rotation capacity

Table 4-5 showed unbraced length limits ($L_{d,ui}/r_y$) and normalized slenderness limits ($\bar{\lambda}_{LT,d,ui}$) for achieving target rotation capacity $R_m=2.0$ calculated by the detailed approaches (Eq. 4-39). **Fig. 4-44** shows the comparison between the analytically derived unbraced length limits and the unbraced length limit in current AISC criteria, $L_p / r_y = 1.76 \cdot \sqrt{E / F_y}$. As indicated in the previous analytical parameter studies, the specimens with low height to width ratio [Type:A], relatively compact web [G:A-W, B-W] I-section, mild steel I-section [M:Ho-349] and hybrid I-section [M:Hy-349-722] show higher rotation capacity.

All specimens of [M:Ho-349] series could satisfy the unbraced limit predicted in current AISC criteria. However, the specimens which could satisfy the current criteria in [M:Ho-722] series are few, as predicted.

In the [M:Ho-722] I-sections, the specimens [G:A-W], [G:B-W] and [G:A-F] which have relatively high effective rigidities ratios by adopting low height-to-width ratios or relatively compact web only satisfy the current AISC criteria. Also, in the [M:Hy-349-722] I-sections, the specimens [G:A-S], [G:A-F], [G:A-S] and [G:B-F] satisfy the current AISC criteria. As mentioned

previously, the hybrid I-section is advantages for ensuring higher rotation capacity.

4.3.6 Simplified approach to derive unbraced length limit for target rotation capacity

In this chapter, simplified approach for deriving unbraced length for target rotation capacity ($L_{d,ui}$) will be discussed. As mentioned in previous chapter 2, **White** (1960) and Lay suggested simplistic format for providing unbraced length for achieving target rotation in AISC spec. By assuming the maximum moment of I-section are equal to the plastic moment and by adopting the effective flexural rigidities ($\alpha_d=(EI_y)_e/(EI_y)$) at the critical curvature (ϕ_{cr}), the unbraced length limit for achieving target rotation capacity is resulted in as **Eq. 4-41**.

$$\begin{aligned} L_{d,Ho,ui} &= \frac{\pi}{k} \cdot \sqrt{\frac{(EI_y)_e}{EI_y}} \cdot \sqrt{\frac{(A/2) \cdot (d-t_f)}{Z_x F_{yf}}} \cdot r_y \cdot \sqrt{E} \\ &= \frac{\pi}{k} \cdot \sqrt{\alpha_d} \cdot \sqrt{\frac{(A/2) \cdot (d-t_f)}{Z_x}} \cdot r_y \cdot \sqrt{\frac{E}{F_{yf}}} \end{aligned} \quad (4-41a)$$

$$\begin{aligned} L_{d,Hy,ui} &= \frac{\pi}{k} \cdot \sqrt{\frac{(EI_y)_e}{EI_y}} \cdot \sqrt{\frac{(A/2) \cdot (d-t_f)}{Z_{xf} F_{yf} + Z_{xw} F_{yw}}} \cdot r_y \cdot \sqrt{E} \\ &= \frac{\pi}{k} \cdot \sqrt{\alpha_d} \cdot \sqrt{\frac{(A/2) \cdot (d-t_f)}{Z_{xf} + Z_{xw} \cdot (F_{yw} / F_{yf})}} \cdot r_y \cdot \sqrt{\frac{E}{F_{yf}}} \end{aligned} \quad (4-41b)$$

where

$L_{d,Ho,ui}$ is unbraced length for achieving target rotation capacity of homogeneous I beam

$L_{d,Hy,ui}$ is unbraced length for achieving target rotation capacity of hybrid I beam

$\alpha_d = (EI_y)_e / (EI_y)$ is the flexural bending stiffness reduction factor at target rotation capacity ($R_{d,ui}$)

$$r_y = \sqrt{\frac{I_y}{A}}$$

$k=0.54$ assuming when continuous lateral bracings provided, $k=1.0$ without continuous bracings

For normalized lateral slenderness $\bar{\lambda}_{LT,0} = \sqrt{M_p / M_e}$ adequate for EC 3, it can be expressed as Eq. 4-42.

$$\bar{\lambda}_{LT,d,ui} = \sqrt{\frac{M_p}{M_e}} = \sqrt{\alpha_d} \quad (4-42)$$

where

$\bar{\lambda}_{LT,d,ui}$ is plateau length in lateral torsional buckling curve for achieving target rotation capacity

$\alpha_d = (EI_y)_e / (EI_y)$ is the flexural bending stiffness reduction factor at target rotation capacity ($R_{d,ui}$)

Table 4-6 showed unbraced length limits ($L_{d,ui}/r_y$) and normalized slenderness limits ($\bar{\lambda}_{LT,d,ui}$) for achieving target rotation capacity ($R_m=2.0$) calculated by the simplified approaches (Eq. 4-41 and Eq. 4-42). Fig. 4-45 graphically showed the L_d/r_y values with the AISC code limits.

Compared with the detailed approaches, by neglecting the torsional rigidities in this simplistic approach, the buckling strength of relatively compact flange I-section are underestimated. However, this approach underestimates the effective rigidities considerably and requires relatively closer bracing limits. Nevertheless, all mild steel I-section models, [M: Ho-349] series, regardless of geometrical variation, could satisfy the unbraced limit predicted in current AISC criteria. However, at high strength I-section

models such [M: Ho-722] and [M: Ho-349-722] series, only thick web I-section [G: A-W] could satisfy the current unbraced length limit.

4.3.7 Summary

1) An analytical procedure to derive a rotation capacity curve at bifurcation ($R_{cr,ui}$) under uniform moment according to unbraced length was proposed, based on the effective rigidities derived in the section 4.1, applicable to both high strength and mild strength, and to the hybrid I-section member. By comparing the rotation capacity curve with the studies by Lee and Galambos (1962), Prasad and Galambos (1963), and Adams, Lay and Galambos (1965), the curve predicts the experimental rotation capacity excellently well and seems to be acceptable for use in parametric model studies (analogous to section 4.2) required for suggesting appropriate design methodologies for controlling LTB of I-shaped members fabricated from all grades of steel.

2) From the analytical results, with regard to the geometrical aspect, the model with low height-to-width ratio [G: Type A (d=250mm, b=150mm)] shows higher rotation capacity than the model with high height-to-width ratio [G: Type B (d=400mm, b=150mm)] since the required buckling strength is increased at high height-to-width ratio without proportionally increasing the effective rigidities. Also, the relatively thick web [G: A-W, B-W] models show higher rotation capacity than the models with an I-section are fabricated from same thick plates [G: A-S, B-S] model and thick flange [G: A-F, B-F]

model. This phenomenon derives from the fact that in the inelastic range, the contribution of the flange to the effective rigidities continuously decreased due to flange yielding (=reduction of tangent modulus), and a considerable portion of the effective rigidities are contributed by the web, where a large part remains in the elastic stages.

3) From the analytical results, with regard to the material aspect, the mild steel I-section models [M: Ho-349] show a definite higher rotation capacity than the high strength I-section models [M: Ho-722] for two reasons as follows. At certain rotation capacities such as a level 3.0, the effective rigidities of the mild steel I-section are significantly higher than those of the high strength I-section. Moreover, the required buckling strength of the high strength I-section is two times higher than that of mild steel, inevitably resulting in more stringent unbraced lengths. Meanwhile, the hybrid I-section [M: Hy-349-722] shows higher rotation capacity than that of the high strength I-section [M: Ho-722] since the required buckling strength decreases considerably when applying a mild steel web while merely decreasing the effective section rigidities.

4) The explicit formula (Eq. 4-31) to derive the unbraced length limit ($L_{d,ui}$) for achieving target rotation capacity ($R_{cr,d,ui}$) under uniform moment is proposed. By comparing the unbraced length limits with the current AISC limit ($L_p / r_y = 1.76 \cdot \sqrt{E / F_y}$), all mild steel models [M: Ho-349] series,

regardless of geometrical variation, could satisfy the unbraced limit predicted in the current AISC criteria with a considerably large margin.

However, only a few high strength models [M: Ho-722] could satisfy the current criteria. The reason for such limited rotation capacities is explained as follows. First, the critical curvature ($\phi_{cr}(\alpha_{2-3})$, $\phi_{cr}(\beta_{2-3})$), when the effective rigidities are under 5% of its initial elastic rigidities ($\alpha_{2-3} = \beta_{2-3} = 0.05$), of high strength models [M: Ho-722] are significantly lower than those of mild steel models [M: Ho-349]. The critical curvature of the high strength I-section model is about 2.5~3.0 times the yield curvature ($\phi_{cr}(\alpha_{2-3, HSA800}) = 2.5 \sim 3.0 \cdot \phi_y$); meanwhile, the critical curvature of the mild steel I-section model is about 10.0 times the yield curvature ($\phi_{cr}(\alpha_{2-3, SM490}) = 10.0 \cdot \phi_y$). Also the required buckling strength (=plastic moment, $M_p = Z_x \cdot F_y$) of [M: Ho-722] is about two times larger than that of [M: Ho-349], inevitably resulting in more stringent unbraced lengths.

Among the high strength I-section models [M: Ho-722], the model with the low height-to-width ratio and the thick web plate, [G: A-W]-[M: Ho-722], shows the highest rotation capacity as predicted, satisfying the current unbraced length limit. Also, the hybrid I-section model with the thick web I-section [G: A-W]-[M: Hy-349-722] shows further rotation capacity since it decreases the required buckling strength considerably with merely a decrease in the effective section rigidities. Therefore, to ensure sufficient rotation

capacity for the high strength I-section, the geometrically low height-to-width [G: Type A] and thick web [G: A-W] I-section should be applied, and in a material aspect, adopting the hybrid I-section is favorable.

4.4 LTB strength under moment gradient

In the previous chapter, the LTB strength under uniform moment has been deal with. In this chapter, the LTB strength under moment gradient will be discussed. In contrast to the uniform moment case where the solution of the governing equation is analytically obtainable by explicit formulas, the solutions of that of the moment gradient case are inevitably depended on the numerical method. The reason adopting such method is that the length and value of the inelastic section rigidities region ($M \geq M_y$) varies along the longitudinal direction according to each load level. Historically, several solution methods have been developed and adopted to solve the governing equation such finite difference, finite integral and finite element methods. In this study, the finite element method via Galerkin method which are the most frequently utilized so as to develop finite element procedure was adopted and utilized for solving these problems.

4.4.1 Overview of LTB under moment gradient

4.4.1.1 Description of the behavior

Fig. 4-46 shows the overall information as inelastic LTB occurred under moment gradient. Fig. 4-46a shows the loading condition triggering moment gradient condition in the middle of I-beam. The position of the lateral constraint located same position with loading point. The laterally unbraced length is indicated by $L_{b,gr}$. Fig. 4-46b shows the moment distribution when the maximum moment reached at the load level higher than the yield moment ($M \geq M_y$). Fig. 4-46c showed the x-z plane (in-plane) deformed shape where the vertical degree of freedom is constraint at the ends. Fig. 4-46c showed the y-z plane (out-of-plane) deformed shape where the lateral degree of freedoms is constraint at the bracing points and ends. It showed that the out-of-plane deformed shape showed sinusoidal profile with zero values at the constraints. Contrary to the uniform moment case, the magnitudes of the sinusoidal profile are specially concentrated to the inelastic region the moment of which is higher than yield moment ($M \geq M_y$). Fig. 4-46d showed the (in-plane) moment-curvature diagram at the loading condition. The curvature distributions in the elastic ($\phi < \phi_y$) and inelastic ($\phi \geq \phi_y$) range are shown depending on the stress-strain profiles of a material. Fig. 4-46e showed the flexural rigidities at the loading condition. The distribution of flexural rigidities in the elastic ($\alpha=1.0$) and inelastic ($\alpha < 1.0$) range are shown depending on the stress-strain profiles of a material. Fig. 4-46f showed the

idealized analytical model with unequal end moments (one end $M_i=M_x$, the other end $M_j=0$) in the braced length region ($L_{b,gr}$). The lateral torsional buckling behavior is usually represented by the cross-sectional rotation ($\gamma(z)$) along the member length.

4.4.1.2 Derivation of LTB strength curve under moment gradient via inelastic section rigidities

Eq. 4-43 showed the external force components of each x' , y' and z' axis under moment gradient loading condition. The moment (M_0) indicates the maximum external force applied in a member. The moment terms in each component varies according to the longitudinal z position. The terms result in that no analytical solution would be derived and the numerical method, discussed below, is required for the solution. Since the internal force in each axis components are the same as the Eq. 4-27, the formula for describing the internal force are omitted.

$$\begin{aligned} M'_{x,ext} &= M_x \cdot \cos(\gamma) \approx M_x = M_0 \cdot [1 - (z/L) \cdot (1 - m_R)] \\ M'_{y,ext} &= -M_x \cdot \sin(\gamma) \approx -\gamma M_x = -\gamma M_0 \cdot [1 - (z/L) \cdot (1 - m_R)] \\ M'_{z,ext} &= d\mu/dz \cdot M_x = d\mu/dz \cdot M_0 \cdot [1 - (z/L) \cdot (1 - m_R)] \end{aligned} \quad (4-43)$$

where

m_R is gradient parameters

$m_R = 1.0$: uniform moment case

$m_R = -1.0$: moment gradient with equal magnitude

(1) Elastic LTB under moment gradient

In this chapter, detailed approach for deriving unbraced length for achieving yield moment ($L_{r,gr}$) will be discussed. Eq. 4-44 describes the governing equation of elastic lateral-torsional buckling under moment gradient. Because all properties remains in elastic stages, the flexural, warping and torsional rigidities are expressed as EI_y , EC_w and GJ . The solution of the governing equation (fourth-order differential equation with respect to cross section rotation γ) is difficult for expressing closed form since it possess the term associated the external force, $[1-(z/L)\cdot(1-m_r)]^2$ which have unknown variable z .

$$\frac{d^4\gamma}{dz^4} - \frac{GJ}{EC_w} \frac{d^2\gamma}{dz^2} - \frac{M_0^2}{EI_y \cdot EC_w} \cdot [1-(z/L)\cdot(1-m_r)]^2 \cdot \gamma = 0 \quad (4-44)$$

where

EI_y is elastic flexural stiffness

EC_w is elastic warping stiffness

GJ is elastic torsional stiffness

γ is the rotation of the cross section

To solve the Eq. 4-44, Galerkin method were adopted and the assumed shape functions which satisfying the torsionally simple boundary conditions (Eq. 4-45) are proposed. In analogous to the Ritz method, the higher order terms such as $n=3, 4, \dots$ are required for convergence of the solution, but no longer required as the condition are satisfied.

$$\gamma(0) = 0, \gamma(L_b) = 0, \gamma''(0) = 0, \gamma''(L_b) = 0 \quad (4-45)$$

$$\gamma(z) = \sum_{i=1,2,3\dots} a_i \cdot \phi_i(z) = \sum_{i=1,2,3\dots} a_i \cdot \sin\left(\frac{i\pi}{L} \cdot z\right)$$

where

$\gamma(z)$ is assumed shape function for the rotation of the cross section

a_i are the undetermined coefficients

ϕ_i are independent continuous functions satisfying boundary conditions

Eq. 4-46 shows the altered governing equation after Galerkin method applied using the assumed shape function Eq. 4-45 as weight function.

$$\int_0^L \left[\frac{d^4 \gamma(z)}{dz^4} - A \frac{d^2 \gamma(z)}{dz^2} - M_0^2 \cdot B \cdot \{1 - (z/L) \cdot (1-c)\}^2 \cdot \gamma(z) \right] \cdot \frac{\partial \gamma(z)}{\partial a_n} dz = 0 \quad (4-46)$$

$$\sum_{i,j=1,2,3\dots}^{i,j=J} a_n \cdot \int_0^L \left[\frac{d^4 \phi_i(z)}{dz^4} - A \frac{d^2 \phi_i(z)}{dz^2} - M_0^2 \cdot B \cdot \{1 - (z/L) \cdot (1-c)\}^2 \cdot \phi_i(z) \right] \cdot \phi_j dz = 0$$

where

$$A = \frac{GJ}{EC_w}, \quad B = \frac{1}{EI_y \cdot EC_w}$$

i, j vary over the range $1 \leq (i, j) \leq J$ result in a square matrix

J is the number of terms required for convergence

Eq. 4-47 shows the matrix format representation of Eq. 4-46. If the value of n and j are equal, the equation derives square matrix $[A]$.

$$[[K] - M_0^2 \cdot [S]] \cdot [a_n] = [0]$$

$$\begin{bmatrix} K_{11} - M_0^2 \cdot S_{11} & K_{12} - M_0^2 \cdot S_{12} & \dots & K_{1J} - M_0^2 \cdot S_{1J} \\ K_{21} - M_0^2 \cdot S_{21} & \dots & \dots & K_{2J} - M_0^2 \cdot S_{2J} \\ \dots & \dots & \dots & \dots \\ K_{J1} - M_0^2 \cdot S_{J1} & K_{J2} - M_0^2 \cdot S_{J2} & \dots & K_{JJ} - M_0^2 \cdot S_{JJ} \end{bmatrix} \begin{bmatrix} a_1 \\ a_2 \\ \dots \\ a_n \end{bmatrix} = \begin{bmatrix} 0 \\ 0 \\ \dots \\ 0 \end{bmatrix} \quad (4-47)$$

where

$$K_{ij} = \int_0^L \left[\frac{d^4 \phi_i(z)}{dz^4} - A \frac{d^2 \phi_i(z)}{dz^2} \right] \cdot \phi_j(z)$$

$$S_{ij} = \int_0^L \left[B \cdot \{1 - (z/L) \cdot (1 - m_R)\}^2 \cdot \phi_i(z) \right] \cdot \phi_j$$

The matrix equations expressed in Eq. 4-47 finally lead a set of equation format as Eq. 4-48a. The [k] matrix represents the internal force associated with the effective rigidities and the [S] matrix represent the external force associated with the applied load (M_0). Non-trivial solutions of Eq. 4-48b define a series of buckling loads ($M_{cr,1}, M_{cr,2}, \dots, M_{cr,n}$) and the lowest buckling load ($M_{cr,1}$) is critical buckling load. For deriving bracing length limit for achieving yield moment ($L_{r,gr}$), iterative process are required to find the point where the lowest buckling load and yield moment become equal as described in Eq. 4-48c.

$$\det [K] - M_{cr,n}^2 \cdot [S] = 0 \quad (4-48a)$$

$$M_{cr} = M_{cr,1} \quad (4-48b)$$

$$M_{cr}(L_{b,gr}, m_R) = M_0 \quad (4-48c)$$

where

$\det |A| = 0$ is the determinant of the matrix A, resulting in a polynomial function with variable $M_{cr,1}, M_{cr,2}, \dots, M_{cr,n}$

$M_{cr,1}$ is the lowest eigenvalue among the eigenvalues, $M_{cr,n}$

$L_{b,gr}$ is required unbraced length for resisting moment gradient M_0

(2) Inelastic LTB under moment gradient

In this chapter, detailed approach for deriving unbraced length for achieving plastic moment ($L_{p,gr}$) will be discussed. Eq. 4-49 describes the

governing equation of inelastic lateral-torsional buckling under moment gradient. In contrast to the elastic lateral-torsional buckling where all properties remains in elastic range, the inelastic section regions the moment of which is higher than yield moment $M \geq M_y$ require inelastic effective rigidities $(EI_y)_e(z)$, $(EC_w)_e(z)$ varies along with the position of z . These terms trigger cumbersome and lengthy re-calculation to define adequate inelastic effective rigidities in the inelastic section regions. Also, it requires at least two divided sub-domains to represent each elastic and inelastic properties of a member.

$$\frac{d^4 \gamma}{dz^4} - \frac{(GJ)_e}{(EC_w)_e} \frac{d^2 \gamma}{dz^2} - \frac{M_0^2}{(EI_y)_e \cdot (EC_w)_e} \cdot [1 - (z/L) \cdot (1 - m_r)]^2 \cdot \gamma = 0 \quad (4-49)$$

where

$(EI_y)_e$ is effective flexural stiffness

$(EC_w)_e$ is effective warping stiffness

$(GJ)_e$ is effective torsional stiffness

The effect of mono-symmetry section $(\beta_x)_t$ is neglected

More specifically, the flexural rigidity is EI_y for $M < M_y$, and it will be $(EI_y)_e(\phi_p)$ at plastic moment M_p . For the effective rigidities $(EI_y)_{e,gr}(z_1)$ between M_y and M_p , sinusoidal representation are would be adequate for the representation as described [Eq. 4-50a](#). The length of inelastic region ($\tau_1 \cdot L_b$) is determined from the different load level between yield moment (M_y) and plastic moment (M_p). For simplify the inelastic effective rigidities as the average value, adopting [Eq. 4-50b](#) is recommended.

$$(EI_y)_{e,gr}(z_1) = \frac{1 + (EI_y)_e(\phi_p)}{2} - \frac{1 - (EI_y)_e(\phi_p)}{2} \cdot \cos\left(\frac{\pi \cdot z_1}{\tau_i L_b}\right) \quad (4-50a)$$

$$(EI_y)_{eq,gr} = \frac{\int_0^{\tau_i L_b} (EI_y)_{e,gr}(z_1) \cdot dz_1}{\tau_i L_b} \quad (4-50b)$$

where

$(EI_y)_e(\phi_p)$ is the effective flexural rigidities at curvature ϕ_p

$(EI_y)_{e,gr}(z_1)$ is effective rigidities located at z_1 position under moment gradient condition

$(EI_y)_{eq,gr}$ is equivalent effective stiffness value in inelastic portion length

$(L_{ie} = \tau_i \cdot L_b)$ under moment gradient condition

$\tau_i = \frac{[1 - (M_y / M_p)]}{(1 - m_R)}$ is the length of inelastic portion in unbraced length (L_b)

ϕ_p is curvature when the plastic moment achieved

z_1 is the coordinate for longitudinal direction

To solve the Eq. 4-49, the finite element method via Galerkin method was adopted as shown in Fig. 4-48. As mentioned previously, at least at least two divided sub-domains(=elements) to represent each elastic and inelastic properties of a member. As for an element, one dimensional line element designated as i and j for each end are assumed. Each end have three degree of freedoms γ , γ' and γ'' and 5th order polynomial equation are adopted for the shape functions. For better understating suppose two elements (#EL1-elastic, #EL2-inelastic) are applied for this model with three nodes (#N1, #N2 and #N3). The length of #EL1 will be L_e and the length of #EL2 will be L_i .

$$\gamma_{ij}(z) = A \cdot z^5 + B \cdot z^4 + C \cdot z^3 + D \cdot z^2 + E \cdot z + F \quad (4-51)$$

$$\gamma(0) = \gamma_i, \quad \gamma'(0) = \gamma'_i, \quad \gamma''(0) = \gamma''_i, \quad \gamma(L_{ij}) = \gamma_j, \quad \gamma'(L_{ij}) = \gamma'_j, \\ \gamma''(L_{ij}) = \gamma''_j$$

$$\begin{bmatrix} 0 & 0 & 0 & 0 & 0 & 1 \\ 0 & 0 & 0 & 0 & 1 & 0 \\ 0 & 0 & 0 & 2 & 0 & 0 \\ L^5 & L^4 & L^3 & L^2 & L & 1 \\ 5L^4 & 4L^3 & 3L^2 & 2L & 1 & 0 \\ 20L^3 & 12L^2 & 6L & 2 & 0 & 0 \end{bmatrix} \begin{bmatrix} A \\ B \\ C \\ D \\ E \\ F \end{bmatrix} = \begin{bmatrix} \gamma_i \\ \gamma'_i \\ \gamma''_i \\ \gamma_j \\ \gamma'_j \\ \gamma''_j \end{bmatrix}$$

$$\gamma_{ij}(z) = H_1(z) \cdot \gamma_i + H_2(z) \cdot \gamma'_i + H_3(z) \cdot \gamma''_i \\ + H_4(z) \cdot \gamma_j + H_5(z) \cdot \gamma'_j + H_6(z) \cdot \gamma''_j$$

where

$\gamma, \gamma', \gamma''$ are rotations of cross section and its derivative

i, j are end joints in a sub-domain

A, B, C, D, E, F are the unknown coefficient

$H_1, H_2, H_3, H_4, H_5, H_6$ are the shape functions

$$H_1(z) = \left[1 - (10/L^3) \cdot z^3 + (15/L^4) \cdot z^4 - (6/L^5) \cdot z^5 \right]$$

$$H_2(z) = \left[z - (6/L^2) \cdot z^3 + (8/L^3) \cdot z^4 - (3/L^4) \cdot z^5 \right]$$

$$H_3(z) = \left[(1/2) \cdot z^2 - (3/(2L)) \cdot z^3 + (3/(2L^2)) \cdot z^4 - (1/(2L^3)) \cdot z^5 \right]$$

$$H_4(z) = \left[(10/L^3) \cdot z^3 - (15/L^4) \cdot z^4 + (6/L^5) \cdot z^5 \right]$$

$$H_5(z) = \left[-(4/L^2) \cdot z^3 + (7/L^3) \cdot z^4 - (3/L^4) \cdot z^5 \right]$$

$$H_6(z) = \left[(1/(2L)) \cdot z^3 - (1/L^2) \cdot z^4 + (1/(2L^3)) \cdot z^5 \right]$$

Eq. 4-52 shows the altered governing equation after Galerkin method applied using the assumed shape function Eq. 4-51 as weight function.

$$\sum_{i=1}^n \int_i^{i+1} \left[\frac{d^4 \gamma_{ij}(z)}{dz^4} - A \frac{d^2 \gamma_{ij}(z)}{dz^2} - M_0^2 \cdot B \cdot \{1 - (z/L) \cdot (1-c)\}^2 \cdot \gamma_{ij}(z) \right] \gamma_{ij}(z) \cdot dz = 0 \quad (4-52)$$

$$\sum_{i=1}^n \int_{z_i}^{z_{i+1}} \left[\begin{matrix} H_1^{iv} \\ H_2^{iv} \\ H_3^{iv} \\ H_4^{iv} \\ H_5^{iv} \\ H_6^{iv} \end{matrix} \right] \begin{matrix} H_1 \\ H_2 \\ H_3 \\ H_4 \\ H_5 \\ H_6 \end{matrix}^T - A \begin{matrix} H_1^* \\ H_2^* \\ H_3^* \\ H_4^* \\ H_5^* \\ H_6^* \end{matrix} \begin{matrix} H_1 \\ H_2 \\ H_3 \\ H_4 \\ H_5 \\ H_6 \end{matrix}^T \cdot dz \begin{matrix} \gamma_i \\ \gamma_i' \\ \gamma_i^* \\ \gamma_{i+1} \\ \gamma_{i+1}' \\ \gamma_{i+1}^* \end{matrix} \right]$$

$$- \sum_{i=1}^n \int_{z_i}^{z_{i+1}} M_0^2 \cdot B \cdot \{1 - (z/L) \cdot (1-c)\}^2 \begin{matrix} H_1 \\ H_2 \\ H_3 \\ H_4 \\ H_5 \\ H_6 \end{matrix} \begin{matrix} H_1 \\ H_2 \\ H_3 \\ H_4 \\ H_5 \\ H_6 \end{matrix}^T \cdot dz \begin{matrix} \gamma_i \\ \gamma_i' \\ \gamma_i^* \\ \gamma_{i+1} \\ \gamma_{i+1}' \\ \gamma_{i+1}^* \end{matrix} = 0$$

where

$$A_{ij} = \frac{(GJ)_e}{(EC_w)_e}, B_{ij} = \frac{1}{(EI_y)_e \cdot (EC_w)_e}$$

is the coefficients for inelastic LTB solution applied in Galerkin method

Eq. 4-53 shows the matrix format representation of Eq. 4-52 with satisfying the torsionally simple boundary conditions at initial and last node of a member.

$$[[K] - M_0^2 \cdot [S]] \cdot [\gamma_n] = [0]$$

$$\begin{bmatrix} 1 & 0 & 0 & 0 & 0 & 0 & 0 \\ K_{2,1} - M_0^2 \cdot S_{2,1} & K_{2,2} - M_0^2 \cdot S_{2,2} & \dots & \dots & \dots & \dots & K_{2,n} - M_0^2 \cdot S_{2,n} \\ 0 & 0 & 1 & 0 & 0 & 0 & 0 \\ \dots & \dots & \dots & \dots & \dots & \dots & \dots \\ 0 & 0 & 0 & 0 & 1 & 0 & 0 \\ K_{n-1,1} - M_0^2 \cdot S_{n-1,1} & \dots & \dots & \dots & \dots & \dots & K_{n-1,n} - M_0^2 \cdot S_{n-1,n} \\ 0 & 0 & 0 & 0 & 0 & 0 & 1 \end{bmatrix} \begin{bmatrix} \gamma_1 \\ \gamma_1' \\ \gamma_1^* \\ \dots \\ \gamma_n \\ \gamma_n' \\ \gamma_n^* \end{bmatrix} = \begin{bmatrix} 0 \\ 0 \\ 0 \\ 0 \\ 0 \\ 0 \\ 0 \end{bmatrix} \quad (4-53)$$

where

$$K_{ij} = \int_i^j \left[H_i^{iv} H_j - A_{ij} \cdot H_i'' H_j \right] dz$$

$$S_{ij} = \int_i^j \left[B_{ij} \cdot \{1 - (z/L) \cdot (1-k)\}^2 \cdot H_i \cdot H_j \right] dz$$

$$A_{ij} = \frac{(GJ)_e}{(EC_w)_e}, \quad B_{ij} = \frac{1}{(EI_y)_e \cdot (EC_w)_e}$$

is the coefficients for inelastic LTB solution applied in Galerkin method

The matrix equations expressed in Eq. 4-53 finally lead a set of equation format as Eq. 4-54a. The [k] matrix represents the internal force associated with the effective rigidities and the [S] matrix represent the external force associated with the applied load. Non-trivial solutions of Eq. 4-54b define a series of buckling load ($M_{cr,1}, M_{cr,2}, \dots, M_{cr,n}$) and the lowest buckling load ($M_{cr,1}$) is critical buckling load. For deriving bracing length limit for achieving plastic moment ($L_{p,gr}$), iterative process are required to find the point where the lowest buckling load and yield moment become equal as described in Eq. 4-54c.

$$\det \left[[K] - M_{cr,n}^2 \cdot [S] \right] = 0 \quad (4-54a)$$

$$M_{cr} = M_{cr,1} \quad (4-54b)$$

$$M_{cr}(L_{p,gr}, m_R) = M_p \quad (4-54c)$$

where

$\det|A| = 0$ is the determinant of the matrix A, resulting in a polynomial function

with variable $M_{cr,1}, M_{cr,2}, \dots, M_{cr,n}$

$M_{cr,1}$ is the lowest eigenvalue among the eigenvalues, $M_{cr,n}$

$L_{p,gr}$ is required unbraced length for achieving plastic moment under moment gradient

Fig. 4-49 showed the effect of moment gradient on LTB strength as compared with uniform moment case calculated by simplified approach. The buckling strength curve under moment gradient is significantly increased as compared to that of uniform moment case. Consequently relaxed unbraced length is permissible for the moment gradient case. The reason for the higher buckling strength results from the limited inelastic rigidities participation. For specifically, at the moment gradient case, the participation of inelastic region is limited to $L_i = \tau_i \cdot L_b$ length, however, at the uniform moment case, the participation of inelastic length is entire total unbraced length L_b .

4.4.2 Simplified T-column approach to derive unbraced length limit for achieving plastic moment

In this chapter, simplified approach for deriving unbraced length for achieving plastic moment ($L_{p,gr}$) will be discussed.

4.4.2.1 Overview and assumption

As mentioned previously, White and Lay propose simplified analytical model to derive unbraced length limit. Among those models, Lay's T-column would be powerful and advantageous for moment gradient case. Therefore, the brief overview of Lay's T-column approach and the method adopted in this study will be described below. The T-column model simply represents the compressive portion of I-section under bending moment situation. Also, the model only considers the flexural bending behavior and neglected the moment

variation and torsional behaviors. The validity of above assumption are well described in [Lay's Ph.D. thesis](#) paper and the model predict more conservative value than experimental results since it neglected several effective terms.

4.4.2.2 Derivation of unbraced length limit for plastic moment

As shown in [Fig. 4-50](#), by assuming a column with two materials (one is elastic and the other is inelastic), the LTB model dramatically simplified as described in [Eq. 4-55](#).

$$(EI_y)_T y_1'' + P_0 \cdot y_1 = 0 \quad (4-55a)$$

$$(EI_y)_{eq,T,gr} \cdot y_2'' + P_0 \cdot y_2 = 0 \quad (4-55b)$$

where

$(EI_y)_T$ is elastic flexural stiffness of T-column in elastic region

$(EI_y)_{eq,T,gr}$ is equivalent effective stiffness value of T-column in inelastic portion length ($L_{ie} = \tau_i \cdot L_b$) under moment gradient condition

In analogous to the detailed approach, for the effective rigidities $(EI_y)_{e,T,gr}(z_1)$ between M_y and M_p , sinusoidal representation are adopted as described [Eq. 4-56a](#). The length of inelastic region ($\tau_i L_b$) is determined from the different load level between yield moment (M_y) and plastic moment (M_p). The averaged inelastic rigidities for assigning in [Eq. 4-56b](#) is recommended.

$$(EI_y)_{e,T,gr}(z_1) = \frac{1 + (EI_y)_{e,T,gr}(\phi_p)}{2} - \frac{1 - (EI_y)_{e,T,gr}(\phi_p)}{2} \cdot \cos\left(\frac{\pi \cdot z_1}{\tau_i L_b}\right) \quad (4-56a)$$

$$(EI_y)_{eq,T,gr} = \frac{\int_0^{\tau_i L_b} (EI_y)_{e,T,gr}(z_1) \cdot dz_1}{\tau_i L_b} \quad (4-56b)$$

where

$(EI_y)_{e,T,gr}(z_1)$ is effective flexural rigidities of T-column located at z_1 position

$(EI_y)_{eq,T,gr}$ is equivalent effective stiffness value of T-column in inelastic portion

length ($L_{ie} = \tau_i \cdot L_b$) under moment gradient condition

The exact solution of Eq. 4-55 is represented by Eq. 4-57.

$$\begin{aligned} y_1 &= A \cdot \cos(k_1 x) + B \cdot \cos(k_1 x) \\ y_2 &= C \cdot \cos(k_2 x) + D \cdot \cos(k_2 x) \end{aligned} \quad (4-57)$$

where

$k_1 = \sqrt{\frac{P_0}{(EI_y)_T}}$ is constant representing elastic property in T-column approach

$k_2 = \sqrt{\frac{P_0}{(EI_y)_{eq,T}}}$ is constant representing inelastic property in T-column approach

The torsional simply boundary conditions and joint compatibility are represented in Eq. 4-58.

$$\begin{aligned} y_1(0) = y_1''(0) = y_2(0) = y_2''(0) &= 0 \\ y_1(L_a) = -y_2(L_b), y_1'(L_a) &= y_2'(L_b) \end{aligned} \quad (4-58)$$

where

L_a is a portion of T-column length in elastic property

L_b is a portion of T-column length in inelastic property

By applying Eq. 4-58 into Eq. 4-57, square matrix format represented are available as Eq. 4-59.

$$\begin{bmatrix} \sin(k_1 L_a) & \sin(k_2 L_b) \\ k_1 \cdot \cos(k_1 L_a) & -k_2 \cdot \cos(k_2 L_b) \end{bmatrix} \begin{bmatrix} B \\ D \end{bmatrix} = 0 \quad (4-59a)$$

$$\det \begin{bmatrix} \sin(k_1 L_a) & \sin(k_2 L_b) \\ k_1 \cdot \cos(k_1 L_a) & -k_2 \cdot \cos(k_2 L_b) \end{bmatrix} = 0 \quad (4-59b)$$

The matrix equations expressed in Eq. 4-59 finally lead a set of characteristic equation format as Eq. 4-60a. Non-trivial solutions of Eq. 4-60a define a series of buckling load ($P_{cr,1}, P_{cr,2}, \dots, P_{cr,n}$) and the lowest buckling load ($P_{cr,1}$) is critical buckling load as Eq. 4-60b. For deriving bracing length limit for achieving plastic moment ($L_{p,T,gr}$), iterative process are required to find the point where the lowest buckling load and plastic moment become equal as described in Eq. 4-60c.

$$\tan(k_1 L_a) + (k_1 / k_2) \cdot \tan(k_2 L_b) = 0 \quad (4-60a)$$

$$\tan(k_1 L_a) + \sqrt{\alpha_{eq,T,gr}} \cdot \tan\left(\frac{k_1}{\sqrt{\alpha_{eq,T,gr}}} L_b\right) = 0 \quad (4-60b)$$

$$P_{cr,1}(L_{p,T,gr}, m_R) = P_y \quad (4-60c)$$

where

$\alpha_{eq,T,gr} = (EI_y)_{eq,T,gr} / (EI_y)$ is the ratio of equivalent effective section stiffness to the elastic section stiffness

$L_{p,T,gr} = L_a + L_b$ is required unbraced length for achieving plastic moment under moment gradient by T-column approach

4.4.3 Summary

1) The analytical procedure to drive moment strength under moment gradient condition according to the unbraced length ($L_{b,gr}$) was proposed, based on the effective rigidities derived in the section 4.1, applicable to both

high strength and mild strength, and to a hybrid I-section member. Contrary to the uniform moment loading, the numerical methods are inevitable; since the moment and effective rigidities are varied along the longitudinal direction, no explicit solution for the governing LTB equation could be derived. Historically, such solutions have been solved using numerical procedures such as finite difference, finite integral, and finite element methods. In this study, by adopting the Galerkin method for the detailed approach and Lay's T-column for the simplified approach, systematic procedures were established to derive the laterally unbraced lengths under moment gradient condition.

2) By applying Galerkin methods for solving the governing equation, the analytical procedure has been performed primarily by recalculating the stiffness (associated with effective rigidities) and the stability matrices (associated with applied moment) from the yield to maximum moment levels. The eigenvalue analysis was then applied to acquire the inelastic buckling strength (=eigenvalue) at the given unbraced length and moment condition. By comparing the derived buckling strength with the applied moment, the adequate unbraced length ($L_{b,gr}$) for resisting the applied moment was finally determined.

3) From the analytical results, the buckling strength curve under moment gradient is significantly increased compared to that of the uniform moment case. The higher buckling strength results from the limited inelastic participation along the member length, resulting in limited stiffness reduction.

Specifically, at the moment gradient case, the participation of the inelastic region is limited in a small portion of the member length, although it depends on the material post-yield properties; however, at the uniform moment case, the total unbraced length participate in the inelastic region at once, inevitably resulting in large stiffness reduction than that of moment gradient case.

Consequently, the unbraced length ($L_{b,gr}$) for moment gradient case is quite relaxed as compared to that ($L_{b,ui}$) of uniform moment case. Therefore the close spacing would not provide higher LTB strength and other buckling phenomenon such as local buckling would govern the beam buckling strength.

4.5 Available rotation capacity under moment gradient

In this chapter, the unbraced length for achieving target rotation capacity under moment gradient condition will be deal with. As discussed in chapter 3, as the rotation capacity under moment gradient case highly affected by the factors such T/Y strain ratio (ϵ_u/ϵ_y), yield plateau length (S) and Y/T strength ratio (Y_R), there are many factors which must be considered to propose the unbraced length. In this study, by considering such factor at once, the methods which are both applicable to conventional steel and high strength steel are will be described.

4.5.1 Description of the behavior

Fig. 4-51 shows the overall information as inelastic LTB occurred under moment gradient degrades the rotation capacity of a member. Fig. 4-51b shows a moment-rotation curve considering the in-plane behavior only. However, the behavior is not fully realized since the out-of-plane behavior such LTB curtail the rotation capacity significantly as shown in Fig. 4-51c.

4.5.2 Derivation of rotation capacity curve under moment gradient via inelastic section rigidities

The required unbraced length ($L_{d,gr}$) for resisting target rotation capacity (R_d) can be calculated as the target rotation capacity is determined as Eq. 4-61. Please refer to chapter 3.3.2.2 for the background of the calculation.

$$R_{d,gr} = \frac{\theta_{cr,d,gr}}{\theta_p} - 1 \approx \frac{\int_0^L \phi_{cr,d,gr}(z) dz}{\int_0^L \phi_y(z) dz} - 1 \quad (4-61)$$

where

$R_{d,gr}$ is target rotation capacity under moment gradient

$\theta_{cr,d,gr}$ is the critical rotation when target rotation capacity achieved under moment gradient

$\phi_{cr,d,gr}$ is the critical curvature when target rotation capacity achieved under moment gradient

For the effective rigidities $(EI_y)_{e,gr}(z_1)$ between M_y and M , sinusoidal representation are adopted as described Eq. 4-62. The moment at the target rotation capacity is also needs to be calculated to determine the length of

inelastic region and assigning the inelastic effective rigidities. The length of inelastic region ($\tau_i L_b$) is determined from the different load level between yield moment (M_y) and target moment (M) as described Eq. 4-62a. For the averaged inelastic rigidities for assigning in LTB equation, Eq. 4-62b is recommended.

$$(EI_y)_{e,gr}(z_1) = \frac{1 + (EI_y)_e(\phi_{cr,d,gr})}{2} - \frac{1 - (EI_y)_e(\phi_{cr,d,gr})}{2} \cdot \cos\left(\frac{\pi \cdot z_1}{\tau_i L_b}\right) \quad (4-62a)$$

$$(EI_y)_{e,gr}(z_1) = \frac{\int_0^{\tau_i L_b} (EI_y)_{e,gr}(z_1) \cdot dz_1}{\tau_i L_b} \quad (4-62b)$$

where

$(EI_y)_e(\phi)$ is the effective flexural rigidities at curvature ϕ

$(EI_y)_{e,gr}(z_1)$ is the effective flexural rigidities located at z_1 position under moment gradient condition

$(EI_y)_{eq,gr}$ is equivalent effective stiffness value in inelastic portion length

$(L_{ie} = \tau_i \cdot L_b)$ under moment gradient condition

Other process such as applying Galerkin method, the matrix format representation are the same as in previous chapter 4.2 The matrix equations finally lead a set of equation format as Eq. 4-63a. The [k] matrix represents the internal force associated with the effective rigidities and the [S] matrix represent the external force associated with the applied load. Non-trivial solutions of Eq. 4-63b define a series of buckling load ($M_{cr,1}, M_{cr,2}, \dots, M_{cr,n}$) and the lowest buckling load ($M_{cr,1}$) is critical buckling load. For deriving bracing length limit for target rotation ($L_{d,gr}$), iterative process are required to find the point where the lowest buckling load and target moment become

equal as described in Eq. 4-63c.

$$\det\left[[K] - M_{cr,n}^2 \cdot [S]\right] = 0 \quad (4-63a)$$

$$M_{cr} = M_{cr,1}, \quad (4-63b)$$

$$M_{cr}(L_{p,gr}, m_R) = M_0(\phi_{cr,d,gr}) \quad (4-63c)$$

where

$\det|A| = 0$ is the determinant of the matrix A, resulting in a polynomial function

with variable $M_{cr,1}, M_{cr,2}, \dots, M_{cr,n}$

$M_{cr,1}$ is the lowest eigenvalue among the eigenvalues, $M_{cr,n}$

$L_{d,gr}$ is required unbraced length in order to achieve target rotation capacity under moment gradient

4.5.3 Simplified T-column approach to derive unbraced length limit for target rotation capacity

By assuming a column with two materials (one is elastic and the other is inelastic), the LTB model dramatically simplified. In analogous to the detailed approach, for the effective rigidities $(EI_y)_{e,T,gr}(z_1)$ between M_y and M , sinusoidal representation are adopted as described Eq. 4-64a . The length of inelastic region ($\tau_i L_b$) is determined from the different load level between yield moment(M_y) and target moment(M). The averaged inelastic rigidities for assigning, Eq. 4-64b is recommended.

$$(EI_y)_{e,T,gr}(z_1) = \frac{1 + (EI_y)_{e,T}(\phi_{cr,d,gr})}{2} - \frac{1 - (EI_y)_{e,T}(\phi_{cr,d,gr})}{2} \cdot \cos\left(\frac{\pi \cdot z_1}{\tau_i L_b}\right) \quad (4-64a)$$

$$(EI_y)_{eq,T,gr} = \frac{\int_0^{\tau_i L_b} (EI_y)_{e,T}(z_1) \cdot dz_1}{\tau_i L_b} \quad (4-64b)$$

where

$(EI_y)_{e,T,gr}(z_1)$ is effective flexural rigidities of T-column located at z_1 position
 $(EI_y)_{eq,T,gr}$ is equivalent effective stiffness value of T-column in inelastic portion
length ($L_{ie} = \tau_i L_b$) under moment gradient condition

Other process such as applying boundary condition and joint compatibility and the matrix format representation are the same as in previous chapter 4.2
The matrix equations finally lead a set of equation as Eq. 4-65a. A series of buckling load ($P_{cr,1}, P_{cr,2}, \dots, P_{cr,n}$) and the lowest buckling load ($P_{cr,1}$) is critical buckling load as Eq. 4-65b. For deriving bracing length limit for achieving target rotation capacity ($L_{d,T,gr}$), iterative process are required to find the point where the lowest buckling load and plastic moment become equal as described in Eq. 4-65c.

$$\tan(k_1 L_a) + (k_1 / k_2) \cdot \tan(k_2 L_a) = 0 \quad (4-65a)$$

$$\tan(k_1 L_a) + \sqrt{\alpha_{eq,T,gr}} \cdot \tan\left(\frac{k_1}{\sqrt{\alpha_{eq,T,gr}}} L_b\right) = 0 \quad (4-65b)$$

$$P_{cr,1}(L_{p,T,gr}, m_R) = P_R \quad (4-65c)$$

where

$\alpha_{eq,T,gr} = (EI_y)_{eq,T,gr} / (EI_y)$ is the ratio of equivalent effective section stiffness to the elastic section stiffness

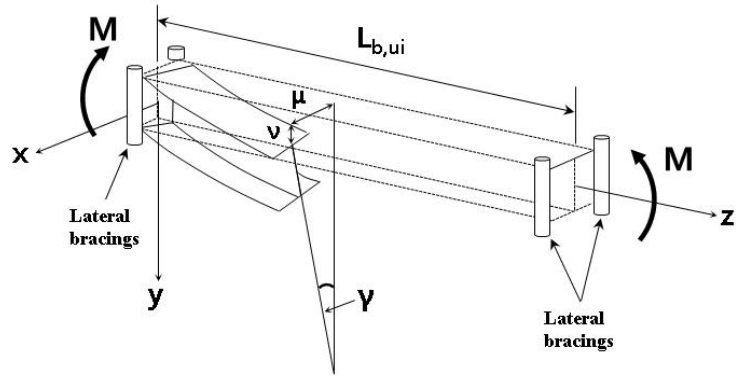
$L_{d,T,gr} = L_a + L_b$ is required unbraced length for achieving plastic moment under moment gradient by T-column approach

4.5.4 Summary

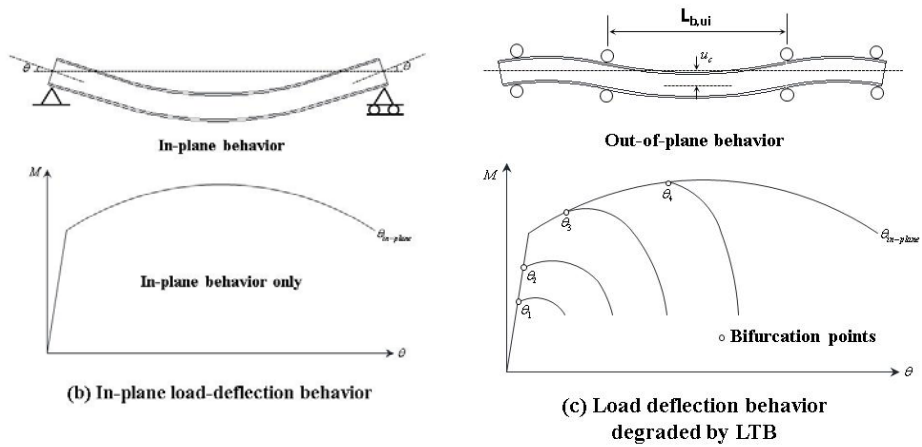
1) The analytical procedure to drive the rotation capacity under the moment gradient condition according to the unbraced length was proposed, based on the effective rigidities derived in the section 4.1, applicable to both high

strength and mild strength, and to the hybrid I-section member. By applying Galerkin methods to solve the governing equation, the analytical procedure was performed primarily by recalculating the stiffness (associated with effective rigidities) and the stability matrices (associated with applied moment) at a target rotation capacity level. The eigenvalue analysis was then applied to acquire the inelastic buckling strength (=eigenvalue) at a given unbraced length and moment condition. By comparing the derived buckling strength with the applied moment, the adequate unbraced length for resisting the target rotation capacity is finally determined.

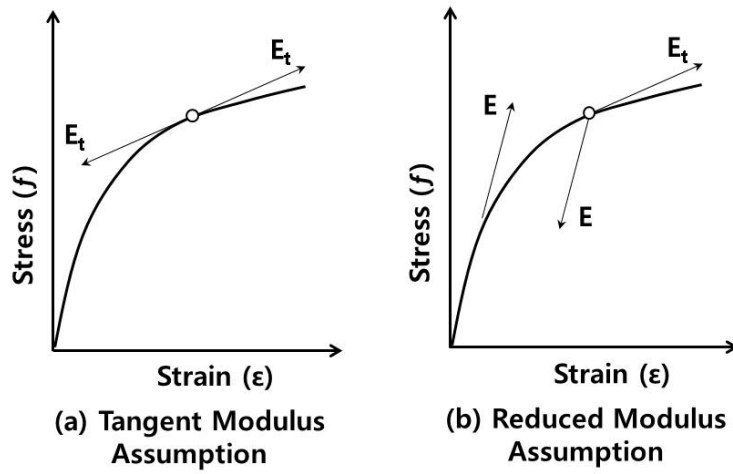
2) To ensure a certain level of rotation capacity under ($R_{cr,gr} \leq 2.0$), a relaxed unbraced length is permissible ($L_{d,gr}$) for the moment gradient case. The reason for the relaxed unbraced length results from the limited inelastic rigidities participation along the length. However, as discussed in chapter 3, since the values of the in-plane rotation capacity (which is affected by Y/T strength ratio, T/Y strain ratio, and yield plateau length) of HSA800 are quite low level, the high LTB resistance at the moment gradient condition does not alone ensure the higher rotation capacity of a member such $R_{cr,gr} \geq 2.0$. Therefore, to increase the rotation capacity of HSA800 I-shaped member under moment gradient condition, the adoption of a material with low Y/T strength ratio or high T/Y strain ratio is inevitable.



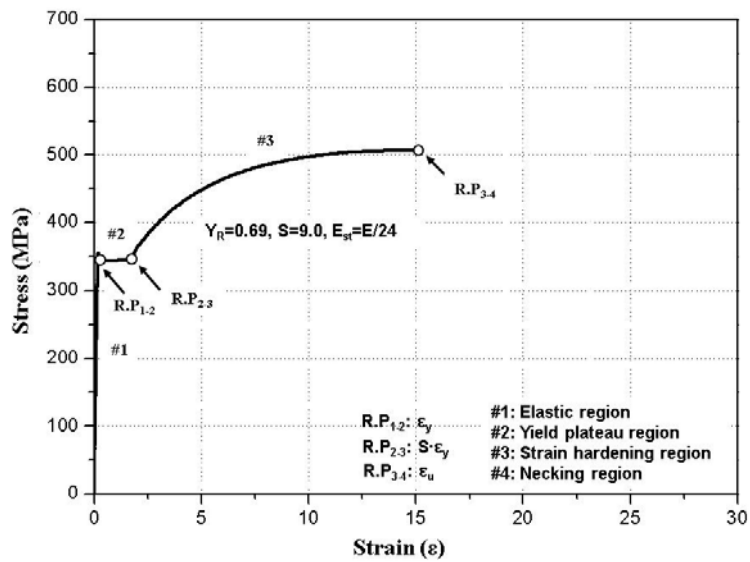
(a) I-shaped member under uniform moment loading



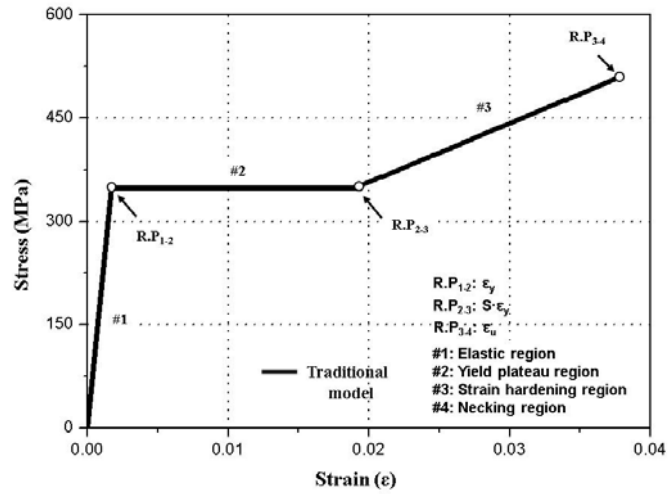
[4-1] Schematic overview of in-plane and out-of-plane behavior of I-shaped beam member (a) I-shaped member under uniform moment loading (b) In-plane load-deflection behavior (c) load-deflection behavior degraded by LTB



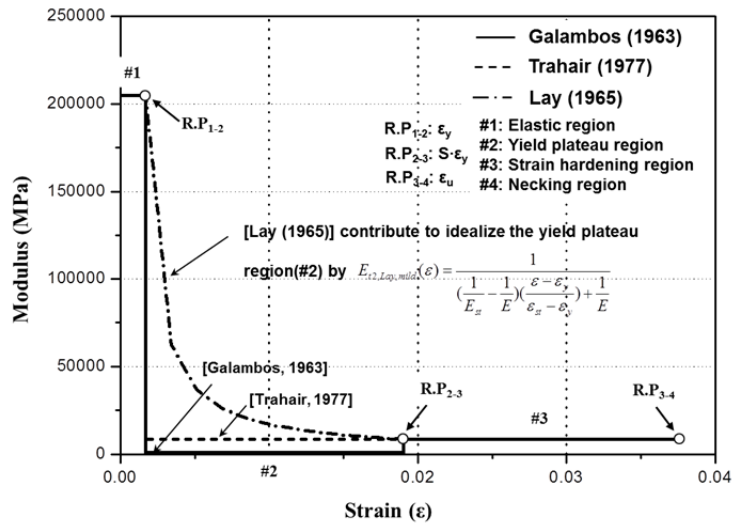
[4-2] Inelastic buckling theories (a) tangent modulus assumption (b) reduced modulus assumption



[4-3] Stress-strain relationships of typical mild steel (SM490)

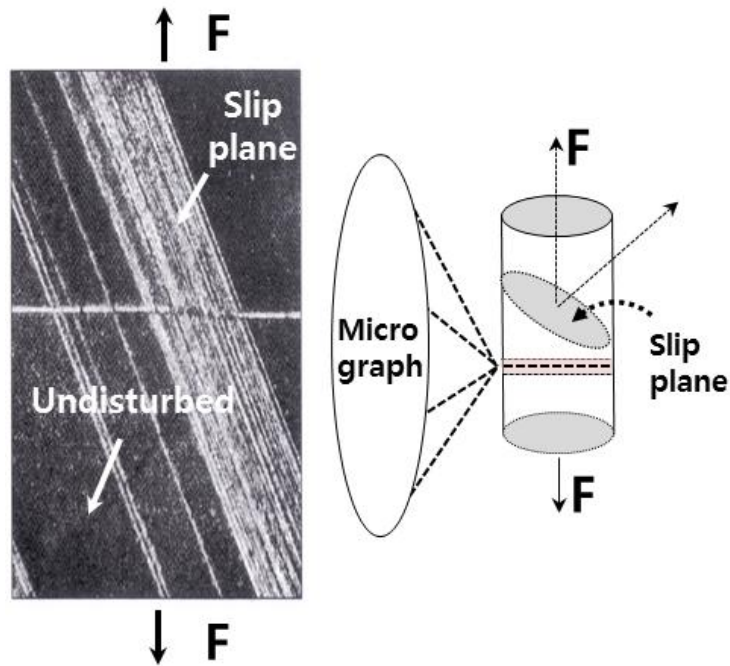


(a) Stress-Strain

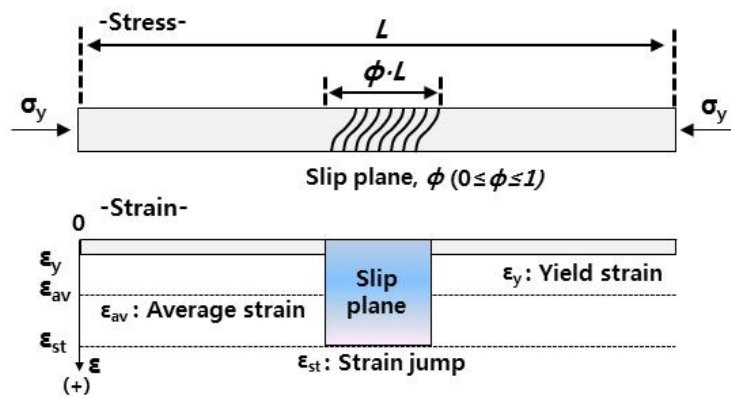


(b) Modulus-strain

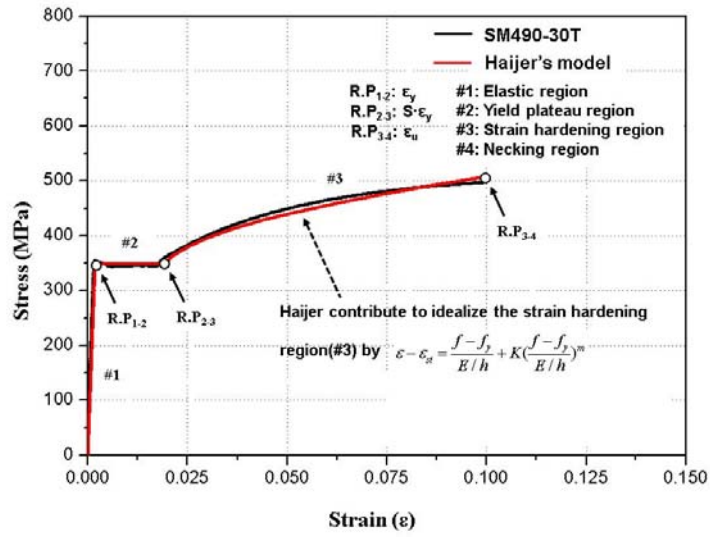
[4-4] Traditional model No.1 for mild steel (a) stress-strain (b) modulus-strain



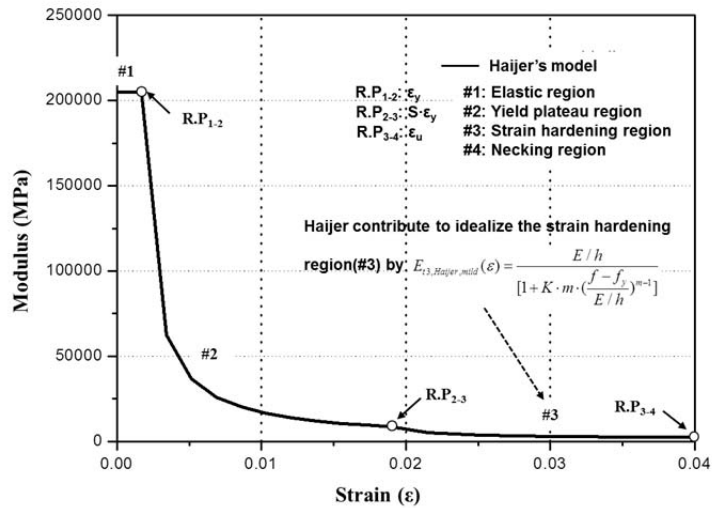
[4-5] Deformation of polycrystalline material: α brass strained 0.2% tension (Henkel and Pense, 2001)



[4-6] Analytical model for deriving tangent modulus by slip theory

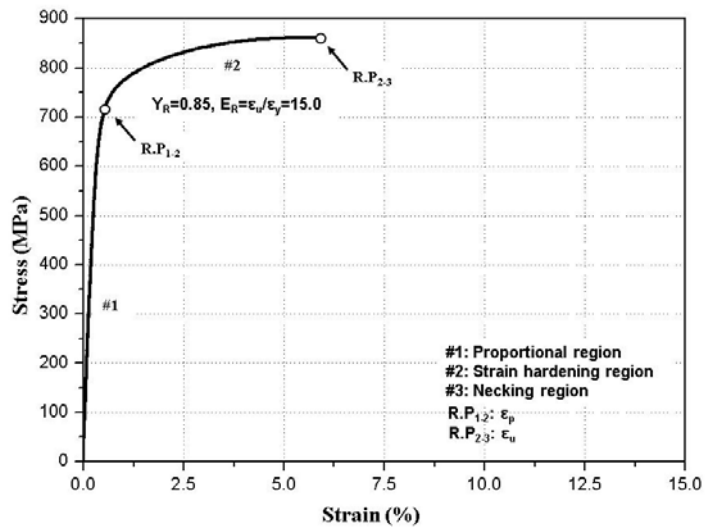


(a) Stress-strain

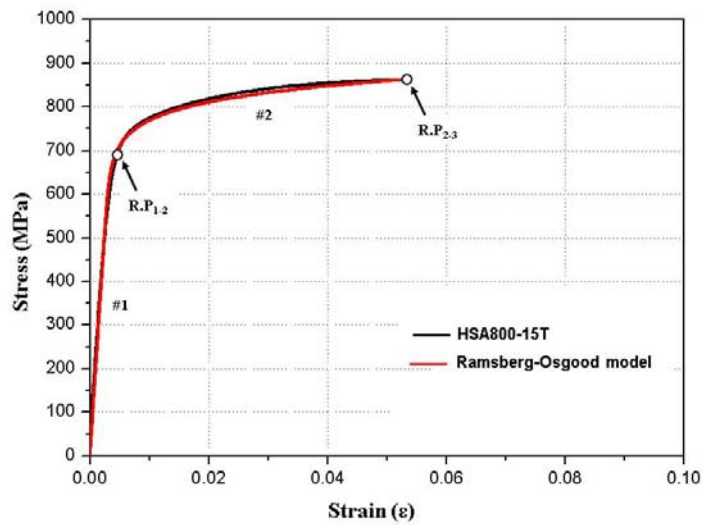


(b) Modulus-strain

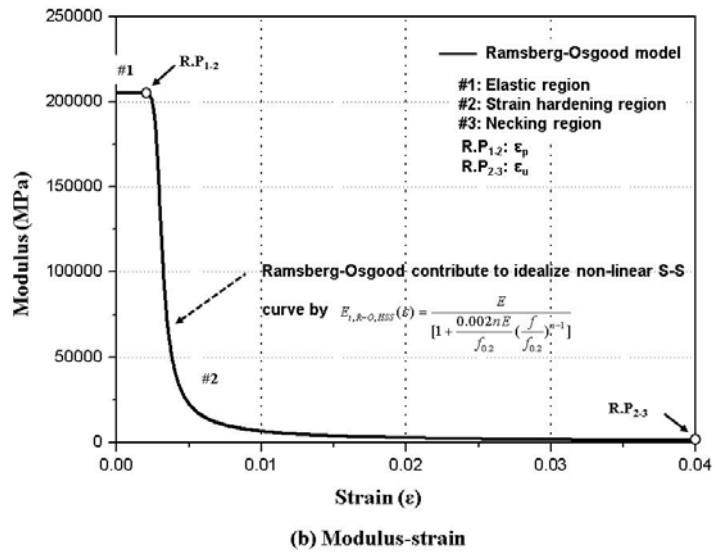
[4-7] Haijer model No. 2 for mild steel (a) stress-strain (b) modulus-strain



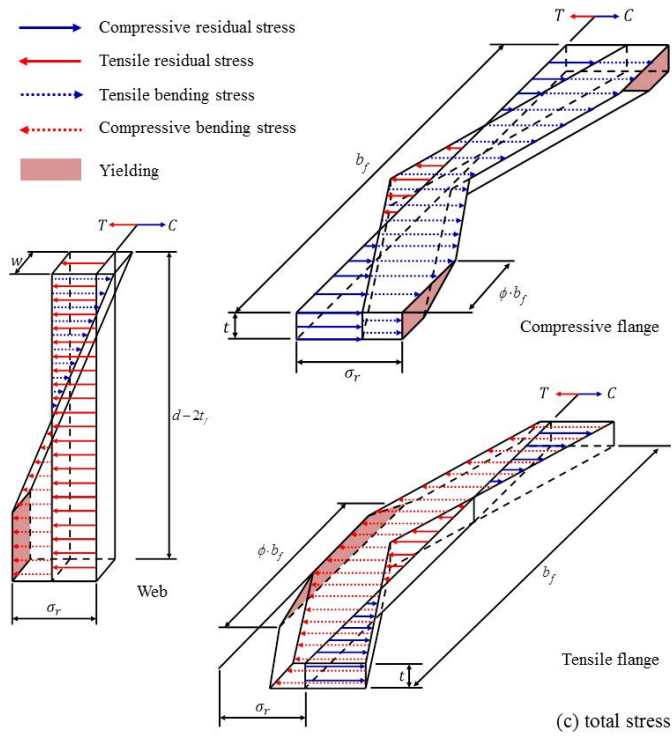
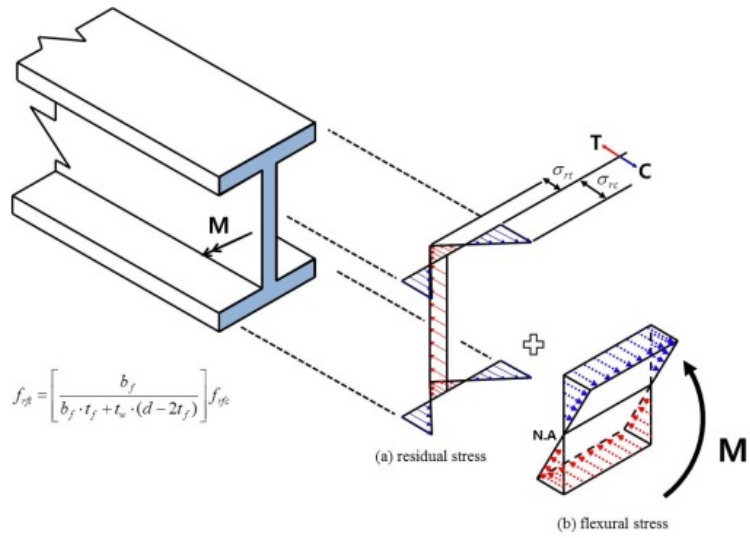
[4-8] Stress-strain relationships of typical high strength steel (HSA800)



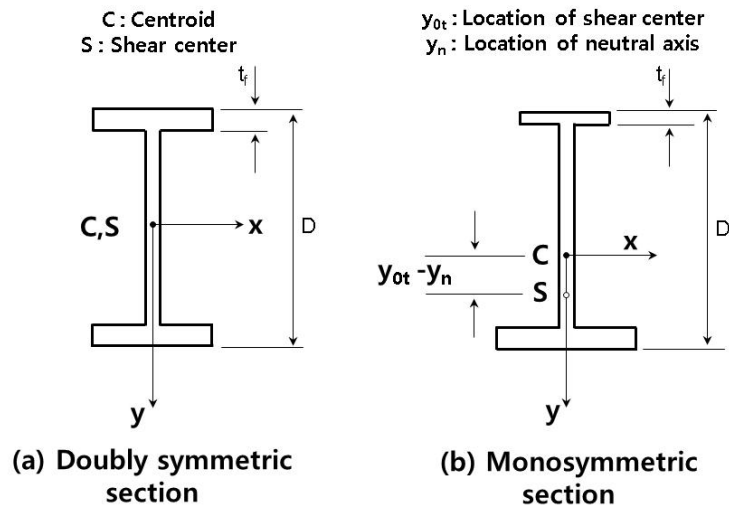
(a) Stress-strain



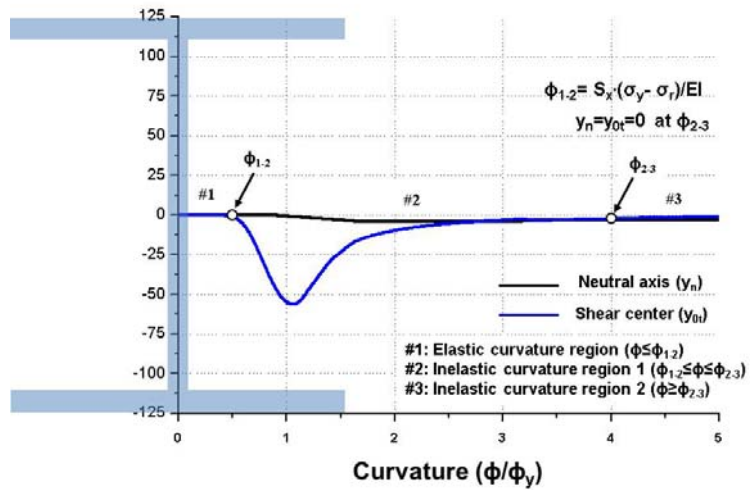
[4-9] Ramberg-Osgood Model No.3 for high strength steel (a) stress-strain (b) modulus-strain



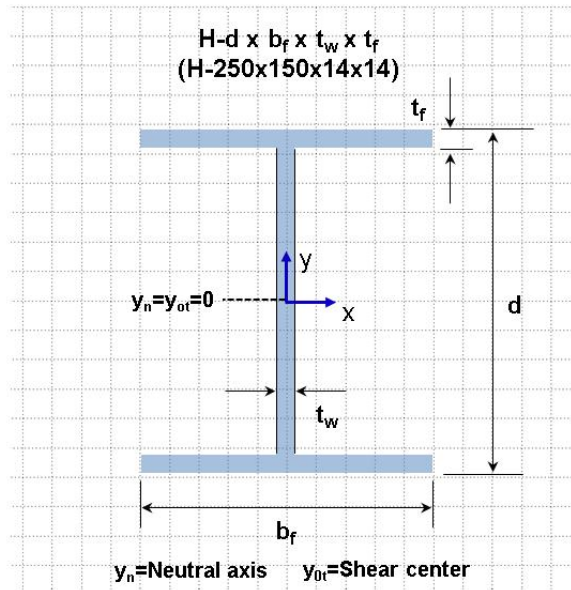
[4-10] Strain and stress distribution (a) residual strain (b) bending strain (c) total stress (Galambos, 1969)



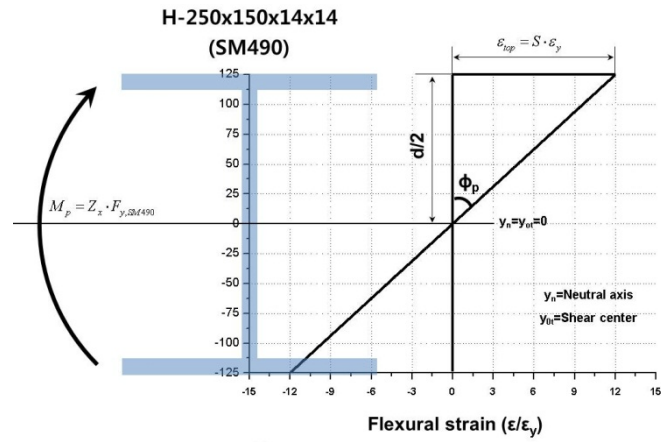
[4-11] Beam cross-section (a) doubly symmetric section (b) monosymmetric section



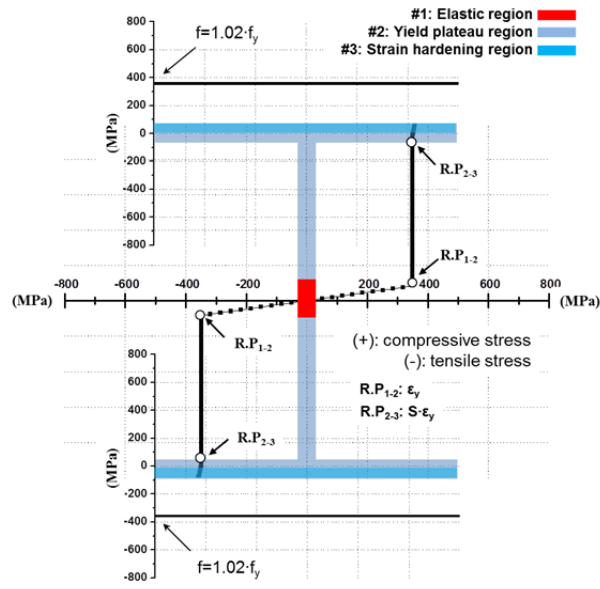
[4-12] Variation of the neutral axis (N.A) and shear center (S.C) according to a curvature



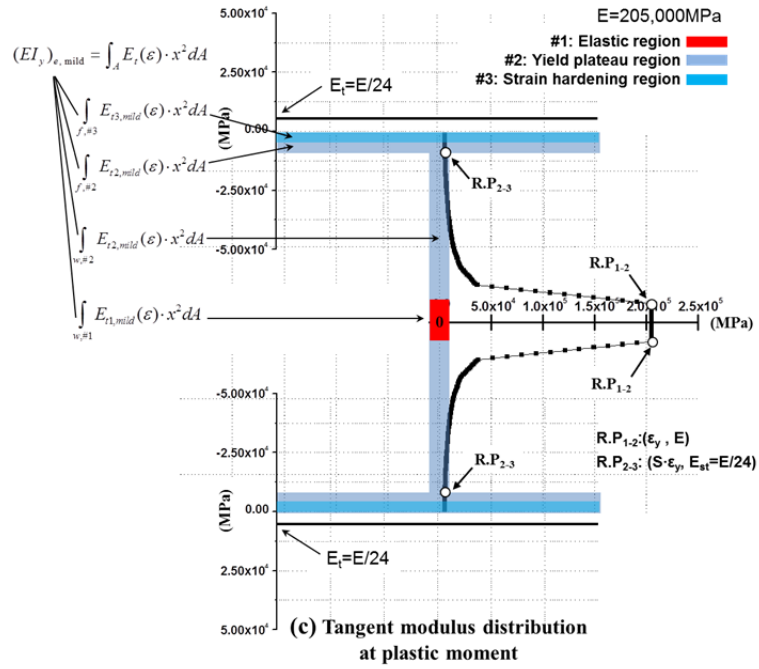
[4-13] Dimension and coordinate of I-section



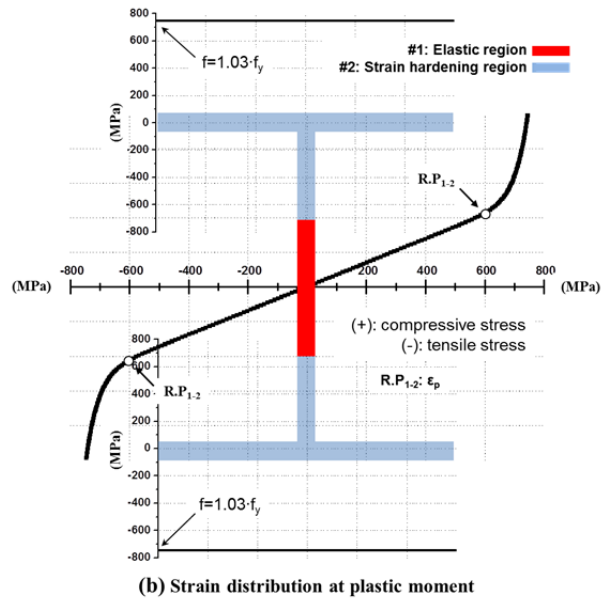
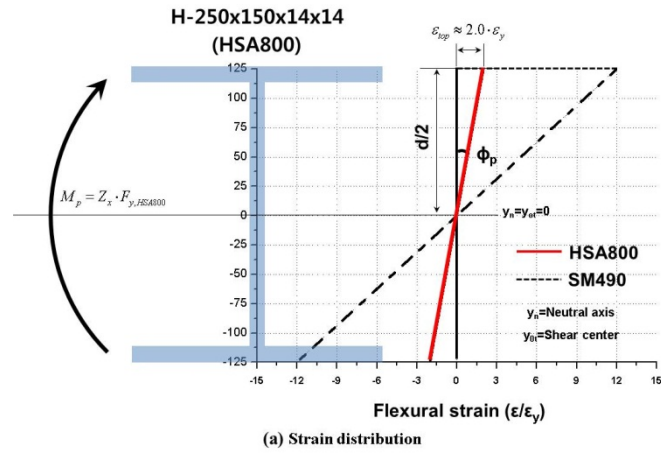
(a) Strain distribution at plastic moment

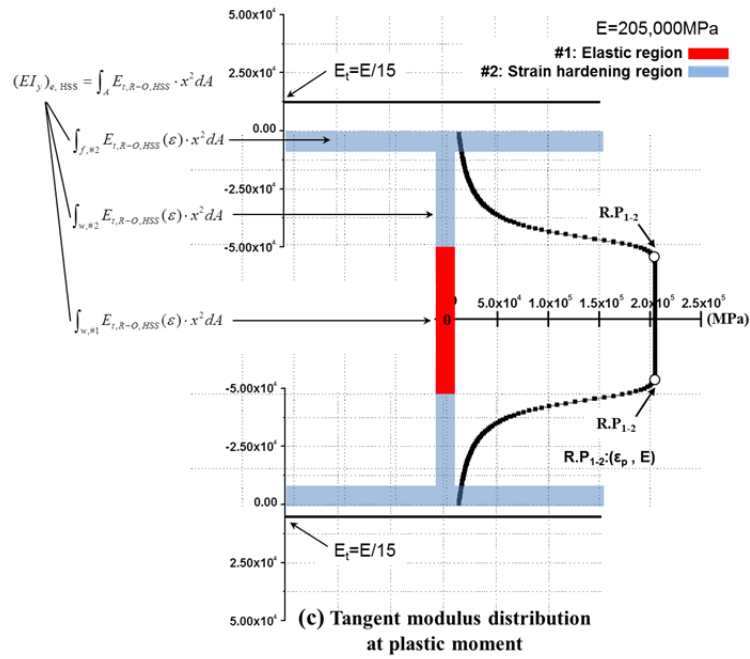


(b) Stress distribution at plastic moment

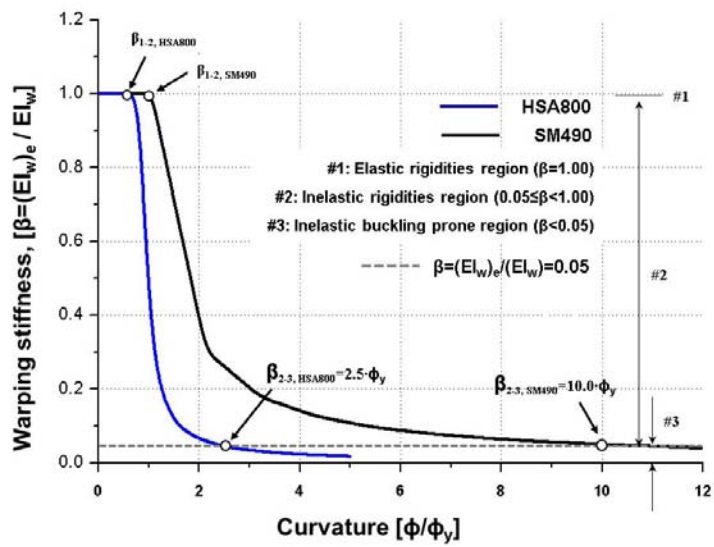
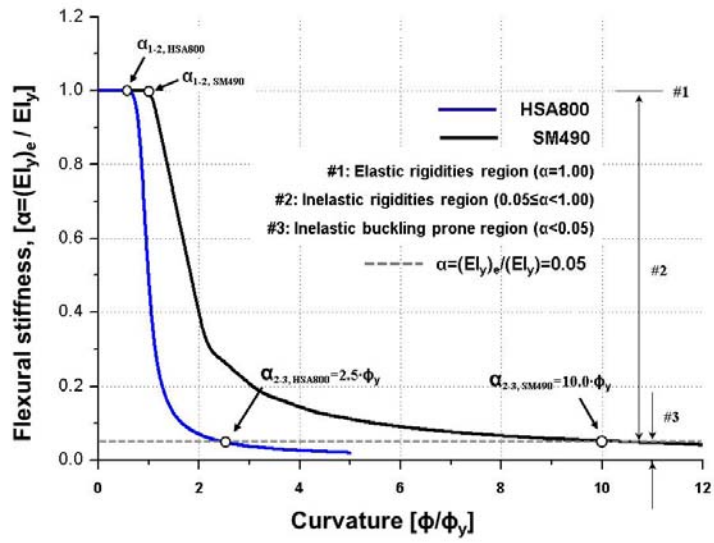


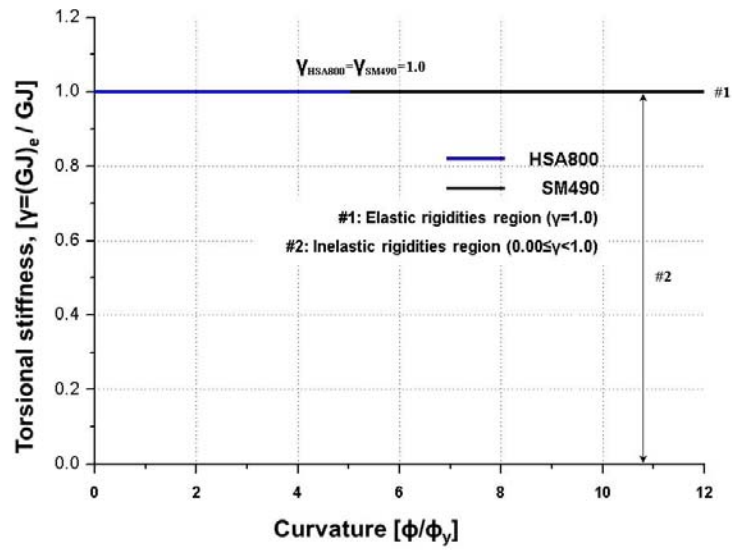
[4-14] Inelastic section characteristics of ideal I-beam fabricated from mild steel (SM490) (a) Strain distribution at plastic moment (b) Stress distribution at plastic moment (c) tangent modulus distribution at plastic moment



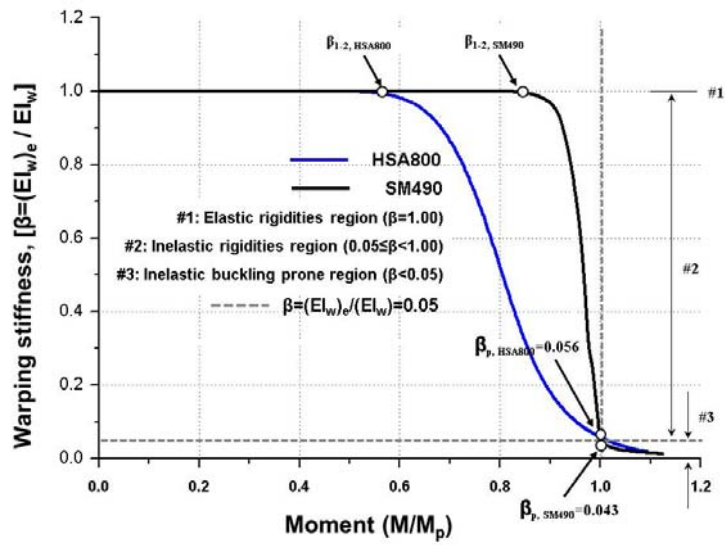
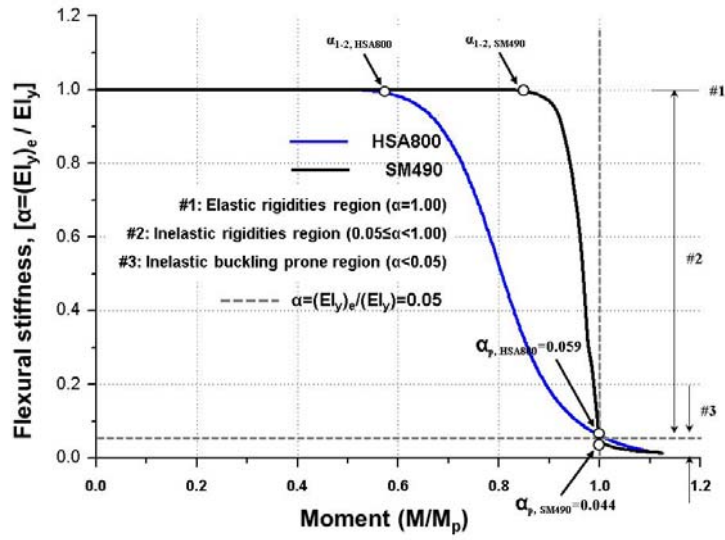


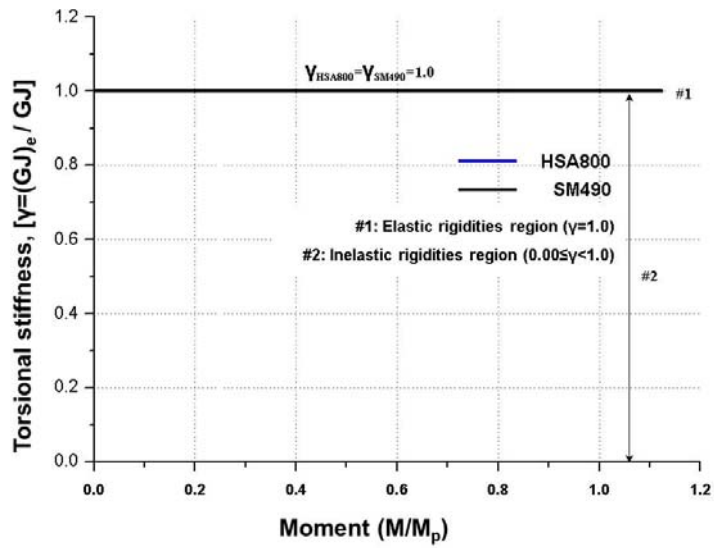
[4-15] Inelastic section characteristics of ideal I-beam fabricated from high strength steel (HSA800) (a) Strain distribution at plastic moment (b) Stress distribution at plastic moment (c) tangent modulus distribution at plastic moment



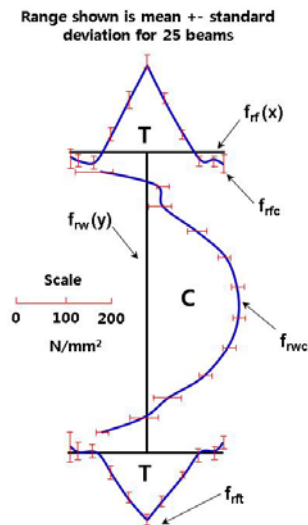


[4-16] Inelastic effective rigidities of ideal I-beam according to curvature (a) effective flexural stiffness (b) effective warping stiffness (c) effective torsional stiffness

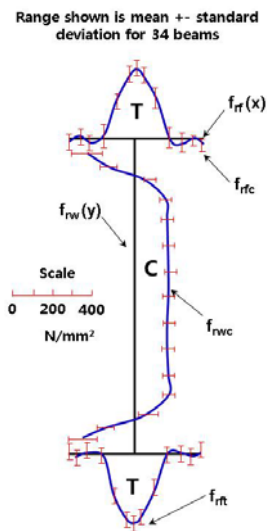




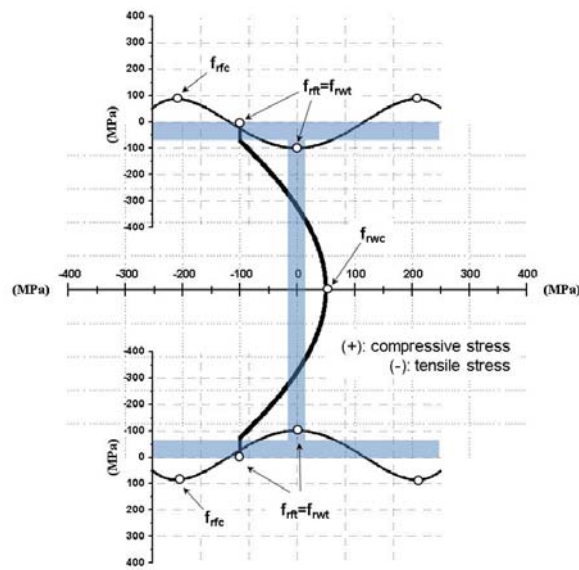
[4-17] Inelastic effective rigidities of ideal I-beam according to moment (a) effective flexural stiffness (b) effective warping stiffness (c) effective torsional stiffness



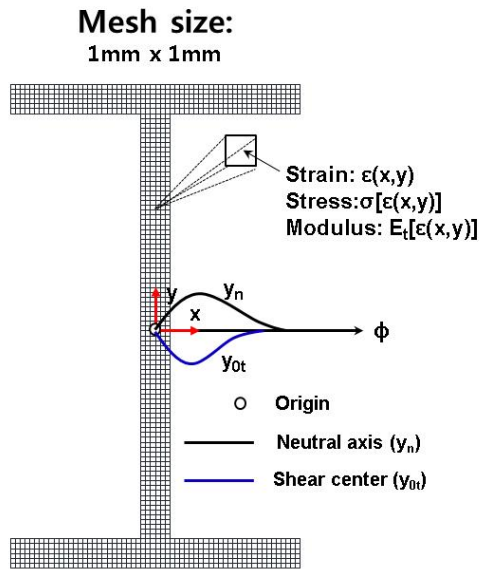
[4-18] Fukumoto's measured residual stress patterns of rolled I beam (Fukumoto et al, 1980)



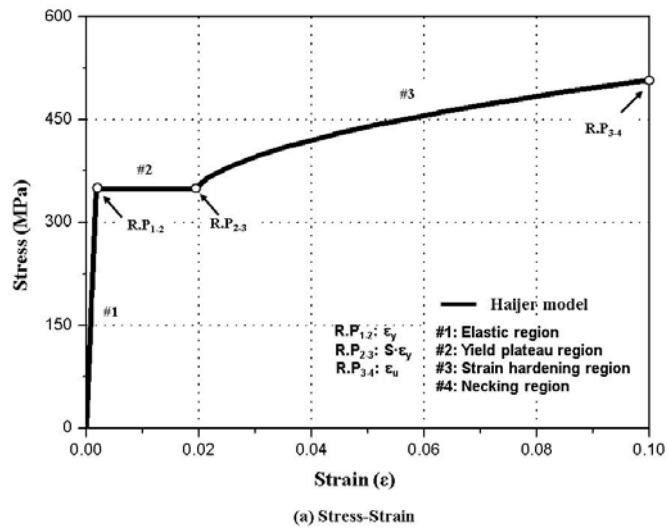
[4-19] Fukumoto's measured residual stress patterns of welded I beam (Fukumoto and Itoh, 1981)

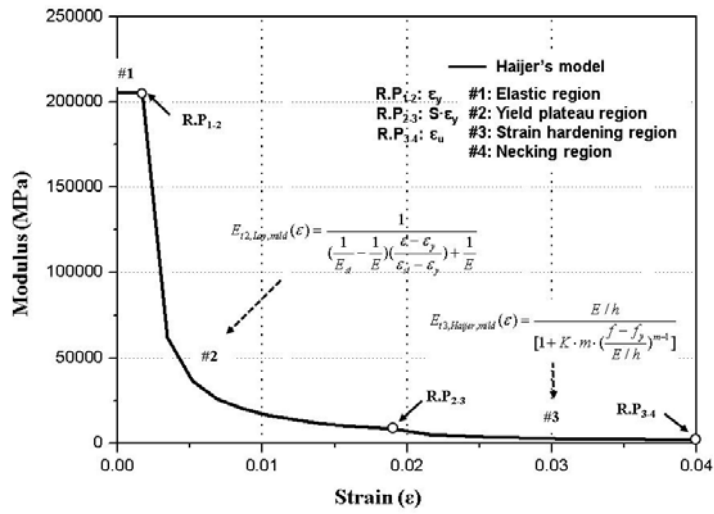


[4-20] Residual stress pattern model No.1

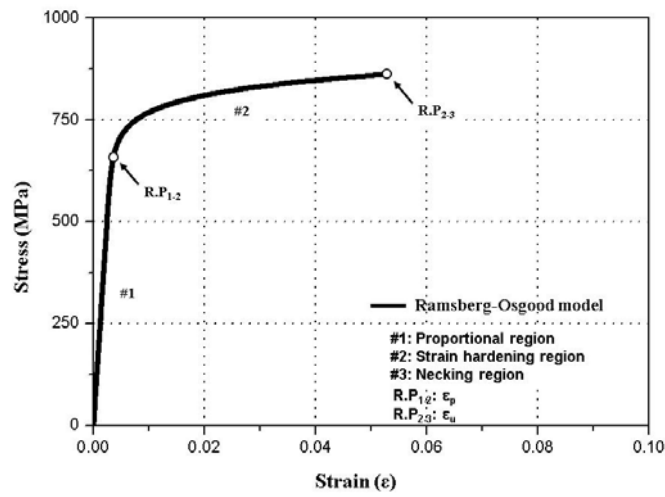


[4-23] Meshed I-section for numerical calculation

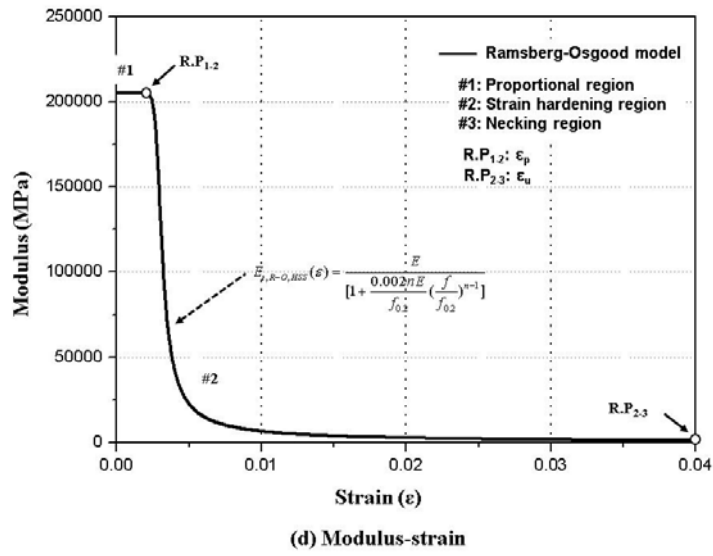




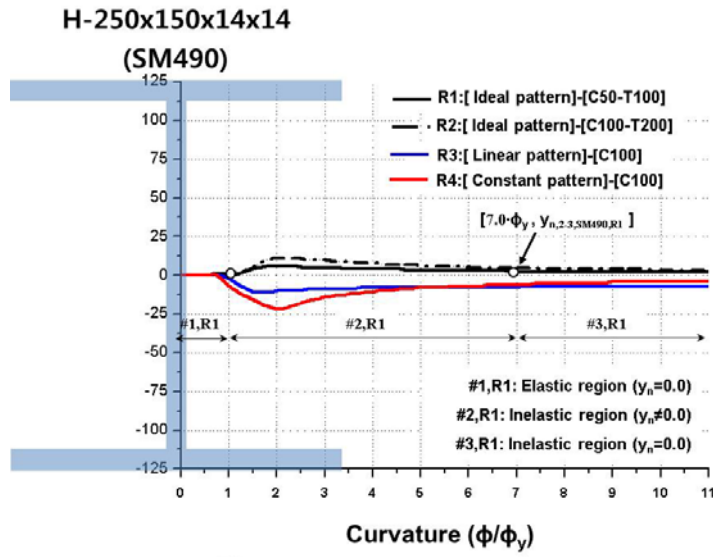
(b) Modulus-strain



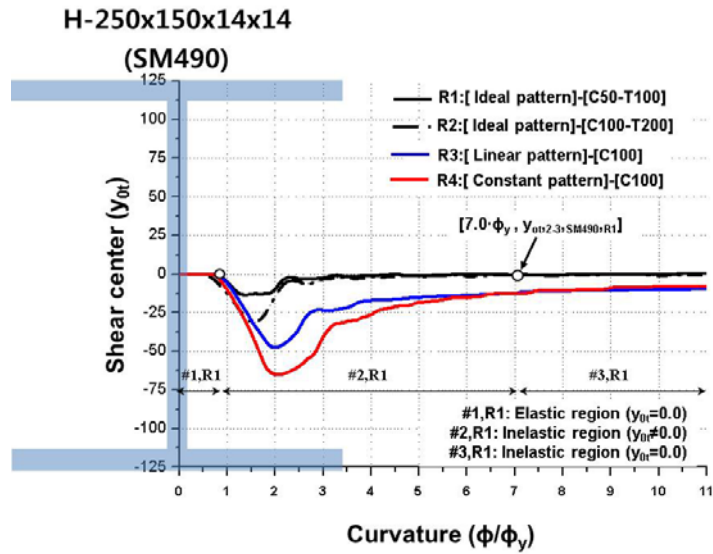
(c) Stress-Strain



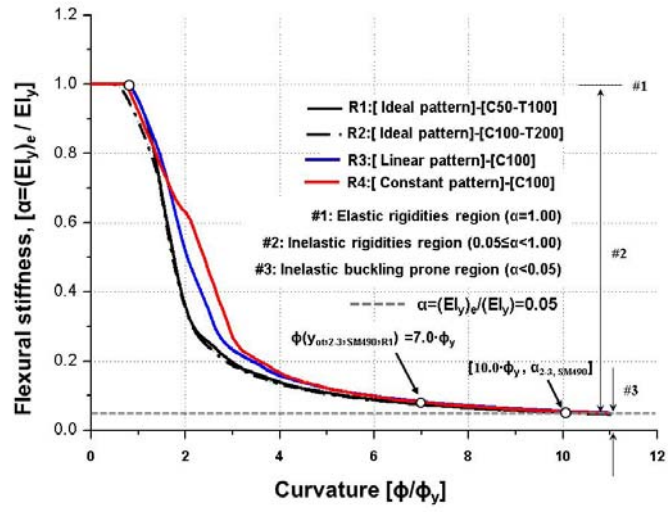
[4-24] Stress and tangent modulus of HSA800 and SM490 according to strain used as subroutines in the numerical calculation program



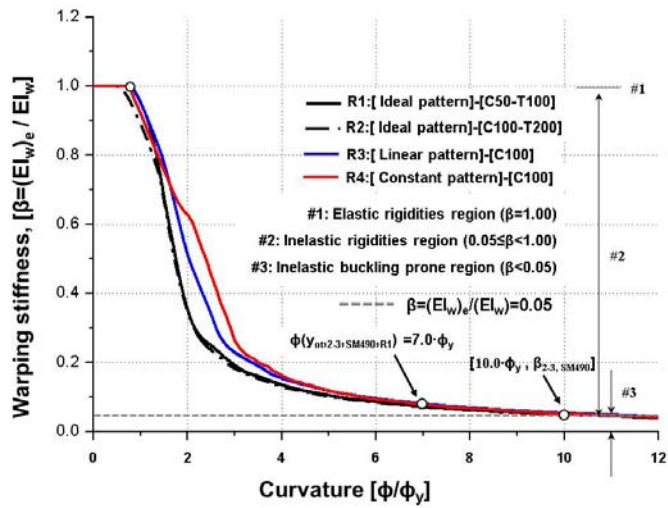
(a) Neutral axis



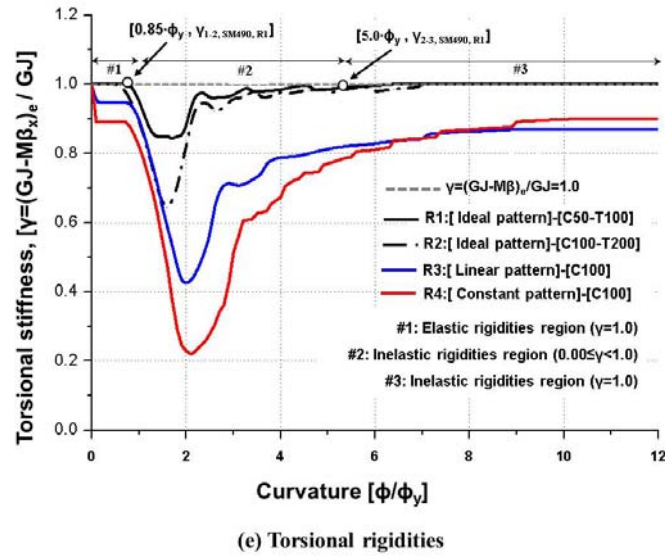
(b) Shear center



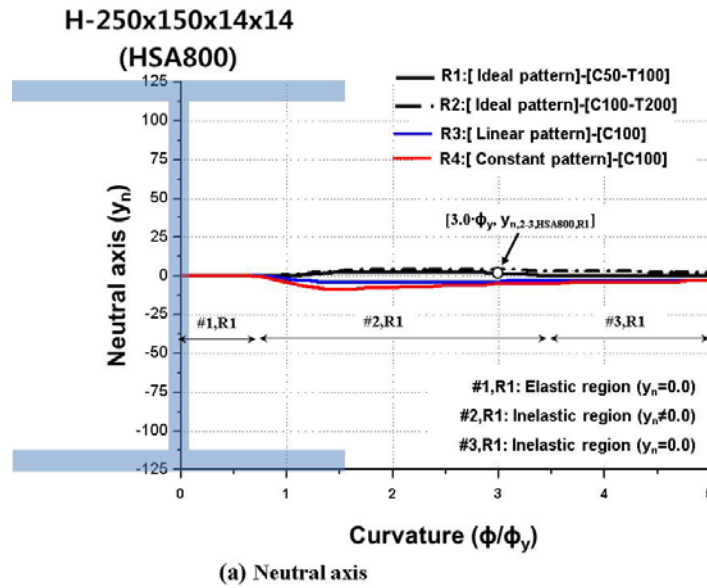
(c) Flexural rigidities

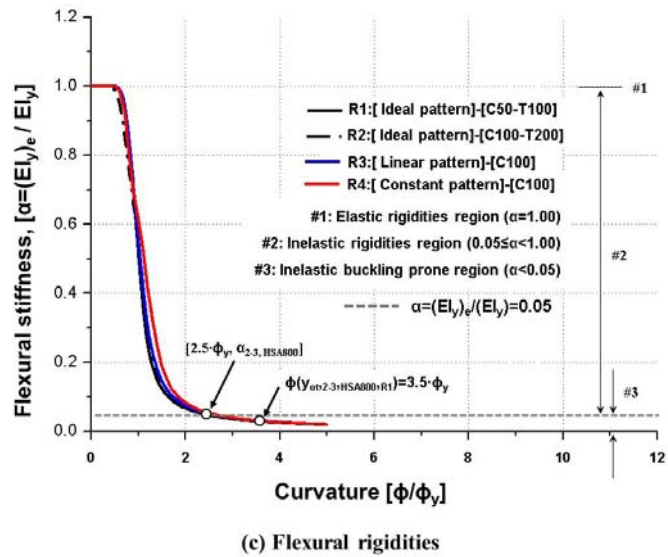
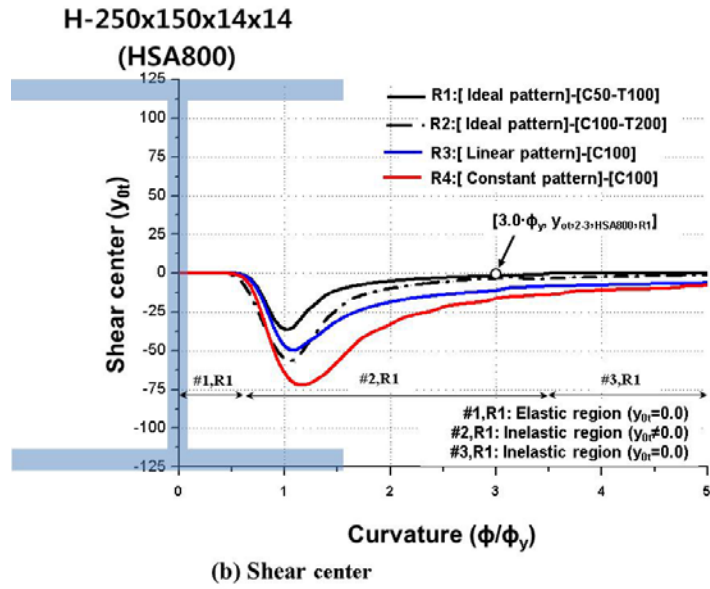


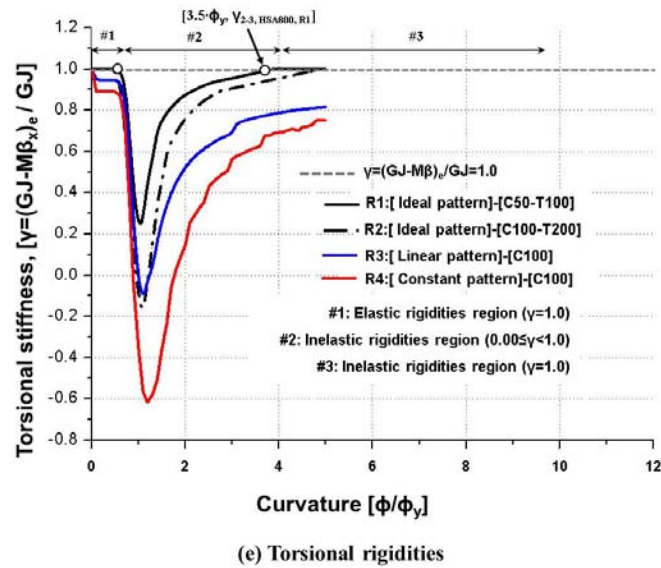
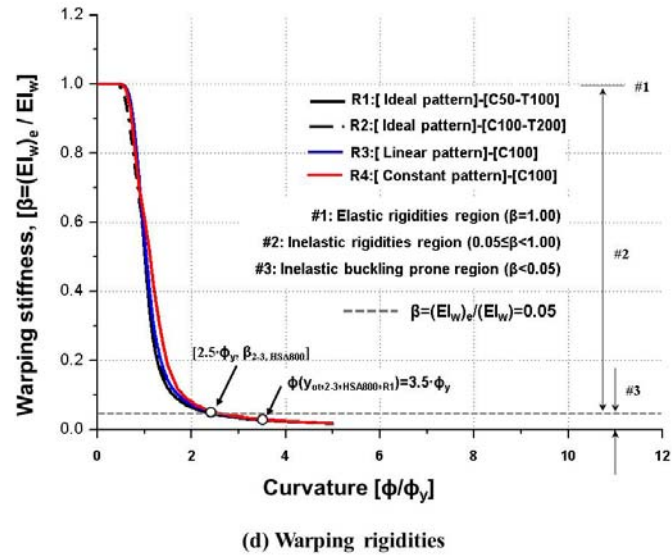
(d) Warping rigidities



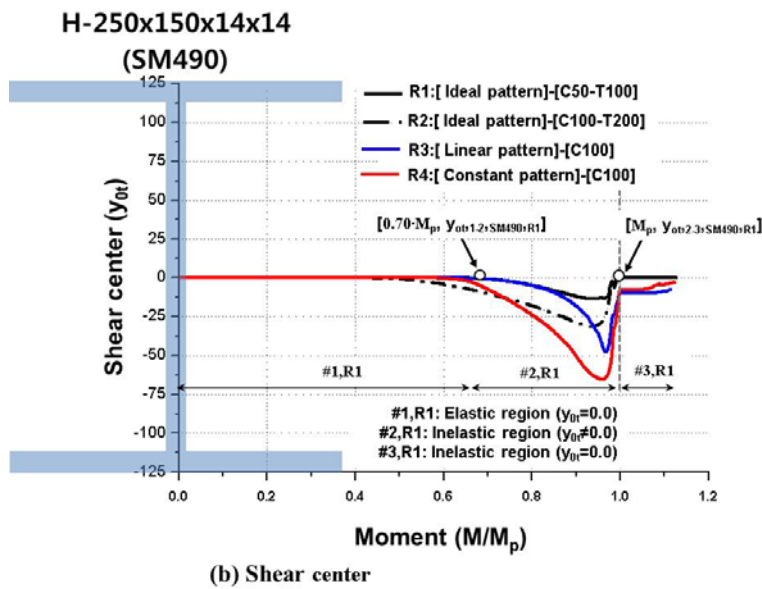
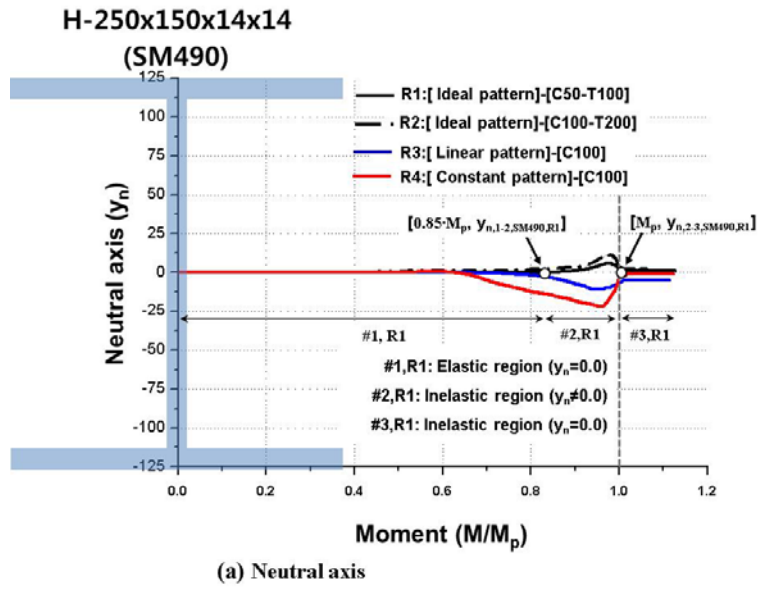
[4-25] Variation of the inelastic rigidities of I-beam fabricated from mild steel (SM490) (a) N.A (b) S.C (c) Inelastic flexural rigidities with curvature (d) Inelastic warping rigidities with curvature (e) Inelastic torsional rigidities with curvature

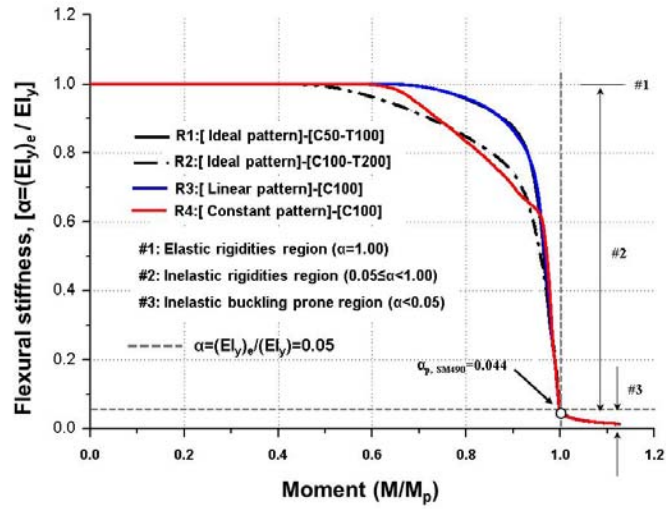




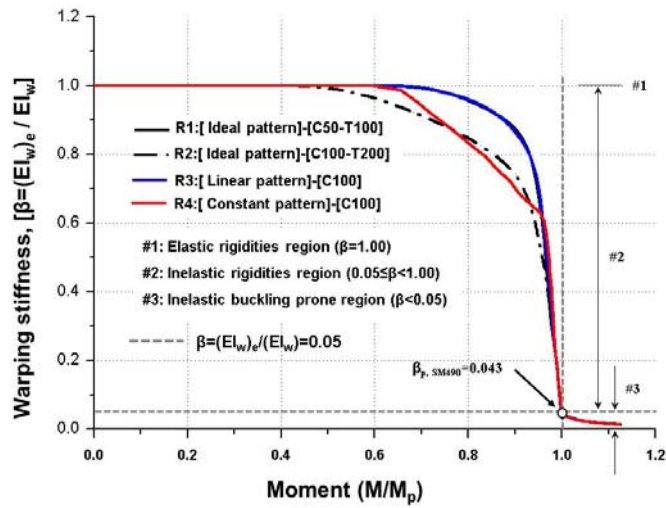


[4-26] Variation of the inelastic rigidities of I-beam fabricated from high strength steel (HSA800) (a) N.A (b) S.C (c) Inelastic flexural rigidities with curvature (d) Inelastic warping rigidities with curvature (e) Inelastic torsional rigidities with curvature

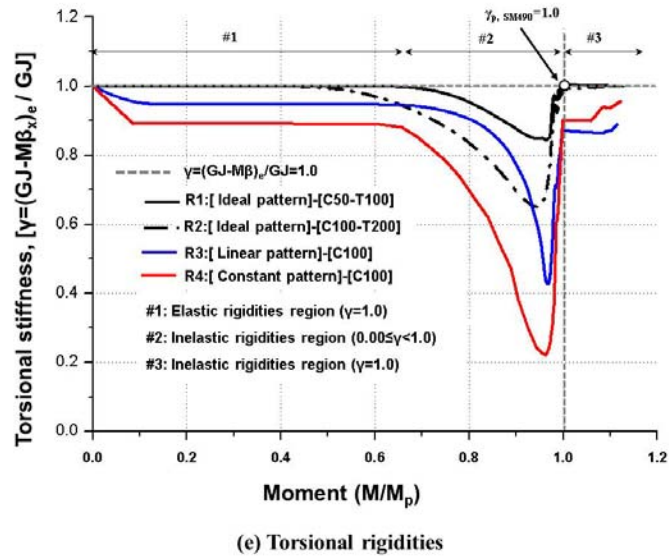




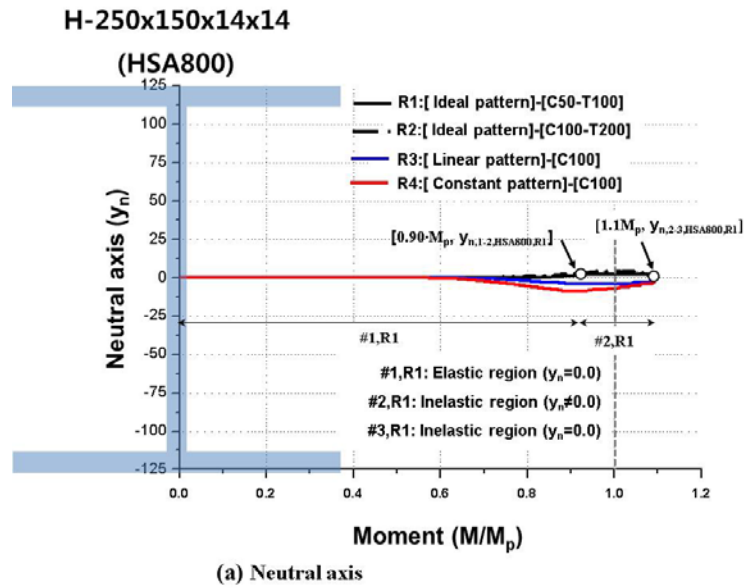
(c) Flexural rigidities

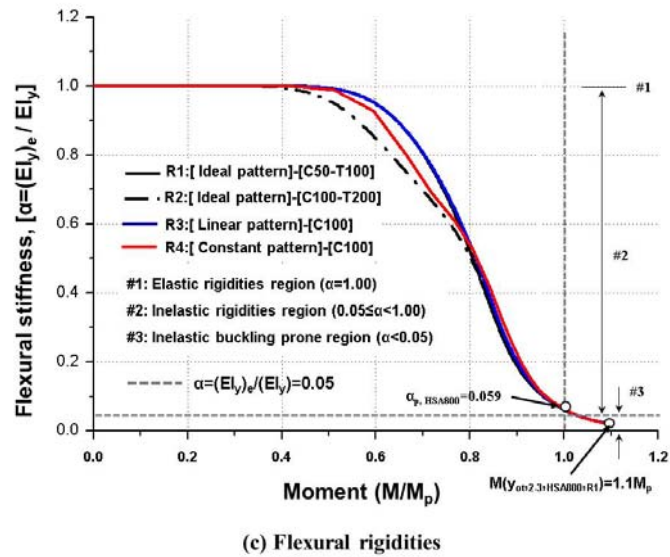
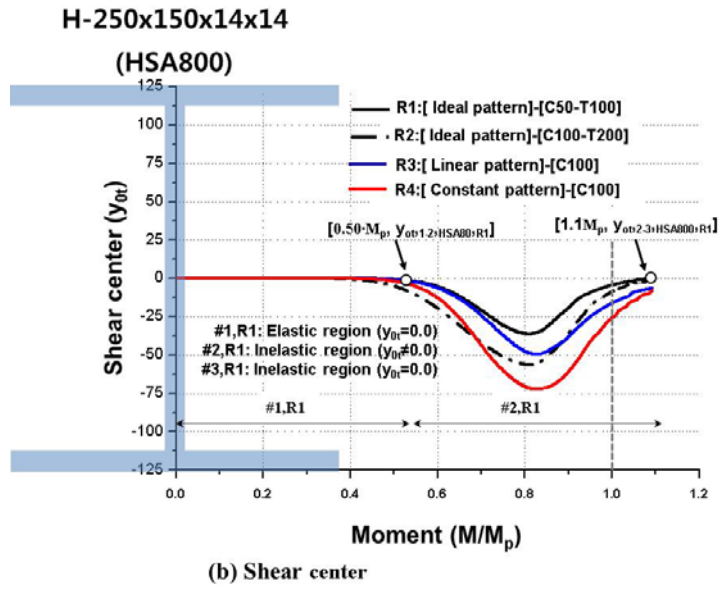


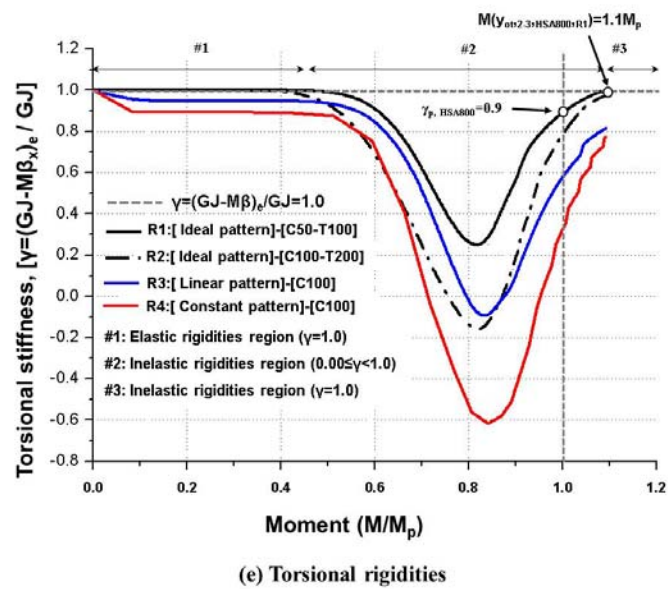
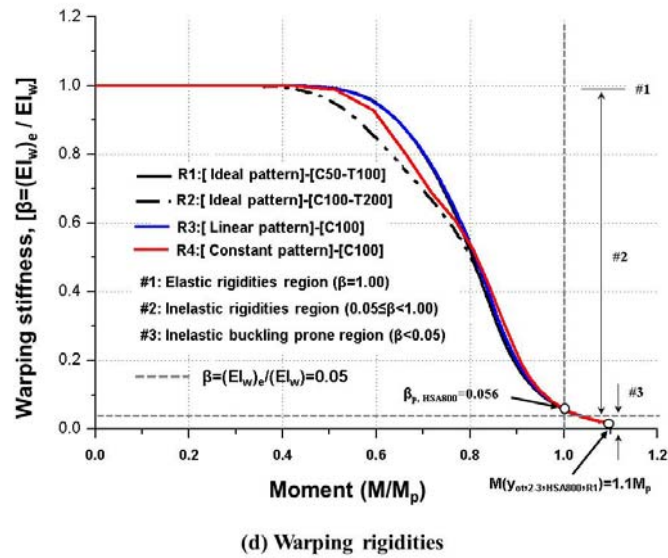
(d) Warping rigidities



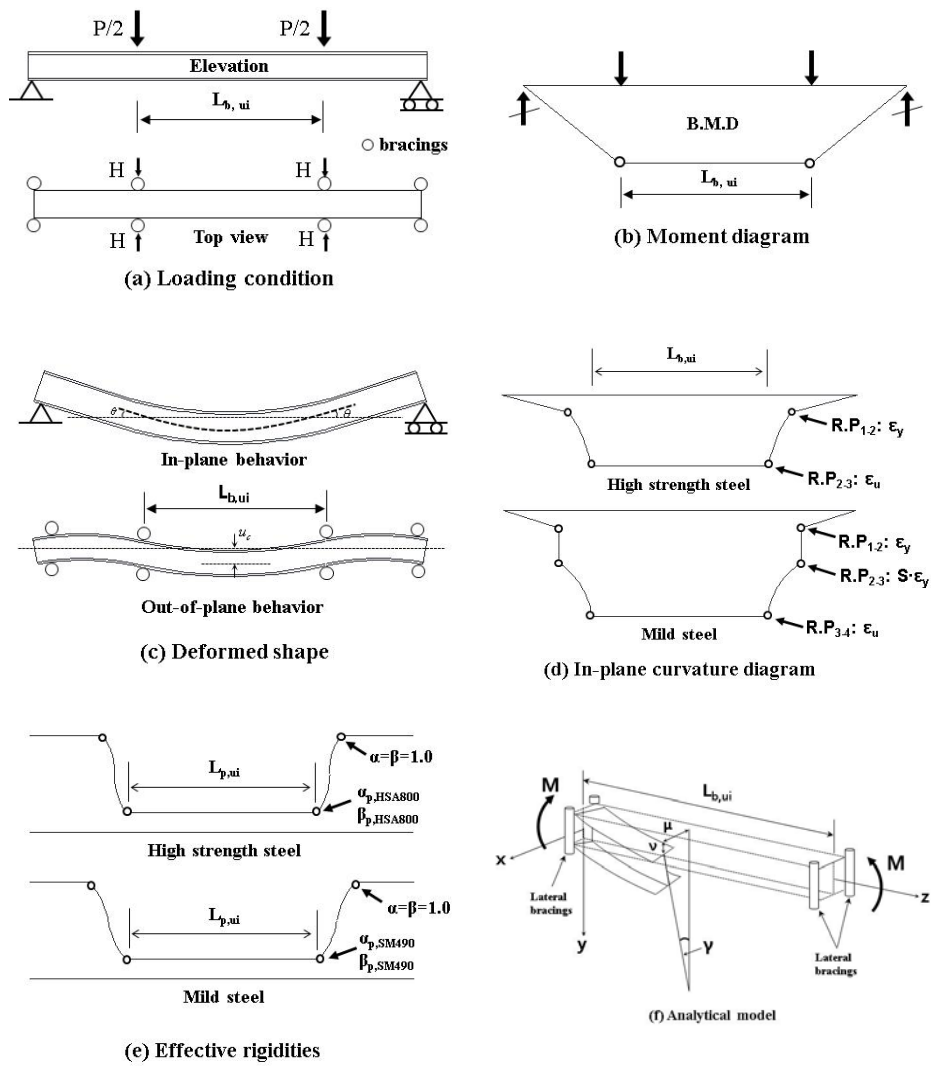
[4-27] Variation of the inelastic rigidities of I-beam fabricated from mild steel (SM490) (a) N.A (b) S.C (c) Inelastic flexural rigidities with moment (d) Inelastic warping rigidities with moment (e) Inelastic torsional rigidities with moment



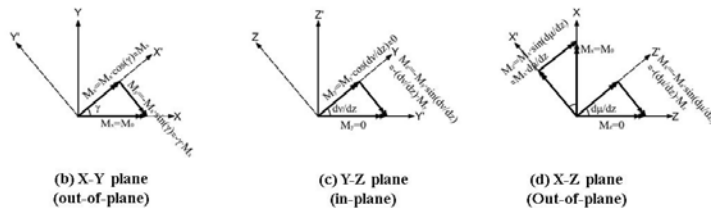
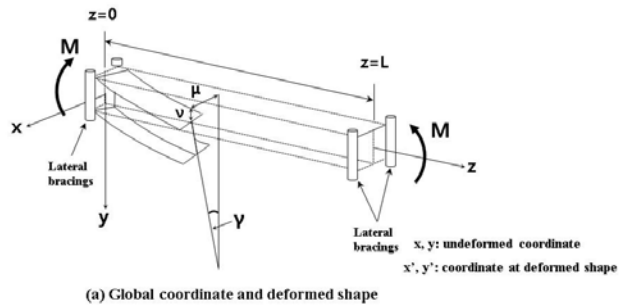




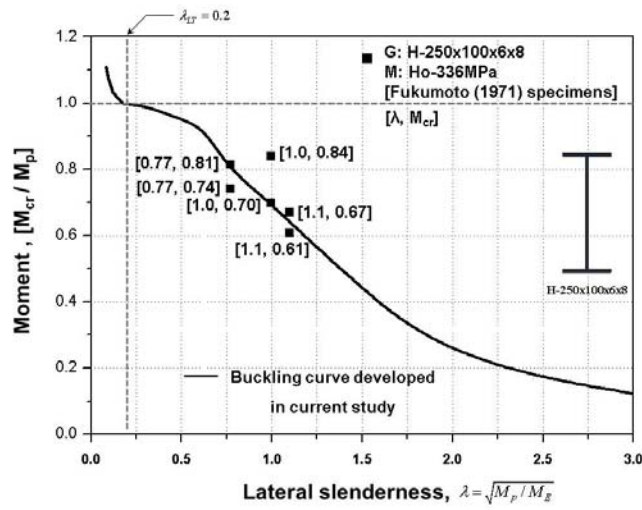
[4-28] Variation of the inelastic rigidities of I-beam fabricated from high strength steel (HSA800) (a) N.A (b) S.C (c) Inelastic flexural rigidities with moment (d) Inelastic warping rigidities with moment (e) Inelastic torsional rigidities with moment

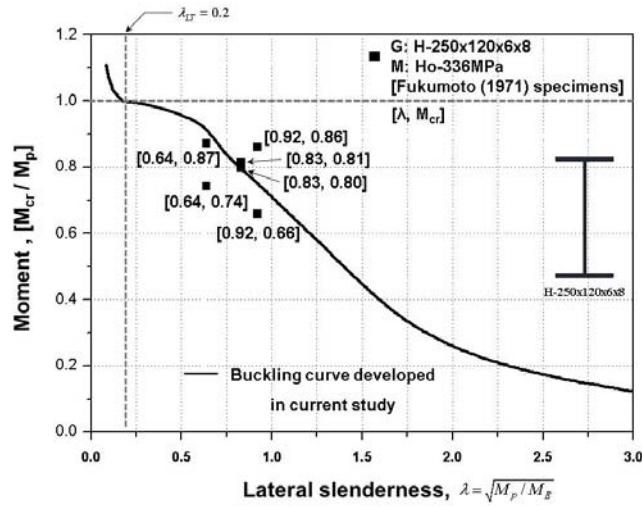


[4-29] Schematic overview of LTB strength problem under uniform moment (a) Loading and beam geometry (b) Moment diagram (c) Deformed shape (in-plane and out-of-plane) (d) Curvature diagram (e) Effective rigidities diagram (f) Analytical model

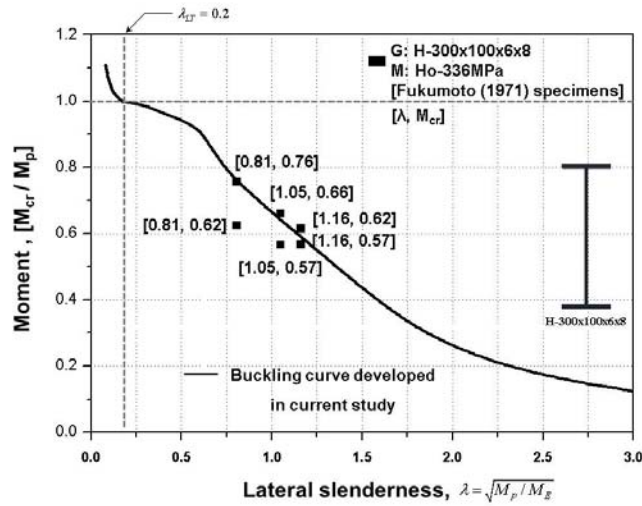


[4-30] External moment decompositions (a) global coordinate and deformed shape (b) x-y plane (c) x-z plane (c) y-z plane



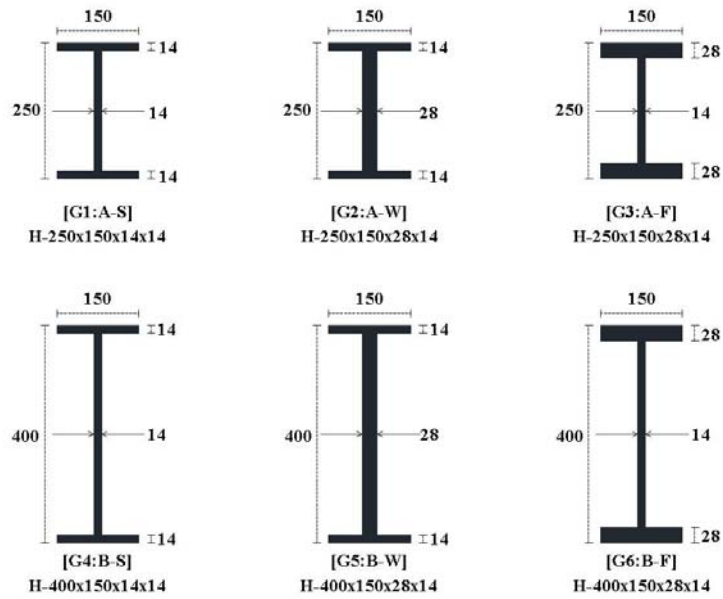


(b) Fukumoto (1971)

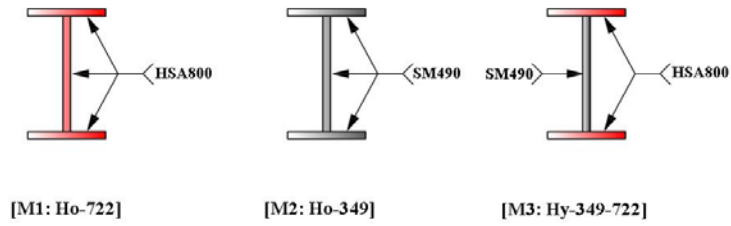


(c) Fukumoto (1971)

[4-31] Validation of the analytically developed critical buckling strength curve with previous experiments (a) Fukumoto, 1971 [G: H-250x100x6x8]-[M: Ho-336] (b) Fukumoto, 1971 [G: H-200x120x6x8]-[M: Ho-336] (c) Fukumoto, 1971 [G: H-300x100x6x8]-[M: Ho-336]

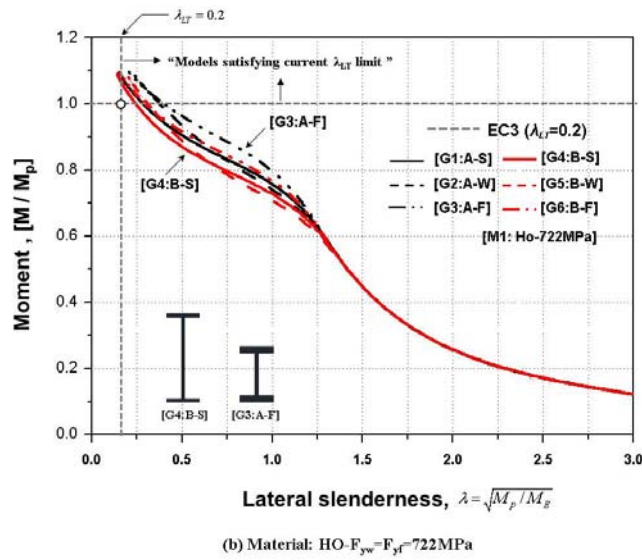
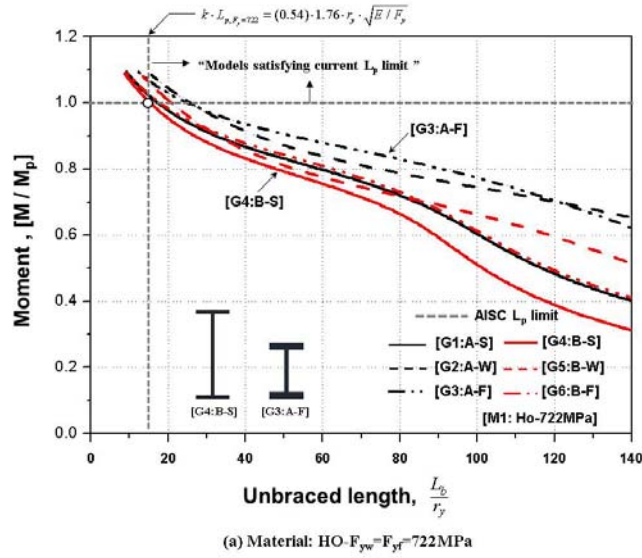


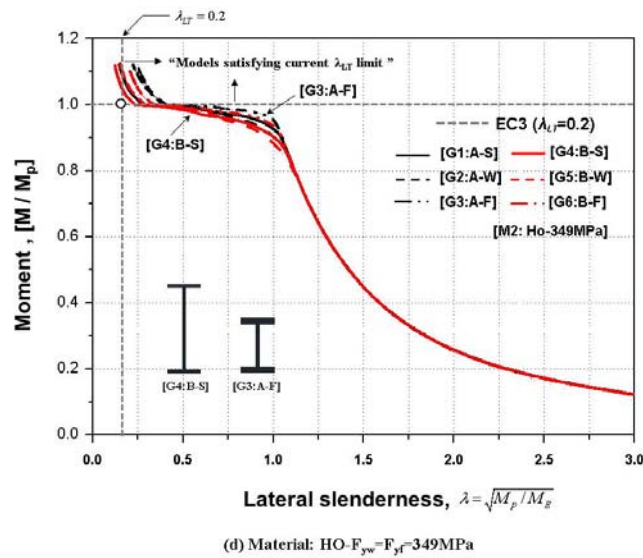
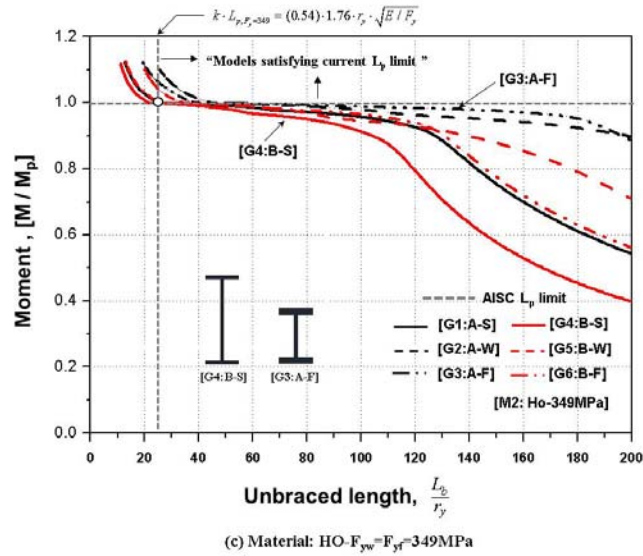
(a) geometrical parameters (G1~G6)



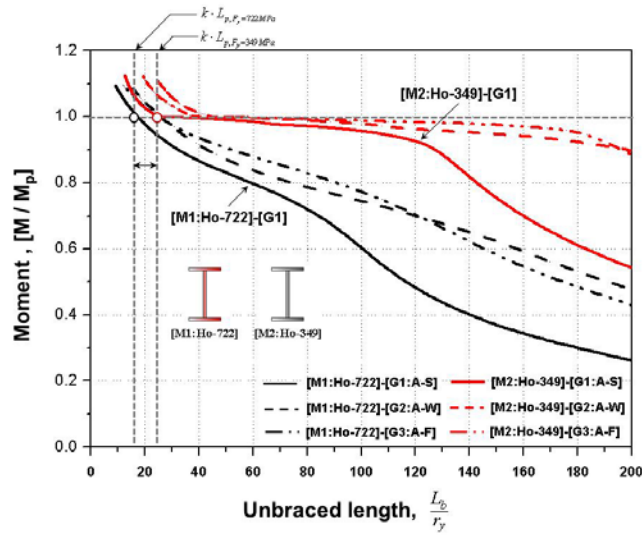
(b) material parameters (M1~M3)

[4-32] Parametric models for analyzing the effects of geometrical and material variations on inelastic LTB behavior (a) geometrical parameters (G1~G6) (b) material parameters (M1~M3)

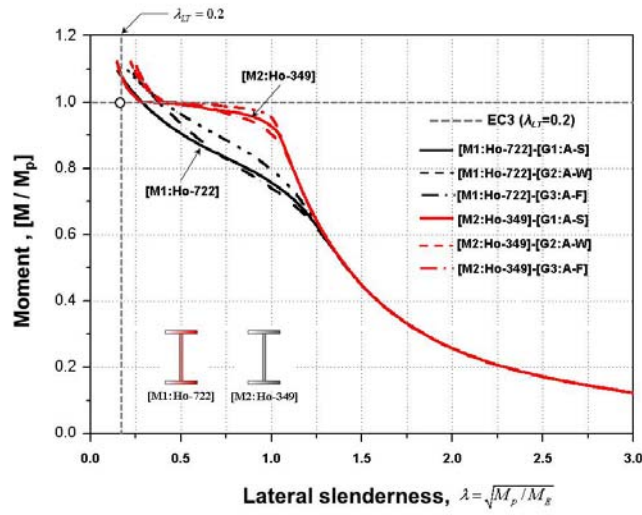




[4-33] Effects of geometrical variation (flange, web and depth) on inelastic LTB strength curve (a) Material: $H_o-F_{yw}=F_{yf}=722\text{MPa}$ represented by AISC format (b) Material: $H_o-F_{yw}=F_{yf}=722\text{MPa}$ represented by EC 3 format (c) Material: $H_o-F_{yw}=F_{yf}=349\text{MPa}$ represented by AISC format (d) Material: $H_o-F_{yw}=F_{yf}=349\text{MPa}$ represented by EC 3 format

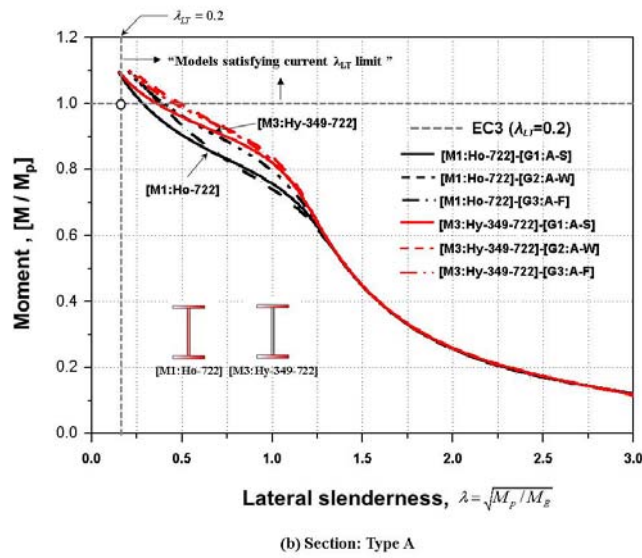
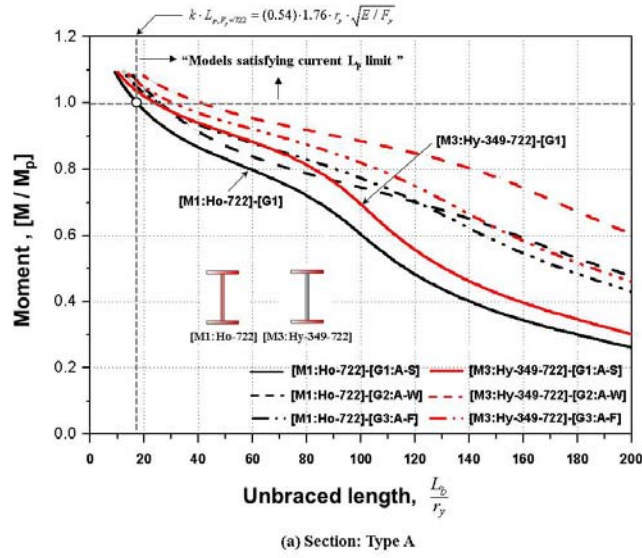


(a) Section: Type A

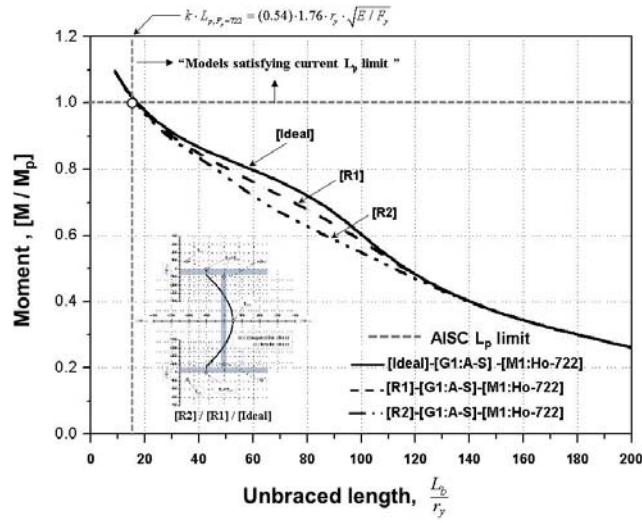


(b) Section: Type A

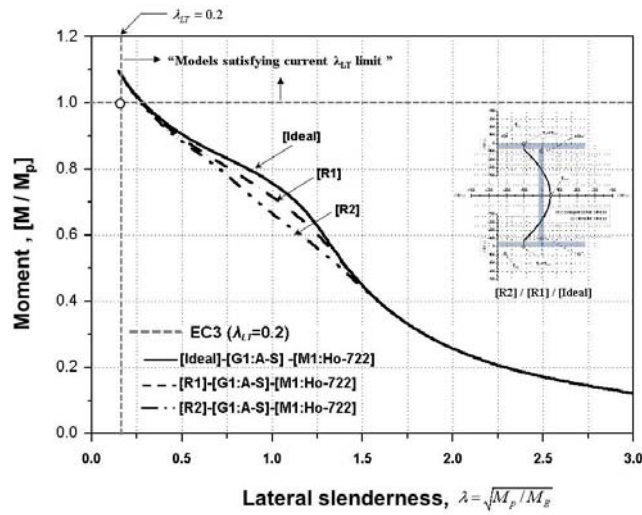
[4-34] Effects of material (high strength vs. mild) on inelastic LTB strength curve (a) Section: Type A [250x150 series] represented by AISC format (b) Section: Type A [250x150 series] represented by EC 3 format



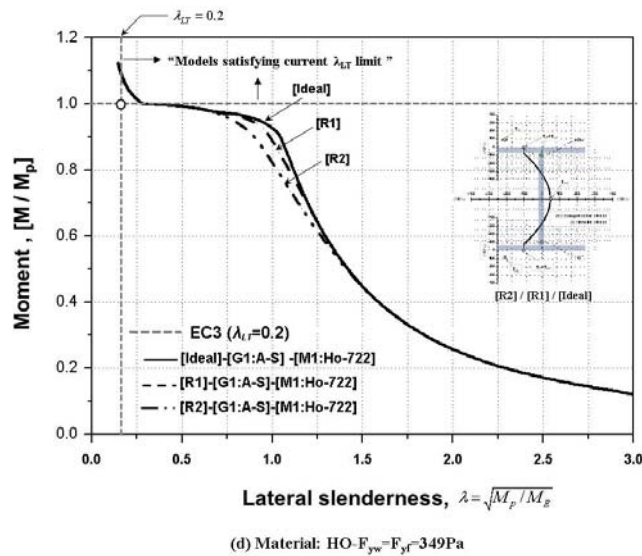
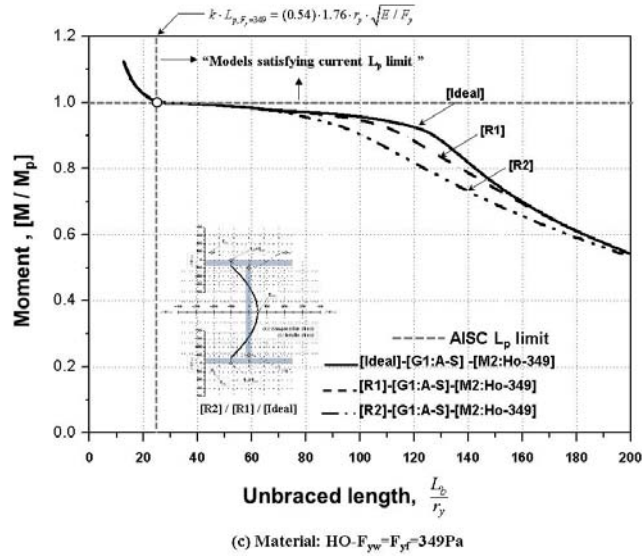
[4-35] Effects of hybrid (homogeneous vs. hybrid) on inelastic LTB strength curve (a) Section: Type A [250x150 series] represented by AISC format (b) Section: Type A [250x150 series] represented by EC 3 format



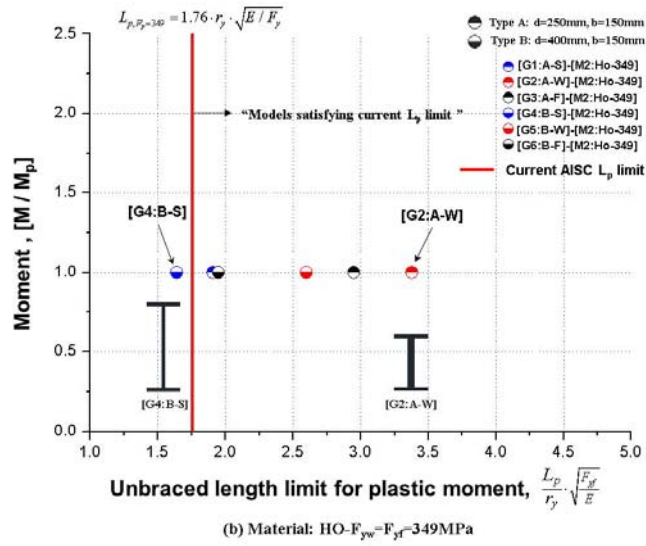
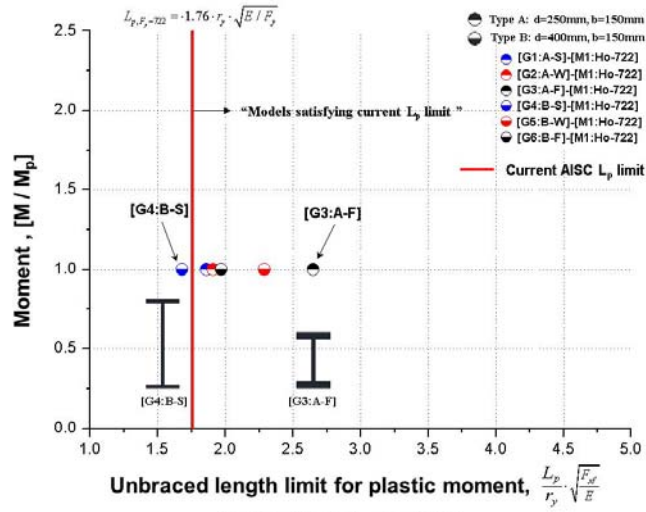
(a) Material: HO- $F_{yw}=F_{yf}=722\text{MPa}$

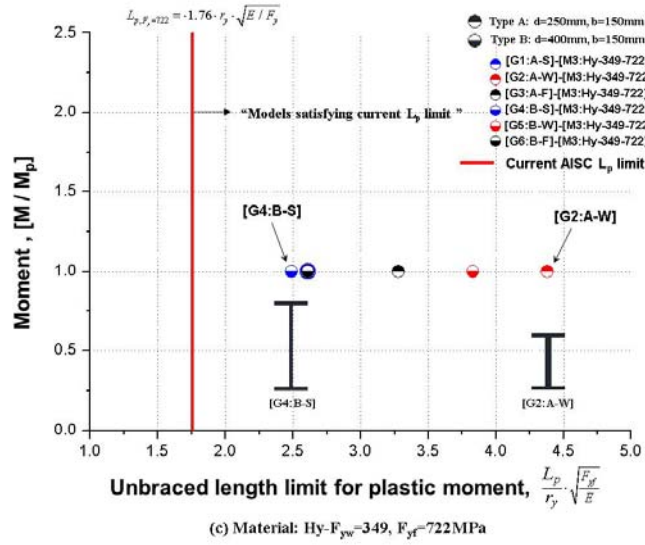


(b) Material: HO- $F_{yw}=F_{yf}=722\text{MPa}$

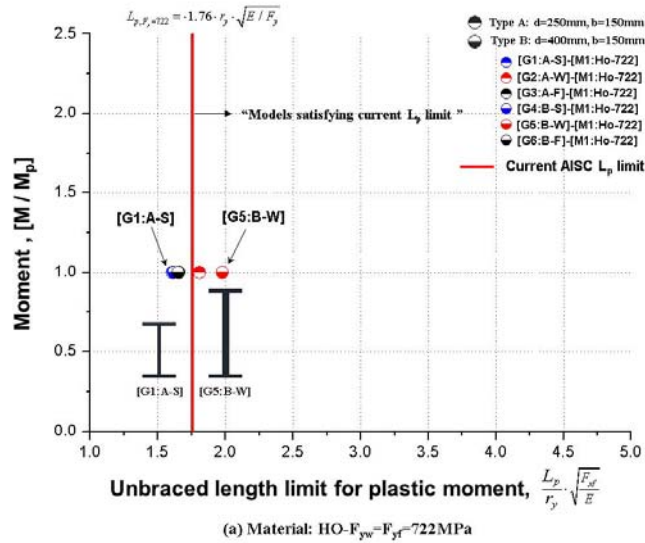


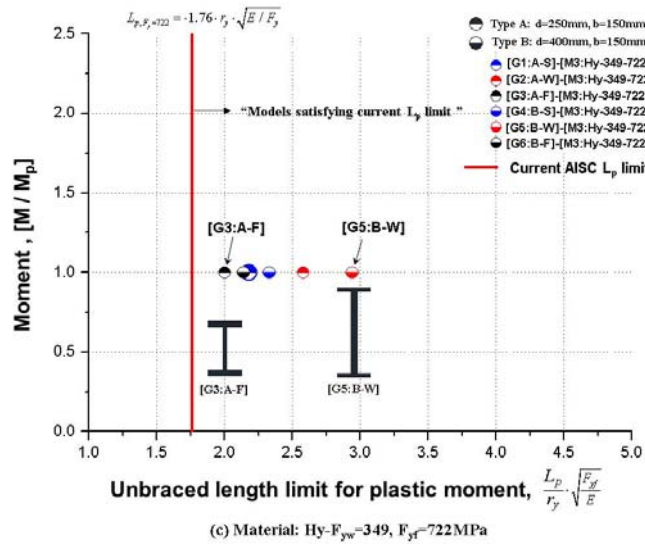
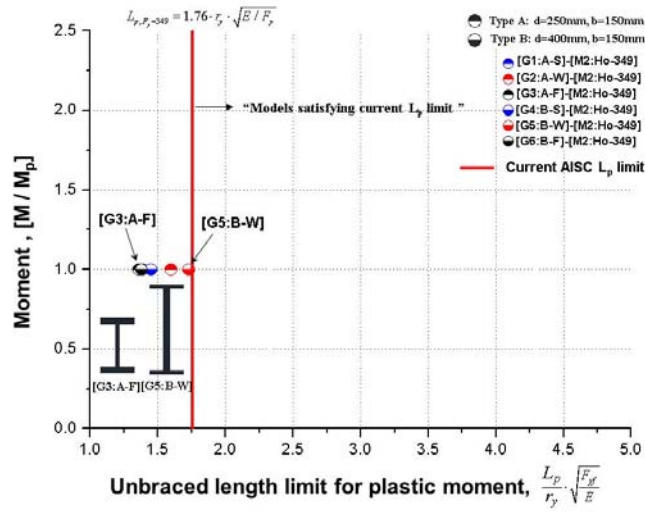
[4-36] Effects of residual stresses (M1-C50-T100, M1-C100-T200) on inelastic LTB strength curve (a) Material: Ho- $F_{yw}=F_{yt}=722\text{MPa}$ represented by AISC format (b) Material: Ho- $F_{yw}=F_{yt}=722\text{MPa}$ represented by EC 3 format (c) Material: Ho- $F_{yw}=F_{yt}=349\text{MPa}$ represented by AISC format (d) Material: Ho- $F_{yw}=F_{yt}=349\text{MPa}$ represented by EC3 format



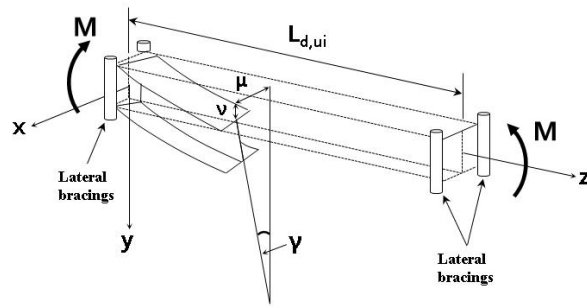


[4-37] Laterally unbraced length limit for achieving plastic moment under uniform moment by the detailed approaches (a) Material: Ho- $F_{yw}=F_{yf}=722$ MPa (b) Material: Ho- $F_{yw}=F_{yf}=349$ MPa (c) Material: Hy- $F_{yw}=349$, $F_{yf}=722$ MPa





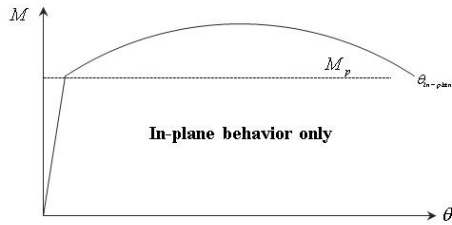
[4-38] Laterally unbraced length limit for achieving plastic moment under uniform moment by the simplified approaches (a) Material: Ho- $F_{yw}=F_{yf}=722\text{MPa}$ (b) Material: Ho- $F_{yw}=F_{yf}=349\text{MPa}$ (c) Material: Hy- $F_{yw}=349, F_{yf}=722\text{MPa}$



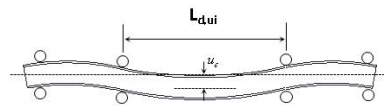
(a) LTB under uniform moment



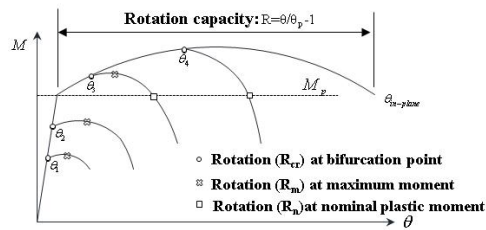
In-plane behavior



(b) Maximum rotation capacity without LTB



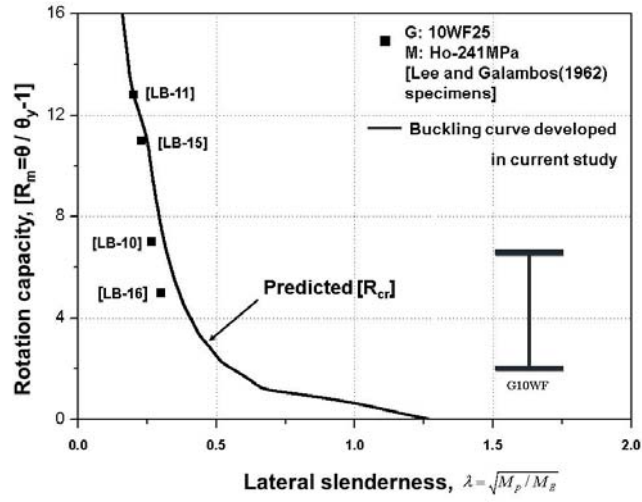
Out-of-plane behavior



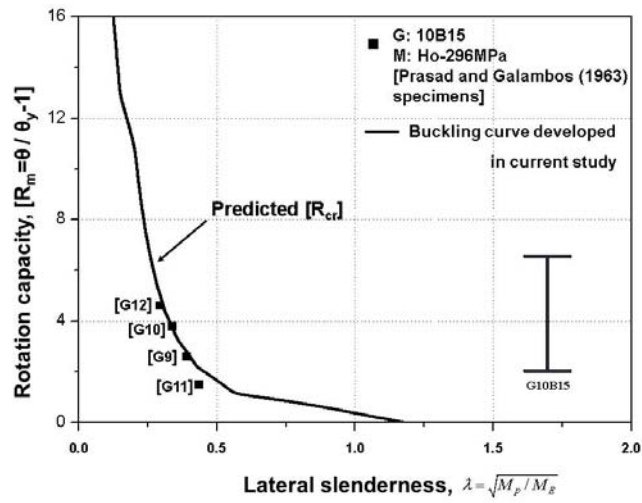
(c) Rotation capacity curves under LTB

[4-39] Schematic overview of rotation capacity problem under uniform moment (a) LTB under uniform moment (b) maximum rotation capacity without LTB (c) Rotation

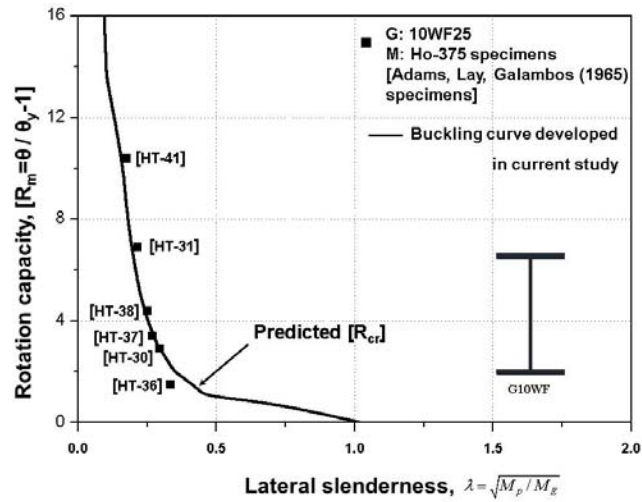
capacity curves under LTB



(a) Lee and Galambos (1962)

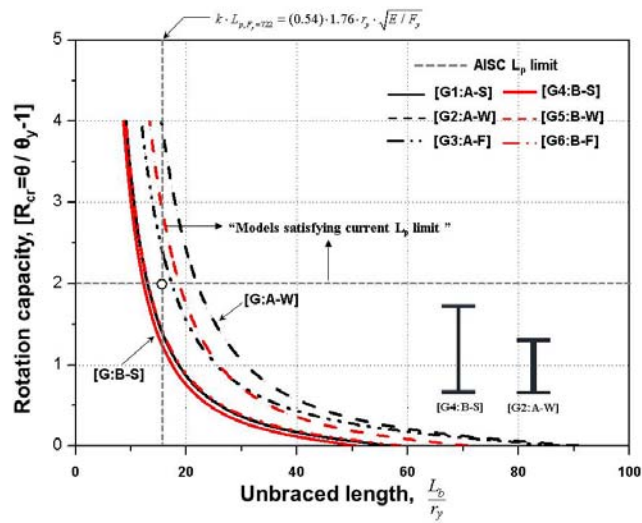


(b) Prasad and Galambos (1963)

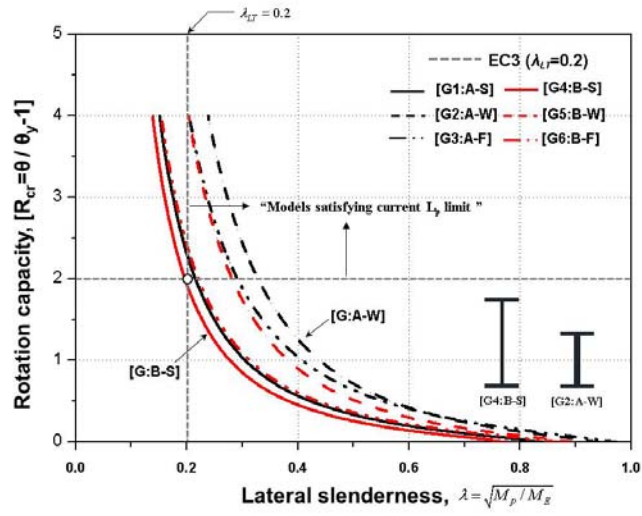


(C) Adams, Lay and Galambos (1965)

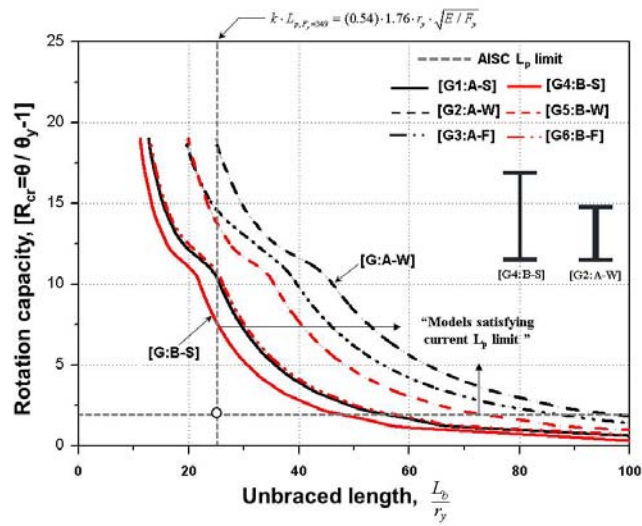
[4-40] Validation of the analytically developed rotation capacity curve with previous experiments (a) Lee and Galambos (1962) (b) Prasad and Galambos (1963) (c) Adams, Lay and Galambos (1965)



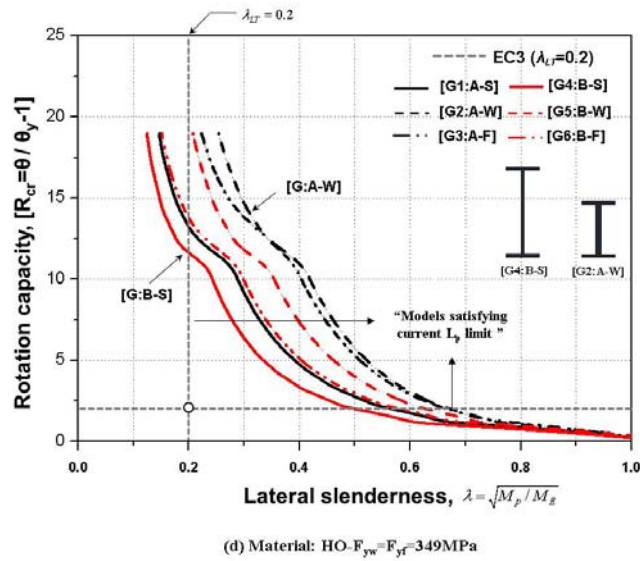
(a) Material: HO- $F_{yw} = F_{yf} = 722$ MPa



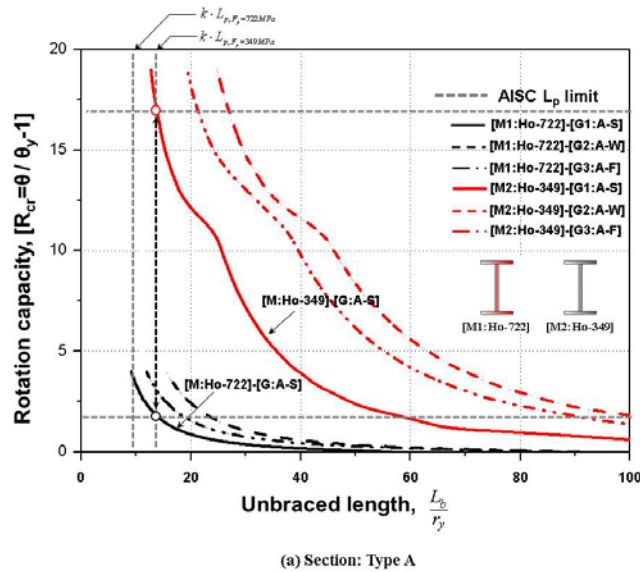
(b) Material: HO- $F_{yw}=F_{yf}=722\text{MPa}$

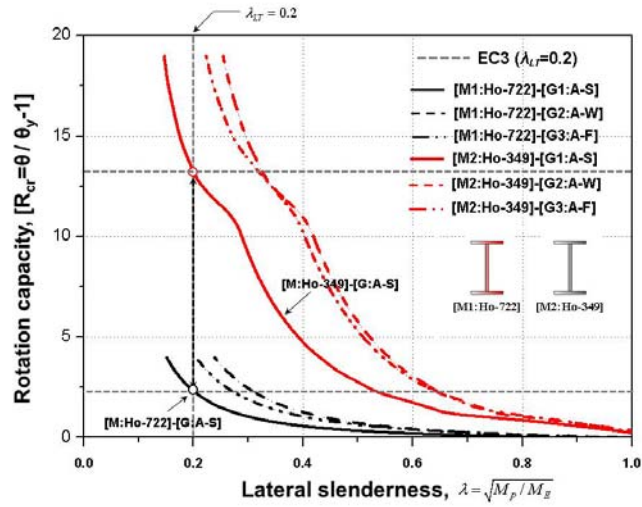


(c) Material: HO- $F_{yw}=F_{yf}=349\text{MPa}$



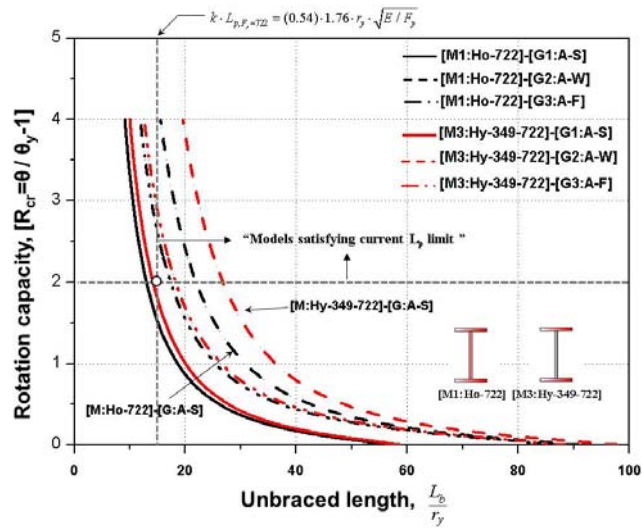
[4-41] Effects of geometrical variation (flange, web and depth) rotation capacity curve
 (a) Material: $H_o-F_{yw}=F_{yf}=722\text{MPa}$ represented by AISC format (b) Material: $H_o-F_{yw}=F_{yf}=722\text{MPa}$ represented by EC 3 format (c) Material: $H_o-F_{yw}=F_{yf}=349\text{MPa}$ represented by AISC format (d) Material: $H_o-F_{yw}=F_{yf}=349\text{MPa}$ represented by EC 3 format



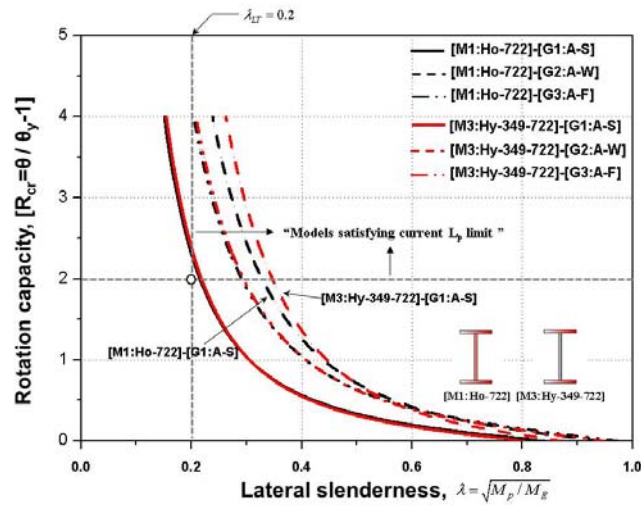


(b) Section: Type A

[4-42] Effects of material (high strength vs. mild) on rotation capacity curve (a) Section: Type A [250x150 series] represented by AISC format (b) Section: Type A [250x150 series] represented by EC 3 format

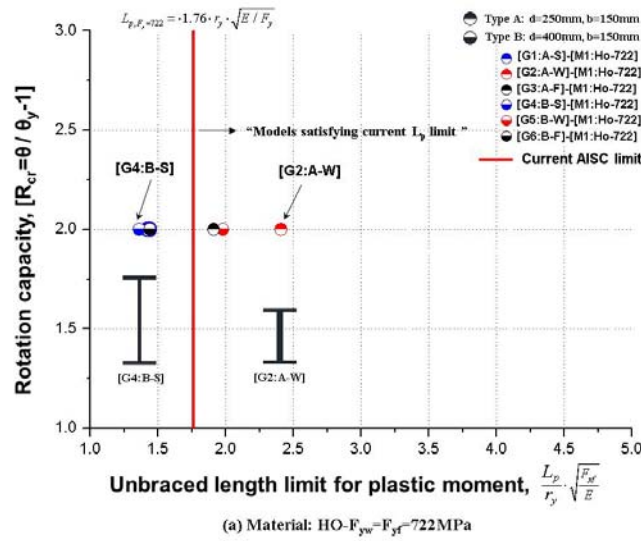


(a) Section: Type A

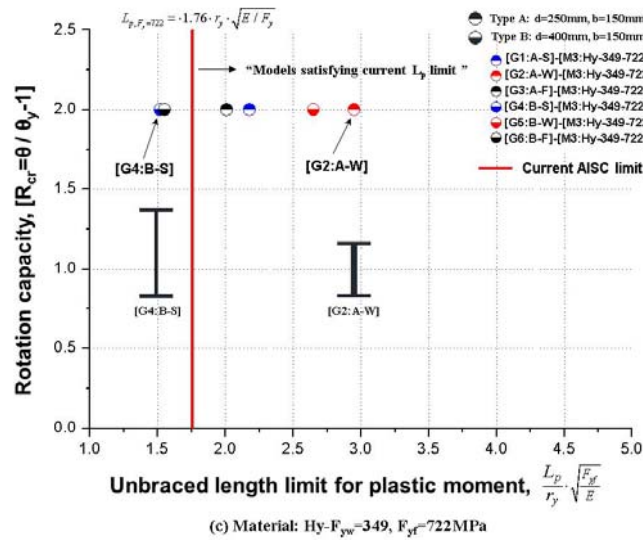
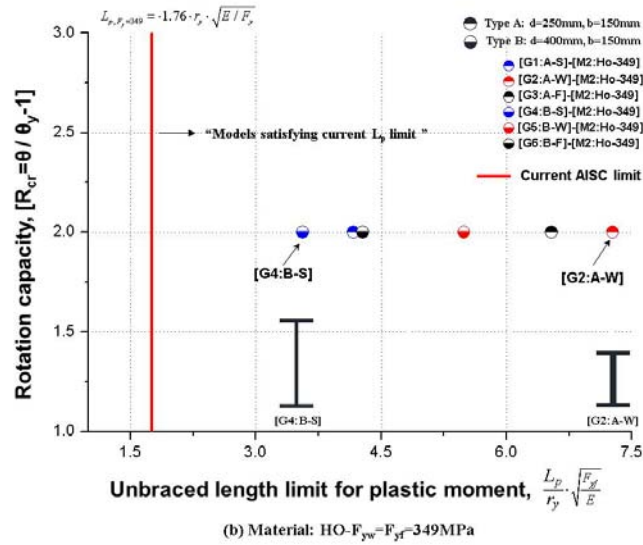


(b) Section: Type A

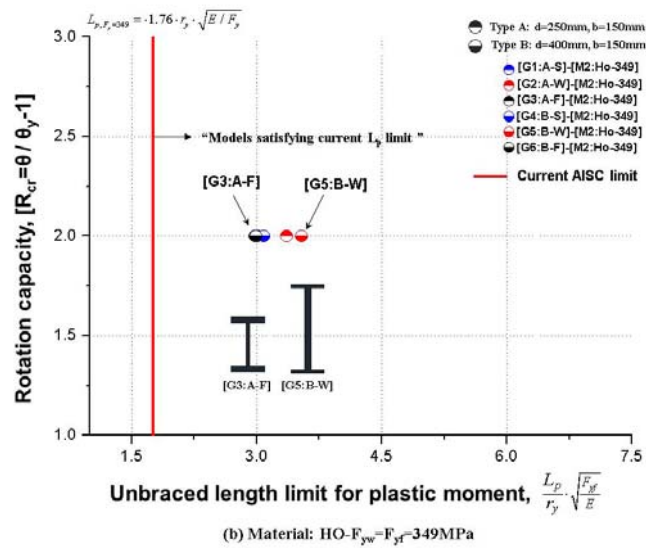
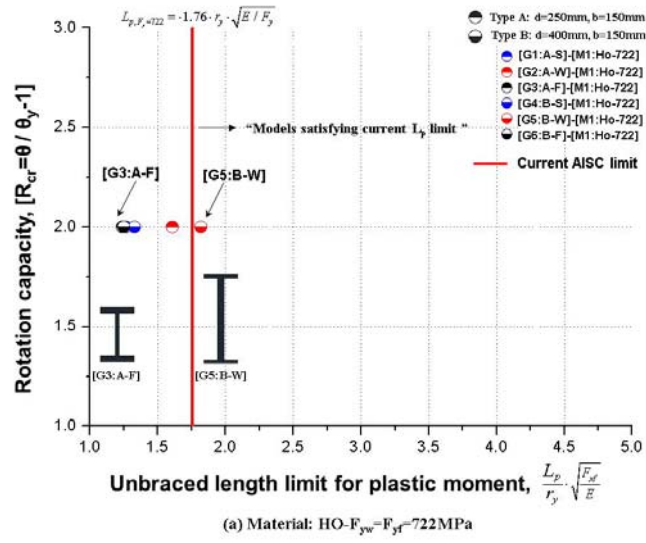
[4-43] Effects of hybrid (homogeneous vs. hybrid) on rotation capacity curve (a) Section: Type A [250x150 series] represented by AISC format (b) Section: Type A [250x150 series] represented by EC 3 format

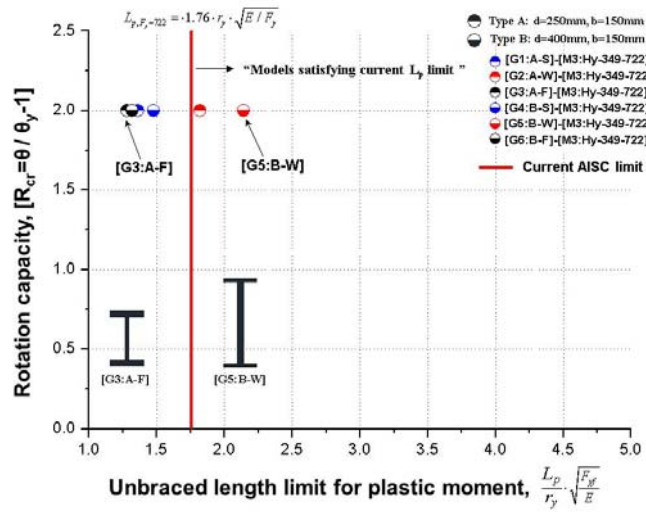


(a) Material: HO- $F_{yw} = F_{yf} = 722$ MPa



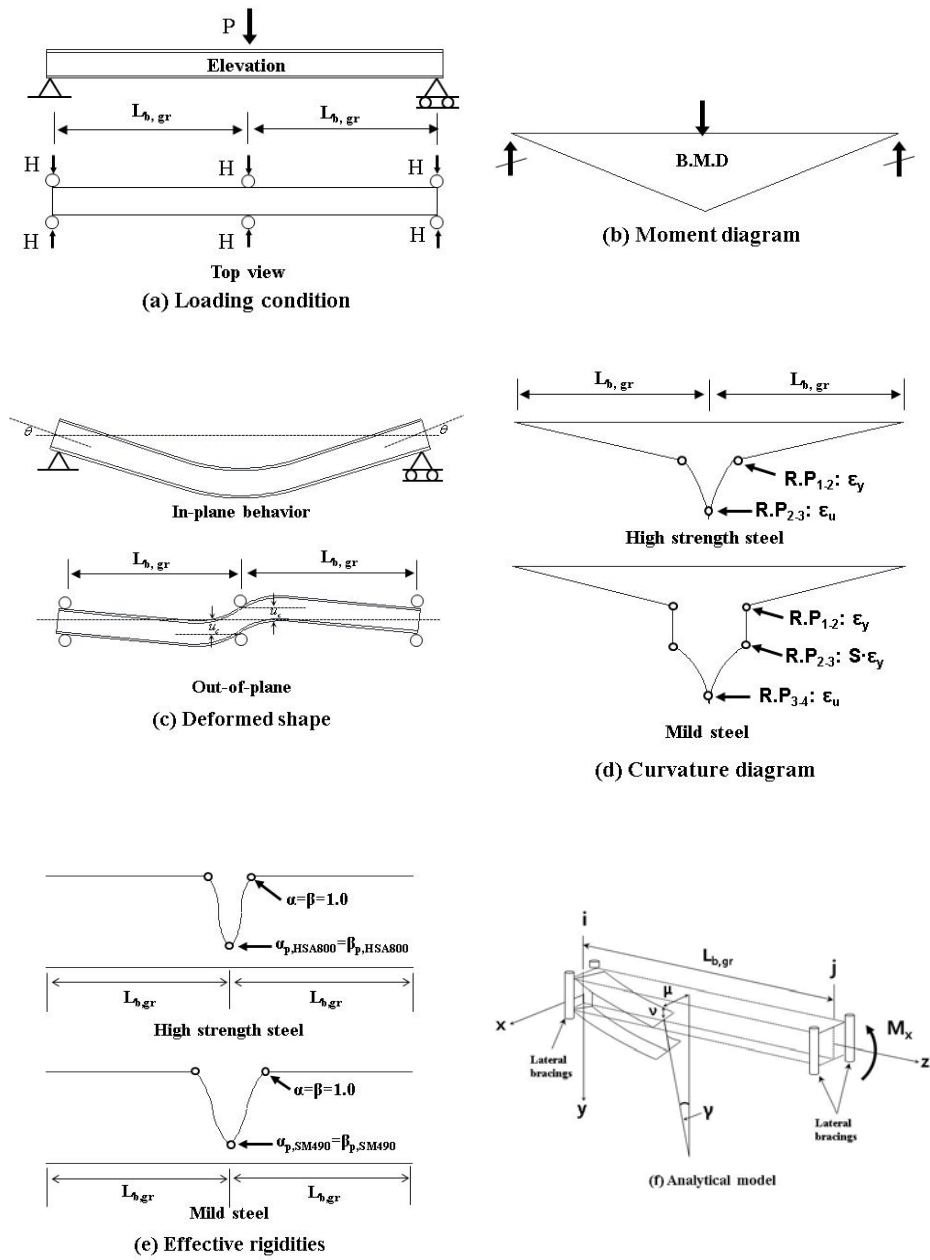
[4-44] Laterally unbraced length limit for achieving target rotation capacity under uniform moment by the detailed approaches (a) Material: Ho- $F_{yw}=F_{yf}=722\text{MPa}$ (b) Material: Ho- $F_{yw}=F_{yf}=349\text{MPa}$ (c) Material: Hy- $F_{yw}=349, F_{yf}=722\text{MPa}$



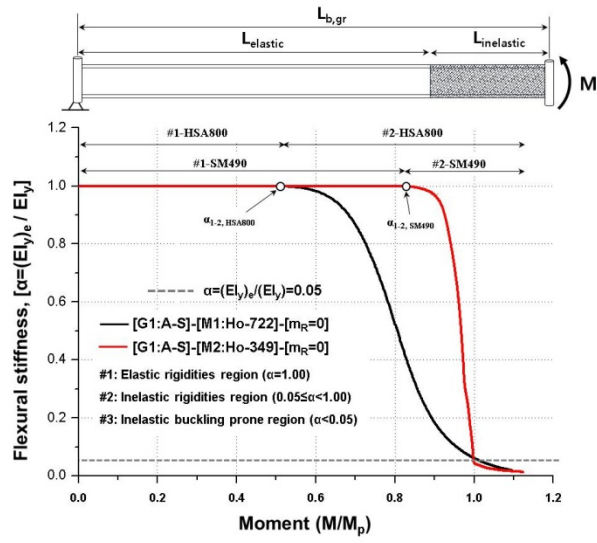


(c) Material: Hy- $F_{yw}=349$, $F_{yt}=722$ MPa

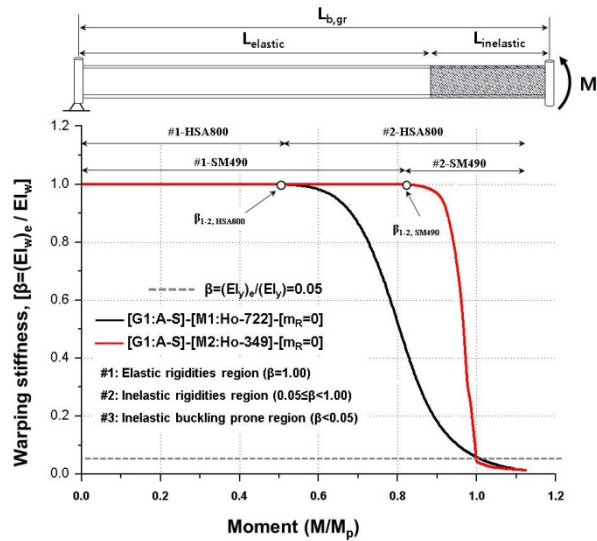
[4-45] Laterally unbraced length limit for achieving target rotation capacity under uniform moment by the simplified approaches (a) Material: Ho- $F_{yw}=F_{yt}=722$ MPa (b) Material: Ho- $F_{yw}=F_{yt}=349$ MPa (c) Material: Hy- $F_{yw}=349$, $F_{yt}=722$ MPa



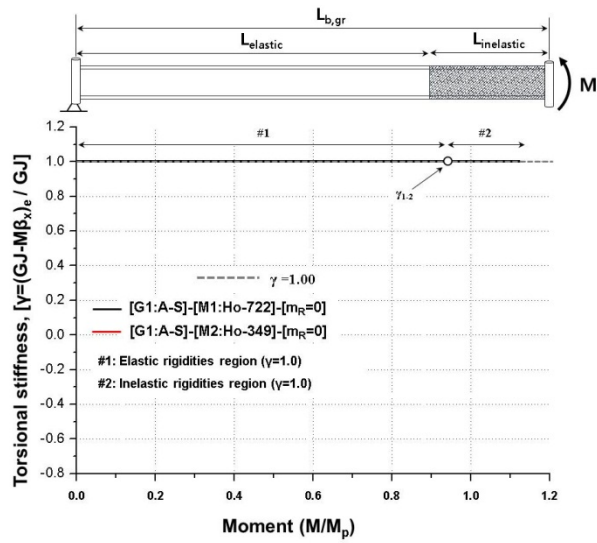
[4-46] Schematic overview of LTB strength problem under moment gradient (a) Loading and beam geometry (b) Moment diagram (c) Deformed shape (in-plane and out-of-plane) (d) Curvature diagram (e) Effective rigidities diagram (f) Analytical model



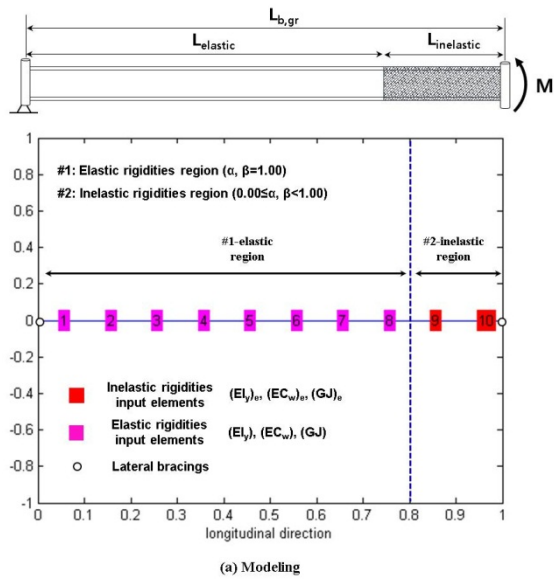
(a) Effective flexural stiffness

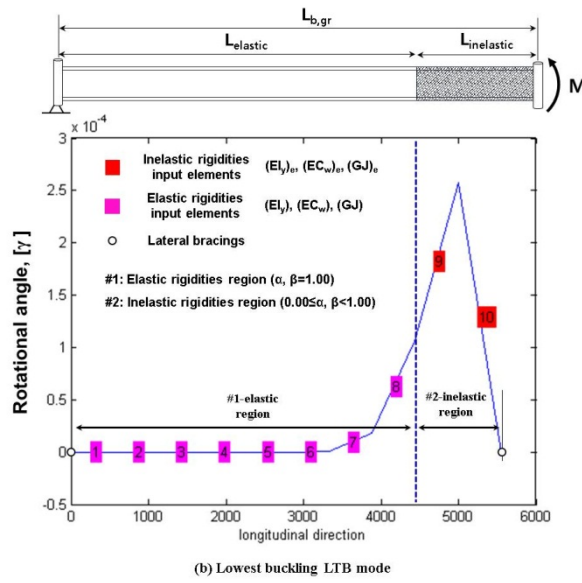


(b) Effective warping stiffness

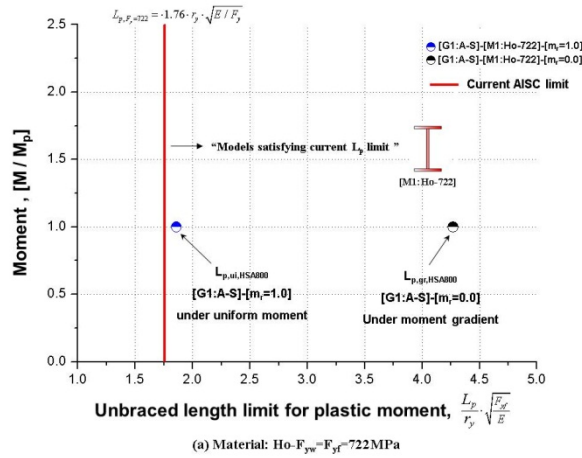


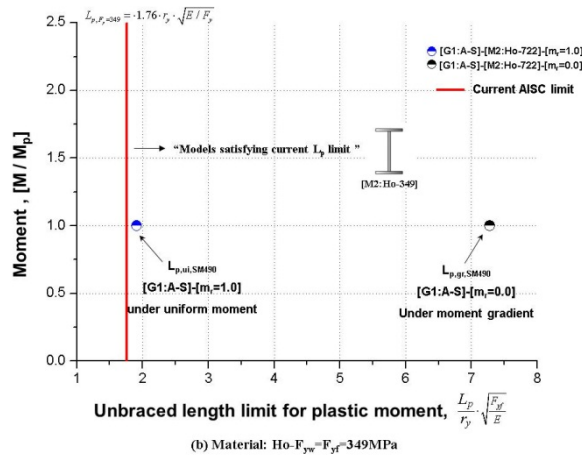
[4-47] Inelastic effective rigidities of ideal I-beam according to moment level under moment gradient condition, $m_R=0$ (a) effective flexural stiffness (b) effective warping stiffness (c) effective torsional stiffness



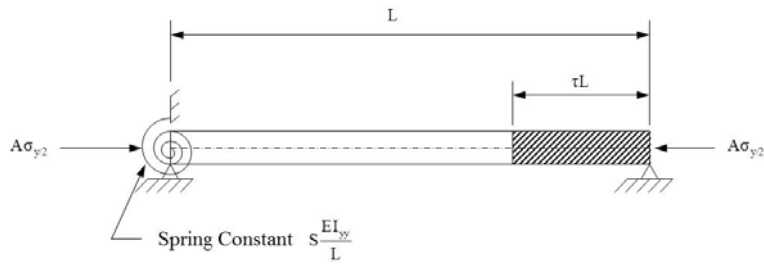


[4-48] Schematic overview of the numerical procedure to calculate LTB strength under moment gradient condition for the detailed approach (a) modeling (b) lowest buckling mode

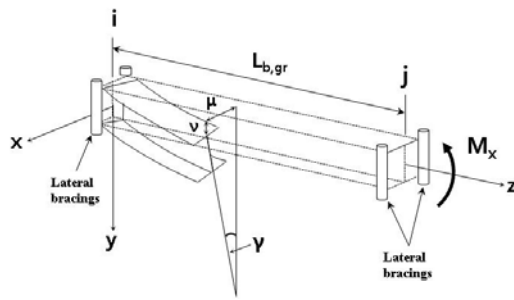




[4-49] Laterally unbraced length limit for achieving plastic moment under moment gradient condition, $m_R=0$ by the detailed approaches (a) Material: $H_o-F_{yw}=F_{yt}=722\text{MPa}$ (b) Material: $H_o-F_{yw}=F_{yt}=349\text{MPa}$



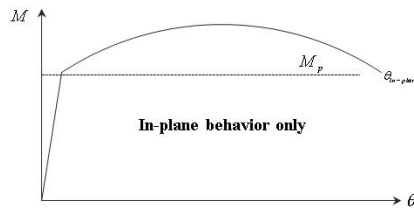
[4-50] Schematic overview of the numerical procedure to calculate LTB strength under moment gradient condition for the simplified approach by Lay and Galambos (1967)



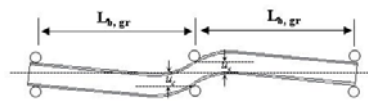
(a) LTB under moment gradient



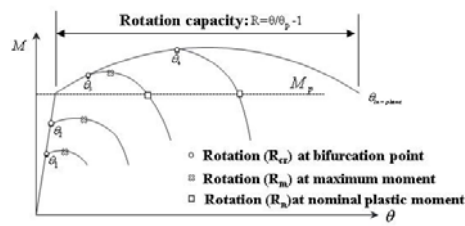
In-plane behavior



(b) Maximum rotation capacity without LTB



Out-of-plane



(c) Rotation capacity curves under LTB

[4-51] Schematic overview of rotation capacity problem under moment gradient (a) LTB under uniform moment (b) maximum rotation capacity without LTB (c) Rotation capacity curves under LTB

[4-1] Residual stresses parameters for analyzing the effects on the effective rigidities

			[M1:Ho ¹⁾ -F _{yw} =F _{yt} =722(#3) ²⁾	[M2:Ho ¹⁾ -F _{yw} =F _{yt} =349(#1) ³⁾
Residual stresses Parameters [R1~R4]	Ideal Pattern	[R1] C50-T100 ⁴⁾	[G:H-250x150x14x14]-[M1:Ho-722]-[R1]	[G:H-250x150x14x14]-[M2:Ho-349]-[R1]
		[R2] C100-T200 ⁵⁾	[G:H-250x150x14x14]-[M1:Ho-722]-[R2]	[G:H-250x150x14x14]-[M2:Ho-349]-[R2]
	Linear Pattern	[R3] C100 ⁶⁾	[G:H-250x150x14x14]-[M1:Ho-722]-[R3]	[G:H-250x150x14x14]-[M2:Ho-349]-[R3]
		[R4] C100 ⁷⁾	[G:H-250x150x14x14]-[M1:Ho-722]-[R4]	[G:H-250x150x14x14]-[M2:Ho-349]-[R4]
1) Ho is abbreviation of homogenous I-section, the flange and web of which are the same grade steel are applied 2) Ramberg-Osgood model No.3 was applied for the analysis 3) Traditional model No.1 was applied for the analysis 4) R1: C50-T100 indicate ideal residual stress pattern model with $f_{rfc} = 50MPa$ and $f_{rft} = f_{rwt} = 100MPa$ 5) R2: C100-T200 indicate ideal residual stress pattern model with $f_{rfc} = 100MPa$ and $f_{rft} = f_{rwt} = 200MPa$ 6) R3: C100 indicate linear residual stress pattern model with $f_{rfc} = 100MPa$ 7) R4: C100 indicate constant residual stress pattern model with $f_{rfc} = 100MPa$				

[4-2] Geometric and material parameters for LTB behavior analysis

			Material parameters [MPa]		
			M1:Ho ¹ -F _{yw} =F _{yt} =722(#3) ³	M2:Ho ¹ -F _{yw} =F _{yt} =349(#1) ⁴	M3:Hy ² -F _{yw} =349-F _{yt} =722
Geometrical parameters [mm]	[250x150 series] Type A	[G:A-S] H-250x150x14x14	A-P1: [G:A-S]-[M1:Ho-722]	A-P2: [G:A-S]-[M2:Ho-349]	A-P3: [G:A-S]-[M3:Hy-349-722]
		[G:A-W] H-250x150x28x14	A-P4: [G:A-W]-[M1:Ho-722]	A-P5: [G:A-W]-[M2:Ho-349]	A-P6: [G:A-W]-[M3:Hy-349-722]
		[G:A-F] H-250x150x14x28	A-P7: [G:A-F]-[M1:Ho-722]	A-P8: [G:A-F]-[M2:Ho-349]	A-P9: [G:A-F]-[M3:Hy-349-722]
	[400x150 series] Type B	[G:B-S] H-400x150x14x14	B-P1: [G:B-S]-[M1:Ho-722]	B-P2: [G:B-S]-[M2:Ho-349]	B-P3: [G:B-S]-[M3:Hy-349-722]
		[G:B-W] H-400x150x28x14	B-P4: [G:B-W]-[M1:Ho-722]	B-P5: [G:B-W]-[M2:Ho-349]	B-P6: [G:B-W]-[M3:Hy-349-722]
		[G:B-F] H-400x150x14x28	B-P7: [G:B-F]-[M1:Ho-722]	B-P8: [G:B-F]-[M2:Ho-349]	B-P9: [G:B-F]-[M3:Hy-349-722]
Residual stresses	Ideal Pattern	[R1] C50-T100 ⁵	A-P1-R1:[G:A-S]-[M1:Ho-722]-[R1]	A-P1-R1:[G:A-S]-[M2:Ho-349]-[R1]	A-P1-R1:[G:A-S]-[M3:Hy-349-722]-[R1]
		[R2] C100-T200 ⁶	A-P1-R2:[G:A-S]-[M1:Ho-722]-[R2]	A-P1-R2:[G:A-S]-[M2:Ho-349]-[R2]	A-P1-R2:[G:A-S]-[M3:Hy-349-722]-[R2]

1) Ho is abbreviation of homogenous I-section, the flange and web of which are the same grade steel are applied
 2) Hy is abbreviation of hybrid I-section, the flange and web of which are the different grade steel are applied
 3) Ramberg-Osgood model No.3 was applied for the analysis
 4) Traditional model No.1 was applied for the analysis
 5) R1: C50-T100 indicate ideal residual stress pattern model with $f_{rfc} = 50MPa$ and $f_{rt} = f_{rwt} = 100MPa$
 6) R2: C100-T200 indicate ideal residual stress pattern model with $f_{rfc} = 100MPa$ and $f_{rt} = f_{rwt} = 200MPa$

[4-3] Unbraced length for achieving plastic moment under uniform moment by the detailed approach

Analytical parameters		$\alpha_p = \frac{(EI_y)_e}{(EI_y)}$	$\beta_p = \frac{(EC_w)_e}{(EC_w)}$	$\gamma_p = \frac{(GJ)_e - M\beta_x}{(GJ)_e}$	$\frac{L_p}{k \cdot r_y} \cdot \sqrt{\frac{F_y}{E}}$	λ_p
		[non]	[non]	[non]	[non]	[non]
[250x150 series] Type A	A-P1: [G:A-S]-[M1:Ho-722]	0.059	0.056	1	1.86	0.28
	A-P2: [G:A-S]-[M2:Ho-349]	0.044	0.043	1	1.91	0.28
	A-P3: [G:A-S]-[M3:Hy-349-722]	0.094	0.091	1	2.61	0.36
	A-P4: [G:A-W]-[M1:Ho-722]	0.066	0.045	1	2.78	0.37
	A-P5: [G:A-W]-[M2:Ho-349]	0.052	0.042	1	3.38	0.41
	A-P6: [G:A-W]-[M3:Hy-349-722]	0.106	0.081	1	4.38	0.48
	A-P7: [G:A-F]-[M1:Ho-722]	0.070	0.069	1	2.65	0.39
	A-P8: [G:A-F]-[M2:Ho-349]	0.047	0.046	1	2.95	0.40
	A-P9: [G:A-F]-[M3:Hy-349-722]	0.095	0.094	1	3.28	0.45
[400x150 series] Type B	B-P1: [G:B-S]-[M1:Ho-722]	0.055	0.050	1	1.68	0.24
	B-P2: [G:B-S]-[M2:Ho-349]	0.044	0.042	1	1.64	0.24
	B-P3: [G:B-S]-[M3:Hy-349-722]	0.092	0.087	1	2.49	0.32
	B-P4: [G:B-W]-[M1:Ho-722]	0.073	0.041	1	2.29	0.31
	B-P5: [G:B-W]-[M2:Ho-349]	0.056	0.040	1	2.60	0.34
	B-P6: [G:B-W]-[M3:Hy-349-722]	0.116	0.077	1	3.83	0.43
	B-P7: [G:B-F]-[M1:Ho-722]	0.065	0.062	1	1.97	0.30
	B-P8: [G:B-F]-[M2:Ho-349]	0.045	0.044	1	1.95	0.29
	B-P9: [G:B-F]-[M3:Hy-349-722]	0.097	0.094	1	2.61	0.37

Continuous lateral bracings where the effective length factor is $k = k_y = k_z = 0.54$ are assumed in the calculation.

[4-4] Unbraced length for achieving plastic moment under uniform moment by the simplified approach

Analytical parameters		$\alpha_p = \frac{(EI_y)_e}{(EI_y)}$	$k = \sqrt{\frac{(A/2) \cdot (d-t_f)}{[Z_f + Z_w \cdot (F_{yw} / F_{yf})]}}$	$\frac{L_p}{k \cdot r_y} \cdot \sqrt{\frac{F_{yf}}{E}}$	λ_p
		[non]	[non]	[non]	[non]
[250x150 series] Type A	A-P1: [G:A-S]-[M1:Ho-722]	0.059	1.14	1.61	0.24
	A-P2: [G:A-S]-[M2:Ho-349]	0.044	1.14	1.39	0.21
	A-P3: [G:A-S]-[M3:Hy-349-722]	0.094	1.22	2.18	0.31
	A-P4: [G:A-W]-[M1:Ho-722]	0.066	1.21	1.81	0.26
	A-P5: [G:A-W]-[M2:Ho-349]	0.052	1.21	1.60	0.23
	A-P6: [G:A-W]-[M3:Hy-349-722]	0.106	1.36	2.58	0.33
	A-P7: [G:A-F]-[M1:Ho-722]	0.070	1.08	1.66	0.26
	A-P8: [G:A-F]-[M2:Ho-349]	0.047	1.08	1.36	0.22
	A-P9: [G:A-F]-[M3:Hy-349-722]	0.095	1.11	2.00	0.31
[400x150 series] Type B	B-P1: [G:B-S]-[M1:Ho-722]	0.055	1.18	1.62	0.23
	B-P2: [G:B-S]-[M2:Ho-349]	0.044	1.18	1.45	0.21
	B-P3: [G:B-S]-[M3:Hy-349-722]	0.092	1.32	2.33	0.30
	B-P4: [G:B-W]-[M1:Ho-722]	0.073	1.26	1.98	0.27
	B-P5: [G:B-W]-[M2:Ho-349]	0.056	1.26	1.73	0.24
	B-P6: [G:B-W]-[M3:Hy-349-722]	0.116	1.49	2.94	0.34
	B-P7: [G:B-F]-[M1:Ho-722]	0.065	1.12	1.65	0.25
	B-P8: [G:B-F]-[M2:Ho-349]	0.045	1.12	1.38	0.21
	B-P9: [G:B-F]-[M3:Hy-349-722]	0.097	1.18	2.14	0.31

Continuous lateral bracings where the effective length factor is $k = k_y = k_z = 0.54$ are assumed in the calculation.

[4-5] Unbraced length for achieving target rotation capacity $R_m=2$ under uniform moment by the detailed approach

Analytical parameters		$\alpha_d = \frac{(EI_y)_e}{(EI_y)}$	$\beta_d = \frac{(EC_w)_e}{(EC_w)}$	$\gamma_d = \frac{(GJ)_e - M\beta_x}{(GJ)_e}$	$\frac{L_d}{k \cdot r_y} \cdot \sqrt{\frac{F_{yf}}{E}}$	λ_d
		[non]	[non]	[non]	[non]	[non]
[250x150 series] Type A	A-P1: [G:A-S]-[M1:Ho-722]	0.037	0.035	1	1.43	0.22
	A-P2: [G:A-S]-[M2:Ho-349]	0.207	0.204	1	4.17	0.57
	A-P3: [G:A-S]-[M3:Hy-349-722]	0.037	0.035	1	1.56	0.22
	A-P4: [G:A-W]-[M1:Ho-722]	0.053	0.035	1	2.41	0.33
	A-P5: [G:A-W]-[M2:Ho-349]	0.228	0.204	1	7.27	0.67
	A-P6: [G:A-W]-[M3:Hy-349-722]	0.053	0.035	1	2.95	0.35
	A-P7: [G:A-F]-[M1:Ho-722]	0.039	0.038	1	1.91	0.29
	A-P8: [G:A-F]-[M2:Ho-349]	0.226	0.225	1	6.54	0.67
	A-P9: [G:A-F]-[M3:Hy-349-722]	0.039	0.038	1	2.01	0.30
[400x150 series] Type B	B-P1: [G:B-S]-[M1:Ho-722]	0.037	0.033	1	1.36	0.20
	B-P2: [G:B-S]-[M2:Ho-349]	0.201	0.196	1	3.56	0.50
	B-P3: [G:B-S]-[M3:Hy-349-722]	0.037	0.033	1	1.52	0.20
	B-P4: [G:B-W]-[M1:Ho-722]	0.062	0.033	1	2.06	0.28
	B-P5: [G:B-W]-[M2:Ho-349]	0.234	0.196	1	5.49	0.63
	B-P6: [G:B-W]-[M3:Hy-349-722]	0.062	0.033	1	2.65	0.30
	B-P7: [G:B-F]-[M1:Ho-722]	0.037	0.035	1	1.44	0.22
	B-P8: [G:B-F]-[M2:Ho-349]	0.212	0.210	1	4.28	0.57
	B-P9: [G:B-F]-[M3:Hy-349-722]	0.037	0.035	1	1.55	0.22

Continuous lateral bracings where the effective length factor is $k = k_y = k_z = 0.54$ are assumed in the calculation.

[4-6] Unbraced length for achieving target rotation capacity $R_m=2$ under uniform moment by the simplified approach

Analytical parameters		$\alpha_d = \frac{(EI_y)_e}{(EI_y)}$	$k = \sqrt{\frac{(A/2) \cdot (d-t_f)}{[Z_f + Z_w \cdot (F_{yw} / F_{yf})]}}$	$\frac{L_d}{k \cdot r_y} \cdot \sqrt{\frac{F_{yf}}{E}}$
		[non]	[non]	[non]
[250x150 series] Type A	A-P1: [G:A-S]-[M1:Ho-722]	0.037	1.14	1.27
	A-P2: [G:A-S]-[M2:Ho-349]	0.207	1.14	3.01
	A-P3: [G:A-S]-[M3:Hy-349-722]	0.037	1.22	1.36
	A-P4: [G:A-W]-[M1:Ho-722]	0.053	1.21	1.61
	A-P5: [G:A-W]-[M2:Ho-349]	0.228	1.21	3.36
	A-P6: [G:A-W]-[M3:Hy-349-722]	0.053	1.36	1.82
	A-P7: [G:A-F]-[M1:Ho-722]	0.039	1.08	1.24
	A-P8: [G:A-F]-[M2:Ho-349]	0.226	1.08	2.98
	A-P9: [G:A-F]-[M3:Hy-349-722]	0.039	1.11	1.28
[400x150 series] Type B	B-P1: [G:B-S]-[M1:Ho-722]	0.037	1.18	1.33
	B-P2: [G:B-S]-[M2:Ho-349]	0.201	1.18	3.09
	B-P3: [G:B-S]-[M3:Hy-349-722]	0.037	1.32	1.48
	B-P4: [G:B-W]-[M1:Ho-722]	0.062	1.26	1.82
	B-P5: [G:B-W]-[M2:Ho-349]	0.234	1.26	3.54
	B-P6: [G:B-W]-[M3:Hy-349-722]	0.062	1.49	2.14
	B-P7: [G:B-F]-[M1:Ho-722]	0.037	1.12	1.25
	B-P8: [G:B-F]-[M2:Ho-349]	0.212	1.12	2.99
	B-P9: [G:B-F]-[M3:Hy-349-722]	0.037	1.18	1.32

Continuous lateral bracings where the effective length factor is $k = k_y = k_z = 0.54$ are assumed in the calculation.

Chapter 5 Experimental Buckling Studies

In previous chapter, the analytical studies with regard to LTB strength and rotation capacity under uniform and moment have been described. In this chapter, experimental LTB studies of welded I-shaped beam will be described. The information with regard to material properties, cross-section geometry, overall test span, bracing length & methods and loading condition is described in detail.

This experiment was carefully prepared in order to derive the tangible results of two major concerns below.

- 1) The first concern is the precise measurement of the inelastic LTB strength and rotation capacity of welded I-beam according to unbraced length since it has been frequently reported that some of previous LTB experiments were halted during the experiments because of the lack of the bracing member stiffness and forces. In addition, some other experiments mistakenly miss the measure of the bifurcation point (=initiation of buckling), which result in incorrectly measured buckling strength (M_{cr}) since the post-buckling strength ($M_m - M_{cr}$) often increase the buckling strength significantly.
- 2) The second concern is the experimental confirmation that the geometrical and material parameters, which have been extensively discussed in the

analytical studies, could actually affect the performance of the inelastic behavior of I-beam.

5.1 Overview of the experimental study

Fig. 5-1 conceptually shows the overall information as inelastic LTB occurred under uniform moment. **Fig. 5-1a** free body diagrams. The vertically applied load (P) is equilibrated by the two reaction forces (R_n). **Fig. 5-1b** shows the internal moment triggered by the test set-up. Two side span (L_{gr}) under moment gradient provide uniform moment in the center span (L_{ui}) as described in **Eq. 5-1a**. The length of L_{gr} were determined about one-fifth of L_{ui} by considering the effect of shear deformation, affected the by span-to-depth ratio. **Fig. 5-2** shows the configuration of the uniform moment region (L_{ui}). is composed of three elements (L_{Δ} , L_{aj} and L_b) as described in **Eq. 5-1b**. First, L_{Δ} indicate the differential length between the loading point and end bracing points. In contrast to the analytical study, where the position of the lateral constraint are assumed at the loading point, the tested condition in this experimental study set the L_{Δ} since the width of the loading zig at the loading point is wider than width of the test specimens. Second, L_{aj} indicate the adjacent span of tested span or unbraced length L_b . By attuning the relative span length ratio L_{aj}/L_b , the effective length ($k=k_y=k_z$) are able to be adjusted, which is required to configure the laterally very closely braced length ($k \cdot L_b$).

Third, L_b indicate the laterally unbraced length, which is the major parameter of this experiment, positioned in the center.

Fig. 5-1c showed the x-z plane (in-plane) deformed shape where the vertical degree of freedom is constraint at the ends, in other words, simply supported beam condition. **Fig. 5-1c** showed the y-z plane (out-of-plane) deformed shape where the torsionally simple condition provided at the bracing points. The lateral bracing conditions are categorized as two types. The unbraced length (L_b) without the adjacent beam condition (L_{aj}) simulate the effective length condition $k = 1.0$; the unbraced length (L_b) with the adjacent beam condition (L_{aj}) simulate the effective length condition $k = 0.55$ and $k = 0.60$ respectively.

Fig. 5-1d shows the (in-plane) curvature distribution along the length. The curvature distribution will depends on the stress-strain profile of a material. **Fig. 5-1e** shows the (out-of-plane) curvature distribution after the LTB is triggered. Depending on the existence of adjacent beam, laterally single or double curvature will be recorded. The sign of the curvature change indicate the inflection points and give the effective length (k).

$$L = L_{ui} + 2 \cdot L_{gr} \quad (5-1a)$$

$$L_{ui} = L_b + 2 \cdot L_{aj} + 2 \cdot L_{\Delta} \quad (5-1b)$$

where

L is test span length

L_{ui} is the span length under uniform moment
 L_{gr} is the span length under moment gradient to trigger uniform moment in L_{ui}
 L_b is unbraced length for LTB testing
 L_{aj} is the adjacent span length which influences on the effective length in L_b
 L_{Δ} is the differential length between loading point and the end bracing point

Fig. 5-2a shows the test set-up of this experiment. The experiment performed by the 10,000KN UTM (Ultra Testing Machine) located at POSCO global R&D center. Loading system (in-plane) is designed to transmit the UTM loading to specimen via loading zigs. The loading zigs are composed of the block zig and UT type zig. The block (zig) is closely reinforced by the bearing stiffeners to prevent any local or global deformation during the loading and bolt connected UT-type zigs are directly toughed, not connected, with the top flange of the specimens.

Fig. 5-2b~d showed the lateral bracing system. Lateral bracing systems was designed to resist the horizontal flange forces of the specimens, developed during LTB behavior, by the reaction frame. Vertical bars, composed of 15mm diameter solid steel bar welded to the edge of adjustable T bar, closely toughing the side flange of the specimens, were prepared for providing the lateral constraints of the top and bottom flanges of specimens. The rear face of the vertical bars were attached to the flange face of the reaction beam (8,320mm long H-458x417x30x50 rolled I-beam with closely reinforced

bearing stiffeners coinciding the working point with the vertical bars) via bolted connection. The reaction beams are finally connected to the strong self-stand reaction frames, which is connected to the reaction floor via heavy screw bolt connection.

5.1.1 Mechanical properties

Table 5-1 shows mechanical properties of the 15mm HSA800 plates, applied to fabricate homogeneous I-shaped member. The average yield strength, tensile strength, yield ratio (Y_R) and tensile strain ratio (E_R) of 15mm plates are $F_y=773.8\text{MPa}$, $F_u=877.3\text{MPa}$, $F_y/F_u=0.88$, and $\epsilon_u/\epsilon_y=13.3$ respectively. By fitting the stress-strain curves with the Ramberg-Osgood model (**Eq. 3-6**), the average values of the strain hardening parameter of 15mm plates are 27.0. No yield plateau was investigated in HSA800 plates.

Table 5-2 shows mechanical properties of the 25mm thick HSA800 plates and 30mm thick SM490 plates, applied to fabricate hybrid I-shaped member. The average yield strength, tensile strength, yield ratio (Y_R) and tensile strain ratio (E_R) of 25mm plates are $F_y=822.3\text{MPa}$, $F_u=937.0\text{MPa}$, $F_y/F_u=0.90$ and $\epsilon_u/\epsilon_y=12.4$ respectively. For 30mm plates of SM490, $F_y=339.0\text{MPa}$, $F_u=515.3\text{MPa}$, $F_y/F_u=0.66$ and $\epsilon_u/\epsilon_y=88.8$ are reported. By fitting the 25mm HSA800 stress-strain curves with the Ramberg-Osgood model (**Eq. 3-6**), the average values of the strain hardening parameter of 25mm plates are 24.0. No

yield plateau was investigated in HSA800 plates. By fitting the 30mm SM490 stress-strain curves with the Haaijer model (Eq. 3-5), the yield plateau length is $\varepsilon_{st}/\varepsilon_y=10.0$ and the initial strain hardening modulus is $E/E_{st}=21.3$.

5.1.2 Instrumentation plan for measurement

The types and installation of instrumentations was planned to carefully measure the in-plane and out-of-plane behaviors of I-beams as shown in Fig. 5-3. The in-plane behaviors are measured by the end rotation (θ) and the vertical displacement (v) of the I-beam. The out-of-plane behaviors (the lateral torsional buckling behavior) are measured by the cross-section rotation (γ) and the lateral bending curvature (ϕ_{LT}). As early indicated by Bansal (1971), the onset-of lateral instability could not be ascertained very well by visual inspection since the lateral deflection (μ) occur from the very beginning of the loading. The actual determination of lateral buckling was obtained by the cross-section rotation and the lateral bending curvature. The rate of γ and ϕ_{LT} remains proportional to that of in-plane rotation until the occurrence of LTB. When the γ and ϕ_{LT} increase at a much faster rate than the in-plane deflections, the point of deviation from the initial slope is determined as the start of lateral instability. Fig.5-4a shows how the behaviors of the cross-section rotation are measured by the instrumentation. Fig. 5-4b shows how the behaviors of the lateral bending are measured by the instrumentation.

In summary, LVDT #1~2(3), #10(11)~12 is critical for measuring the end

rotation; LVDT #2~3, LVDT #10~11 is critical for measuring the vertical displacement; LVDT #6~7 is critical for measuring the cross-section rotation; Strain gauges #6~7 is critical for measuring the lateral bending curvature.

5.1.3 Data processing method

Eq. 5-2~5.8 describe the data processing method to analyze the behaviors of the tested specimens. For deriving the moment-rotation graphs, Eq. 5-2~Eq. 5-6 was applied. The external moment (M_0) is calculated by Eq. 5-2.

$$M_0 = \frac{1}{2} P \cdot L_{gr} \quad (5-2)$$

where

P is UTM force

M_0 is the external moment

For normalizing the measured moment strength (M_0), the yield moment strength (M_{yf}) and plastic moment strength (M_p) are calculated by the Eq. 5-3 and Eq. 5-4 respectively. For homogeneous I-shaped section, Eq. 5-3a and Eq. 5-4a are applicable for deriving yield moment and plastic moment. For hybrid I-shaped section, Eq. 5-3b and Eq. 5-4b are applicable for deriving flange yield moment and plastic moment.

$$M_{yf} = S_x F_{yf} \quad (5-3a)$$

$$M_{yf} = S_x F_{yf} - (1/2)(A_{wy})(F_{yf} - F_{yw})(d_{wy}) \quad (5-3b)$$

where

M_{yf} is the flange yield moments, Eq. (5-3a) is applicable to

homogeneous I section, Eq. (5-3b) is applicable to hybrid I section

$A_{wy} = (h - 2t_f - h_{we})(t_w)$ is the area of the yielded web at the flange
yield moment M_{yf} in hybrid I-section

$d_{wy} = 2 \cdot \left[\frac{2}{3}(h/2 - t_f - h_{we}/2) + h_{we}/2 \right]$ is the distance between the

centroid of the yielded web section at flange yield moment in hybrid I-section

$h_{we} = \frac{F_{yw}}{F_{yf}} \cdot h$ is the elastic web height in hybrid I-section

F_{yf} is the flange yield strength

F_{yw} is the web yield strength

$$M_p = Z_x F_{yf} \quad (5-4a)$$

$$M_p = Z_{xf} F_{yf} + Z_{xw} F_{yw} \quad (5-4b)$$

where

M_p is the plastic moment, Eq. (5-4a) is applicable to homogeneous I section, Eq. (5-4b) is applicable to hybrid I section

$Z_x = Z_{xf} + Z_{xw}$ is plastic section modulus about x-x' axis

$Z_{xf} = (A_f / 2)(d - t_f)$ is the flange plastic section modulus

$Z_{xw} = (A_w / 2)[(1/2) \cdot (d - t_f)]$ is the web plastic section modulus

For normalizing the measured end rotation (θ , Eq. 5-5), the elastic rotation (θ_p) and deflection (Δ_p) at plastic moment achieved are calculated by the Eq. 5-6.

$$\theta = \frac{(\Delta_1 - \Delta_2)}{b_{12}} \quad (5-5)$$

where

Δ_1, Δ_2 is measured vertical displacement for end rotation

b_{12} is the longitudinal distance of the two measurement instruments

$$\theta_{p,e} = \left(\frac{1}{2}\right) \cdot \phi_{p,e} \cdot L_{ui} \quad (5-6a)$$

$$\Delta_{p,e} = \left[\left(\frac{1}{2} \right) \cdot \phi_{p,e} \cdot L_{ui} + \left(\frac{1}{3} \right) \cdot \phi_{p,e} \cdot L_{gr} \right] \cdot L_{gr} \quad (5-6b)$$

where

$\phi_{p,e} = M_p / EI$ is elastic curvature at plastic moment achieved

The cross-section rotation (γ) and the lateral bending curvature (ϕ_{LT}) are calculated by Eq. 5-7.

$$\gamma = \frac{(\Delta_L - \Delta_R)}{b_{LR}} \quad (5-7a)$$

$$\phi_b = \frac{(\varepsilon_L - \varepsilon_R)}{b_{LR}} \quad (5-7b)$$

where

γ is cross section rotation

ϕ_b is lateral bending curvature

Δ_L, Δ_R are measured vertical displacements for cross section rotation

$\varepsilon_L, \varepsilon_R$ are longitudinal strains for cross section rotation

b_{LR} is the transverse distance of two measurement instruments

The effective length factor (k), the effective lateral slenderness ($k \cdot L_b / r_y$) and the normalized slenderness ($\overline{\lambda}_{LT}$) are calculated by Eq. 5-8, Eq. 5-9 and Eq. 5-10 respectively.

$$\phi_b(z_i) = 0, \quad \phi_b(z_j) = 0 \quad (5-8a)$$

$$k = \frac{z_j - z_i}{L_b} \quad (5-8b)$$

where

z_i, z_j is the longitudinal location where lateral bending curvature is

zero

k is effective (lateral bending) length factor adjusted by L_b and

$$\frac{L_{aj}}{r_y} = \frac{k \cdot L_b}{r_y} \quad (5-9)$$

where

$\frac{k \cdot L_b}{r_y}$ is the effective slenderness ratio

k is effective (lateral bending) length factor

L_b is unbraced length for LTB testing

$$\lambda = \sqrt{\frac{M_p}{M_e}} \quad (5-10)$$

where

$M_e = \frac{\pi}{k_y \cdot L_b} \sqrt{(EI_y)(GJ) + \frac{\pi^2 (EI_y)(EC_w)}{(k_z \cdot L_b)^2}}$ is the elastic LTB strength in the

given unbraced length L_b

L_b is unbraced length for LTB testing

5.1.4 Description of test parameter

Table 5.3 summarized the parameters being tested in this study. Geometrical parameter is designated as [G: H- depth x width x web thickness x flange thickness], the representation of which follows the Korea industrial standard. Material parameter is designated as [M: Ho- F_{yw} - F_{yf}] or [M: Hy- F_{yw} - F_{yf}]. The yield strength of flange and web are designated as F_{yf} and F_{yw} . When the yield strength of flange and web is identical the I-section are designated as [Ho] abbreviated from homogeneous. Otherwise, the yield strength of flange and web is different the I-section are designated as [Hy] abbreviated from

hybrid.

Many factors have been considered to determine of the test specimens. The first geometrical consideration is the height-to-width ratio (H/B). As specified in the lateral torsional buckling curve in EC 3, a welded cross section, the height-to-width ratio of which is higher than 2 ($H/B \geq 2$), is designated to follow the most disadvantageous buckling curve D. On the other hand, a welded cross section, the height-to-width ratio is lower than 2 ($H/B \leq 2$), is indicated to follow buckling curve C.

The second geometrical consideration is the web height-to-thickness ratio (h/t_w). As observed in earlier analytical studies, the I-section with relatively thicker web (=compact) shows the higher buckling strength and the rotation capacity at the identical slenderness. The high performance of the I-section is come from the fact that the web thickness reinforcement contribute to increase the effective rigidities $[(EI_y)_e$ and $(GJ)_e]$ in inelastic ranges while the external force (=in-plane moment strength) are slightly increase.

The third materialistic consideration is the hybrid I-section. As [Mitsuru et al. \(2005\)](#) experimentally observed the hybrid I-section have more inelastic rotation capacity compared to homogenous I-section. Also, as observed in earlier analytical studies, the hybrid I-section would show the higher buckling strength and the rotation capacity at the identical slenderness. The reason of the higher performance is that the effective rigidities of hybrid I-section are

slightly decreased or marginally same as compared to that of homogeneous I-section, however the relative effect of the reduced external force (M_0) is significant.

Fig. 5-5a and Fig. 5-5b show the section and length of the test specimens. Test specimens [H-250x150x15x15] and [H-400x150x15x15] were fabricated with the flange and web plates cut from the same 15mm HSA800 plate. The longitudinal partial joint penetration (PJP) welds joining the flange and web plate were made using gas-shielded, flux-cored arc welding (FCAW). Fillet welds used to attach the bearing stiffener plates by the FCAW process. Full height stiffener was applied at the loading pint and at the reaction points except specimens S6 where the partial height stiffener was applied at the loading point.

Fig. 5-5c shows the section and length of the test specimens. Test specimens [H-350x150x30x25] were fabricated with the flange and web plates cut from the same 30mm SM490 plate and 25mm HSA800 plate. The longitudinal PJP welds joining the flange and web plate were made using gas-shielded, flux-cored arc welding (FCAW). Fillet welds used to attach the bearing stiffener plates by the FCAW process. Full height stiffener was applied at the reaction points and the partial height stiffener was applied at the loading point, by expecting the large plastic rotation at the location.

The specimens with [G: H-250x150x15x15] and [M: Ho- F_{yw} - F_{yf} =775], the height-to-width ratio is 1.67. The yield moment (M_{yf}) and plastic moment (M_p)

are 468.2 KN-m and 550.4 KN-m respectively. The (weak-axis) flexural rigidities, warping rigidities and torsional rigidities are $8,499,375 \cdot E$ [$N \cdot mm^2$], $116,490,234,375 \cdot E$ [$N \cdot mm^4$] and $601,875 \cdot E$ [$N \cdot mm^2$] respectively. The ratio flexural rigidities, warping rigidities and torsional rigidities to plastic moment are 3,165 [mm], 43,384,084 [mm^3], and 86 [mm] respectively.

The specimens with [G: H-400x150x15x15] and [M: Ho- $F_{yw}=F_{yf}=775$], the height-to-width ratio is 2.67. The yield moment (M_{yf}) and plastic moment (M_p) are 891.8 KN-m and 1,069.2 KN-m respectively. The (weak-axis) flexural rigidities, warping rigidities and torsional rigidities are $8,541,563 \cdot E$ [$N \cdot mm^2$], $312,662,109,375 \cdot E$ [$N \cdot mm^4$] and $770,625 \cdot E$ [$N \cdot mm^2$] respectively. The ratio flexural rigidities, warping rigidities and torsional rigidities to plastic moment are 1,638 [mm], 59,946,849 [mm^3], and 57 [mm] respectively. Comparing with the value of Type A, the ratios of flexural, warping and torsional rigidities are $0.52(=1,638/3,165)$, $1.38(=43,384,084/59,946,849)$, $0.66(=57/86)$ respectively.

The specimens with [G: H-350x150x30x25] and [M: Ho- $F_{yw}=349, F_{yf}=822$], the height-to-width ratio is 2.34. The yield moment (M_{yf}) and plastic moment (M_p) are 1,120.7 KN-m and 1,243.5 KN-m respectively. The (weak-axis) flexural rigidities, warping rigidities and torsional rigidities are $14,737,500 \cdot E$ [$N \cdot mm^2$], $371,337,890,625 \cdot E$ [$N \cdot mm^4$] and $4,487,500 \cdot E$ [$N \cdot mm^2$] respectively. The ratio flexural rigidities, warping rigidities and torsional rigidities to plastic moment are 2,430 [mm], 61,218,669 [mm^3], and 285 [mm]

respectively. Comparing with the value of Type A, the ratios of the flexural, warping and torsional ratios are $0.77(=2,430/3,165)$, $1.41(=61,218,669/43,384,084)$, $3.31(=285/86)$ respectively.

5.2 Experimental test results

In this chapter, the experimental test results of the specimens are described. As summarized in Table 5.4, three specimens with [G: H-250x150x15x15] and [M: Ho- $F_{yw}=F_{yf}=775$] were tested with given effective slenderness ratio ($k \cdot L_b/r_y$) 84.8, 72.7 and 30.0 respectively; Three specimens with [G: H-400x150x15x15] and [M: Ho- $F_{yw}=F_{yf}=775$] were tested with the given effective slenderness ratio ($k \cdot L_b/r_y$) 96.0, 34.0 and 28.8 respectively. Four specimens with [G: H-350x150x30x15] and [M: Ho- $F_{yw}=349$, $F_{yf}=722$] were tested with the given effective slenderness ratio ($k \cdot L_b/r_y$) 93.7, 80.3, 33.1 and 28.1 respectively.

Fig. 5-6b, Fig. 5-8b and Fig. 5-10b show the cross section rotation (γ) and the lateral bending curvature (ϕ_{LT}) of tested specimens. As pointed out, the on-set of lateral instability was well measured by the installed instrumentation. However, the tendency of the cross section rotation for specimens with [G: H-350x150x30x15] and [M: Hy- $F_{yw}=349$, $F_{yf}=722$] showed less accurate result than expected. The results were result from the different anchoring methods at the specimens. In detail, at the specimens with type A and B, the settlement of

the thread, connecting the end of LVDTs and tension flanges of the specimens, are established by tying the wire on the face of the threaded portion of anchored screw bolts via tightening two nuts. While, at the specimens with type C, the settlement of the thread, are established by tying the wire on slippery face of the anchored ring, which connected to the screw bolts. Therefore, the lateral instability of specimen type A and B are reported by the data from the cross section rotation (γ) and that of specimen type C are reported by the data from the lateral bending curvature (ϕ_{LT}).

5.2.1 Specimen Type A: [G: H-250x150x15x15]-[M: H0-775]

5.2.1.1 Failure modes

Fig. 5-6c shows the failure modes of specimen type A. All specimens are failed by the inelastic LTB buckling. As described in the analytical studies, the in-plane behaviors were curtailed or prevented when LTB was triggered in the specimens, resulting in limited strength and rotation capacities. The behavior could be generalized as below. At the low loading level such as $M/M_p \leq 0.5$, the specimens shows the in-plane behavior and no specific LTB were observed. As the loading level is increased and become the load level equal to critical buckling strength ($M/M_{cr} \approx 1.0$) according to unbraced length, the specimens start to bifurcate and sinusoidal deformed shapes are investigated.

Fig. 5-7 shows the out-of-deformations measured at the top flanges, bottom flanges and web. At the top flanges, identical compressive strains are measured prior to bifurcation point. However, after LTB occurred, the measured compressive strains become different as below. For the strain located at the LTB triggered side, the additional compressive strain is induced because of the out-of-plane behavior. In contrast, for the strain located at the other side, the addition tensile strain is induced because of the out-of-plane behavior. The difference between two measured strains is significantly magnified as the magnitudes of the out-of-plane behavior are increased.

Similarly, at the bottom flanges, identical tensile strains are measured prior to bifurcation point. After LTB was occurred the measured tensile strains become different as below. For the stain located at the LTB triggered side, the additional tensile strain is induced because of the out-of-plane behavior. For the strain located as the other side, the additional compressive strain is induced because of the out-of-plane behavior. The difference between two measured strains is significantly magnified as the magnitudes of the out-of-plane behavior are increased.

At the web, where strain gauges are located along the height, the strains shows linearly increased strain distributions prior to bifurcation point. However, after LTB occurred, the linearly increased strain distribution could not be maintained, resulting in altered strain distributions.

5.2.1.2 Measured strength and rotation capacities

Fig. 5-6a and shows the moment (M/M_p) versus end rotation (θ/θ_p) behaviors and Fig. 5-6b shows the cross section rotation (γ) versus end rotation (θ/θ_p) respectively. Table 5-4 summarized the results. At the given effective slenderness ratios ($k \cdot L_b/r_y$) 84.8, 72.7 and 30.0, the on-set of the lateral instability (=bifurcation) are measured at the end rotation (θ_{cr}/θ_p) 1.3, 1.6 and 2.2 respectively. The critical buckling strengths (M_{cr}/M_p), measured strength at the on-set of the lateral instability, are 0.90, 1.01 and 1.08 respectively. The inelastic instability strengths (M_m/M_p), measured strength at the maximum strength, are 1.00, 1.16 and 1.18 respectively. The post-buckling strengths ($(M_m - M_{cr})/M_p$) are 0.10, 0.15 and 0.10 respectively.

The rotation capacities at the maximum strength (R_m) in the ascending part are 0.67, 2.00 and 2.67 respectively. The rotation capacities at the nominal strength (R_n) in the descending part are 0.67 for specimen A-S, 2.50 for specimen A-2. For specimens A-3, the rotation capacities at the nominal strength could not be measured since the tension flange crack at the vicinity of the HAZ of the full height stiffeners significantly curtailed the inelastic rotations. It should have applied partial height stiffener at the loading point, since the full height stiffener was not recommend at the expected large plastic rotation points as specified in the specifications.

5.2.2 Specimen Type B: [G: H-400x150x15x15]-[M: H0-775]

5.2.2.1 Failure modes

Fig. 5-8c shows the failure modes of specimen type B. All specimens are failed by the elastic or inelastic LTB buckling. As described in the analytical studies, the in-plane behaviors were curtailed or prevented when LTB was triggered in the specimens, resulting in limited strength and rotation capacities. The behavior could be generalized as below. At the low loading level such as $M/M_p \leq 0.5$, the specimens shows the in-plane behavior and no specific LTB were observed. As the loading level is increased and become the load level equal to critical buckling strength ($M/M_{cr} \approx 1.0$) according to unbraced length, the specimens start to bifurcate and sinusoidal deformed shapes are investigated.

Fig. 5-9 shows the out-of-deformations measured at the top flanges, bottom flanges and web. At the top flanges, identical compressive strains are measured prior to bifurcation point. However, after LTB occurred, the measured compressive strains become different as below. For the strain located at the LTB triggered side, the additional compressive strain is induced because of the out-of-plane behavior. In contrast, for the strain located at the other side, the addition tensile strain is induced because of the out-of-plane behavior. The difference between two measured strains is significantly magnified as the magnitudes of the out-of-plane behavior are increased.

Similarly, at the bottom flanges, identical tensile strains are measured prior to bifurcation point. After LTB was occurred the measured tensile strains become different as below. For the stain located at the LTB triggered side, the additional tensile strain is induced because of the out-of-plane behavior. For the strain located as the other side, the additional compressive strain is induced because of the out-of-plane behavior. The difference between two measured strains is significantly magnified as the magnitudes of the out-of-plane behavior are increased. As compared with the specimen type A, the magnitudes are relatively severe, indicating that severe LTB triggered in the type B specimens.

At the web, where strain gauges are located along the height, the strains shows linearly increased strain distributions prior to bifurcation point. However, after LTB occurred, the linearly increased strain distribution could not be maintained, resulting in altered strain distributions. As compared with the specimen type A, the magnitude of altered distribution is relatively severe, indicating that sever LTB triggered in the type B specimens.

5.2.1.2 Measured strength and rotation capacities

Fig. 5-8a and **Fig. 5-8b** shows the moment (M/M_p) versus end rotation (θ/θ_p) behaviors and the cross section rotation (γ) versus end rotation (θ/θ_p). **Table 5-2** summarized the results. At the given effective slenderness ratios ($k \cdot L_b/r_y$) 96.0, 34.0 and 28.8, the on-set of the lateral instability (=bifurcation) are

measured at the end rotation (θ_{cr}/θ_p) 0.9, 1.4 and 1.8 respectively. The critical buckling strengths (M_{cr}/M_p), measured strength at the on-set of the lateral instability, are 0.66, 0.98 and 1.04 respectively. The inelastic instability strengths (M_m/M_p), measured strength at the maximum strength, are 0.86, 1.10 and 1.12 respectively. The post-buckling strengths ($(M_m - M_{cr})/M_p$) are 0.20, 0.12 and 0.08 respectively.

The rotation capacities at the maximum strength (R_m) in the ascending part are 0.85 for specimens B-2 and 1.25 for specimen B-3 respectively. The rotation capacities at the nominal strength (R_n) in the descending part are 1.32 for specimen B-2 and 1.77 for specimen B-3. For specimens B-1, the rotation was not reported since the measured strength does not achieve the plastic moment strength (M_p).

By comparing the specimens type A and type B, type B specimens showed a sudden drop after reaching the peak moment, while type A specimens were able to sustain the moments. This phenomenon indicate that the increased plastic moment (=external force or required buckling strength) without increased the flexural rigidities, warping rigidities and torsional rigidities together will have less inelastic rotation capacity at the same tested condition as shown in this study, which are already discussed in analytical studies. Also, the second order loading effect after the initiation of the LTB needs to be investigated for further researches.

5.2.3 Specimen Type C: [G: H-350x150x30x25]-[M: Hy-349-827]

5.2.3.1 Failure modes

Fig. 5-10c shows the failure modes of specimen type C. All specimens are failed by the elastic or inelastic LTB buckling. As described in the analytical studies, the in-plane behaviors were curtailed or prevented when LTB was triggered in the specimens, resulting in limited strength and rotation capacities. The behavior could be generalized as below. At the low loading level such as $M/M_p \leq 0.5$, the specimens shows the in-plane behavior and no specific LTB were observed. As the loading level is increased and become the load level equal to critical buckling strength ($M/M_{cr} \approx 1.0$) according to unbraced length, the specimens start to bifurcate and sinusoidal deformed shapes are investigated.

Fig. 5-11 shows the out-of-deformations measured at the top flanges and web. At the top flanges, identical compressive strains are measured prior to bifurcations point. However, after LTB occurred, the measured compressive strains become different as below. For the strain located at the LTB triggered side, the additional compressive strain is induced because of the out-of-plane behavior. In contrast, for the strain located at the other side, the addition tensile strain is induced because of the out-of-plane behavior. The difference between two measured strains is significantly magnified as the magnitudes of the out-of-plane behavior are increased. As compared with the specimen type

A, the magnitudes are relatively less severe, indicating that less severe LTB triggered in the type C specimens

At the web, where strain gauges are located along the height, the strains shows linearly increased strain distributions prior to bifurcation point. However, after LTB occurred, the linearly increased strain distribution could not be maintained, resulting in altered strain distributions. As compared with the specimen type A, the magnitude of altered distribution is relatively less severe, indicating that less sever LTB triggered in the type C specimens.

5.2.3.2 Measured strength and rotation capacities

Fig. 5-11a and Fig. 5-11b shows the moment (M/M_p) versus end rotation (θ/θ_p) behaviors and the cross section rotation (γ) versus end rotation (θ/θ_p). Table 5-2 summarized the results. At the given effective slenderness ratios ($k \cdot L_b/r_y$) 93.7, 80.3, 33.1 and 28.1, the on-set of the lateral instability (=bifurcation) are measured at the end rotation (θ_{cr}/θ_p) 1.6, 2.1, 3.1 and 3.5 respectively. The critical buckling strengths (M_{cr}/M_p), measured strength at the on-set of the lateral instability, are 1.05, 1.05, 1.16 and 1.15 respectively. The inelastic instability strengths (M_m/M_p), measured strength at the maximum strength, are 1.08, 1.07, 1.17 and 1.21 respectively. The post-buckling strengths ($(M_m - M_{cr})/M_p$) are 0.03, 0.02, 0.01 and 0.06 respectively. The rotation capacities at the maximum strength (R_m) in the ascending part are

1.25, 1.98, 3.00 and 4.00 respectively. The rotation capacities at the nominal strength (R_n) in the descending part are 1.60, 3.80, 4.60 and 5.40 respectively.

As compared to the specimens type A and type B, type C specimens showed larger inelastic rotation capacity at the same tested condition. This phenomenon indicate that the relatively higher effective rigidities values as compared to the plastic moment (=external force or required buckling strength) lead the superior inelastic rotation capacity. Therefore, the dimension and the materials of I-shaped beams should be determined by considering both effective inelastic rigidities and plastic moment simultaneously in order to achieve higher inelastic rotation capacity, as discussed in analytical studies. In addition, it seems that, as indicated by Mitsuru et al. (2005), the large yield region in the web plate of hybrid I-girder contribute a larger inelastic rotation than that of homogeneous I-girder.

5.3 Evaluation of the experimental results

In this chapter, the present test results are analyzed in three aspects.

1) First, the present test results are compared with the design value specified in the AISC spec. and EC 3. By comparing the value, the possibility whether the current code would applicable to the high strength steel are could evaluated.

2) Second, the present test results are compared with the previous LTB

experiments available. Although the information of the previous test results is limited or rare, the available test results are modified to make those results comparable with the present test results.

3) Third, the present test results are compared with the analytically developed buckling curve in chapter IV. By comparing the results, the validity of the analytical studies are estimated.

5.3.1 Comparison with the code prediction

5.3.1.1 AISC-LTB strength curve

Fig. 5-12a~14a compared the present critical buckling strengths with the design value specified in the AISC spec. As shown the figures, current AISC spec. predicts conservative buckling strength to all specimens. However, depending on the section types, the code predicts different load levels as compared to measured buckling strength.

For specimens type A, where the effective rigidities to plastic moment ratios are relative high, at the given effective slenderness ratios ($L_b/r_y L_b / r_y$) 93.7, 80.3, 33.1 and 28.1, AISC predict the buckling strength 0.68, 0.73 and 0.93 respectively. The measured critical buckling strengths (M_{cr}/M_p), measured strength at the on-set of the lateral instability, are 0.90, 1.01 and 1.08 respectively. The measured buckling strength to AISC predicted buckling strength ratios are 1.32, 1.38 and 1.16 respectively.

For specimens type B, where the effective rigidities to plastic moment ratios are relatively low, at the given effective slenderness ratios (L_b/r_y) 96.0, 34.0, and 28.8, AISC predict the buckling strength 0.58, 0.90 and 0.93 respectively. The measured critical buckling strengths (M_{cr}/M_p) are 0.66, 0.98 and 1.04 respectively. The measured buckling strength to AISC predicted buckling strength ratios are 1.14, 1.09 and 1.12 respectively, indicating that the current code predict less conservative values as compared to specimen type A. As indicated in the analytical studies, the specimens with high height to width ratio [G: Type B] without the reinforcement such as compact web or compact flange I-section showed inferior buckling strengths than that of other specimens. It should be noted that as specified in the lateral torsional buckling curve in EC 3, a welded cross section, the height-to-width ratio of which is higher than 2 ($H/B \geq 2$), is designated to follow the most disadvantageous buckling curve D. On the other hand, a welded cross section, the height-to-width ratio is lower than 2 ($H/B \leq 2$), is indicated to follow buckling curve C.

For specimens type C, where the effective rigidities to plastic moment ratios are relatively high, at the given effective slenderness ratios (L_b/r_y) 93.7, 80.3, 33.1 and 28.1, AISC predict the buckling strength 0.76, 0.80, 0.94 and 0.96 respectively. The measured critical buckling strengths (M_{cr}/M_p) are 1.05, 1.05, 1.16 and 1.15 respectively. The measured buckling strength to AISC predicted buckling strength ratios are 1.38, 1.31, 1.23 and 1.20 respectively,

indicating that the current code predict more conservative values as compared to specimen type B. As indicated in the analytical studies, the specimens with the high effective rigidities to plastic moment ratios showed superior buckling strengths than that of other specimens.

5.3.1.2 AISC-Specified rotation capacity curve

Fig. 5-12b~14b compared the rotation capacity with the L_p specified in the AISC spec. The rotation capacities were measured at the nominal strength (R_n) in the descending part of the moment-rotation curves. As shown the figures, current AISC spec. L_p predicts different levels of rotation capacities depending on the geometrical shapes of I-section. For specimens type A, where the effective rigidities to plastic moment ratios are relatively moderate, the current L_p predicts the rotation capacities 3.0 or higher level. For specimens type B, where the effective rigidities to plastic moment ratios are relatively low, the current L_p predicts the rotation capacities 2.0 or lower level. For specimens type C, where the effective rigidities to plastic moment ratios are relatively high, the current L_p predicts the rotation capacities 5.0~6.0 or higher level.

In contrast to the mild steel experiments (Fig. 5-15b) and analytical studies (Fig. 4-42), where high rotation capacities such 7.0 or higher level could be ensured by the current AISC spec. L_p regardless of section types, careful considerations are required for determining a section type of high strength

steel I-shaped member to achieve rotation capacities 3.0 or higher level. The major reason such limited rotation capacities of the high strength steel I-shaped member are result from the early degradation of the effective rigidities under 5% of its initial elastic values as analyzed in chapter 4. On the other hand, the effective rigidities of the mild steel are decreased very slowly, which results in higher rotation capacities as shown in Fig. 4-16.

Considering the experimental and analytical studies, to ensure the rotation capacities 3 or higher level for HSA800 I-shaped member, specimens with low height to width ratios or relatively compact web I-section were recommended. Also, hybrid I-section where mild steel are applied in the web will be beneficial.

5.3.2 Comparison with the previous experiments

5.3.2.1 Buckling strength

Fig. 5-15 shows the present critical buckling strength with previous LTB experiments. Three experimental results 1) Fukumoto 1976 experiments: welded I-beam with [G: H-300x100x6x8], [G: H-250x100x6x8], [G: H-250x120x6x8] fabricated from [M: Ho- $F_{yw}=F_{yf}=336$]; 2) Fukumoto 1976 experiments: welded I-beam with [G: H-300x100x7x10], [G: H-250x100x7x10], [G: H-250x120x7x10] fabricated from [M: Ho- $F_{yw}=F_{yf}=769$]; 3) Fukumoto 1976 experiments: welded I-beam with [G: H-800x110x6x10], [G: H-800x130x6x10] fabricated from [M: Hy- $F_{yw}=650$, $F_{yf}=770$], [M: Hy-

$F_{yw}=460$, $F_{yt}=770$]; are selected to compare the LTB strength under uniform moment.

Fig. 5-15a shows the critical buckling strength of current experiments with the previous experiments: [G: H-300x100x6x8], [G: H-250x100x6x8], [G: H-250x120x6x8] fabricated from [M: Ho- $F_{yw}=F_{yt}=336$]. Similar phenomenons were investigated as analyzed early. Specimens with high height-to-width ratio [G: H-300x100x6x8], where effective rigidities to plastic moment is relatively low, the measured buckling strengths (M_{cr}/M_p) are relatively low as compared to other specimens. At the given lateral slenderness ratios (λ_{LT}) 0.807, 0.807, 1.048, 1.048, 1.161 and 1.61, the measured critical buckling strengths (M_{cr}/M_p) are 0.624, 0.757, 0.661, 0.566, 0.615 and 0.567 respectively. Whereas, specimens with low height-to-width ratio [G:H-250x120x6x8], where effective rigidities to plastic moment is relative high, the measured buckling strength (M_{cr}/M_p) are relatively high as compared to other specimens. At the given lateral slenderness ratios (λ_{LT}) 0.638, 0.638, 0.83, 0.83, 0.921 and 0.921, the measured critical buckling strengths (M_{cr}/M_p) are 0.872, 0.742, 0.798, 0.813, 0.861 and 0.659 respectively.

Also, it should be noted that the measured buckling strength distributions are far away from the elastic-plastic buckling curve, indicating that the residual stresses (also possibly geometrical imperfection) are influential on the inelastic buckling strength considerably.

Fig. 5-15b shows the critical buckling strength of current experiments with the previous experiment: [G: H-300x100x7x10], [G: H-250x100x7x10], [G: H-250x120x7x10] fabricated from [M: Ho- $F_{yw}=F_{yf}=769$]. Regardless of the high strength or mild strength steel, similar phenomenons were investigated. Specimens with high height-to-width ratio [G: H-300x100x7x10], where effective rigidities to plastic moment is relatively low, the measured buckling strengths (M_{cr}/M_p) are relatively low as compared to other specimens. At the given lateral slenderness ratios (λ_{LT}) 0.967, 1.142 and 1.31, the measured critical buckling strengths (M_{cr}/M_p) are 0.786, 0.669 and 0.62 respectively. Whereas, specimens with low height-to-width ratio [G:H-250x120x7x10], where effective rigidities to plastic moment is relative high, the measured buckling strength (M_{cr}/M_p) are relatively high as compared to other specimens. At the given lateral slenderness ratios (λ_{LT}) 0.766, 0.906 and 1.041, the measured critical buckling strengths (M_{cr}/M_p) are 0.887, 0.818 and 0.764 respectively.

Comparing with the previous [M: Ho- $F_{yw}=F_{yf}=336$] specimens, the measured buckling strength distributions are close to the elasto-plastic buckling curve, indicating that the influence of the residual stress to the inelastic buckling strength become less as the material strength of the parent material are increased. As discussed in previous chapter, the magnitude of the residual stresses (f_{rfc} , f_{rwc}) are about 40.8MPa and 175.0MPa respectively

although it depends on the section geometry and heat input in the arc-welding process. In general, the magnitude would not be increased unless higher heat input is performed in the arc welding process. Therefore, the effects of the residual stress become negligible as the parent metal strength are increased as shown in the experimental results.

Fig. 5-15c shows the critical buckling strength of current experiments with the previous experiment: [G: H-800x110x6x10], [G: H-800x130x6x10] fabricated from [M: Hy- $F_{yw}=650$, $F_{yf}=770$] and [G: H-800x110x6x10], fabricated from [M: Hy- $F_{yw}=460$, $F_{yf}=770$]. Similar phenomenons were investigated as the previous case. At the given lateral slenderness ratios (λ_{LT}) 1.1369, 1.164, 1.12, 0.952 and 1.272, the measured critical buckling strengths (M_{cr}/M_p) are 0.501, 0.649, 0.673, 0.764 and 0.59 respectively.

5.3.2.2 Rotation capacity

Fig. 5-16 shows the inelastic rotation capacities of current experiments with the previous experiment: [G: H-262x146x6x11], [G: H-254x102x6x6], [G: H-262x146x6x11] fabricated from [M: Ho- $F_{yw}=F_{yf}=241$], [M: Ho- $F_{yw}=F_{yf}=296$] and [M: Ho- $F_{yw}=F_{yf}=375$] respectively.

The rotation capacities of the member ensure 7~13 levels, depending on the specimen types, at the given lateral slenderness ratio ($\lambda_{LT}=0.2$). More specifically, the specimens with relatively low ($1.8=252/146$) height –to–width ratio such [G:H-262x146x6x11], where the effective rigidities to plastic

moment ratio is relatively high, the inelastic rotation capacities are relatively high such 13.0 level. Whereas, the specimens with relatively high ($2.5=254/102$) height –to-width ratio such [G:H-254x102x6x6], where the effective rigidities to plastic moment ratio is relatively low, the inelastic rotation capacities are relatively low such 7.0 level.

Meanwhile, specimens in current studies such [G:H-350x150x30x25,M:Ho-349-822] could not show such high rotation capacities. This phenomenon could be explained as follow. As investigated in the inelastic rigidities according to a curvature (Fig. 4-16), the values of the effective rigidities of mild steel such [M:Ho-296] or [M:Ho-375] material are decreased very slowly as compared to that of high strength steel such [M: Ho-822] or [M:Ho-722] materials, indicating that the mild steel have sufficient inelastic rigidities to resist high rotation capacities. By comparing the critical curvature (ϕ_{cr}) when the effective rigidities are under 5% of its initial elastic rigidities, which is very important to estimate the rotation capacity of a material, the ϕ_{cr} of the mild steel is about $10.0 \cdot \phi_y$. However, the ϕ_{cr} of the high strength steel is about $3.0 \cdot \phi_y$. Please note that the critical values are varied depending on the section geometries.

In summary, by analyzing the critical curvatures, this studies explain why the I-section of [M:Ho-722] is more vulnerable to LTB than that of [M:Ho-349] in terms of ensuring the rotation capacity. It also implies that for ensuring adequate rotation capacities such as $R=3.0$ in high strength steel, a

strategy or section selection to increase the effective rigidities to plastic moment ratio is required.

Fig. 5-17 shows the inelastic rotation capacities of current experiments with the previous experiment:

1) Rolled I-shapes member-[G: H-211.8x170.2x9.8x14.1], [G: H-211.8x141.7x9.7x14.4], [G: H-211.6x113.0x9.8x14.2] fabricated from [M: Ho- $F_{yw}=F_{yf}=824$].

2) Welded I-shapes member-[G: H-237.2x100.8x6.5x15.8], [G: H-238.3x150.9x6.8x15.7] fabricated from [M: Ho- $F_{yw}=F_{yf}=809$].

The rotation capacities of the member ensure 4~6 levels, depending on the specimen types, at the given lateral slenderness ratio ($\lambda_{LT}=0.2$). More specifically, the specimens with relatively low ($1.2=211.8/170.2$) height-to-width ratio such [G:H-211.8x170.2x9.8x14.1], where the effective rigidities to plastic moment ratio is relatively high, the inelastic rotation capacities are relatively high such 6.0 level. Whereas, the specimens with relatively high ($1.9=211.6/113.0$) height-to-width ratio such [G:H-211.6x113.0x9.8x14.2], where the effective rigidities to plastic moment ratio is relatively low, the inelastic rotation capacities are relatively low such 4.0 level.

As discussed previously, the experimental results clearly shows that the high strength steel show less rotation capacities as compared to mild steel at the given lateral slenderness ratio. Also, it proved that just closer bracing itself

could not ensure the high rotation capacities since the effective rigidities are rapidly decreased as the curvature becomes higher than 3.0 ranges.

For ensuring target rotation capacity such $R_n=3.0$ specified in AISC specification, low height-to-width ratio specimen or web compact or hybrid web strategies are inevitable. By applying the strategies, the high strength I-shaped member could ensure higher rotation capacity exceeding the target value ($R_n=3.0$).

5.3.3 Comparison with the analytically developed buckling curve

In this chapter, the experimental data will be compared to the analytically developed LTB curves (L_b versus M_{cr}) and inelastic rotation capacities curves (L_b versus R_m). Many LTB strength curves according to unbraced length were already proposed by many researchers, applying tangent modulus approach and conventional steel material model. However, those curves only treated the I-shaped member fabricated from mild steel plates and applying those curve to high strength steel are limited or unacceptable. In this study, the critical buckling strength curves for I-shaped member fabricated from high strength steel were developed. The curve adopted the tangent modulus approach and Ramberg-Osgood model, already described in detail in chapter IV.

Meanwhile, the rotation capacity curves according to unbraced length were

very rare. It seems that only Kemp (1996) recently propose the rotation capacity prediction curve by adopting the effective slenderness ratio. However, the curve is strongly depended on the statistical regression method and the effective slenderness ratio which excluding the material aspect could not well explain the high-strength I-shaped member behavior. As shown in Fig. 5-18a, even the curve statically predict the rotation capacity, numerous data are deviated or scattered from the curve. Whereas, the rotation capacity curve developed in this study, by considering the slenderness and material characteristic simultaneously, the rotation capacity of past experiments are well predicted as shown in Fig. 5-18b.

Fig. 5-19 shows the classification of the rotation capacities. First point is the rotation capacities at the bifurcation points (R_{cr}). The points indicate the initiation of buckles as reported in Fig. 5-6, Fig. 5-8 and Fig. 5-10. The analytically derived curve predicts the bifurcation points, therefore, exactly speaking, to compare the analytical developed rotation capacity curve with the experimental data, R_{cr} should be reported.

However, a number of researchers have been adopting the rotation capacities at the second points. The second point is the rotation capacities at the maximum moment (R_m). The points indicate the end rotation when the moment-rotation curves are reached at the maximum moment. It has been called “inelastic instability points”. By considering that the moment-deflection curves are in the middle of ascending branch even the bifurcation

(=start of buckle) is occurred, it seems to be reasonable estimations to measure the ductile capacity of a member.

Third point is the rotation capacities at the nominal moment (R_n). The points indicate that the end rotation when the moment-rotation curves are reached at the nominal moment after reaching the peak values. Current AISC code adopts the rotation capacities and requires the values are three times larger than that of elastic rotation ($R_n \geq 3.0$). However, the predictions of the rotation capacities are very complicated or unstable. The major reason such difficulties come from that the values are highly dependent on the experiment setting condition and the prediction by such F.E.M does not provide stable algorithm to predict the descending branch. Therefore, the rotation capacities at maximum moment (R_m) are seems to relevant data for this comparison.

Fig. 5-20 show the present critical buckling and rotation capacity with the analytically developed buckling curve for Type A specimens. In the analytical prediction curve, the effects residual stress are neglected since the effect of the residual stress become negligible as the yield strength of the parent material becomes high. At the given effective slenderness ratios (L_b/r_y) 84.8, 72.7 and 30.3, the analytically developed buckling curve predict the buckling strength 0.73, 0.77 and 0.92 respectively. The measured critical buckling strengths (M_{cr}/M_p) are 0.90, 1.01 and 1.08 respectively. The measured buckling strength to the predicted (analytically derived) buckling strength

ratios are 1.24, 1.31 and 1.17 respectively.

For the ductility, the experimentally measured rotation capacities are best fitted by multiplying the bifurcation prediction curve (A) with 2.5 values ($2.5 \cdot L_b$). It seems that specimens with low height-to-width ratios would show higher rotation capacities as predicted. In other words, even the bifurcation has been occurred in early stages, the inelastic instability points are reached at the late time, which is beneficial for ensuring high rotation capacities.

Fig. 5-21 show the present critical buckling and rotation capacity with the analytically developed buckling curve for Type B specimens. At the given effective slenderness ratios (L_b/r_y) 96.0, 34.0 and 28.8, the analytically developed buckling curve predict the buckling strength 0.55, 0.86 and 0.89 respectively. The measured critical buckling strengths (M_{cr}/M_p) are 0.66, 0.98 and 1.04 respectively. The measured critical buckling strengths (M_{cr}/M_p) are 0.90, 1.01 and 1.08 respectively. The measured buckling strength to the predicted (analytically derived) buckling strength ratios are 1.21, 1.14 and 1.17 respectively.

For the ductility, the experimentally measured rotation capacities are best fitted by multiplying the bifurcation prediction curve (A) with 1.8 values ($1.8 \cdot L_b$). It seems that specimens with high height-to-width ratios would show relatively lower rotation capacities as compared to that of specimen Type A.

Fig. 5-22 show the present critical buckling and rotation capacity with the analytically developed buckling curve for Type C specimens. At the given

effective slenderness ratios (L_b/r_y) 93.7, 80.3, 33.1 and 28.1, the analytically developed buckling curve predict the buckling strength 0.86, 0.89, 1.00 and 1.02 respectively. The measured critical buckling strengths (M_{cr}/M_p) are 1.05, 1.05, 1.16 and 1.15 respectively. The measured buckling strength to the predicted (analytically derived) buckling strength ratios are 1.22, 1.18, 1.16 and 1.13 respectively. For the ductility, the experimentally measured rotation capacities are best fitted by multiplying the bifurcation prediction curve (A) with 1.7 values ($1.7 \cdot L_b$).

In summary, for critical buckling strength, the derived curve predict the critical buckling strength (M_{cr}) with 10~20% conservative level as compared to measured buckling strength. Considering the tangent modulus approach are well-known for the conservative approximation, the prediction curve are seems to be acceptable. For rotation capacities, the derived curve predicts the rotation capacity rather conservative value for high strength steel, as compared to that of mild steel case, where accurate prediction were abled It seems that the different material characteristic of high strength steel such no-yield plateau and continuous hardening, would affect the reduced modulus (such elastic flange unloading at the half of the width) after LTB, giving conservation rotation capacity values at the prediction based on the tangent modulus approach (please note that the rotation capacity of the mild steel easily curtailed at the initiation of LTB, as shown in [Fig. 5-23](#) indicating that $R_{cr} \approx R_m$). Judging by the statistical approach only, the estimating the rotation

capacity with multiplying factor 1.5 in the analytically derived unbraced length seems to be acceptable for high strength steel for section height-to-width (H/B) ratio under 2.7.

5.4. Summary

1) Experimental studies on the elastic and inelastic LTB of welded I-shaped members have been performed with carefully measuring the in-plane and the out-of-plane behavior. The mechanical properties of the applied 15mm and 25mm thick high strength steel plates are $F_y=775\sim 825\text{MPa}$, $F_u=877\sim 937\text{MPa}$, $Y_R=0.88\sim 0.90$, and $E_R=12.4\sim 13.3$ respectively.

2) Three types of weld I-shaped specimens were designed by considering the geometrical and material effects such height-to-width ratios (d/b), relatively thick web or hybrid I-section on LTB behavior. The dimensions and material information of type-A, type-B, and type-C specimens are [G:H-250x150x15x15]-[M:Ho-775], [G:H-400x150x15x15]-[Ho-775], and [G:350x150x30x25]-[Hy:349-822], respectively. Classifying the specimens according to the effective rigidities to plastic moment ratios such as effective flexural and effective torsional rigidities ($(EI_y)_e/M_p$, $(GJ)_e/M_p$), type-A specimens have relatively large flexural rigidities and type-C specimens have relatively large torsional rigidities. However, type-B specimens have relatively low flexural and torsional rigidities, implying that they are expected

to be more vulnerable to buckling.

With regard to fabrication, all test specimens were fabricated from the 15mm and 25mm thick HSA800 plate and 30mm thick SM490 plate by flame cutting. To join the flange and web plates, longitudinal partial joint penetration welding was performed using a gas-shielded, flux-cored arc welding (FCAW) process.

3) All specimens failed by LTB, triggering the sinusoidal shape failure mode. By comparing the measured critical buckling strength (M_{cr}) with the current AISC specification and EC 3, the codes predict conservative buckling strength for all specimens. However, the prediction levels differ depending on the specimen types. In other words, the type-A and type -C specimens (where effective section rigidities to plastic moment ratios are relatively higher than those of type B), show a higher measured buckling strength level compared to that of the type B specimen.

4) By comparing the measured rotation capacity at nominal strength ($R_{n,ui}$) with the unbraced length limit for achieving the plastic moment (L_p) specified in the current AISC specification, the current limit predicts different level of rotation capacities depending on the type of specimen. For type A and type C specimens (where the effective section rigidities to plastic moment are relatively high), current L_p predicts the rotation capacities to be about a 3.0~5.5 level. However, for type B specimens (where the effective section rigidities to plastic moment are relatively low), the current unbraced length

limit predicts the rotation capacities to be about 2.0 or a lower level.

5) Previous LTB experiment (Fukumoto, 1976) were compared to the measured buckling strengths (M_{cr}) and a similar tendency has been reported. In other words, regardless of the yield strength of materials, specimens where the effective rigidities to plastic moment are relatively high, the measured buckling strength showed higher values compared to other specimens. In addition, in contrast to the mild steel I-members, the critical buckling strengths of the high strength I-members are closely distributed to the elasto LTB-plastic strength curve, even in the inelastic LTB ranges, implying that the influence of the residual stresses to the inelastic buckling strength become less or decrease as the yield strength of the parent material increases. It should be noted that the magnitude of the residual stress is not dependent on the yield strength of a material, but dependent on the section geometry and heat-input in the arc-welding processes.

6) By comparing the measured rotation capacities with previous LTB experiments (Lee and Galambos, 1962; Prasad and Galambos, 1963; Adams, Lay and Galambos, 1965), the lateral slenderness ratio ($\bar{\lambda}_{LT} = 0.2$) predicts rotation capacities of about a 7.0~13.0 level in mild steel I-shaped members, even for specimen types such height-to-width ratios:1.8~2.5. However, the current specimens (=high strength I-shaped member) could not show such high rotation capacities at the lateral slenderness ratio, $\bar{\lambda}_{LT} = 0.2$. Such

behaviors are well explained in analytical studies by analyzing the inelastic rigidities according to a curvature (ϕ). The major reason for these behaviors is that the inelastic effective rigidities of the mild steel decrease relatively slowly compared to those of high strength steel, where inelastic rigidities decrease rapidly as inelastic rotation capacity increases, indicating that mild steel I-shaped members have sufficient effective rigidities to resist such high rotation.

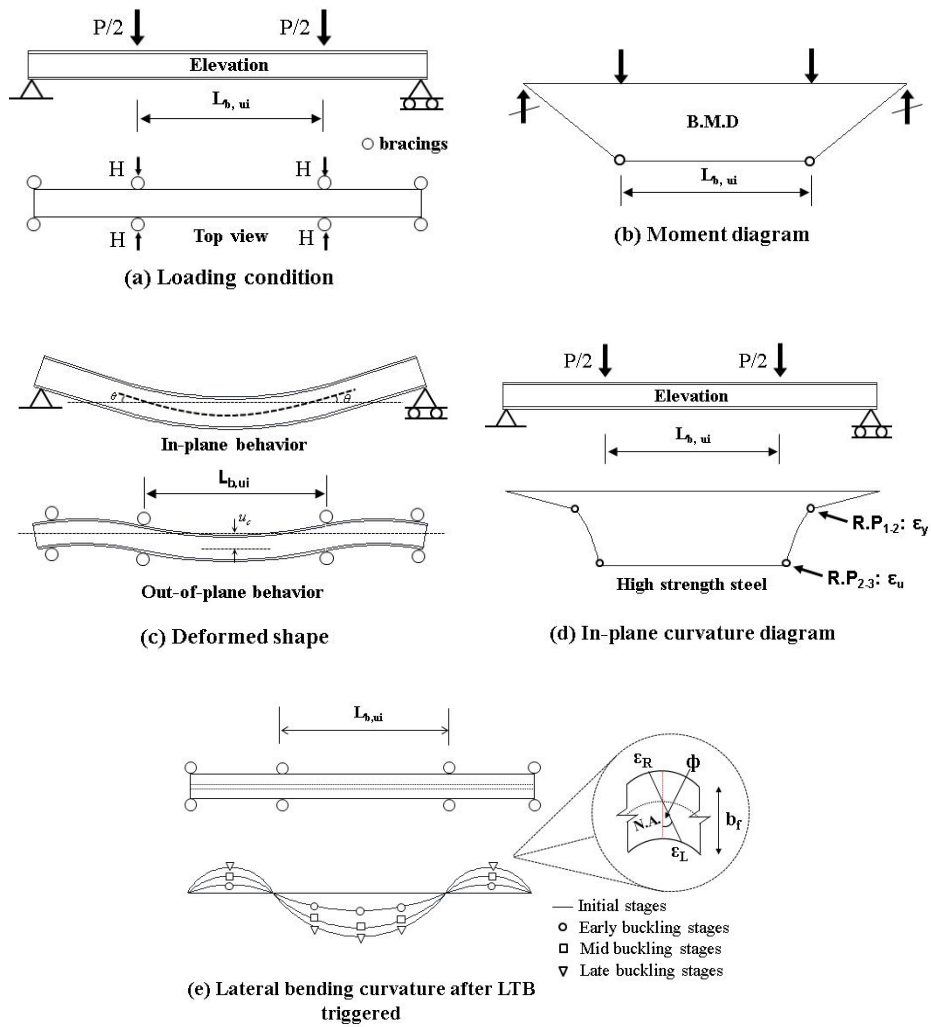
As discussed in the section 4.1, the critical curvature when the effective rigidities are less than 5% of the initial values ($\alpha_{2-3} = \beta_{2-3} = 0.05$), the critical curvature of the mild steel I-member is about 10.0 times of yield curvature ($\phi_{cr}(\alpha_{2-3, SM490}) = 10.0 \cdot \phi_y$), although the critical curvature of a high strength steel I-member is about 3.0 times of yield curvature ($\phi_{cr}(\alpha_{2-3, HSA800}) = 3.0 \cdot \phi_y$), even if the values fluctuate depending on the section geometries. Therefore, to ensure high rotation capacities for the high strength I-member, strategies to increase the effective rigidities to plastic moment ratios such as a low height-to-width ratios I-section or a relatively compact web or hybrid I-section are inevitable.

7) Derived buckling strength curve in chapter 4 were compared to the measured buckling strengths. The derived critical buckling curve predicts 10%~20% level conservative strengths compared to the measured buckling strength. Considering the tangent modulus approach is well-known for the

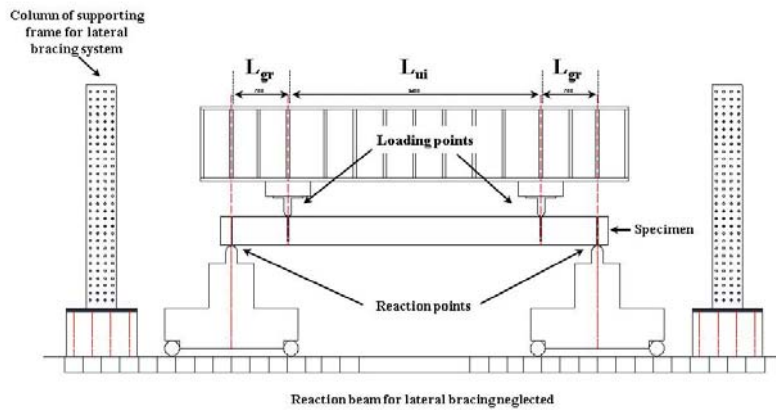
conservative approximation compared to the reduced modulus, the prediction curve seems to be acceptable.

For rotation capacities, the analytically derived curve well predicts the rotation capacity at bifurcation point (R_{cr}), however, the derived curve conservatively predicts the rotation capacity at maximum moment (R_m) for high strength I-shaped member. On the other hand, at the mild steel case, derived curve excellently predict the rotation capacity at maximum moment (R_m). It seems that the different material characteristics of high strength steel, such as no-yield plateau and continuous hardening, would affect the inelastic behavior after the initiation of bifurcation point (R_{cr}), giving further strength increase until R_m is reached. It should be noted that the rotation capacities of the mild steel are easily curtailed as the initiation of LTB, implying that the value of R_{cr} and R_m of mild steel would be very close. Therefore, further studies are required to accurately predict the rotation capacities (R_m) of high strength steel, by using such reduced modulus concept which consider the elastic flange unloading at half of the width in the I-section.

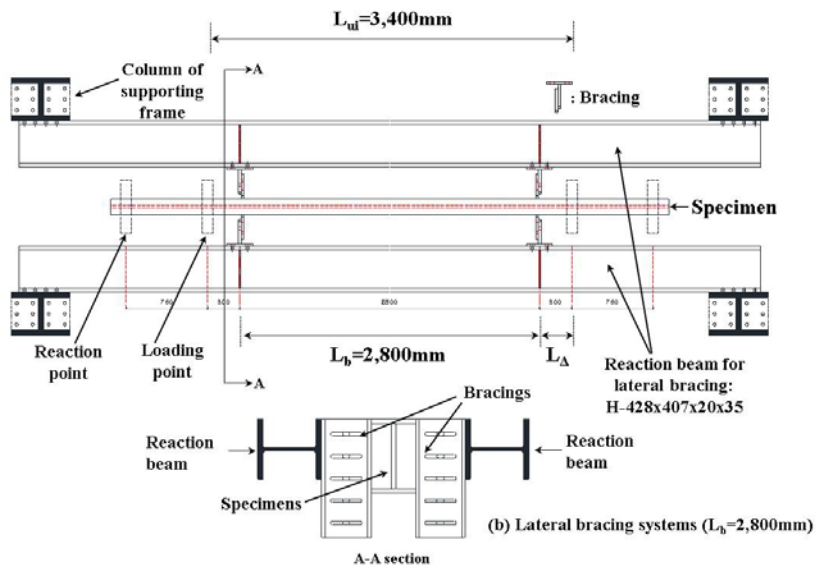
Judging by the statistical data only, estimating the rotation capacity at maximum moment (R_m) of high strength I-shaped member, where height-to-width ratios are under 2.7 (=400/150) level, would be conservatively predicted with a multiplying factor of 1.5 to the derived unbraced length ($L_{d,ui}$) in current study.



[5-1] Schematic overview of experimental LTB testing under uniform moment (a) Initial geometry (b) Moment diagram (c) Deformed shape (d) In-plane curvature diagram (e) Lateral bending curvature after LTB triggered

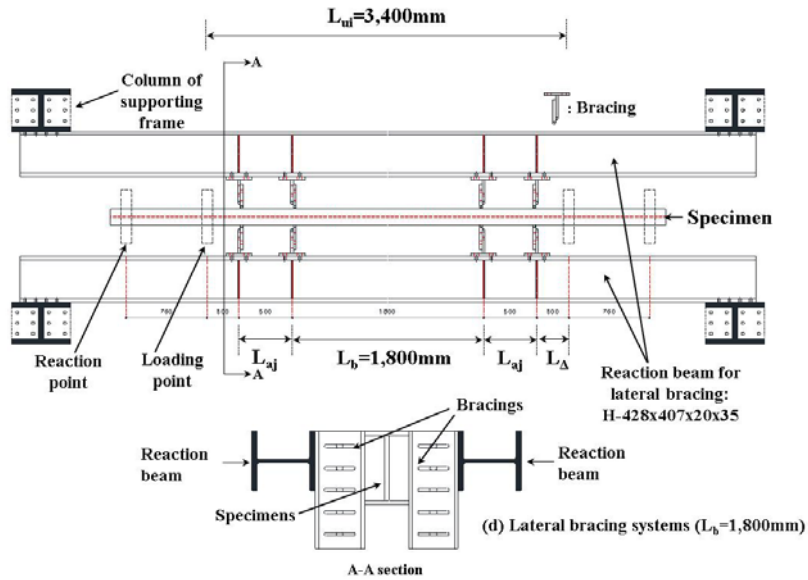
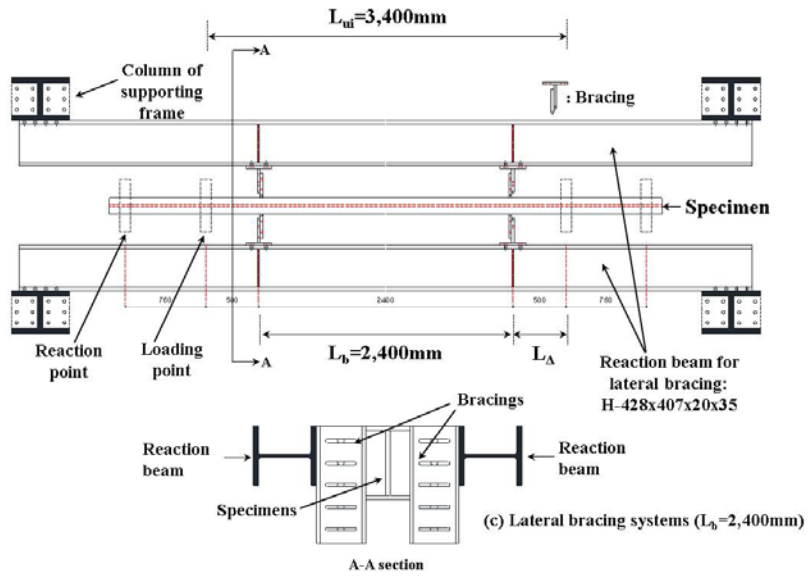


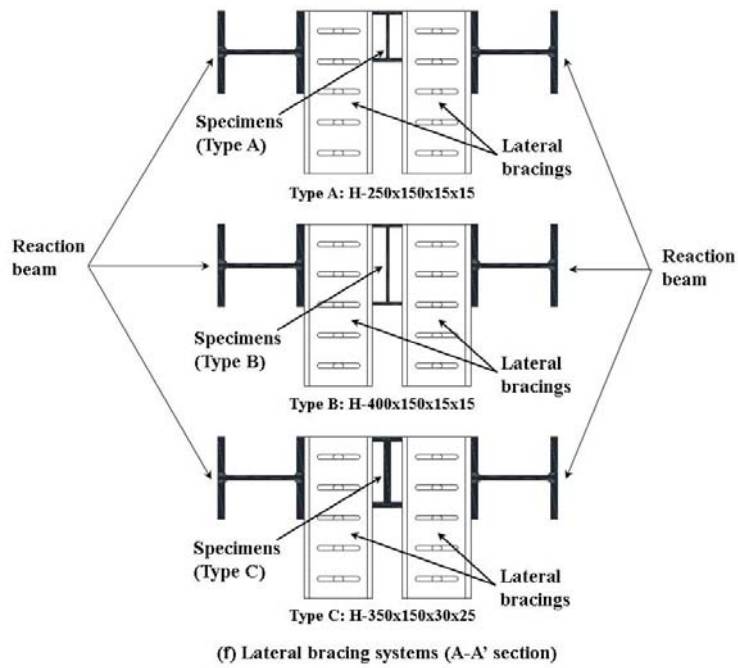
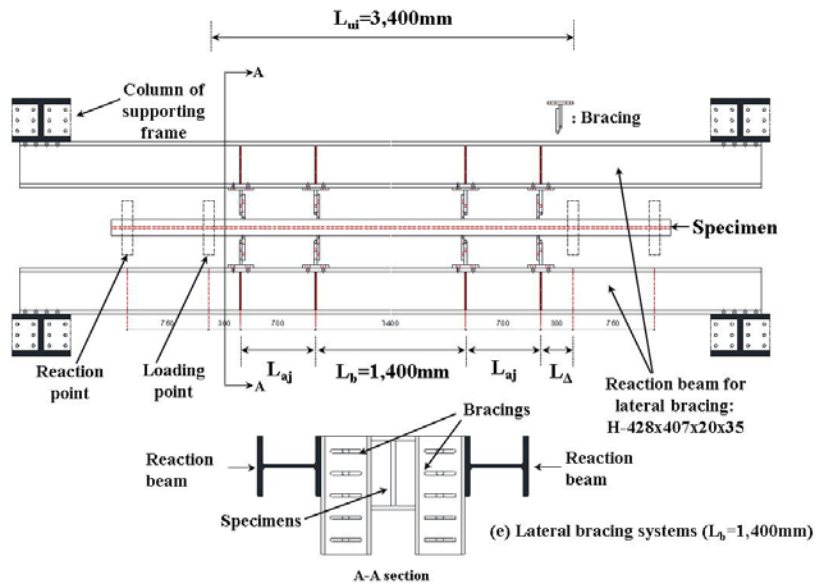
(a) Loading systems

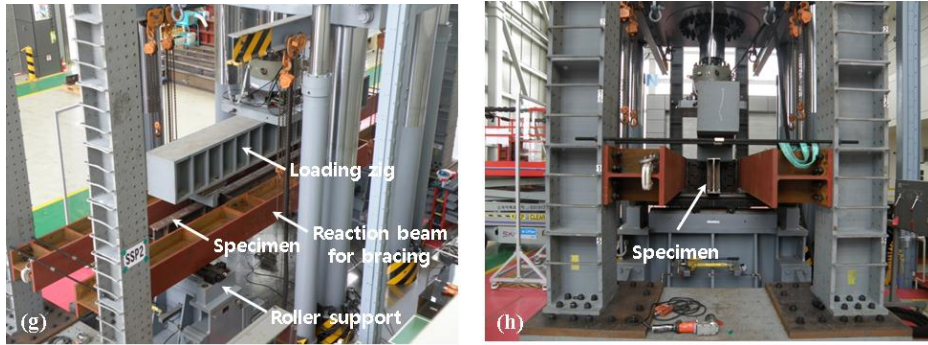


(b) Lateral bracing systems ($L_b=2,800\text{mm}$)

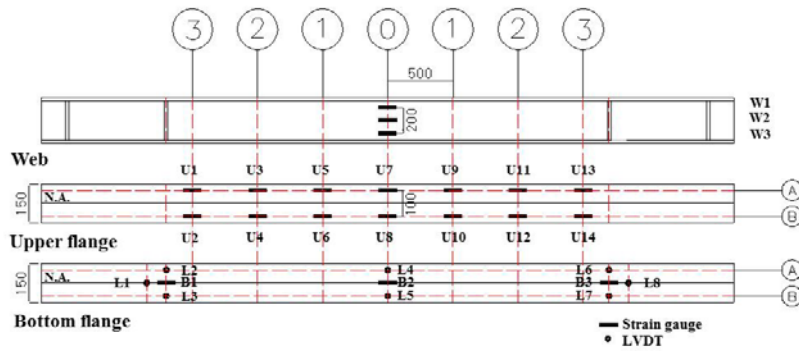
A-A section







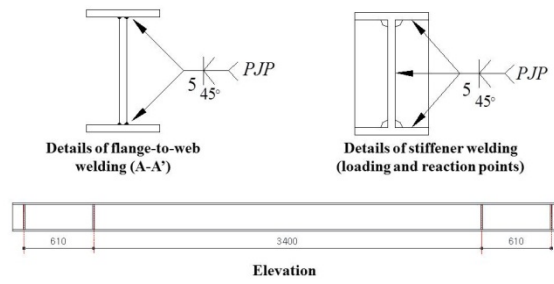
[5-2] Test set-up (a) Loading systems (b) Lateral bracing systems $L_b=2800\text{mm}$ (c) Lateral bracing systems $L_b=2400\text{mm}$ (d) Lateral bracing systems $L_b=1,800\text{mm}$ (e) Lateral bracing systems $L_b=1,400\text{mm}$ (f) Lateral bracing systems (A-A' section) (g) Overall view of test set-up (h) Side view of test set-up



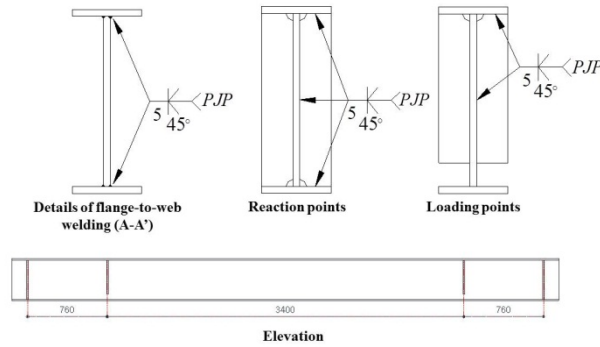
[5-3] Instrumentation plan for measuring In-plane and out-of-plan behavior



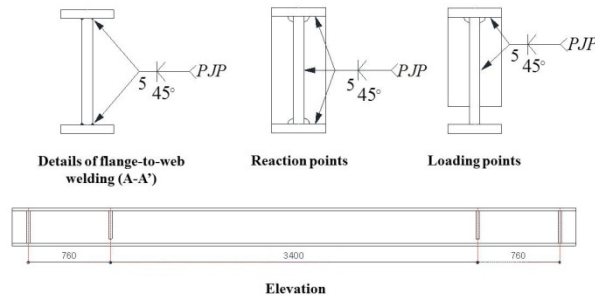
[5-4] Instrumentation for measuring out-of-plane behavior (LTB bifurcation) (a) Cross-section rotation measurements (b) Lateral bending curvature measurements



(a) Specimen [G: H-250x150x15x15]-[M:Ho-775]

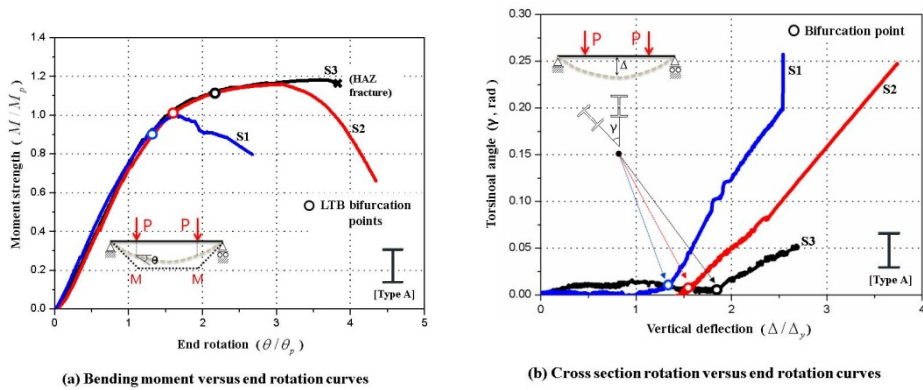


(b) Specimen [G: H-400x150x15x15]-[M:Ho-775]



(c) Specimen [G: H-300x150x30x25]-[M:Hy-349-775]

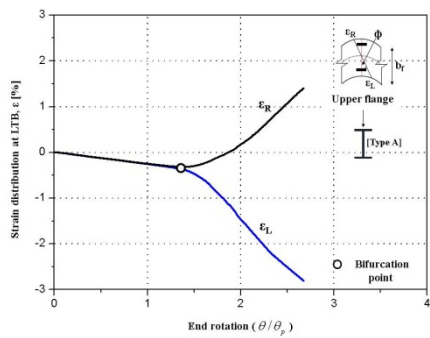
[5-5] Test specimens layout and fabrication details (a) Specimens [G: H-250x150x15x15]-[M: Ho-775] (b) Specimens [G: H400x150x15x15]-[M: Ho-775] (c) Specimens [G: 350x150x30x25]-[M: Hy-349-827]



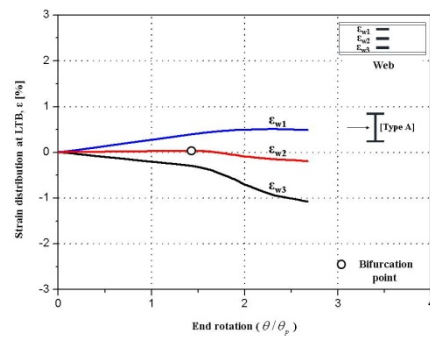
Specimen	LTB and failure mode	
S1		
S2		
S3		

(c) Failure modes

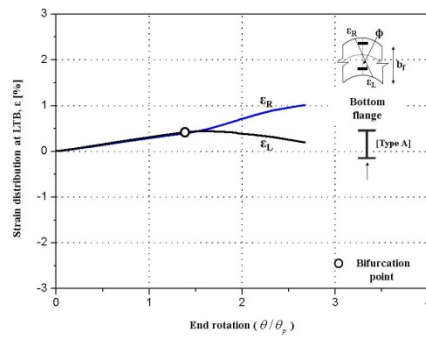
[5-6] Global responses of the specimens [G: H-250x150x15x15]-[M: Ho-775] (a) Bending moment versus end rotation curves (b) Cross section rotation versus center vertical deflection curves (c) Failure modes



(a) Strain response of the top flange (S1)

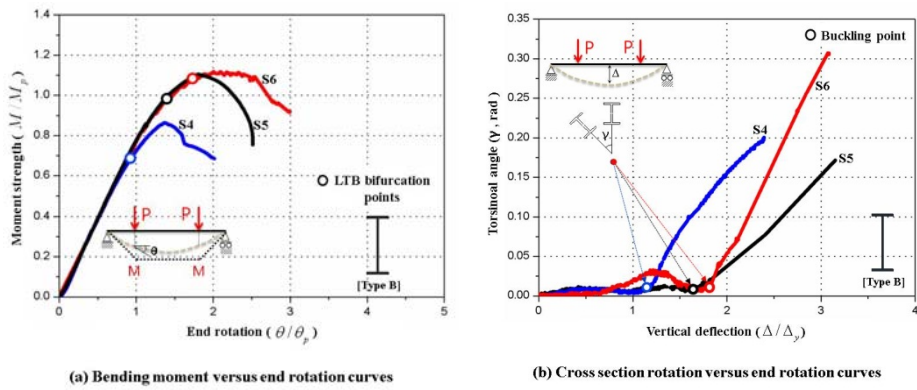


(b) Strain response of the web (S1)



(c) Strain response of the bottom flange (S1)

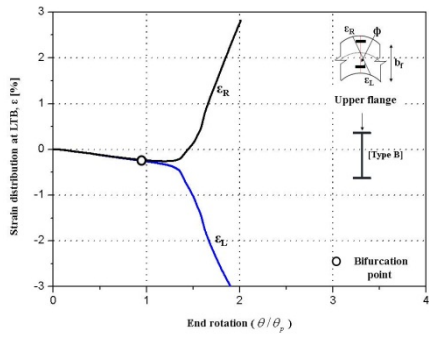
[5-7] Local responses of the specimens [G: H-250x150x15x15]-[M: Ho-775] (a) Strain response of the top flange (b) Strain responses of the web (c) Strain response of the bottom flange



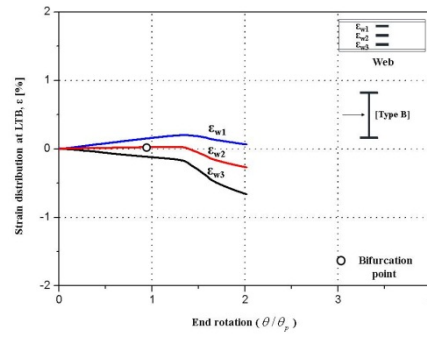
Specimen	LTB and failure mode	
S4		
S5		
S6		

(c) Failure modes

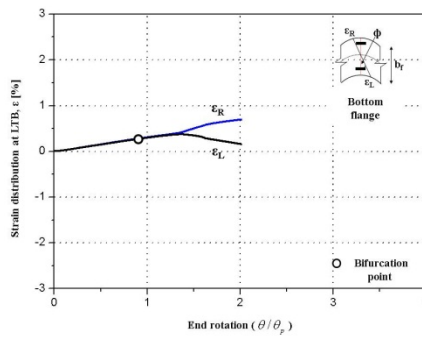
[5-8] Global responses of the specimens [G: H-400x150x15x15]-[M: Ho-775] (a) Bending moment versus end rotation curves (b) Cross section rotation versus center vertical deflection curves (c) Failure modes



(a) Strain response of the top flange (S4)

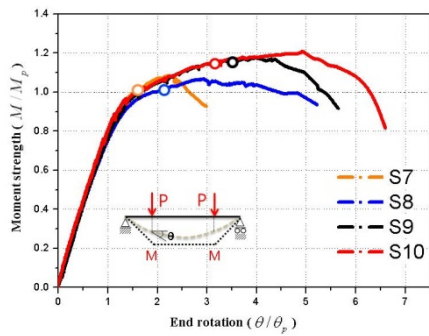


(b) Strain response of the web (S4)

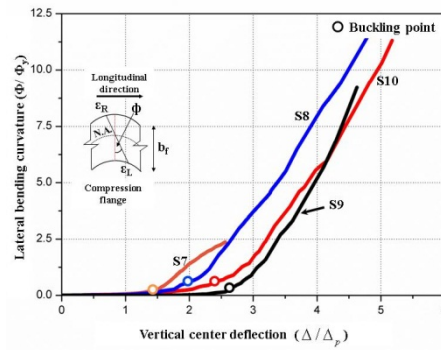


(c) Strain response of the bottom flange (S4)

[5-9] Local responses of the specimens [G: H-400x150x15x15]-[M: Ho-775] (a) Strain response of the top flange (b) Strain responses of the web (c) Strain response of the bottom flange



(a) Bending moment versus end rotation curves



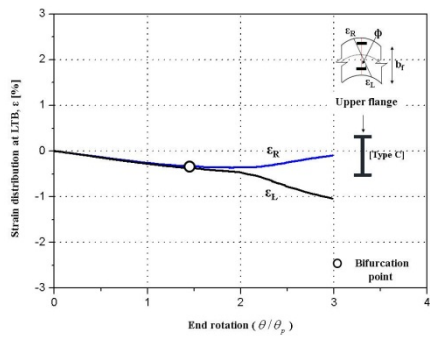
(b) Cross section rotation versus end rotation curves

Specimen	LTB and failure mode	
S7		
S8		
S9		
S10		

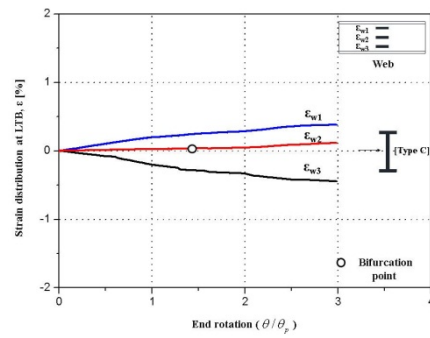
(c) Failure modes

[5-10] Global responses of the specimens [G: H-350x150x30x25]-[M: Hy-349-722]

(a) Bending moment versus end rotation curves (b) Cross section rotation versus center vertical deflection curves (c) Failure modes

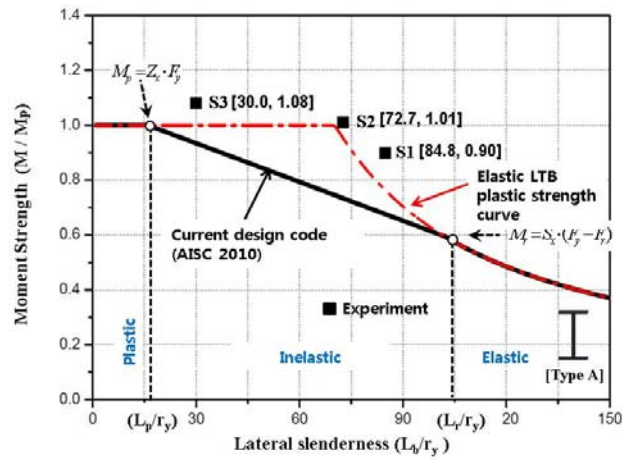


(a) Strain response of the top flange (S7)

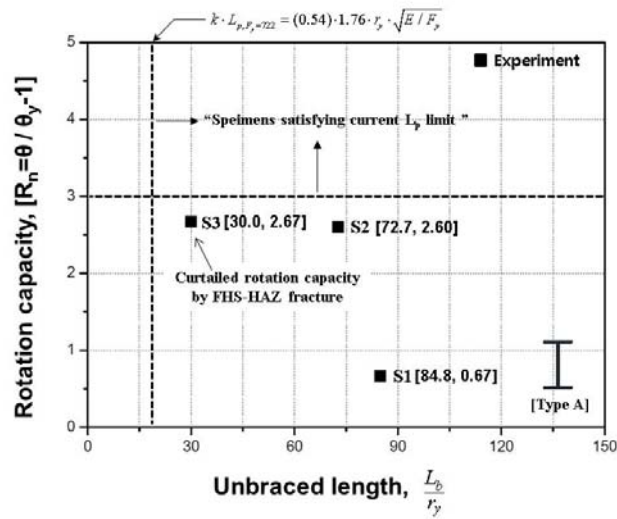


(b) Strain response of the web (S7)

[5-11] Local responses of the specimens [G: H-350x150x30x25]-[M: Hy-349-722] (a) Strain response of the top flange (b) Strain responses of the web

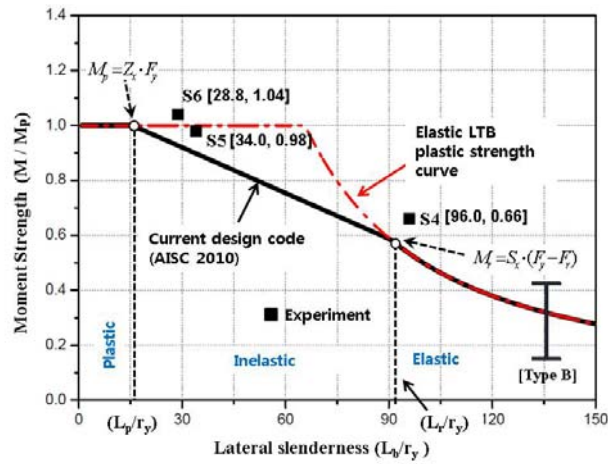


(a) AISC-critical buckling strength (M_{cr})

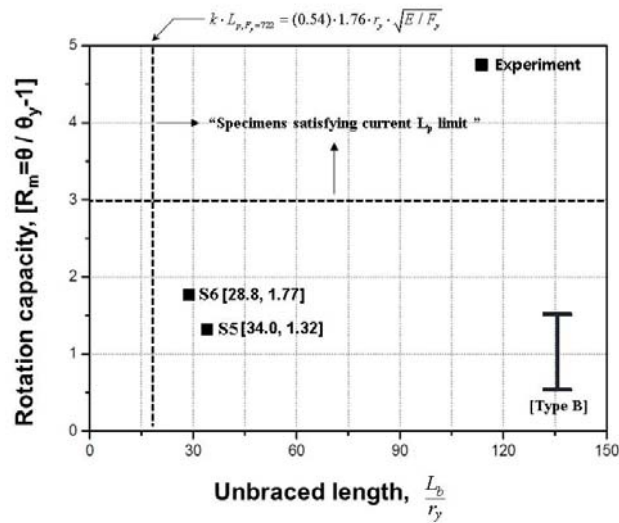


(b) AISC-rotation capacity (R_n)

[5-12] Critical buckling strength and rotation capacity of specimens [G: H-250x150x15x15]-[M: Ho-775] compared with current design codes (a) AISC, M_{cr} (b) AISC, R_n

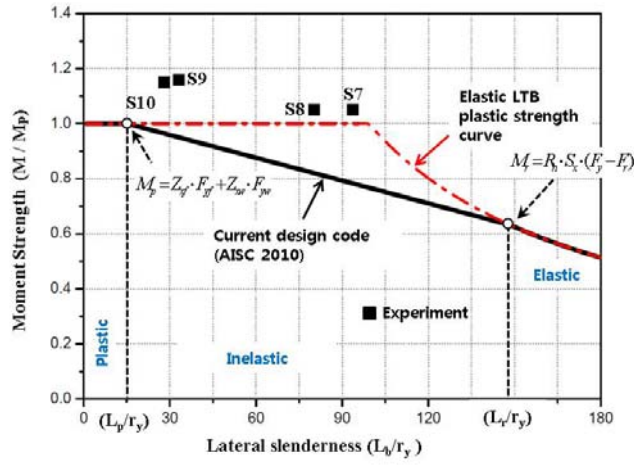


(a) AISC-critical buckling strength (M_{cr})

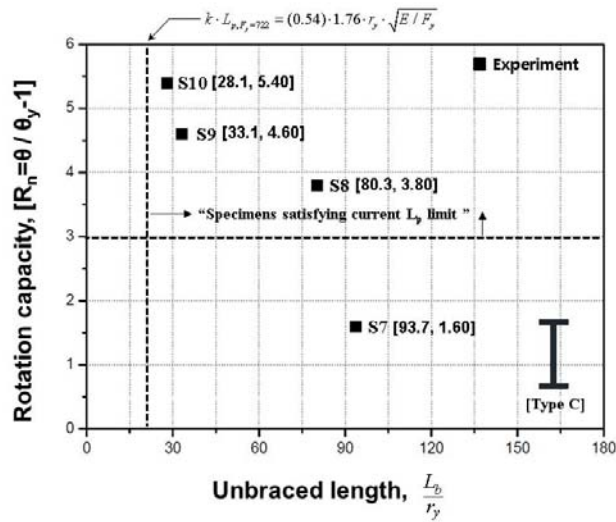


(b) AISC-rotation capacity (R_m)

[5-13] Critical buckling strength and rotation capacity of specimens [G: H-400x150x15x15]-[M: Ho-775] compared with current design codes (a) AISC, M_{cr} (b) AISC, R_m

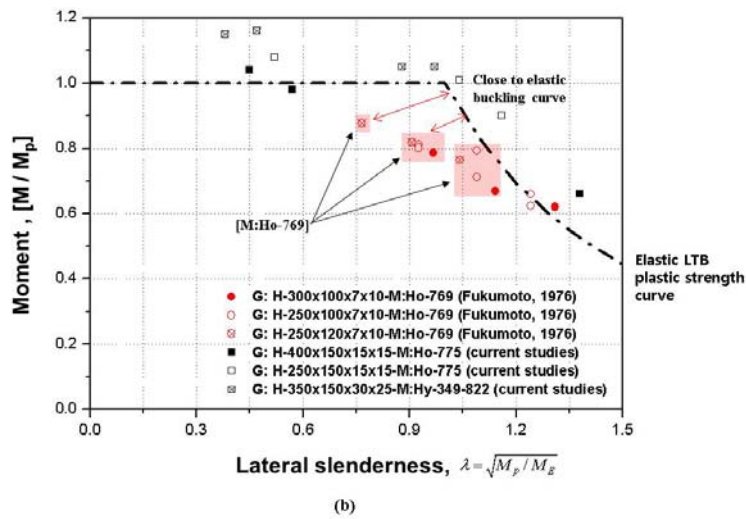
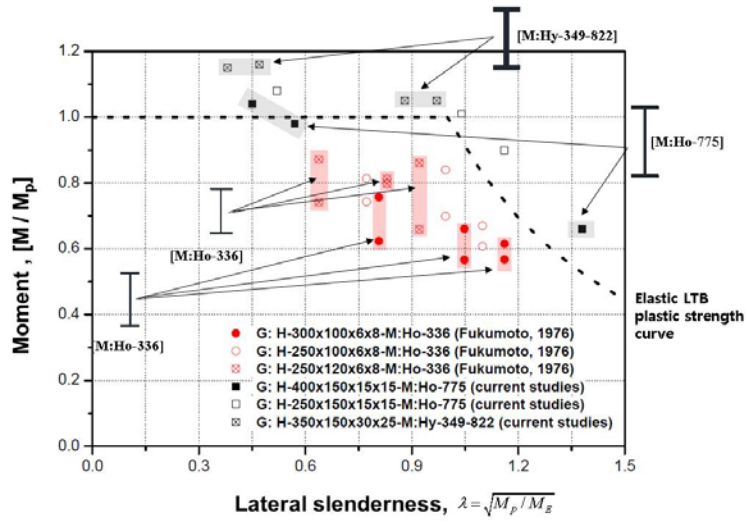


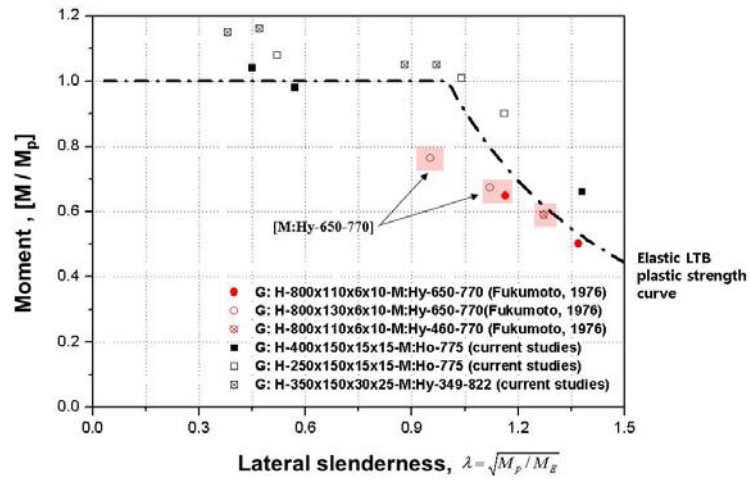
(a) AISC-critical buckling strength (M_{cr})



(b) AISC-rotation capacity (R_n)

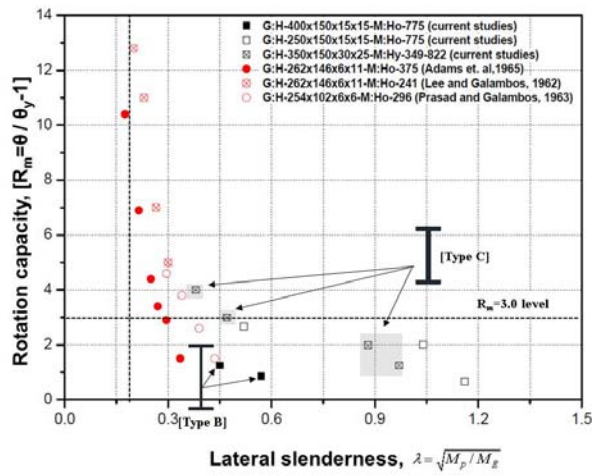
[5-14] Critical buckling strength and rotation capacity of specimens [G: H-350x150x30x25]-[M: Hy-349-722] compared with current design codes (a) AISC, M_{cr} (b) AISC, R_n



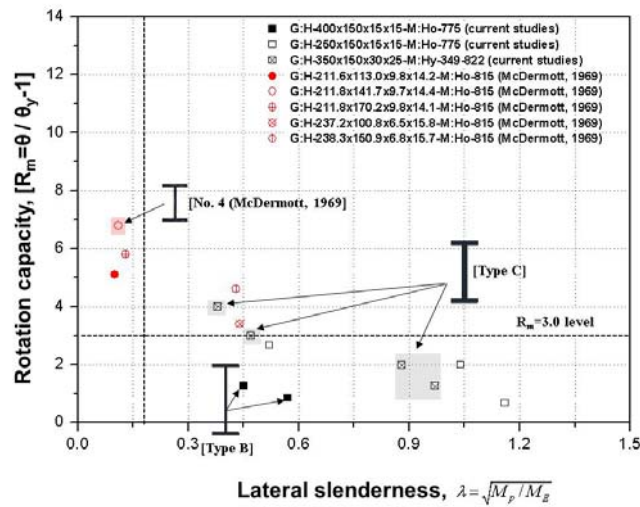


(c)

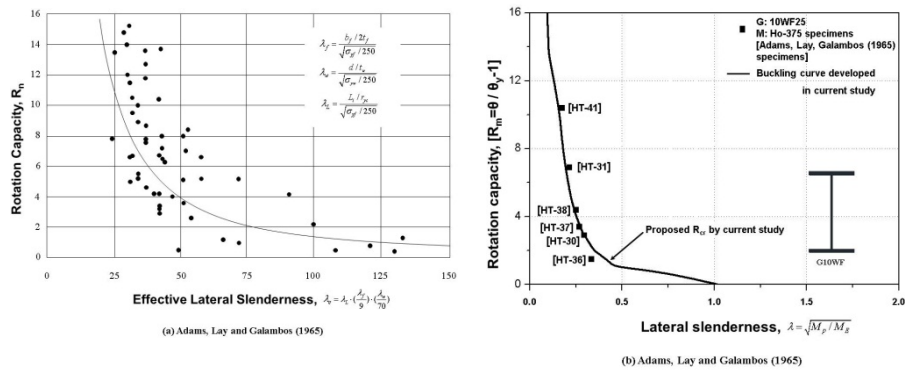
[5-15] Comparison critical buckling strength of specimens with previous experiments
 (a) Fukumoto, 1976 [M: Ho-336] series (b) Fukumoto, 1976 [M: Ho-769] (c)
 Fukumoto, 1976 [M: Hy-650-770] and [M:Hy-460-770] series



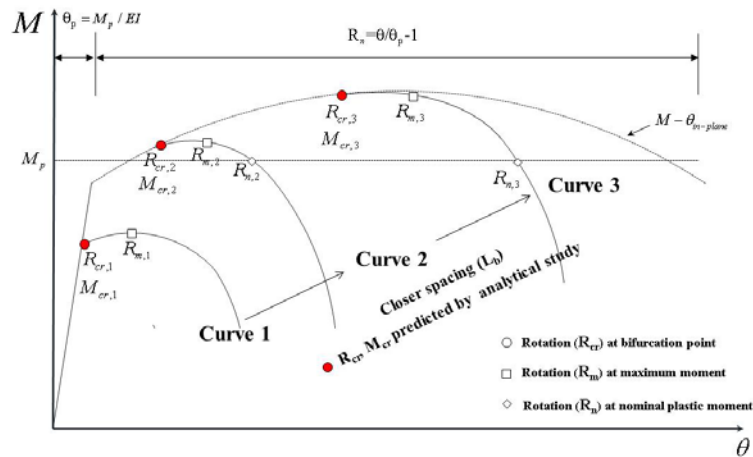
[5-16] Comparison rotation capacity of specimens with previous experiments (Lee and Galambos, 1962 [M:Ho-241] series; Prasad and Galambos, 1963 [M:Ho-296] series; Adams, Lay and Galambos, 1965 [M:Ho-375] series)



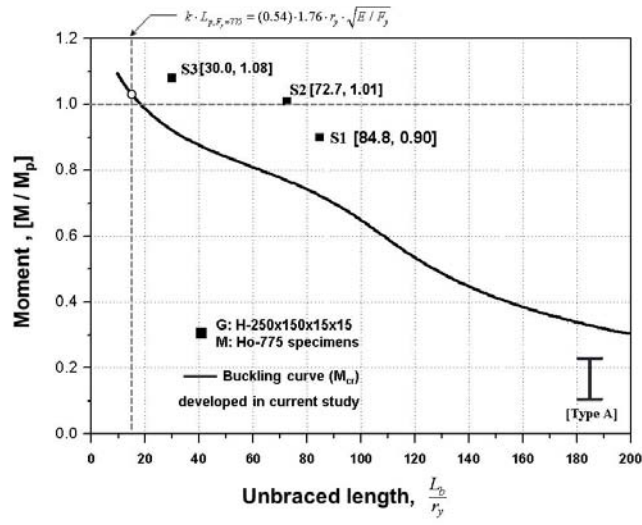
[5-17] Comparison rotation capacity of specimens with previous experiment (McDermott, 1969 [M:Ho-815] series)



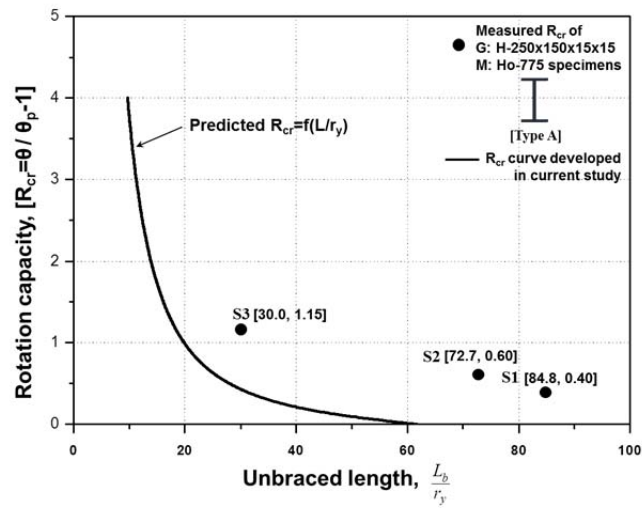
[5-18] Validation of the analytically developed rotation capacities curves (a) Proposed curve by Kemp based on the Experimental Test Data (1986) (b) Proposed curve in current studies



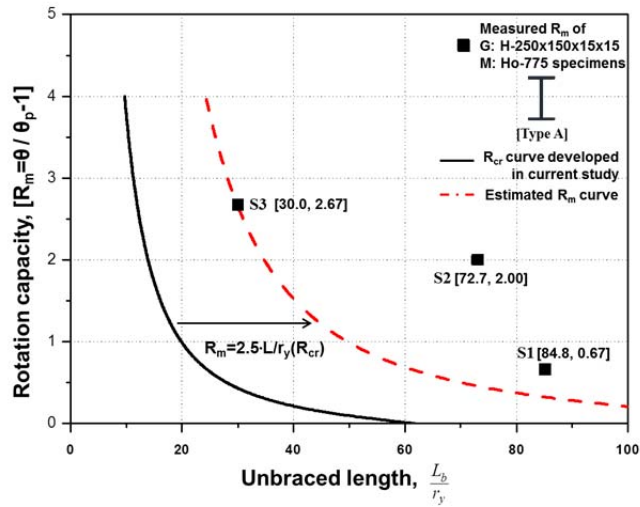
[5-19] Critical buckling strength (M_{cr}) and rotation capacity (R_{cr} , R_m and R_n) measurement points in the $M-\theta$ curve (a) R_{cr} , rotation capacities at bifurcation points (b) R_m , rotation capacities at maximum strength (c) R_n , rotation capacities at nominal strength



(a) AISC-critical buckling strength (M_{cr})

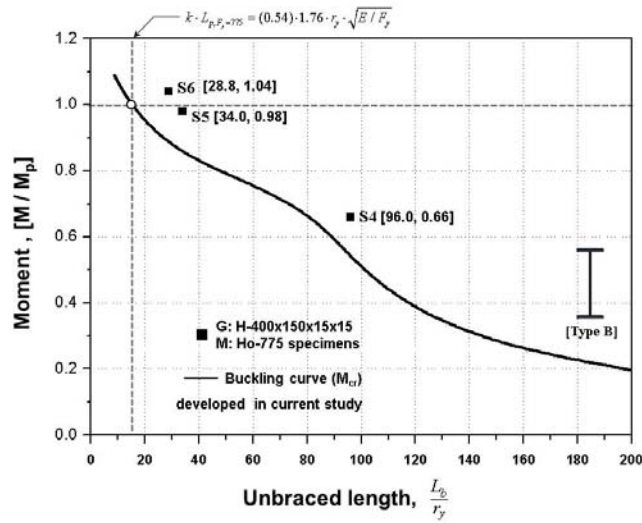


(b) AISC-rotation capacity (R_{cr})

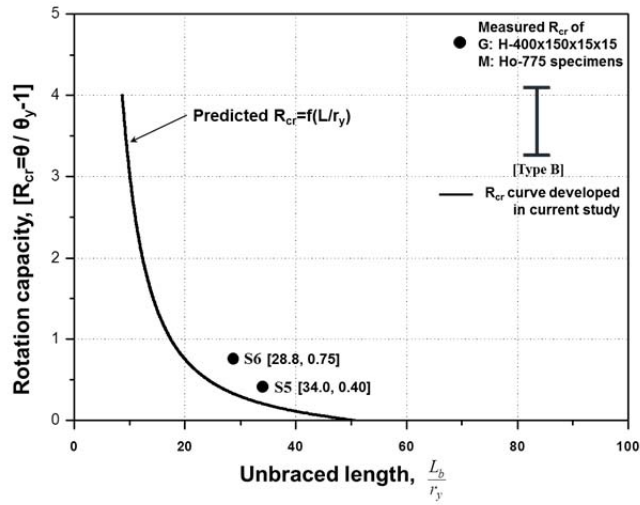


(c) AISC-rotation capacity (R_m)

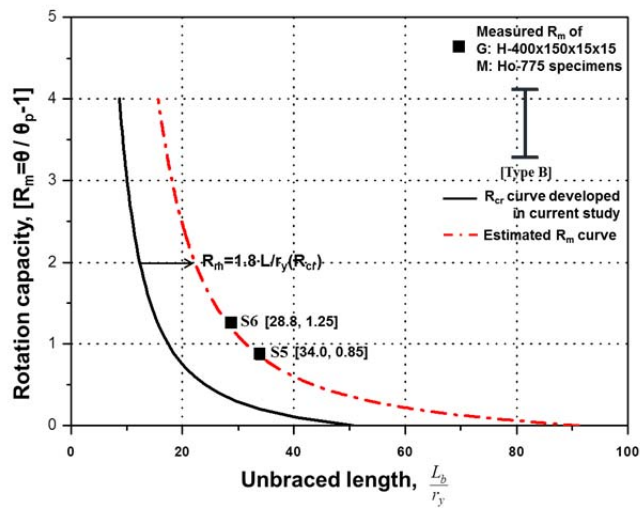
[5-20] Critical buckling strength and rotation capacity of specimens [G: H-250x150x15x15]-[M: Ho-775] compared with the analytically developed buckling curves (a) AISC, M_{cr} (b) AISC, R_{cr} (c) AISC, R_m



(a) AISC-critical buckling strength (M_{cr})

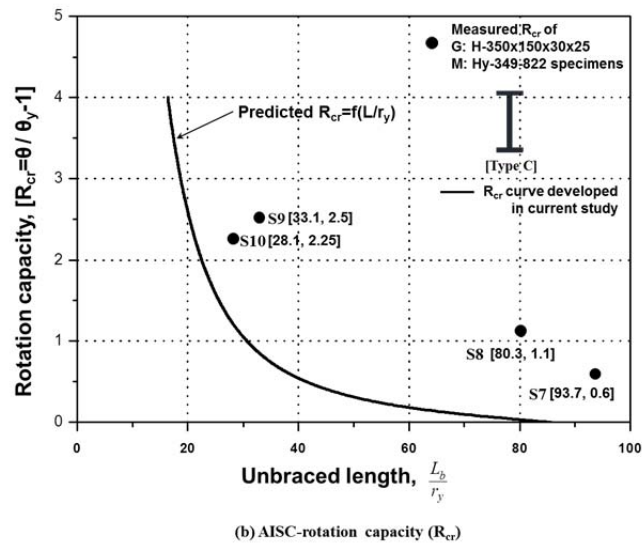
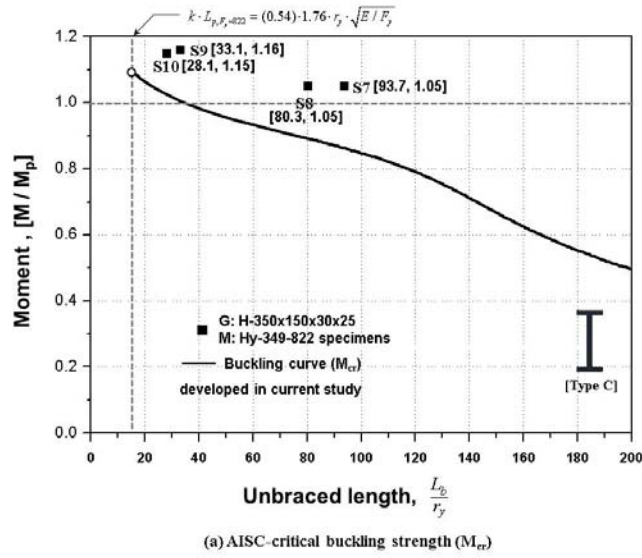


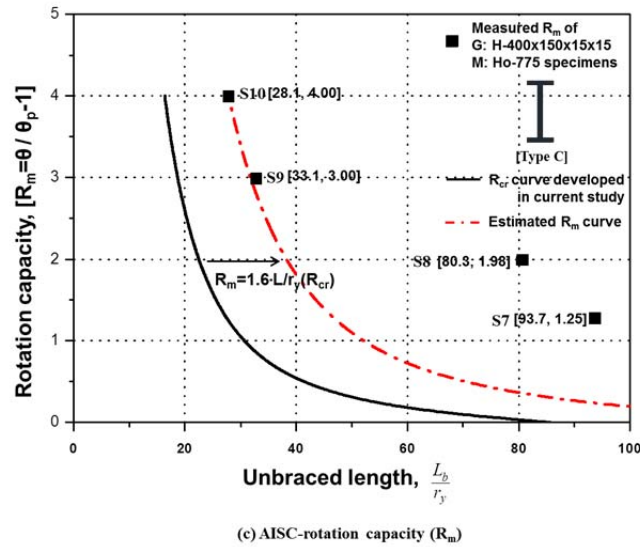
(b) AISC-rotation capacity (R_{cr})



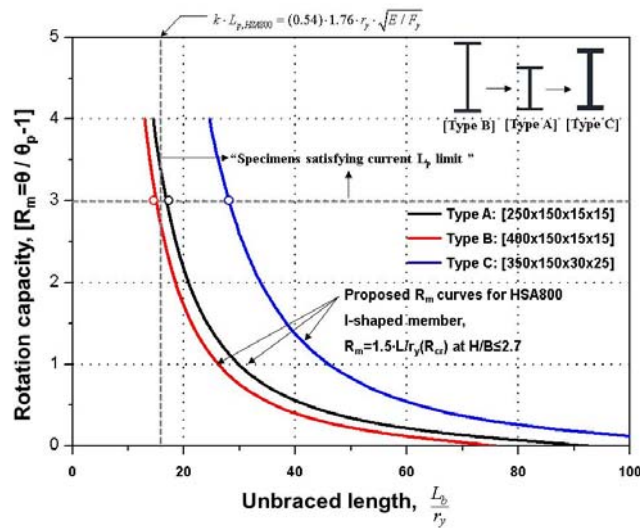
(c) AISC-rotation capacity (R_m)

[5-21] Critical buckling strength and rotation capacity of specimens [G: H-400x150x15x15]-[M: Ho-775] compared with the analytically developed buckling curves (a) AISC, M_{cr} (b) AISC, R_{cr} (c) AISC, R_m

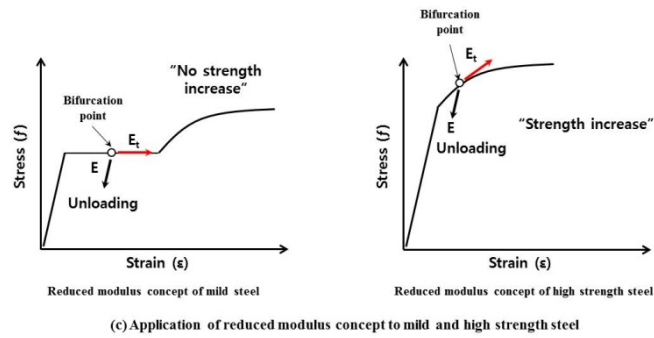
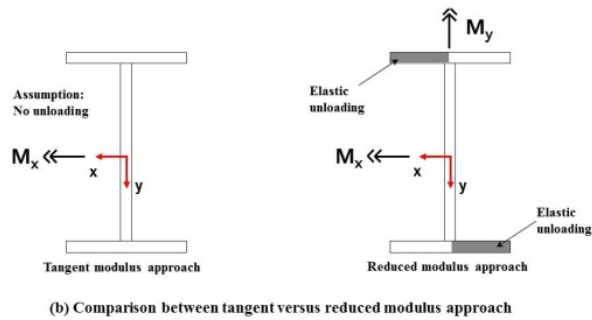
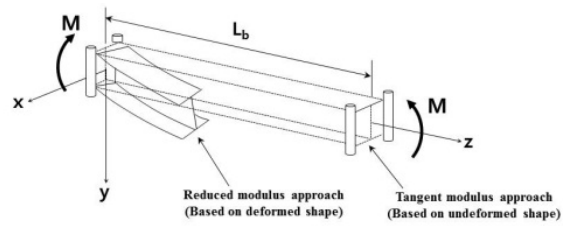
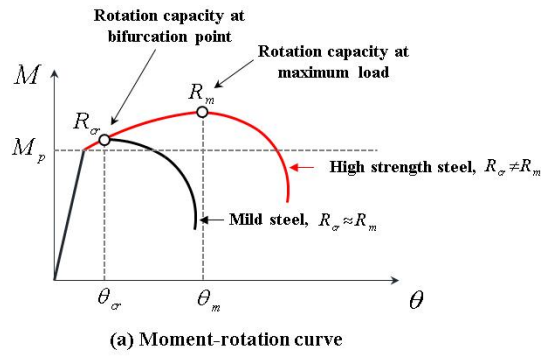




[5-22] Critical buckling strength and rotation capacity of specimens [G: H-350x150x30x25]-[M: Hy-349-722] compared with the analytically developed buckling curves (a) AISC, M_{cr} (b) AISC, R_{cr} (c) AISC, R_m



[5-23] Proposed rotation capacities curves (R_m) for HSA800 I-shaped member



[5-24] Schematic post-buckling behaviors of mild and high strength I-shaped steel after LTB triggered (a) Moment-rotation relationship (b) comparison between tangent

modulus versus reduced modulus approach (c) application of reduced modulus
concept to mild and high strength steel

[5-1] Tensile coupon properties of HSA800 steel plates

Name of Specimen	E	F_y ¹⁾	F_u	$Y_R = F_y / F_u$	$E_{st,R} = \varepsilon_{st} / \varepsilon_y$ ²⁾	$E_R = \varepsilon_u / \varepsilon_y$	n ³⁾
	[MPa]	[MPa]	[MPa]				
HSA800-15T-1	205,000 ⁴⁾	803.49	888.53	0.91	1	11.9	33
HSA800-15T-2		806.33	883.24	0.91	1	12.4	35
HSA800-15T-3		762.43	875.76	0.87	1	12.0	22
HSA800-15T-4		809.56	898.54	0.90	1	13.8	32
HSA800-15T-5		722.16	861.87	0.84	1	15.3	18
HSA800-15T-6		741.79	858.10	0.86	1	14.0	22
HSA800-25T-1		826.09	940.26	0.88	1	13.3	25
HSA800-25T-2		810.94	927.97	0.87	1	12.2	23
HSA800-25T-3		829.38	943.00	0.88	1	11.6	24

1) 0.2% offset method applied
2) $\varepsilon_y = F_y / E$
3) Proposed hardening parameter according to Ramberg-Osgood model calculated by Eq. (3-6)
4) Nominal value

[5-2] Tensile coupon properties of SM490 steel plates

Name of Specimen	E	F_y ¹⁾	F_u	$Y_R = F_y / F_u$	$E_{st,R} = \varepsilon_{st} / \varepsilon_y$ ²⁾	$E_R = \varepsilon_u / \varepsilon_y$	E / E_{st} ³⁾
	[MPa]	[MPa]	[MPa]				
SM490-30T-1	205,000 ⁴⁾	349.08	507.82	0.69	11.2	90.5	24
SM490-30T-2		328.67	518.13	0.63	9.7	90.3	20
SM490-30T-3		339.44	520.68	0.65	9.0	85.6	20

1) 0.2% offset method applied
 2) $\varepsilon_y = F_y / E$
 3) Stress-Strain relationship in strain-hardening range expressed by Haaijjer model calculated by Eq. (3-5) with $m = 2$ and $K = 180$
 4) Nominal value

[5-3] Test matrix summary

Specimen Type		Loading Condition	$\frac{b_f}{2t_f} \sqrt{\frac{F_{yf}}{E}}$	$\frac{h}{t_w} \sqrt{\frac{F_{yw}}{E}}$	L_b [mm]	k	$k \cdot L_b$	$\frac{k \cdot L_b}{r_y}$	$\frac{k \cdot L_b}{r_y} \sqrt{\frac{F_{yf}}{E}}$	λ_{IT}	Steel Material	Planned failure mode
[250x150] Series Type: A	[G: H-250x150x15x15] [M: Ho-775]	S1	0.31 (0.38) ³	0.92 (3.76) ⁴	2,800	1.00	2,800	84.8	5.21 (0.95) ⁵	1.14	HSA800	LTB
		S2			2,400	1.00	2,400	72.7	4.47 (0.95) ⁵	1.03		LTB
		S3			1,800	0.55	990	30.0	1.84 (0.95) ⁵	0.51		LTB
[400x150] Series Type: B	[G: H-400x150x15x15] [M: Ho-775]	S4	0.31 (0.38) ³	1.54 (3.76) ⁴	2,800	1.00	2,800	96.0	5.90 (0.95) ⁵	1.37	HSA800	LTB
		S5			1,800	0.55	990	34.0	2.09 (0.95) ⁵	0.57		LTB
		S6			1,400	0.60	840	28.8	1.77 (0.95) ⁵	0.45		LTB
[350x150] series Type: C	[G: H-350x150x30x25] [M: Hy-349-827]	S7	0.19 (0.38) ³	0.64 (3.76) ⁴	2,800	1.00	2,800	93.7	5.95 (0.95) ⁵	0.97	Flange: HSA800	LTB
		S8			2,400	1.00	2,400	80.3	5.10 (0.95) ⁵	0.88		LTB
		S9			1,800	0.55	990	33.1	2.10 (0.95) ⁵	0.47	Web: SM490	LTB
		S10			1,400	0.60	840	28.1	1.78 (0.95) ⁵	0.38		LTB

1) Ho is abbreviation of homogenous I-section, the flange and web of which are the same grade steel are applied
 2) Hy is abbreviation of hybrid I-section, the flange and web of which are the different grade steel are applied
 3) Flange slenderness limit for compact section
 4) Web slenderness limit for compact section
 5) Lateral slenderness limit for plastic moment

[5-4] Test results

Specimen Type		AISC			EC3		Measured					Steel Material	Observed failure mode	
		$\frac{k \cdot L_b}{r_y}$	$\frac{k \cdot L_b}{r_y} \sqrt{\frac{F_{yf}}{E}}$	$M_{cr} / M_p^{3)}$	λ_{LT}	$M_{cr} / M_p^{4)}$	$M_{cr} / M_p^{5)}$	$M_m / M_p^{6)}$	$R_{cr}^{7)}$	$R_m^{8)}$	$R_n^{9)}$			
[250x150] Series Type: A	[G: H-250x150x15x15] [M: Ho-775]	S1	84.8	5.21 (0.95) ²⁾	0.68	1.14	0.46	0.90	1.00	0.40	0.67	0.67	HSA800	LTB
		S2	72.7	4.47 (0.95) ²⁾	0.73	1.03	0.53	1.01	1.16	0.60	2.00	2.60		LTB
		S3	30.0	1.84 (0.95) ²⁾	0.93	0.51	0.85	1.08	1.18	1.15	2.67	2.67 ¹⁾		LTB/ HAZ crack
[400x150] Series Type: B	[G: H-400x150x15x15] [M: Ho-775]	S4	96.0	5.90 (0.95) ²⁾	0.58	1.37	0.31	0.66	0.86	-	-	-	HSA800	LTB
		S5	34.0	2.09 (0.95) ²⁾	0.90	0.57	0.75	0.98	1.10	0.40	0.85	1.32		LTB
		S6	28.8	1.77 (0.95) ²⁾	0.93	0.45	0.80	1.04	1.12	0.75	1.25	1.77		LTB
[350x150] series Type: C	[G: H-350x150x30x25] [M: Hy-349-827]	S7	93.7	5.95 (0.95) ²⁾	0.76	0.97	0.48	1.05	1.08	0.60	1.25	1.60	Flange: HSA800 Web: SM490	LTB
		S8	80.3	5.10 (0.95) ²⁾	0.80	0.88	0.53	1.05	1.07	1.10	1.98	3.80		LTB
		S9	33.1	2.10 (0.95) ²⁾	0.94	0.47	0.81	1.16	1.17	2.50	3.00	4.60		LTB
		S10	28.1	1.78 (0.95) ²⁾	0.96	0.38	0.85	1.15	1.21	2.25	4.00	5.40		LTB

1) The crack at the vicinity of the Full height stiffener(FHZ) curtailed the further inelastic rotation after R_m had been reached.
 2) Lateral slenderness limit for plastic moment
 3) Predicted moment strength by AISC-LRFD 2010 specification
 4) Predicted moment strength by EC 3
 5) Measured moment strength at bifurcation point
 6) Measured moment strength at maximum load
 7) Measured rotation capacity at bifurcation point
 8) Measured rotation capacity at maximum load
 9) Measured rotation capacity at nominal strength

Chapter 6 Conclusions

This research has been focused on the inelastic behavior of structural I-shaped members fabricated from 800MPa high strength steel (HSA800). HSA800, a new generation of high performance steel, produced by thermo-mechanical controlling process, has advantages to acquire the high strength as well high toughness and relatively low carbon equivalent value. However, due to lack of sufficient research on the effects of the different post-yield range characteristics of the high strength steel to the structural behavior, the current code directly or indirectly restricts high strength steel by adopting limiting parameters such upper yield-to-tensile (Y/T) strength ratio limit or a certain level of ductility capacity (rotation capacity).

The primary target of this research is to experimentally and analytically quantify the effects of the post-yield range characteristics of mild and high strength steel on I-shaped flexural members. In addition, this study attempts to establish a methodology to provide adequate unbraced length limit to ensure inelastic lateral torsional buckling strength and a certain level of rotation capacity, related to the existing AISC-LRFD specification and EC 3 code. The objective was achieved by means of five major activities: stress-strain curve idealizations for both mild ($F_u=490\text{MPa}$) and high strength ($F_u=800\text{MPa}$)

steels, estimation of in-plane rotation capacities of both mild and high strength I-shaped beam member, quantifying the inelastic section stiffnesses for both mild and high strength steels by using the tangent modulus theories, establishment LTB strength and rotation capacity curves of mild and high strength I-shaped flexural members under uniform and moment gradient conditions, and experimental work.

In the stress-strain curve idealizations, four idealized material models are discussed and verified with tensile coupon test data to indicate adequate stress and inelastic modulus according to post-yield range strain, which is crucial data for in-plane and out-of-plane analysis. The traditional piecewise model (#1) and Haaijer model (#2) were appropriate to idealize mild steel. The Ramberg-Osgood model (#3) was adequate to idealize the shape of the stress-strain curve of high strength steel. In addition, for in-plane behavior analysis only, a piecewise linear model (#4) could be applicable for idealizing the various materials by increasing the number of polylines according to material nonlinearity.

In the estimation of in-plane rotation capacities, the effects of the Y/T strength ratio, T/Y strain ratio, and YP length of both mild and high strength steels on the rotation capacity were analyzed. At the uniform moment loading condition, the rotation capacity ($R_{m,ui}$) is directly proportional to the T/Y strain

ratios. Other parameters such as Y/T strength ratio and YP length are not influential under the uniform loading condition. On the other hand, under the moment gradient loading condition, three parameters (Y/T strength ratio, T/Y strain ratio, and YP length) all together influence the rotation capacity ($R_{m,gr}$) and their contributions are summarized. Due to high Y/T strength ratio and low T/Y strain ratio of HSA800, the in-plane rotation capacity of HSA800 I-shaped member is inevitably low as compared to other grades (SM570 and SM490) of steel under moment gradient loading condition.

In the inelastic section stiffnesses, the explicit formulas for quantifying the inelastic (minor-axis) flexural, warping and torsional stiffnesses of I-section for mild (adopting Haaijer's stress-strain model) and high strength steels (adopting Ramberg-Osgood's stress-strain model) were proposed. By applying the formula to mild and high strength I-section (H-250x150x14x14) respectively, different variations of the flexural and warping stiffnesses in inelastic range were confirmed. Specially, the value of the inelastic stiffnesses of high strength I-section decrease rapidly below 5% of its elastic value as the curvature reaches beyond three or four times the yield curvature. This implies that the high strength steel I-member would have little or weak resistance sustaining high rotation capacity unless very close lateral bracing length or other geometrically high LTB resistance sections are provided.

Based on the derived inelastic section stiffnesses, the LTB strength and rotation capacity curves under uniform and moment gradient conditions were proposed and verified with previous experimental studies. In detail, for uniform moment loading condition, explicit formulas were proposed for deriving adequate unbraced length limit to achieve target strength and rotation capacity. Meanwhile, explicit formulas were not enabled under moment gradient loading condition since the governing inelastic LTB equation case is not explicitly solved. Therefore, a numerical method (Galerkin method) was adopted to propose adequate unbraced length limit for moment gradient case.

In the experimental studies, three types of weld I-shaped specimens were designed and experimented. The dimensions and material information of type-A, type-B, and type-C specimens are [H-250x150x15x15]-[Homogeneous- $F_y=775\text{MPa}$ steels], [H-400x150x15x15]-[Homogeneous- $F_y=775\text{MPa}$], and [H-350x150x30x25]-[Hybrid- $F_{yw}=349\text{MPa}$, $F_{yt}=822\text{MPa}$] respectively. Classifying the specimens according to the inelastic section stiffness, type-A specimens have relatively large flexural stiffness and type-C specimens have relatively large torsional stiffness. However, type-B specimens have relatively low flexural and torsional stiffnesses, implying that it is expected to be more vulnerable to LTB.

All specimens failed by LTB, triggering the sinusoidal shape failure mode.

By comparing the measured buckling strength and rotation capacity, it was confirmed that, as expected, type-A and type-C specimens shows higher LTB resistance as compared to that of type-B specimen. Also, the analytically derived curves in chapter 4 well predict the measured critical buckling strength (M_{cr}) and measured rotation capacity at bifurcation point (R_{cr}). Based on this validation, it is justified that the proposed buckling strength and rotation capacity formula (Eq. 4-31 and Eq. 4-39) in this study could be utilized for the rational LTB design criteria of high strength I-shaped member.

In summary, this study has proposed new LTB design criteria reflecting the different post-yield range characteristics of high strength steel. Based on this study, the relaxation of the current code limitation on the high strength steel is justified and the current AISC-LTB design criteria could be substituted in rational way.

-The end of conclusion-

References

- Adams, P. F., Lay, M. G., and Galambos, T. V. (1964). *Experiments on High Strength Steel Members*. Fritz Engineering Laboratory Reports, Lehigh University, Bethlehem, Pennsylvania.
- Aglietti, R. A., Galambos, T. V., and Lay, M. G. (1964). *Tests on A-F6 and A441 Steel Beam-columns*. Fritz Engineering Laboratory Reports, Lehigh University, Bethlehem, Pennsylvania.
- AISC. (1989). *Specification for Structural Steel Building-Allowable Stress Design and Plastic Design*. American Institute of Steel Construction, Chicago, Illinois.
- AISC. (2002). *Seismic Provisions for Structural Steel Buildings*. American Institute of Steel Construction, Chicago, Illinois.
- AISC. (2010). *Specification for Structural Steel Buildings*. American Institute of Steel Construction, Chicago, Illinois.
- Bannister, A. C. (1998a). *Assessment of the Occurrence and Significance of Yield Plateaus in Structural Steels*. British steel/Corus group.
- Bannister, A. C. (1998b). *Contribution to Sub-Task 2.3: Assessment of the Occurrence and Significance of Yield Plateaus in Structural Steels*. Report No. SINTAP/BS/19.
- Bannister, A. C., Ocejo, J. R., and Gutierrez-Solana, F. (2000). *Implications of the Yield Stress/Tensile Stress Ratio to the Sintap Failure Assessment Diagrams for Homogeneous Materials*. Engineering Fracture Mechanics, 67(6), 547-562.
- Bannister, A. C., and Trail, S. J. (1996). *Structural Integrity Assessment Procedures*

- for European Industry*. British steel/Corus group.
- Bansal, J. P. (1971). *The Lateral Instability of Continuous Beams* AISI Project, 157, University of Texas, Austin.
- Bjorhovde, R. (2014). *Current Developments for International Steel Design Codes*. Paper presented at the Pacific Steel Structure Conference 2013, Singapore.
- Booker, J. R., and Kitipornchai, S. (1971). *Torsion of Multilayered Rectangular Section*. Journal of the Engineering Mechanics Division, 97(5), 1451-1468.
- Bradford, M. A. (1992). *Lateral-Distortional Buckling of Steel I-Section Members*. Journal of Constructional Steel Research, 23(1), 97-116.
- Bradford, M. A., Cuk, P. E., Gizejowski, M. A., and Trahair, N. S. (1987). *Inelastic Lateral Buckling of Beam-Columns*. Journal of Structural Engineering-ASCE, 113(11), 2259-2277.
- Bradford, M. A., and Trahair, N. S. (1985). *Inelastic Buckling of Beam-Columns with Unequal End Moments*. Journal of Constructional Steel Research, 5(3), 195-212.
- Brockenbrough, R. L. (1995). *Effect of Yield-Tensile Ratio on Structural Behavior-High-Performance Steels for Bridge Construction*. Final Rep. to Naval Surface Warfare Center and Federal Highway Administration.
- Chen, W. F., and Lui, E. M. (1987). *Structural Stability: Theory and Implementation*. Elsevier, New York.
- Chen, W. F., and Lui, E. M. (1991). *Stability Design of Steel Frames*. CRC press.
- de Normalisation, C. E. (1992). *Eurocode 3: Design of Steel Structures: Part 1-1: General Rules and Rules for Buildings*. European Committee for Standardization.

References

- Dexter, R. J., and Melendrez, M. I. (2000). *Through-Thickness Properties of Column Flanges in Welded Moment Connections*. Journal of Structural Engineering-ASCE, 126(1), 24-31.
- Dibley, J. E. (1969). *Lateral Torsional Buckling of I-Sections in Grade 55 Steel*. Paper presented at the ICE Proceedings, 43(4), 599-627
- Driscoll, G. C. (1965). *Plastic Design of Multi-Story Frames*. Fritz Engineering Laboratory Reports, Lehigh University, Bethlehem, Pennsylvania.
- Dumont, C., and Hill, H. N. (1937). *The Lateral Instability of Deep Rectangular Beams*. National Advisory Committee for Aeronautics.
- Dumont, C., and Hill, H. N. (1940). *The Lateral Stability of Equal-Flanged Alu-Alloy I-Beams in Pure Bending*. NACA Tech Note 770, 22 (4).
- Dux, P. F., and Kitipornchai, S. (1983). *Inelastic Beam Buckling Experiments*. Journal of Constructional Steel Research, 3(1), 3-9.
- Earls, C. J. (1999). *On the Inelastic Failure of High Strength Steel I-Shaped Beams*. Journal of Constructional Steel Research, 49(1), 1-24.
- Earls, C. J. (2000). *Geometric Factors Influencing Structural Ductility in Compact I-Shaped Beams*. Journal of Structural Engineering-ASCE, 126(7), 780-789.
- Earls, C. J. (2001a). *Geometric Axis Compactness Criteria for Equal Leg Angles: Horizontal Leg Compression*. Journal of Constructional Steel Research, 57(4), 351-373.
- Earls, C. J. (2001b). *Single Angle Geometric Axis Flexural Compactness Criteria: Horizontal Leg Tension*. Journal of Structural Engineering-ASCE, 127(6), 616-624.
- Earls, C. J. (2001c). *Single Angle Geometric Axis Flexure I. Background and Model*

- Verification*. Journal of Constructional Steel Research, 57(6), 603-622.
- Earls, C. J. (2001d). *Single Angle Geometric Axis Flexure II. Design Recommendations*. Journal of Constructional Steel Research, 57(6), 623-646.
- Fukumoto, Y., and Itoh, Y. (1981a). *Numerical Data Bank for the System Evaluating the Ultimate Strength of Steel Structural Members*. JSCE J, 312, 59-72.
- Fukumoto, Y., and Itoh, Y. (1981b). *Statistical Study of Experiments on Welded Beams*. Journal of the Structural Division-ASCE, 107(1), 89-103.
- Fukumoto, Y., Itoh, Y., and Hattori, R. (1982). *Lateral Buckling Tests on Welded Continuous Beams*. Journal of the Structural Division-ASCE, 108(10), 2245-2262.
- Fukumoto, Y., Itoh, Y., and Kubo, M. (1980). *Strength Variation of Laterally Unsupported Beams*. Journal of the Structural Division-ASCE, 106(1), 165-181.
- Fukumoto, Y., and Kubo, M. (1977a). *An Experimental Review of Lateral Buckling of Beams and Girders*. Paper presented at the Stability of Structures Under Static and Dynamic Loads, SSRC-ASCE, Bethlehem, Pennsylvania.
- Fukumoto, Y., and Kubo, M. (1977b). *A Supplement to a Survey of Tests on Lateral Buckling Strength of Beams*. Paper presented at the Final Report, 2nd Int. Colloquium on Stability of Steel Structures (4th Edn), ECCS-IABSE, Liege.
- Fukumoto, Y., and Kubo, M. (1977c). *A Survey of Tests on Lateral Buckling Strength of Beams*. Paper presented at the Preliminary Report, 2nd Int. Colloquium on Stability of Steel Structures (4th Edn), ECCS-IABSE, Liege.
- Galambos, T. V. (1960). *Report on the Beam-Column Experiments*. Fritz Engineering Laboratory Reports, Lehigh University, Bethlehem, Pennsylvania.

References

- Galambos, T. V. (1963). *Inelastic Lateral Buckling of Beams*. Journal of the Structural Division, 89(5).
- Galambos, T. V. (1998). *Guide to Stability Design Criteria for Metal Structures*. John Wiley & Sons.
- Galambos, T. V., Adams, P. F., and Fukumoto, Y. (1965). *Further Studies on the Lateral-Torsional Buckling of Steel Beam-Columns*. Fritz Engineering Laboratory Reports, Lehigh University, Bethlehem, Pennsylvania.
- Galambos, T. V., and Fukumoto, Y. (1963). *Inelastic Lateral-Torsional Buckling of Beam-Columns*. Fritz Engineering Laboratory Reports, Lehigh University, Bethlehem, Pennsylvania.
- Galambos, T. V., Hajjar, J. F., Earls, C. J., and Gross, J. L. (1997). *Required Properties of High-Performance Steels*. National Institute of Standards and Technology, Building and Fire Research Laboratory.
- Galambos, T. V., and Lay, M. G. (1962). *End Moment-End Rotation Characteristics for Beam-columns*. Fritz Engineering Laboratory Reports, Lehigh University, Bethlehem, Pennsylvania.
- Galambos, T. V., and Lay, M. G. (1964). *Plastic Design in High Strength Steel: The Ductility of Steel Structures*. Fritz Engineering Laboratory Reports, Lehigh University, Bethlehem, Pennsylvania.
- Galambos, T. V., and Ravindra, M. K. (1974). *Load and Resistance Factor Design Criteria for Steel Beams*. Department of Civil and Environmental Engineering, Washington University.
- Gedies, R. W. (1983). *Beam Buckling Tests with Various Brace Stiffnesses*. University of Texas, Austin.

- Gogou, E. (2012). *Use of High Strength Steel Grades for Economical Bridge Design*. TU Delft.
- Green, P. S. (2000). *The Inelastic Behavior of Flexural Members Fabricated from High Performance Steel*. Lehigh University.
- Haaijer, G. (1959). *Plate Buckling in the Strain-Hardening Range*, Transactions of the American Society of Civil Engineers, 124, 117-148.
- Hechtman, R. A., Hatstrup, J. S., Styer, E. F., and Tiedemann, J. L. (1957). *Lateral Buckling of Rolled Steel Beams*. Transactions of the American Society of Civil Engineers, 122(1), 823-843.
- Hibbitt, Karlsson, and Sorensen. (2001). *ABAQUS/Standard user's manual (Vol. 1)*. Hibbitt, Karlsson & Sorensen.
- Hrennikoff, A. P. (1965). *Importance of Strain Hardening in Plastic Design*. Journal of the Structural Division-ASCE, 91(4), 23-34.
- HSU, T. R. (1966). *Application of Dislocation Theory to the Yield Drop in Mild Steel*. Micromechanics of Solids Laboratory Report 66-4.
- Ito, M., Nozaka, K., Shirosaki, T., and Yamasaki, K. (2005). *Experimental Study on Moment-Plastic Rotation Capacity of Hybrid Beams*. Journal of Bridge Engineering, 10(4), 490-496.
- Kemp, A. R. (1985). *Interaction of Plastic Local and Lateral Buckling*. Journal of Structural Engineering-ASCE, 111(10), 2181-2196.
- Kemp, A. R. (1996). *Inelastic Local and Lateral Buckling in Design Codes*. Journal of Structural Engineering-ASCE, 122(4), 374-382.
- Kim, J. R., and Rasmussen. (2003). *Full-Range Stress-Strain Curves for Stainless Steel Alloys*. Journal of Constructional Steel Research, 59(1), 47-61.

References

- Kitipornchai, S., and Trahair, N. S. (1975a). *Buckling of Inelastic I-Beams under Moment Gradient*. Journal of the Structural Division-ASCE, 101(5), 991-1004.
- Kitipornchai, S., and Trahair, N. S. (1975b). *Elastic Behavior of Tapered Monosymmetric I-Beams*. Journal of the Structural Division-ASCE, 101(8), 1661-1678.
- Kitipornchai, S., and Trahair, N. S. (1975c). *Inelastic Buckling of Simply Supported Steel I-Beams*. Journal of the Structural Division-ASCE, 101(7), 1333-1347.
- Kitipornchai, S., Wang, C. M., and Trahair, N. S. (1986). *Buckling of Monosymmetric I-Beams under Moment Gradient*. Journal of Structural Engineering-ASCE, 112(4), 781-799.
- Lay, M. G. (1962). *A Brief Survey of U.S. Structural Steel Types*. Fritz Engineering Laboratory Reports, Bethlehem, Pennsylvania.
- Lay, M. G. (1963). *The Experimental Bases for Plastic Design-A Survey of the Literature*. Fritz Engineering Laboratory Reports, Bethlehem, Pennsylvania.
- Lay, M. G. (1964a). *The Mechanics of Column Deflection Curves*. Lehigh University, Bethlehem, Pennsylvania.
- Lay, M. G. (1964b). *Some Studies of Flange Local Buckling in Wide-Flange Shapes*. Lehigh University, Bethlehem, Pennsylvania.
- Lay, M. G. (1964c). *The Static Load-Deformation Behavior of Planar Steel Structure*. Lehigh University, Bethlehem, Pennsylvania.
- Lay, M. G. (1965). *Yielding of Uniformly Loaded Steel Members*. Journal of the Structural Division-ASCE, 91(6), 49.
- Lay, M. G., Aglietti, R. A., and Galambos, T. V. (1963). *Testing Techniques for Restrained Beam-Columns*, Fritz Engineering Laboratory Reports, Bethlehem,

- Pennsylvania.
- Lay, M. G., and Galambos, T. V. (1963). *Lateral Bracing Force of Steel I-beams*. Fritz Engineering Laboratory Reports, Bethlehem, Pennsylvania.
- Lay, M. G., and Galambos, T. V. (1964a). *Bracing Requirements for Inelastic Steel Beams*. Fritz Engineering Laboratory Reports, Bethlehem, Pennsylvania.
- Lay, M. G., and Galambos, T. V. (1964b). *The Experimental Behavior of Beam and Column Subassemblages*. Fritz Engineering Laboratory Reports, Bethlehem, Pennsylvania.
- Lay, M. G., and Galambos, T. V. (1964c). *The Inelastic Behavior of Closely Braced Steel Beams under Uniform Moment*. Lehigh University, Bethlehem, Pennsylvania.
- Lay, M. G., and Galambos, T. V. (1964d). *The Inelastic Behaviour of Beams under Moment Gradient*. Lehigh University, Bethlehem, Pennsylvania.
- Lay, M. G., and Galambos, T. V. (1965). *Inelastic Steel Beams under Uniform Moment*. Journal of the Structural Division, ASCE, 91(6), 67-93.
- Lay, M. G., and Gimsing, N. (1964). *Further Studies of the Moment-Thrust-Curvature Relationship*. DTIC Document.
- Lay, M. G., and Smith, P. D. (1965). *Role of Strain Hardening in Plastic Design*. Journal of the Structural Division, ASCE, 91(3), 25-44
- Lee, C. H., Han, K. H., Uang, C. M., Kim, D. K., Park, C. H., and Kim, J. H. (2012). *Flexural Strength and Rotation Capacity of I-Shaped Beams Fabricated from 800MPa Steel*. Journal of Structural Engineering, 139(6), 1043-1058.
- Lee, G. C. (1959). *Literature Survey on Lateral Instability and Lateral Bracing Requirements*. Fritz Engineering Laboratory Reports, Bethlehem,

References

- Pennsylvania.
- Lee, G. C. (1960). *Proposal on Lateral Buckling and Lateral Bracing Experiments*. Fritz Engineering Laboratory Reports, Bethlehem, Pennsylvania.
- Lee, G. C., and Galambos, T. V. (1962). *The Post-Buckling Strength of Wide-Flange Beams*. Fritz Engineering Laboratory Reports, Bethlehem, Pennsylvania.
- Lim, L. C. (1970). *The Strength and Behavior of Laterally Unsupported Columns*. Fritz Engineering Laboratory Reports, Bethlehem, Pennsylvania.
- Mandal, P., and Calladine, C. R. (2002). *Lateral-Torsional Buckling of Beams and the Southwell Plot*. International Journal of Mechanical Sciences, 44(12), 2557-2571.
- McDermott, J. F. (1969). *Plastic Bending of A514 Steel Beams*. Journal of Structural Division, 95(9), 1851-1871.
- Moen, L. A., Hopperstad, O. S., and Langseth, M. (1999). *Rotational Capacity of Aluminum Beams under Moment Gradient. I: Experiments*. Journal of Structural Engineering-ASCE, 125(8), 910-920.
- Moen, L. A., Matteis, G. D., Hopperstad, O. S., Langseth, M., Landolfo, R., and Mazzolani, F. M. (1999). *Rotational Capacity of Aluminum Beams Under Moment Gradient. II: Numerical Simulations*. Journal of Structural Engineering, 125(8), 921-929.
- Nethercot, D. A. (1972). *Factors Affecting the Buckling Stability of Partially Plastic Beams*. Paper presented at the ICE Proceedings, 53, 285-304.
- Nethercot, D. A. (1974). *Residual Stresses and their Influence upon the Lateral Buckling of Rolled Steel Beams*. The Structural Engineer, 52(3), 86-96.
- Nethercot, D. A. (1976). *Buckling of Welded Hybrid Steel I-Beams*. Journal of the

- Structural Division-ASCE, 102(3), 461-474.
- Nethercot, D. A., and Trahair, N. S. (1976). *Inelastic Lateral Buckling of Determinate Beams*. Journal of the Structural Division-ASCE, 102(4), 701-717.
- Nethercot, D. A., and Trahair, N. S. (1983). *Design of Laterally Unsupported Beams. Beams and Beam Columns: Stability and Strength*, Applied Science Publishers, London, 71-94.
- Nishino, F., Tall, L., and Okumura, T. (1968). *Residual Stress and Torsional Buckling Strength of H and Cruciform Columns*. Jap. Soc. Civil Engrs. Trans, 160, 75-87.
- Noordhoek, C., Verheul, A., Foeken, R. J., Bolt, H. M., and Wicks, P. J. (1996). *Static Strength of High Strength Steel Tubular Joints*. ECSC agreement number 7210-MC, 602.
- Nozaka, K., Masuda, T., Suzuki, M., and Ito, M. (2005). *Experimental Study on Inelastic Rotation Capacity of Hybrid I-Girders with High Strength Steel HT690*. Paper presented at the NASCC 2004.
- O'Eachteirn, P., and Nethercot, D. A. (1988). *Lateral Buckling Tests on Monosymmetric Plate Girders*. Journal of Constructional Steel Research, 11(4), 241-259.
- Park, J. S., Stallings, J. M., and Kang, Y. J. (2004). *Lateral-Torsional Buckling of Prismatic Beams with Continuous Top-Flange Bracing*. Journal of Constructional Steel Research, 60(2), 147-160.
- Pi, Y. L., and Trahair, N. S. (1997). *Lateral-Distortional Buckling of Hollow Flange Beams*. Journal of Structural Engineering-ASCE, 123(6), 695-702.
- Ramberg, W, and Osgood, R. (1943). *Description of Stress-Strain Curves by Three*

References

- Parameters*. Technical Note 902, NACA, Washington, D.C.
- Schilling, C. G. (1968). *Design of Hybrid Steel Beams*. Journal of the Structural Division, 94(6), 1397-1426.
- Suzuki, T., and Iwamoto, I. (2001). *Lateral Buckling and Flexural Torsional Behavior of Z-Section Beams*. Journal of Structural and Construction Engineering(Japan), 540, 127-131.
- Timoshenko, S. P., and Gere, J. M. (2012). *Theory of Elastic Stability*. Dover Publications.
- Timoshenko, S. P., Woinowsky-Krieger, S., and Woinowsky, S. (1959). *Theory of Plates and Shells (Vol. 2)*. McGraw-hill, New York.
- Trahair, N. S. (1969a). *Deformations of geometrically imperfect beams*. Journal of the Structural Division, 95(7), 1475-1496.
- Trahair, N. S. (1986). *Design Strengths of Steel Beam Columns*. Canadian Journal of Civil Engineering, 13(6), 639-646.
- Trahair, N. S. (1996). *Laterally Unsupported Beams*. Engineering structures, 18(10), 759-768.
- Trahair, N. S., and Kitipornchai, S. (1972). *Buckling of Inelastic I-beams under Uniform Moment*. Journal of the Structural Division, 98(11), 2551-2566.
- Wakabayashi, M., and Nakamura, T. (1983). *Buckling of Laterally Braced Beams*. Engineering structures, 5(2), 108-118.
- Webster, S., and Bannister, A. (2000). *Structural Integrity Assessment Procedure for Europe in the SINTAP Programme Overview*. Engineering Fracture Mechanics, 67(6), 481-514.
- White, D. W. (1960). *Inelastic Lateral Instability of Beams and Their Bracing*

Requirements. Ph. D. Thesis, Lehigh University, Bethlehem, Pennsylvania.

White, D. W. (2008). *Unified Flexural Resistance Equations for Stability Design of Steel I-Section Members: Overview*. Journal of Structural Engineering-ASCE, 134(9), 1405-1424.

White, D. W., and Jung, S. K. (2008). *Unified Flexural Resistance Equations for Stability Design of Steel I-Section Members: Uniform Bending Tests*. Journal of Structural Engineering-ASCE, 134(9), 1450-1470.

White, D. W., and Kim, Y. D. (2008). *Unified Flexural Resistance Equations for Stability Design of Steel I-Section Members: Moment Gradient Tests*. Journal of Structural Engineering-ASCE, 134(9), 1471-1486.

Yoshida, H., and Imoto, Y. (1973). *Inelastic Lateral Buckling of Restrained Beams*. Journal of the Engineering Mechanics Division, 99(2), 343-366.

Yura, J. A., Ravindra, M. K., and Galambos, T. V. (1978). *The Bending Resistance of Steel Beams*. Journal of the Structural Division, 104(9), 1355-1370.

Keywords

Accelerated cooling (ACC)
Acicular ferrite microstructure
Analytical LTB model
Available rotation capacity

Bifurcation point

Carbon equivalent value (CEV)
Charpy-V notch (impact) energy
Compact section
Critical buckling strength
Critical curvature
Critical metal parameter (PCM)
Curvature diagram

Decoupling
Doubly-symmetric I-section
Ductile-brittle transition temperature (DBTT)

Effective flexural rigidity
Effective rigidities
Effective torsional rigidity
Effective warping rigidity
Elongation at fracture (EF)
Elongation at onset of strain hardening (EST)
Elongation at tensile strength (ET)
End rotation
Experimental specimens

Finite element method (F.E.M)

Galerkin method
Governing equation of elastic FLB
Governing equation of elastic LTB
Governing equation of inelastic FLB
Governing equation of inelastic LTB
Granville weldability diagram

Haaiker's stress-strain model
Height-to-width ratio
High strength steel (HSS)

Homogeneous I-shaped member
Hot-rolled I-section member
HSA800
Hybrid I-shaped member

Ideal I-section without residual stresses
Inelastic buckling strength
Inelastic instability
Inelastic participation length
Inelastic section stiffnesses
Initial strain hardening modulus (EST)
In-plane behavior
In-plane (=maximum) rotation capacity
I-section with residual stresses
I-shaped member

Lateral deflection
Lateral slenderness
Lateral torsional buckling (LTB)
Local buckling
LTB strength curve
LTB under moment gradient
LTB under uniform moment

Material property
Member stability requirement
Microstructure
Mild steel
Moment gradient loading
Moment-rotation relationship
Mono-symmetric section

Neutral axis (N.A)
Normalizing

Out-of-plane behavior

Parametric model
Pearson correlations coefficient
Piecewise-linear model
Plastic moment
Post-buckling strength
Post-yield curvature
Post-yield range properties

Quenching & Tempering	Uniform moment loading
	Upper Y/T strength ratio limit
	Upper yield strength limit
Ramberg-Osgood stress-strain model	
Reduced modulus	Welded I-section member
Residual stress	Width-to-thickness ratio
Residual stress magnitude	
Residual stress pattern model	Yield curvature
Residual stress patterns	Yield moment
Rotation capacity	Yield plateau
Rotation capacity at bifurcation point	Yield plateau length (YP length)
Rotation capacity at maximum load	Yield strength (YS)
Rotation capacity at nominal strength	Yield-to-tensile strength ratio (Y/T strength ratio)
Rotation capacity curve	
Shear center (S.C)	
Simply-supported beam	
Slenderness ratio	
Slenderness (ratio) limit	
Slip theory	
SM490	
SM570	
Strain hardening parameter (n)	
Strain-hardening magnitude	
Strain-hardening rate ($E_{st}(\epsilon)$)	
Strain-jump	
Stress-strain characteristics	
Stress-strain model	
Tangent modulus	
Tangent modulus theory	
Target rotation capacity	
Tensile coupon test	
Tensile strength (TS)	
Tensile-to-yield strain ratio (T/Y strain ratio)	
Thermo-mechanical rolling (TMR)	
TMC process (TMCP)	
Traditional material model	
Tri-linear stress-strain model	
Unbraced length	
Unbraced length limit for plastic moment	
Unbraced length limit for target rotation capacity	

초 록

본 연구는 인장강도 800MPa급(HSA800) 고강도 빌트업 H형강의 비탄성 거동에 대한 연구이다. HSA800은 열가공제어법을 통해 높은 강도와 인성을 발현하면서도 상대적으로 낮은 탄소당량을 유지하는 고성능강재의 일종으로, 적절한 설계 및 제작법이 뒷받침된다면 건설시장에서 활용성이 높은 신재료로서 최근들어 학계 및 산업계의 상당한 주목을 받고 있다. 그러나, 현행기준에서는 (AISC 2010, EC 3 및 KBC 2009) 항복이후 일반강재와 다른 응력-변형률 특성을 갖는 고강도 강재의 사용이 구조적 거동에 미치는 영향에 대한 연구가 부족함에 따라 항복강도제한, 항복비제한, 회전능력 제한 등의 여러 제약조건을 도입하여 고강재의 사용을 직·간접적으로 제한하고 있다. 따라서 본 연구는 일반강재와 응력-변형률 특성이 다른 고강도 H형강 강재의 구조적 거동을 분석하고, 고강도 H형강이 소정의 횡비틀림좌굴강도 및 회전능력을 발현할 수 있는 방안을 제시함으로써 현행 기준식의 연장 적용 시 적절성을 평가하고, 고강도 강재의 활용성을 높이기 위해 수행된 연구이다.

본 논문의 구성은 크게 4가지로 이루어져 있다. 응력-변형률 모델 제안, 면내최대회전능력분석, 비탄성 횡비틀림좌굴거동의 해석적 연구, 그리고 비탄성 횡비틀림좌굴거동의 실험적 연구이다.

먼저, 응력-변형률 모델의 제안에서는 HSA800, SM570 및 SM490 강재의 인장시편데이터 값을 바탕으로 강도의 변화에 따라 항복비 (F_y/F_u)와 인장변형률비 (ϵ_u/ϵ_y)를 예측하는 회귀분석식을 바탕으로 일반강재 및 고강도 강재를 이상화할 수 있는 네 가지 재료모델을 제안하였다. 일반강재의 경우 전통적 삼선형 응력-변형률 모델(#1) 및 Haaijer가 제안한 응력-변형률 모델(#2)을 통해 실제 응력-변형률 곡선을 적절히 이상화 할 수 있는 것으로 판단되었다. 고강도강재의

경우 Ramberg-Osgood이 제안한 응력-변형률 모델(#3)을 이용할 경우 실제 응력-변형률 곡선을 적절히 이상화 할 수 있는 것으로 판단되었다. 추가적으로, 다중선형 응력-변형률 모델(#4)은 적절한 포인트를 가정하여 다양한 비선형적인 응력-변형률 곡선을 쉽게 표현할 수 있으므로 일반강도 및 고강도 강재에 범용적으로 적용할 수 있는 것으로 판단되었다.

두 번째, 면내최대회전능력예측에서는 등분포모멘트 및 모멘트구배 시에 HSA800, SM570 및 SM490강재로 제작된 H형강의 최대회전능력을 다중선형 응력-변형률 모델 (#4)을 바탕으로 예측하는 방법을 제안하였다. 이를 통해, 등분포모멘트시 면내최대회전능력(R_m)은 다른 요소의 영향과 무관하게 단순히 인장변형률비에 비례한 것으로 나타났다. 하지만, 모멘트구배시 면내최대회전능력은 항복비, 인장변형률비 및 항복참길이 세 가지 변수에 영향을 받는 것으로 나타났으며, 항복비가 높고 인장변형률비가 낮은 HSA800 H형강 부재는 SM570 및 SM490 강종에 비해 모멘트구배 시 면내최대회전능력이 낮을 수 밖에 없는 것으로 나타났다. 추가적으로 HSA800강종의 항복비와 인장변형률비의 독립적인 변화가 면내최대회전능력에 미치는 영향을 분석한 결과 HSA800강종의 면내최대회전능력의 증가를 위해서는 항복비를 낮추는 것보다 인장변형률비를 늘리는 것이 더욱 효과적인것으로 판단되었다.

세 번째, 비탄성 횡비틀림좌굴거동의 해석적 연구에서는 일반강재 및 고강도강재로 이루어진 H형강 단면이 항복이후 지니는 비탄성단면강성을 접선계수이론을 적용하여 정량화하는 방법을 제안하였다. 여기서 유도된 비탄성단면강성 데이터를 바탕으로 일반강도 및 고강도강재의 횡비틀림좌굴강도곡선 및 회전능력곡선 개발하고, 대표적인 선행연구 실험결과와 비교함으로써 본 접근방법의 타당성을 입증하였다. 마지막으로 다양한 고강도 H형강 단면의 좌굴강도 및 회전능력을 분석하는 변수해석 연구를 수행하여 고강도강재를 적용

하더라도 현행코드가 염두하는 소정의 강도 및 회전능력을 만족시키는 단면을 선정하는 방법을 제안하였다.

네 번째로 비탄성 횡비틀림좌굴의 해석적 연구에서는 동종(타입 A, B) 및 이종강재(타입 C)로 구성된 세 가지 빌트업 실험체(타입 A-[H-250x150x15x15]-[$F_y=775\text{MPa}$], 타입 B-[H-400x150x15x15]-[$F_y=775\text{MPa}$], 타입 C-[H-350x150x30x25]-[$F_{yw}=349\text{MPa}$, $F_{yf}=822\text{MPa}$])를 제작하고, 등분포모멘트 조건에서 실험을 수행하여 기학적 변수와 재료적 변수가 비탄성횡좌굴에 미치는 영향을 실험적으로 분석하였다. 모든 실험체는 사인형태의 좌굴모드를 유발하며 횡비틀림좌굴에 의해 파괴되었다. 실험결과, 소성강도에 비해 비탄성단면강성에 상대적으로 큰 타입 A 및 타입 C 실험체는 현행 기준식을 연장적용하여도 소정의 강도 및 연성능력을 만족시키는 결과를 보여주었다. 반면, 소성강도에 비해 비탄성단면강성이 상대적으로 작고, 춤-폭비가 높은 타입 B 실험체는 현행의 기준식이 연장적용될 경우 소정의 연성능력을 발현하는데 안전측이 아닐 수 있음이 나타났으며, 연성능력을 만족시키기 위해서는 단면의 재선정 혹은 더욱 촘촘한 횡지지거 요구되었다. 마지막으로 해석적 연구에서 유도된 좌굴강도 및 회전능력 값과 실험에서 측정된 임계좌굴강도 및 임계회전능력을 비교한 결과, 본 연구에서 제시하는 고강도 H형강 좌굴강도 및 회전능력곡선은 측정된 실험결과를 충분히 잘 예측하는 것으로 판단되었다.

주요어 : 고강도강재; 다중선형 응력-변형률 모델; 면내최대회전능력; 비탄성단면강성; 열가공제어법; 인장변형률비; 일반강재; 전통적 삼선형 응력-변형률 모델; 탄소당량; 항복비; 항복참길이; 회전능력; 횡비틀림좌굴강도; 횡세장비; 횡지지거리; H형강부재; Haaijer 응력-변형률 모델; Ramberg-Osgood 응력-변형률 모델;

학 번 : 2010-30165